Ed Spitzer

REPORT NO. FAA-RD-77-68

PROCEEDINGS
OF THE
AIRCRAFT WAKE VORTICES CONFERENCE

March 15-17, 1977

J. N. Hallock, Editor

June 1977

DOCUMENT IS AVAILABLE TO THE U.S. PUBLIC
THROUGH THE NATIONAL TECHNICAL
INFORMATION SERVICE, SPRINGFIELD,
VIRGINIA 22161

DEPARTMENT OF TRANSPORTATION ★ UNITED STATES OF AMERICA ★

HELD AT THE TRANSPORTATION SYSTEMS CENTER, KENDALL SQUARE, CAMBRIDGE MA 02142

NOTICE

NOTICE

TECHNICAL REPORT DOCUMENTATION PAGE

1. Report No.
FAA-RD-77-68

2. Government Accession No.

3. Recipient's Catalog No.

4. Title and Subtitle
PROCEEDINGS OF THE AIRCRAFT WAKE VORTICES CONFERENCE

5. Report Date
June 1977

6. Performing Organization Code

7. Author(s)
J. N. Hallock, Editor

8. Performing Organization Report No.
DOT-TSC-FAA-77-12

9. Performing Organization Name and Address
U.S. Department of Transportation
Transportation Systems Center
Kendall Square
Cambridge MA 02142

10. Work Unit No.
FA705/R8106

11. Contract or Grant No.

12. Sponsoring Agency Name and Address
U.S. Department of Transportation
Federal Aviation Administration
Systems Research and Development Service
Washington DC 20591

13. Type of Report and Period Covered
Conference Proceedings
March 15-17, 1977

14. Sponsoring Agency Code

15. Supplementary Notes

16. Abstract

This volume contains the proceedings of a conference on aircraft wake vortices held at the DOT Transportation Systems Center on March 15-17, 1977. The contributed papers discuss technological advances in the knowledge of the phenomenon, its effects on aircraft, alleviation techniques, and vortex avoidance systems designed to permit decreases in delays at major airports.

17. Key Words
Aircraft Wake Vortices
Vortices
Alleviation
Vortex Hazard
Sensors
Wake Behavior

18. Distribution Statement
DOCUMENT IS AVAILABLE TO THE U.S. PUBLIC THROUGH THE NATIONAL TECHNICAL INFORMATION SERVICE, SPRINGFIELD, VIRGINIA 22161

19. Security Classif. (of this report)
Unclassified

20. Security Classif. (of this page)
Unclassified

21. No. of Pages
352

22. Price

FOREWORD

This international conference on aircraft wake vortices was sponsored by the Transportation Systems Center and supported by the Federal Aviation Administration, U.S. Department of Transportation.

Twenty-nine papers were presented in five sessions. The titles of the sessions and the respective session chairmen were:

Session I:	The Wake Vortex Hazard; James Andersen, Director, Office of Air and Marine Systems, Transportation Systems Center
Session II:	Vortex Sensors and Data; Robert Wedan, Deputy Director, Systems Research and Development Service, Federal Aviation Administration
Session III:	Vortex Structure; Alfred Gessow, Chief, Fluid and Flight Dynamics Branch, NASA Headquarters
Session IV:	Vortex Alleviation; Joseph Tymczyszyn, Special Projects and Advanced Planning, FAA Western Region
Session V:	Vortex Behavior and the VAS; James Hallock, Traffic and Operations Branch, Transportation Systems Center.

I wish to express my appreciation to my fellow session chairmen for helping to give some semblance of order to a diversity of papers.

James N. Hallock
Conference Chairman

METRIC CONVERSION FACTORS

Approximate Conversions to Metric Measures

Symbol	When You Know	Multiply by	To Find	Symbol
		LENGTH		
in	inches	2.5	centimeters	cm
ft	feet	30	centimeters	cm
yd	yards	0.9	meters	m
mi	miles	1.6	kilometers	km
		AREA		
in^2	square inches	6.5	square centimeters	cm^2
ft^2	square feet	0.09	square meters	m^2
yd^2	square yards	0.8	square meters	m^2
mi^2	square miles	2.6	square kilometers	km^2
	acres	0.4	hectares	ha
		MASS (weight)		
oz	ounces	28	grams	g
lb	pounds	0.45	kilograms	kg
	short tons (2000 lb)	0.9	tonnes	t
		VOLUME		
tsp	teaspoons	5	milliliters	ml
Tbsp	tablespoons	15	milliliters	ml
fl oz	fluid ounces	30	milliliters	ml
c	cups	0.24	liters	l
pt	pints	0.47	liters	l
qt	quarts	0.95	liters	l
gal	gallons	3.8	liters	l
ft^3	cubic feet	0.03	cubic meters	m^3
yd^3	cubic yards	0.76	cubic meters	m^3
		TEMPERATURE (exact)		
°F	Fahrenheit temperature	5/9 (after subtracting 32)	Celsius temperature	°C

Approximate Conversions from Metric Measures

Symbol	When You Know	Multiply by	To Find	Symbol
		LENGTH		
mm	millimeters	0.04	inches	in
cm	centimeters	0.4	inches	in
m	meters	3.3	feet	ft
m	meters	1.1	yards	yd
km	kilometers	0.6	miles	mi
		AREA		
cm^2	square centimeters	0.16	square inches	in^2
m^2	square meters	1.2	square yards	yd^2
km^2	square kilometers	0.4	square miles	mi^2
ha	hectares (10,000 m^2)	2.5	acres	
		MASS (weight)		
g	grams	0.035	ounces	oz
kg	kilograms	2.2	pounds	lb
t	tonnes (1000 kg)	1.1	short tons	
		VOLUME		
ml	milliliters	0.03	fluid ounces	fl oz
l	liters	2.1	pints	pt
l	liters	1.06	quarts	qt
l	liters	0.26	gallons	gal
m^3	cubic meters	35	cubic feet	ft^3
m^3	cubic meters	1.3	cubic yards	yd^3
		TEMPERATURE (exact)		
°C	Celsius temperature	9/5 (then add 32)	Fahrenheit temperature	°F

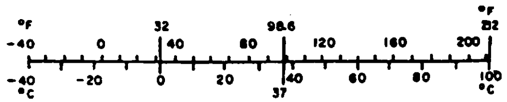

PROCEEDINGS
OF THE AIRCRAFT WAKE VORTICES CONFERENCE

CAMBRIDGE MA **MARCH 1977**

CONTENTS

WELCOME

JAMES P. ANDERSEN
Acting Director of Air and Marine Systems
U.S. Department of Transportation
Transportation Systems Center
Cambridge MA 02142

On behalf of Dr. Costantino and the staff, I would like to welcome you to Cambridge, to the Transportation Systems Center, and to this Conference on Aircraft Wake Vortices. Dr. Costantino could not be here today as he is in Washington appearing before a Congressional subcommittee on programs of DOT and TSC.

This three-day meeting is sponsored by TSC and supported by the Federal Aviation Administration. It is designed to bring together in one place transportation and aeronautical specialists from other countries, our own government, the aircraft industry, and universities to discuss the progress being made in analyzing wake vortices and the experimental systems and alleviation devices developed to cope with the vortex problem. We are most pleased with the outstanding papers that you will be hearing during the next three days.

The Transportation Systems Center itself has been analyzing the wake vortex phenomenon for some years and has collected a large amount of data on vortex behavior. This work, guided by Bill Wood, Head of our Traffic and Operations Branch, has culminated in the Vortex Advisory System now being tested at Chicago's O'Hare Airport. A paper will be presented on this system on Thursday.

To give you a broad overview of our role here in Cambridge, this Center is DOT's major research and development facility for air, highway, rail, and marine transportation. We carry out, with a 60-million dollar annual budget and staff of about 650 people, major parts of the R&D programs for the Office of the Secretary of Transportation and for all major administrations within DOT, including Federal Aviation, Federal Railroad, National Highway Traffic Safety, Urban Mass Transportation, Federal Highway, the Office of Deepwater Ports, Saint Lawrence Seaway Development Corporation, and the Coast Guard. We provide DOT, state and local governments, and private industry with key transportation statistical information and engineering, economic, and environmental planning information. We are involved with problems of urban, intercity, rural and national passenger and freight transport, and provide analytical support to the entire Department with a skilled professional staff of engineers, community planners, economists, mathematicians, lawyers, sociologists, and computer specialists.

We are engaged in a unique diversity of projects. They include vehicle research on fuel use, emissions, noise, testing of rubber tires; bus scheduling and routing; public transportation needs for the elderly and handicapped; subway station design and construction; studies of rail passenger service between Boston and New York and Washington — the so-called Northeast Corridor; railroad safety research to detect flaws in tracks and rail equipment; antihijack-sensing devices to detect explosives and weapons; air traffic control in the air and on the ground; evaluations of energy use and its economic implications; and the forecasting of transportation systems needs. We also work on very specific problems, like answering the questions "why are the new GE SPD-40 locomotives derailing?", and "what is the true noise and vibration effect of the Concorde SST flying into the U.S.A.?"

These are just some of the 120 on-going projects that the Transportation Systems Center has in progress.

In summation, we are here to integrate transportation technology through state-of-the-art research and development, always taking into consideration the social and economic ramifications of our work. The results of our work lead directly to national decisions and policy implemented by both the

Secretary of our Department and the President.

Our extensive agenda for this conference reflects, I believe, the state-of-the-art research and analytical developments on wake vortices. It includes some 30 presentations divided into five major sections.

Our Opening Remarks Speaker today is someone well known to you and to us at TSC, Mr. Robert W. Wedan, Deputy Director of the Systems Research and Development Service of the Federal Aviation Administration. Prior to his work for the FAA, Bob Wedan was Director of Transportation Systems Development here at TSC. Bob has held high-level management positions also with the NASA Electronics Research Center in Cambridge, and before that, worked for Honeywell in Minnesota and St. Petersburg. He received his Bachelor's and Masters' Degrees from MIT. Bob is the owner of a Beech Bonanza and is a very expert IFR pilot, both single and twin. It's my pleasure to welcome back to TSC and Cambridge and introduce to you Bob Wedan.

OPENING REMARKS

ROBERT W. WEDAN
Deputy Director, Systems Research and Development Service
Federal Aviation Administration
Washington DC

The growth of aviation is progressing at a rapid rate, and current projections indicate that aviation activity will continue to rise over the next decade. For example, the number of passengers carried by scheduled U.S. carriers is expected to increase from the 212 million carried in 1976 to 388 million in 1986. That represents about an 83 percent increase in activity. General aviation activity is also projected to have a similar vigorous growth, with general aviation intercity carriage growing from 156 million in 1976 to an estimated 233 million in 1986, and that represents about a 50 percent expected increase over the decade. These numbers, by the way, were put together by the aviation-forecasting group in Washington.

These increases establish a great demand for airport facilities to accommodate the traffic flow not only safely but also efficiently. This in turn dictates that every possible effort be expended to develop automatic capabilities to aid the human or manual activities or capabilities in the National Airspace System to achieve optimum use of these existing facilities. The system planned for use in the 1980's to about the end of the century is known as the Upgraded Third Generation Air Traffic Control System. This is the system whose component parts are under development by the FAA at this time. It is intended and designed to meet the goals of maintaining or improving safety, of constraining or reducing costs of operating the system, of increasing or improving performance and, finally, to meet energy conservation and environmental needs. One of the major features of this Upgraded Third Generation System deals with the subject of this conference — Aircraft Wake Vortices. The vortex problem must be dealt with before the potential benefits of the Upgraded Third System can be realized.

The most critical element of the National Airspace System is the airport, and the airport is capacity-limited. Present and predicted demands being placed on airports cannot be met by indiscriminate construction of new runways and airports in the present economic and social environment. To make matters more difficult, in recent years runway capacity has actually declined at the Nation's airports. Noise restrictions and wake vortex separation standards have resulted in significant increases in delays and delay-related fuel consumption. A number that was given to me before I came here was that we are experiencing a reduction in capacity at O'Hare due to increasing the separation standards of the order of 4 to 8 percent. This may not sound like a lot; but when you convert this to delay, delay is increased 8 to 10 percent. That gives you some sort of a feel for the magnitude of the problem as it exists at O'Hare; please don't extend that in your own thinking to all airports; but at that one airport, this is what we're seeing now with the present separation standards.

Now in spite of this, over the next few years, the FAA has accepted as a broad development objective the need to double airport and airway systems in the decade ending in 1980. It appears that airports can achieve a twofold increase in capacity with such improvements as dual-lane runways, the microwave instrument-landing system, an improved beacon system, the automation of the terminal radar vector service, a reduced separation to 2500 feet between independent parallel IFR runways, and reduced longitudinal separation of aircraft on final approach. The operational capacity of the limited number of runway options that exist must be increased if airports are to meet the increase of traffic in the next few years. Today, there exists the technology to develop the landing aids which will substantially increase runway capacity; that is, by employing these planned techniques of the Upgraded Third System, but until the wake vortex problem has been alleviated, these improvements cannot be used to their full potential.

The vortex problem has been recognized for a long time — the Wright brothers are known to have studied vortices in their wind tunnel. Of course, it is well known that the wake vortex is a phenomenon that is a direct result or a direct consequence of the generation of lift. But it was the introduction of the wide-bodied jets with their increased weight and hence stronger vortices which rekindled our interest in the phenomenon.

Vortex strength measurements made by the Transportation Systems Center for the FAA led to the revised separation standards which were promulgated in November 1975 for lighter aircraft following heavier aircraft. History and measurements have shown that the present separation standards are safe. However, the time has come to examine these standards to determine if we have been in some circumstances and under some conditions excessively conservative. The overall objective of the aircraft wake vortex program is the increasing of capacity at the major high-density air terminals. Thus, the problem is gaining capacity without sacrificing the present level of safety.

There are two major approaches to the solution of the problem of minimization or elimination of the impediment on air traffic flow caused by aircraft vortices. One approach is the use of various techniques to break up or appropriately to alter the characteristics of the vortices to decrease the hazard caused by them. The FAA has recognized, of course, the expertise that exists within NASA and has supported the Office of Aeronautics and Space Technology in their efforts to accelerate vortex decay or dissipation at the source; that is, by the aircraft itself or modifications to the aircraft. The second approach is the development of a wake vortex avoidance system; that is, to detect the presence and to prevent following aircraft from entering into the vortex caused by the leading aircraft. In concept, this system will insure that the aircraft will avoid an inadvertent encounter with a hazardous vortex by tailoring interarrival aircraft spacings commensurate with the vortex hazard. With the assistance of the Transportation Systems Center, the FAA has pursued the latter approach. A first-generation wake vortex avoidance system has been deployed at the Chicago O'Hare International Airport for demonstration and testing. This system, known as the Vortex Advisory System, uses a measurement of the ambient winds in the approach corridors to decide when it is safe to decrease aircraft separations to a uniform three nautical miles.

The Chicago O'Hare Delay Task Force Study has pointed out that O'Hare annually processes about 9 percent of the United States air passengers and that the airport is experiencing significant annual delay-related costs: over 44-million dollars to aircraft operators, 67-million gallons of fuel, and over 4½-million hours of passenger delays (that is, approximately 525 years of passenger delay). The task force also foresaw that a wake vortex avoidance system as well as upgrading the air traffic control automation in the form of automated metering-and-spacing can have a major favorable impact on O'Hare's capacity and delay.

Now we come to the specifics of this conference. The conference was convened because the FAA felt that the time was right to share insights on the wake vortex work that has been underway these past few years. The first symposium on the subject was held in September 1970. This was sponsored by the Air Force Office of Scientific Research and the Boeing Company. In the summer of 1971, the FAA sponsored a conference on turbulence, both clear air turbulence and wake turbulence, in Washington DC. In July 1974, the Air Force conducted a two-day workshop on the phenomenon at Wright-Patterson Air Force Base. NASA conducted a review of the minimization concepts in February 1976 in Washington DC. Over two and a half years have passed since the last get-together of the entire wake vortex technical community, so for this reason we felt it's time we should meet again.

The first session we'll hear today deals with the wake vortex hazard. Everyone has an intuitive feeling for the seriousness of an inadvertent vortex encounter, but it is important to quantify these feelings. What is the problem? How often does it occur? Are there specific aircraft which are involved more often than others? How does the phase of flight affect pilot response? What is the extent of the hazard? These are the kinds of questions that will be addressed in this first session.

The second session is about vortex sensors and data collection. It would seem that a swirling mass of air would lend itself to simple measurement techniques. However, the elusive vortex requires specialized detection devices and data-processing methods. Numerous schemes have been devised and many tested. Practically the entire electromagnetic spectrum and various mechanical techniques have been examined for their applicability to the remote sensing of vortices. As the sensors and sensing techniques become available, the data on vortex behavior expanded. The laser-Doppler velocimeter has become an important research instrument in the study of wake vortices as each of the papers in session two will reference. Most of the data, however, has been collected using less sophisticated sensors.

Vortex structure is the subject of the next session. The status of some computational methods will be discussed as well as results applicable for the near term in the near wake. The importance of modeling is acknowledged, particularly when theory agrees with experiment. Perhaps we are really beginning to comprehend fully the phenomenon of wake vortices from their birth all the way through to their death or demise. Knowing how vortices form can also be used to good advantage in the design of future aircraft. In an operational system, to make the system available at the largest number of airports, it is important that we find low-cost techniques; you will be hearing in this session about indirect methods of obtaining the same information that one would obtain by direct measurement and, of course, hopefully at a considerable reduction in cost.

Alleviation techniques will be discussed after that. Various devices have been tested in wind tunnels, water channels and flights using full-scale aircraft. Splines, mass injections, wing modifications, differential flap settings, spoiler deployment, and so on have been considered. The fourth session will examine some of these techniques as well as how the alleviation systems affect the vortex-generating aircraft. Flight test investigations of the alleviation schemes will be discussed.

The final session is on vortex behavior and the Vortex Advisory System. The atmosphere has a profound effect on how vortices move and die. The papers will point out the effects of meteorology on vortex behavior and describe how this knowledge was used to develop the first wake vortex avoidance system now being tested at Chicago's O'Hare International Airport.

I now add my welcome to all of you to the conference. The problem is a real one, and the need for the solution to this problem is of paramount importance, so let us share our thoughts on the subject in the best interests of the aviation community.

COLLECTION OF OPERATIONAL DATA ON WAKE VORTEX INCIDENTS IN THE UK

OLIVER B. ST. JOHN
Civil Aviation Authority
London, England

ABSTRACT: Data relating to pilots' reports of a total of over 300 incidents have been collated and analyzed covering a 5-year period.

INTRODUCTION

The Civil Aviation Authority (CAA) wake vortex incident reporting scheme was formally initiated in July 1972; reports had previously been collected on an informal basis and reasonably complete information is available on incidents occurring from January 1972 onwards. Pilots who believe their aircraft to have encountered a wake vortex are asked to complete a detailed questionnaire. Whenever possible, the reports are supplemented by spacing data supplied by the air traffic controllers and by meteorological data; this extra information is received as a matter of course when incidents are reported in the neighbourhood of London Heathrow airport. In some cases it has been possible to examine flight data recordings from aircraft involved in reported incidents. No accidents attributable to wake vortices occurred.

This paper presents some of the data collected during the five-year period 1972-1976, concentrating on the reported incidents occurring on the approach to London Heathrow airport, which account for about 70% of the 316 reports received. Particular attention is paid to the altitude at which the incidents occurred, the reported wind conditions at the time of occurrence, and the effect of the change in separation standards introduced in March 1974.

CLASSIFICATION OF REPORTED INCIDENTS

Between January 1972 and December 1976, a total of 316 reports were received, excluding those which, on further investigation, did not appear to have been caused by wake vortices or where insufficient data was available for analysis.

Classification by Phase of Flight.

Table 1 shows the total numbers of incidents reported during the period, classified according to the phase of flight of the two aircraft involved; cases where the aircraft generating the wake (the 'leader') was in a different phase of flight from the aircraft encountering it (the 'follower') are classified as 'other'. About 70% of the reported incidents have occurred to aircraft approaching London Heathrow airport, and these incidents have been subdivided into those occurring at or below 3000 ft ("final approach") and those occurring above 3000 ft ("intermediate approach").

Table 1. Summary of Reported Incidents

	1972	1973	1974	1975	1976	Total
Intermediate approach at Heathrow	4	6	3	9	11	33
Final approach at Heathrow	40	49	18	27	59	193
Approach elsewhere	4	3	3	3	4	17
Take-off	5	8	2	4	19	38
En route	3	5	1	5	6	20
Other	3	3	2	3	4	15
TOTAL	59	74	29	51	103	316

Classification by Severity of Disturbance.

The characteristic effect on an aircraft encountering a vortex wake is a sudden upset about the roll axis. The severity of the disturbance is measured by the reported magnitude of this upset, on the assumption that the pilot is taking corrective action. When a large disturbance is reported, the flight data recording (if available) is consulted to establish the precise nature and magnitude of the upset. In general, the flight data recording shows a roll angle somewhat less than was estimated by the pilot, though in one en-route case a roll reported by the pilot as 40°-60° was found to have been 69°.

Reported incidents are divided into three classes as shown in Table 2, according to the angle of bank reported by the pilot. The actual hazard involved in any incident depends on several factors, particularly on the altitude at which the encounter occurs.

Table 2. Classification of Incident Severity

Class	Reported Roll Excursion
A Severe	30° or more
B Moderate	Between 10° and 30°
C Slight	Less than 10°

Table 3 shows the numbers of incidents reported in each class.

Table 3. Reported Incidents Classified by Severity

	All Incidents			
	A	B	C	Total
1972	14	24	21	59
1973	14	30	30	74
1974	7	13	9	29
1975	9	17	25	51
1976	15	39	49	103
TOTAL	59	123	134	316

Classification by Aircraft Weight.

The magnitude of the effect that the wake of one aircraft can have on another aircraft is a complex function of the aircrafts' relative weights, spans, etc., and of the controllability of the following aircraft. Initial experience, however, has shown that it is helpful to classify reported incidents according to the weights of the two aircraft involved. For this purpose, aircraft are grouped into broad categories according to their maximum certificated take-off weight as shown in Table 4.

Table 4. Aircraft Weight Groupings

	Maximum Certificated Take-off Weight	
	(kg)	(lb)
B747-group	Over 170,000	Over 375,000
B707-group	136,000 - 170,000	300,000 - 375,000
B720-group	100,000 - 136,000	220,000 - 300,000
Trident-group	40,000 - 100,000	88,000 - 220,000
Viscount-group	10,000 - 40,000	22,000 - 88,000
Learjet-group	7,000 - 10,000	15,000 - 22,000
GA-group	Below 7,000	Below 15,000

ANALYSIS OF INCIDENTS REPORTED ON APPROACH TO HEATHROW

Analysis by Severity and Altitude.

Table 5 gives the number of incidents in each class of severity reported on approach to Heathrow in the whole five-year period in various altitude bands, excluding 21 incidents for which the altitude of occurrence was not recorded.

Table 5. Heathrow Approach Incidents by Severity and Altitude

Altitude (ft)	Severity A	B	C	Total
0 - 200	5	34	21	60
201 - 500	1	3	3	7
501 - 1000	0	5	3	8
1001 - 2000	11	13	15	39
2001 - 3000	12	22	32	66
above 3000	7	10	8	25
TOTAL	36	87	82	205

Table 6 gives details of the six severe incidents which have occurred at altitudes below 1000 ft.

Analysis by Prevailing Wind Conditions.

Figure 1 shows the incidents reported at 1000 ft or below on approach to Heathrow, plotted against the headwind (or tailwind) and crosswind component recorded at the time of the incident by the Meteorological Office anemometer positioned about 220 metres south of the threshold of runway 10R. The Mk5 Munro anemometer measures the wind at 10 metres above ground level and the measurements are averaged over a 10-minute period. It should be observed that the wind

Table 6. Details of Severe Incidents Occurring Below 1000 ft

INCIDENT	AIRCRAFT		ROLL	HEIGHT	HEADWIND Component	CROSSWIND Component	SEPARATION	
No.	Leader	Follower	Degrees	Feet	Kts	Kts	nm	REMARKS
53	B747	Trident 1E	30	200	0	0	4	No natural turbulence — B747 had landed and turned off runway. Separation should have been 5 nm (1972).
86	B707	Viscount	30	100	2	4	3	B707 just cleared runway as Viscount was over approach lights when roll was experienced.
97	B747	Viscount	30	300	5	1	5	Viscount experienced very strong rolling moments in both directions from 300 ft to 100 ft agl.
126	B747	Viscount	—	300	0	0	6	B747 just cleared runway. Pilot was too busy to assess roll angle, but turbulence was so bad an overshoot was considered.
157	IL62	Viscount	45	70	1	3	4	IL62 just cleared runway. Sharp right wing drop required full corrective aileron. Turbulence ceased 20 ft agl.
225	VC10	HS125	30	200	-3	3	5	VC10 had cleared runway when HS125 encountered wake turbulence at 200 ft agl.

speeds recorded in this way are not always representative of the conditions at the point where the vortex encounter took place.

Also shown on Figure 1 is the "wind ellipse" derived by the US DOT Transportation Systems Center as a result of measurements at Heathrow and elsewhere. When the wind conditions, as measured by an anemometer 15 metres above ground level close to the threshold of the runway in use, and averaged over 1 minute, lie outside this ellipse, it has been observed that vortices of landing aircraft do not remain active for more than 80 seconds in a zone of unlimited height extending to a distance of 45 metres on each side of the extended runway centreline. Although it is of interest to relate reported incidents to this wind ellipse, the difference between the two types of wind measurement used must be kept in mind.

The figure shows that almost all incidents (70 out of 73 when the wind was recorded) occurred when the reported wind conditions lay inside or on the boundary of the ellipse. All severe incidents occurred in wind conditions well inside the ellipse. The three incidents which occurred in wind conditions outside the ellipse all occurred on approaches to the northern runway, and the two substantially outside the ellipse occurred at an altitude of 1000 ft. It is interesting to note that many incidents occur above 1000 ft

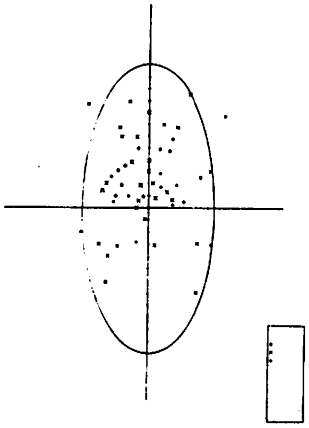

Figure 1. The winds for the incidents reported at 1000 feet or below on approach to Heathrow.

in wind conditions outside the ellipse; during the five year period a total of 51 such incidents, including 9 severe incidents, were reported on final approach to Heathrow.

Incidents where the Leading Aircraft was in the B747 or B707 Weight Group.

Out of the 226 reported incidents (37 severe) on the approach to Heathrow, 190 (29 severe) occurred behind aircraft in the B747 or B707 weight group. Tables 7 and 8 give the numbers of incidents reported behind aircraft in these groups, together with estimates of the annual numbers of landings of these aircraft types at Heathrow.

Analysis of the Relative Frequencies of Reported Incidents.

In March 1974, following analysis of the early results from this programme, the spacing given in the UK to aircraft in UK group 2 (10,000 - 170,000 kg) on approach behind UK group 1 (over 170,000 kg) was increased from 5 to 6 nautical miles. Thus it is interesting, in analysing the frequencies of reported incidents, to compare the periods January 1972 to March 1974 and April 1974 to December 1976.

Table 9 shows the number of severe incidents reported for selected leader-follower pairs in the two periods and also the frequencies of these incidents expressed as the number per 10^5 occasions on which each leader-follower pair occurred. The frequencies are expressed in this form to take account of the different and changing proportions of landings at Heathrow by the various aircraft types.

Table 7. Incidents Behind Aircraft Above 170,000 kg

Year	A	B	C	TOTAL	% all incidents	landings	% all landings
1972	2	8	8	18	41	7700	6
1973	5	10	7	22	40	9600	7
1974	1	5	2	8	38	9800	7
1975	1	6	9	16	44	13500	10
1976	3	8	20	31	44	16000	12

Table 8. Incidents Behind Aircraft Between 136,000 and 170,000 kg

Year	A	B	C	TOTAL	% all incidents	landings	% all landings
1972	4	9	7	20	45	26600	19
1973	1	12	8	21	38	25500	18
1974	3	3	2	8	38	24400	17
1975	2	3	7	12	33	23600	18
1976	7	15	12	34	48	21900	16

CONCLUSION

The analysis of over 300 reported wake vortex incidents received during a period of 5 years shows considerable fluctuations, as is to be expected from what is statistically a small sample, but also some consistent features. For example, although the total number of incidents reported annually has ranged from 29 in 1974 to 103 in 1976, the proportion occurring on approach to Heathrow has always been about 70%, and the proportion of these Heathrow approach incidents attributable to aircraft in the B747 weight group has remained close to 40% despite the increasing numbers of these aircraft in service. The frequency of severe incidents reported behind this group on approach to Heathrow dropped from 35 per 100,000 landings before April 1974, when the separation behind such aircraft was changed from 5 to 6

Table 9. Numbers and Relative Frequencies of Heathrow Approach Severe Incidents for Various Leader-Follower Combinations

Leader's group	Follower's group	Jan '72 - Mar '74 Total	Jan '72 - Mar '74 per 10^5 landings	Apr '74 - Dec '76 Total	Apr '74 - Dec '76 per 10^5 landings
B747	Trident	3	30	4	20
	Viscount	4	300	1	30
	All	7	35	5	15
B707	Trident	2	6	7	20
	Viscount	4	80	4	70
	All	6	10	11	15
All	All	18	5.6	19	4.9

miles, to 15 per 100,000 landings thereafter. Since the frequency of severe incidents reported behind other large aircraft (above 136,000 kg) rose slightly from 10 to 15 per 100,000 landings, the change in separation would appear to have been fully justified operationally as having led to a more consistent level of safety behind all large aircraft.

It is difficult to make a convincing estimate of the absolute level of safety being achieved. An attempt to do so was made in 1973 by a small group comprising representatives of NATS, Directorate of Flight Safety, Airworthiness Division and Chief Scientist's Division from CAA, and of RAE Bedford. This group examined all the severe incidents reported up to that time and came to the conclusion that the likelihood of an accident could be assumed to be of the order of 1/100 of that of a severe incident, this being regarded as a pessimistic assumption. On this basis, the figures given in Table 9 for frequencies of severe incidents per 100,000 landings would represent the number of occasions in 10^7 landings on which an accident might be expected. The generally accepted target level of safety is represented by a figure of one fatal accident in 10^7 flights; consequently some of the figures in these Tables could be seen as giving rise to a measure of concern.

Subsequent to March 1974, the highest frequency of severe incidents, 70 per 10^5 landings, has been experienced by aircraft in the Viscount weight group behind those in the B707 group (136,000 - 170,000 kg). The number of movements by Viscount group aircraft is comparatively small — less than 10% of all movements at Heathrow — and is declining as the Viscounts themselves retire from service and are only partially replaced by newer aircraft in the same weight group. In addition, only a proportion of the severe incidents occurred in the height band where the risk of an accident is thought to be significant. Thus the figures by themselves may not be a reliable guide to the importance of this problem.

Virtually all incidents below 1000 ft on approach to Heathrow take place in wind conditions lying inside the 'wind ellipse' shown in Figure 1. This implies that, when the wind conditions lie outside this ellipse, the separations applied currently are greater than is necessary to ensure adequate safety in this phase of flight. However, it must be noted that a substantial number of incidents, including some severe incidents, occur at altitudes between 1000 ft and 3000 ft in wind conditions outside the ellipse and a reduction in separations could be expected to increase the frequency and severity of such incidents.

ACKNOWLEDGMENT

The author would wish to acknowledge the help of B. A. M. Piggott and J. A. Pask, both of Chief Scientist's Division, CAA, who were responsible for both the data collection and analysis of results.

ESTIMATION OF VORTEX-INDUCED ROLL EXCURSIONS BASED ON FLIGHT AND SIMULATION RESULTS

BRUCE E. TINLING
NASA Ames Research Center
Moffett Field CA

ABSTRACT: The results of flight measurements at altitude were combined with an analytical procedure to estimate the wake vortex roll excursions for aircraft ranging in size from small business jets to jumbo jets. The roll excursion estimates were compared with a bank-angle boundary developed from piloted simulation. The estimates indicate that if the vortex from a jet transport of medium size or larger should be encountered out of ground effect at current separation distance standards, the resulting maximum bank angle exceeds the boundary for all following aircraft except the large heavy transports. The possible bank-angle excursion for small aircraft, even though their separation distances are greater, exceeds the boundary by a large amount. In view of this apparent hazard, it is reasoned that the current extremely low accident rate exists because the specified separation allows sufficient time for the vortices to be removed from the path of following aircraft by winds and by their mutual induction, and because the vortex strength is dissipated at low altitudes by ground effect.

NOMENCLATURE

$\overline{AR}$ = aspect ratio, b^2/S
b = wing span
C_1, C_2 = constants
g = gravitational acceleration
p = roll rate
$\dot{p}$ = roll acceleration
S = wing area
V = airspeed
$V_{\theta_{max}}$ = maximum vortex tangential velocity
W = aircraft weight
x = downstream distance
Γ_0 = large radius circulation
Δt = vortex encounter duration
ρ = air density
σ = radius of gyration
ϕ = bank angle.

Subscripts

f = following or encountering aircraft
g = vortex generating aircraft.

INTRODUCTION

A solution to the wake vortex problem that permits airport capacity to be increased with no reduction in safety is essential to the success of the upgraded third generation air traffic control system proposed for the 1980s [1]. Research is in progress on two different approaches to the solution of this problem. One is to develop a wake vortex avoidance system for the terminal airspace. Such a system is being developed by the DOT Transportation Systems Center. The other approach to the wake vortex problem, finding an aerodynamic means to reduce the hazard, has been the subject of a NASA research program for several years. A number of alleviation techniques were developed in the NASA ground-based research facilities, and several have shown sufficient promise to warrant evaluation in flight.

Within the last year, the research programs have provided sufficient information to estimate the maximum roll excursions that can be imposed on following aircraft by jet transports and to determine if such excursions are likely to represent a potential hazard during the final phases of the landing approach. This information can be used to evaluate the roll excursions under current separation standards in the event of a vortex encounter for a variety of aircraft pairs, to evaluate the roll excursions of aerodynamically alleviated configurations at reduced separations, and to estimate the level of aerodynamic alleviation required if an encounter is to be nonhazardous.

The procedure for estimating the roll excursions is outlined in Figure 1. The following are key elements of this procedure:

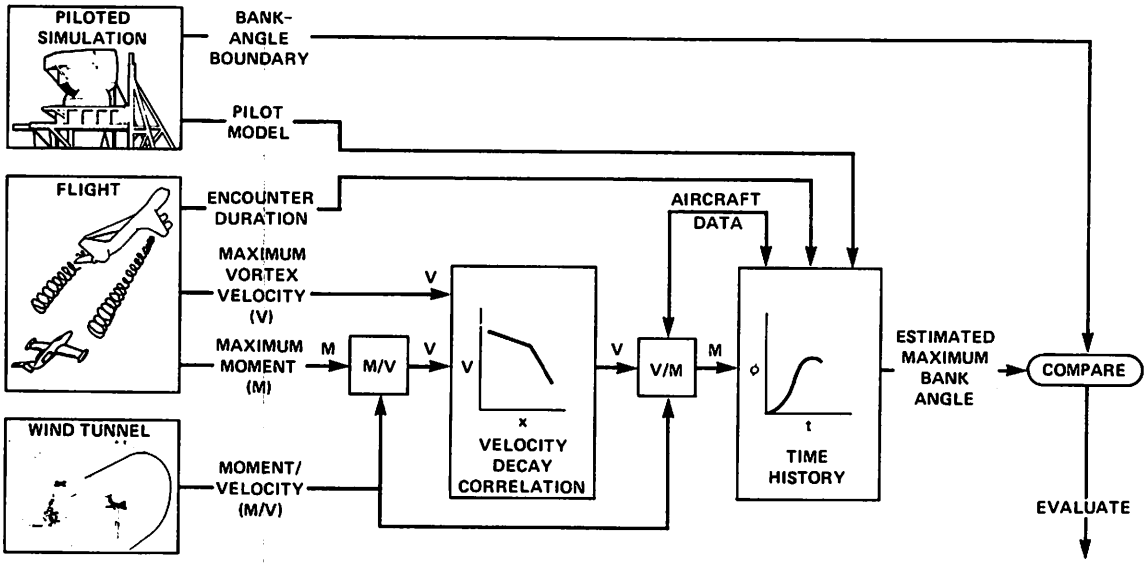

Figure 1. Procedure for estimation and evaluation of vortex-induced roll excursions.

1. Verification of calculations of rolling moment on aircraft that encounter a wake vortex by making flight measurements of upsets and vortex velocity fields;
2. Correlation of flight results to obtain vortex decay histories for jet transport aircraft in terms of correlation parameters given by Iversen [2];
3. Estimation of the maximum duration of an encounter from flight-test data;
4. Calculation of roll time histories using a pilot response model developed from moving-base simulation results;
5. Evaluation of the roll excursion in terms of a bank-angle boundary developed from simulation results.

DATA ANALYSIS

The flight data on vortex-induced rolling moments and maximum vortex tangential velocity were obtained at altitudes of several thousand feet or more. The estimated maximum excursions, therefore, correspond to those that might occur out of ground effect, that is, at an altitude greater than one span length of the aircraft that generated the vortex. The key assumptions in the analysis of the data are:

1. Rolling moments are computed for a worst-case situation where the aircraft is centered in a vortex. The envelope of vortex-induced rolling moments measured during intentional encounters during flight test represents this condition.
2. The large radius circulation is invariant with increasing separation and is equal to that for an elliptically loaded wing.
3. The velocity distribution within the vortex is that given by the variable eddy-viscosity solution by Iversen [2].
4. The duration of unintentional encounters by any aircraft can be represented in the worst case by the maximum for intentional encounters by the small probe aircraft used in flight test.
5. The bank-angle boundary determined from piloted motion-base simulation separates possibly hazardous encoun-

ters from nonhazardous encounters. Exceeding the boundary, therefore, does not necessarily imply a hazardous situation.

CORRELATION OF FLIGHT-TEST RESULTS

Rolling Moment and Maximum Vortex Tangential Velocity.

The principal method employed by NASA to evaluate vortex alleviation techniques is to measure the rolling moment on a following aircraft. This method has been used in ground-based facilities as well as in flight where the rolling moments are inferred from the measured time histories of aircraft motion following an intentional encounter with a marked vortex. Many encounters are made and it is assumed that the envelope of the rolling-moment variation with distance represents the maximum. A limitation of such results is that they cannot be generalized for direct application to other aircraft pairs. This is because the vortex core enlarges as the decay progresses, and the effect of a change in core size on rolling moment varies nonlinearly with the span of the penetrating aircraft. This limitation can be circumvented if the vortex velocity field can be inferred from the rolling-moment measurements and vice versa. A method of inferring velocities was developed and the results compared with velocity measurements made in flight. These were obtained with a hot-wire anemometer as a probe aircraft traversed the vortex wake. Reference 3 gives a more complete description of the flight-test techniques used in making both the velocity and the rolling-moment measurements.

The estimation of vortex velocity from measured rolling moments is based on the work of Rossow et al. [4] and Iversen [2]. Rossow et al. compared maximum vortex-induced rolling moments measured in the wind tunnel with those estimated by several methods. He demonstrated that a method based on simple strip theory yields results that agree with experiment as well as more elaborate lifting surface methods. Iversen demonstrated that a procedure based on a variable eddy-viscosity solution for the decay of a single line vortex leads to parameters that successfully collapse the maximum vortex velocities from a number of data sources to a single curve. In Iversen's vortex model, the large radius circulation is assumed to be constant and dissipation occurs in the vortex core. His model was combined with the rolling-moment calculation proposed by Rossow et al. to allow vortex velocities to be inferred from the rolling moments. The inverse calculation obviously is also feasible; that is, the rolling moment can be estimated from the peak tangential-velocity correlation for arbitrary vortex generating and penetrating aircraft.

A time history of a vortex encounter typical of those from which estimates of peak velocity were made is shown in Figure 2. This particular record is unique in that it represents the only instance known to the author where a large upset has been measured at approach speeds on a 3° glide slope. The generating aircraft was Boeing-727 and the probe aircraft was a Lear Jet-23.

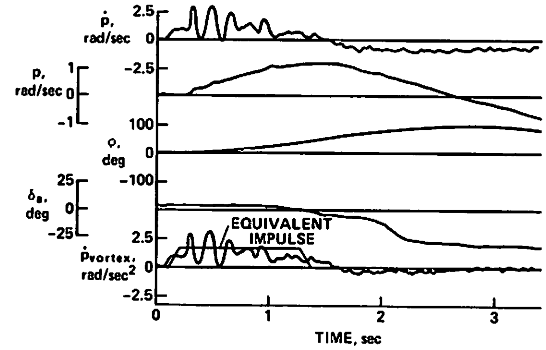

Figure 2. Time history of the roll response of Lear Jet-23 encountering the vortex of a B-727 on a 3° approach path with a separation of 2.7 n. mi.

The recorded roll acceleration for any encounter is typically oscillatory, as shown. This high-frequency oscillation is believed to be structural in origin and was ignored in the estimation of peak vortex-induced roll acceleration. The procedure used in this estimate was first to correct the measured acceleration for aerodynamic moments caused by control inputs and by aircraft motion. The principal contributions to this correction come from aileron deflection and roll damping. The peak vortex-induced roll acceleration was then chosen as shown in Figure 2, with the peaks caused by structural oscillation averaged.

The peak tangential velocities calculated from the rolling moments determined in flight are presented in Figure 3 in terms of the correlation parameters developed by Iversen. The data presented include results obtained during tests of B-747 and B-727 aircraft in the landing configuration with the Lear Jet-23 used as a probe aircraft. Also shown in Figure 3 are results of direct velocity measurements made in the wake of the B-747. It can be seen that the results of the two types of measurement are in reasonable agreement with each other and with Iversen's correlation for values of the dimensionless downstream distance parameter of less than about 900. This implies that the method of computing rolling moment from the known vortex field yields reasonable results.

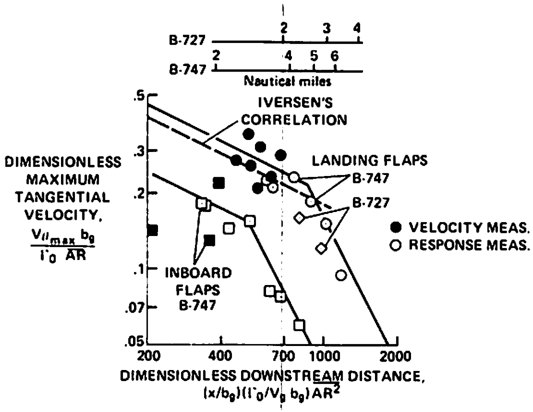

Figure 3. Correlation of maximum vortex tangential velocity determined from response measurements and by direct velocity measurement.

At values of the downstream distance parameter greater than 900, the data can be bounded by a line with a slope of −2, rather than −1/2 as in Iversen's original correlation. This rapid decay has also been observed in a correlation of in-flight measurements of the wake velocities of the C-5A. For purposes of this analysis, the vortex decay for the B-747 and B-727 with landing flaps has been assumed to be as shown in Figure 3. However, there is no reason to believe that the dimensionless distance parameter, as developed by Iversen for decay of a line vortex, will also correlate with the point where rapid decay occurs. It should also be recognized that the point for rapid decay will be influenced by atmospheric turbulence and possibly by ground effect.

One aerodynamic alleviation technique that proved promising from results obtained in ground-based facilities is modification of the span-load distribution. In particular, a sizable reduction in rolling moment was realized when only the inner segments of the flaps of the B-747 were lowered. Unfortunately, the flight tests showed that the alleviation was nearly eliminated when the gear was lowered or when small amounts of sideslip were introduced. The results from flight tests of this modified flap configuration with the gear retracted have been included here because they represent the highest level of aerodynamic alleviation achieved to date.

The results given in Figure 3 show two beneficial effects of lowering only the inboard flap segments as an alleviation technique. The first is the lowering of the peak tangential velocity at relatively small separation distances. This effect, observed in tests in ground-based facilities, led to the flight-test program. An equally important effect, not evident prior to correlating the flight-test data in terms of Iversen's parameters, is that the distance at which the rapid decay occurs is reduced. As shown in Figure 3, this effect causes reductions in peak vortex velocity of the order of 4 at values of the dimensionless distance parameter, $(x/b)(\Gamma/V_g b_g)\overline{AR}^2$, greater than about 900 in contrast to about 2 in the near field.

The apparent sensitivity of the distance at which rapid decay of the wake vortex occurs to the aircraft configuration is not understood. The discovery of the fundamental factors or parameters that influence this distance might lead to the development of more effective vortex alleviation techniques.

Encounter Duration.

The ultimate objective of the data analysis is to obtain sufficient information to calculate the time history of the aircraft motion following an encounter. This requires that the time history of the rolling moment induced on the encountering aircraft be represented. Examination of the flight records indicated that there is no typical rolling acceleration time history. The strategy adopted was to integrate the rolling-moment acceleration due to the vortex to obtain the total impulse. An equivalent impulse having the same area was then specified as indicated in Figure 2. The amplitude was chosen to be equal to the maximum acceleration because of the vortex, and the rise and decay times were always assumed to be 0.1 sec.

The duration of a large number of encounters is shown in Figure 4 as computed by the method described. Data from many more encounters are included in this figure in contrast to Figure 3 where only data representing the largest upsets at a given separation distance are shown. The encounter duration data show no correlation between $\dot{p}$ and Δt, and that, with one exception, the encounters last less than 1 sec. The exception is the encounter shown previously in Figure 2 which was obtained with the probe aircraft in the landing configuration and at approach speed. All other encounters were made with the probe at an airspeed about 40% greater with the probe either clean or with partial flaps. It is likely that the lower airspeed typical of the approach increased the duration of the encounter. There are insufficient data to determine if the size of the generating aircraft influences encounter duration. The few points that are available from tests of the B-727 – Lear Jet combination are distributed from about 0.4 to 1.27 sec.

On the basis of the data in Figure 4, the duration of the encounter was chosen to be 1 sec. In view of the airspeed of the probe aircraft, this encounter duration might be shorter than would normally be experienced during a landing approach. Selection of an increased duration will cause a nearly proportional increase in the calculated maximum bank angle.

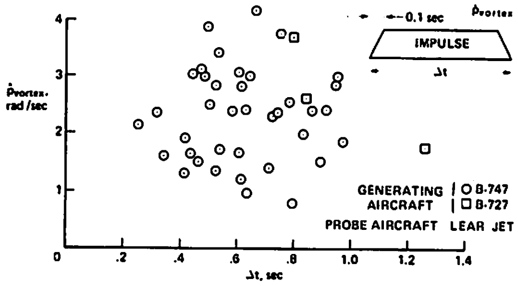

Figure 4. Duration of vortex encounters.

BANK-ANGLE BOUNDARY

Piloted simulations were conducted on the Flight Simulator for Advanced Aircraft at Ames Research Center to determine hazard criteria for vortex encounters. A bank-angle boundary was determined for jet aircraft in the 10,000-lb class (Lear Jet-23) and for the 150,000-lb class (Boeing 707/720) (see reference 5). In both simulations only the final approach flight condition was considered. The pilot control task was to fly an approach on a 3° glide slope in an environment of calm air or light turbulence and an occasional wake vortex encounter. Both VFR and IFR approaches were simulated.

To achieve the most realistic simulation results, several things were done to enhance the element of surprise so that the pilot could not anticipate the vortex upset. Although the pilot knew he was flying a vortex encounter simulation, he could not anticipate the upset because the altitude of the encounter, the magnitude of the vortex strength, and the direction of vortex flow (clockwise or counterclockwise) were all varied in a random manner from one approach to the next. In addition, during some approaches, there would be no vortex encounter. To further surprise the pilot, the encounter upset features were varied so that he could not adapt a standard response once he determined an encounter was occurring. This was done by simulating encounters from any one of several directions which caused different conditions to be associated with each upset occurrence. For example, encounters at a shallow entry angle from beneath the vortex result in a monotonically increasing bank angle in the absence of pilot control, and shallow angle encounters directly from the side result in a roll in one direction followed by a larger roll in the opposite direction in the absence of pilot control.

The pilots were asked to rate the encounters as either hazardous or nonhazardous. An encounter was to be rated nonhazardous only if the possibility of an accident due to the upset was considered by the pilot to be extremely low. The analysis of the data indicated that the best separation of the data into nonhazardous and possibly hazardous regions could be made on the basis of maximum vortex-induced bank angle. Typical results are shown in Figure 5. The bank-angle boundary is drawn to separate the data into nonhazardous and possibly hazardous regions. On the basis of similar results for both aircraft for VFR and IFR approach conditions, the boundary for purposes of the analysis was chosen to lie between 8° and 10° of bank angle.

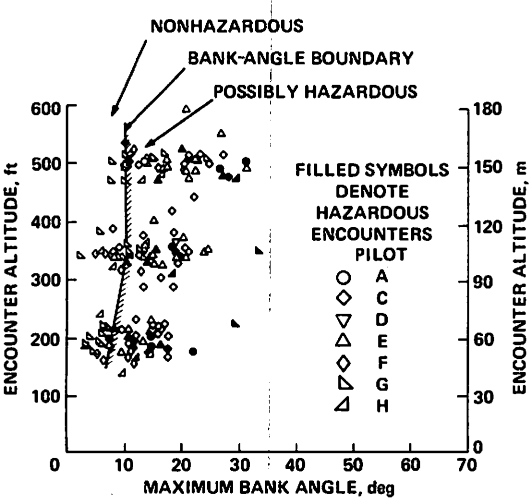

Figure 5. Bank-angle boundary determined from piloted, moving-base simulation of Boeing 707/720/IFR.

Pilot Model.

A model for the human pilot response to a wake vortex encounter was developed from the simulation results by Systems Technology, Inc., under contract to the FAA [6]. The model is limited to those encounters in which the rolling moment is in one direction only; this is typical for the landing approach where the vortex would be entered from above.

As an example of the use of the pilot model, the response was calculated to the vortex acceleration time history shown in Figure 2. The results are presented in Figure 6. The computed bank angle is considerably less than experienced in flight where the pilot purposely held the controls fixed during the encounter. The phases of pilot activity pertinent to the computation of maximum bank angle are termed A through C. In phase A, the pilot is responding to normal turbulence, if any, with aileron response to roll rate and roll angle governed by derived gain constants with a time delay of about 0.4 sec. After encountering the vortex, the switching logic of the model enters phase B once a threshold roll rate of 0.05 rad/sec or about 2.9°/sec is exceeded. During phase B, the pilot applies lateral control to produce roll acceleration proportional to roll rate, also with a 0.4-sec time delay. When the aileron input rate reaches zero, the model switches to phase C which represents a period during which the pilot waits for the bank angle to start decreasing.

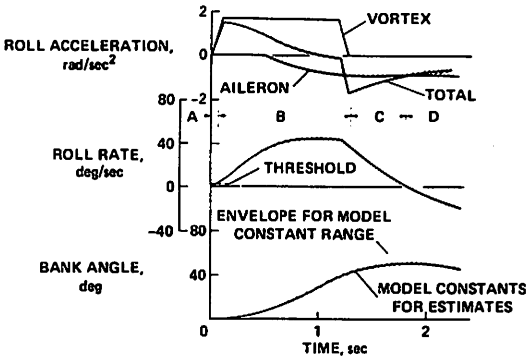

Figure 6. Typical response to a vortex encounter according to human pilot model.

During phase C, the pilot applies additional aileron control at a rate proportional to the wheel deflection. The change in aileron input is small in this phase and may be slightly positive or negative. During phase D, the pilot applies lateral control proportional to bank angle to effect his recovery with some roll rate gain to generate lead to offset his time delay. Phase D, however, is of negligible importance in determining the maximum bank angle which is of interest for this analysis.

The magnitude of the maximum bank angle will be influenced by the size of the gain constants assigned to phases B and C and the magnitude of the time delay. As Figure 6 shows, variation of these constants and the time delay within the limits observed during the simulation experiments can change the maximum bank angle between limits of about +20% and −10%.

EFFECTS OF AIRCRAFT SIZE

Before proceeding to the results of the computations of vortex upset, it is instructive to consider the importance of aircraft size to the vortex upset problem. Aerodynamicists consider the upset in terms of rolling-moment coefficient and measure progress toward reducing upset in terms of this parameter. However, when the vortex upset is considered in terms of rolling acceleration or maximum bank angle, the importance of the variation of moment of inertia with size of the encountering aircraft becomes evident.

Consider the various parameters of importance to the vortex upset problem as illustrated in Figure 7. The circulation in the vortex system shed by the generating aircraft is proportional to the weight per unit span. For geometrically similar aircraft having equal wing loading, weight will vary as the square of the span; therefore, circulation will vary as some constant, designated K_1 in Figure 7, times the span. The rolling moment induced on the following aircraft is somewhat more complicated and depends on the circulation of the generating aircraft, the square of the span of the following aircraft, and some function of separation distance and the spans of the aircraft pair. This function expresses how much the vortex has decayed and how much the resulting expanded core affects the rolling moment of the encountering aircraft. As the sketch in Figure 7 indicates, the change in rolling moment on the larger aircraft because of vortex decay would be expected to be much smaller than on the smaller aircraft where the core enlargement has reduced the vortex velocity over much of the wing span. Ignoring this factor for the moment, it is shown that the rolling moment is proportional to the span of the generator multiplied by the square of the span of the follower.

$W_g/S_g = C_1; W_f/S_f = C_2$

QUANTITY	EQUATION	VARIATION WITH SPAN
CIRCULATION, Γ_g	$4W_g/\pi\rho\, b_g V_g$	$K_1 b_g$
ROLLING MOMENT, L_f	$\Gamma_g b_f^2 \rho V_f \underbrace{[f(x, b_g, b_f)]}$ 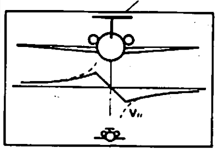 	$K_2 b_g b_f^2 [f(x, b_f, b_g)]$
MOMENT OF INERTIA, I_f	$(W_f/g)\rho^2$	$K_3 b_f^4$
ROLLING ACCELERATION, $\dot{p}$	L/I	$K_4 (b_g/b_f^2)[f(x, b_f, b_g)]$

Figure 7. Variation with aircraft size of quantities affecting response to a vortex encounter by geometrically similar aircraft.

The moment of inertia of the encountering aircraft is the most significant factor, dependent on aircraft size, that determines the severity of the upset due to a vortex encounter. The rolling moment of inertia can be expressed as the aircraft mass, W/g, times the square of the radius of gyration. For aircraft having identical wing loading, the moment of inertia is found to vary roughly as the fourth power of the span. This corresponds to the case when all the mass is uniformly distributed in a plane. Differences in engine location will cause some differences in this variation.

Finally, the rolling acceleration is shown to be proportional to the span of the generator divided by the square of the span of the follower, multiplied by the function that expresses the effect of vortex decay. It is extremely interesting to consider the results when a series of aircraft pairs, each of ever decreasing size, are assumed to be at a common separation distance. Ignoring the decay function for the moment, the expression indicates that if the aircraft have identical wing loading, the bank-angle excursion should become more severe as the aircraft pairs become smaller!

Results of calculations to study this effect of aircraft size, based on the correlation of experimental data discussed earlier, are shown in Figure 8. The expected variation of rolling-moment coefficient and $\dot{p}$, without considering the effects of vortex decay, are shown as the solid lines, assigning the value of 1 to a pair of B-747's with a separation of 3 n. mi. The rolling-moment coefficient on the aircraft following would be expected to remain constant as size is reduced, and the rolling acceleration would be expected to increase as b_{747}/b. The actual values computed for the pairs of B-747's, B-727's, and Lear Jet-23's have been compared on the same basis. In making these computations, the variation of vortex velocity with distance implied by Figure 3 was assumed to apply to all aircraft. The calculated value of $\dot{p}$ for the pair of B-727's exceeds the expected value because the placement of engines on this aircraft causes a smaller moment of inertia than given by the assumed variation.

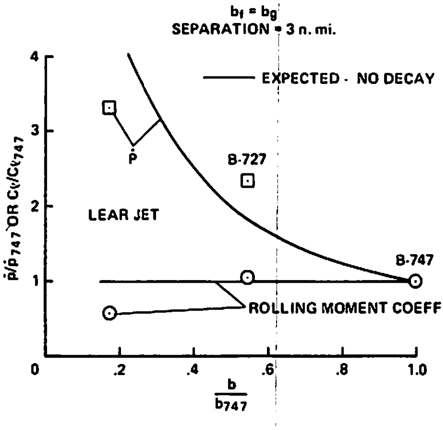

Figure 8. Variation with aircraft size on the severity of the encounter for identical generating and following aircraft.

The calculated rolling-moment coefficient for the Lear Jet-23 pair is considerably less than the expected value because of vortex decay. However, even this much lower calculated value exceeds what our experience indicates will occur. The calculation of rolling moment, in this case, depends on the estimation of the rolling moment at dimensionless downstream distances that exceed by about 50% the limits of the data on which Iversen's correlation is based. The data available from flight tests indicate a rapid decay in this region. Further, the decay may be more rapid than the slope of −2 shown in Figure 3.

In other words, extrapolation of the results to predict upset for small aircraft pairs is questionable. However, there is evidence that the decay of the vortex from the B-727 is sufficiently close to that of the B-747, in dimensionless terms, to expect that the rolling-moment coefficients would be very nearly the same, as shown in Figure 8. In this event, the rolling acceleration will vary roughly inversely as the span, and the upset to a B-727 encountering a vortex from another B-727 would be expected to be more severe than the upset of a B-747 caused by a B-747 at the same distance.

CALCULATED BANK-ANGLE EXCURSIONS FOR CURRENT SEPARATION STANDARDS

Iversen's correlation has been shown to collapse vortex decay data from many sources to a single curve. On the basis of this result, the vortex decay data shown in Figure 3 would be expected to apply to the B-727 as well as to the B-747 in the range of dimensionless downstream distances where the slope of −1/2, as given by Iversen, applies. However, the point at which the decay process apparently changes and is better represented by a slope of −2 might not be the same for both aircraft. The two data points shown in Figure 3 for the B-727 represent the most severe encounters obtained during the flight tests reported in reference 7. A slope of −2 drawn through these points would reduce the peak tangential velocity at separations of 3 and 4 n. mi. by about 40%. The corresponding reduction in rolling moment will depend on the span of the penetrating aircraft and will be considerably smaller than 40%. However, for purposes of this analysis the solid lines in Figure 3 were assumed to apply to both the B-747 and the B-727.

The calculated maximum bank angles are shown in Figure 9. Also shown are estimates of bank angles made by Nelson [8]. Nelson's calculation used a different vortex model, a simpler pilot model, and the calculation consisted of a six-degrees-of-freedom digital simulation of the encounter with the encounter duration determined by the path of the aircraft. Nelson's estimates are for different aircraft pairs and cannot be compared directly with those made herein, but when the effects of aircraft size are considered his procedure appears to result in somewhat greater values of maximum bank angles.

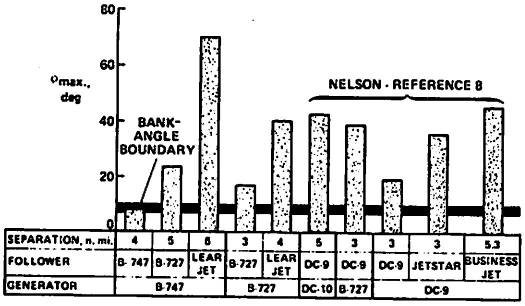

Figure 9. Calculated upset magnitudes for current separation standards.

Both sets of calculations show the dominant effects of aircraft size and that the maximum bank angles for the small aircraft exceed the bank-angle boundary by factors of from 4 to 7 even though the separation distances for these aircraft are greater. This relatively large estimated response of the small aircraft to a vortex encounter is consistent with the trend of accident statistics reported in reference 9 where it is stated that the vortex-related accident rate is lower by an order of magnitude for air carriers than it is for general aviation.

In view of the large estimated bank angles, it is logical to ask why there have not been more wake vortex accidents and incidents. Landing accidents attributable to the wake vortex, for instance, are reported in reference 9 to be only about one in 3 million landings. Reasons for the low accident rate in view of the apparent hazard are: (1) the low probability of a "maximum" encounter in which an aircraft penetrates the center of the vortex; (2) the wake vortex in ground effect is considerably weaker than at the altitudes where the data for this study were obtained; and (3) the bank-angle boundary drawn on the basis of the simulation results is very conservative.

"Maximum" encounters of the type considered in this study can be shown to be extremely rare events. Surveys of the presence of the vortex in an area 46 m on either side of the runway centerline [10] show the vortex to be present about 1% of the time at a separation of 3 n. mi. (see Figure 10). At separations of 4 n. mi. or more, the occurrence is reported to be less than 0.1%. For a maximum encounter, the aircraft must be centered in the vortex core, which is of the order of a few meters in diameter. Thus the probability of a core penetration is considerably lower than that stated above.

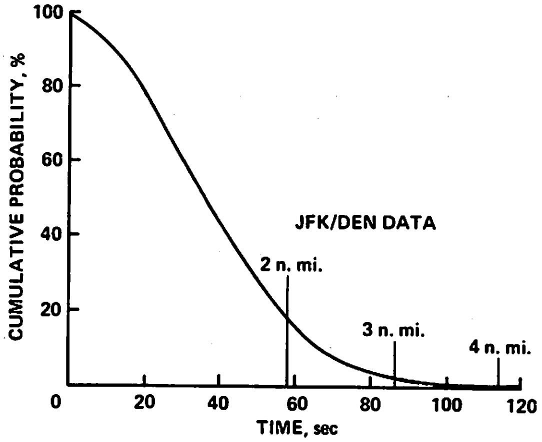

Figure 10. Results of surveys by DOT near runway threshold to determine vortex presence within 46 m of runway centerline.

The effect of the proximity of the ground on vortex strength possibly also influences the frequency with which the vortex will lie within the landing area. It will also have a large effect on the severity of an encounter if an encounter should occur. Surveys by the DOT using acoustic radar in the region of the runway threshold [11] have indicated circulation strengths that are lower than would be expected out of ground effect by a factor of 2 or more at a separation of 2 n. mi. Further reductions would be expected as the separation is increased. This is extremely important since the vortex tends to lie well below the flight path until its descent is arrested by the ground. It is in this region that the 10-year statistics reported in reference 9 indicate that more than 70% of the encounters leading to accidents occur.

Finally, the bank-angle boundary is very conservative. The pilots participating in the simulation program were instructed to rate an encounter as hazardous if there was more than a "very low" probability that an accident would result. The boundary was then drawn as a lower bound to all of the maximum bank angles for encounters rated as hazardous. The boundary therefore identifies a nonhazardous region, but exceeding the boundary by a modest amount does not necessarily imply a hazardous situation.

AERODYNAMIC ALLEVIATION OF THE WAKE VORTEX HAZARD

In the previous section it was demonstrated that a vortex encounter under current separation standards can exceed the bank-angle boundary and that the bank angle for small aircraft can be of the order of 70°. From this it can be concluded that the current extremely low wake vortex accident rate is a consequence of the vortex usually being removed by ambient winds or, at extremely low altitudes, dissipated by ground effect. A reduction in separation distance, which is the goal for the aerodynamic alleviation program, will allow less time for these favorable effects to occur and is therefore likely to cause increases in the number of vortex encounters. For instance, the cumulative probability of vortex presence over the runway increases markedly when the separation is decreased (see Figure 10). The possibility of encountering the vortex outside of ground effect, where it is evidently stronger, will also increase. This is important for IFR operations where the bank-angle boundary was determined to be at about 10° even at an altitude of 160 m. One reason for the increased encounter probability is that the downwash will have less time to carry the vortex pair below the flight path of the following aircraft. Hence, the probability of encounters caused by glidepath errors of either aircraft or by the presence of large scale turbulence is increased.

To assess the progress of the aerodynamic alleviation program toward producing benign encounters, calculations were made of upsets that could be caused by the wake of jet transports with only the inner segments of the flaps lowered (30/1). This particular configuration has produced the greatest alleviation in flight observed to date. The maximum tangential velocity is shown in Figure 3 to be about halved at 3 n. mi. for the B-747 and reduced to possibly 1/4 for the same modification to a B-727. Estimates of the maximum bank angles for various aircraft encountering the wake of this alleviated configuration are shown in Figure 11.

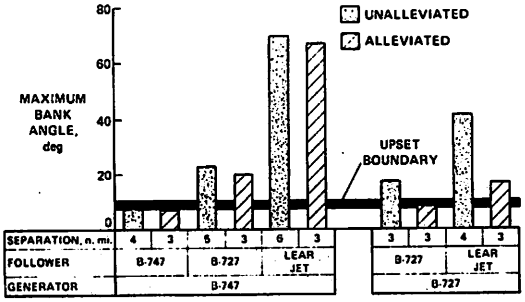

Figure 11. Comparison of upset magnitudes of alleviated configuration at 3 n. mi. separation with unalleviated configuration at standard separation distance.

The modified flap configuration (30/1) is shown to be effective in reducing the maximum bank angle to a level that is less at a separation of 3 n. mi. than it is for the standard flap configuration (30/30) at current separation distances. However, the only aircraft combinations for which the maximum bank angle lies within the boundary are the B-747 and the B-727 encountering their own wake. As noted previously, the bank-angle boundary is conservative. Another important reference is the bank angle for the B-727 with 30/30 flaps encountering its own wake. In view of the large number of operations occurring daily for this and the other combinations of aircraft of this class without any accidents, it must be concluded that the level of maximum bank angle and encounter probability associated with a separation of 3 n. mi. is representative of an adequate level of safety. The maximum bank angle for this situation is shown to be about 18°. This is exceeded by several degrees when the B-727 encounters the wake of the B-747 with 30/1 flaps and by a factor of about 3 when the Lear Jet encounters this wake at the reduced separation. The maximum bank angle for the Lear Jet is only slightly less than it is for the unmodified flaps at a separation of 6 n. mi. In view of the magnitude of the maximum bank angle, safety must be provided for the small aircraft through other means, such as enhanced flight control characteristics or by a very low encounter probability afforded by a large separation distance. Therefore, even though the wake alleviation technique makes it possible to obtain roughly the same bank-angle magnitudes at half the separation distance for small aircraft, it does not follow directly that a significant reduction in separation distance is possible without reducing the level of safety.

CONCLUDING REMARKS

A method has been developed for estimating the maximum roll excursions of aircraft encountering the wake vortex that is based on flight and simulation results. The method relies on a correlation of the maximum wake velocity with distance in terms of parameters derived by Iversen that have been shown to collapse wake data from a number of sources and aircraft configurations to a single curve. The method therefore permits flight data from a particular vortex generating and probe aircraft combination to be applied to estimate the roll excursions for other aircraft combinations.

An analysis of the flight measurements in terms of Iversen's correlation parameters indicates that aerodynamic alleviation has two distinct effects that are important to the indicated reduction of the wake vortex upset. The first is a uniform reduction in maximum vortex velocity at distances less than about 3 n. mi. behind a large heavy transport. This phenomenon has been observed during tests in ground-based facilities. The second effect is a marked reduction in the distance at which the decay process apparently changes, causing the peak velocities to vary approximately inversely with the square of further increases in separation distance. An understanding of the basic reasons for this latter effect might lead to more effective vortex alleviation techniques.

Estimates indicate that the best configuration for aerodynamic alleviation of the wake vortex will produce bank-angle levels at 3 n. mi. that are comparable to those of unalleviated aircraft at current separation distances. However, the maximum bank angle for small aircraft is estimated to be large in either case and to exceed the bank-angle boundary by a large amount. It must be concluded that safety for small aircraft is currently provided by an extremely low vortex encounter probability which is likely to be jeopardized by a decrease in separation.

REFERENCES

1. Israel, D.R., "Air Traffic Control: Upgrading the Third Generation," *Tech. Rev.*, Vol. 77, Feb. 1975, p. 14-24.

2. Iversen, J.A., "Correlation of Turbulent Trailing Vortex Decay Data," *J. Aircraft*, Vol. 13, May 1976, p. 338-342.

3. Jacobsen, R.A. and Barber, M.R., "Flight-Test Techniques for Wake Vortex Minimization Studies," NASA Symposium on Wake Vortex Minimization, Feb. 25-26, 1976, p. 191-217.

4. Rossow, V.J., Corsiglia, V.R., Schwind, R.G., Frick, J.K.D., and Lemmer, O.J., "Velocity and Rolling-Moment Measurements in the Wake of a Swept-Wing Model in the 40- by 80-Foot Wind Tunnel," NASA TM X-62,414, Apr. 1975, Ames Research Center, Moffett Field, CA.

5. Sammonds, R.I., Stinnett, G.W., Jr., and Larsen, W.E., "Wake Vortex Encounter Hazard Criteria for Two Aircraft Classes," NASA TM X-73,113, June 1976, Ames Research Center, Moffett Field, CA.

6. Johnson, W.A. and Meyers, T.T., "A Model for Human Pilot Behavior During Wake Vortex Encounter Upsets," FAA-RD-76-8, April 1976, Systems Tech. Inc., Hawthorne, CA.

7. Kurkowski, R.L., Barber, M.R., and Garodz, L.J., "Characteristics of Wake Vortex Generated by a Boeing 727 Jet Transport During Two-Segment and Normal ILS Approach Flight Paths," NASA TN D-8222, 1975.

8. Nelson, R.C., "The Response of Aircraft Encountering Wake Turbulence," AFFDL-TR-74-29, June 1974, Flight Dynamics Lab., Wright-Patterson Air Force Base, Ohio.

9. Gupta, V., "Vortex-Related Accidents Over the Ten-Year Period 1964-73," FAA-EM-75-6, April 1975, MITRE Corp., McLean, VA.

10. Hallock, J.N., Wood, W.D., and Spitzer, E.A., "Predictive Techniques for Wake Vortex Avoidance," AGARD Guidance and Control Panel 20th Symposium on Plans and Developments for Air Traffic Systems, Paper 23, 1975.

11. Hallock, J.N., "Wake Vortex Decay Near the Ground," AIAA Paper 75-882, 8th Fluid and Plasma Dynamics Conference, Hartford, CT, June 16-18, 1975.

HAZARD EXTENT ABOUT AIRCRAFT TRAILING WAKE VORTICES — ANALYTIC APPROACH

IAN G. McWILLIAMS
U.S. Department of Transportation
Transportation Systems Center
Cambridge MA 02142

ABSTRACT: The proposed Vortex Advisory System makes use of the fact that under certain wind conditions, vortices cannot be detected within a protected corridor after 80 seconds. The width of the corridor is dependent upon the hazard extent about vortices. Two methods for estimating the hazard extent are presented: a static calculation of the rolling moment on a generic aircraft as a function of distance from the vortex axis; and a dynamic simulation of a B-720 encountering vortices at varying distances. Both of these methods were found to be in substantial agreement and yielded a value of 30 meters as a conservative estimate for the hazard extent about vortices.

INTRODUCTION

The term "hazard definition" is generally used to describe all of the circumstances under which a vortex wake can be dangerous to a following aircraft. Such a description would have to include: generator type, follower type, altitude, flight configuration of both aircraft, geometry of penetration, separation between aircraft, and the meteorological conditions. At present there is not enough knowledge of vortex behavior to make a determination of whether a vortex encounter would be hazardous for all combinations of the variables mentioned above.

An ideal solution to the problem of hazard definition would be to run a series of flight tests in which several types of instrumented aircraft would probe known vortex flow fields. In these tests the encounter upset could be measured as a function of vortex strength and position. Unfortunately, in this type of experiment, it becomes too difficult to control all of the important variables. Nevertheless, a considerable amount of information can be gleaned from an encounter flight test.

NASA has conducted a series of flight tests to evaluate the response of probe aircraft to a vortex wake [1, 2]. The wake-generating aircraft included C-5A, B-747, DC-10, CV-880, B-727 and DC-9, while the list of probe aircraft included the DC-10, DC-9, T-3A, Lear Jet, and the Cessna 210. Vortex encounter probes were made at distances ranging from 1 nm to 15 nm behind the generator aircraft. Distance was measured either by precision radar or onboard DME. The pilot of the probe aircraft tried to keep the aircraft in the center of the vortex which was usually marked with smoke. Roll response was found to be the principal effect in vortex encounters. Analysis of the data showed good correlation between the separation distance at which roll acceleration just exceeded the roll control capability and the minimum separation the test pilots judged as adequate for safety. It has been suggested that just such a methodology be used to establish separation standards.

There are serious limitations to relying solely on flight test for hazard definition. For the sake of safety, all of the encounter probes took place at an altitude of approximately 3,000 m AGL. It is evident that if there is a radical difference in the time scale of vortex decay between 3,000 m AGL and 150 m AGL, then the separation distances found in the flight tests are not directly applicable to approach and landing operations.

Until the present, it has not been possible to measure the vortex flow field and the probe aircraft response simultaneously for a near parallel encounter. The distance behind the generator aircraft was used to extrapolate the vortex strength. In addition, all of the probes were central encounters, i.e., the probe aircraft were flown into the visual center of the vortex; consequently, there is only qualitative information on the spatial extent of the hazard region.

The Vortex Advisory System (VAS) [3] uses a wind measurement algorithm to determine the conditions under which aircraft separation standards can be reduced to 3 nautical miles for every combination of aircraft. The VAS algorithm is based on a large number of measured vortex tracks at three airports: New York's JFK, Denver's Stapleton, and London's Heathrow [4, 5]. It has been found that whenever the surface wind vector, as measured near landing threshold, lies outside an ellipse whose minor axis is 5.5 knots in the lateral or crosswind direction and whose major axis is 12 knots in the longitudinal direction, vortices have not been detected within a protected corridor 90 meters wide and centered on the runway centerline after 80 seconds from aircraft passage.

The hazard extent of vortices is one of the factors which goes into the determination of the width of the corridor used in the VAS algorithm. The hazard extent of a vortex is the minimum lateral distance which a landing aircraft can be displaced from the vortex axis without experiencing unacceptable upsets. The function of the VAS is to ensure that an approaching aircraft's flight path is always displaced at least a distance equal to the hazard extent from any vortices remaining after 80 seconds. For the VAS algorithm, the hazard extent is defined without regard for the type of aircraft which is the generator and which is the follower and without taking vortex decay directly into consideration.

In order to arrive at an estimation of vortex hazard extent, a number of simplifying assumptions will have to be made. First, it will be assumed that we are dealing only with aircraft on final approach at an altitude of 60 meters or less, that is, in a region where vortices are known to sink to near the ground and vortex vertical descent will not clear the vortices from the flight path. The second assumption is that the vortex flow field is the worst case possible in today's air traffic mix, such as the 747 or DC-10 vortex.

There are two approaches to the establishment of a hazard extent considered here. One is a static calculation of the vortex-induced rolling moment of a generic aircraft displaced various distances from the vortex axis. A simplified rolling moment calculation employing a reciprocal theorem of Heaslet and Spreiter [6] which overestimates the vortex-induced rolling moment will be used. The calculated rolling moment will be compared to the roll authority for encountering aircraft of varying wing spans, and the hazard extent will be defined as the distance from the vortex axis at which the ratio of the induced rolling moment to the roll authority falls below a prescribed value. The hazard extent corresponding to several values of this ratio, 1.0, .75 and .5, will be examined.

The second approach is to use a dynamic simulation of a particular aircraft, B-720, to probe the vortex flow field. In this method the probe aircraft flys a 3° glide-slope approach. The vortex, whose axis is parallel to and displaced from the extended runway centerline, acts as a disturbance to the probe aircraft. For this case the hazard extent is defined as the distance beyond which the total roll excursion falls below a prescribed hazard criterion value derived from the NASA-Ames/FAA simulation [7]. It will be seen that the two methods outlined above produce consistent results.

HAZARD EXTENT DERIVED FROM A GENERIC AIRCRAFT ROLLING-MOMENT CALCULATION

One of the simplest methods of deriving a formulation for the rolling moment of an aircraft in the flow field of a vortex is to use a version of strip theory. Barrows [8] has used a similar formulation using the reciprocal theorem of Heaslet and Spreiter [6] which relates the rolling moment on a wing in an arbitrary flow field to that of a wing rolling at a uniform rate. For an aircraft flying in the flow field w(y) of a vortex (Figure 1) with forward velocity V, the rolling moment can be written

$$L = \int_{-b/2}^{b/2} \left[\ell(y)\right]_{\alpha_V(y)} y \, dy , \qquad (1)$$

where $[\ell(y)]_{\alpha_V(y)}$ is the sectional loading induced by the flow field represented by $\alpha_V(y)$.

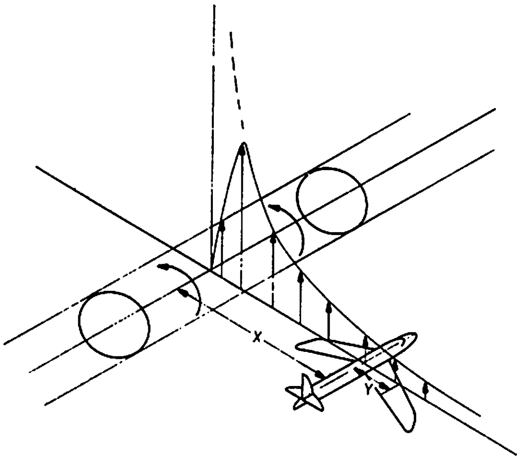

Figure 1. Geometry of rolling-moment calculation.

Consider now the same aircraft rolling at a uniform rate p. Then

$$\alpha_p(y) = \frac{p}{V}\, y \qquad \text{or} \qquad y = \frac{V}{p}\, \alpha_p.$$

Equation (1) can be rewritten

$$L = \frac{V}{p}\int_{-b/2}^{b/2} \left[\ell(y)\right]_{\alpha_v(y)} \alpha_p(y)\, dy. \quad (2)$$

The right side of Equation (2) is a constant times the integral over the span of a sectional loading due to the vortex angle of attack distribution times the angle of attack of an aircraft rolling at rate p. The reciprocal theorem allows us to reverse the roles of the two angles of attack, that is

$$\int_{-b/2}^{b/2} \left[\ell(y)\right]_{\alpha v} \alpha_p(y)\, dy =$$

$$\int_{-b/2}^{b/2} \left[\ell(y)\right]_{\alpha_p} \alpha_v(y)\, dy\,,$$

where $[\ell(y)]_{\alpha p(y)}$ is the sectional loading of the aircraft wing rolling at rate p. Then

$$L = \frac{V}{p}\int_{-b/2}^{b/2} \left[\ell(y)\right]_{\alpha_p} \alpha_v(y)\, dy.$$

For p= 2V/b we have

$$L = \frac{b}{2}\int_{-b/2}^{b/2} \left[\ell(y)\right]_{\alpha_p} \alpha_v(y)\, dy. \quad (3)$$

Equation (3) allows us to calculate the rolling moment on an aircraft due to an arbitrary flow field $\alpha_v(y)$ by means of simple strip integration once the sectional loading for the same aircraft in uniform rolling motion is calculated.

Eggleston and Diederich [9] have expressed the rolling-moment coefficient in terms of the roll damping coefficient

$$C_\ell = \frac{-C_{\ell p}}{4}\int_{-1}^{+1} \gamma\left(\frac{2y}{b}\right) \alpha_v\left(\frac{2y}{b}\right) d\left(\frac{2y}{b}\right),$$

where $\gamma(2y/b)$is a weighting function derived from a calculation of the rolling moment of the aircraft in uniform rolling motion.

Following Barrows [8], the rolling-moment coefficient is calculated for a Betz model vortex field given by

$$\Gamma_o = \frac{2}{\pi}\left(\frac{VC_L S}{b}\right)_g\,,$$

$$w(x) = \frac{\Gamma_o}{2\pi}\, f\left(\frac{2x}{b_g}\right),$$

$$f\left(\frac{2x}{b_g}\right) = \begin{cases} \left[3\left(\frac{2x}{b_g}\right) - \frac{9}{4}\left(\frac{2x}{b_g}\right)^2\right]^{1/2}, & \frac{2x}{b_g} \leq 2/3\,, \\ \quad , & \frac{2x}{b_g} > 2/3\,, \end{cases}$$

where the g subscripts refer to parameters of the vortex-generating aircraft. The corresponding roll-moment coefficient for the following aircraft (Figure 1) can be written

$$C_{\ell_v} = \frac{C_{\ell_p}}{2\pi^2}\left(\frac{C_L}{AR}\right)_g \frac{V_g b_g}{V_f b_f}\int_{-1}^{1}\frac{\gamma\left(\frac{2y}{b_f}\right) f\left(\frac{2x}{b_g}\right) d\left(\frac{2y}{b_f}\right)}{(2y/b_f) - (2x/b_f)}$$

where the f subscripts refer to parameters of the following aircraft. Let

$$R = \frac{C_{\ell_v}}{(C_\ell)_{\text{max control}}}$$

be the ratio of the vortex-induced rolling moment to the maximum roll-control moment.

The maximum roll control available can be related to the roll-damping coefficient by

$$(C_\ell)_{\text{max control}} = C_{\ell_p}\left(\frac{pb}{2V}\right)_{\text{max}} = C_{\ell_p}\hat{p}_{\text{max}} \; .$$

Then

$$R = \frac{1}{\hat{p}_{\text{max}}}\left(\frac{C_L}{AR}\right)_g \frac{V_g}{V_f}\frac{b_g}{b_f}\, I\left(\frac{2x}{b_f}\right),$$

where

$$I\left(\frac{2x}{b_f}\right) = \frac{1}{2\pi^2}\int_{-1}^{1}\frac{\gamma\left(\frac{2y}{b_f}\right) f\left(\frac{2x}{b_g}\right) d\left(\frac{2y}{b_f}\right)}{\left(\frac{2y}{b_f}\right) - \left(\frac{2x}{b_f}\right)}$$

is a dimensionless quantity describing how the rolling moment varies with displacement x from the vortex axis. $I(2x/b_f)$ is plotted in Figure 2 using an elliptical weighting function in the integral for three values of b_f/b_g.

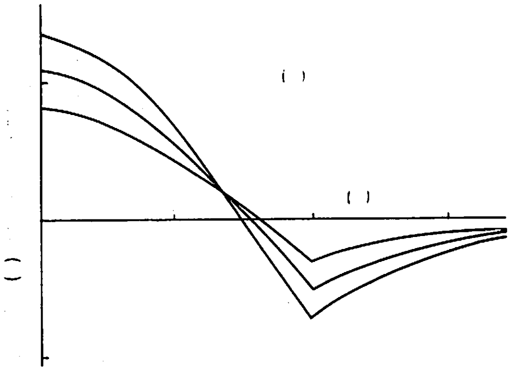

Figure 2. Plot of the dimensionless rolling moment for various values of the follower-to-generator wingspan ratio.

The rolling moment is a maximum when the following aircraft is centered at the vortex axis and falls off continuously as the follower is displaced, reversing sign at about .8 semispans and reaching a negative maximum at one semispan. The negative maximum, occurring when the wing tip is in the vortex core, represents a rolling moment with the opposite sense of rotation as the vortex. When the wing tip is completely outside of the vortex core, the rolling moment falls off rapidly as a function of distance.

Using typical aircraft parameters: $\hat{p}_{\text{max}}=0.8$, $C_L=1.0$, $AR=7$, $V_g=V_f$, and $b_g=60$m, we obtain (with b_f in meters)

$$R = \frac{106.8}{b_f}\, I\left(\frac{2x}{b_f}\right)$$

We can now define the hazard extent as the distance from the vortex beyond which R is always less than some chosen value R_{min}. Figure 3 is a plot of hazard extent for three values of R_{min} (1, .75 and .5).

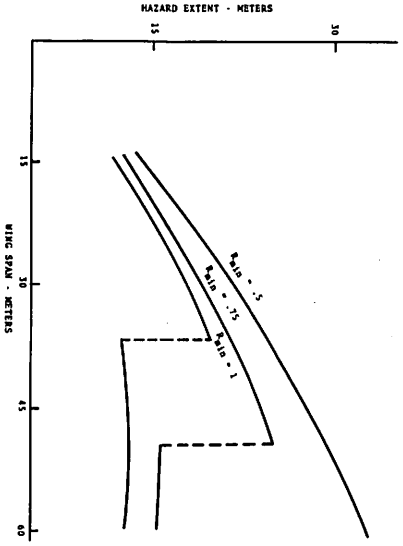

Figure 3. Hazard extent.

For the $R_{min} = .75$ case, the hazard extent curve rises to a maximum of 24 meters and then drops discontinuously to a value of 12 meters. The reason for the discontinuity is the following: For values of b_f less than 50 meters, there is some value of R greater than R_{min} for $2x/b_f$ greater than one that is beyond the negative maximum of $I(2x/b_f)$. For b_f values greater than 50 meters, the condition that $R = R_{min}$ occurs only near the central maximum of $I(2x/b_f)$. A similar discontinuity occurs for the case $R_{min} = 1$.

It should be noted here that a number of assumptions were made which make the value of hazard extent somewhat conservative:

1) The vortex was considered not to have decayed.

2) $\gamma(2y/b_f)$ was based on an elliptically loaded wing; while for most aircraft in the landing configuration, the loading is concentrated further in-board.

3) The vortices for landing aircraft are not in the form of a simple Betz-model vortex, but rather take the form of multiple vortices for which the resultant rolling moment is less than for a single concentration of vorticity.

It could therefore be concluded that if one required that the maximum induced rolling moment experienced by a landing aircraft not exceed one half the roll control power for any following aircraft, a protected corridor of 30 meters is adequate.

DYNAMIC SIMULATION OF AIRCRAFT-VORTEX ENCOUNTERS

In order to probe the spacial extent of vortex hazard, a computer simulation of a vortex encounter has been developed at TSC [10]. A strip-theory model of the aerodynamics was used to calculate the forces and moments due to a non-uniform wind field which the vortex represents. Initial attempts at a fixed-stick simulation demonstrated that the probe aircraft was easily pushed away from the vortex center making a severe encounter difficult to recreate. An autopilot was added in order to constrain the probe to a given task such as completing an approach and letting the vortex act as a perturbation. The region around the vortex could thus be probed and a hazard volume mapped out. The hybrid computer consists of a Beckman 2200 analog computer and a XDS 3600 digital computer.

The TSC Encounter Simulation program is a hybrid program which uses a modified strip-theory calculation of forces and moments. The aerodynamic coefficients are calculated on the digital computer as are the various coordinate transformations (e.g., body axes to navigation axes). The equations of motion are solved on the analog computer, and the updated coordinates and their rates are fed back to the digital computer via A/D lines.

There are two principal coordinate systems used to solve the equations of motion. One, the navigation axes, is basically a flat earth approximation in which the z axis points in the direction of the gravity vector and x and y point north and east, respectively. The navigation frame can be considered an inertial frame. It is in the navigation axes coordinate system that the equations of motion are solved. Without loss of generality, the runway direction can be orientated in the x direction, so that the vortex flow field can be written in a particularly simple form in the navigation axes frame.

The general procedure in the simulation computation is to compute the vortex-induced moments in the body-fixed frame and to solve the equations of motion for the Euler angles. The resultant Euler angles are then used in the transformation matrix to convert from the navigation frame to the body-fixed frame for another iteration. Similarly, the velocity vector is integrated to update the aircraft's position. The program organization is shown in Figure 4.

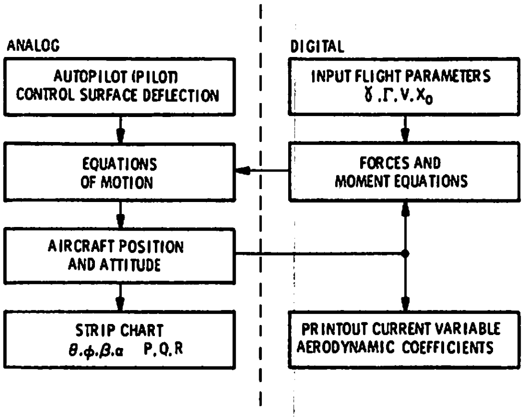

Figure 4. Program organization.

In an aircraft encounter with a vortex wake, the forces and moments vary considerably over the whole aircraft structure due to the non-uniform wind field which the wake represents. For example, the spanwise changes of lift produce a rapidly changing rolling moment as the aircraft passes through the vortex. The usual procedure for calculating the forces and moments is to lump all of the contributions from the various parts of the aircraft into one aerodynamic coefficient; whereas for vortex encounters, some method of distributing the forces has to be used. In the encounter simulation, a modified form of strip theory is used. The encountering aircraft is broken down into 16 wing segments, 3 horizontal stabilizer segments, and 1 vertical tail section as shown in Figure 5.

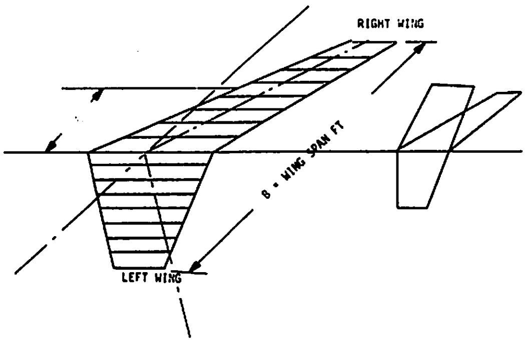

Figure 5. Aircraft model.

The rolling moment is given by

$$L = \frac{Sq}{16}\left\{\sum_{i=1}^{16} F_i \, C_{L\alpha_w} \, \xi_i \alpha_i - b\left[C_{\ell p}\,\hat{p} + C_{\ell_{\delta\alpha}}\,\delta_\alpha\right]\right\},$$

where C_L and the F_i have been adjusted to obtain the correct total lift and roll damping coefficient.

The strip theory summation to calculate the coefficients is carried out in the digital computer using the local angle of attack for each wing section. At the start of each computation cycle, a routine is called which calculates the vortex flow field at each wing and tail station. The contribution to each coefficient is summed over the 20 segments, and the total coefficient is fed back to the analog computer where the equations of motion are solved. The vortex flow field used in the simulation could take any form which could be programmed as a function of the coordinates. For the purposes of the simulation, it was found that the exact form of the flow field was not critical, but rather the total circulation and, to a lesser extent, core radius were the important parameters. Therefore, the bulk of the simulation runs were made using the simple Rankine model:

$$w(r) = \begin{cases} \dfrac{\Gamma_0 r}{2\pi r_c^2}, & r < r_c \\ \dfrac{\Gamma_0}{2\pi r}, & r \geq r_c \end{cases}$$

In general, four vortices were used (two real vortices and their images) and $r_c = 2.1$ meters.

In addition, a ground-effect correction is made to each of the wing section lift coefficients. The ground-effect correction multiplier is a non-linear function which is unity on the ground and zero at 30 meters AGL. During the digital computation, the program tests for both angle of attack and height above touchdown.

The geometry of the encounter simulation is shown in Figure 6. The probe aircraft descends from an altitude of 90 meters proceeding down a 3° glide slope toward touchdown. The vortex axis is parallel to the runway centerline at an altitude of 30 meters. The displacement of the vortex-ground projection from the extended runway centerline was varied from run to run along with the value of circulation.

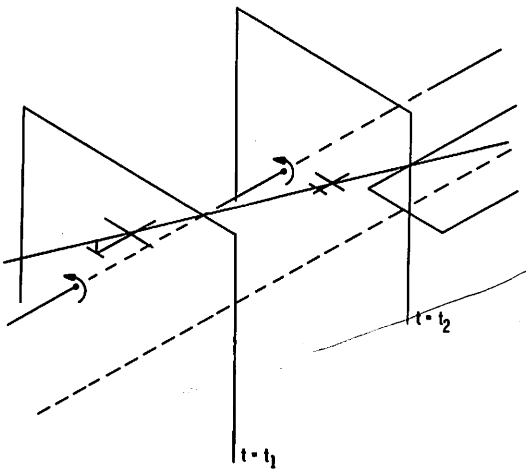

Figure 6. Geometry of simulation.

Figure 7 shows the projection of the aircraft's motion on a vertical plane normal to the vortex axis for a typical case. The case being simulated is that of a B-720 following a 3° glide slope influenced by a vortex with a strength of 460 meter²/sec which has been displaced a distance of 22.5 meters from the flight path. The wingspan of the B720 is 39.0 meters so that the closest approach of the wingtip to the vortex is about 3 meters. The induced roll angle is seen to be small until the wing passes through a region at about 8 meters radius where the roll angle becomes as great as 11°.

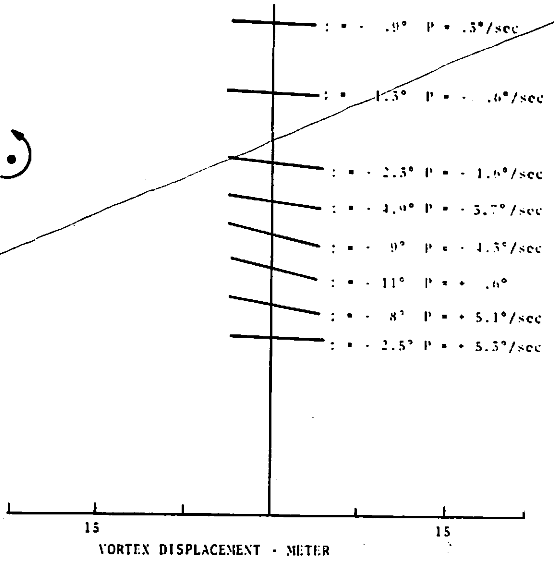

Figure 7. Typical simulation roll history.

The maximum roll angle, a quantity which correlated with pilot assessment of hazard in a previous simulation [7] is plotted as a function of the displacement of the vortex from the intended flight path in Figure 8. It is seen that the roll upset caused by the vortex falls off rapidly with distance from 22.5 meters; the maximum induced roll angle is not a monotonic function of displacement of the vortex axis from the intended flight path since lateral motion makes the actual displacement during the simulation impossible to control. Only the data from 22.5 meters to 37.5 meters is plotted. Two values for the hazard criteria, 7° and 10° maximum roll angle, were applied to the maximum roll angle curve in Figure 8. Because of the steepness of the curves in this region, the value of hazard extent obtained for the two values of criteria agree to within one meter. For the B720 this method gives a value for the hazard extent of 25 meters.

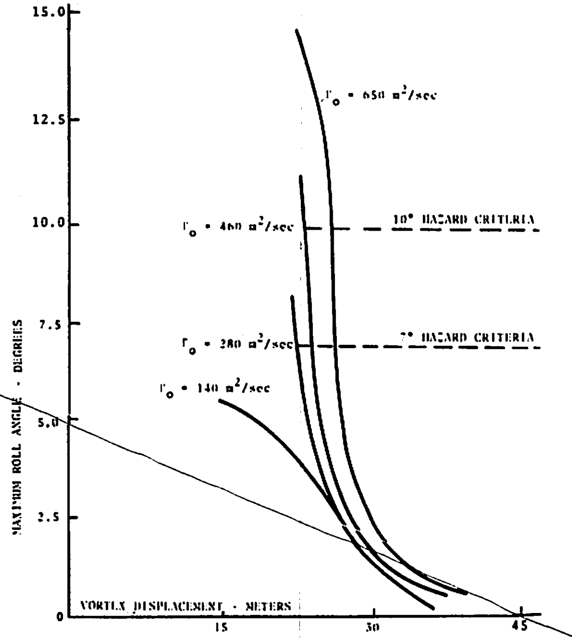

Figure 8. Maximum induced roll moment versus aircraft displacement.

CONCLUSIONS

Two different methods were used to determine the hazard extent about trailing wake vortices. One method used a static calculation of the rolling moment induced on a generic aircraft in the proximity of a vortex. The hazard extent is dependent upon the choice of hazard criteria for the larger span aircraft; a value of 30 meters for the hazard extent encompasses all of the aircraft in todays aircraft mix and those presently under design. One advantage the dynamic simulation has over the static calculation is that the hazard criterion is based on the total upset that occurs over the encountering period. It is seen, however, that both methods give similar results which is a consequence of the fact that the vortex-induced moments fall off rapidly when the following aircraft wing tip is displaced more than 5 meters from the vortex.

It should be pointed out that the concept of hazard extent is only applicable to a system which predicts that vortices move outside of a corridor or die completely in a certain period of time. For more sophistocated systems predicated on vortex decay, a more comprehensive definition of vortex hazard will have to be employed. Such a definition would have to include consideration of minimal upsets produced by central encounters for various classes of aircraft.

REFERENCES

1. Andrews, W.H., Robinson, G.H., and Larson, R.R., "Exploratory Flight Investigations of Aircraft Response to the Wing Vortex Wake of Jet Transport Aircraft," NASA TN 6655, Mar. 1972.

2. Andrews, W.H., Tymczyszyn, J.J., Jacobsen, R.A., and Drinkwater, F.J., "Flight Investigation of the Response of Wide-Body Tri-Jet to the Wing Vortex Wake Generated By Large Transport Aircraft," FWP-35, Feb. 1973, NASA Flight Research Center, Edwards, CA.

3. Hallock, J.N., Wood, W.D., and Spitzer, E.A., "Vortex Advisory System," Proceedings of Seventh Conference on Aerospace and Aeronautical Meteorology and Symposium on Remote Sensing from Satellites, American Meteorological Society, Melbourne, FL, Nov. 1976.

4. Hallock, J.N., Wood, W.D., and Spitzer, E.A., "The Motion of Wake Vortices in the Terminal Environment," Proceedings of the AIAA/AMS Sixth Conference on Aerospace and Aeronautical Meteorology, El Paso, TX, 1974.

5. Hallock, J.N. and Wood, W.D., "Joint US/UK Vortex Tracking Program at Heathrow International Airport," FAA-RD-76-58, Mar. 1976, Transportation Systems Center, Cambridge, MA.

6. Heaslet, M.A. and Spreiter, J.R., "Reciprocity Relations in Aerodynamics," NACA Report 1119, 1953.

7. Sammonds, R.T., Stinnett, G.W., and Larsen, W.E., "Wake Vortex Encounter Hazard Criteria for Two Aircraft Classes," NASA TM X-73,113, June 1976.

8. Barrows, T.M., "Simplified Methods of Predicting Aircraft Rolling Moments Due to Vortex Encounters," AIAA paper 76-61, AIAA 14th Aero-space Sciences Meeting, Washington, DC, Jan. 1976.

9. Eggleston, J.M. and Diederich, F.W., "Theoretical Calculation of the Power Spectra of the Rolling and Yawing Moments on a Wing in Random Turbulence," NACA Report 1321, 1957.

10. Harlan, R.B. and Madden, S.J., "Hazard Definition for Wake Turbulence Encounter, During Terminal Area Operations," MIT-MSL-RE-81, Mar. 1973, MIT Measurements Systems Lab., Cambridge, MA.

SOME REMARKS ON AIRCRAFT WAKE VORTEX ANALYSIS

K.K. BOFAH
Aerodynamic Research Unit
Boeing Commercial Airplane Company
Seattle WA 98124

ABSTRACT: Analysis techniques for aircraft trailing vortices are presented. Employing vortex theories by Saffman and Moore, predictive methods for vortex-induced rolling moments and coalescence time for a vortex pair are obtained. The predictions compare favorably with published data in the far field.

NOMENCLATURE

A	wing aspect ratio
a	wing sectional lift-curve slope
b	wing span
C_L	wing lift coefficient
C_{ℓ_v}	vortex induced rolling-moment coefficient: rolling moment/ $(1/2\rho U^2 Sb)$
$C_{\ell,\delta_{max}}$	maximum available roll control
C_0	rolling moment parameter
D	vortex hazard index
h	point vortex distance from wall
l	vortex center distance
M	number of sectors per quadrant
N	number of dividing circles
P	roll rate
r	radial coordinate
r_1	vortex core radius
r_0	vorticity radius
S	wing reference area
s	point vortex-pair separation distance
T	period of vortex pair rotation
t	time (vortex age)
U	wing speed or free-stream velocity
V_1	maximum tangential velocity
x	downstream distance
$\bar{y}$	center of gravity (y coordinate)
α	vortex pair strength ratio
Γ	circulation
Γ_1	vortex core circulation
Γ_0	wing-root circulation or vortex strength
ζ_1	nondimensional core radius
ζ_0	nondimensional vorticity radius
ξ,η	cartesian coordinates
Θ	ellipse major-to-minor axes ratio
Θ_c	critical axes ratio
λ	wing-taper ratio
ρ	fluid density
Φ	function (Equation 10)
ϕ	distance ratio (Equation 14)
ν	kinematic viscosity
χ	function (Equation 3)
σ	constant.

Subscripts

f	vortex-penetrating airplane
g	vortex-generating airplane
m	merging of vortex pair.

INTRODUCTION

The hazard of trailing vortices to other aircraft is largely due to severe rolling moments induced by the vortex. The severity of the induced rolling moments depends on the flow characteristics of the wake vortex and design loading characteristics of the encountering wing. In addition to these factors, the hazard index is a function of roll control power available, pilot input, dynamic response of the encounter airplane and also ground proximity. Atmospheric turbulence and vortex instability are also important in defining the wake vortex hazard. Treatment of the vortex encounter problem, where all these factors and others can be considered, appears to be formidable. Various treatments of the problem can be found in references 1 and 2. A recent paper by Nelson [3] treats the dynamic response of an aircraft encountering a vortex system. Bisgood, Maltby and Dee [2] and Condit and Tracy [2] use an eddy viscosity vortex model to calculate roll rate and rolling moments.

In the first part of this paper a turbulent vortex model by Saffman [4] is used to calculate induced rolling moments by employing a simple two-dimensional strip theory. The calculation is valid for large downstream distances where vortex sheet roll-up and multiple vortex merging are complete. Agreement with data is quite encouraging.

There is some experimental evidence that vortex merging leads to reduction in induced-rolling moments [5]. The second part of the paper examines the coalescence of a vortex pair. Estimates of time for complete mergence are obtained and found to compare favorably with data.

TRAILING VORTEX THEORY OUTLINE

For convenience, pertinent results of trailing vortex theories by Saffman and Moore [6-8] are summarized below. The theory assumes a circular axisymmetric vortex and is valid in the far field where a well behaved counterrotating vortex pair exists.

Laminar Vortex.

In a laminar vortex that trails behind an elliptically loaded wing, the maximum tangential velocity is given by [7]

$$v_1 = 0.19\,\Gamma_0\,b^{-\frac{1}{2}}\,(\nu t)^{-\frac{1}{2}}$$

at a radius $r_1=2.92(\nu t)^{\frac{1}{2}}$. Here ν is the kinematic viscosity, t is vortex age, b is the wing span and Γ_0 is the wing root circulation. The theory is valid for light loading and/or far downstream distances. The usual relation $t=x/U$ (where x is the distance downstream and U is the wing speed) is thus applicable. In non-dimensional terms, the maximum tangential velocity is [7]

$$\frac{V_1}{U}\left(\frac{\Gamma_0}{Ub}\right)^{-1} = 0.19\left[\frac{\nu}{\Gamma_0}\left(\frac{\Gamma_0}{Ub}\right)\left(\frac{x}{b}\right)\right]^{-\frac{1}{2}}, \quad (1)$$

and the core radius becomes [7]

$$\frac{r_1}{b} = 2.92\left[\frac{\nu}{\Gamma_0}\left(\frac{\Gamma_0}{Ub}\right)\left(\frac{x}{b}\right)\right]^{\frac{1}{2}}. \quad (2)$$

The quantity Γ_0/ν is the Reynolds number. For an elliptically loaded wing,

$$\frac{\Gamma_0}{Ub} = \frac{2}{\pi}\,\frac{C_L}{A},$$

where C_L is the wing lift coefficient and A is the aspect ratio.

Turbulent Vortex.

The mean circulation distribution in a turbulent vortex is given in three radial regions as follows [4]:

$$\Gamma = \Gamma_1\,\frac{r^2}{r_1^{\,2}}, \quad r < r_1,$$

$$\Gamma = \Gamma_1\left(\ell n\,\frac{r}{r_1} + 1\right), \quad r_1 < r \ll r_0,$$

and

$$\Gamma = \Gamma_0 + \Gamma_1\left[\ell n\,\frac{r}{r_0} + 1 - x(t)\,\frac{r}{r_0} + \left\{x(t) - 1\right\}\frac{r^2}{r_0^{\,2}}\right],$$

$$r_1 < r < r_0. \quad (3)$$

For an elliptic wing,

$$x = \frac{1}{30}\,\frac{b^2}{r_0^{\,2}}\,\frac{\Gamma_0}{\Gamma_1} \to 0 \text{ as } t \to \infty.$$

The circulation distribution is characterized by an overshoot [4] which is believed to be a feature of the turbulent vortex. The existence of an overshoot would imply instability which could be beneficial (in hazard context) to an early demise of the vortex. However, this feature has not been satisfactorily observed in experiments. The vortex core radius where $\Gamma=\Gamma_1$ and the outer edge radius where $\Gamma=\Gamma_0$ are, respectively

$$r_1 \doteq 2\ (\nu\Gamma_1)^{1/4}\ t^{1/2}, \tag{4}$$

and

$$r_0 \doteq \tfrac{1}{2}\ (\Gamma_1 t)^{1/2}. \tag{5}$$

Putting $t = x/U$, the core radius in nondimensional terms becomes [4]

$$\frac{r_1}{b} = 2\left(\frac{\Gamma_0}{\Gamma_1}\right)^{-1/4}\left(\frac{\Gamma_0}{\nu}\right)^{-1/4}\left(\frac{\Gamma_0}{Ub}\right)^{1/2}\left(\frac{x}{b}\right)^{1/2}. \tag{6}$$

The maximum tangential velocity, $V_1=\Gamma_1/2\pi r_1$, is [4]

$$\frac{V_1}{U}\left(\frac{\Gamma_0}{Ub}\right)^{-1} = \frac{1}{4\pi}\left(\frac{\Gamma_0}{\Gamma_1}\right)^{-3/4}\left(\frac{\Gamma_0}{\nu}\right)^{1/4}\left(\frac{\Gamma_0}{Ub}\right)^{-1/2}\left(\frac{x}{b}\right)^{-1/2}. \tag{7}$$

The ratio Γ_0/Γ_1 is weakly dependent on the Reynolds number Γ_0/ν and is given implicitly by [4]

$$\frac{\Gamma_0}{\nu} \doteq \left[4\ \exp\left\{\frac{\Gamma_0}{\Gamma_1} + \tfrac{1}{4}\ \ell n\ \frac{\Gamma_0}{\Gamma_1}\right\}\right]^4. \tag{8}$$

For most flight tests $\Gamma_0/\Gamma_1\approx2$. In the range $10^5<\Gamma_0/\nu<10^8$,

$$\frac{\Gamma_0}{\Gamma_1} \approx \frac{2}{9}\ \ell n\ \frac{\Gamma_0}{\nu} - 1.16. \tag{9}$$

The theory is valid after the vortex sheet roll-up is complete; for a turbulent vortex $x/b \geqslant 0.2\ Ub/\Gamma_0$, and for a laminar vortex $x/b \geqslant 0.5\ Ub/\Gamma_0$.

The vortex theory outlined above reveals the scaling parameters that characterize the flow and may be used in correlating vortex data. In this light, NAFEC (National Aviation Facilities Experimental Center) tower-fly-by data [9-12] are examined to see if any information of interest may be gleaned from them. The peak tangential velocities are plotted in Figure 1 according to the nondimensional parameters in Equation (1). There is large scatter in the data. However, it is interesting to note that the 747 data demonstrate a plateau region; a feature that was not indicated quite well in the original NAFEC analysis.

Further, the data for the 727, DC7 and DC9, which do not adequately cover the plateau region, all fall between the laminar and turbulent predictions. The DC9 data extend to large downstream distances. Observe that, after 120-span lengths downstream, the scatter in the data reduces substantially and the decay rate then follows the $x^{-1/2}$ turbulent decay law. It is, perhaps, plausible to suppose that the vortex undergoes a laminar-turbulent transition. Reliable data (by laser-Doppler velocimeter) will be necessary for any definite conclusions.

VORTEX-INDUCED ROLLING MOMENTS

In the proximity of a vortex, a lifting wing experiences a change in lift distribution due to the vortex induced velocities. The change in lift distribution results in an induced rolling moment on the wing. Reasonable estimates of the induced rolling moments can be made by use of simple two-dimensional strip theory. Assume a thin wing (with taper ratio λ) encounters a turbulent vortex that possesses the flow characteristics outlined above. Then, for an encounter where the wing is centered on the vortex axis, the rolling-moment coefficient can be easily calculated. It is

$$C_{\ell_v} = \frac{a}{2\pi}\,\frac{2}{1+\lambda}\left(\frac{\Gamma_1}{\Gamma_0}\right)\left(\frac{U_g}{U_f}\right)\left(\frac{b_g}{b_f}\right)\left(\frac{\Gamma_0}{Ub}\right)_g \Phi\ (\zeta_1), \tag{10}$$

where

$$\Phi(\zeta_1) = \left[1/3 - 1/4\ (1-\lambda)\right]\zeta_1^{-2},\quad \zeta_1 > 1\ ,$$

and

$$\begin{aligned}\Phi(\zeta_1) = {} & 1/3\,\zeta_1 - \ell n\ \zeta_1 - 1/4\ (1-\lambda)(1 - 2\ \ell n\ \zeta_1) \\ & - \Big[1/2x\ (1-\zeta_1^{2})\ \zeta_0^{-1} - 1/3\ \Big\{(x-1)\ \zeta_0^{-2} \\ & + x(1-\lambda)\ \zeta_0^{-1}\Big\}(1-\zeta_1^{3}) \\ & + 1/4\ (1-\lambda)\ (x-1)\ (1-\zeta_1^{-4})\ \zeta_0^{-2}\Big],\quad \zeta_1 < 1.\end{aligned}$$

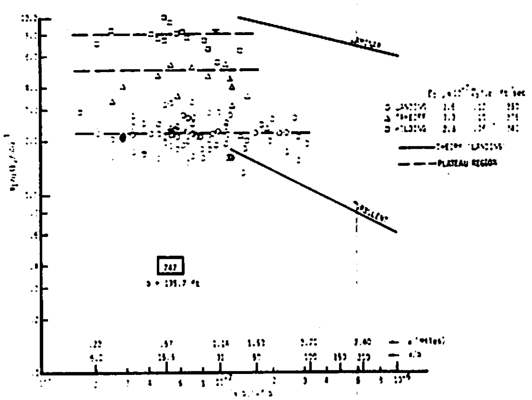

Figure 1a. Dimensionless peak tangential velocities in trailing vortices of Boeing 747.

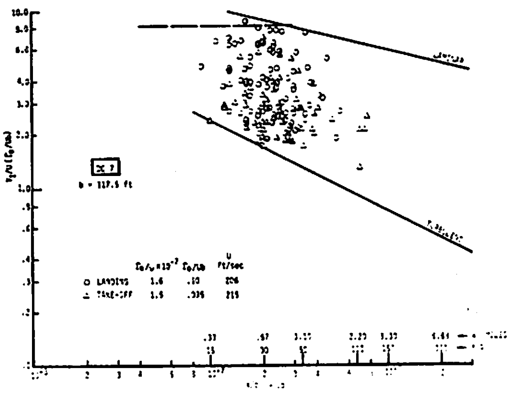

Figure 1c. Dimensionless peak tangential velocities in trailing vortices of Douglas DC-7.

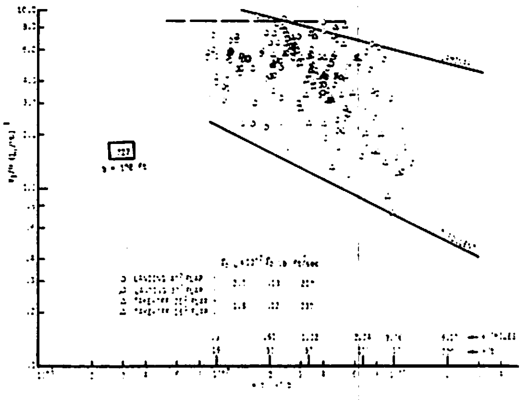

Figure 1b. Dimensionless peak tangential velocities in trailing vortices of Boeing 727.

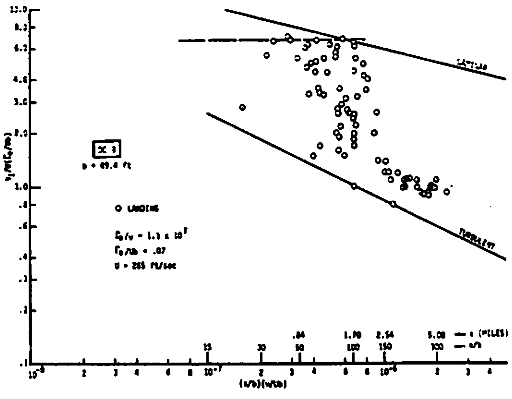

Figure 1d. Dimensionless peak tangential velocities in trailing vortices of Douglas DC-9.

The roll rate P can be obtained as

$$\bar{P} = \frac{b_f P}{2U_f} = \frac{1}{\pi}\left[1/3 - 1/4\ (1 - \lambda)\right]^{-1}$$

$$\left(\frac{\Gamma_1}{\Gamma_o}\right)\left(\frac{\Gamma_o}{Ub}\right)_g\left(\frac{U_g}{U_f}\right)\left(\frac{b_g}{b_f}\right)\Phi(\zeta_1).$$

Further, $\zeta_1 = 2r_1/b_f$ and $\zeta_0 = 2r_0/b_f$ are the vortex core and outer edge diameters nondimensionalized by the encountering wing span b_f. U_f is the encounter speed and a is the wing sectional lift-curve slope. The lift-curve slope is a function of the wing aspect ratio A. An appropriate expression for the strip theory is uncertain. The aspect ratio dependence may be put in the form

$$a = \frac{2\pi A}{A+2n},\quad n = 0,\ 1,\ 2,\ 3.$$

The case n=0 gives the two-dimensional value; n=1 is the elliptic wing correction. Rolling moment analysis by Barrows [13] leads to n=2 and Rossow [1] uses n=3 in his analysis in the near field. To be conservative, the elliptic wing correction is used here.

In Figure 2 published data [14-17] are compared to the theoretical prediction (Equation 10). Despite the approximate nature of the theory, the agreement with data is fairly good for x/b>13. The far field deviation of theory from the data could be partially due to failure to achieve axial penetration. Furthermore, a body inserted in a vortex core is bound to alter the vortex structure; vortex meandering occurs and vortex breakdown may even be induced [18]. In flight tests, it is almost impossible to penetrate the vortex eye due to the tendency of the airplane to be swept out of the vortex core [3]. It is noted in reference 17 that in the C54/PA-28 test (Figure 2) only 80-90 percent of the rolling moment could be measured. This is roughly of the same order of magnitude as the discrepancy between the data and theory.

All far-field data considered are presented as a single plot in Figure 3. The data are for λ=1. The rolling moment parameter $\Phi = C_{\ell_v}/C_0$ is plotted against ζ_1, where

$$C_o = \frac{a}{2\pi}\left(\frac{2}{1+\lambda}\right)_f\left(\frac{\Gamma_1}{\Gamma_o}\right)_g\left(\frac{\Gamma_o}{Ub}\right)_g\left(\frac{U_g}{U_f}\right)\left(\frac{b_g}{b_f}\right).$$

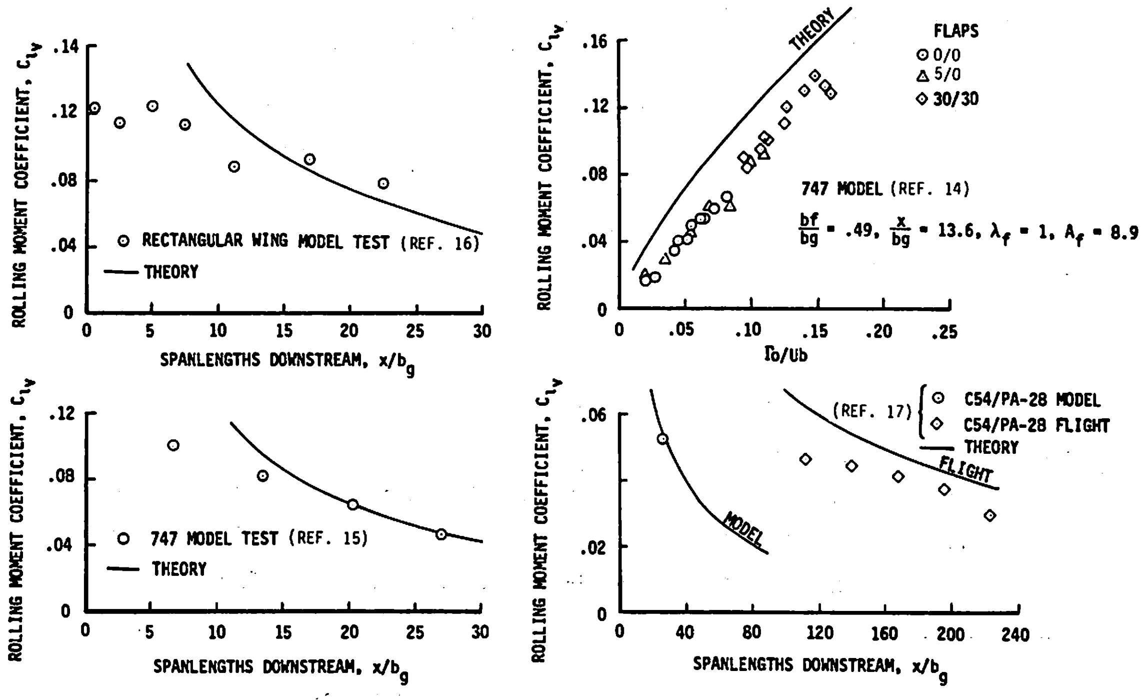

Figure 2. Comparison of vortex induced rolling-moment data with theory.

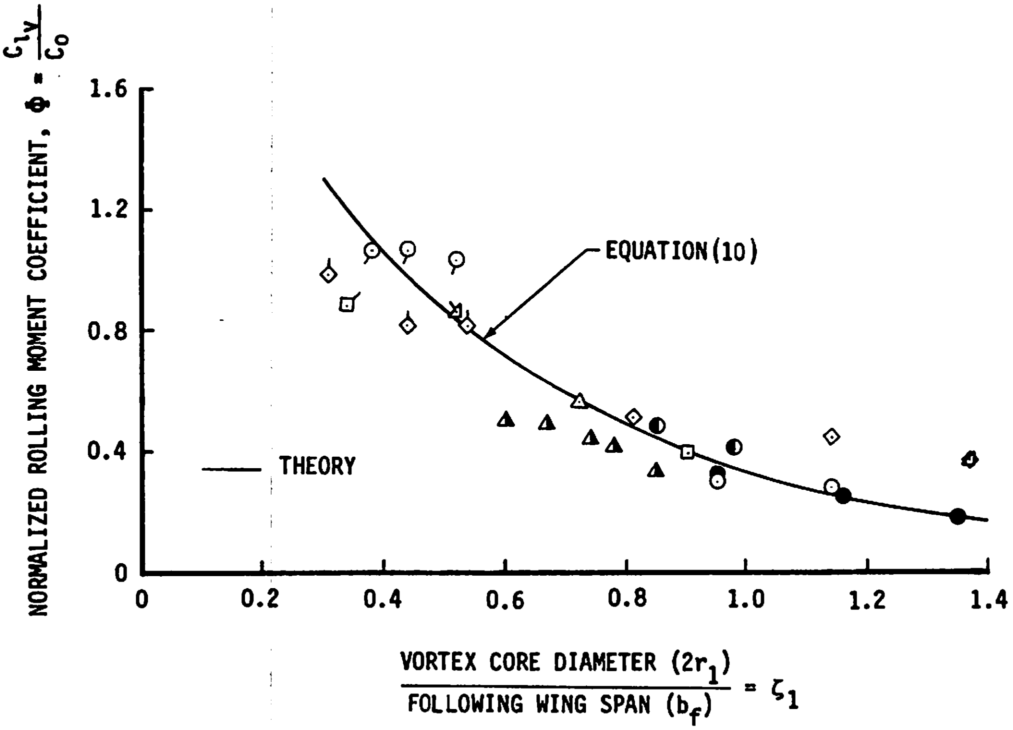

Figure 3. Correlation of rolling-moment theory, flight and model data.

SYM	$\frac{\Gamma o}{\nu} \times 10^{-6}$	$\frac{\Gamma o}{Ub}$	$\frac{b_f}{b_g}$	$\frac{U_f}{U_g}$	b_g m.	A_g	A_f	U_g m/sec	TEST	REF.
⚲	.37	.11	.476	1	1.79	6.96	8.7	27.4	747/RECT.	10
○	.37	.11	.182	1	↓	↓	5.45	↓	MODEL	↓
◈	.79	.11	.476	1			8.7		↓	
◇	.79	.11	.182	1			5.45			
⊠	.37	.11	.476	1			8.7			
◿	.37	.11	.182	1			5.45			
⊡	.54	.11	.476	1			8.7	40.		
□	.54	.11	.182	1			5.45	40.		
●	.37	.11	.182	1			5.45	27.4		8
◐	.46	.10	.25	1	2.44	8	6.67	27.4	RECT./RECT. MODEL	9
△	.27	.054	.255	1	2.51	9.4	5.6	30.5	C54/PA-28 MODEL	11
▲	7.0	.057	.255	.8	35.81	9.4	5.6	59.2	C54/PA-28 FLIGHT	11

C54 IN CRUISE, ALL OTHERS IN LANDING CONFIGURATION.

TABLE 1. LEGEND TO FIGURE 3

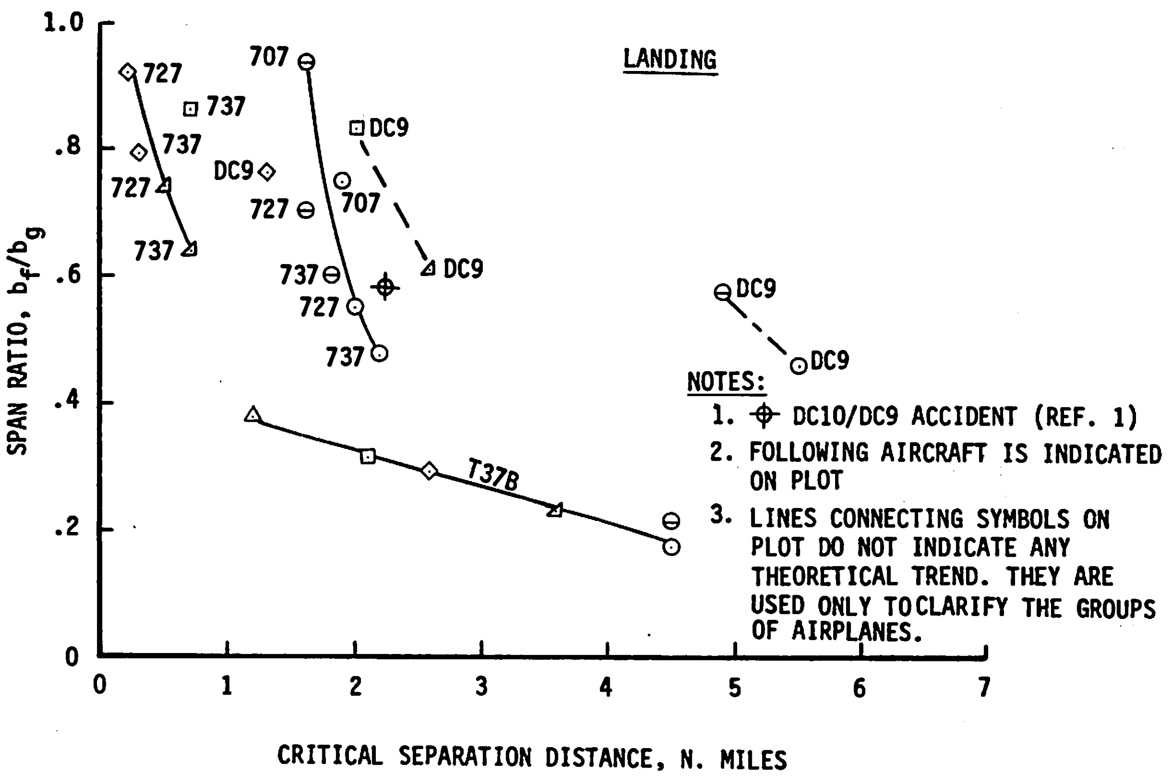

NOTES:

1. ⌖ DC10/DC9 ACCIDENT (REF. 1)
2. FOLLOWING AIRCRAFT IS INDICATED ON PLOT
3. LINES CONNECTING SYMBOLS ON PLOT DO NOT INDICATE ANY THEORETICAL TREND. THEY ARE USED ONLY TO CLARIFY THE GROUPS OF AIRPLANES.

Figure 4. Calculated critical aircraft separation distances.

SYM	VORTEX GENERATING AIRCRAFT	$\frac{\Gamma_o}{\nu} \times 10^{-7}$	$\frac{\Gamma_o}{Ub}$
⊙	747	3.6	.12
⊖	DC 10	3.5	.14
⊡	727	2.0	.13
⊿	707	2.4	.11
◇	DC 7	1.6	.10
△	DC 9	1.1	.07

FOLLOWING AIRCRAFT	SPAN, b_f FT.	AVAILABLE ROLL CONTROL $C_{l_\delta}\delta$ max
747	195.7	.068
707	145.8	.080
727	108	.092
737	93	.097
DC9	89.4	.067
T37B	33.8	.060
LEAR JET	34	.047

TABLE 2. LEGEND TO FIGURE 4

The plot indicates a reasonable correlation between model and flight test data, and the theory.

The simplest wake vortex hazard index may be defined as

$$D = \frac{C_{\ell_v}}{C_{\ell_\delta}\,\delta_{max}},$$

where $C_{\ell_\delta}\delta_{max}$ is the maximum available roll control of the penetrating airplane. Vortex encounter is unsafe if $D \geq 1$. Employing this simple criterion in conjunction with the rolling moment prediction, estimates of critical separation distances for various airplane combinations are obtained. The results appear on Figure 4 for landing configuration using mean values of Γ_0/ν and Γ_0/Ub from the NAFEC data. It should be emphasized here that the results are approximate and are for comparison purposes only. The wake vortex hazard is far more complicated than the simple picture given here. The vortices are not usually in the calm organized state as assumed. Complex effects of atmospheric turbulence, vortex instabilities, etc., need to be considered. Ground proximity, pilot input, and the airplane response to vortex encounter are all important in defining the vortex hazard.

COALESCENCE OF A VORTEX PAIR

A vortex pair shed by a flapped wing (Figure 5a) will eventually coalesce if the two vortices have a tendency to rotate about each other. The relative motion of the vortex pair can be studied by considering the motion of a point vortex pair in the presence of a wall as shown in Figure 5b. From the energy and impulse invariants of the equations of motion, the relative motion of the vortex pair can be easily obtained (see for example page 127 of reference 19). The path of the relative motion is

$$\xi^2 = \frac{\left(\bar{y} - \frac{2}{1+\alpha}\eta\right)^{\alpha}\left(\bar{y} + \frac{2\alpha}{1+\alpha}\eta\right)^{1/\alpha}\left(\bar{y} + \frac{\alpha-1}{\alpha+1}\eta\right)^{2} - \sigma^2\eta^2}{\sigma^2 - \left(\bar{y} - \frac{2}{1+\alpha}\eta\right)^{\alpha}\left(\bar{y} + \frac{2\alpha}{1+\alpha}\eta\right)^{1/\alpha}} . \qquad (11)$$

Here $\alpha = \Gamma_1/\Gamma_2$ is the strength ratio of the two vortices; $\bar{y}$ is the y coordinate of their center of gravity and is invariant, and σ^2 is a positive constant determinable from known coordinates of the vortex pair. It is interesting to observe that the streamlines of a counter-rotating equistrength vortex pair can be obtained from Equation (11) by requiring $\alpha \rightarrow \infty$.

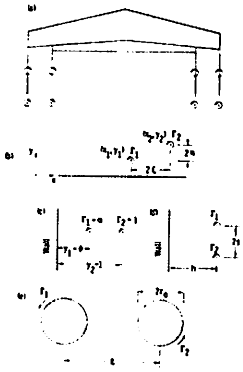

Figure 5. Vortex pair configurations
- a) Two vortex pair behind a flapped wing.
- b) Vortex pair in the presence of a wall.
- c) Point vortex pair in a plane normal to the wall.
- d) Point vortex pair in a plane parallel to the wall.
- e) Vortex pair with uniform vorticity core.

Depending on the value of σ^2, Equation (11) describes one of two cases of motion: cyclic or non-cyclic motion. In the former type of motion, the two vortices rotate about each other at all times. In the latter case, the vortices go on diverging paths. A necessary condition for cyclic motion is that at $\eta = 0$,

$$\sigma^2 > \bar{y}^{\alpha + \frac{1}{\alpha}}, \qquad (12)$$

and, of course, $\bar{y} > 0$. Acton [20] uses Equation (12) as a sufficient condition for cyclic motion. It is incorrect; it is true only when $\alpha = 1$ where the path (Equation (11)) is symmetric about both η and ξ axes. If $\alpha = 1$, an additional condition is necessary for cyclic motion. Sufficient conditions for all α can be obtained by use of elementary algebra to examine the roots of Equation (11). The results follow.

First, $\alpha > 0$. The sufficient condition for cyclic motion is

$$\sigma^2 > \alpha^{\alpha}\left(\frac{1+\alpha}{1+\alpha^2}\right)^{\alpha + \frac{1}{\alpha}} \bar{y}^{\alpha + \frac{1}{\alpha}} . \qquad (13)$$

Consider an initial configuration where the two vortices lie in a plane normal to the wall (Figure 5c). Put $y_1/y_2=\phi$ (≤ 1). Then

$$\bar{y} = \frac{1+\alpha\phi}{1+\alpha} \quad \text{and} \quad \sigma^2 = \phi^\alpha \left(\frac{1+\phi}{1-\phi}\right)^2 .$$

Equation (13) then becomes

$$\left(\frac{1+\phi}{1-\phi}\right)^2 > \left(\frac{\alpha}{\phi}\right)^\alpha \left(\frac{1+\alpha\phi}{1+\alpha^2}\right)^{\alpha+\frac{1}{\alpha}} . \tag{14}$$

Now for $\alpha<0$. A general solution for σ^2 appears difficult. However, for the same initial configuration above, the sufficiency condition can be easily obtained. For $-1<\alpha<0$, the sufficient condition for cyclic motion is

$$\alpha < -\frac{3\phi + \phi^3}{1 + 3\phi^2} \tag{15}$$

This condition can also be obtained by inspection of the initial induced velocities.

Note that the dividing boundary for cyclic motion in the (α',ϕ') plane where $/\alpha'/>1$ may be obtained by a simple transformation of the boundary in the (α,ϕ) plane where $/\alpha/<1$. By virtue of the physical nature of the problem, there exist identical paths in both regions. The transformation is

$$\alpha' = \frac{1}{\alpha} \text{ and } C' = C,$$

where

$$C = \sigma^2 \, \bar{y}^\alpha + \frac{1}{\alpha} .$$

Observe that the transformation leaves Equation (13) unchanged. The required boundary for $\alpha<-1$ is obtained by applying the transformation to Equation (15).

An initial configuration of interest is the case where the vortices lie in a plane parallel to the wall. This is equivalent to vortices behind a biplane. Let the vortices be at a distance 2s apart and h from the wall (Figure 5d), then $\sigma^2=(1+h^2/s^2)$ and $\bar{y}=h$. For $\alpha>0$, the cyclic motion condition is given by

$$\frac{s}{h} > \left[\alpha^\alpha \left(\frac{1 + \alpha}{1 + \alpha^2}\right)^{\alpha + \frac{1}{\alpha}} - 1\right]^{-\frac{1}{2}} . \tag{16}$$

Note that Equation (16) remains unchanged if α is replaced by $1/\alpha$ as should be expected. In fact one needs to consider $/\alpha/\leq 1$ only. For $-1<\alpha<0$, the dividing boundary for cyclic motion can be obtained through the following parametric relation:

$$\alpha = -\frac{3\phi + \phi^3}{1 + 3\phi^2} , \quad 0 < \phi < 1 ,$$

$$\frac{s}{h} = \left[\phi^\alpha \left(\frac{1 + \phi}{1 - \phi}\right)^2 \left(\frac{1 + \alpha\phi}{1 + \alpha}\right)^{-\alpha - \frac{1}{\alpha}} - 1\right]^{-\frac{1}{2}} . \tag{17}$$

Figure 6 presents charts (similar to that by Donaldson and Bilanin [21]) for determining cyclic and noncyclic motion of a vortex pair according to the sufficient conditions above. The region of cyclic motion lies to the left of the arrow direction. The broken line is Equation (12) which appears to be adequate when α is in the neighborhood of unity. Typical paths of motion relative to the center of gravity are presented in Figure 7. Wall effect on the relative motion for $\alpha=1$ is shown in Figure 8 where the major to minor axes ratio Θ is plotted against the distance ratio ϕ. In the absence of the wall, the vortex pair rotates around each other on the same circular path ($\Theta=1$). Figure 8 indicates the wall presence is not felt by the vortices until $\phi\leq .6$, where $\Theta=1.05$ approximately.

Effects of Finite Core.

The analysis given above is not adequate in describing vortex pair interaction in a real flow. In a real fluid, a vortex is characterized by a finite core of vorticity. The vortex pair will coalesce if the vortices are in close enough proximity. Numerical calculations by Roberts and Christiansen [22] and Rossow [23] demonstrate the vortex merging phenomenon. Moore and Saffman's [6, 8] analytical studies of vortex motion in a straining field give a reasonable estimate of the critical separation distance of the vortex pair. Appendix A of reference 8 treats the case of an equistrength vortex pair with uniform vorticity. The analysis can be generalized to include two vortices of unequal strength.

Consider two circular vortices having

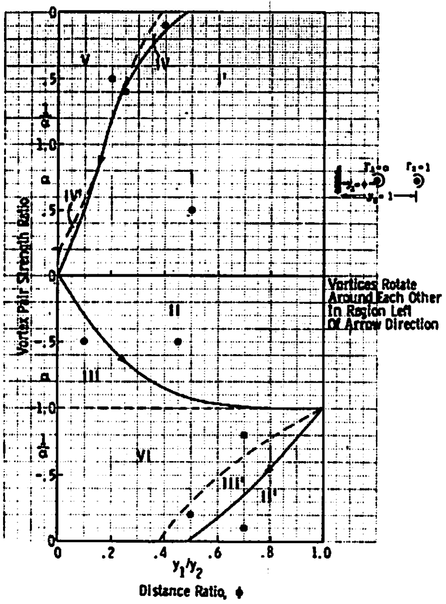

Figure 6a. Regions of cyclic and non-cyclic motions of a vortex pair near a wall. Vortex pair initially lies in a plane normal to the wall (as in Figure 5c).

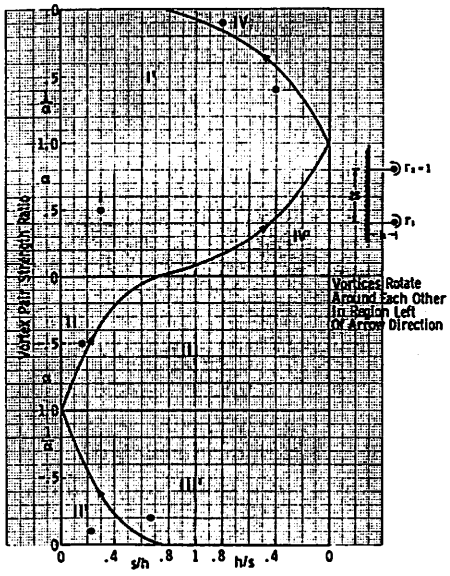

Figure 6b. Regions of cyclic and non-cyclic motions of a vortex pair near a wall. Vortex pair initially lies in a plane parallel to the wall (as in Figure 5d).

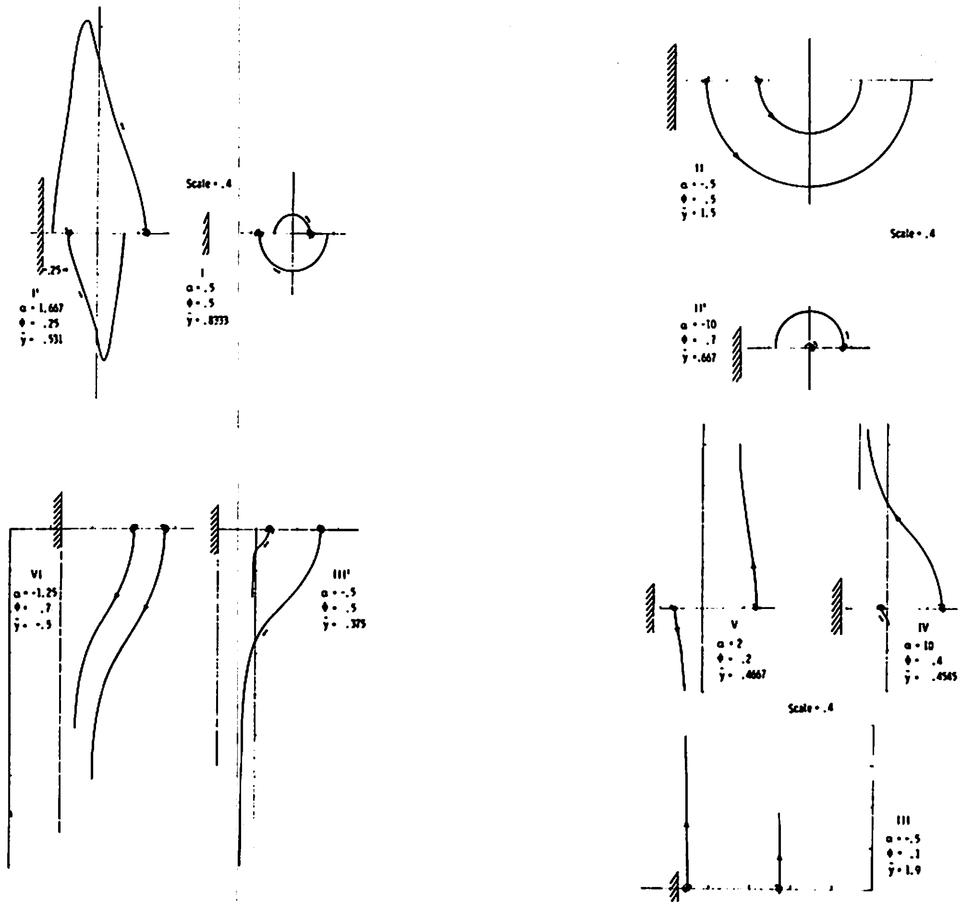

Figure 7. Relative motions of vortex pair.

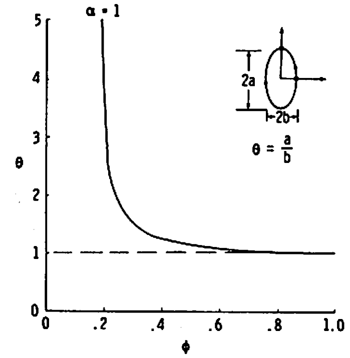

Figure 8. Wall effect on equistrength vortex pair.

radius r_0 and strengths Γ_1 and Γ_2. Let the vortex centers be l apart (Figure 5e). Then the analyses in references 6 and 8 show the circular vortex in the straining field of the other will deform into an ellipse with major to minor axes ratio $\Theta(>1)$, where

$$\frac{\Theta + 1}{\Theta - 1} + 1 + \alpha = 2\left(\frac{\ell^2}{r_o^2} - 1 - \alpha\right)\frac{\Theta}{\Theta^2 + 1} \tag{18}$$

with the major axes along the vortex centers. Here $\alpha = \Gamma_1/\Gamma_2$ is the vortex strength ratio. Equation (18) has two or no solutions. Moore and Saffman's stability analysis [6] further shows that the more elongated ellipse of the two solutions (when they exist) is unstable to two-dimensional disturbances. Equation (18) has real roots $(\Theta>1)$ if

$$2\left(\frac{\ell^2}{r_o^2} - 1 - \alpha\right) > \frac{3(2 + \alpha)\,\Theta_c^2 - 2\alpha\Theta_c + 2 + \alpha}{2\Theta_c - 1}. \tag{19a}$$

where

$$(2 + \alpha)\Theta_c^4 - 2(2 + \alpha)\Theta_c^3 - 2\Theta_c^2 + 2\alpha\Theta_c - \alpha = 0. \tag{19b}$$

Here Θ_C is the critical axes ratio. When relation (19) is satisfied, the circular vortex deforms into an ellipse that can persist in the straining field, otherwise it will disintegrate or amalgamate with the other vortex. As given in reference 8, for $\alpha=1$ and $\Theta_C=2.2$, $2r_0=1.43$ which compares favorably with Roberts and Christiansen's [22] value of 1.7. Rossow [23] gives a value of 1.9 and points out that the discrepancy might be due to the few point vortices used to simulate the vortex core. Appropriate discretization of the vortex core resolves the discrepancy.

NUMERICAL CALCULATION

The circular core of uniform vorticity (unit radius and unit strength) is divided into N anulii of equal net vorticity. The radii of the dividing circles (Figure 9) are given by

$$r_j = (j/N)^{\frac{1}{2}}, \quad j = 1, 2, \ldots N.$$

Each quadrant is then divided into M sectors of equal net vorticity. The resulting discrete regions then have equal net vorticity $\Gamma_j=(4MN)^{-1}$ and is represented by a point vortex of equal strength located at the vorticity centroid,

$$r_j = \frac{8}{3\pi}\left[j^{\frac{3}{2}} - (j - 1)^{\frac{3}{2}}\right]\frac{M}{N^{\frac{1}{2}}}\sin\left(\frac{\pi}{4M}\right).$$

Thus, each vortex is represented by an array of 4MN point vortices. The motion of the point vortices are followed in time by integrating numerically the usual differential equations of motion. In the calculations presented here, N=M=3 (the same number of point vortices used by Rossow) and a fourth-order Runge-Kutta integration scheme is used on the CDC-6600 computer. Time is normalized by the period of revolution of the vortex pair at initial separation distance. Thus,

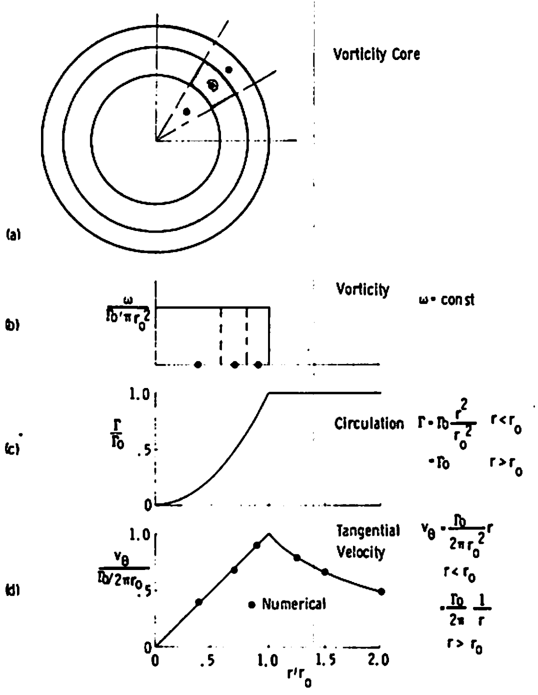

Figure 9. Uniform vorticity core vortex model.
a) Discretization of vorticity core.
b) Uniform vorticity distribution.
c) Circulation distribution.
d) Tangential velocity distribution.

$$t^* = t/T,$$

where $T=4\pi^2\ell^2/(\Gamma_1+\Gamma_2)$. Distances are normalized with ℓ. When the two vortices are identical in strength and diameter, reflectional symmetry is used to save computer time. No recipe for surpressing chaotic motion of the point vortices is used. Computation accuracy is checked by evaluating the center of gravity and energy invariants of point vortex motion. These invariants remained constant at all times considered.

Figure 10 presents typical computer runs. A numerically obtained merging boundary in the (α, $\ell/2r_0$) plane is shown on Figure 11a along with the analytical stability boundary from Equation (19). For $\alpha=1$, the critical separation distance $\ell/2r_0 \approx 1.65$. This is consistent with the 1.7 value obtained by Roberts and Christiansen's more sophisticated vortex code approach. According to this analysis, Rossow's point vortices [23] represent a vortex diameter 10 percent larger than the diameter used.

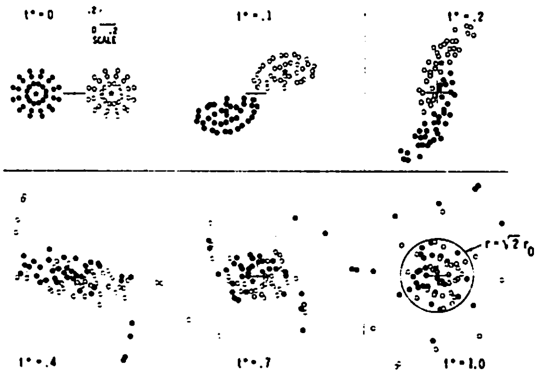

Figure 10a. Numerical calculation of vortex pair interaction ($\alpha=\Gamma_1/\Gamma_2=1$, $\ell/2r_0=1.43$).

When the two vortices do not merge, they deform into ellipses and precess around each other. The predicted deformed ellipse (Equation (18)) is shown to agree quite well with the numerical shape (Figure 10b). The wall effect on the merging boundary is shown in Figure 11b for an equistrength vortex pair. As in the case of the point vortex pair, the wall effect is negligible until $\phi \leq .6$ (roughly). Unequal vortex diameters do not change the merging boundary. However, when merging occurs, the larger vortex wraps around the smaller vortex in a spiral faction as illustrated in Figure 10c. This type of deformation also occurs when one vortex is much weaker than the other.

Note (Figure 10a) the circularization of the merged vortical region at $t^*=1$; merging may be considered essentially complete here. If it is assumed that the vortex pair merges to form a single circular vortex, the vortical area invariance gives the radius of the merged vortex to be $\sqrt{2}r_0$. To conserve angular momentum, the merged vortex must necessarily be centered on the center of gravity of the vortex pair. The rate of concentra-

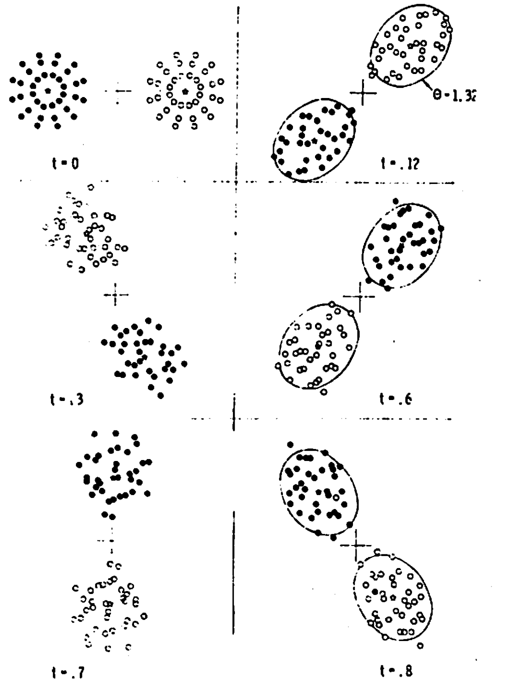

Figure 10b. Numerical calculation of vortex pair interaction ($\alpha = 1$, $\ell/2r_0 = 1.7$).

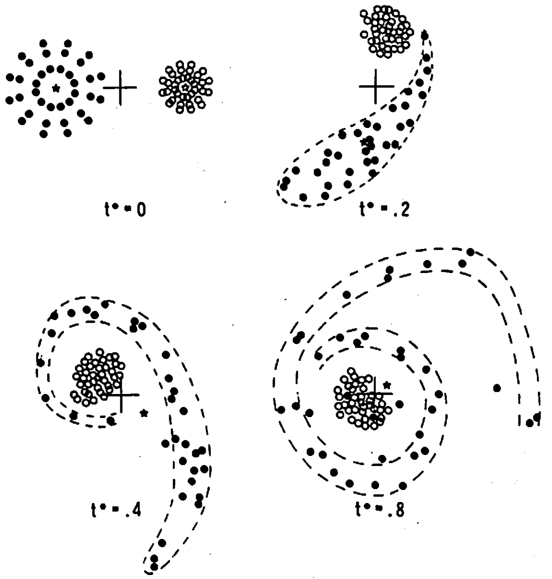

Figure 10c. Numerical calculation of vortex pair interaction ($\alpha = 1$, $(\ell/2r_0)_1 = 2.5$, $(\ell/2r_0)_2 = 1.25$).

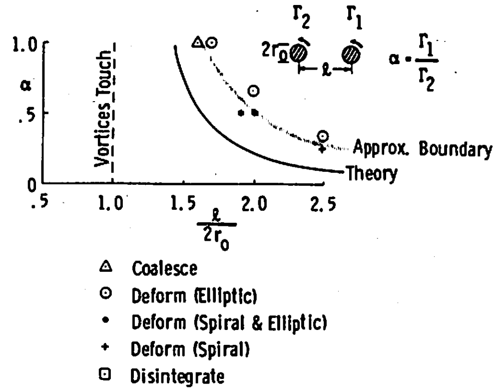

Figure 11a. Merging boundary of vortex pair.

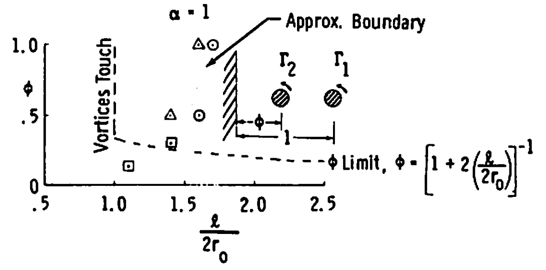

Figure 11b. Wall effect on merging, $\alpha = 1$.

tion of vorticity into a circle of radius $\sqrt{2}r_0$ with center at the centroid of vorticity of the vortex pair was obtained numerically. The result is shown in Figure 12 where g, the fraction of net vorticity that coalesces, is plotted against time. It is apparent that the rate of vorticity concentration goes to zero at about $t^*=1$, demonstrating again the completion of merging. It appears that only 70 percent of the initial net vorticity merges. In a real fluid, the remaining vorticity hangs in a diffused cloud which viscosity eventually annihilates. The reduction in vortex strength and increase in core size leads to equivalent reduction in vortex induced rolling moments. One can easily show that the percentage reduction in vorticity is approximately equal to the percentage reduction in induced rolling moments after vortex merging, if the vortex penetrating span is not much greater than the vortex core diameter. Experiments by Iversen and Brandt [5] indicate a rolling moment reduction of 25 to 29 percent which compares well with the numerically obtained 30 percent vortex strength reduction.

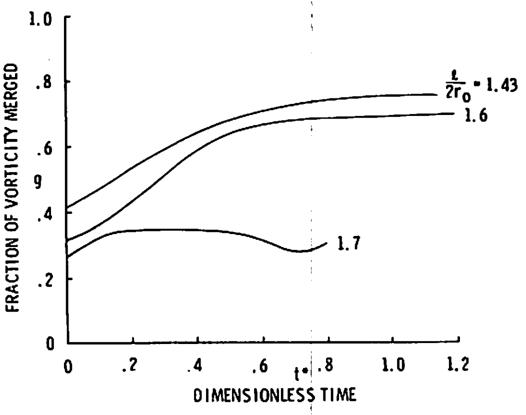

Figure 12. Rate of vorticity concentration in merged vortex.

ESTIMATE OF MERGING DISTANCE

A pair of diffusing vortices, such as those shed by a flapped wing, will eventually merge downstream if there is a tendency for the vortices to rotate about each other. An attempt is made here to determine the merging distance for such a pair of vortices. Using the usual two dimensional approximation, assume that a vortex pair is created at $t=0$ and that the vorticity core grows according to the turbulent prediction (Equation (5)). Taking a typical value of $\Gamma_0/\Gamma_1=2$, the vorticity radius grows like

$$r_0 \doteq 0.35\,(\Gamma_0 t)^{1/2}\,.$$

Moore and Saffman's analysis predicts a critical separation distance (for an equistrength vortex pair) of $\ell=2.86\ r_0$. Then the time taken by the vortex pair to reach the critical state is given by

$$t_c = \ell^2/\Gamma_0\,.$$

Merging may be considered essentially complete when the centers of vorticity coincide and circularization of the merged vortical region sets in. If it is assumed that the merging process is entirely inviscid (calculations by Lo and Ting [24] indicate little Reynolds-number effect), then dimensional analysis indicates a time scale of the form ℓ^2/Γ_0. The numerical results presented earlier give the merging time (after the vortices reach a critical distance apart) to be in the order of magnitude of the period of rotation. Thus

$$\Delta t_m \doteq 2\pi^2\ell^2/\Gamma_0\,.$$

The total time t_m for merging since creation of the vortex pair is then estimated to be

$$t_m = t_c + \Delta t_m = 20.7\ell^2/\Gamma_0\,.$$

In terms of downstream stations, put $x=Ut$. Then in nondimensional terms, the vortex pair merges at x_m where

$$\frac{\ell}{b}\left(\frac{\Gamma_0}{Ub}\right)^{-\frac{1}{2}} = 0.22\left(\frac{x_m}{b}\right)^{\frac{1}{2}}. \qquad (20)$$

Calculations by Lo and Ting [24] for an exponentially decaying vortex (Lamb vortex) give the numerical constant in Equation (20) to be 0.2 for Reynolds number $\Gamma_0/\nu=100$.

Vortex merging data [5] are replotted in Figure 13, according to the nondimensional parameters in Equation (20). The data correlation is seen to be excellent and agreement with the simply derived prediction is quite good for x/b>3. Deviation of the data from the prediction is seen to occur in the vortex sheet roll-up region. In fact x/b=3 is roughly the predicted station when roll-up is complete.

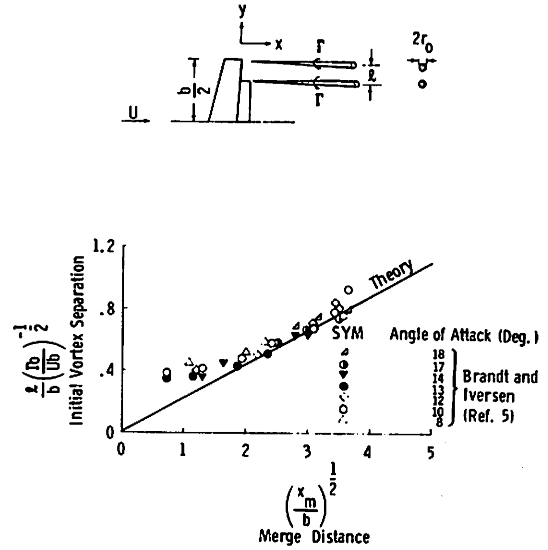

Figure 13. Correlation of vortex pair merging distance data and theory.

REFERENCES

1. Anon., "NASA Symposium on Wake Vortex Minimization," Feb. 1976, SP-409.

2. Olsen, J., Goldburg, A., and Rogers, M., Eds., *Aircraft Wake Turbulence and Its Detection*, Plenum Press, New York, NY, 1971.

3. Nelson, R.C., "Dynamic Behaviour of An Aircraft Encountering Aircraft Wake Turbulence," *J. Aircraft*, Vol. 13, No. 9, Sep. 1976, p. 704-708.

4. Saffman, P.G., "The Structure and Decay of Trailing Vortices," *Archives Mech.*, 26, 3, 1974.

5. Brandt, S.A. and Iversen, J.D., "Merging of Aircraft Trailing Vortices," AIAA Paper No. 77-8, Los Angeles, CA., 1977.

6. Moore, D.W. and Saffman, P.G., "Structure of a Line Vortex in an Imposed Strain," in *Aircraft Wake Turbulence and Its Detection*, Plenum Press, New York, NY, 1971, p. 339.

7. Moore, D.W. and Saffman, P.G., "Axial Flow in Laminar Trailing Vortices," *Proc. Roy. Soc.*, A333, June 1973, p. 491-508.

8. Moore, D.W. and Saffman, P.G., "Density of Organized Vortices in a Turbulent Mixing Layer," *J. Fluid Mech.*, Vol. 69, part 3, 1975, p. 465-473.

9. Garodz, L.J., Lawrence, D., and Miller, N., "The Measurement of the McDonnell-Douglas DC-9 Trailing Vortex System Using the Tower Fly By Technique," FAA-RD-74-173, 1974.

10. Garodz, L.J., Miller, N.J., and Lawrence, D., "The Measurement of the Boeing 747 Trailing Vortex System Using the Tower Fly-By Technique," FAA-RD-73-156, 1974.

11. Garodz, L.J., Miller, N.J., and Lawrence, D., "The Measurement of the Boeing 727 Trailing Vortex System Using the Tower Fly-By Technique," FAA-RD-73-90, 1974.

12. Garodz, L.J., Miller, N.J., and Lawrence, D., "The Measurements of the Douglas DC 7 Trailing Vortex System Using the Tower Fly-By Technique," FAA-RD-73-141, 1974.

13. Barrows, T.M., "Simplified Methods of Predicting Aircraft Rolling Moments Due to Vortex Encounters," AIAA Paper No. 76-61, Washington, DC, 1976.

14. Corsiglia, V.R. and Dunham, R.E., "Aircraft Wake-Vortex Minimization by Use of Flaps," NASA Symposium on Wake Vortex Minimization, SP-409, 1976.

15. Croom, D.R., "Low-Speed Wind-Tunnel Investigation of Various Segments of Flight Spoilers as Trailing-Vortex Alleviation Devices on a Transport Aircraft Model," NASA TN D-8161, 1976.

16. Croom, D.R., "Low-Speed Wind-Tunnel Investigation of Forward Located Spoilers and Trailing Splines as Trailing Vortex Hazard Alleviation Devices on an Aspect-Ratio-8 Wing Model," NASA TM X-3166, 1976.

17. Patterson, J.R., Hastings, J.C., Jr., and Jordon, F.L., Jr., "Ground Development and Flight Correlation of a Vortex Attenuating Spline Device," NASA Symposium on Wake Vortex Minimization, SP-409, 1976.

18. Baker, G.R., Barker, S.J., Bofah, K.K., and Saffman, P.G., "Laser Anemometer Measurements of Trailing Vortices in Water," *J. Fluid Mech.*, Vol. 65, part 2, 1974, p. 325-336.

19. Friederichs, K.O., *Special Topics in Fluid Dynamics*, Gordon and Breach, New York, NY, 1966, p. 121.

20. Acton, E., "The Modelling of Large Eddies in a Two-dimensional Shear Layer," *J. Fluid Mech.*, Vol. 76, Part 3, 1976, p. 561-592.

21. Donaldson, C. duP. and Bilanin, A.J., "Vortex Wakes of Conventional Aircraft," AGARDograph-204, 1975.

22. Roberts, K.V. and Christiansen, J.P., "Topics in Computational Fluid Mechanics," *Comp. Phys.* Comm. (Suppl.), 3, 1972, p. 14-32.

23. Rossow, V.J., "Convective Merging of Vortex Cores in Lift-Generated Wakes," AIAA paper No. 76-415, 1976.

24. Lo, R.K.C., and Ting, L., "Studies of the Merging of Vortices," *Phys. Fluids*, Vol. 19, No. 6, 1976, p. 912-913.

REVIEW OF VORTEX SENSOR DEVELOPMENT SINCE 1970

DAVID C. BURNHAM
U.S. Department of Transportation
Transportation Systems Center
Cambridge MA 02142

ABSTRACT: The various sensing techniques developed since 1970 and used for studying aircraft wake vortices are described. The inherent advantages and limitations of each technique are discussed. Emphasis is placed on those sensors used for data collection at airports.

INTRODUCTION

In 1970 the Transportation Systems Center (TSC) became involved in the development of sensors for aircraft wake vortices. As reported at the first wake vortex conference [1], held in 1970, the sensing techniques available at that time required dedicated flight tests. Subsequent development of remote sensors by TSC and others produced systems which operate satisfactorily at airports during normal operations. Some of these systems have been used to compile large data bases on wake vortex behavior. This paper will emphasize those systems used for extensive data collection. Another report [2] discusses all the sensing techniques proposed or evaluated for use in wake vortex studies.

Figure 1 shows the historical development of the eight sensing techniques which have provided the current understanding of aircraft wake vortices. The first three require a physical intrusion into the vortex and are therefore suited only for dedicated flight tests. The other five are remote sensors which have been operated for data collection at various airports as indicated in the figure. Each sensing system will be described in detail with an emphasis on its capabilities and limitations. The intended goal of this paper is to allow a realistic evaluation of the data produced by each technique.

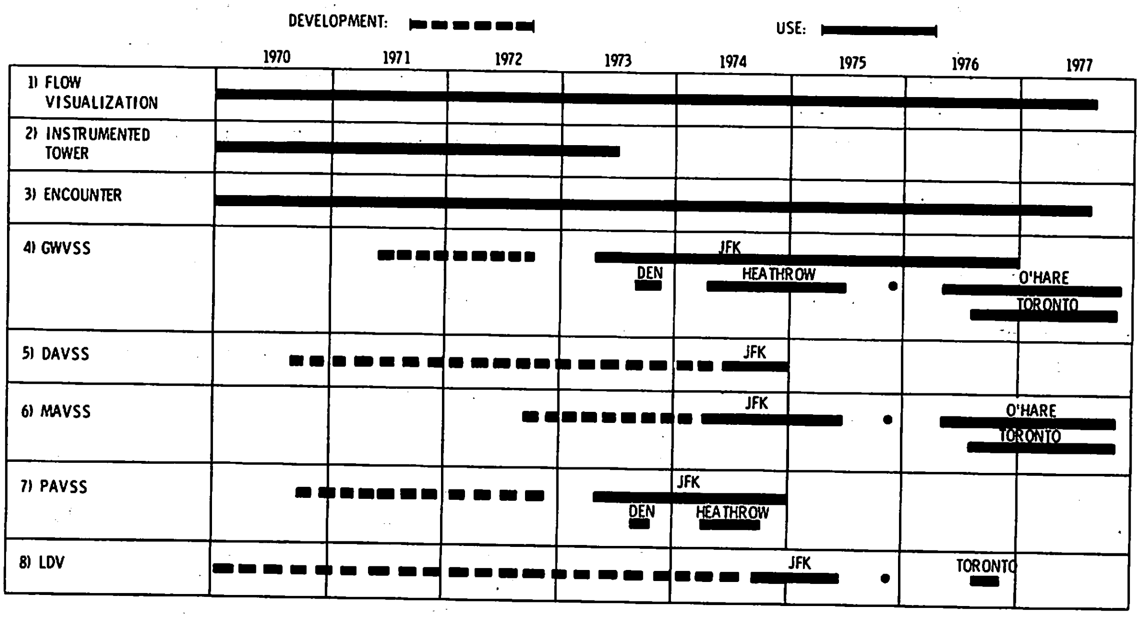

Figure 1. History of wake vortex sensor development and use since 1970.

Before presenting the various sensors, it is helpful to consider the nature of wake vortex sensing from a more philosophical point of view. Studies of vortex hazard [3] have indicated that the vortex strength (circulation) is the most important indicator of hazard. An axially symmetric vortex is characterized by its tangential velocity profile v(r), where r is the radius from the vortex center. The circulation is given by

$$\Gamma(r) = 2\pi r\ v(r), \tag{1}$$

A vortex with a well-defined core region will have a constant circulation Γ_∞ defined as the strength of the vortex for large values of r. One useful index of vortex hazard can be derived from the circulation profile:

$$\Gamma'(s) = \frac{1}{s}\int_{o}^{s} \Gamma(r)\ dr. \tag{2}$$

The average circulation up to radius s, $\Gamma'(s)$, can be shown to be proportional to the maximum rolling moment on a wing of span 2s under some simple assumptions.

It is difficult to determine Γ_∞ from measured velocity profiles since velocity errors become troublesome at large radii where the vortex velocities are small according to Equation (1). A determination of Γ' is much more stable since the integral over the measured velocities tends to average out velocity errors.

The basic functions performed by wake vortex sensors are detection, tracking, and measurement. Each of these functions successively involves a higher order of complexity. Some sensors can detect and track but cannot measure. Normally, the most important vortex parameter to be measured is its strength. For those sensors which can measure strength the detection and tracking functions were usually implemented first before strength measurement was attempted. One must be careful in making use of vortex data which do not include a determination of vortex strength.

Each wake vortex sensor interacts with some physical property of the vortex. The usefulness of a sensor depends upon how closely the property sensed is related to the property which is to be determined. For example, smoke injected into the vortex by the generating aircraft is very useful for marking the vortex location, but it provides virtually no information on vortex strength. The question of the appropriateness of a sensor is particularly important for sensors which are intended to monitor the decay of wake vortex hazard. The property sensed may decay more quickly or more slowly than the actual hazard. The former case results in missed hazards while the latter leads to false alarms. These uncertainties have led to the strong emphasis in recent work on sensors which measure vortex strength.

FLOW VISUALIZATION

Considerable information about wake vortex behavior can be obtained if the normally invisible vortex core is marked by light scattering particles. Such marking allows one to track the vortex and to observe its decay. One must beware of assuming that the vortex has disappeared when the marking is gone. Some recent tests have shown that a coherent vortex flow can remain long after the marking has dissipated.

Under certain natural conditions (high-altitude flight or high humidity), water vapor condenses in the wake vortices and remains trapped until the vortices dissipate. The effect is familiar to anyone who observes contrails. Under normal atmospheric conditions, particles must be added to make vortices visible. Two techniques have been developed for dedicated flight tests. In the first, smoke grenades or smoke generators are mounted on an aircraft in an appropriate spot to mark the core of the wake vortex. In the second, smoke grenades are mounted on a tower through which the wake drifts after the aircraft has passed. Figure 2 shows some photographs of the second technique. The proper analysis of the photographs in Figure 2 requires careful corrections for the effects of the ambient wind.

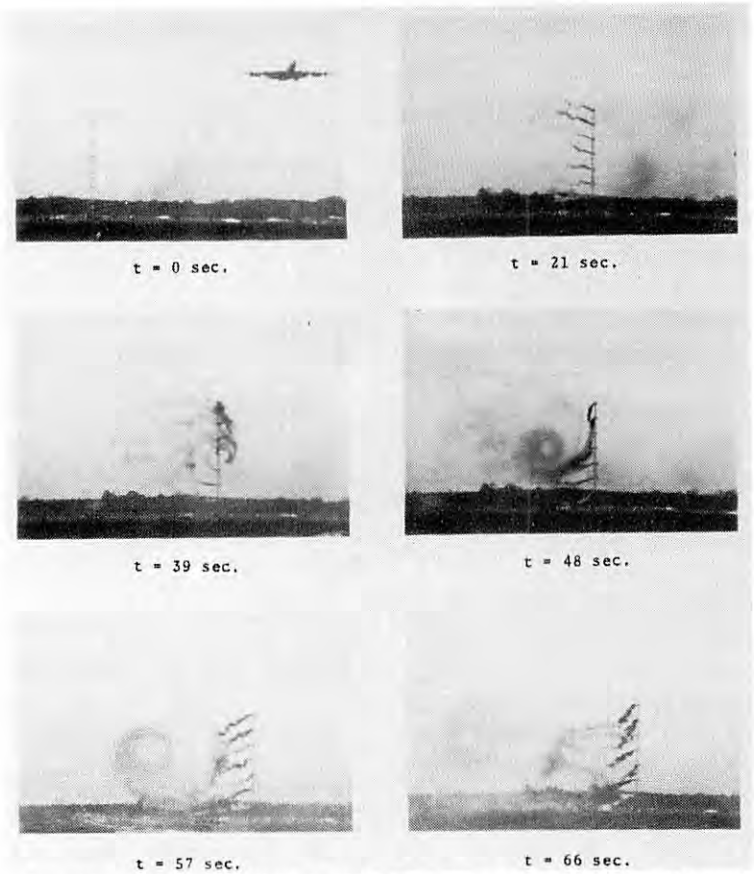

Figure 2. Time history of an aircraft wake drifting through a tower equipped with smoke grenades.

INSTRUMENTED TOWER

The detailed structure of an aircraft's wake can be studied by flying the aircraft past a tall instrumented tower (see Figure 2). The wake profile is measured as it drifts past the tower. Normally hot-wire anemometers are used to sense the wake vortices. The highest resolution was achieved in measurements [4] at NAFEC which had one-foot sensor spacing. Although this technique has produced the most detailed vortex velocity profiles, it suffers from a number of difficulties. A tower can make only one vortex measurement for each aircraft fly-by, thus making it difficult to measure vortex decay. Moreover, the tower interacts with the vortex, affecting its decay and interfering with measurements of the vortex wind. For the single-wire anemometers normally used the data processing is difficult because the sensor responds to the ambient wind as well as to the vortex wind.

AIRCRAFT ENCOUNTER

One of the simplest techniques for studying wake vortices is to fly a probe airplane through the marked wake of another aircraft. The probe aircraft can be regarded as the sensor by measuring its response to the vortex encounter [5] or it can be instrumented to measure the wake directly [6]. While this technique offers the most direct observation of the dynamics of a wake vortex encounter, it suffers from a number of difficulties. It is difficult to determine the exact location of the probe aircraft in the wake; consequently, the data have a lot of scatter and cannot be easily compared with encounter simulations. In addition, it can be difficult for the probe aircraft to locate a partially decayed vortex which has lost its smoke marking but not necessarily its strength.

GWVSS

Although tall instrumented towers cannot be installed near airport runways, experience has shown that anemometers located near the ground can successfully detect and track wake vortices generated near the ground. Such a system, called the Ground Wind Vortex Sensing System (GWVSS), has produced the bulk of the currently available data on wake vortex transport in the airport environment. First tested in 1972, the system was subsequently installed at Kennedy, Stapleton, Heathrow, O'Hare, and Toronto International Airports for data collection.

The GWVSS consists of an array of single-axis anemometers installed on a baseline perpendicular to the aircraft path. Since the wake vortices induce winds near the ground which are perpendicular to the flight path, the anemometers are oriented to respond only to the perpendicular component of the wind (the crosswind). The theoretical crosswind at the ground produced by a pair of counter-rotating vortices is given by the expression

$$v_x = \frac{\Gamma_\infty}{\pi}\left[\frac{h_2}{h_2^2 + (x-x_2)^2} - \frac{h_1}{h_1^2 + (x-x_1)^2}\right] , \qquad (3)$$

as a function of lateral position x, where x_1 and x_2 are the lateral positions of the two vortices, and h_1 and h_2 are the altitudes of the two vortices. Figure 3 shows the expected crosswind vortex signatures for three different vortex altitudes. It is assumed that the vortex-induced winds can be simply superimposed on the ambient crosswind.

The effects of the two vortices are easily distinguished since they are of opposite sign. When the vortices are at altitudes significantly less than their lateral separation, the peak vortex winds are located directly below the vortex centers. For altitudes greater than the vortex separation, the vortex signature deteriorates because the winds from the two vortices tend to cancel; the signal amplitude diminishes more rapidly than 1/h and the signature no longer clearly indicates the vortex locations. The success of the GWVSS is the result of the normal behavior of wake vortices near the ground. After creation, the vortices descend toward the ground at a rate of 1 to 2 m/sec. According to classical theory [7], when the vortices approach the ground they begin to separate and eventually reach an altitude of half of their initial spacing with a separation rate of twice their initial descent rate. Thus, the vortex motion produces the exact conditions needed to give good GWVSS signatures; namely, low altitudes and large lateral separations. The theory also predicts a maximum GWVSS crosswind of four times the initial descent rate; i.e., 4 to 8 m/sec.

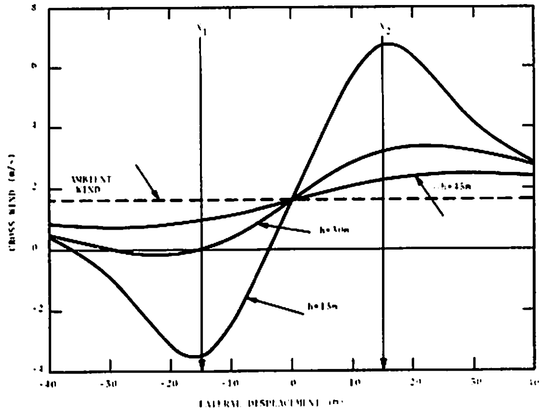

Figure 3. Theoretical GWVSS signatures.

Figure 4 shows some experimental data from the Heathrow GWVSS installation [8]. The wind measured simultaneously at each anemometer is presented as a bar graph obtained by successively sampling each anemometer output in turn. The motion of the vortices to the left is evidenced by the displacement of the vortex peaks at different times. The algorithm used to obtain the vortex positions from GWVSS data simply designates the location of the anemometer reading the highest crosswind velocity as the lateral position of one vortex and the location of the anemometer reading the lowest velocity as the position of the other vortex. Figure 5 shows the stepped vortex tracks obtained from this algorithm. When the vortex signals decay to the level of ambient turbulence, the vortex locations given by the algorithm become random. The termination of the vortex tracks can be made automatic by means of consistency requirements.

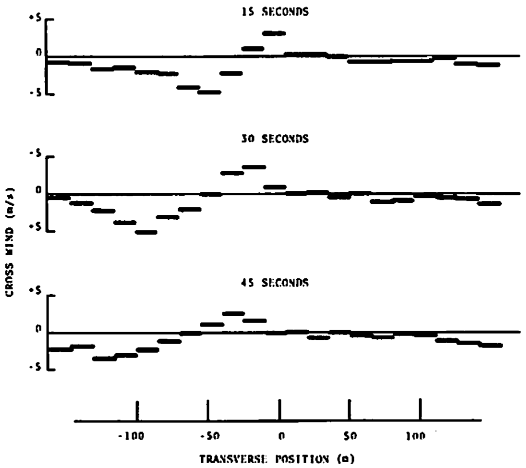

Figure 4. GWVSS data.

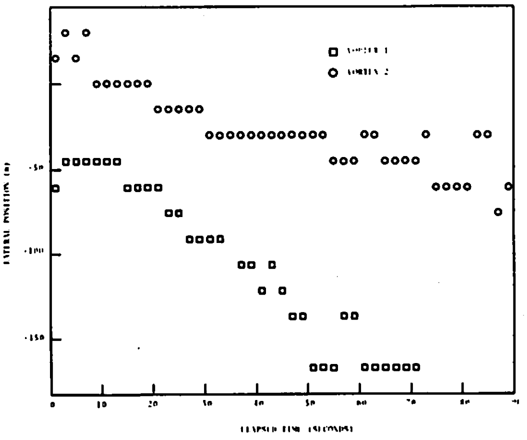

Figure 5. GWVSS vortex tracks.

The accuracy of the GWVSS vortex locations was evaluated in 1972 flight tests at NAFEC. Figure 6 shows some data from those tests plotted as time histories of the crosswind at each anemometer. Comparisons with photographic tracks of smoke entrained in the vortices showed that the peak in the anemometer response accurately measures the time when the vortex is directly above the anemometer. Because the vortex peak becomes asymmetrical as the vortex ages, the stepped track of Figure 5 tends to display a bias compared to the actual vortex tracks. The peak response representing the vortex arrival typically occurs considerally before the middle of the total time the vortex position is assigned to a particular anemometer location.

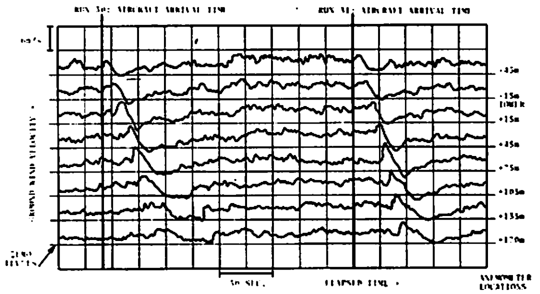

Figure 6. GWVSS signals: time histories.

A typical GWVSS installation is shown in Figure 7. Fixed-axis propeller anemometers using d-c generators are mounted on posts about 3-m high with lateral spacing of about 15 m. The spacing between anemometers should be roughly equal to the expected minimum vortex altitude (about 3/8 of the wing span), so that vortices are not lost between sensors. The altitude of the anemometers is not critical but they should be well above any obstructions which could disrupt the wind flow. The 3-m height was selected to discourage unauthorized removal of the anemometers as much as for clearance to eliminate ground effects from the data. Proper orientation of the anemometers is important for reliable vortex tracking. A single anemometer skewed into the wind can falsely indicate the presence of a vortex at its location.

Figure 7. Vortex sensor baseline at JFK Airport.

The GWVSS is well established as a reliable technique for obtaining the transverse positions of wake vortices located near the ground. However, the current tracking algorithm makes no use of the nagnitude of the vortex signal which could perhaps give some indication of vortex height h or strength Γ_∞. The peak vortex signal from Equation (3) is $\Gamma_\infty/\pi h$ for $h << (x_2-x_1)$. A basic limitation of the GWVSS is that the decrease or disappearance of a vortex signal could be caused by the decay of Γ_∞, and hence a decay in hazard, or to an increase in h which could even increase the hazard to a following aircraft. The data-collection efforts using the GWVSS have usually included another vortex sensor sensitive to height to verify the disappearance of a vortex signal. At present, the boundary-layer effects on GWVSS vortex signatures are not well enough understood to allow the influence of Γ_∞ and h to be disentangled from GWVSS data alone.

ACOUSTIC SENSORS

The three acoustic sensors, the Doppler Acoustic Vortex Sensing System (DAVSS), the Monostatic Acoustic Vortex Sensing System (MAVSS) and the Pulsed Acoustic Vortex Sensing System (PAVSS), share some common features which will be discussed before each is considered in turn. Acoustic sensors all suffer from sensitivity to ambient noise. The major noise sources which limit the performance of acoustic sensors in the airport environment are aircraft operations and meteorological effects such as rain hitting the antenna and wind whistling around the antenna. At the current state of development, no acoustic sensor can be designated as an "all-weather" system.

The capabilities of an acoustic-sensing system are normally limited by the tradeoffs involved in antenna design. Since most sources of ambient noise and spurious reflections are located on the ground, antennas are designed to have low side response. The standard acoustic antenna consists of a transducer and horn at the focus of a parabolic dish. Low side response is achieved by surrounding the antenna with a shield which is covered on the inside with sound-absorbing material to eliminate internal reflections. One should note that mechanically scanned antennas such as used in radars are generally impracticable for acoustic antennas because of limitations posed by the slow speed of sound. Consequently, multiple-beam antennas are often used to span an area, and can be constructed simply by using an array of transducers in the same dish. One of the limitations of the horn-dish-shield antenna configuration is that the feasible angular coverage of a single antenna is probably less than 50 degrees. Morover, as the angular coverage increases, the side response also tends to increase, thus leading to lower signal-to-noise ratios.

One of the critical parameters for acoustic sensors is the frequency of operation. The acoustic absorption of air increases rapidly with frequency, and has a strongly peaked dependence on the absolute humidity [9]. Acoustic absorption serves both to attenuate the desired vortex signals and to reduce the ambient noise from distant sources. Proper selection of the frequency requires a balancing of the relative advantages of high frequency: smaller antennas and less ambient noise; and those of low frequency: longer range for a given signal loss and greater transducer efficiency. One pitfall in frequency selection should be noted. If the frequency chosen for a particular range is just satisfactory under normal meteorological conditions, the humidity-absorption peak can severely degrade the range capabilities under conditions of low absolute humidity.

Sound waves interact with wake vortices via a number of scattering mechanisms. Turbulent fluctuations in the air cause some of the sound to be scattered in all directions. The scattered signals are Doppler-shifted by the mean wind in which the turbulence is imbedded. The change in frequency Δf is given by

$$\Delta f = 2f_0 \, (w/c) \sin\left(\frac{1}{2}\theta\right), \qquad (4)$$

where f_0 is the transmitted frequency, Θ is the scattering angle, w is the mean velocity component of the wind in the direction bisecting the angle between the transmitted and received beams, and c is the speed of sound.

The angular distribution of the acoustic energy scattered from turbulence depends upon the nature of the associated fluctuations [10]. The cross section decreases rapidly with angle and reaches a null at 90 degrees. An additional null occurs at 180-degree scattering for velocity fluctuations. The positions of these nulls have influenced the design of the Doppler Acoustic Vortex-Sensing Systems (DAVSS). Although a bistatic (separated transmitter and receiver) acoustic sensor can respond to both velocity and temperature fluctuations, a monostatic (single-location) sensor views 180-degree scattering which can be produced only by temperature fluctuations. The characteristics of a monostatic acoustic sensor are, therefore, strongly dependent upon the distribution of thermal fluctuations in the wake, which may vary considerably with aircraft-engine placement. Because of this uncertainty, the first DAVSS experiments [11, 12] employed bistatic configurations rather than the simpler monostatic configuration which would also provide greater velocity resolution according to Equation (4).

Another mechanism for acoustic scattering is the modification of acoustic propagation by the non-fluctuating properties of the vortex. The dominant effect is a deflection or refraction of the sound propagating through the vortex core. The scattering cross section for refraction is much larger than that for fluctuation scattering for two reasons. First, the entire incident beam is scattered, not just a fraction of it. Second, the beam is scattered into a plane, rather than a sphere of resultant propagation directions. One can calculate [13] a maximum scattering angle

$$\theta_m = \Gamma_\infty / \pi c \bar{r}, \qquad (5)$$

where $\bar{r}$ is mean vortex radius weighted according to the radial variation in vorticity.

The approximations leading to Equation (5) become inaccurate as Θ_m approaches 1.0 radian. The aircraft dependence of Equation (5) lies in the two parameters Γ_∞ and $\bar{r}$. For aircraft operating with the same coefficient of lift and wing shape (a reasonable approximation for commercial jet transports), Γ_∞ is proportional to the wing span b. The maximum scattering angle is then inversely proportional to $\bar{r}/b$, the relative size of the core with respect to the wing span. A factor-of-three variation in Θ_m has been observed [14] for different types of landing aircraft. The observed variation can be related to the proximity of engine-jet blast to the vortex core during the wake roll-up process [15]. When the jet blast is near the origin of the vortex core (i.e., for aircraft with four wing-mounted engines), the vortex core is enlarged and the resulting maximum scattering angle is smaller than that for aircraft with engines far away from the vortex core (e.g., on the tail). Because of the strong variation in Θ_m with aircraft type, a sensing system based on refractive scattering; e.g., the PAVSS, is highly sensitive to aircraft type. It is also incapable of measuring the vortex-wind distribution. Since the scattering is produced coherently by the vortex as a whole, Doppler shifts in the scattered signals characterize only the vortex-transport velocity and not the wind velocity within the vortex. Because of these limitations the PAVSS was phased out when the DAVSS and MAVSS became available.

Spatial resolution in acoustic sensors is achieved by using narrow angular beams and/or short transmitted pulses. Since two dimensions must be specified to define a point in a plane, three basic configurations are available for resolving vortex location:

a) Two beam angles,
b) One beam angle plus one pulse arrival time, and
c) Two pulse arrival times.

Figure 8 illustrates how each of these three configurations can be used to provide bistatic coverage of a plane perpendicular to the aircraft flight path. Each beam angle to be resolved requires a fan of narrow antenna beams. Each time to be resolved requires a wide beam antenna. The roles of transmitting and receiving antennas are interchangeable as far as spatial resolution is concerned. For the monostatic configuration, illustrated in Figure 9, spatial resolution is achieved by range and beam-angle measurements.

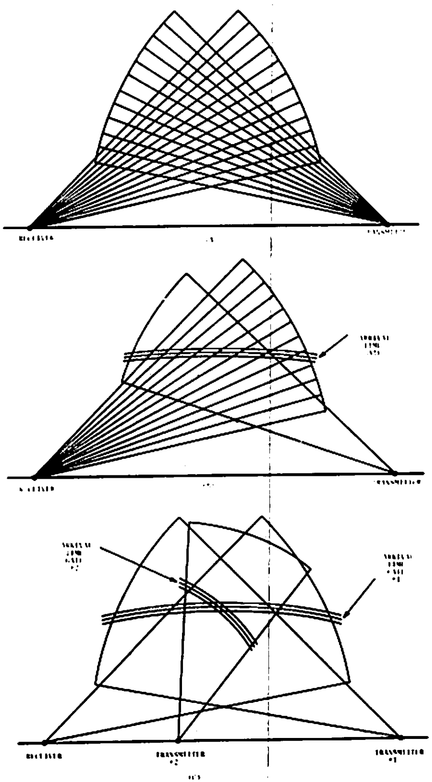

Figure 8. Acoustic antenna configurations.

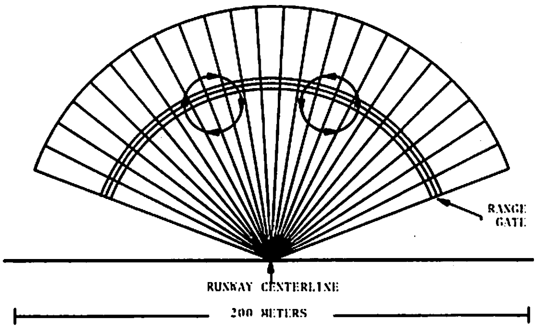

Figure 9. Monostatic configuration.

From the viewpoint of operational use, the monostatic configuration is superior to the bistatic configurations because it can be installed directly under the flight corridor to be monitored where the real estate is normally already available at airport sites. Moreover, the monostatic configuration minimizes the range to the vortex (and hence, the acoustic attenuation), and maximizes the spatial resolution for a given antenna beam width. The specific configuration of Figure 9 is designed for monitoring wake vortices at the middle marker location of the approach corridor (1100 m from the runway threshold) using a maximum range of 100 m.

DAVSS

The term Doppler Acoustic Vortex-Sensing System (DAVSS) does not refer to a particular sensor configuration, but rather to a host of sensor configurations sharing the common feature that the acoustic returns from turbulence within a vortex are spectrally analyzed to yield information on the velocity profile of the vortex. Doppler processing of the turbulence-scattering signals is necessary for reliable vortex-tracking even if the velocity information is not required.

Since the turbulence is distributed throughout the vortex, the vortex center cannot be consistently identified by a maximum in the scattered signal. In fact under some atmospheric conditions, the scattering from ambient turbulence is so large that even the presence of a vortex cannot be detected by the magnitude of the scattered signals.

The first DAVSS development work was done by the Xonics Corporation. In late 1970 and early 1971 they experimented with Doppler-scattering from aircraft vortices at airport test sites. They then carried out two series of flight tests under FAA sponsorship at NAFEC in the fall of 1971 [11] and the spring of 1972 [12]. Two types of experiments using bistatic configurations were carried out during these tests:

The first involved a detailed comparison of acoustic velocity measurements with those from hot-wire anemometers mounted on a 43-m tower. A CW transmitter radiated into a narrow vertical beam near the tower. The scattered signals were received by an antenna with multiple beams which intersected the transmitted beam at various heights. The DAVSS and instrumented tower measurements showed reasonable agreement after suitable corrections were made for the different resolution of the two types of sensor. A model for the Doppler spectra expected from vortex-scattering was developed to aid in the interpretation of the DAVSS data. The data from the tower comparison tests were also processed to yield vortex strength.

The second type of experiment was designed to explore the high-altitude tracking capabilities of the DAVSS. Both configurations (a) and (b) in Figure 8 were explored. The transmitter consisted of a phased array of transducers. In configuration (a) eight beams were synthesized by proper phasing. The beams were scanned sequentially, two at a time using two distinct transmitted frequencies. The location of the wake vortices was determined by the pair of beams showing the greatest Doppler spread. Vortices were detected at altitudes as high as 400 m with configuration (a).

Late in 1972, work began on DAVSS monostatic configurations. Work at Xonics led to a demonstration of a monostatic DAVSS designed to track wake vortices in real time [16]. TSC collected some monostatic acoustic wake vortex scattering data during the fall 1972 sensor-calibration tests at NAFEC. The success of this simple data-collection effort led to the development of the Monostatic Acoustic Vortex-Sensing System (MAVSS) for studying the decay of wake vortex strength. The MAVSS is simply a particular DAVSS configuration, but it is discussed as a separate sensor because of its important role in data collection at airports.

In 1973, the Avco Corporation built an engineered DAVSS with real-time vortex-tracking capability and the versatility to operate in any DAVSS configuration. The Avco DAVSS was installed in 1974 at Kennedy International Airport to test both bistatic and monostatic configurations. Figure 10 shows the bistatic Avco DAVSS configuration designed to monitor the landing glide-slope window with two transmitting and two receiving antennas. Depending upon transmitter and frequency selections, it can be operated in the cw or pulsed mode and in the forward- or back-scatter modes. A comparison between the monostatic and bistatic vortex data showed the former to be much more useful because of larger Doppler shifts (Equation (4)), higher spatial resolution, and lower noise levels (because the receiving antennas were elevated farther above the horizon).

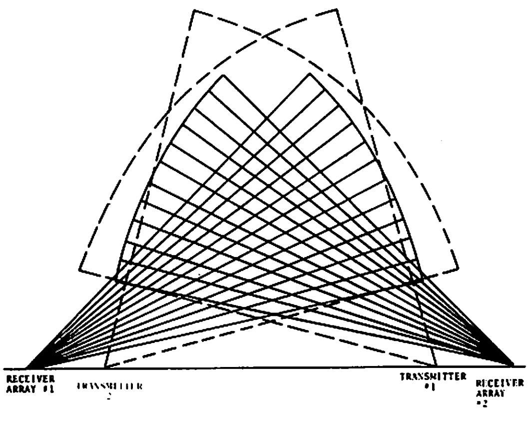

Figure 10. Avco bistatic DAVSS configuration.

The 24-beam monostatic DAVSS configuration shown in Figure 9 was used for data collection. Figure 11 shows a photograph of this installation. The need for four 36-degree receiving antennas to sense a plane through the approach corridor is a cumbersome consequence of the previously mentioned angle limitations of horn-dish antennas. It is unlikely that fewer than three antennas could span the corridor without a radical change in antenna design. One attempt to simplify the antenna configuration used three 50-degree fan-beam antennas (one vertical and one tilted to each side) to span the whole corridor. It was found that the tilted antennas had too much response to surface noise sources to give satisfactory performance.

Figure 11. Photograph of Avco monostatic DAVSS configuration.

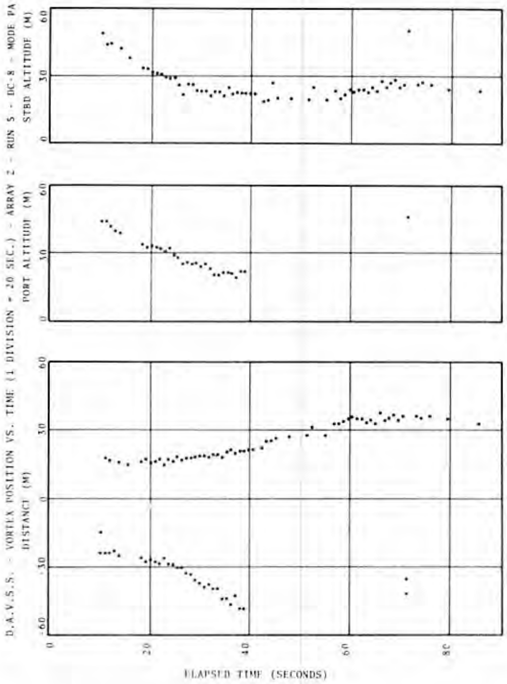

Figure 12. Vortex tracks from the Avco DAVSS.

In the Avco DAVSS, the received signals go to a computerized processor which produces real-time displays and digital records of vortex locations. The processor simultaneously analyzes the signals from 24 receiver beams using a 6-frequency comb filter to characterize the Doppler spectrum of each signal. The spectral characteristics feed into a search algorithm which locates any vortices in the field of the antennas and determines their sense of rotation. The current algorithm also provides a crude estimate of vortex strength. Figure 12 shows some vortex tracks produced by the Avco DAVSS. The lateral position and altitude of the port and starboard vortices are plotted as a function of time after aircraft passage. In this run, the vortices are seen to drop toward the ground and separate as predicted by the classical theory in the case of a small crosswind. The port vortex drifts out of the sensor field of view, but the starboard vortex remains within the sensitive area until it dissipates.

MAVSS

The MAVSS antenna configuration illustrated in Figure 13 was originally conceived as a simple test for studying the 180-degree acoustic-scattering properties of wake vortices. The Doppler shifts in this configuration depend only upon the vertical component of the wind in the sensitive volume. The test data showed scattered signals large enough to allow accurate measurement of the vertical wind profile of the aircraft wake (see Figure 14). In fact, the analysis of the test data proved the simple MAVSS configuration to be a promising technique for studying vortex strength.

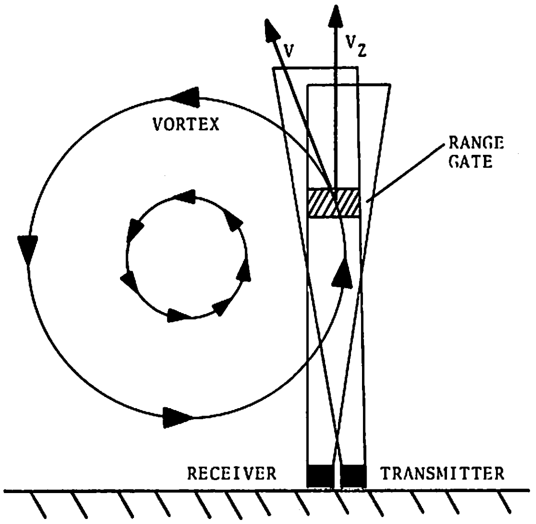

Figure 13. MAVSS configuration.

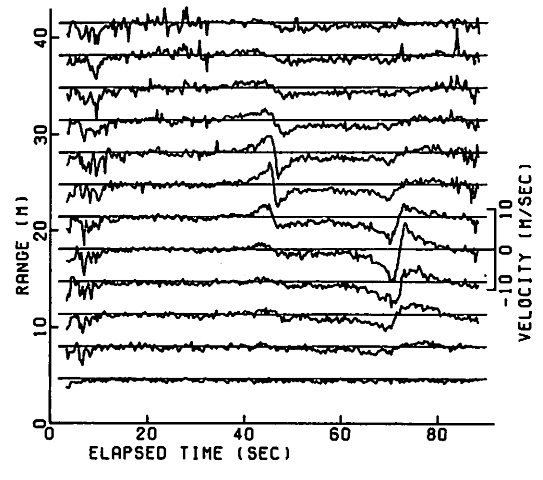

Figure 14. MAVSS vertical wind profile of the wake from a B-707 aircraft.

The MAVSS configuration is superior to the more complex DAVSS configurations for vortex-measurement studies because the vortex measurements are not contaminated by the ambient wind which has little vertical component. Moreover, the simplicity of the MAVSS configuration allows a whole array of MAVSS antennas to be processed with the same effort required for a single DAVSS configuration. For example, the DAVSS NAFEC tower comparison tests gave vortex-strength information similar to that from the MAVSS but required Doppler-processing of twelve signals instead of one.

The choice between the MAVSS and DAVSS configurations for data collection on vortex decay poses a dilemma. Since vortices are likely to drift laterally under most meteorological conditions, a MAVSS array laid out perpendicular to the flight path will usually give a more complete history of vortex decay than a single DAVSS located under the flight path. Unfortunately, a MAVSS array cannot measure the decay of vortices which do not drift at a significant speed. Since the primary wake vortex hazard is produced by the infrequent vortices which stall near the flight path, one is left with the difficult data-collection question of collecting much data on vortices which are not in dangerous locations, or collecting skimpy data on vortices which remain in dangerous locations. An understanding of the influence of vortex motion on vortex decay is needed to resolve the dilemma.

The analysis of MAVSS data [17] to yield vortex strength starts with the vertical velocity profile such as that shown in Figure 14 for a B-707 aircraft. In the figure, the velocity at each range gate is plotted as a function of time after aircraft passage. The arrival times of the two wake vortices over the antenna can be located by the rapid reversal in the direction of the vertical wind. The vertical wind is negative between the vortices as one would expect. The height of a vortex is indicated by the range gate with the largest velocities. If one can estimate the transport velocity of the vortex past the antenna, the time data of Figure 14 can be converted to a spatial picture under the assumption that the vortex decay is negligible during the time of passage. Figure 15 shows the results of such a transformation on the data of Figure 14 for the range gates where the vortex core is located. In this case, the range-gate velocity is a direct measurement of the vortex tangential velocity averaged over the beam angle and range-gate resolution of the system.

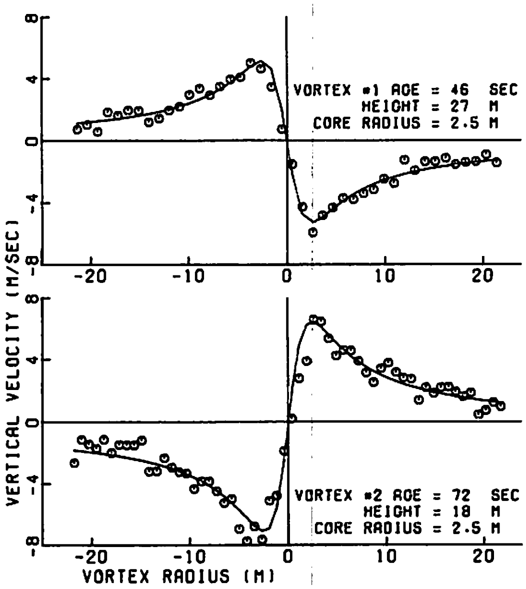

Figure 15. Vortex tangential velocity profiles for the B-707 data.

Figure 16 shows the radial dependence of the circulation from Equation (1) for the velocity data in Figure 15. The circulation values for positive and negative radius are averaged to eliminate some sources of bias. The solid lines in Figure 16 are a weighted least-squares fit to the data of the two parameter form:

$$\Gamma(r) = \frac{\Gamma_\infty}{1+(r/r_c)^2}, \qquad (7)$$

where Γ_∞ is the vortex strength and r_c is the vortex core radius. This simple vortex model generally fits the MAVSS data reasonably well, and it has the virtue that r_c is both the radius of maximum velocity and of half-circulation ($\Gamma(r_c) = \Gamma_\infty/2$). The value of r_c obtained in the data-fitting is not necessarily related to the actual core radius. Only if the core radius is larger than the antenna beamwidth can one assign a physical significance to r_c. The average circulation (Equation 2), which is proportional to the rolling moment on a wing, is plotted in Figure 17 for the same data. It is notably smoother than the raw circulation data of Figure 16 because of the averaging. The techniques of vortex parameterization discussed here assume that the vortex is isolated. The assumption is reasonable for old vortices which have had time to separate, but it leads to errors for fresh vortices which are still close together.

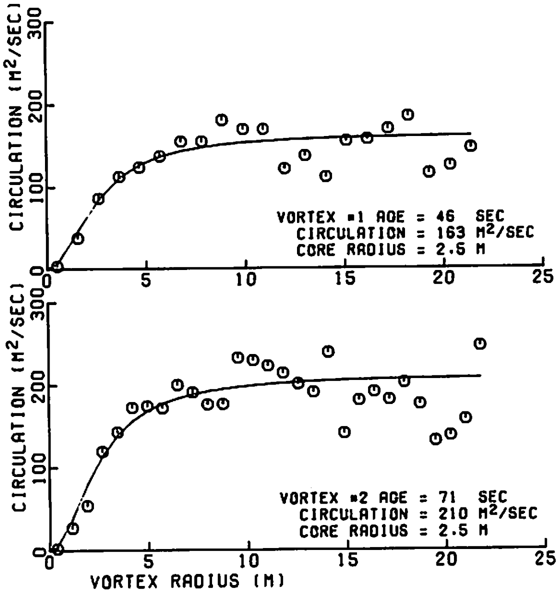

Figure 16. Vortex circulation profiles for the B-707 data.

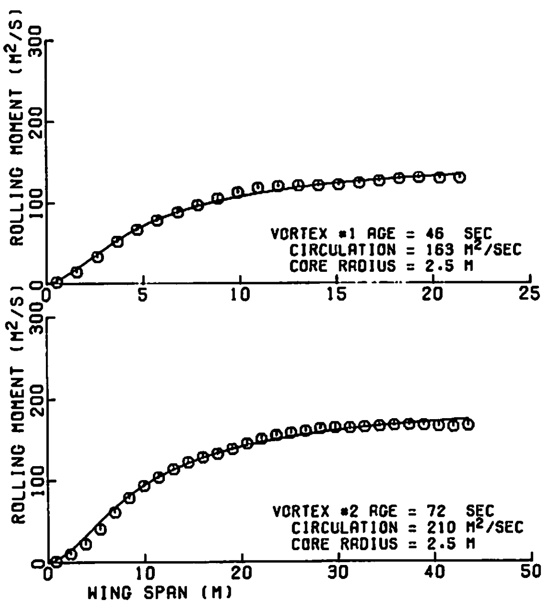

Figure 17. Average circulation vs. twice the radius for the B-707 data.

The measurement of wake vortex decay with the MAVSS uses an array of antennas to sequentially probe the vortices as they drift past. Figures 18 and 19 show some MAVSS data obtained from a four-antenna array. The vortex tracks in Figure 18 are determined by the arrival time and altitude at each antenna. The time variations in the vortex parameters of strength Γ_∞, core radius r_c and rolling moment $\Gamma'(r=30\text{ m})$ are shown in Figure 19. The values of Γ' and Γ_∞ tend to agree for the large radius $r=30$ m. It should be noted that the measurements for short times are less accurate because of interference from the other vortex, aircraft noise, and poorer estimates of the transport velocity.

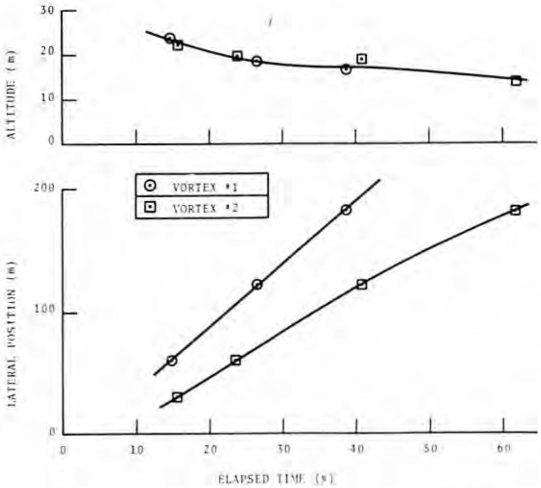

Figure 18. MAVSS vortex location vs. elapsed time.

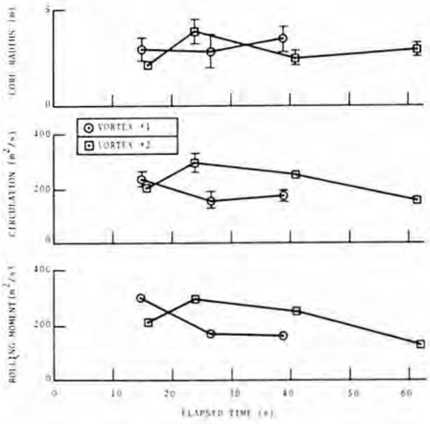

Figure 19. MAVSS vortex parameters vs. elapsed time.

The MAVSS configuration is essentially a meteorological acoustic sounder modified for wake vortex studies which require shorter ranges and higher resolution. Separate transmitting and receiving antennas, shown in Figure 20, eliminate antenna-ringing which could obscure low-altitude returns up to perhaps 15 m. Each antenna consists of a 1.2-m square dish (0.8-m focal length) and a horn-driver transducer surrounded by the acoustic shield which can be seen in Figure 20. A transmitted carrier is modulated by 20-msec pulse (3.5-m resolution) near 3-kHz frequency with a smooth envelope to minimize the intrinsic frequency spread. The return signals are recorded and subsequently analyzed with a real-time spectrum analyzer. The mean frequency of the power spectrum is used in Equation (4) to give the vertical velocity. The deviation of the spectrum about the mean is also calculated to indicate the reliability of the velocity measurement which can be degraded by noise and by strong velocity gradients. The rms deviation of the spectrum from the mean corresponds to about 1.2 m/sec for good data. In the absence of vortices, the pulse-to-pulse standard deviation in mean velocity is typically less than 0.6 m/sec.

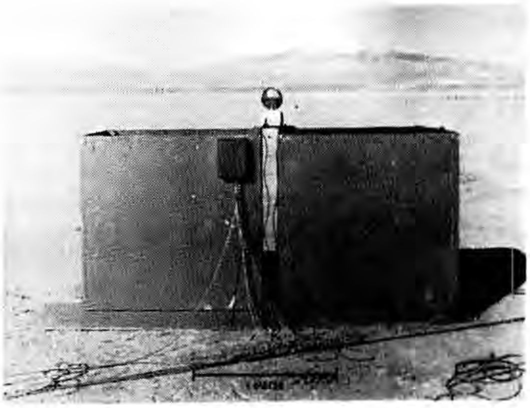

Figure 20. Photograph of MAVSS antennas.

PAVSS

The Pulsed Acoustic Vortex-Sensing System (PAVSS) makes use of refractive-scattering to locate a wake vortex by means of time delays [13]. The first refractive signals from aircraft wake vortices were observed in January 1971 [14]. In the spring of 1971, the basic PAVSS tracking system shown in Figure 21 was tested. This configuration is essentially a forward-scattering version of that shown in Figure 8c. The sensitive area is scanned by one wide fan-beam transmitter and two wide fan-beam receivers. The antenna response extends down to the horizon, so that two signals are received, one directly along the ground and one scattered from the vortex. Since refractive-scattering is produced by a bending of the propagation path in the direction of vortex rotation, only one of the two vortices will be seen by a particular transmitter-receiver pair (see Figure 21).

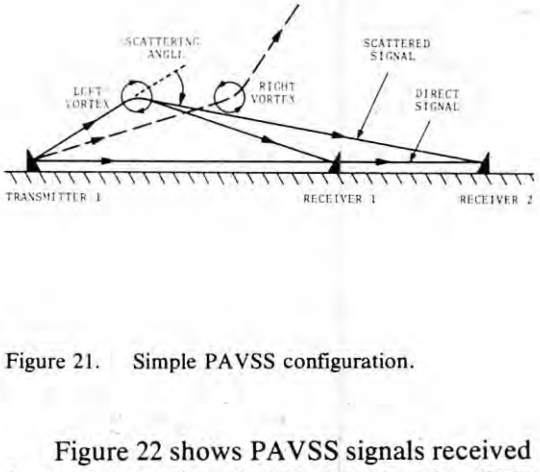

Figure 21. Simple PAVSS configuration.

Figure 22 shows PAVSS signals received from one receiver in Figure 21. The CRT intensity indicates the received acoustic intensity. The picture is scanned rapidly in the vertical direction in synchronization with the transmitter pulses (5-msec long with a 60-msec period). A slow horizontal scan gives the dependence of the signals as a function of the time after aircraft passage. The direct signal appears as a horizontal band near the bottom of the picture. The vortex signal is vertically displaced (delayed) with respect to the direct signal by an amount which depends upon the vortex location, and hence, varies with time. The time delay in arrival of the scattered signal determines that the vortex lies on an ellipse with foci at the transmitter and receiver. The exact vortex location can then be determined by the intersection of ellipses from two different transmitter-receiver pairs (see Figure 23).

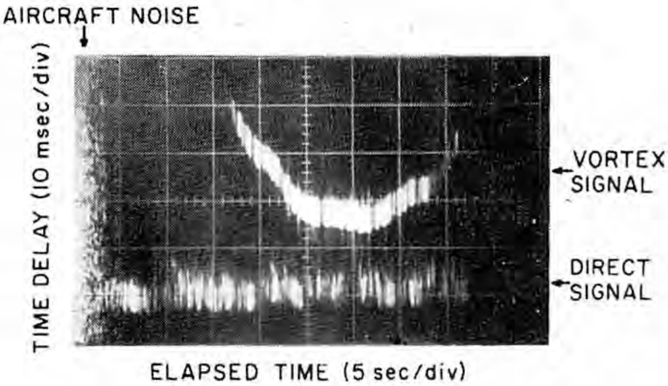

Figure 22. PAVSS signals.

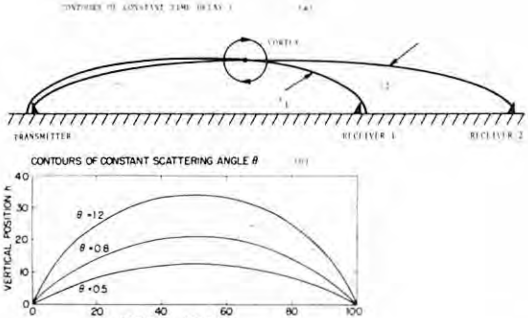

Figure 23. Contours of constant time delay and scattering angle for the simple PAVSS configuration.

Comparisons with the NAFEC tower in the summer of 1971 [18] showed that the PAVSS gave reasonably accurate vortex locations. The PAVSS was then developed to its final configuration by the winter of 1971

[19]. Frequencies in the 2- to 3-kHz range and pulse widths of 2 to 3 msec are used. Three antennas are placed on either side of the runway centerline. Each alternately transmits and receives, so that both vortices can be detected. The multiplicity of antennas is needed to give the desired spatial coverage while maintaining reasonable location accuracy. The tracking limitations of the PAVSS are discussed below.

PAVSS development continued with calibration tests at NAFEC during the fall of 1972, studies of take-off vortices at Logan Airport during the winter of 1973, and the demonstration of real-time tracking using a minicomputer during the spring of 1973. The calibration tests further verified that the PAVSS gives accurate vortex locations when properly configured for the altitudes of interest. Increasing the antenna separation to 800 m was found to increase the PAVSS altitude range to 200 m.

The Avco Corporation built an engineered version of the PAVSS which could measure vortex locations in real-time simultaneously at two different distances from the runway threshold. The system was installed at Kennedy Airport during the spring of 1974. Figure 7 shows some of the wide-beam antenna used in the Avco PAVSS. Figure 24 shows some vortex tracks obtained from the Avco PAVSS.

The ability of the PAVSS to detect and track wake vortices is strongly dependent upon the scattering angle Θ_m defined in Figure 21. Because the refractive scattering angles are small, the two ellipses in Figure 23a are very flat. Consequently, the horizontal position determined by their intersection can have large errors for small errors in the time-delay measurements. The vortex height is much less influenced by timing errors, and therefore, is given more accurately by the PAVSS. The timing errors in the signal delay measurements are typically several msec. Errors of this size lead to a horizontal position accuracy which is useless unless one of the scattering angles is greater than 0.5 radian. Smaller values of Θ also lead to difficulty in separating the direct and scattered signals since the time delays are proportional to Θ^2 for small Θ. The difficulty is illustrated in Figure 24 where the vortex signals are lost for a time when the port-vortex altitude is so low that the resultant scattering angles and time delays are too small.

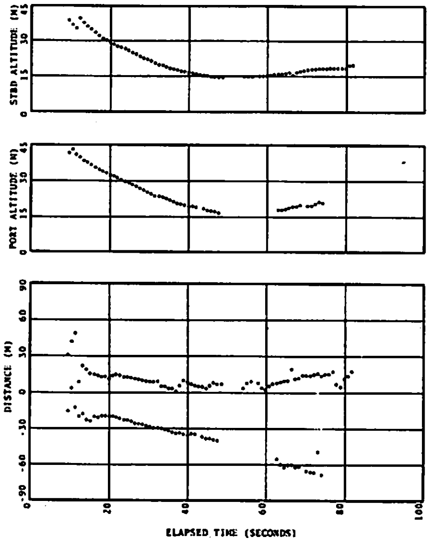

Figure 24. Vortex tracks from the Avco PAVSS.

The maximum vortex-scattering angle Θ_m (Equation (5)) determines the area where a vortex can be detected. Figure 23b shows the detection limits for three values of scattering angle. The useful tracking area is roughly the region between the 0.5-radian contour and the Θ_m contour. As discussed previously, the values of Θ_m range from 0.5 to 1.2 radians for different types of aircraft [14]. The PAVSS is thus very useful for B-727 vortices (Θ_m=1.2 radians) and is worthless for B-707 vortices (Θ_m=0.5).

LDV

The vortex-sensing Laser-Doppler Velocimeter (LDV) operates in the far infrared at the CO_2 laser wavelength λ of 10.6 microns. This wavelength selection offers the advantages of high available power, low personnel hazard, long range in fog, and feasible heterodyne detection. The LDV operates in the CW backscatter mode, making use of naturally occurring aerosols as scattering targets. The Doppler shifts in the return signals measure the component of the wind along the laser beam line-of-sight. The Doppler shifts (Equation 4 with Θ = 180 degrees and c = the speed of light) are much larger than those observed in acoustic scattering (1.9 MHz for 10 m/sec velocity). The laser frequencies are reduced to the MHz region by means of heterodyne detection which also serves to give a good signal-to-noise ratio at the detector. If the scattered light is simply mixed with the transmitted signal, the resultant velocity measurement has a sign ambiguity which can be confusing in many cases. The ambiguity can be removed if the mixing signal is offset or translated with respect to the transmitted signal.

The spatial resolution of the LDV is achieved by focusing the CW laser beam at the desired range D. For ranges much larger than the optics diameter d, the focal spot diameter is approximately λF where $F = D/d$ is the f-number of focus distance. The length of the focal spot is approximately equal to $F^2\lambda$, and therefore, is much larger than the focal width for the usual values of F. Since the length of the focal region increases as the square of the range, there is a limiting range beyond which the LDV gives no range resolution. For a 30-cm diameter beam, the half-power focus length is about 4.5 m at range of 100 m. The maximum useful range for such a beam diameter is roughly 500 m. The focusing technique for achieving spatial resolution also suffers from the fact that the response does not fall off rapidly outside the focal region [20]. This limitation can cause some difficulty in signal processing, especially if the concentration of scatterers varies along the beam.

The question may be asked: Why not use a pulsed laser to achieve range resolution, as in Doppler radar and Doppler acoustic sensors, instead of using the complicated focusing system of the LDV? The answer is that, for a specific desired spatial resolution, the single pulse-velocity resolution at $\lambda = 10.6$ microns is a factor of 100 worse than for a 3-kHz Doppler acoustic sensor. Moreover, it may not be possible to integrate over many pulses, as in a Doppler radar, because the coherence time of the scattered signal is limited by diffusion of the aerosol scatters.

The LDV can map the line-of-sight velocity field in a region by scanning its beam direction and the focal distance. The allowed scan rate is limited by the requirement that the same focal region must be observed for a time approximately equal to the inverse of the desired Doppler frequency resolution. This requirement is normally more restrictive for angle rather than range scans. The maximum rate of angle change is roughly 200 degrees/second for a beam diameter of 30 cm and a frequency resolution of 100 kHz.

The basic data generated by the LDV is the Doppler spectrum of the scattered signal. Figure 25 shows the non-translated spectrum expected when the LDV is focused near a wake vortex. The shape of the spectrum can be understood by examining Figure 26. The LDV beam probes a line through the vortex. The resulting spectrum, assuming a uniform distribution of scatterers, is given by the contribution of the line-of-sight velocity at each point along the line weighted by the LDV range response at that point. There are two regions where large contributions will occur: the first is the focal range and the second is the point where the beam is tangent to the vortex velocity and therefore measures the same velocity over a considerable distance. Since this tangential velocity is the highest velocity observed along the beam, it can be identified by the largest frequency shift seen in the spectrum (see Figure 25). Since the tangential velocity tends to give a peak in the spectrum, it can be distinguished even when the focal point is located some distance away from the tangent point.

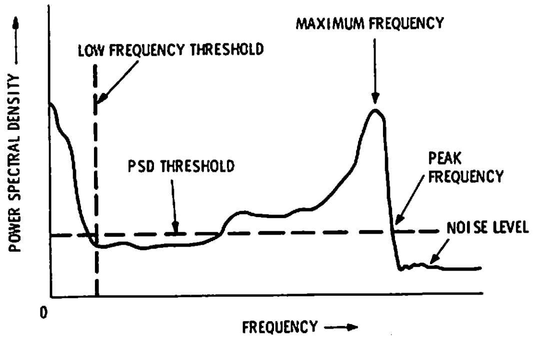

Figure 25. LDV spectrum.

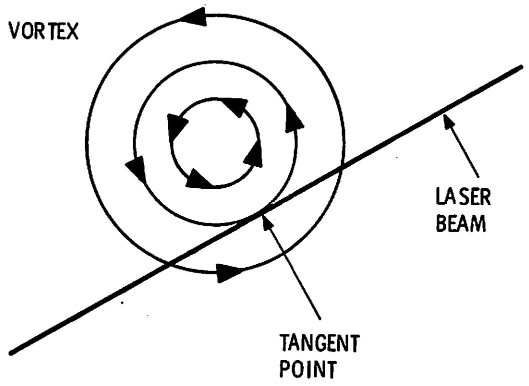

Figure 26. Intersection of the LDV beam with a vortex.

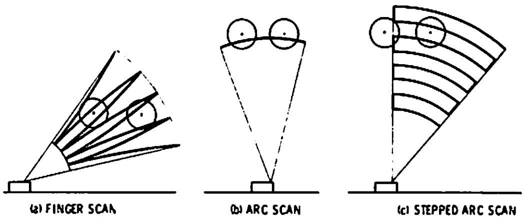

Figure 27. LDV scan modes.

Three LDV scan modes, shown in Figure 27, have been used to study wake vortices. The finger-scan mode (Figure 27a) has been used for most data collection efforts because it provides the fastest scan over a plane subject to the constraints imposed by the scanner. The range can be varied much more rapidly (7 Hz) than the angle (0.5 Hz) because the mirror to be moved is much smaller. Unfortunately, the finger-scan mode is inefficient because the data tend to be redundant. The rapid motion of the scan in range is in the direction of poor resolution so that data samples are not independent for high data rates. Moreover, the scan tends to retrace itself at the reversal points of both the range and angle scans. Figure 28 shows a vortex tangential-velocity profile generated from finger-scan data. The most notable feature is the gaps left where the focal distance was too far from the vortex to yield valid data. These gaps make the velocity profile somewhat difficult to use and also can make the determination of vortex location very difficult for non-translated data.

The arc scan mode (Figure 27b) has been used only in special tests where more detailed velocity profiles were desired. The range of the scan is selected manually. A sample velocity profile is shown in Figure 29. The arc scan mode gives good velocity profiles when the scan is near the vortex, but it is not very useful for studying vortex transport and decay since the vortex can get lost.

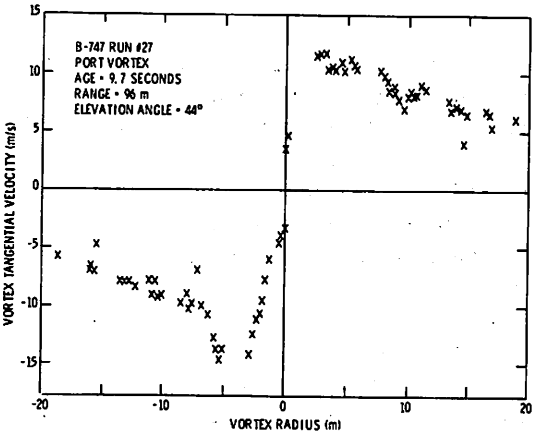

Figure 28. Vortex velocity profile from a single 2.5-second frame of LDV finger scan data. The other vortex is located in the negative direction.

(It should be noted that both Figures 28 and 29 were made from non-translated data where the velocity sign was simply reversed for one side of the vortex).

The desirability of arc-scan data for velocity measurements and accurate tracking led to the stepped arc-scan mode shown in Figure 27c. This mode can scan one frame in eight seconds and is totally nonredundant since the range can be quickly changed at the end of each arc. This mode will soon be used in measurements of vortex descent and decay for aircraft altitudes between 200 and 400 meters.

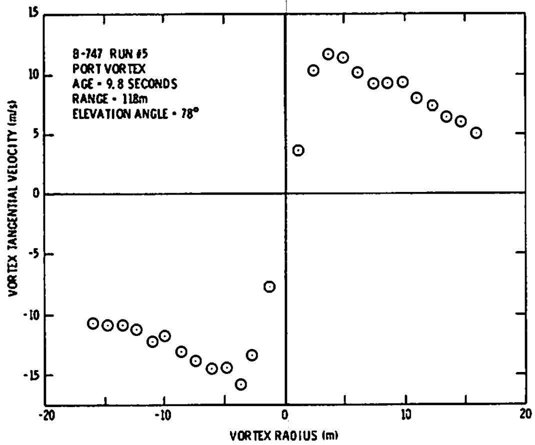

Figure 29. Vortex velocity profile from a single 1.0 second arc scan. The other vortex is located in the negative direction.

A number of different options have been used in collecting LDV data. The first choice is the type of spectrum analyzer used. The NASA Marshall Space Flight Center (MSFC) LDV system (discussed later) uses a real-time spectrum analyzer (surface acoustic wave) to make use of all the scattered power. The Lockheed LDV system uses a swept frequency spectrum analyzer which discards much of the scattered power and also takes longer to obtain a complete spectrum. Once a rate for spectrum generation has been set, the total data rate to be recorded depends upon how much of the spectral data is retained. One can keep the whole spectrum, only those spectral points above a threshold (see Figure 25) or only the spectral point corresponding to the highest spectral point or the highest frequency point with intensity above the threshold. If the intensity threshold is set too high in the last two modes, the vortex data can be extremely difficult to interpret, particularly for the non-translate mode.

The scanning LDV for use in vortex measurements was developed by the NASA Marshall Space Flight Center. It was used at the JFK Airport to detect, track, and measure the vortices generated by aircraft in the approach corridor of runway 31R between September 1974 and May 1975 [21]. The JFK installation consisted of two LDV units each scanning in range and elevation perpendicular to the landing corridor. Figure 30 shows some vortex tracks obtained with this system. The algorithms used to generate these tracks make use of the maximum spectral intensity for each data point. The spectral intensity gives more consistent vortex tracking than velocity parameters, probably because of the elevated aerosol content of wake vortices relative to the ambient level and the complex dependence of the vortex spectrum upon range.

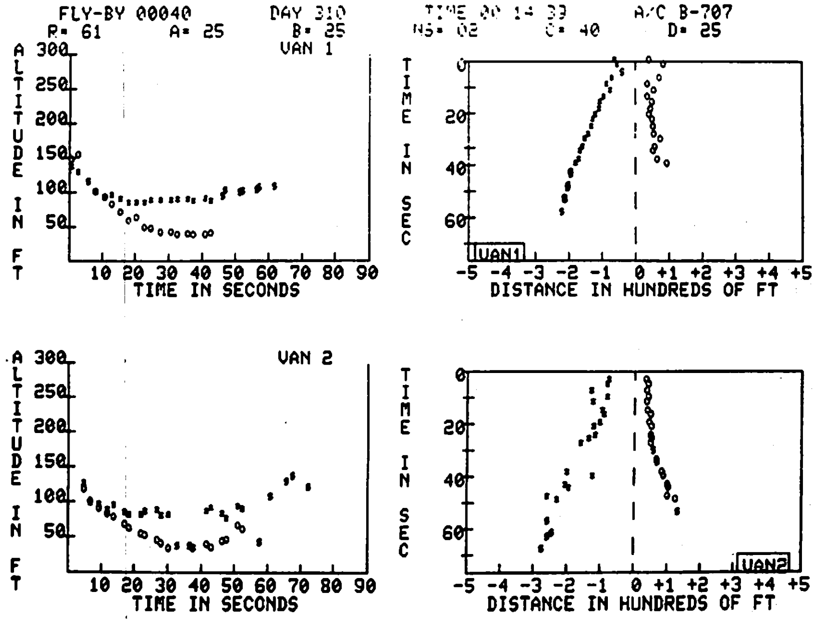

Figure 30. Simultaneous vortex tracks from the two LDV systems at JFK Airport.

Subsequent to the JFK work, a mobile LDV system was developed by Lockheed. The system has more limited real-time processing capability than the NASA LDV, but is easily moved and has a more versatile beam scanner. The system has been used to collect wake vortex data at a variety of airports and at some special B-747 vortex tests conducted at a California dry lake, from which the data in Figures 28 and 29 were taken.

The basic LDV consists of a very stable single-frequency CO_2 laser, a Mach-Zehnder interferometer, a variable focus Cassegrainian telescope, an angle scanner, a sensitive infrared detector, and (optionally) a Bragg cell frequency translator. Figure 31 shows the layout of this equipment. In addition, a scan control system and a data processing and storage system are required.

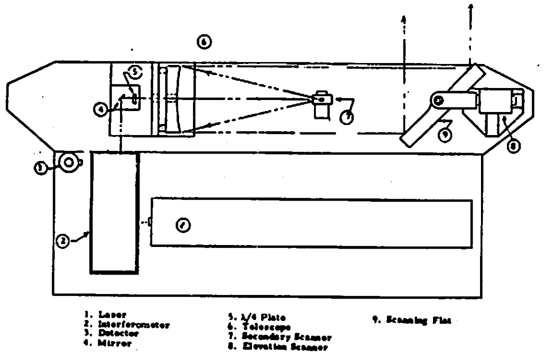

Figure 31. LDV optical layout.

COMBINATION TECHNIQUES

A combination of techniques may be more useful than a single one if the strengths and weaknesses are complementary. Two combination techniques have been suggested during the wake vortex sensor development.

The first combines the PAVSS and the GWVSS. If the lateral position of a vortex is known from the GWVSS, the vortex height could be accurately determined by a pair of PAVSS antennas. Such a system would still be subject to the aircraft-type limitations of the PAVSS.

The second combines the MAVSS and the GWVSS to yield a direct measurement of circulation for vortices stalled near the runway centerline. The circulation within an area is computed directly as a line integral around the area. The MAVSS is ideally suited for measuring the velocity-line integral along a vertical line. The measured line integrals are in reasonable agreement with the theoretical values based on the vortex strength measurement. Two MAVSS antennas would measure the vortex-line integrals along the sides of the area. The GWVSS sensors would complete the integral between the two MAVSS antennas. For low-altitude vortices, the top of the area makes no significant contribution to the line integral. Data have been collected for this configuration but have not yet been processed.

REFERENCES

1. *Aircraft Wake Turbulence and Its Detection*, edited by J.H. Olsen, A. Goldberg, and M. Rogers, Plenum Press, New York, NY, 1971.

2. "Aircraft Wake Vortices: A State-of-the-Art Review of the United States R&D Program," Edited by J.N. Hallock and W.R. Eberle, FAA-RD-77-23, Apr. 1977, Transportation Systems Center, Cambridge, MA.

3. Madden, S.J., Jr. and Harlan, R.B., "A Program to Analyze and Model Trailing Vortices on Airports," MIT Measurement Systems Laboratory Report RN-69, Oct. 1971.

4. Garodz, L.J., Lawrence, D.M., and Miller, N.J., "Measurements of the Trailing Vortex Systems of Large Transport Aircraft Using Tower Fly-By and Flow Visualization (summary, comparison and application)," FAA-RD-75-127, May 1975, NAFEC, Atlantic City, NJ.

5. Smith, H.J., "A Flight Test Investigation of the Rolling Moments Induced on a T-37B Airplane in the Wake of a B-747 Airplane," TM X-56031, Apr. 1975, NASA Flight Research Center, Edwards, CA.

6. Tombach, I.H., Bate, E.R., and MacCready, P.B., "Investigation of the Motion and Decay of the Vortex Wake of a Light Twin-Engine Aircraft," AV-FR-439, Oct. 1974, AeroVironment, Pasadena, CA.

7. Brown, C.E., "Pressure Field of a Vortex Wake in Ground Effect," *J. Aircraft*, Vol. 12, No. 2, Feb. 1975, p. 120-121.

8. Hallock, J.N. and Wood, W.D., "Joint US/UK Vortex Tracking Program at Heathrow International Airport," Volume I: Executive Summary, FAA-RD-76-58, Mar. 1976, Transportation Systems Center, Cambridge, MA.

9. Harris, C.M., "Absorption of Sound in Air versus Humidity and Temperature," *J. Acoustical Soc. Am.*, Vol. 40, No. 1, July 1966, p. 148-159.

10. Little, C.G., "Acoustic Methods for the Remote Probing of the Lower Atmosphere," *Proceedings of the IEEE*, Vol. 57, No. 4, Apr. 1969, p. 571-578.

11. Balser, M., Nagy, A.E., and Proudian, A.P., "Vortex Observations by the Xonics Acoustic Radar at NAFEC," FAA-RD-71-103, Dec. 1972, Xonics Corp., Van Nuys, CA.

12. Balser, M., McNary, C., and Nagy, A., "Acoustic Analysis of Aircraft Vortex Characteristics," FAA-RD-72-81, July 1972, Xonics Corp., Van Nuys, CA.

13. Burnham, D.C., "Characteristics of a Wake Vortex Tracking System Based on Acoustic Ray-Bending Scattering," *J. Acoustical Soc. Am.*, Vol. 61, No. 3, March 1977, p. 647-654.

14. Burnham, D., Kodis, R., and Sullivan, T., "Observations of Acoustic Ray Deflection by Aircraft Wake Vortices," *J. Acoust. Soc. Am.*, Vol. 52, Pt. 2, July 1972, p. 431-433.

15. Burnham, D.C. and Sullivan, T.E., "Influence of Flaps and Engines on Aircraft Wake Vortices," *J. Aircraft*, Vol. 11, Sep. 1974, p. 591-592.

16. Balser, M., McNary, C.A., and Nagy, A.E., "Acoustic Back Scatter Radar System for Tracking Aircraft Trailing Vortices," *J. Aircraf*, Vol. 11, Sep. 1974, p. 556-562.

17. Burnham, D.C., Sullivan, T.E., and Wilk, L.S., "Measurement of Wake Vortex Strength by Means of Acoustic Back Scattering," *J. Aircraft*, Vol. 13, No. 11, November 1976, p. 889-894.

18. Burnham, D.C., Hallock, J., Kodis, R., and Sullivan, T., "Vortex Sensing Tests at NAFEC," DOT-TSC-FAA-72-2, Jan. 1972, Transportation Systems Center, Cambridge, MA.

19. Sullivan, T., Burnham, D., and Kodis, R., "Vortex Sensing Tests at Logan and Kennedy Airports," FAA-RD-72-141, Dec. 1972, Transportation Systems Center, Cambridge, MA.

20. Sonnenschein, C.M. and Horrigan, F.A., "Signal to Noise Relationships for Coaxial Systems that Heterodyne Backscatter from the Atmosphere," *Applied Optics*, Vol. 10, No. 7, July 1971, p. 1600-1604.

21. Bilbro, J.W., Jeffreys, H.B., Weaver, E.A., Huffaker, R.M., Craig, G.D., George, R.W., and Marrero, P.J., "Laser Doppler Velocimeter Wake Vortex Tests," FAA-RD-76-11 and NASA TM X-64988, Marshall Space Flight Center, Huntsville, AL.

TSC WAKE VORTEX DATA BASE AND APPLICATIONS

JAMES N. HALLOCK, BERL P. WINSTON,
THOMAS E. SULLIVAN, AND DAVID C. BURNHAM
U.S. Department of Transportation
Transportation Systems Center
Cambridge MA 02142

ABSTRACT: An extensive data base is being compiled on the motion and decay of wake vortices near the ground. To date, data for over 40,000 vortex pairs have been recorded, analyzed, and entered into the data base. The rationale for the data collection program at each site is presented along with a description of the entries into the data base and the results of some preliminary studies using the data base.

RATIONALE FOR DATA COLLECTION

Under the sponsorship of the Federal Aviation Administration (FAA), the Transportation Systems Center (TSC) has been working on the subject of aircraft wake vortices since 1970. Prior to July 1973, the emphasis of the work was on the development of sensors to detect and to track vortices. Since July 1973 the emphasis has been on collecting data on vortex behavior and applying the knowledge of vortex behavior to the development of systems for increasing the capacity of an airport. Burnham [1] describes the sensor development effort and Spitzer, et al. [2] the vortex avoidance systems. This paper reviews the data collection which commenced in July of 1973.

JFK Tests, First Phase, and DEN Tests.

After limited tests had been conducted at Boston's Logan International Airport, the John F. Kennedy International Airport (JFK) became the first extensive test site to be instrumented in order to fully evaluate two TSC-developed vortex sensing systems, the Ground-Wind Vortex Sensing System (GWVSS) and the Pulsed Acoustic Vortex Sensing System (PAVSS). Each system consists of sensors strategically placed on lines perpendicular to the extended runway centerline. The instrumentation (two GWVSS lines and one PAVSS line) was set up in the approach region of runway 31R. In addition to the vortex tracking equipment, a meteorological tower was erected to monitor simultaneously the winds.

At the time the JFK site was being established, the FAA requested that the Instrument Flight Rules (IFR) and vortex separations be checked to ascertain their adequacy for protecting commercial aircraft from an inadvertant vortex encounter. Because of the expected limited traffic using runway 31R at JFK, it was decided to instrument a second runway. Since JFK did not have adequate real estate for the vortex tracking equipment on the approaches to their other runways, a second airport was selected: Denver's Stapleton International Airport (DEN). The choice of DEN was prompted by: (1) available real estate on the approach to runway 26L, (2) the different climate as compared to Jamaica, New York, and (3) the chance to record aircraft types which do not frequent JFK (e.g., B-737). Two GWVSS, one PAVSS, and two meteorological towers were set up at DEN.

Data collection began at JFK in July 1973 and at DEN in August 1973. By November 1973, at which time the DEN site was closed, vortices from over 10,000 aircraft had been monitored (3100+ at JFK and 6900+ at DEN). From the data it was shown that the IFR and vortex separations were indeed adequate for preventing a vortex encounter. In fact, the data base indicated that most of the time the separations were unnecessarily restrictive.

For the next two and a half years, the JFK site was used as it was originally intended — an operational site for testing and evaluating vortex sensors including laser sensors and other acoustic devices (see Burnham [1] for descriptions of these sensors).

LHR Tests.

From June 1970 onwards, unsolicited reports of possible vortex encounters were received by air traffic control officers at the London Heathrow International Airport (LHR). Consequently, the Civil Aviation Authority (CAA) instituted a program to gather information on wake behavior under operational conditions, and on the effect of a wake vortex encounter by various civil aircraft [3]. The majority of incidents occurred at or near Heathrow and on final approach. In some cases, the encounter took place very near to the ground. Incidents were reported from a wide variety of aircraft pairs (leader/follower) and it was found that the heaviest jets (B-747 and L-1011) caused 40% of all incidents, in spite of the fact that they constituted only about 12% of all traffic at Heathrow during peak periods. After consideration of the incident reports and consultation with the appropriate operations groups, the approach separation distance for lighter aircraft following a widebody jet in the United Kingdom was increased in March 1974 from 5 to 6 nautical miles.

There has been close liaison between the CAA and the FAA on wake vortex research for some years. They jointly agreed in late 1973 that it would be beneficial if equipment similar to that tested at DEN and JFK could be installed at LHR. The test program would afford the opportunity to expand significantly the vortex track and meteorological data base under new and varied environmental conditions, to correlate reported vortex incidents with measured vortex and meteorological conditions, and to track vortices from a number of aircraft rarely seen in the United States, e.g., Trident, Viscount, and A-300B.

The equipment (two GWVSS, one PAVSS and two meteorological towers) were emplaced on the approach to runway 28R and became fully operational in May 1974. Data collection continued through June 1975. A total of 12,950 landings were monitored [4]. As a result of the LHR tests, the correlation between the ambient meteorology and vortex behavior was underscored. It was noted that it would be safe to use decreased aircraft separations often and the concept of the Vortex Advisory System (see Spitzer, et al. [2]) was born.

JFK Tests, Second Phase.

Tests were continued at JFK to assist in the design of the Vortex Advisory System (VAS) and to study the decay of vortices in the terminal area. Parts of the tests began in the Fall of 1975 but the full tests began in March 1976 and continued to the closing of the JFK site in January 1977. Over 4700 aircraft passages were monitored in the March 1976 to January 1977 time frame.

Two facets of vortex lateral motion are being examined. First, how far can vortices drift in ground effect? One GWVSS line was extended to allow the tracking of vortices to a distance of 3000 feet from the extended runway centerline. The data (still being evaluated) should indicate how far apart parallel runways need to be in order to be considered independent with respect to a possible vortex encounter. Second, three GWVSS lines (located at the threshold of the runway, approximately 2000 feet from the threshold, and approximately 4000 feet from the threshold) were installed to reveal the variation in vortex lateral motion as a function of distance from the runways threshold, or, alternatively, as a function of the height of the vortex-generating aircraft.

The decay of vortices was studied at JFK using a Monostatic Acoustic Vortex Sensing System (MAVSS) as described by Burnham [1] and Burnham et al. [5]. The analysis of the data [6] led to a revision of the IFR and vortex separation standards for General Aviation aircraft following commercial aircraft — aircraft with a certificated gross takeoff weight less than 12,500 pounds are spaced 4 nautical miles behind aircraft with certificated gross takeoff weights between 12,500 pounds and 300,000 pounds, and are spaced 6 nautical miles behind aircraft with certificated gross takeoff weights in excess of 300,000 pounds. The new rule was promulgated in November 1975.

A new question also arose. The United States defines a "Heavy" aircraft as one that has a certificated gross takeoff weight in excess of 300,000 pounds. The United Kingdom defines a Heavy aircraft as one that has a certificated gross takeoff weight in excess of 375,000 pounds. Thus, the 320 and 420 series of the B-707 and the 60's series of the DC-8 are categorized as "Heavy" in the United States but not in the United Kingdom. Thus, for light aircraft in the United States, a 5-mile separation was required behind the "Heavy" 707's and DC-8's while in the United Kingdom, only 4 miles was required. This difference has a large impact on the peak traffic flow rate and it was decided to try to resolve the discrepancy. The appropriate designation can be determined by studying the vortex strength/decay and the influence upon following aircraft. A limited amount of applicable data was collected at JFK and additional data is now being collected at Chicago's O'Hare International Airport (ORD).

ORD Tests.

The primary purpose of the ORD tests is the evaluation of the Vortex Advisory System [2]. The approach region of runways 32L, 14R and 27R were each instrumented with a GWVSS line. Outputs from the VAS are being compared with actual vortex behavior as measured by the three GWVSS. Since July 1976 when the tests began, over 13,000 vortex pairs have been recorded and the data reduced.

A MAVSS has also been installed in the approach region of runways 32L and 14R. The strength of vortices and their subsequent decay is being studied. In particular, the B-707 and DC-8 aircraft, both regular and those designated as "Heavy", are receiving special attention, with the assistance of the Air Transport Association and three of the major airlines operating B-707's and DC-8's at ORD (UAL, TWA, AAL). The individual landing weights of each of these aircraft are being obtained from the airlines and entered into a data base consisting of the aircraft type and flight number, time code, vortex strength as a function of vortex age, meteorological conditions, etc.

The YYZ Tests.

The Vortex Advisory System is based on an algorithm of wind criterion which has been shown to be valid for landing aircraft. A lesser but still important problem is the delay encountered by aircraft queuing to take off. One would optimistically hope that the VAS wind-criterion algorithm either as is or slightly modified could be used also for controlling the spacing of aircraft taking off. A joint program has been initiated with the Canadian Ministry of Transport to address this question. The vortices shed by aircraft departing on runway 23L at the Toronto International Airport (YYZ) are being monitored by three GSVSS lines, one MAVSS line and a photographic system which determines the height of the aircraft over the sensor lines. The tests began in August 1976 and will continue through August 1977. To date, over 3000 takeoffs have been recorded.

RECORDED DATA

Tables 1 to 5 list the data compiled in the TSC wake vortex data base. Unless otherwise noted, the vortex data discussed were obtained from the GWVSS. Most of the table entries are self-explanatory; the remainder are discussed below.

The winds were measured using tower-mounted anemometers. Each tower was instrumented at one or more levels or "positions." For example, in Table 1 the early JFK tests used only one tower and one anemometer pair for the wind measurements. The later tests used two towers instrumented at two heights yielding four "positions." The DEN tests used two towers but only the upwind tower values were retained (a vortex often passed over the downwind tower and corrupted the ambient wind measurements). Heathrow employed two towers instrumented at two heights. Toronto has one tower instrumented at two heights with the lower height containing two sets of sensors. Except for the ORD work, the atmospheric turbulence was calculated using the measured winds and a selected time constant.

Table 1. JFK International Airport

July 18, 1973 — November 10, 1973

GWVSS	
Aircraft Type	(B-727, B-707, DC-8, B-747, B-737, etc.)
Headwind	(20-second average; one position)
Crosswind	(20-second average; one position)
Horizontal Wind	(20-second magnitude average; one position)
Turbulence	(5-second time constant $\epsilon^{1/3}$ value; one position)
Port and Starboard Vortex Residence Time	(time to next aircraft; based on sample rate)
Run Duration	

September 10, 1974 — November 23, 1974

MAVSS	
Aircraft Type	(B-727, B-707, B-747, DC-8, B-737, etc.)
Time Code	(hour:minute:second)
Observed Time of Vortex Crossover	(since start of run)
Vortex Strength	
Vortex Core Height	
Estimated Vortex Transport Velocity	
Headwind	(60-second mean, σ; two positions)
Crosswind	(60-second mean, σ; two positions)
Vertical Wind	(60-second mean, σ; two positions)
Horizontal Wind	(60-second magnitude mean, σ; two positions)
Turbulence	(60-second $\epsilon^{1/3}$ mean; two positions)

March 8, 1976 — January 13, 1977

GWVSS	
Aircraft Type	(B-727, B-707, DC-10, L-1011, B-747, etc.)
Time Code	(day:hour:minute:second)
Weather	(sunny, overcast, sunny/10% clouds, rain, etc.)
Headwind	(60-second mean, σ; four positions)
Crosswind	(60-second mean, σ; four positions)
Vertical Wind	(60-second mean, σ; four positions)
Horizontal Wind	(60-second magnitude mean, σ; four positions)
Relative Solar Flux	(from pyranograph readings)
Aircraft Ground Speed	(between baselines 1 and 2, 2 and 3, 1 and 3)
Baselines #1, #2, #3	
— Port and Starboard Vortices	
-Residence Time	
-Death Time (end of track time)	
-Death Position	

Table 2. Stapleton International Airport

August 24, 1973 — November 21, 1973

GWVSS	
Aircraft Type	(B-727, B-707, DC-8, Business Jet, etc.)
Headwind	(20-second average; one position)
Crosswind	(20-second average; one position)
Horizontal Wind	(20-second magnitude average; one position)
Turbulence	(5-second time constant $\epsilon^{1/3}$ value; one position)
Inner and Outer Baselines	
— Port and Starboard Vortices	
-Residence Time	
Run Duration	(time to next aircraft; based on sample rate)

Table 3. Heathrow International Airport

	April 28, 1974 — June 30, 1975
GWVSS	
Aircraft Type	(B-727, B-747, L-1011, Trident, BAC-111, etc.)
Time Code	(hour:minute:second; at inner baseline)
Headwind	(60-second mean, σ; four positions)
Crosswind	(60-second mean, σ; four positions)
Vertical Wind	(60-second mean, σ; four positions)
Horizontal Wind	(60-second magnitude mean, σ; four positions)
Turbulence	(60-second $\epsilon^{1/3}$ mean, σ; four positions)
Estimated Aircraft Ground speed from aircraft detectors	
B-747 weight when provided	
Inner and Outer Baselines	
— Port and Starboard Vortices	
-Residence Time	
-Death Time (end of track time)	
-Death Position	

Table 4. O'Hare International Airport

	July 14, 1976 — Present
GWVSS	
Runway	(32L, 14R, 27R)
Aircraft Type	(B-727, B-707, DC-8H, B-747, etc.)
Time Code	(day:hour:minute:second)
Weather	(sunny, overcast, sunny/10% clouds, rain, etc.)
Headwind	(60-second average, calculated through VAS)
Crosswind	(60-second average, calculated through VAS)
Turbulence	(measured using Sigma meter)
Temperature	
Pressure	
B-707 and DC-8 weight and flight number, when provided	
VAS Runway Status (Red, Green, Red/Green, Off)	
Port and Starboard Vortex Residence Time	
MAVSS	
Observed Time of Vortex Crossover (since start of run)	
Vortex Strength (Γ' at 5, 10, 20, 30 meters from core center)	
Vortex Core Height	
Estimated Vortex Transport Velocity	

Since it was anticipated that vortices from a landing aircraft usually move away or dissipate before a following aircraft arrives, it was decided to analyze the extensive amount of vortex track data in terms of how soon the vortices exit a "safety region." The safety region is centered on the extended runway centerline. The width of the safety region was determined by considering two points: First, a measurement program by TSC at DEN showed that 3σ or 99.74% of all landing aircraft were within 50 feet of the extended runway centerline at 1500 feet from threshold. Second, 6-degree-of-freedom aircraft-vortex encounter simulations [7] indicated that if the fuselage of any aircraft were at least 100 feet from the center of any vortex, the encountering aircraft would not experience an unacceptable disturbance. The figure is conservative, and represents the worst case of a light general aviation aircraft approaching a vortex formed by a wide-body jet; the exact figure depends upon the individual characteristics of the vortex-generating aircraft and the encountering aircraft. Thus, the safety region was selected to have a width of 50 + 100 or 150 feet on both sides of the extended runway centerline. If

Table 5. Toronto International Airport

August 13, 1976 — Present

Aircraft Type	(B-727, B-707, DC-8, B-747, L-1011, etc.)
Time Code	(day:hour:minute:second)
Weather	(sunny, overcast, sunny/10% clouds, rain, etc.)
Aircraft Ground Speed	(between baselines 1 and 2, 1 and 3, 2 and 3)
Headwind	(60-second mean, σ: three positions)
Crosswind	(60-second mean, σ: three positions)
Vertical Wind	(60-second mean, σ: three positions)
Horizontal Wind	(60-second magnitude mean, σ: three positions)
Turbulence	(60-second $\epsilon^{1/3}$ mean, σ: three positions)
Temperature	
Lapse Rate	

Baselines #1, #2, #3
  — Port and Starboard Vortices
    -Position at 30, 60, 90, 120 seconds after start of run
    -Death Time (end of track time)
    -Death Position

MAVSS
  Observed Time of Vortex Crossover (since start of run)
  Vortex Strength (Γ' at 5, 10, 20, 30 meters from core center)
  Vortex Core Height
  Estimated Vortex Transport Velocity

both vortices are clear of the safety region, they cannot pose any threat to a following descending aircraft landing on the same runway. The size of the safety region is very conservative; even if both the following aircraft and a vortex from a preceding aircraft are observed to be in the safety region at the same time, the vortex may have decayed sufficiently that it could not affect the following aircraft. Additionally, the aircraft and vortex can be separated by as much as 200 feet and yet both be within the safety region.

In the tables and in the ensuing discussion of the data, the term "residence time" refers to the time it takes for both vortices to exit the safety region. Each vortex may either be blown out of the safety region or be eliminated by a decay process while the vortex is still within the safety region. Note that the existence of a vortex within the safety region at a given time does not necessarily imply that it could constitute a hazard to a following aircraft: The vortex could have decayed to a strength sufficiently below the hazard threshold of the encountering aircraft, the vortex being tracked may have been generated by an aircraft whose vortices will not affect the following aircraft (e.g., a Twin Otter followed by a B-747), or the vortex of the oncoming aircraft might be separated by sufficient lateral distance such that the aircraft will barely detect the presence of the vortex in the safety region.

DATA ANALYSES — VORTEX BEHAVIOR

Vortex behavior can be examined by retrieving particular information from the data base. Figure 1 shows the probability of finding a vortex in the safety region as a function of the time after an aircraft passed over the vortex-tracking equipment. For example, 16 percent of the data yielded a vortex in the safety region after one minute; in the remaining 84 percent of the cases, the vortices either exited the safety region or decayed within it. The figure is a composite of data recorded at Denver, Kennedy, Heathrow, and Chicago Airports and represents the results of approximately 40,000 aircraft.

In the following subsections, the information in Figure 1 is re-examined to ascertain the dependence on aircraft type, the winds, the mode of exiting the safety region (drifting out or decaying), the different vortex behavior at various sensor baseline locations, the time between the first and second vortex exiting the safety region, and the conditions which lead to residence times in excess of 80 seconds.

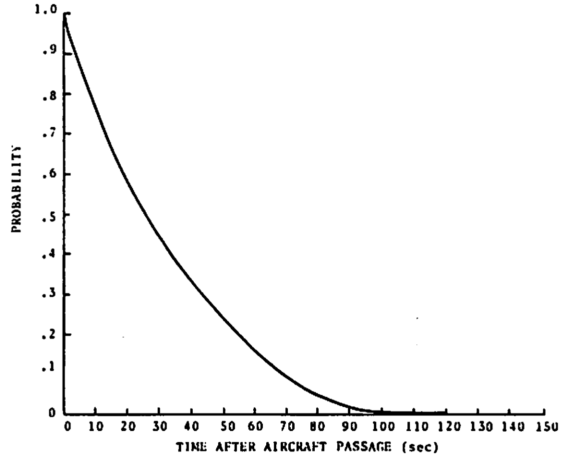

Figure 1. The probability of finding a vortex in the safety region as a function of the time after the aircraft has passed.

Residence Times by Aircraft Type.

In Figure 2, the data of Figure 1 is reproduced along with curves for the wide-body jets (B-747, DC-10, and L-1011) and for small commercial jets (DC-9 and BAC-111). The type of aircraft generating the vortices plays an important role on the longevity of a vortex within the safety region. The wide-body jets constitute a significant portion of the older residence-time cases. If a vortex is found inside the safety region after 80 seconds, the probability is very high that the vortex was shed by a wide-body aircraft.

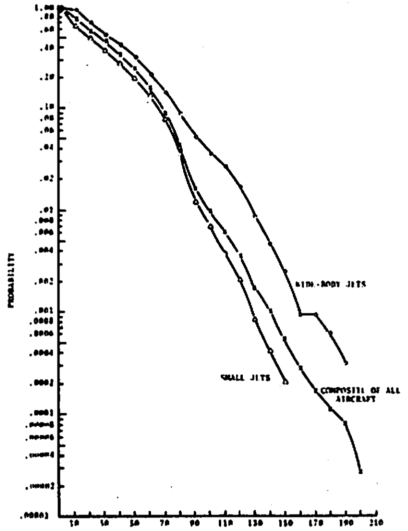

Figure 2. The probability of finding a vortex in the safety zone as a function of the time after the aircraft has passed.

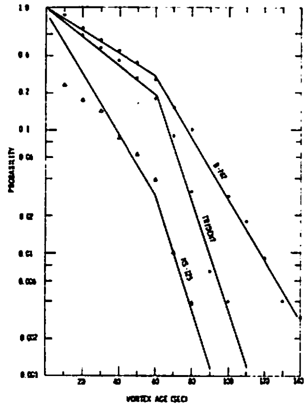

Figure 3. The probability of finding a vortex in the safety zone as a function of the vortex age.

Figure 3 further breaks down the data to specific aircraft. Except for the TU-134 and the Mystere, all the aircraft types exhibited a discontinuity at 60 seconds. The probability of finding a vortex in the safety region can thus be described by two exponentials. It is conjectured that the first exponential (short times) is fundamentally the probability that the vortices translate out of the safety region, and the second exponential (long times) is the probability that the vortices decay in the safety zone. For times between 0 and 60 seconds (0 and 40 seconds for the TU-134 and the Mystere), the probability is

$$e^{-\alpha_1 t}$$

and for times greater than or equal to 60 seconds,

$$Ae^{-\alpha_2 (t-60)}$$

the exponent will contain the term (t-40) for the Mystere and the TU-144; in the ensuing discussion, these two aircraft will be omitted for convenience. The coefficient A is the probability of finding a vortex in the safety region at 60 seconds. Table 6 gives the relevant constants as determined from the Heathrow data. Note that the exponential forms will overestimate the probabilities at large times. For instance, no vortex was found in the safety region in excess of 120 seconds for a B-727, yet the exponential form will yield a non-zero probability.

Table 6. Coefficients for Probability of Finding a Vortex in Safety Zone

AIRCRAFT TYPE	α_1	A	α_2
IL-62	0.0215	0.275	0.0552
B-747	0.0230	0.252	0.0554
L-1011	0.0229	0.252	0.0742
A-300	0.0245	0.230	0.0583
VC-10	0.0245	0.230	0.0777
DC-8	0.0245	0.230	0.0784
B-727	0.0256	0.219	0.1027
B-707	0.0262	0.207	0.0649
B-720	0.0288	0.178	0.0353
DC-9	0.0291	0.175	0.0763
Trident	0.0292	0.173	0.1031
Caravelle	0.0300	0.165	0.0758
B-737	0.0316	0.148	0.0702
BAC-111	0.0335	0.143	0.0715
Viscount	0.0332	0.136	0.1070
F-27	0.0334	0.135	0.2453
Herald	0.0415	0.083	0.2209
HS-125	0.0541	0.038	0.1181

The aircraft in Table 6 are arranged in decreasing order of the coefficient A, the probability of finding a vortex in the safety region at 60 seconds. It is of note that the ordering closely follows that of decreasing aircraft weight.

Residence Times — Wind Effects.

Crosswind magnitude plays an important role in the motion of the vortices. Figure 4 shows the probability of a vortex remaining in the safety region for various crosswinds. The figure is a composite of all aircraft types; the data for specific aircraft types are similar; the lighter the vortex-generating aircraft, the closer the curves approach the origin of the graph. Eighty seconds represents an aircraft-to-aircraft spacing of less than three nautical miles for the approach speeds of most aircraft. On the basis of Figure 4, it is reasonable to predict that wake vortices are unlikely to be troublesome when there are crosswinds greater than 5 knots.

For a specific crosswind, the average residence time increases with aircraft size. The largest average residence times occur at a higher crosswind magnitude for the jumbo jets than for all other aircraft. These trends are related to the fact that the stronger the vortex, the higher the crosswind required to stall the vortex in the safety region.

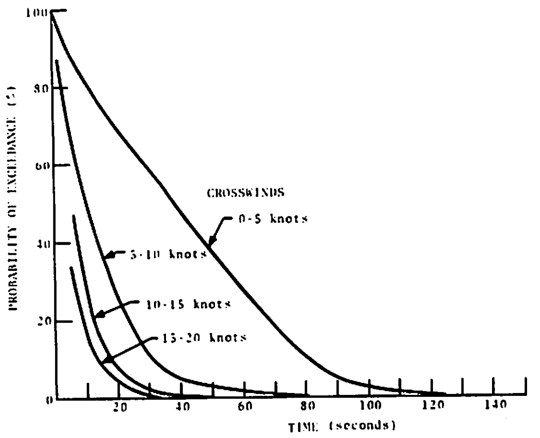

Figure 4. The probability of finding a vortex in the safety zone as a function of vortex age and crosswind.

Residence Times — How Vortices Exit Safety Region.

Vortices exit the safety region by either transporting out or by decaying in the region. Most of the vortices with a residence time in excess of 40 seconds decay in the safety region while most of the vortices with a residence time of 40 seconds or less move out of the region.

Vortex Behavior at Various Sensor Baselines.

Near the runway threshold the aircraft generating the vortices are well within ground effect. The downwash field causes the vortices initially to descend and to interact very strongly with the ground. Usually, one of the vortices (the upwind vortex) very quickly disappears, most likely because of a catastrophic interaction with the ground. The remaining vortex then moves away very quickly. It is a rare event when a vortex shed near the runway threshold persists for 80 seconds; because of the strong ground interaction, it is unlikely that such a vortex could have sufficient strength to affect another aircraft.

At or beyond the middle marker location (3500 feet from the runway threshold), the aircraft are over 200 feet above the ground, so that the vortices are barely within ground effect. For the first 10 to 20 seconds, the vortices move with the wind, and, usually, do not remain in the safety region for any significant amount of time. When a vortex stalls, it usually is outside the region or at least is low enough below the typical aircraft glide path that it is unlikely that the vortex could cause an unacceptable disturbance to a following aircraft. Most of the cases in this location where a vortex is found in the safety region after 80 seconds are those in which the vortex either exited the region and re-entered or stalled near the extreme edge of the region.

The sensor baselines positioned about 2000 feet from a runway threshold are the important baselines. Here, when a vortex lingers, the vortex is at about the same altitude as a following aircraft would be, and these vortices, in a probabilistic sense, are the ones which can linger longer than those

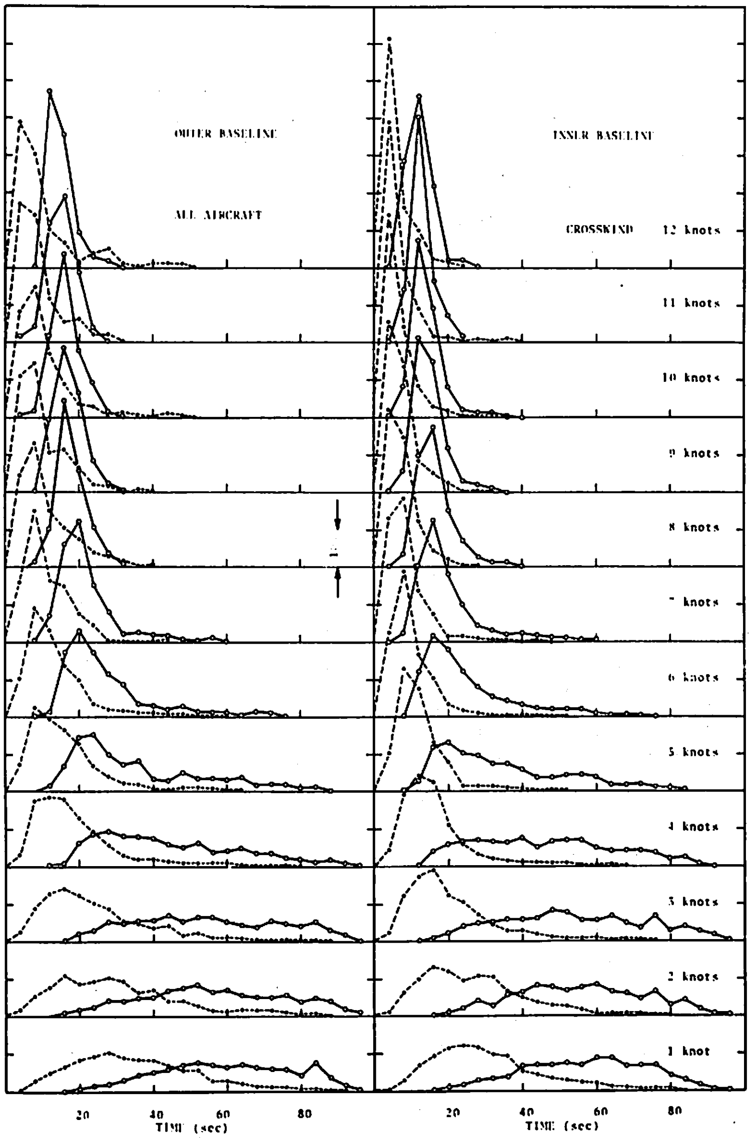

Figure 5. The probability of finding both vortices in the safety zone as a function of both vortex age and crosswind.

near the runway threshold or the middle marker. Each test site always was provided with a sensor baseline in this region. All the data presented in the figures refer to the 2000-foot region.

The residence times for two sensor lines (Heathrow) which were both in the intermediate regime (1200 and 2300 feet from the runway threshold) were compared. Since the aircraft altitude is about the same over both baselines, the residence times should be about the same. The wind at the two sensor lines need not be the same, particularly with low winds, and should be reflected in a random variation between the residence times and lead to a non-negligible standard deviation. For the Heathrow data, the residence times differed by only 1.6 seconds on the average with a standard deviation of 23.7 seconds; the lower the winds (and hence, the larger the variation in the winds between the two baselines), the higher the standard deviation (a maximum of 36.1 seconds). With high winds, particularly high crosswinds, the standard deviation decreased to a minimum of 7.9 seconds.

First and Second Vortex Crossings.

Residence time was defined as the time required for both vortices to exit the safety region; in other words, the time the second vortex leaves the safety region. Suppose the time of the exiting of the first vortex is known, can the time that the second vortex exits be predicted?

Figure 5 shows the distributions of the crossing times as a function of the crosswind (data from the Heathrow tests). The broken lines indicate the distributions of the first crossing, and the solid lines indicate the second crossing. As the crosswind magnitude increases, the first vortex exits sooner (the peak of the distribution), and the distribution becomes narrower. The second vortex seems to exit the safety region almost randomly for crosswinds up to 4 knots, but the distribution becomes more peaked, and the vortex exits sooner as the crosswind increases. Similar distributions exist for specific aircraft types, only the location of the peaks of the distributions differ (earlier times for the lighter aircraft, and later times for the heavier aircraft). The crosswind magnitude, however, appears to be the most important quantity for estimating when the safety region will be clear of vortices. If a high confidence level is necessary (as indeed it would be for any predictive system), knowing the time at which the first vortex exits does not significantly improve a prediction of the residence time.

Residence Times — Cases Which Exceed 80 Seconds.

One method for decreasing delays at an airport would be to determine those times during which all aircraft separations on final approach could be safely decreased to 3 nautical miles (instead of the current 3, 4, 5 or 6 nautical miles depending on the type of lead and following aircraft). It would be expected that such times are dependent on the wind velocity; e.g., crosswinds in excess of 5 knots were shown previously to appear to alleviate the wake vortex problem.

To identify the appropriate wind conditions, data on the heavy aircraft (B-747, DC-10, L-1011, stretched versions of DC-8 and B-707, Super VC-10, IL-62, and A-300) whose vortices had a residence time of 80 seconds or more were segregated from the data base. A ground speed of 135 knots means that 3 nautical miles is equivalent to 80 seconds. All the 80-second or more data are contained within an ellipse with a semi-major axis (headwind/tailwind axis) of 12 knots and a semi-minor axis (crosswind axis) of 5.5 knots. Any number of geometrical patterns could have been used to enclose the data, but the ellipse is a convenient pattern with a low enclosed area. This ellipse became the wind-criterion algorithm for the VAS.

It should be noted that just because winds are measured to be within the ellipse does not mean that every vortex will remain in the safety region for 80 seconds or more. It a vortex has lingered within the safety region for 80 seconds or more, then the winds have been within the ellipse. When the winds are within the ellipse, less than 5 percent of the vortices will persist in the safety region in excess of 80 seconds. The overly conservative dimensions of the safety region, the ignoring of aircraft types, the ignoring of vortex decay because of atmospheric turbulence or the nonstability of the atmosphere, etc., all contribute to restricting the times when the separations could be decreased. Additional research now underway should provide other criteria to shrink the size of the ellipse.

VORTEX DECAY

Although vortices have been detected in the safety region for times in excess of 80 seconds, nothing is as yet known about the strength of these vortices. The data discussed in the previous sections were collected using baselines of propeller anemometers. It is possible that only remnants of the vortices are being tracked which would be unable to affect an aircraft which inadvertantly penetrated or encountered them. In this section, the demise of vortices as indicated by the wealth of anemometer data will be discussed first. The section will close with a discussion of the ongoing program to measure directly the strength or circulation decay of vortices in the terminal environment.

Anemometer Data.

Various studies have shown that the demise of vortices correlates best with the magnitude of the total wind. The lower the wind magnitude, the longer a vortex will survive on the average. McGowan devised a curve to indicate the maximum lifetime of a vortex as a function of the total wind. He obtained the relationship by fairing a curve to all the known (in 1970) vortex lifetime data in such a manner that all the data were included under this curve. McGowan's curve has been widely used. The TSC data includes conditions omitted from the McGowan curve. Most of the data that McGowan had available came from tower tests. Smoke from cannisters on a tower became imbedded in the vortices shed by aircraft making low passes upwind of the tower. Decay was assessed visually. By necessity, this type of data involved mainly a crosswind component since a crosswind was required to translate the vortices to and past the tower. At Heathrow, the winds were from all directions, and a particular component of the wind was not required to move the vortex, so that it could be tracked. What McGowan's curve neglects is the effect of winds along the direction of the vortex. Winds along the vortex axis seems to suppress meanderings of the vortex and thus delays at least one of the known decay modes (sinuous or Crow instability). When the wind is orthogonal to the vortex axis, the shearing action of the wind across the vortex can aid in the dissipation process. Thus, the data alter the McGowan curve for the high winds as shown in Figure 6.

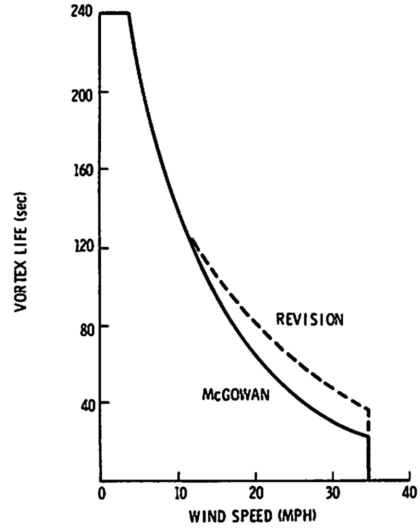

Figure 6. The McGowan life-time curve and the proposed revision.

Figures 7 and 8 present the probability of finding a vortex still active at a given age for various total wind magnitudes. The vortex lifetime for each increment of the horizontal wind can be fitted with the form

$$T_{life}(t) = 1.0, \qquad t \leq T_A,$$
$$= e - \beta^{(t-T_A)}, \qquad t > T_A.$$

For the two cases shown, the B-747 and the Trident, T_A was found to be dependent on the horizontal wind. The natural turbulence in the wind appears to dissipate the vortices in high winds. When the winds exceeded 20 knots, no vortices existed for more than 60 seconds. The vortices of light aircraft very often were not detected in high winds; HS-125 vortices were never detected when the wind exceeded 15 knots, but this may be attributed to the increased sensor-noise level. When using anemometers, a vortex is said to have died when the vortex signal is not distinguishable from the ambient wind.

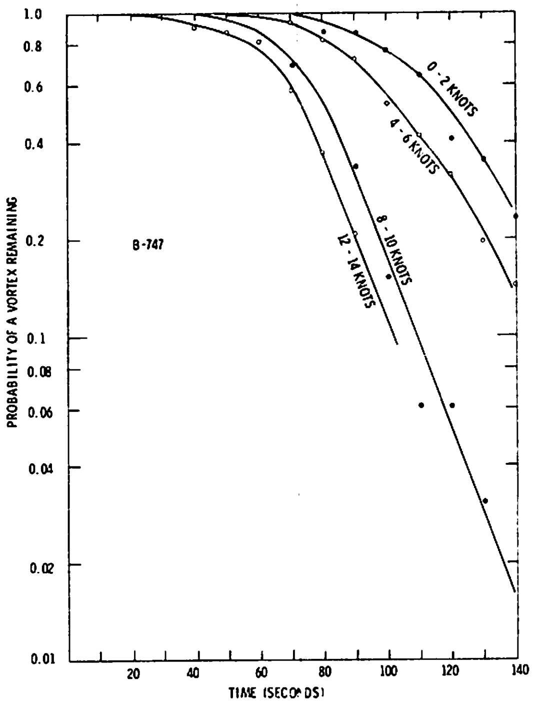

Figure 7. The probability of a B-747 vortex existing as a function of the total wind.

Monitoring Vortex Decay.

As part of the extensive program to monitor the behavior of wake vortices in the terminal environment, the strength or circulation of vortices was briefly measured for aircraft landing on runway 31R at JFK Airport in New York. Further work is now in progress at Chicago's O'Hare where vortex strength is being recorded for aircraft landing on runways 32L and 14R, and at Toronto's International Airport where vortex strength is being recorded for aircraft departing from runway 23L. Arrays of monostatic acoustic sensors are used to measure vortex vertical velocity fields; successive measurements of the velocity field of the same vortex are obtained as the vortex passes over each sensor.

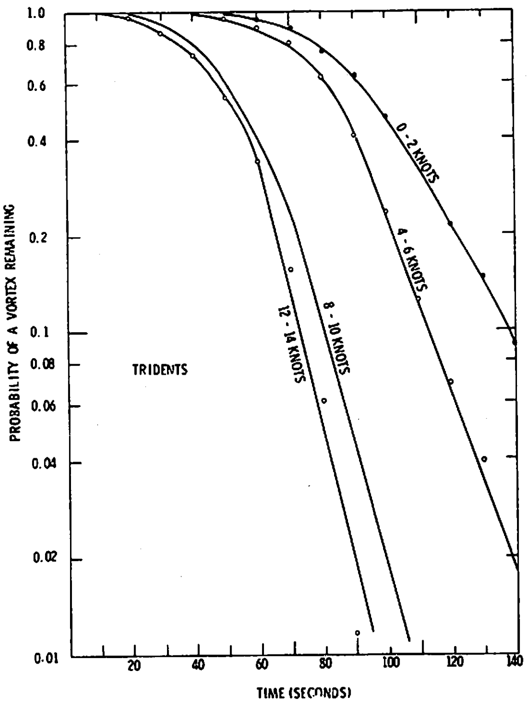

Figure 8. The probability of a Trident vortex existing as a function of the total wind.

The vertical velocity distributions are used to calculate an "effective" strength. The "effective" strength is the circulation of an equivalent line vortex producing the same torque on a wing as would be produced by the measured vortex velocities. In other words, the first moment of the measured vertical velocity distribution is equated to the first moment of a potential or line vortex:

$$\int_{-b/2}^{b/2} v_{\text{potential}}\ r\ dr = \int_{-b/2}^{b/2} v_{\text{measured}}\ r\ dr.$$

Since $v_{\text{potential}} = \Gamma/(2\pi r)$,

$$\Gamma = \frac{2\pi}{b}\int_{-b/2}^{b/2} v_{\text{measured}}\ r\ dr,$$

where Γ is the "effective" strength, b is the wing span of a hypothetical vortex-encountering aircraft, and V_{measured} are the vertical velocities measured by the monostatic acoustic sensors. To perform the integration, the radial parameter is transformed to time as the measured velocities are recorded as time histories. Thus, $r = V_T t$, where V_T is the horizontal transport velocity of a vortex over each sensor (obtained by noting the time at which the vortex is directly over each sensor and assuming a constant transport velocity between sensors).

Figures 9, 10, and 11 show examples of the data from the brief trials at Kennedy Airport; each figure exhibits an apparently different but equally probable mode of decay. Up to four independent measurements of effective vortex strength can be made for each vortex (noisy channels often precluded obtaining all four measurements). Solid lines in the figures connect the data for the same vortex. In Figure 9, four of the cases have been extended with broken lines; here, the vortex was not seen in the next sensor as the strength decayed below the instrumental threshold.

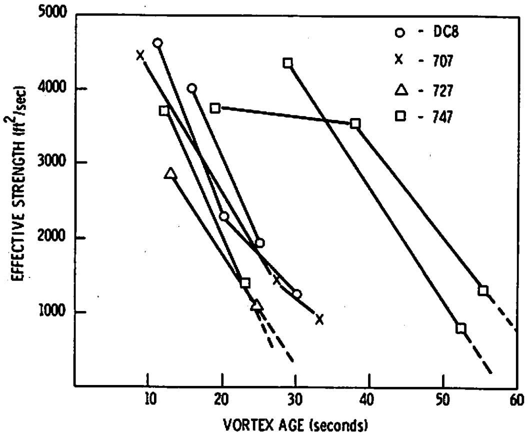

Figure 9. Vortex decay via linking with the ground.

Figure 9 displays cases where the strength very rapidly decays. Once the rapid decay commences, the strength is seen to decrease by a factor of 2 in approximately 15 seconds. Two trends have been observed: (a) the rapid decay begins sooner, and occurs more often when the ambient turbulence is high, and (b) for a given turbulence level, the larger aircraft begin the rapid decay later than the smaller aircraft. It is suggested that the rapid decay is caused by a sinusoidal instability in which the vortex has linked with its image vortex.

Gradual decay is depicted in Figure 10. The strength appears slowly to erode to a negligible value (at least below the instrumental threshold) with a halving of strength every 30 to 60 seconds. The dissipation of the vortex varies as $(\text{time})^{-1}$, and is probably a turbulent diffusion process.

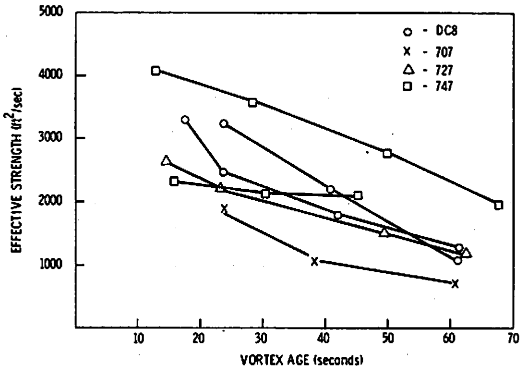

Figure 10. Vortex decay via turbulent diffusion.

Figure 11 exhibits a third mechanism: the vortex experiences a rapid decay which ultimately is curtailed leaving behind a relatively constant but weaker vortex or remnant in its stead. It is suggested that vortex breakdown or core-bursting has occurred leaving behind a remnant which mixes little with the atmosphere. The strength of the remnant correlates with the size of the vortex-generating aircraft: B-727 vortex remnants are weaker than B-707 or DC-8 remnants which in turn are weaker than B-747 remnants. In flight tests where smoke has been injected into the cores of the vortices, often after a vortex has "burst" a smaller core becomes discernible

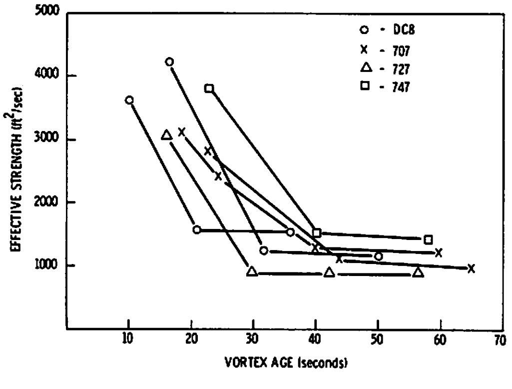

Figure 11. Vortex decay via core bursting.

as smoke is transported by the axial flow in the vortex from an unburst portion to the remnant.

CONCLUSIONS

An extensive data base on vortex motion and decay has been compiled and is continually being expanded. The vortices from over 40,000 landing aircraft and over 3000 departing aircraft have been monitored to date. Detailed studies of the behavior of wake vortices have really just begun; once the data collection phase is complete, statistical techniques can be used to examine the predictability of particular phases of vortex motion and decay.

However, the data base has already been used to establish important aspects of vortex dynamics: The present IFR and vortex separation rules have been shown to be safe (vortex-wise) for the terminal environment. Use of a VAS elliptical wind criterion will permit reducing aircraft separations to a uniform three nautical miles for all aircraft. Finally, the intricate behavior of vortices near the ground is becoming more understandable and even predictable in a statistical sense.

REFERENCES

1. Burnham, D.C., "Review of Vortex Sensor Development Since 1970," Proceedings of Aircraft Wake Vortices Conference, DOT Transportation Systems Center, Cambridge, MA, Mar. 1977.

2. Spitzer, E.A., Hallock, J.N., and Wood, W.D., "Status of the Vortex Advisory System," Proceedings of Aircraft Wake Vortices Conference, DOT Transportation Systems Center, Cambridge, MA, Mar. 1977.

3. St. John, O., "The Collection of Operational Data on Wake Vortex Incidents in the UK," Proceedings of Aircraft Wake Vortices Conference, DOT Transportation Systems Center, Cambridge, MA, Mar. 1977.

4. Hallock, J.N. and Wood, W.D., "Joint US/UK Vortex Tracking Program at Heathrow International Airport; Vol. I, An Executive Summary," Report FAA-RD-76-58I, Mar. 1976, Transportation Systems Center, Cambridge, MA.

5. Burnham, D.C., Sullivan, T.E., and Wilk, L.S., "Measurement of Wake Vortex Strength by Means of Acoustic Back Scattering," *J. Aircraft*, Vol. 13, No. 11, Nov. 1976, p. 889-894.

6. Hallock, J.N., "Monitoring Wake Vortex Strength Decay Near the Ground," *J. Aircraft*, Vol. 13, No. 10, Oct. 1976, p. 830-832.

7. McWilliams, I.G., "Hazard Extent About Aircraft Wake Vortices — An Analytic Approach," Proceedings of Aircraft Wake Vortices Conference, DOT Transportation Systems Center, Cambridge, MA, Mar. 1977.

LASER DOPPLER VORTEX MEASUREMENTS
AT
JOHN F. KENNEDY INTERNATIONAL AIRPORT

J.W. BILBRO, G.D. CRAIG, R.W. GEORGE, H.B. JEFFREYS,
P.J. MARRERO, AND E.A. WEAVER
NASA, George C. Marshall Space Flight Center
Huntsville AL 35812

M.C. KRAUSE
Lockheed Missiles and Space Company
Huntsville AL 35807

T.L. DUNN
M&S Computing, Incorporated
Huntsville AL 35807

C.A. DiMARZIO, C.E. HARRIS, C.M. SONNENSCHEIN, AND
D.W. TOOMEY
Raytheon Company
Sudbury MA 01776

ABSTRACT: Marshall Space Flight Center in cooperation with the Federal Aviation Administration has developed a Scanning Laser-Doppler Velocimeter System which has been used to detect, track, and measure the velocity flow fields of wake vortices of aircraft landing at John F. Kennedy International Airport. The tests were performed with the cooperation of the Transportation Systems Center and the National Aviation Facilities Experiment Center, and resulted in detailed velocity and track data on the vortices generated by over 1600 landings of 13 different aircraft types. The paper describes the overall operation and performance of the system as well as the operation of the individual components. It discusses the data-handling capabilities of the system and the algorithms used in processing the laser-Doppler data, both in real time and in post analysis. Selected runs are examined for the spectral characteristics of vortices, their transport, velocity flow fields, and circulation. A summary of the results and a description of the Kennedy tests are also provided.

INTRODUCTION

The utilization of laser-Doppler systems in vortex flow-field measurement is the outgrowth of extensive research into the application of the laser-Doppler principle to flow-field problems, both in the wind tunnel and in the atmosphere. The initial success of the application of the laser-Doppler technique in wind-tunnel research at the Marshall Space Flight Center (MSFC) in the early 1960s resulted in the extension of this work to measuring atmospheric flow fields and associated turbulence. Turbulence of particular interest was that known to be a hazard to aviation, such as the naturally occurring Clear Air Turbulence (CAT) and the artificially induced vortex.

Demonstration of the feasibility of laser-Doppler vortex measurements was performed in 1969 at MSFC in a series of flybys of a DC-3 aircraft. The success of this demonstration led to further investigations into atmospheric flow-field research, resulting in improved component development and system design, as well as improved scan techniques such as planar scanning for vortex tracking and conical scanning for three-dimensional wind flow-field measurements.

In 1972, the Federal Aviation Administration (FAA) requested the National Aeronautics and Space Administration (NASA) to accelerate their applied research activity to provide assistance in the alleviation of the aircraft wake vortex problem on takeoff and landing. This request resulted in the establishment of an interagency agreement between NASA and FAA in which a program was established for MSFC to develop a Scanning Laser-Doppler Velocimeter (SLDV) System which would be deployed at the John F. Kennedy International Airport (JFK) for vortex monitoring tests. Three major objectives were established for this program:

a. The first and primary objective was to detect and track the vortices in the landing corridor and to provide their positions with time, thereby establishing the SLDV as a standard against which other vortex sensors could be compared.

b. The second objective was to evaluate the SLDV for use in an operational mode at airports.

c. The third objective was to measure the vortex velocity fields and their transport and decay characteristics.

In September 1974, approximately one and one-half years after the initiation of the program, two SLDV systems were installed at JFK (Figure 1). These two independent systems were located in such a way as to provide comparison data on the vortex tracks, thereby serving as a check on system accuracy and also providing a means of further increasing the ability to locate vortex positions by triangulation, if desired.

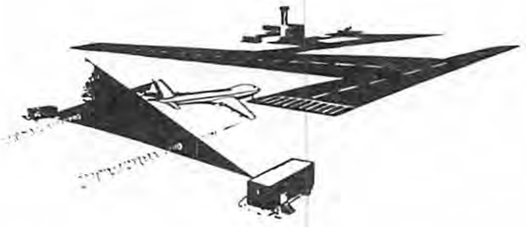

Figure 1. Scanning laser Doppler airport operations (JFK).

During the two phases of testing at JFK (September – December 1974 and March – June 1975), vortex data were collected on over 1600 aircraft landings. This data included position and velocity-profile information which in turn permitted the calculation of transport and circulation.

SYSTEM DESCRIPTION

Principle of Operation.

The principle of laser-Doppler detection is the same as that of conventional Doppler radar with the primary difference being in the wavelength. While the wavelength of the conventional Doppler radar is on the order of centimeters, the wavelength of the SLDV is 10.6 micrometers, and consequently, where conventional radar can only detect scattering from large objects (tens of centimeters), laser-Doppler detection can come from scattering by objects as small as one micrometer in size. Objects of this size are normally contained in the atmosphere in the form of dust and pollen, and are responsible for the backscattered radiation as shown in Figure 2. Since these particles are extremely small, they will follow the motion of the atmospheric wind.

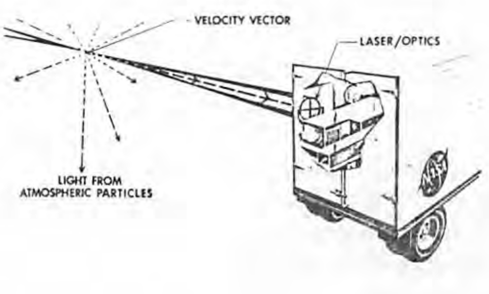

Figure 2. Laser-Doppler principle.

The Doppler shift in the backscattered radiation caused by the motion of these particles can be considered to be due to the wind velocity component that is along the line of sight of the SLDV. The magnitude of this Doppler shift, Δf, is given by:

$$\Delta f = \frac{2V_{\parallel}}{\lambda}, \tag{1}$$

where $V_{\parallel}$ is the line of sight velocity component and λ is the laser radiation wavelength. At 10.6 micrometers, this corresponds to 0.53 m/s per 100 kHz.

The signal-to-noise ratio of the SLDV system is given by

$$S/N = \frac{\eta P_T \beta(\pi)\ \pi R^2}{2Bh\nu} \int_{L_1}^{L_2} \frac{dL}{L^2\left[1 + \left(\frac{\pi R^2}{\lambda L}\right)^2 \left(1 - \frac{L}{f}\right)^2\right]}, \tag{2}$$

where:

η = detector quantum efficiency,
P_T = transmitter power,
$\beta(\pi)$ = backscatter coefficient,
R = radius of the transmitting optics,
B = system bandwidth,
L = particle range,
h = Planck's constant,
ν = frequency of transmitted radiation,
λ = wavelength of transmitted radiation,
and
f = transmitter/receiver focal length, equivalent to range to focus.

Integration from L_1 to L_2 yields:

$$S/N = \frac{\eta P_T \beta(\pi)\lambda}{2Bh\nu}\left\{\tan^{-1}\left[\frac{\lambda L_2}{\pi R^2} - \frac{\pi R^2}{\lambda f}\left(1 - \frac{L_2}{f}\right)\right] - \tan^{-1}\left[\frac{\lambda L_1}{\pi R^2} - \frac{\pi R^2}{\lambda f}\left(1 - \frac{L_1}{f}\right)\right]\right\}. \tag{3}$$

The focal volume of the system can be defined by calculating the length of the range element that produces one-half the coherent backscattered signal received from the entire range $L_1=0$ to $L_2=\infty$.

System Operation.

The SLDV is composed of two main subsystems: optics and signal processing. The optics subsystem is made up of a laser, interferometer, translator, telescope, telescope scan controller, and detector. The signal processing subsystem is comprised of receiver and detector bias electronics, a signal processor, algorithm processor, displays, and recording electronics. A block diagram of the overall system is shown in Figure 3.

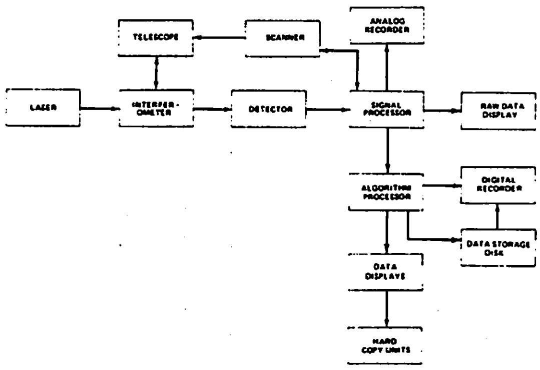

Figure 3. SLDV overall block diagram.

The SLDV operational description can best be communicated by tracing the coherent output radiation from the CO_2 laser transmitter through the optics, to the atmosphere, and back to the data algorithm processor and its displays [1]. As shown in Figure 4, the horizontally polarized collimated 6-mm beam exits the CO_2 laser and impinges on the first beamsplitter which is oriented at 45° to the beam path. Approximately ten percent of this beam is passed through the beamsplitter to be used as a local-oscillator signal. This portion then passes through either a Bragg cell frequency translator or a series of attenuators. In the translated mode, the Bragg cell shifts the frequency by 24 MHz to create an offset zero frequency for which positive and negative Doppler shifts can be observed. In the nontranslated mode, the beam attenuators reduce the local oscillator power to a level for satisfactory operation of the detector. In this mode, positive and negative Doppler shifts and the direction of the velocity cannot be determined. The local oscillator beam is then reflected 90° by a mirror placed at 45° to the beam path. The beam then passes through a half-wave plate, changing the beam polarization from horizontal to vertical, and a recombining beamsplitter where it is mixed with the return signal onto the detector. The main portion of the exit beam from the laser is reflected 90° by the first beamsplitter and passes through a Brewster window that is aligned in such a way that it transmits horizontally polarized light and reflects vertically polarized light. The exit beam is then reflected 90° and passes through a quarter-wave plate that changes the polarization of the beam to right-hand circular. The direction of polarization is reversed at the transmit telescope's secondary mirror and again at the primary mirror so that the radiation impinging on the scanning flat mirror is again right-hand circularly polarized. Upon reflection from the primary, the beam expands to approximately 25.4 cm in diameter, strikes the scanning mirror at 45°, and focuses at positions in space by movement of the secondary mirror and the scanning flat.

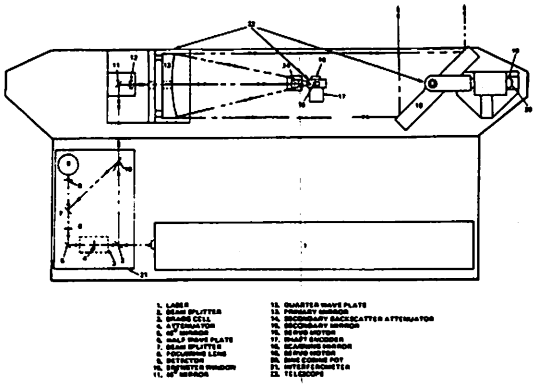

Figure 4. Optical block diagram.

The right-hand circularly polarized radiation is reflected by atmospheric aerosols in the focal volume as left-hand circularly polarized radiation, and at the same time is shifted in frequency by an amount proportional to the velocity of the aerosols along the line of sight. This return signal travels back along the same path as the exit beam until it reaches the quarter-wave plate where, because the direction of polarization has been reversed by the atmospheric backscatter, it passes through and is converted to vertical polarization. This vertically polarized return signal is then reflected by the Brewster window to the recombining beamsplitter where it is mixed with the local-oscillator beam. The mixing of these two beams creates an interference pattern that is imaged by the focusing lens on the face of the detector. This pattern varies with time according to the difference frequency of the two beams. The detector converts the radiation energy to electrical energy, and the result is an electrical beat signal that is proportional to the Doppler shift created by the motion of the atmospheric aerosols. This signal is then amplified by the receiver network to the level required for operation of the signal processor.

Upon entering the signal processor, the Doppler signal is mixed with a chirp pulse and fed to a surface-acoustic-wave delay line. The serial output of the delay line is a continuous, analog spectrum analysis of the Doppler signal where the frequency is proportional to time. The signal is then sent to a sample-and-hold unit, the output of which provides a series of discrete spectrum samples (104 samples in the maximum case). Each sample is representative of a particular Doppler-frequency interval approximately 100 kHz wide. Each sample is then A/D converted and incoherently integrated by summation averaging. At the end of a selected integration time (0.5 ms to 64 ms), a complete Doppler-velocity distribution, in the form of 100-kHz wide velocity cells, is provided for the aerosols contained in the coherent focal volume of the beam for that time and position in space.

This information, along with the position coordinates, is then recorded on high speed, pulsed-code-modulated (PCM) analog tape at a maximum data rate of approximately 2 × 10^6 bits/s. The signal next goes through a velocity and signal amplitude discrimination process in which different velocities and amplitudes of the signal may be eliminated, leaving only a selected portion of the spectrum. This portion of the spectrum, depicted in Figure 5, is further examined by the signal processor and the following information is extracted: V_{max}, the velocity with the highest amplitude; V_{pk}, the highest velocity with signal above the amplitude threshold; I_{pk}, the magnitude of the highest signal amplitude (digital number between 1 and 256); and N, the total number of velocity cells with signal amplitude above amplitude threshold. The information is sent to the data algorithm processor along with position and time information where it is recorded on tape and/or stored in computer memory for processing on a scan-frame by scan-frame basis in real time. The results of the data algorithm processor are then displayed, automatically hardcopied, and written on disk for later transfer to magnetic tape for permanent storage.

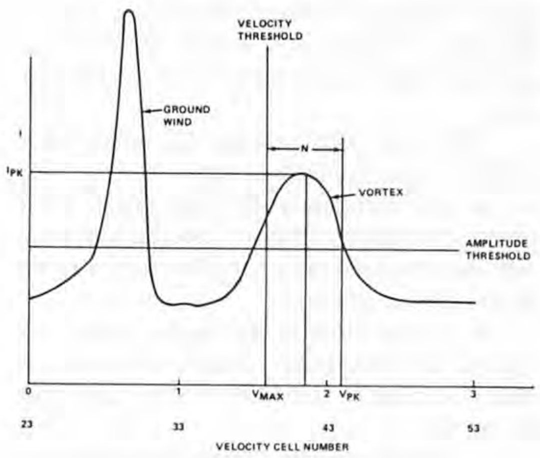

Figure 5. Vortex signal spectrum (untranslated).

Data Collection.

The two SLDV units installed at JFK were located near the middle marker of runway 31 right, approximately 121 m on either side of the centerline. This configuration permitted the two independent sensor units to scan a common planar area perpendicular to the aircraft landing corridor (Figure 6). The area of prime interest for vortex detection and monitoring is indicated in Figure 6 to be 61 m to either side of the runway centerline and 91 m in altitude.

In vortex detection, the velocity threshold is set approximately 1.8 m/s above the peak wind velocity in the scan plane, and the amplitude threshold is set approximately 6 dB below the system wind-signal amplitude. This allows only those data points that have high S/N and high velocities; i.e., those that are associated with the vortices, to be sent to the data algorithm processor.

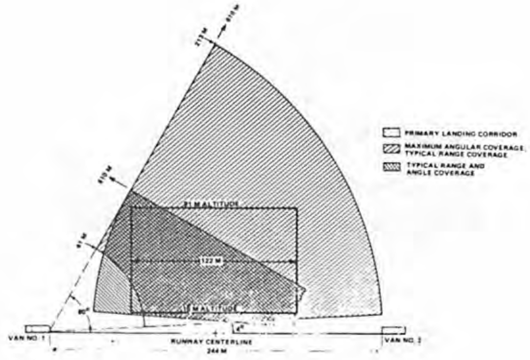

Figure 6. Typical scan coverage requirements with resulting system scan requirements.

The real time vortex-location algorithm processes the raw data to locate the vortex centers. The data are screened to ascertain that a sufficient number of data points exist to define a vortex center and that the maximum peak velocity meets an established minimum. If these criteria are not met, a vortex center cannot be defined. When these criteria are satisfied, a correlation region is defined that contains all data points within a given radius of the point possessing the maximum peak velocity. This region is verified as containing a vortex center if B percent of the points possess velocities that are at least A percent of the maximum peak velocity where A and B are specified by the operator. If the requirement is not met, the point having the maximum peak velocity (V_{pk}) is rejected as a noise spike, and the entire process is repeated until either a noise-spike limit is exceeded or a valid region is found. When a valid region is found, the vortex center is computed by the algorithm in Figure 7. The figure also shows the correlation circle drawn about the data point with the maximum peak velocity. Once a vortex center is located, the points that were used to determine its location are eliminated, and an attempt is made to locate a second vortex by repeating the process. After a second vortex center is located, or it has been established that one cannot be defined, the chosen output data are displayed and recorded.

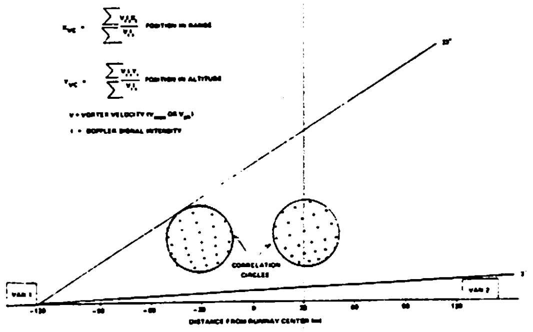

Figure 7. Vortex location algorithm outline.

A series of real-time displays are available to the operator and are shown in Figures 8 through 10. The time-based plot (Figure 8) displays the altitude and horizontal location of the port (*) and starboard (°) vortex centroids as a function of time. When only one vortex centroid is found in the scan plane, an (S) is used to denote its position. The x-y plot (Figure 9) displays the vortex centroids in the vertical scan plane with frame one data represented by A, frame two data by B, etc., for 26 frames, at which point the cycle is repeated. The typical time between scan frames for the JFK operation was 2.5 s. The tabular data output (Figure 10) gives the frame number, the number of data points contained in that frame, the number of points contained in the correlation region for each vortex, the number of noise spikes found while determining each vortex center, the minimum and maximum elevation angles at which data points were found, the maximum peak velocities in each correlation region, the time at which the vortex centers were detected, and the location of the vortex centers.

The total data package [2] collected at JFK includes the following:

a. Approximately 80 high speed PCM tapes containing complete spectral and location information concerning the scan area for detailed post analysis.

b. Approximately 19 digital tapes containing the threshold velocity and position data for input to the PDP-11 data algorithm processor.

c. Approximately 1600 hardcopies of vortex tracks.

d. Approximately 19 digital tapes containing the track and velocity information.

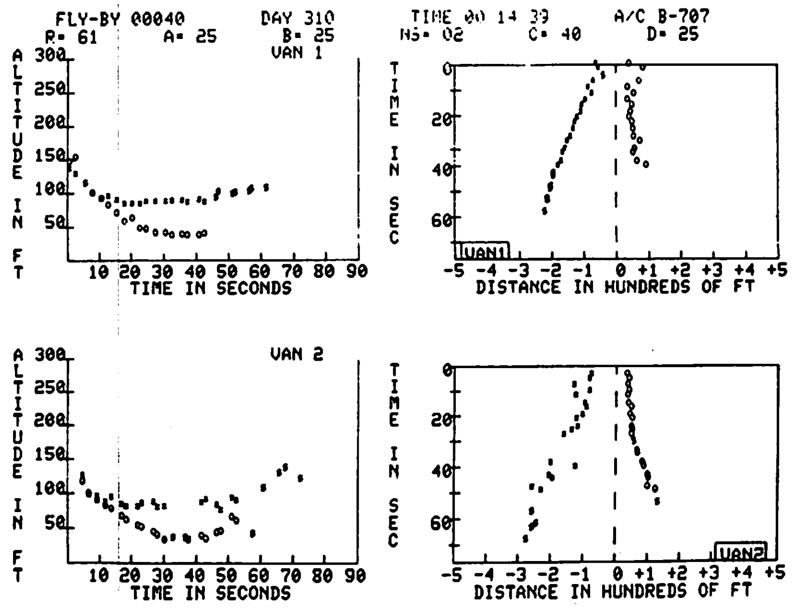

Figure 8. Sample time-based data plot.

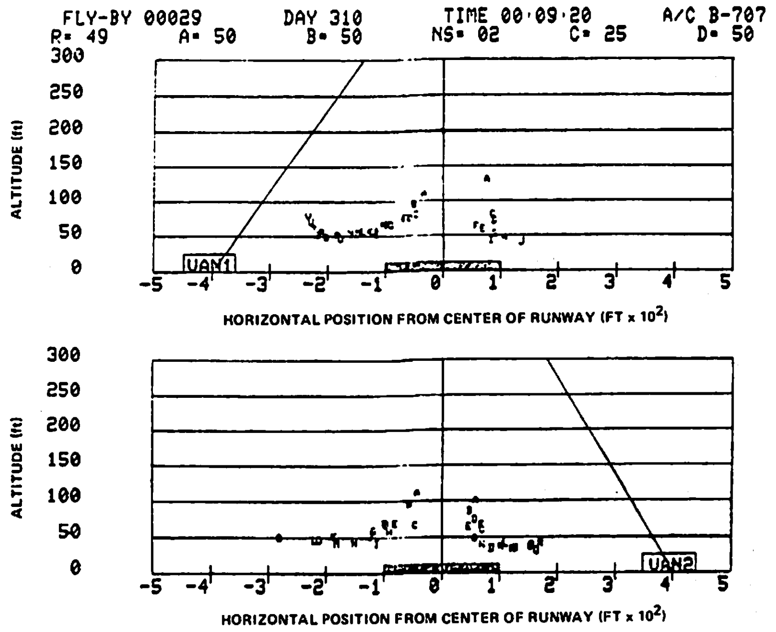

Figure 9. Sample x-y plot.

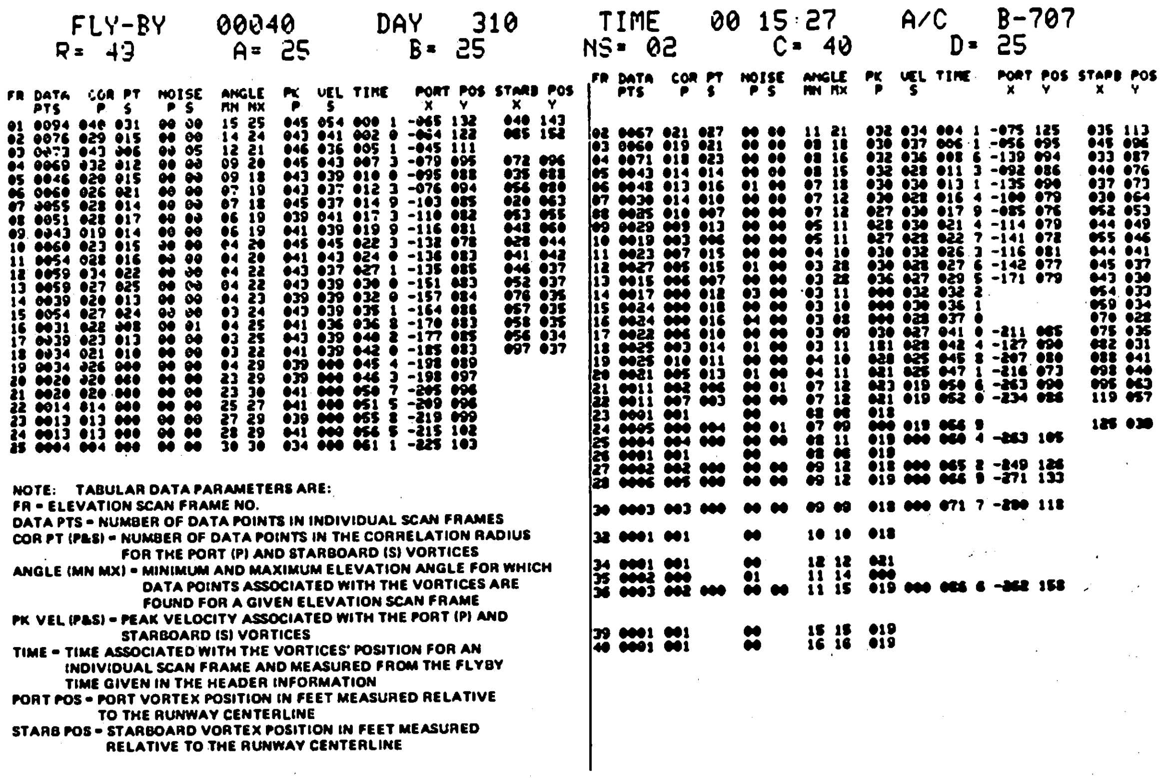

```
     FLY-BY    00040        DAY    310        TIME    00 15:27      A/C    B-707
    R=  43          A=  25        B=  25         NS=  02          C=  40          D=  25

FR DATA  COR PT  NOISE  ANGLE  PK  VEL TIME    PORT POS STARB POS
    PTS   P   S    P S  MN MX  P    S            X   Y     X   Y
01 0094 040 031  00 00  15 25 045 054 000 1 -065 132   040 143
02 0076 029 015  00 00  14 24 043 041 002 0 -064 122   005 152
03 0073 043 006  00 05  12 21 046 036 005 1 -045 111
04 0069 032 012  00 00  09 20 045 043 007 3 -079 095   072 096
05 0046 020 015  00 00  09 18 043 039 010 0 -095 088   035 088
06 0060 026 021  00 00  07 19 043 037 012 3 -076 094   056 080
07 0055 028 014  00 00  07 18 045 037 014 9 -103 085   020 063
08 0051 028 017  00 00  06 19 039 041 017 3 -110 082   053 055
09 0043 019 014  00 00  06 19 041 039 019 9 -116 081   048 060
10 0060 023 015  00 00  04 20 045 045 022 3 -138 078   028 044
11 0054 028 016  00 00  04 20 041 043 024 0 -136 083   041 042
12 0059 034 022  00 00  04 22 043 037 027 1 -135 085   046 037
13 0059 027 025  00 00  04 22 043 039 030 0 -151 083   052 037
14 0039 020 013  00 00  04 23 039 039 032 0 -157 084   076 035
15 0054 027 024  00 00  03 24 043 039 035 1 -164 086   057 035
16 0031 022 008  00 01  04 25 041 036 036 8 -170 083   058 035
17 0039 023 013  00 00  03 25 043 039 040 2 -177 085   056 034
18 0034 021 010  00 00  03 22 041 039 042 0 -185 083   097 037
19 0034 026 000  00 00  04 29 039 000 045 4 -198 089
20 0020 020 000  00 00  23 29 039 000 046 3 -198 097
21 0020 020 000  00 00  23 30 041 000 050 7 -205 096
22 0014 014 000  00 00  25 27 041 000 051 5 -209 096
23 0013 013 000  00 00  27 29 039 000 055 8 -219 099
24 0013 013 000  00 00  28 29 041 000 056 5 -215 102
25 0004 004 000  00 00  30 30 034 000 061 1 -225 103
```

NOTE: TABULAR DATA PARAMETERS ARE:

FR = ELEVATION SCAN FRAME NO.

DATA PTS = NUMBER OF DATA POINTS IN INDIVIDUAL SCAN FRAMES

COR PT (P&S) = NUMBER OF DATA POINTS IN THE CORRELATION RADIUS FOR THE PORT (P) AND STARBOARD (S) VORTICES

ANGLE (MN MX) = MINIMUM AND MAXIMUM ELEVATION ANGLE FOR WHICH DATA POINTS ASSOCIATED WITH THE VORTICES ARE FOUND FOR A GIVEN ELEVATION SCAN FRAME

PK VEL (P&S) = PEAK VELOCITY ASSOCIATED WITH THE PORT (P) AND STARBOARD (S) VORTICES

TIME = TIME ASSOCIATED WITH THE VORTICES' POSITION FOR AN INDIVIDUAL SCAN FRAME AND MEASURED FROM THE FLYBY TIME GIVEN IN THE HEADER INFORMATION

PORT POS = PORT VORTEX POSITION IN FEET MEASURED RELATIVE TO THE RUNWAY CENTERLINE

STARB POS = STARBOARD VORTEX POSITION IN FEET MEASURED RELATIVE TO THE RUNWAY CENTERLINE

```
FR DATA  COR PT  NOISE  ANGLE  PK  VEL TIME    PORT POS  STARB POS
    PTS   P   S    P S  MN MX  P    S            X   Y      X   Y

02 0067 021 027  00 00  11 21 032 034 004 1 -075 125    035 113
03 0060 019 021  00 00  08 18 030 037 006 1 -056 095    045 096
04 0071 018 023  00 00  08 16 032 036 008 6 -139 094    033 087
05 0043 014 014  00 00  08 15 032 028 011 3 -092 086    040 076
06 0048 013 016  01 00  07 18 030 030 013 1 -135 090    037 073
07 0030 014 010  00 00  07 12 030 028 016 4 -100 079    030 064
08 0025 010 007  00 00  07 12 027 030 017 9 -085 076    052 053
09 0029 009 013  00 00  05 11 028 030 021 4 -114 079    044 049
10 0019 003 006  00 00  05 11 027 028 022 7 -141 078    055 046
11 0023 007 015  00 00  04 10 030 032 026 3 -116 081    044 041
12 0027 005 015  01 00  03 28 030 028 027 6 -142 077    045 037
13 0015 006 007  00 00  03 22 036 027 029 5 -171 079    043 030
14 0017 000 012  03 00  03 11 000 032 032 2             054 033
15 0024 000 018  00 00  03 10 000 030 036 1             059 034
16 0024 000 016  04 00  03 08 000 028 037 0             070 028
17 0022 006 010  00 00  03 09 030 027 041 0 -211 085    075 035
18 0025 003 014  01 00  03 11 181 028 042 4 -127 090    082 031
19 0025 010 011  00 00  04 10 028 025 045 8 -207 080    088 041
20 0021 005 013  01 00  04 11 021 025 047 1 -216 073    098 040
21 0011 002 006  00 01  07 12 023 019 050 6 -263 090    095 063
22 0011 007 003  00 00  07 12 021 019 052 0 -234 086    119 057
23 0001 001      00     08 08 018
24 0005 000 004  00 01  07 09 000 019 064 9             128 030
25 0004 004 000  00 00  08 11 019 000 060 4 -263 105
26 0001 001      00     08 08 019
27 0002 002 000  00 00  09 12 018 000 065 2 -249 128
28 0006 005 000  00 00  09 12 019 000 066 9 -271 133

30 0003 003 000  00 00  09 09 018 000 071 7 -280 118

32 0001 001      00     10 10 018

34 0001 001      00     12 12 021
35 0002 000      01     11 14 000
36 0003 002 000  00 00  11 15 019 000 066 6 -262 158


39 0001 001      00     15 15 019
40 0001 001      00     16 16 019
```

Figure 10. Sample tabular data output.

The analysis of the above data package has of course resulted in an expanded data package too large to tabulate.

DATA ANALYSIS

Initially, the data analysis effort, involving the PCM data tapes, concentrated on diagnostic applications such as evaluating signal-to-noise ratios, range resolution, and algorithm results. As a result, a number of computer programs were created to analyze calibration runs, print and plot raw data, and analyze flow field information.

In the evaluation and comparison of various algorithms for vortex location, the simplest form of an aircraft wake was used, consisting of a pair of counter-rotating vortices as shown in Figure 11. In this idealization, one vortex is shed from each wing with the centers being separated by $\pi/4$ times the wing span. The direction of rotation is that which produces a downward velocity component between the vortices. According to the theory of line vortices, in the absence of any wind or other influence, the transport of the vortex center is determined by the induced velocity of the remaining vortex. If the pair is close to the ground, the interaction becomes more complicated due to the boundary condition of zero vertical velocity component at the ground. This condition may be handled by the introduction of reflections of the vortices where these reflections or images, when combined with the actual vortices, satisfy the boundary condition and provide a simple means of determining vortex transport. While it is evident that this simplistic vortex model will not provide realistic results under many conditions, it has served to provide a general standard in determining the ability of the SLDV system to resolve vortex tracks.

The extension of post-analysis techniques to obtain detailed information in selected cases was a natural result following the completion of the initial evaluation. The algorithm which was used primarily in post analysis closely paralleled the real-time algorithm [3]. In this algorithm, the scan is determined by observing the turnaround in angle after smoothing to remove the fluctuations. For each scan the maximum values of V_{pk}, V_{max}, I_{pk}, and S, and the average value of S are recorded (S is the integrated signal). The location of the vortices is performed using an iterated centroid method. The location of one vortex is determined by locating the highest I_{pk}, considering all of the points falling within a correlation circle of specified radius of this point, and calculating the centroid, weighted with the amplitude above the threshold. A similar procedure is used to determine if a second vortex was present using the highest I_{pk} outside the correlation circle defined for the first one. Points occurring in both circles are considered to be associated with both vortices for purposes of the centroid. The locations thus determined are used as centers for new centroids. If a majority of the points in either vortex are in the overlap region, the point which initiated the location of the second is deleted and the iteration procedure is begun again. The x and y locations of each center are printed out after each stage of the iteration. The algorithm, in addition to providing location, also provides time histories of the above parameters as well as scatter plots generated for V_{pk}, V_{max}, I_{pk}, and the integrated signal S. A velocity-versus-angle plot is also constructed for each vortex in each scan for use in determining the flow field parameters.

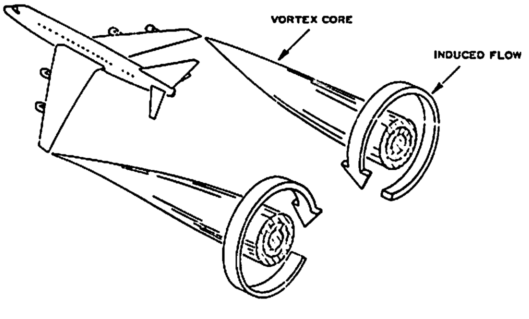

Figure 11. Trailing vortex wake.

Vortex Flow Fields.

By analyzing the function V_{pk} versus angle, it is possible to obtain a plot of the tangential velocity profile of the vortex using the assumption of circular symmetry. V_{pk} is especially useful for this purpose because it does not require that the system be focused at the correct range for the given vortex. Considering ranges which fall within the range bin of the vortex range (±10 m), the value of V_{pk} for any point in this range should be a measure of the tangential velocity of the given vortex at the angle associated with that point. A typical plot of V_{pk} as a function of angle is shown in Figure 12. It may be seen that the vortex consists of two high-velocity regions which may be associated with opposite sides of the vortex core, and a null between them which may be associated with the vortex center. It will be noted that one of the velocity peaks is higher than the other, indicating that one side of the vortex had a velocity which added to the ambient wind velocity. It will also be noted that the high velocities expected at the vortex core are absent. This is believed to be a result of the fact that the regions of high velocity are too small to be seen by the system, since, with a given signal-to-noise ratio from the wind signal, there is a minimum detectable target length below which the system will not receive a signal above threshold. This length is proportional to the range resolution, and for a typical case the minimum detectable target is slightly greater in size than two-tenths of a range-resolution element (corresponds to a length of approximately 3 m at a range of 150 m).

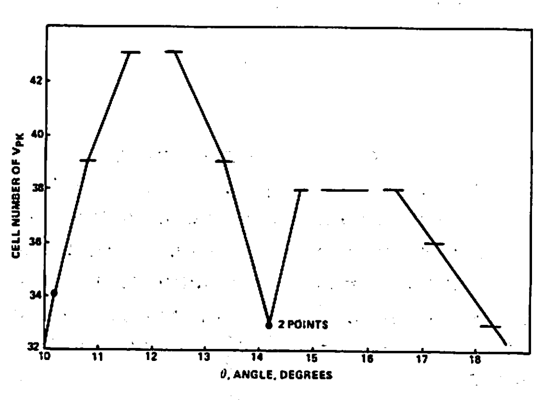

Figure 12. V_{pk} versus Θ for a B-707 vortex; day 310, run 1029, scan 1, vortex 1, range = 100 ± 20 m.

Typical vortex velocity profiles are illustrated in Figure 13 where lines of constant parallel component of velocity are shown. The figures show the vortex velocity profiles for conditions of no wind, a moderate cross-wind, and a reasonably strong cross-wind. The maximum tangential velocity of the vortex is assumed to be 30 m/s. It may be seen that the regions containing velocities greater than 23 m/s are extremely small. Furthermore, as the cross-wind velocity increases, the regions on the side of the vortex which oppose the wind become even smaller and those on the other side become larger. Since these regions are extremely small, it is anticipated that they will not be seen with the Laser-Doppler System.

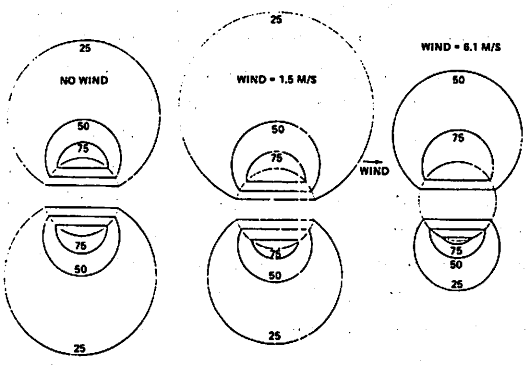

Figure 13. Interaction of vortex and wind; vortex V_{max} = 31 m/s.

In addition, the cross-wind increases the size of the regions on the side of the vortex which add to the wind and makes the detection of these regions more probable than the detection of the same velocity on the opposite side of the vortex. The result of this is a high probability that the top of one vortex and the bottom of the other vortex of the pair will be located by the system. This leads to an altitude difference between the vortices immediately after their formation, with the down-wind vortex being lower in altitude. This has been observed in most of the data which has been analyzed where a significant cross-wind was present.

Vortex Transport.

The transport was compared to the components of the wind velocity for four runs. The wind-velocity components were measured by sensors mounted on a meteorological tower located between the middle marker and runway 22L-4R. Figure 14 shows a vortex pair from an L-1011 being transported at about −3 m/s. After 15 seconds, one vortex left the scan plane. The other continued to fall and changed its velocity until it was traveling in the opposite direction at an altitude of about 12 m. After that, it rose in altitude and returned to its original transport for the rest of the 75 seconds for which it was observed. The measured cross-wind was −2 m/s at 12-m altitude and −.2 m/s at 6 m. The run shows evidence of a shear going from −3 m/s at 50 m to 0 m/s at the ground. The wind velocity may reverse near the minimum altitude of the vortex or the reversal of transport velocity may be due to the induced velocity caused by ground effect. A headwind of 4 m/s was observed on this run.

It is difficult to make a quantitative estimate of the correlation between vortex transport and wind data since the wind data is taken from a 12-m tower while the vortices were seldom at that low an altitude. Furthermore, when the vortices descend to 12 m, the effect of ground interaction becomes significant. The transport data obtained in post analysis are in good agreement with those obtained in real time and reflect both the velocity of the local wind and the induced velocities from the interaction of the vortices and the ground.

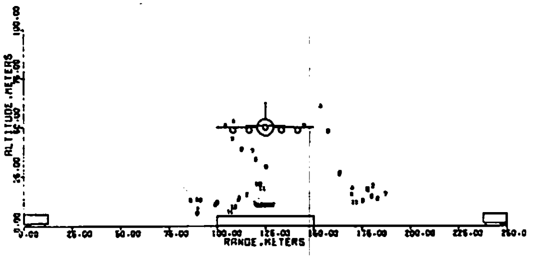

Figure 14. Sample vortex transport.

Vortex Circulation.

The effective circulation of a vortex may be calculated from the LDV data in one of three ways. All approaches make use of plots of the peak velocity versus angle. These plots are restricted to include the vortex of interest by including only data collected with ranges within 10 m of the vortex range. Thus, two velocity versus angle plots are generated for each scan (if two vortices are present). Each plot contains data from a 20-m range bin centered at the vortex range. The highest velocity in the spectrum at each point is assumed to be the velocity of the vortex along the given line of sight.

Since no frequency translation was used in collecting the data, no sign change occurred in the velocity profile across the vortex, therefore it was necessary to locate the center of the vortex in angle and assume that a sign change occurred at this point. This was done by finding two angles having high velocities and having a relative minimum velocity between them. The two peaks were assumed to correspond to the two sides of the core while the null was identified as the angular location of the vortex center.

The easiest circulation estimate is obtained by selecting a point on the velocity versus angle plot, determining its radial distance from the center (using the angles and range), and calculating

$$\Gamma = 2\pi r V, \qquad (4)$$

where r is the radial distance to the vortex center and V is the peak velocity at that point. This method has the advantage of being easy and the disadvantage of using very little of the data. Furthermore, it is not necessarily related to any wake effects which would be experienced by an encountering aircraft.

The second approach is a least-square fit which assumes a specific vortex model with variable parameters and fits it to the data to obtain the best values for these parameters. One of the resulting parameters may be used to calculate the circulation. The method makes use of more of the data, but, again, does not necessarily relate to the effect on an encountering aircraft since the calculated circulation is dependent on the model chosen.

The third approach, the rolling-moment method, makes use of all the data and produces a circulation estimate which is significant to the encountering aircraft [4]. The procedure is to calculate the rolling moment on a hypothetical aircraft of wingspan b, using the LDV data:

$$M = \int_{-b/2}^{b/2} Vr dr. \tag{5}$$

This quantity, in the constant-circulation model of a vortex, is proportional to the wingspan in such a way that the circulation is:

$$\Gamma = 2\pi \frac{dM}{db}. \tag{6}$$

For an actual vortex, this equation will not hold for all values of b. However, it is possible to determine an effective circulation by applying the equation in a region where the M versus b curve is linear. Thus, the effective circulation is defined as the circulation of that model vortex which produces a rolling moment, on a hypothetical encountering aircraft wing of span b, which varies with b in the same way as that of the actual vortex. The method has produced good results in moderate cross-winds for vortices at least 10 to 15 seconds old.

The effective-circulation calculations have been performed using the latter approach on wake vortices from a variety of aircraft types in different wind conditions. The calculation has been performed on each vortex for every scan in several runs to produce a time history of effective circulation for each vortex. An example is shown in Figure 15 for a B-747. The B-747 results indicate that reasonable values are obtained after 10 seconds; however, most of the results for run 1019, on day 115, are low based on the expected values and on the results of other B-747 runs. This may be due to the use of too high an amplitude threshold. A few scans produced reasonable results and these are in good agreement with the results from van 2. Both runs 2011 (day 118) and 2019 (day 115) produced high effective circulation in the first few scans. The DC-8 results in low to moderate cross-winds behave in a similar fashion, while the high cross-wind run has an effective circulation which is too high throughout most of the run. This may be due to changes in the vortex velocity due to the wind, which do not cancel out, because of the folding of the LDV spectrum about zero.

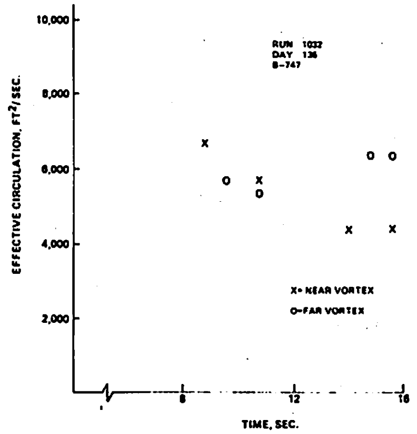

Figure 15. Vortex circulation versus time.

With three runs processed earlier, the overall result of the effective-circulation calculations include usable data on 10 out of 12 runs. There is considerable scatter in some of the data, but the overall trends are readily apparent. Overall, it is felt that the rolling-moment method usually produces reasonable values of effective circulation which may be used as a measure of vortex strength. The calculations have been performed for every scan of several runs lasting up to 60 seconds. From these calculations, it has been determined that the effective-circulation calculation is quite sensitive to the amplitude threshold and that the optimum threshold may be different for vortex location and effective-circulation calculation. For the latter, the threshold should be as close to the noise floor as possible without causing a high false-alarm rate. In addition, it has been observed that the effective-circulation calculation is almost always too high during the first few scans; this is probably due to the existence of multiple vortices which were ignored in the calculations.

Multiple Vortices.

The study of multiple vortices has become of interest for a number of reasons. First, experimental and theoretical studies have been undertaken to determine if multiple vortices can be made to interfere, producing a vortex system which decays more rapidly than those in present aircraft wakes. Additionally, several phenomena observed in the JFK data are difficult to interpret on the basis of a simple vortex-pair model. In particular, excessive effective circulations have usually been obtained during the first ten seconds after vortex generation.

Work performed on the JFK data has indicated that multiple vortices may be studied by using spectral analysis and velocity versus angle plots. Lifetimes of multiple vortex systems have been estimated at 10 to 20 seconds based on observations of spectra, velocity profiles, and effective circulation results. After this time, the vortices apparently merge into a well defined vortex pair.

The spectral characteristics of an aircraft wake change with time. The spectra of young wakes typically contain high velocities, have wide bandwidths, and often exhibit multiple peaks with deep nulls between them. The spectrum is clearly that of a complicated velocity and/or backscatter coefficient distribution rather than that of a simple vortex in a uniform atmosphere. Typical peak velocities are on the order of 15 m/s. Often significant signals are obtained at all velocities between 2 m/s and 15 m/s resulting in a signal bandwidth of close to 3 MHz.

These spectra typically have a number of peaks and valleys indicating that there is significant backscatter from several regions of different velocities. This may arise in one of two ways. First, for a single vortex, locally high concentration of particulate in small regions may be moved about by the vortex flow field. Their velocity components would differ because of their different locations within the vortex. If this is the case, the ratio between peaks and nulls should be equal to the ratio of maximum to minimum backscatter coefficient along the line of sight. This has been measured to be as high as 18 dB (day 115, run 2019, frame 5918), which seems excessive, based on this explanation. The other possibility is that the velocity component along the line of sight undergoes irregular changes as would be the case if the line of sight penetrated several vortices.

As the wake ages, a number of changes occur in the spectra. Most notably, the peak velocity falls, more or less smoothly by about 2 to 3 meters per second in 20 seconds, and continues to fall throughout the life of the wake. The peak velocity usually falls below a threshold of 5 m/s about 60 to 90 seconds after vortex generation.

Evidence of multiple vortices is also apparent on some occasions in plots of the vortex velocity components as functions of angle. A detailed analysis of the multiple-vortex problem is not possible with this data due to the low angular-data density available. However, it has been noted in many runs that considerable structure exists which is more complicated than what would be expected from a single vortex system.

CONCLUSION

The SLDV system, developed by MSFC, was deployed for six months of field operations at JFK Airport to detect, track, and measure aircraft wake vortices. The SLDV operated reliably throughout the test period under a variety of adverse environmental conditions including rain, snow, temperature extremes, and acoustic vibrations. Of these conditions, temperatures in excess of 90°F had the only significant adverse effect on the operation of the system. The problem can be alleviated to a great extent by increasing the air conditioning available to the electronic hardware.

During the JFK Airport operations, information was collected on more than 1600 aircraft landings. The information was stored on magnetic tape from three different data processing points in the system for analysis. This included velocity and position of the flow field of the entire scan plane, the flow field of the vortex, and the track of the vortex centers. In addition, information on vortex centers was obtained on hard copy and placed on microfiche.

Analysis of the JFK Airport data indicates that vortex locations to within 3 m were achieved in real time and that vortices were tracked to a range of 457 m and for a duration in excess of 80 s. Vertical and horizontal transport of the vortices as well as vortex circulation information were also obtained. In addition, the presence of multiple vortices in the JFK data was indicated by spectral analysis, velocity profiles, and effective-circulation calculations and descent rates. The most promising means of studying multiple vortices is felt to be an arc-scan with high angular-data density and a short scan time. Using the existing data, the best approach would be a detailed spectral analysis considering the ratios of peaks and valleys in the spectra. This could yield some size and peak-velocity data which could be compared to simple models. Evaluation of descent rates could also be useful if the models were processed to determine theoretical descent rates for comparison.

ACKNOWLEDGMENTS

The authors wish to acknowledge their many colleagues who participated in the program at MSFC and elsewhere. In particular, several companies supported the program. The Computer Sciences Corporation assisted in data reduction, analysis, formatting, and presentation. Lockheed's Huntsville Research and Engineering Center was responsible for the telescope, the servo scan controls, and the integration and system tests. The graphics capability was the responsibility of M&S Computing, Inc. Physical Dynamics, Inc., provided system modeling concepts and portions of the conceptual design and data analysis techniques. The Raytheon Company was responsible for the laser, frequency translator, detector, interferometer, and signal processor development, and also for part of the data analysis and algorithm design.

The outstanding efforts of these people led to the successful deployment and operation of a highly complex system. It is with deep appreciation that the efforts of individuals who worked on this program are acknowledged.

REFERENCES

1. Huffaker, R.M., Jeffreys, H.B., Weaver, E.A., and Bilbro, J.W., "Development of a Laser Doppler System for the Detection, Tracking, and Measurement of Aircraft Wake Vortices," FAA-RD-74-213 and NASA TMX-66868, Mar. 1975.

2. Bilbro, J.W., Jeffreys, H.B., Weaver, E.A., Huffaker, R.M., Craig, G.D., George, R.W., and Marrero, P.J., "Laser Doppler Velocimeter Wake Vortex Tests," FAA-RD-76-11 and NASA TMX-64988, Mar. 1976.

3. Sonnenschein, C., DiMarzio, C., Clippinger, D., Toomey, D., "Aviation Safety Research/Hazard Avoidance and Elimination," Final Report, NAS8-30795, Raytheon Company, Sudbury, MA, Aug. 1976.

4. Hallock, J.N., "Wake Vortex Decay Near the Ground," AIAA Paper 75-882, 8th Fluid and Plasma Dynamics Conference, Hartford, CT, June 1975.

SIMULATION AND DATA ANALYSIS OF A SCANNING LASER DOPPLER VELOCIMETER SYSTEM FOR SENSING AIRCRAFT WAKE VORTICES

J.C.S. MENG
Science Applications, Inc.
LaJolla CA 92038

J.A.L. THOMSON
Physical Dynamics, Inc.
Berkeley CA 94701

ABSTRACT: The objectives of this study are to simulate the response of a Scanning Laser Doppler Velocimeter System (SLDVS) in an aircraft wake environment and to display the expected spatial signatures. From analysis of these simulated signatures as well as flight data, optimal tactics for determining wake location and strength can be established.

INTRODUCTION

The particular purpose of the simulation program described here is to provide a detailed but flexible model of the SLDVS that will complement the design, development, and implementation of a laser Doppler anemometer for the detection and analysis of aircraft vortex wakes. The purpose is to assist in design of a LDV instrument to locate the hazardous high velocity vortex cores in the aircraft wakes, estimate their strength, and to obtain, where possible, details of the field. A basic problem is the very localized motion of the vortex cores (a few tens of feet) and the large areas of space which must be probed. The LDV system has an incoherent limitation in range resolution and at long ranges the vortex cannot be resolved. The data analysis and particularly the analysis of detection probabilities and reliabilities in the presence of a complex wind shear field is not easy in this type of situation.

The motivation of the approach we will describe is to construct a simulation model of both the instrument, the atmosphere and the vortex wake of the aircraft and to use this model to develop a variety of detection and processing algorithms at a substantially lower cost than repeated field tests. Thus the system to be described is not simply an atmospheric wind anemometer, it is a vortex detection system and a major feature of the design is to define optimal strategies for localizing the signature as well as reducing the false alarm rate. We describe the approach used in the hope that the same type of approach may be valuable in other anemometric applications which involve the construction of a complex data processing procedure.

The simulation does basically two tasks: starting with a fairly general model of the atmosphere and aircraft wake at an initial time, it follows the subsequent atmospheric motion dynamically and simultaneously constructs a simulation of the raw data produced from one or two SLDVS units; and a second part of the program then processes and displays these data. The objective of the simulation program is to provide a well defined and controlled numerical model of the atmosphere and sensor that can be used for testing and evaluating a variety of data processing algorithms. In this way, optimum operational procedures can be determined. In addition, the model provides a method for determining system capability (e.g., vortex location accuracy, false signals, effects of unusual weather or unusual viewing geometry). For the latter goal, it is necessary that the model provide a faithful representation of the actual system, and detailed comparisons with the raw and processed data are necessary to validate or modify the model. A second data processing numerical program was constructed to process actual flight data by the same methods used in the simulation.

It is known that several factors affect the development of the vortex wake and its transport through the atmosphere following aircraft passage. The hydrodynamic model includes most of these influences, and is therefore rather complex. Since a detailed description has been given elsewhere [1], we will merely list the effects which are incorporated in the model:

1) Arbitrary spanwise wing loading (in order to treat any flap configuration),
2) Development of the wake, including initial roll-up into whatever number of vortex regions is consistent with the wing loading,
3) Wind shear in the atmospheric boundary layer within which the low altitude wake is embedded,
4) Image vortices below the ground plane,
5) Atmospheric turbulence (simulated by constructing a detailed realization of a turbulence spectrum),
6) Buoyancy and stratification effects in the atmosphere and in the exhaust jets from the aircraft engines.

Axial flows are neglected. The model is two-dimensional, and treats motion in a vertical plane normal to the aircraft track.

The SLDV simulation model applies to a CW, focused, coaxial, coherent laser system. The system scans in range and elevation in a vertical plane. Range resolution is obtained by utilizing a depth-of-field effect. The system simulation model was developed for the purpose of evaluating various system designs and is also flexible. The applications described in this paper are those in which the magnitude but not the sign of the velocity is sensed. This is not an inherent limitation either in the system or the simulation model.

Detailed descriptions of these models and data processing programs are available in reference 1. Simulations and data analysis have been carried out for several aircraft and are described in detail in references 1 and 2.

The SLDV system is modeled by calculating the system response as the focal point is moved in range and elevation angle in the scan plane. When the system is focused at a given point in space, the Doppler spectrum response is calculated by considering contributions from each range point and superposing these, multiplied by a theoretical range response function. The velocity components are obtained from the hydrodynamical model at various times. A unique feature of the modeling of the hydrodynamics [1] allows the tip vortices to be treated with high spatial resolution by invoking specific models of the core structure while at the same time retaining a lower resolution representation of the larger scale features. The range response function is constructed from a previous analysis (in the appendix of reference 3) of the optical system for Gaussian beams. Effects of finite truncation and blocking of the primary mirror have been treated by a detailed two-dimensional propagation analysis. In the system model these effects are included by simply degrading the Gaussian beam analysis appropriately.

The spectrum is calculated by multiplying the aerosol density by the response function at each range point and cumulating this contribution in the appropriate velocity (or frequency) channel. The aerosol density in the neighborhood of the core is affected by centrifuging at late time, and a model for this has been developed [1]. However, in the present simulation calculations, a uniform particle density is assumed.

Once the spectrum has been evaluated, simulations of the data analysis procedure are carried out. Various moments of the spectrum (the mean velocity, variance, skewness and kurtosis) and certain other characteristics of the spectrum are calculated: the velocity of the highest channel above threshold (V_{peak}), the velocity of the channel having the peak signal (V_{max}), and the signal level in this channel (I_{peak}). All of these data, in addition to the fundamental input (the value of the line-of-sight velocity component at the particular range point) are presented on a three-dimensional range-elevation angle plot. Also plotted are the actual locations of the vortex cores. The geometry of the simulated laser scan pattern together with the vortex wake motion are separately displayed. This entire procedure is repeated for each step of interest.

A data analysis program has been constructed to assess the SLDV system performance, to validate the simulation model, and to test various vortex location algorithms. The program takes either real or simulated Doppler spectra versus range and elevation, calculates the spatial distributions of various spectral moments (mean velocity, variance, skewness, kurtosis) or other spectral characteristics (V_{peak}, V_{max}, I_{peak}, I_{sum}). These data (either real or simulated) are then subjected to various processing procedures to enhance the patterns and to determine vortex locations. The final output is displayed as contour plots in an x-y coordinate system.

Direct comparisons between the simulation results and the flight test data are possible through this data analysis program by a parallel data processing procedure. Conclusions drawn from examination of the simulation data and comparisons with the flight test data can then be made.

SPECTRAL SIGNAL CHARACTERISTICS FOR COAXIAL SLDV SYSTEMS

Characteristics of NASA/MSFC SLDV systems are described in detail in references 4 and 5. In the present paper we are concerned only with the parameters relevant to the simulation of spectral response.

Signal-to-Noise Ratio.

Coherent heterodyne laser detection systems are commonly operated in a shot noise limited condition; that is, the noise is determined entirely by the number of scattered photons detected, not by the receiver electronics. The performance of a general coherent laser system detecting the radiation scattered from a continuously distributed aerosol has been analyzed previously [3]. In the present case of a coaxial system (that is, the received scattered signal is collected through the transmitting optics), the signal-to-noise ratio is given by

$$S/N = \frac{\eta P_\omega}{2\Delta\omega}\left(\frac{\lambda}{\pi\gamma}\right)^2 \int_0^\infty \frac{\overline{n_f\sigma}(L)}{(L-L^*)^2 + \Delta L^2}\, \partial L. \quad (1)$$

Here $\overline{n_f\sigma}$ is the differential backscattering cross-section per unit range per steradian, η the overall loss factor (atmospheric absorption, optics and electronics), P_ω the transmitter power that is scattered into the bandwidth $\Delta\omega$ (i.e., $P_\omega\Delta\omega$ is proportional to the number of photons transmitted which would be scattered into the frequency internal $\Delta\omega$ in an ideal system). We have assumed that both transmitter and receiver have a Gaussian apodization with radii R_t and R_r, respectively, at the e^{-2} intensity points. The transmitted wave fronts are focused at a range f_t and the receiver section is focused at f_r. The focal point for the receiver is determined by locating the position of the virtual image of the local oscillator. In terms of these optics parameters, the various parameters in Equation (1) are given by the relations

$$\gamma = \sqrt{\theta_{geom}^2 + \theta_{diff}^2}\ , \quad (2)$$

$$\theta_{geom} = \sqrt{R_r^2 + R_t^2}\ /f_2\ , \quad (3)$$

$$\theta_{diff} = \lambda\sqrt{R_t^2 + R_r^2/R_tR_r}\ , \quad (4)$$

$$f_1 = \left(\frac{R_r^2}{f_r} + \frac{R_t^2}{f_t}\right) \Bigg/ \left(\frac{R_r^2}{f_r^2} + \frac{R_t^2}{f_t^2}\right), \quad (5)$$

$$f_2 = \left[\frac{R_t^2 + R_r^2}{\frac{R_r^2}{f_r^2} + \frac{R_t^2}{f_t^2}}\right]^{1/2} \quad (6)$$

$$L^* = \frac{f_1}{1 + (\lambda f_2/\pi R_tR_r)^2}\ , \quad (7)$$

where λ is the wavelength and

$$\Delta L = \left\{ \left[\frac{\lambda f_1/\pi R_t R_r}{1 + \left(\frac{\lambda f_2}{\pi R_t R_r}\right)^2} \right]^2 + \frac{\left[\frac{R_r R_t}{R_r^2 + R_t^2} \left(\frac{f_2}{f_t} - \frac{f_2}{f_r} \right)^2 \right]}{\left[1 + \left(\frac{\lambda f_2}{\pi R_t R_r} \right)^2 \right]} \right\}^{1/2} f_2 \; . \qquad (8)$$

When the atmospheric backscattering properties of the Doppler signal vary negligibly across the depth of field $\pi\Delta L$, the signal-to-noise ratio takes the form

$$S/N = \frac{\pi}{2} \frac{\eta P_\omega}{\Delta\omega\Delta L} \left(\frac{\lambda}{\pi\gamma}\right)^2 \overline{n_f\sigma} \left(\frac{1}{2} + \frac{1}{\pi} \tan^{-1} \frac{L^*}{\Delta L}\right) \; . \qquad (9)$$

In order that significant range resolution be achieved, the aperture must be chosen so that ΔL is small compared to L^*, i.e., so that the scattering particles are well within the near field ($\lambda f/\pi R^2 << 1$). In this limit, the signal-to-noise is independent of range

$$S/N = \eta \frac{P_\omega}{\Delta\omega} \overline{n_f\sigma} \frac{\lambda}{4} \; , \qquad (10)$$

and the range resolution (the region from which comes half the scattered energy) is

$$\pi\Delta L = \lambda L^2/R^2 \; . \qquad (11)$$

The signal-to-noise given in Equation (11) represents a mean value averaged over the band width $\Delta\omega$. When the receiver channel width exceeds the Doppler width of the scattered signal, $\Delta\omega$ is to be set equal to the receiver channel bandwidth. When the Doppler spread is large enough to cover more than one receiver channel, $\Delta\omega$ is to be set equal to the Doppler width of the incoming signal. In this case, the signal-to-noise is independent of the individual receiver channel bandwidths.

When the magnitude of the scattered power changes only slightly in a time equal to the reciprocal of the individual receiver channel bandwidths, further improvement in the single-to-noise ratio can be achieved by incoherent integration of the power level at the output of the receiver channels. The increase is essentially equal to $\sqrt{\Delta\omega_c\tau_i}$, where τ_i is the allowed integration time and $\Delta\omega_c$ the receiver channel bandwidth. For the optimum performance, the integration time should be matched to the dwell time.

Spectral-Response.

A typical configuration for a single SLDV system is shown in Figure 1. In the scan plane there are 21 beams at 1.5° apart, each covering a range between 60 and 250 meters. Superimposed in the same figure is the location of the trailing vortex sheet. The flow velocity along each line of sight (parallel velocity $V_{\parallel}$) are presented in Figure 2. These plots would indicate the response of an SLDV system which had infinitely high range resolution. At large lateral separations from the vortices, that is, at the top and bottom of the figure, only a very weak velocity perturbation is seen. As the line of sight gets closer to the vortex, the velocity peaks near the vortex location (C). However, if the line of sight passes directly through the vortex only a small component of velocity parallel to the line of sight is obtained (B). Lines of sight which pass between the vortex pair sense both vortices (A). The peak value of the parallel velocity changes sign as the line of sight crosses the vortex center and maximizes at the edges of the core.

The finite range resolution as defined by Equation (11) smears out this velocity profile to a greater or lesser extent depending on range. The SLDV system senses the Doppler spectrum as averaged over the range re-

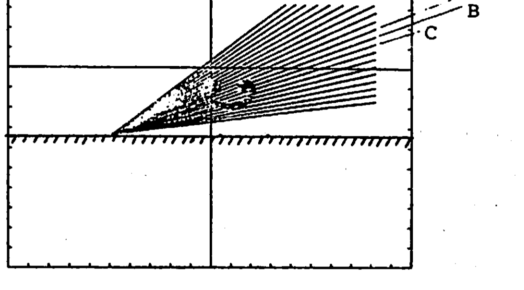

Figure 1. LDV fan beam configuration.

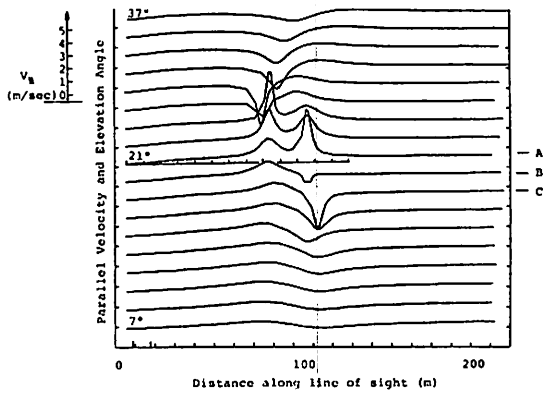

Figure 2. r, Θ-plot for the parallel velocity ($V_\parallel$).

sponse function of the instrument. Various moments or mean properties of the velocity spectrum may be calculated from the relation

$$\bar{f}(s,\theta) = \frac{\int^{\infty} f(V'')\, I(s,\theta,V'')dV''}{\int I(s,\theta,V'')dV''}, \quad (12)$$

where I(s,Θ,V″) is the Doppler spectral intensity, s is range, and Θ is elevation angle. This intensity in turn depends on the atmospheric backscattering properties and the range response function $g_s(s,s')$. For Gaussian aperture apodization, the range response function has the form

$$g_s(s,s') = \frac{1}{1 + 4\left(\frac{s-s'}{\Delta s}\right)^2}, \quad (13)$$

where Δs is the range resolution (between 3db points) obtained by multiplying Equation (11) by 2:

$$(\Delta s)_{gaussian} = 2\frac{\lambda}{\pi}\left(\frac{s}{R}\right)^2 . \quad (14)$$

Here s is the range to the focal point and R is the aperture radius (e^{-2} intensity). To account for finite truncation of the telescope mirror in the simulation model, we simply degrade the resolution by a fixed factor:

$$\Delta s = 2f\,\frac{\lambda}{\pi}\,(s/R)^2 . \quad (15)$$

Detailed propagation calculations have been carried out to examine the effects of finite apertures and blocking of the mirror. For a Gaussian beam truncated at the e^{-2} radius, f is computed to be 2.1.

Two modes of operation are possible, in general: one where the sign of the Doppler shift is sensed and the other where only the magnitude is used. All of the calculations presented here assume the latter mode, although either or both modes can be implemented.

The calculation of the spectrum begins with the parallel velocity profile versus range. When the system is focused at the range s, the spectrum level in the velocity channel V_k is obtained from a finite difference representation of

$$I(s,\theta,V_k) = I_0 \int_0^{\infty} \frac{\overline{n\sigma}(s')\, g_v\left(|V(s') - V_k|\right) ds'/\Delta s}{\pi\left[1 + 4\left(\frac{s-s'}{\Delta s}\right)^2\right]} . \quad (16)$$

Here $g_v(\delta V)$ is the frequency response of the filter and is taken to have the form

$$g_v(\delta V) = \frac{1}{\left[1 + \left(2\frac{\delta V}{\Delta V}\right)^{2p}\right]}, \quad (17)$$

where ΔV is the velocity resolution (0.545 meters/sec in the current simulation) and p is a parameter. The value p = 1 gives a reasonable representation for simple (6 db/octave) rolloff. Filters with sharper cutoffs correspond to larger values of p. No great differences are expected between the different values of p and the current demonstration calculations have all assumed p = ∞.

General Description of SLDV Simulation Code.

The model of the SLDV system response described in the preceding sections is formulated as a numerical computer program. This program calculates as a function of time, the response of a pair of LDV scanning systems which view the region below and near the aircraft track. Each system is described by a prespecified number of equally spaced lines of sight which uniformly cover elevation angles between a given maximum and minimum value. In the present formulation, the program "tracks" the wake, locates the elevation angle of the midpoint between the two tip vortices and automatically centers the elevation angle scan on this point. At regularly spaced time intervals, the simulated LDV system response is calculated as a function of range (to some maximum range) for each elevation angle.

The output of the program is displayed in a series of plots. The vortex sheet shed from the aircraft wing, as well as the tip vortices, are first presented on an x-y plot along with the locations of all the distributed wind shear vortices. The SLDV system configuration is displayed by superposing individual lines of sight of the two beams on a plot of the vortex sheet location.

The SLDV system response is calculated from the distribution of the parallel wind velocity component along each line of sight. Before presenting simulations of the system response, a high resolution 'three-dimensional' plot of this parallel velocity component is presented. This is the basic quantity sensed by all Doppler radar backscatter systems (laser, acoustic or microwave). Here the velocity is plotted versus range for each elevation angle and an entire scan frame is presented in a single range-elevation angle plot. Curves for different elevation angles are displaced in the vertical direction by an amount proportional to the angle.

The Doppler spectral intensity I(V) is then calculated at each point in space. Because of the large amount of data, only samples of these spectra at selected elevation angles are presented.

After the spectrum is computed, a number of spectral moments are determined. At present there are ten different variables or moments that are calculated at each range-elevation point. These are:

1) The parallel velocity $V_{\parallel}$; the actual component along the line of sight as computed directly from the hydrodynamic model.

2) The (unrectified) mean parallel velocity ($\bar{V}_1$); this is the parallel velocity simply averaged over the theoretical range resolution function

$$\bar{V}_1(s) = \int_0^\infty g_s(s-s')V(s')ds' \Big/ \int_0^\infty g_s(s-s')ds' . \tag{19}$$

3) The (rectified) mean parallel velocity $\bar{V}$; this is the parallel velocity as sensed by the LDV system with finite range resolution:

$$\bar{V} = \sum_{|V_k|>V_0} \left[I(k) - I_0(k)\right] |V_k| \Big/ I_{sum} . \tag{20}$$

Here V_k is the velocity of the kth channel, I(k) the computed intensity in this channel, $I_0(k)$ a threshold intensity level (to be discussed subsequently), and V_0 a velocity threshold. I_{sum} is the total intensity in all channels (above threshold):

$$I_{sum} = \sum_{|V_k|>V_0} (I(k) - I_0(k)) . \tag{21}$$

In all moment calculations, no contribution is included for intensities below a given intensity threshold (i.e., only non-zero contributions for $I(k) > I_0(k)$ are allowed). In this computation the system is assumed incapable of distinguishing positive from negative Doppler frequencies.

4) The velocity variance σ:

$$\sigma = \sum_{|V_k|>V_0} \frac{(|V_k| - \bar{V})^2 (I(k) - I_0(k))}{I_{sum}} . \tag{22}$$

5) The skewness β:

$$\beta = \sum_{|V_k|>V_0} \frac{(|V_k| - \bar{V})^3 (I(k) - I_0(k))}{I_{sum}} . \tag{23}$$

6) The kurtosis:

$$k = \sum_{|V_k|>V_0} \frac{(|V_k| - \bar{V})^4 (I(k) - I_0(k))}{I_{sum}} . \tag{24}$$

7) The peak velocity (V_{peak}); the velocity of the highest frequency channel having a spectral intensity exceeding the threshold value (and if $V_{peak} > V_0$).

8) The velocity of the maximum intensity (V_{max}); the velocity of the channel having the highest value of $I(k) - I_0(k)$ and for which $V_k > V_0$.

9) The maximum intensity (I_{peak}); the largest value of $I(k) - I_0(k)$ for all velocities greater than V_0.

10) Sum of intensity (I_{sum}); the total signal strength above the intensity and velocity thresholds:

$$I_{sum} = \sum_{|V_k|>V_0} (I(k) - I_0(k)) . \qquad (25)$$

All of these quantities are presented in the range elevation angle plots described previously. To illustrate the relationship between the variations of each variable and the tip vortices, we also superposed on the plots the location of the vortex sheet and the tip vortices.

DATA ANALYSIS

In general, each range scan of the system concerned is composed of approximately 50 points, and about 25 lines of sight for a complete angle scan so that there are approximately 1250 range points in each frame. The SLDV return signal is in the form of a spectrum (intensity versus velocity) at each point in space. For each focal point in space, there are six numbers to record its frame sequential number, x,y coordinates, range r, angle Θ and the clock time plus one number to record the signal intensity for each of the 104 velocity channels. From the spectrum, values of the derived variables ($\overline{V}$ through I_{sum}) described in the previous section are computed for each point in space. These variables are plotted both as functions of range at constant elevation angle and as contour plots in Cartesian coordinates. The R-Θ plot shows range-angle correlations, while the contour plot shows the spatial variation in the scan plane.

The effects of applying intensity and velocity thresholds to the spectra have been examined. The optimal intensity threshold I_{th} is found by successive approximation, increasing I_{th} until a clear contrast is achieved between the localized vortex return and the distributed background return. The results of this process can be summarized as follows:

1) A low intensity threshold results in a noisy "vortex" signature broadly distributed in space for all of the variables derived from the spectrum, except higher order moments of velocity which show localized signatures.

2) Medium intensity thresholds result in I_{sum} (and also I_{peak}, for non-zero velocity thresholds) being localized near the vortex core. Other variables are noisy and broadly distributed.

3) High intensity thresholds result in localized distributions for all variables; I_{sum} is most localized.

A velocity threshold can also be applied. In this study only two velocity thresholds V_{th} (4 and 20 m/sec) have been examined, and no systematic investigations of the effects of the value of V_{th} have been carried out.

RESULTS OF A B-720 SIMULATION

Figures 3 and 4 show simulations of the vortex wake of a B720 aircraft. The altitude at time zero was taken to be 55.3 meters and the total circulation of one wing is 190 m^2/sec. A light wind was assumed according to $u_{wind} = 0.5\, ln(1+y/2)$ m/sec. Two SLDV systems were assumed located on opposite sides of the aircraft track. Figures 3a and 4a show the overall geometry at an elapsed time of 18 seconds for both SLDV1 and SLDV2.

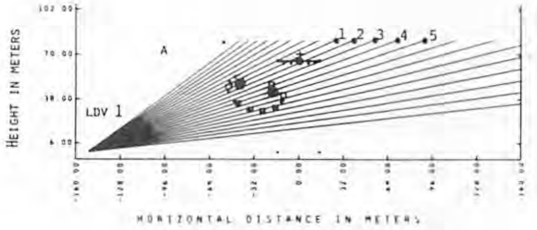

Figure 3a. Fan beam configuration for LDV1.

In Figures 3b to 3g and 4b to 4g, we show range-elevation plots of the following series of variables: $V_{\parallel}$, $\overline{V}_{\parallel}$, $\overline{V}$, σ, β, κ. In all cases to be discussed, the intensity and velocity thresholds were taken to be zero. Five particular lines of sight are identified in Figure 3 and exhibit various characteristics of the signature. In general, both vortices can be identified (at least at this range) in all lines of sight which pass between the two vortices. The line of sight 3 passes near the midpoint and shows two comparable peaks in Figures 3b and 3f. Lines of sight passing near the edge of a vortex core (but not through the core) show a strong peak (e.g., lines 2 and 4); however, when the line of sight passes directly through a vortex core (e.g., line 1), only the broad maximum from the other vortex is discernible. These features are particularly marked in the higher moments of velocity (that is, σ, β and κ in Figure 3e, f, g) where the core edges are quite visible on the line, whereas the line of sight passing through the center of the core shows no signature.

By comparing Figures 3b to 3c for the line of sight 5, the effect of finite range resolution can be seen. Similarly, by comparing Figures 3c to 3d of the same line, the effect of velocity rectification can be demonstrated.

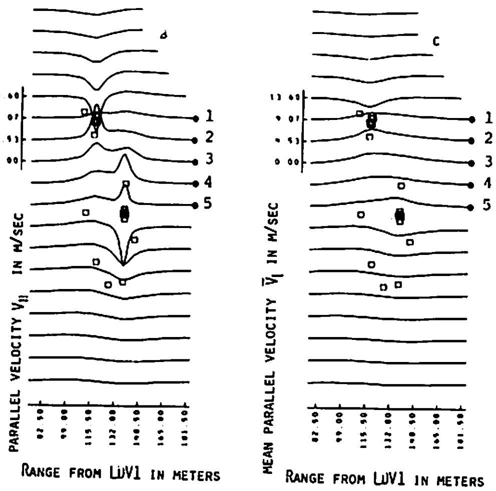

Figure 3bc. Fan beam configuration and distributions of $V_{\parallel}$ and $\overline{V}_{\parallel}$ along various lines of sight for LDV1 located at mean range to wake: 120 meters (B-720 simulations at 18 seconds).

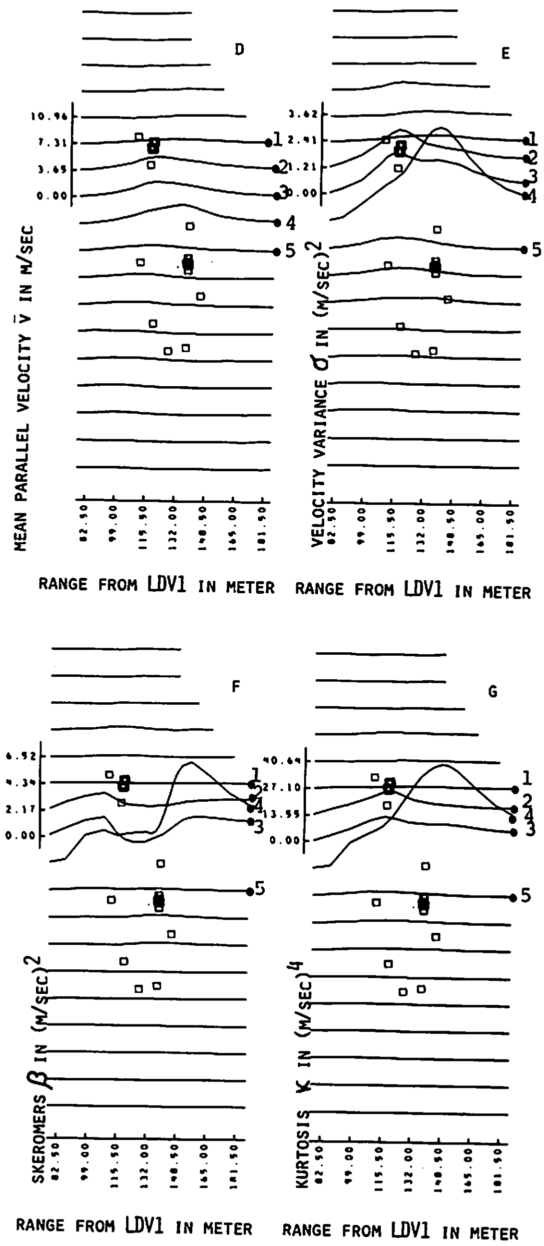

Figure 3defg. Distributions of various spectral moments for LDV1 located at mean range to wake: 120 meters (B-720 simulation at 18 seconds).

Signatures for all variables, except for $V_{\parallel}$ in Figure 3b which was computed with infinite range resolution, are confined in the region between the vortices. Only two beam separations (3°) away from it the signature becomes invisible. The visibility of signature increases with the order of moment of velocity, and angle resolution also improves with higher velocity moments. The spread range is a function of range resolution only; using higher moments does not reduce it. Although it is not clearly shown here, the skewness becomes negative at close range (less than 120 meters) on lines connecting two vortices.

Figure 4 shows the signatures as seen by the second SLDV system (SLDV2) at 18 seconds after fly-by. The mean range to wake is about 160 meters. The vortices in this case lie along a single line of sight from the instrument, and are not separated in angle. Line of sight 2 (passing through both cores) in Figure 4 shows no discernible signature for all variables, while lines of sight 1 and 3 (on either side) show clear signatures. The signatures of the vortices are partially merged together at this range (~ 160 meters) even though there are several peaks in Figures 4defg. More detailed discussions and simulations of other aircraft and wind conditions are given in reference 1.

COMPARISONS OF SIMULATION RESULTS TO FLIGHT TEST DATA

Simultaneous processing for both actual flight and simulated data tapes was carried out. The rasters of measured or recorded points are shown in Figures 5a and 5b, where Figure 5a shows the flight data and Figure 5b shows the simulation data. Both horizontal and vertical coordinates have the same scale. The caption near the top of the raster describes the lowest and highest elevation angles, as well as the initial and final clock times in seconds. The simulation run (Figure 5b) uses a fan of lines of sight separated by a constant angle of 1.5° and is extended from the aperture all the way to the outer boundaries of the computation mesh. The higher density of range points near the vortex locations is the result of finer integration steps used in the simulation model to resolve the higher velocity gradient there.

In this paper we will concentrate on discussion of only one representative flight which has been designated as RUN1023 by NASA/MSFC, to demonstrate the nature of the data. That flight test was conducted at Marshall Space Flight Center, National Aeronautics and Space Administration, on July 20, 1974. A B737 was flown from north to south. The first LDV system was located

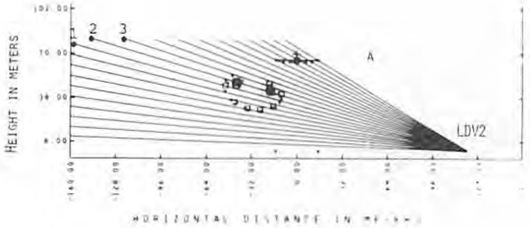

Figure 4a. Fan beam configuration for LDV2.

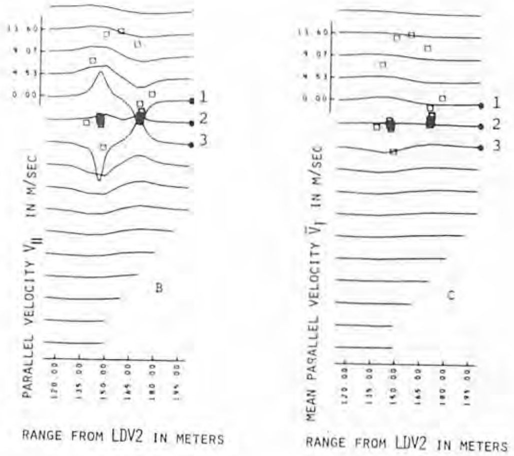

Figure 4bc. Fan beam configuration and distributions of $V_\parallel$ and $V_|$ along various lines of sight for LDV2 located at mean range to wake: 160 meters (B-720 simulations at 18 seconds).

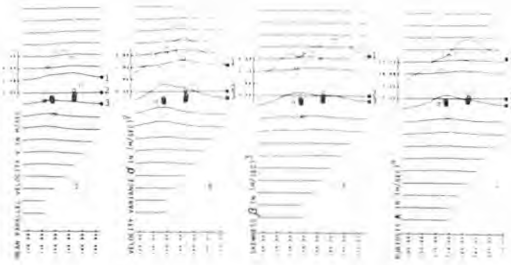

Figure 4defg. Distributions of various spectral moments for LDV2 located at mean range to wake: 120 meters, (B-720 simulation at 18 seconds).

at 61.11 meters to the west, and the second system was at 240 meters to the east of the aircraft track: the wind was blowing from the west.

Figures 6 and 7 show the comparisons of contours for both $\overline{V}$ and V_{max} between the simulated and flight test data. Due to the complexity involved in an uncontrollable atmospheric environment, it was not possible to make an exact simulation of the flight test, and only qualitative comparisons can be made. In the figures, the ground level is indicated by a horizontal line at $y = 0$, and the SLDV systems are located at coordinate (0,0). Both axes are drawn in units of meters.

In Figures 6a and 7a, the vortex locations from the hydrodynamic modeling are indicated by the symbols "+". The SLDV system observes a maximum value for both $\overline{V}$ and V_{max} which lies between the vortices. It is a direct consequence of the interaction between the wind shear and the vortices; i.e., enhancement (or cancellation) along (or against) the wind direction.

Figures 6b and 7b show contours of $\overline{V}$ and V_{max} for the flight test data. Both plots were obtained by applying a constant intensity threshold of 60 to all velocity channels and "no" velocity threshold. Note that the scales for the flight test are not the same as for the simulation. The flight vortex signatures appear similar in shape to those of the simulation. Contours of other variables are discussed in detail in reference 2. The results detailed there can be summarized as follows: at high intensity thresholds, the low order velocity moments yield smooth but rather broadly distributed contours. The high order moments yield contours which are more localized, but weaker signals can be lost. The

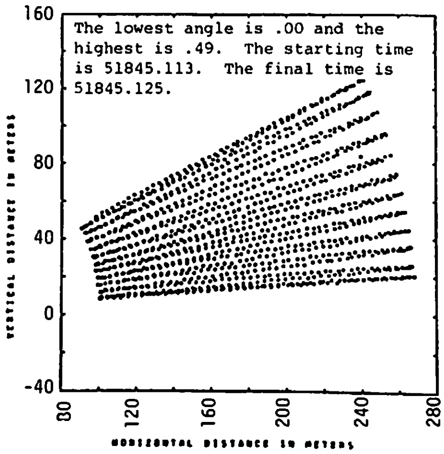

Figure 5a. Fan beam configuration for run 1023.

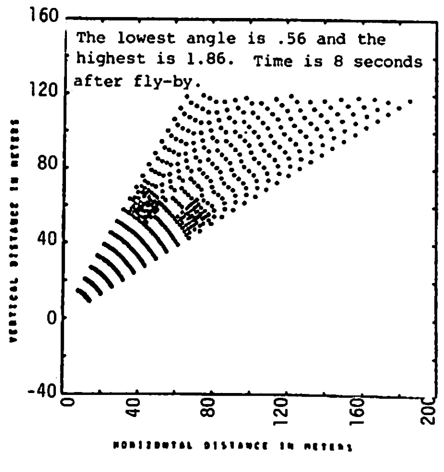

Figure 5b. Fan beam configuration for simulation data.

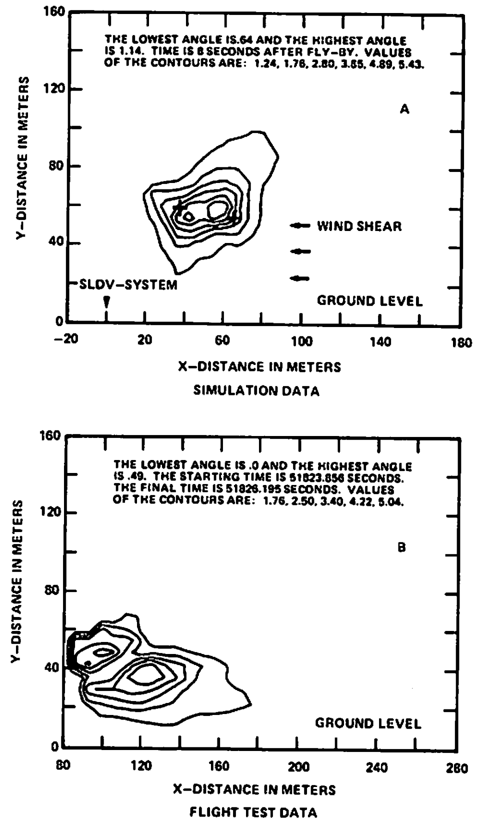

Figure 6. Contours of averaged velocity $\overline{V}$ for both simulation and flight test data, SLDV system is located at coordinate (0,0) for both cases. "+" indicates known locations of vortices for simulation case.

choice of the intensity threshold is important for all variables examined, but is less critical for I_{sum} and I_{peak}. I_{sum} contours are well localized at the vortex positions, as are I_{peak} contours if a velocity threshold is applied.

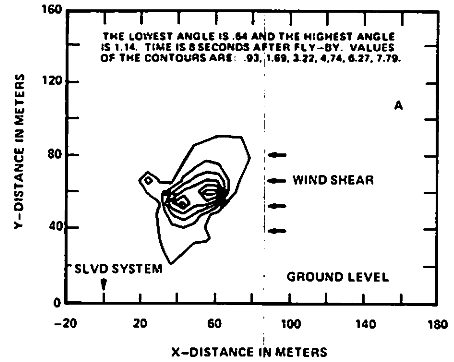

SIMULATION DATA

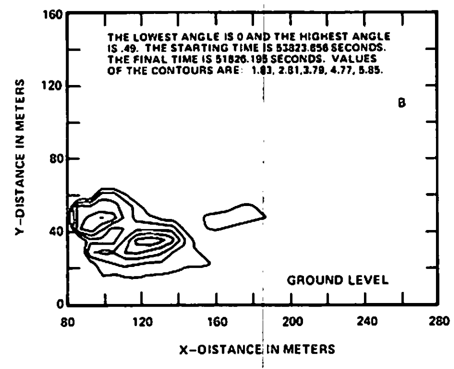

FLIGHT TEST DATA

Figure 7. Contours of maximum velocity V_{max} for both simulation and flight test data, SLDV system is located at coordinate (0,0) for both cases. "+" indicates known location of vortices for simulation case.

A series of contour plots for I_{sum}, generated with a constant intensity threshold $I_0(k) = 60$ but no velocity threshold, are shown in Figure 8. The simulation studies have shown that the maxima of $\overline{V}$, σ, β, and κ are well correlated with the vortex location if the range is greater than 100 meters. The flight data show that the locations of maxima in $\overline{V}$ are closely correlated with those in I_{sum}. One could postulate that a maximum in I_{sum} identifies the vortex core location, and plot the location of these maxima as functions of time in order to obtain vortex tracks. Without going into detail, it can be seen that the plots appear to show two vortices moving from left to right at a speed of about 1.85 m/sec and descending at ~1.08 m/sec. The average vortex separation is about 30 meters, so that the total circulation contained in the vortex is about 204 m^2/sec (2205 ft^2/sec), which is also close to the theoretical prediction of 2360 ft^2/sec.

Another interesting quantity which can be inferred from the data is the range resolution as defined by Equation (15) or the following equation.

$$\Delta s = 0.000629 \ s^2 \tag{26}$$

where Δs and s are both in meters. The constant coefficient is obtained assuming f = 2.1, λ = 10.6μ and R = 0.15m for the NASA/MSFC SLDVS. Defining Δs as the halfwidth of I_{sum} contour plots (shown in Figures 8), we can compare them with Equation (26). Figure 9 shows there is a fair agreement between the data and Equation (26).

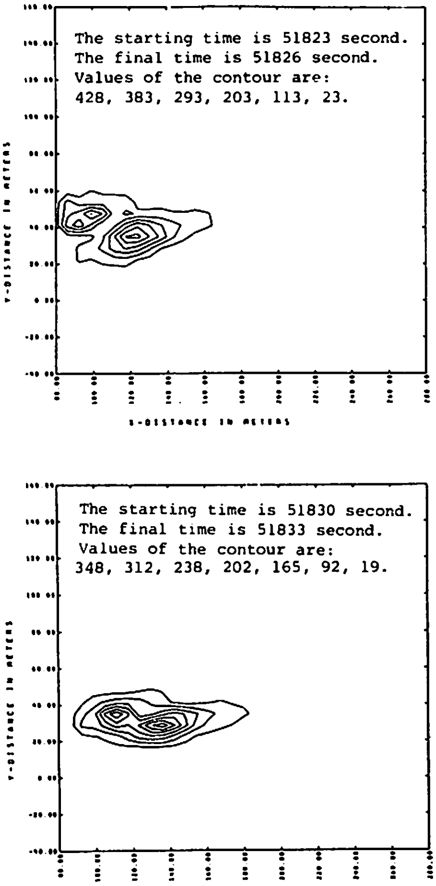

Figure 8. Time sequence of I_{sum}.

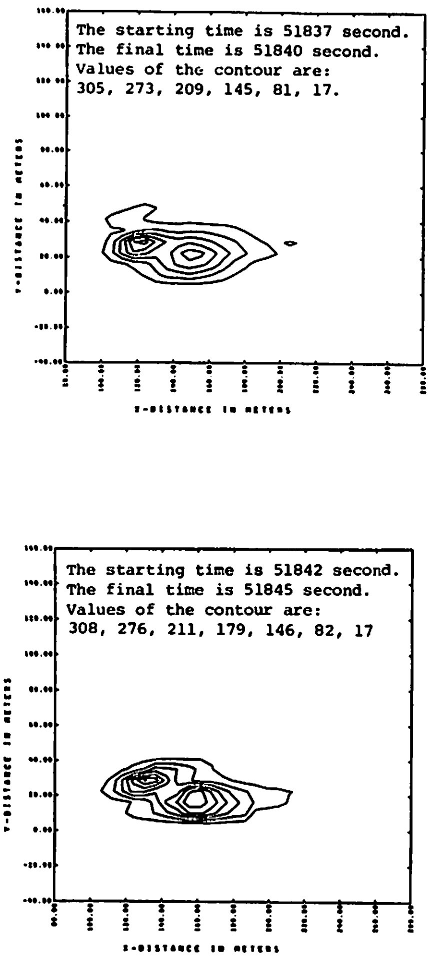

Figure 8. Concluded.

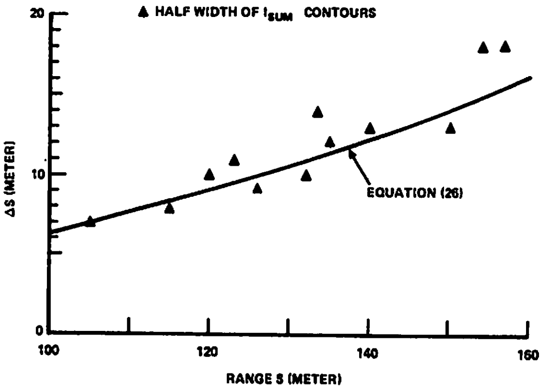

Figure 9. Values of range resolution versus range.

ACKNOWLEDGEMENT

The authors are greatly indebted to Frederick P. Boynton for reviewing the manuscript and helping to prepare it for publication. We also thank both R. Milton Huffaker and Harold Jeffries of NASA/MSFC for their many suggestions and in-depth discussions.

REFERENCES

1. Thomson, J.A. and Meng, J.C.S., "Laser Doppler Velocimeter System Simulation for Sensing Aircraft Wake Vortices. Part I. Simulation Model," PD-74-058, Dec. 1974, Physical Dynamics, Inc., Berkely, CA. (Also appeared in *J. Aircraft*, Vol. 13, number 8, Aug. 1976, p. 605-613.)

2. Meng, J.C.S. and Thomson, J.A.L., "Laser Doppler Velocimeter System Simulation for Sensing Aircraft Wake Vortices, Part II: Processing and Analysis of LDV Data (for runs 1023 and 2023)", PD-75-077, Feb. 1975, Physical Dynamics, Inc., Berkeley, CA.

3. Thomson, J.A., "Study of Conceptual and Operational Feasibility of Laser Doppler Detection Systems," Progress Report to Nov. 30, 1970, for contract NAS8-24810, Research Institute of Engineering Sciences, Wayne State University, Detroit, MI.

4. Krause, M.C., Morrison, L.K., Craven, C.E., Logan, N.A. and Lawrence, T.R., "Development of Theory and Experiments to Improve Understanding of Laser Doppler Systems," LMSC-HREC TR-D306632, June 1973, Lockheed, Huntsville, AL.

5. Wilson, D.J., Krause, M.C., Coffey, E.W., Huang, C.C., Edwards, B.B., Shrider, K.R., Jetton, J.L., and Morrison, L.K., "Development and Testing of Laser Doppler Components for Wake Vortex Monitoring. Volume I. Scanning Development, Laboratory and Field Testing and System Modeling," LMSC-HREC TR-D390159-I, Aug. 1974, Lockheed, Huntsville, AL.

LASER DOPPLER FLIGHT TEST MEASUREMENTS OF B-747 WAKE VORTEX CHARACTERISTICS

M.R. BRASHEARS AND A.D. ZALAY
Lockheed Missiles & Space Company, Inc.
Huntsville, AL 35807

J.N. HALLOCK AND D.C. BURNHAM
U.S. Department of Transportation
Transportation Systems Center
Cambridge, MA 02142

ABSTRACT: In order to determine the behavior of aircraft wake vortices at low altitudes and to measure the wake vortex decay process behind a wide-body transport aircraft as a function of altitude above ground, flap and spoiler settings, and different flight configurations: a B-747 aircraft flew 54 passes at low level over a ground-based laser-Doppler velocimeter (LDV) system. From the LDV measurements, the location and velocity distribution of the wake vortices and the general vortex rollup, transport, and decay trends were obtained. Results of the study indicated that the deployment of spoilers and flaps enhanced the decay of the vortex peak tangential velocity in the near wake while aircraft altitude, flight path angle, and landing gear deployment had little effect. The paper discusses the LDV wake vortex measurement including the instrumentation used, the experimental test sequence, and the results of the wake measurements in terms of the vortex rollup, transport and decay trends. A comparison of the wake vortex characteristics for different aircraft configurations is also presented.

INTRODUCTION

Wake vortex transport and decay parameters near the ground are important factors in determining safe aircraft separation distances for terminal areas. For an operational Wake Vortex Avoidance System (WVAS) a knowledge of the location and intensity of wake vortices near the runway threshold is necessary to determine the minimum-delay safe spacings [1]. Under light crosswind conditions, a wake vortex can remain in the approach corridor for more than 40 seconds and the minimum aircraft separation is dictated primarily by the wake decay process near the ground. Therefore, an important consideration in determining safe aircraft separations is the decay of the wake vortex near the ground. While numerous vortex decay theories have been proposed [2-4] there is little full-scale experimental data available for comparison, particularly near the ground.

Experimental vortex decay data near the ground are also lacking for aerodynamic wake minimization concepts where variations in aircraft geometry are utilized to tailor the wake vortex flow. Flight tests by NASA have shown that certain flap and spoiler settings can reduce the imposed rolling moments on following aircraft in the near wake [5]; however, wake vortex measurements near the ground for full-scale aircraft with different wake minimization concepts are needed.

In order to determine the behavior of aircraft wake vortices at low altitudes a flight test program was conducted by DOT and NASA. The primary goal of the test program was to measure the wake vortex decay process behind a wide-body transport aircraft as a function of altitude above ground, flap and spoiler settings, and different flight configurations. To isolate the influence of aircraft and flight parameters on the wake decay process, the flight tests were conducted at the Rosamond Dry Lake test area near Edwards Air Force Base, California, during the early morning hours when calm atmospheric conditions prevailed. The laser Doppler Velocimeter (LDV) wake decay measurements were sought to quantify the effect of burst, link and viscous decay parameters on the wake vortex dissipation process.

DESCRIPTION OF EXPERIMENTAL TESTS

A two-day test sequence was carried out to determine the wake vortex characteristics of a B-747 aircraft as a function of spoiler, flap and landing gear settings and altitude above ground and flight path angle. The test consisted of 54 low altitude passes over a mobile LDV system deployed at Rosamond Dry Lake near Edwards AFB, California, on 2-3 December 1975.

Flight Test Program.

The aircraft used for the tests was a Boeing 747-123 aircraft. Aircraft configuration varied from run to run, with dominant emphasis on as close to a normal landing configuration as operating conditions would allow. The clean configuration was also studied, and special flap and spoiler configurations were investigated for vortex alleviation effectiveness. The Boeing 747 flew at 30-250 m above the ground level of 700 m MSL. Runs were made in level flight as well as in descending and climbing flight. Descents were at about 250 m/min. A lift coefficient of approximately 1.4 was used for all flaps-down runs.

Of the 54 runs, 35 were made with the inboard flaps lowered 30 deg and the outboard flaps lowered 30 deg (denoted 30/30); 8 with 10/10 flaps and 5 with flaps retracted. The remaining six runs had the inboard flaps lowered 30 deg and the outboard flaps lowered 1 deg, to test the effects of this configuration on vortex alleviation. For each flap setting, both gear down and gear retracted runs were made and some runs had spoilers 1, 2 and 11, 12 deployed (the extension angle was always 41 deg) in addition to the flap. Reference 6 describes the tests in detail including other sensors which were used to study the decay of the B-747 vortices.

LDV Instrumentation.

Wake vortex measurements were carried out by means of a scanning laser Doppler velocimeter system contained in a mobile van. Preliminary processing of the data was carried out with a computer aboard the van. Reduction and analysis of the vortex signatures were carried out by off-line processing software. A description of the instrumentation and data processing for the studies is summarized briefly below.

The laser Doppler velocimeter was utilized to measure the line-of-sight velocity component of the vortex during the Rosamond flight tests. These wake velocity measurements were accomplished as follows: (1) the wake generated by the aircraft was scanned by the CO_2 laser; (2) the radiation backscattered from the aerosol in the wake was collected; (3) the radiation was photomixed with a portion of the transmitted beam on a photodetector; and (4) the intensity and Doppler shift frequency of the signal were displayed and were translated into an along-optic-axis velocity. A sketch of the optical and electronic equipment for measuring the intensity and frequency spectrum of the coherent backscatter from the focal volume is shown in Figure 1 and is described in more detail in reference 7.

The laser beam was focused through a Cassegrainian telescope; the focal volume of the beam was a needle-shaped region of dimension $\Delta f = 9.84 \times 10^{-4}$ (m^{-1}) f^2 along the

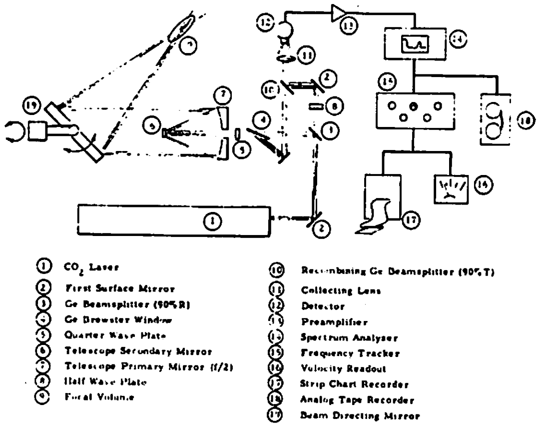

Figure 1. Basic laser Doppler configuration.

optical line of sight and of radius $\Delta r = 3.28 \times 10^{-5}$ f perpendicular to the line-of-sight where f is the target range. The focal volume of the LDV is a measure of the coherent spatial resolution of the system; i.e., the range increment at which the Doppler signal deteriorates to the one-half power level. For example, when the LDV system was tracking wake vortices at a typical range of 60 m, a needle-shaped volume of the vortex 3.5 m long along the optic axis and 4 mm in diameter was sampled. Hence, the typical spatial resolution due to the spreading of the focal volume was 3.5 m.

The pertinent operating characteristics of the LDV during the Rosamond tests are summarized as follows:

Performance
1. Velocity Measurement Threshold: 0.5 m/sec
2. Velocity Range: 0.5 to 28 m/sec

Sample Rate
1. Low Data Rate: 70 Hz
2. High Data Rate: 500 Hz (using NASA filter bank)

Spatial Resolution
1. Range Accuracy: ±0.4 m at 30 m, ±44 m at 300 m
2. Elevation Angle Accuracy: ±0.25 deg.

The characteristic output signature from the LDV, the amplitude-velocity spectrum, is given in Figure 2. The output signature shows the motion of particles within the wake vortex (indicated by the peak labeled vortex signal) as well as a low frequency noise peak and background noise. To facilitate processing the LDV signature, velocity and amplitude thresholds were applied to the signal and the velocities (frequencies) associated with the highest intensity, V_{ms}, and highest velocity, V_{pk}, above the threshold settings were extracted from the spectrum. The velocity V_{ms} is the line-of-sight velocity of the most intense signal. The velocity V_{pk} is a measure of the maximum velocity above threshold encountered in the focal volume. In the case of wake vortex measurements, when the vortex range is near the focal volume of the system, the velocity V_{pk} is associated with the tangential velocity of the vortex at the radius where the line of sight is tangent to the vortex velocity.

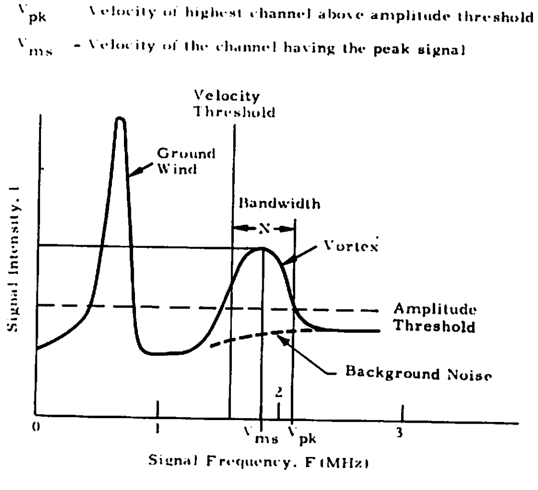

Figure 2. Definition of laser Doppler velocimeter output signature.

Operation of LDV.

During the B-747 flight tests, a total of 53 aircraft fly-bys were recorded with the LDV system. In order to maximize the amount of data collected regarding wake vortex trajectories, velocity profiles, and decay rates, the LDV was operated in two different scan modes: arc scan and finger scan. The wake vortex surveys were conducted in the following manner.

On the first test day the LDV was located directly under the flight path and scanned arcs in a plane perpendicular to the flight path (Figure 3) with a complete arc every second. Scans were at a fixed range until the vortex passed through the scan arc, at which time the sensor range was lowered and remained fixed again until the vortex descended through the new range. The objective of the overhead arc scan measurements was the measurement of the initial downwash field and the wake vortex rollup process.

On the second test day the LDV was moved 60 m north of the flight path and scanned simultaneously in elevation and range (finger-scan mode) at a frequency of 0.2 and 2 - 2.5 Hz, respectively (Figure 4). The objective of the finger-scan measurements was to track the location of the

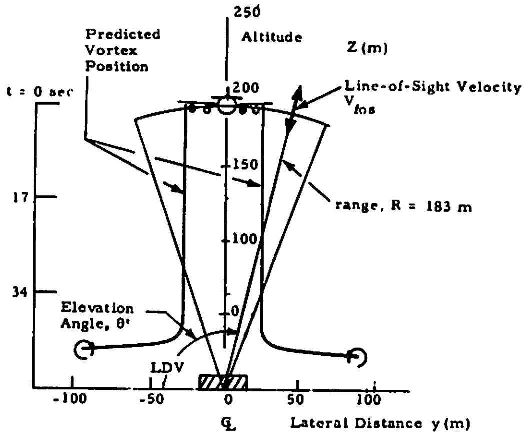

Figure 3. Typical overhead arc-scan configuration.

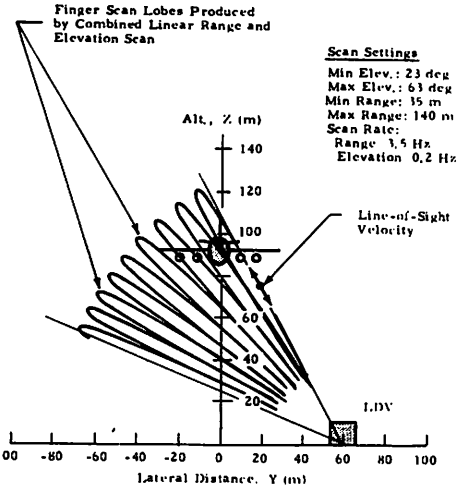

Figure 4. Typical finger-scan configuration.

vortex pair and to observe the vortex decay rates. The finger scan range and elevation settings were selected so that one or more of the trailing vortices would remain in the field of view for extended periods and one or more "cuts" would be made through the vortex core during each elevation scan.

RESULTS OF LDV MEASUREMENTS

The LDV measurements from the B-747 fly-bys have been analyzed to determine the dominant characteristics of the aircraft wake. Particular attention was given to the vortex rollup, transport and decay parameters as a function of aircraft operating characteristics.

Vortex Roll-Up.

The LDV arc-scan measurements have been processed to determine the wake vortex formation characteristics. A sample of the raw line-of-sight velocity, $|V_{pk}|$, versus horizontal distance observed by the LDV system in the wake of a B-747 in the normal landing configuration and with the 1, 2, 11, 12 spoilers deployed is shown in Figures 5 and 6, respectively. Since the arc scan essentially intersected the centroid of the wake vortex during the wake surveys, the $|V_{pk}|$ versus lateral distance plots are a measure of the rotational velocity distribution of the trailing vortices in the aircraft wake. The distinct double peak velocity signatures in Figures 5 and 6 indicate the high rotational velocity at the vortex core radius and the low velocity at the vortex center. Note that the peak tangential velocity is on the order of 16 and 8 m/sec and the core diameter is 5 and 14 m for the normal landing and 1, 2, 11, 12 spoiler configurations, respectively. The sample measurements show that the deployment of spoilers reduces the vortex rotational velocity and increases the viscous core diameter while the core circulation strength remains approximately the same. (The nonlinear distance scales in Figures 5 and 6 are caused by nonlinearities in the angle scan.)

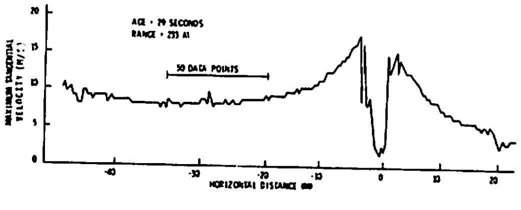

Figure 5. $|V_{pk}|$ as a function of horizontal distance for a 30/30 flaps, gear down flyby.

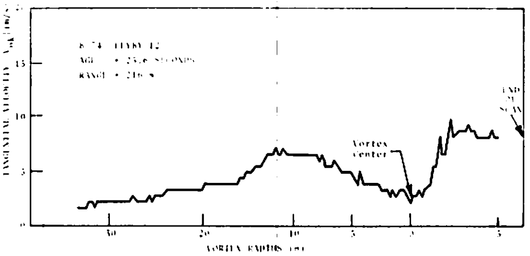

Figure 6. V_{pk} as a function of horizontal distance for a 30/30 flaps, gear down, and spoilers deployed flyby.

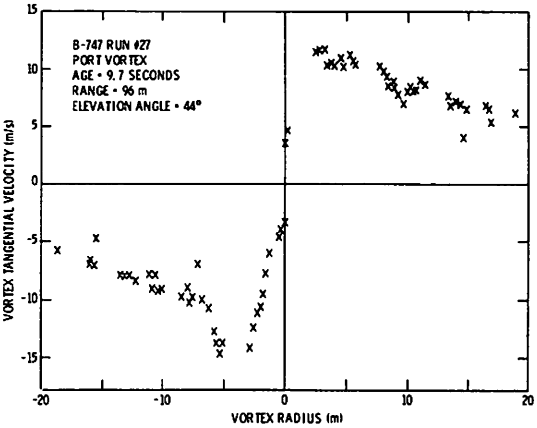

Figure 7. Wake vortex velocity distribution for a 30/30 flaps, gear down flyby.

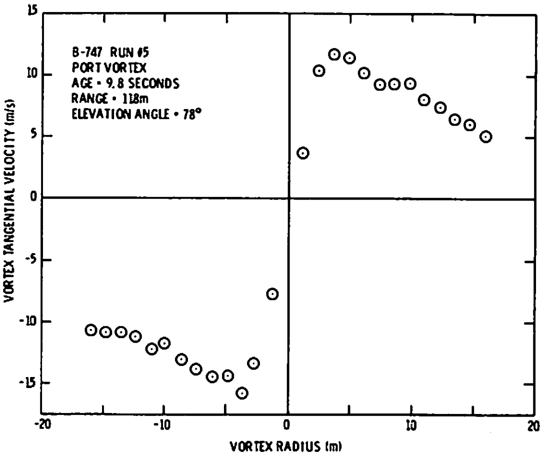

Figure 8. Wake vortex velocity distribution for a 30/30 flaps, gear down flyby.

From the type of line-of-sight velocity distributions illustrated above, the vortex rotational velocity and circulation distributions were calculated. The vortex center was determined to be midway between the two high velocity peaks where the velocity was minimum. The velocity field was derectified using the vortex center as a reference. A sample of the processed vortex tangential velocity distribution for the B-747 in normal landing configuration is shown in Figure 7. The gaps in the velocity plot are a result of the finger-scan mode of data collection. The peak tangential velocity is 13 m/sec and the core diameter is 8 m. A sample of the vortex tangential velocity distribution for the B-747 in the landing configuration but in level flight and at a higher altitude is shown in Figure 8. Use of the arc-scan mode gives continuous velocity measurements, but the range is uncertain. Again, the peak tangential velocity is 13 m/sec and the core diameter is 8 m. These results indicate that aircraft altitude and flight path angle do not influence the vortex formation process significantly for the parameters tested. It is also noted that the vortex rollup occurs rapidly so that at about 10 seconds a distinct and coherent core structure is evident.

The circulation distribution in the wake of the B-747 computed from the velocity distribution in Figure 8, assuming circular symmetry, is illustrated in Figure 9. The circulation strength measured in the vortex wake increases with radial distance from the vortex center. For example, at the vortex core radius, $r_c = 4$ m, the circulation is $\Gamma_c = 326$ m²/sec whereas at 4 radii from the center, $r = 16$ m, the circulation is more than doubled, $\Gamma = 725$ m²/sec. In comparison, the computed bound circulation strength of the wing is $\Gamma = U_\infty \bar{c} C_L/(2K) = 620$ m²/sec where $U_\infty = 74.15$ m/sec, $\bar{c} = 8.3$ m, $C_L = 1.41$, and $K = 0.7$. This discrepancy is likely due to the vortex range error of the arc-scan mode.

Vortex descent to 20 m below the LDV scan would give agreement. The circulation distribution measured with the LDV system agrees well with the theoretical Hoffman and Joubert turbulent vortex model [8] shown by the dashed line in Figure 9 and given by the relationship $\Gamma/\Gamma_c = 1.83\ (r/r_c)^2$ and $\Gamma/\Gamma_c = [1 + 2.14 \log_{10}(r/r_c)]$ in the inner and outer core regions, respectively.

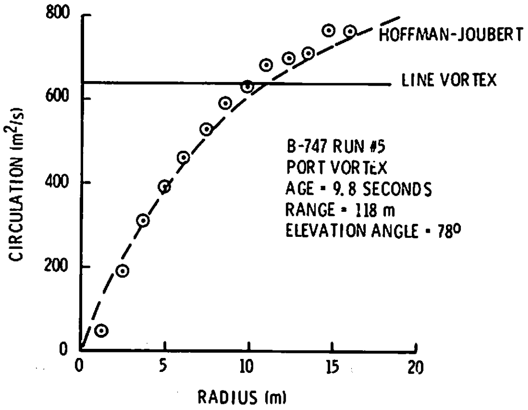

Figure 9. Wake vortex circulation distribution for a 30/30 flaps, gear down flyby.

Vortex Transport.

The line-of-sight velocity measurements obtained with the LDV system in the finger-scan mode have been used to determine the location of the center of the trailing vortices. A vortex-tracking criterion was used which identified the vortex position from the region of maximum backscatter and took into account the spatial resolution of the LDV. The vortex tracking criteria was an improvement over the tracking algorithm described in reference 7. The wake vortex tracks observed with the LDV system are shown in Figure 10 along with the photographic and computed vortex locations. The computed trajectories were generated from a theoretical model using aircraft location, wingspan, weight and airspeed as inputs and assuming no crosswinds. The vortex tracks measured by the LDV system show a gradual descent of the wake with little lateral motion, trends which are in general agreement with the vortex motion determined photographically and predicted theoretically.

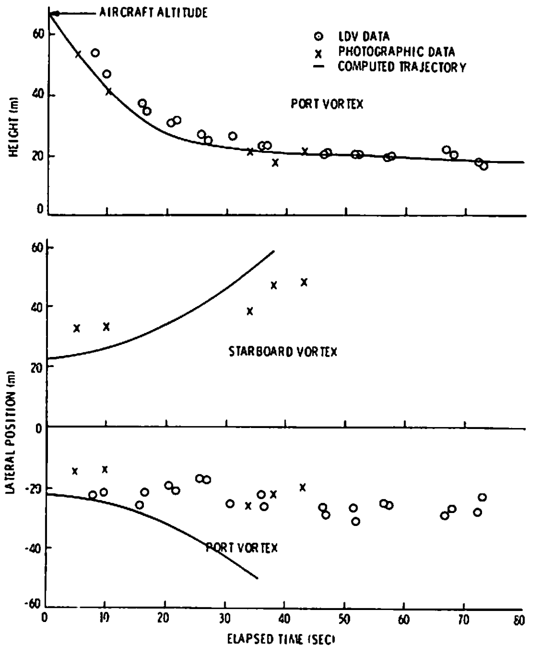

Figure 10. Wake vortex trajectories for a 30/30 flaps, gear down flyby.

Vortex Decay.

Information regarding the decay of the wake vortices including the time history of the vortex rotational velocity, core radius, and circulation was obtained from the line-of-sight velocity distributions measured by the LDV system. In the aircraft near wake, the LDV measurements indicated a relatively constant peak tangential velocity, core radius, and vortex strength. An example of the circulation time history of the trailing vortex observed for the B-747 in normal landing configuration is shown in Figure 11 for different averaging radii. It is noted that the circulation of the vortex remains essentially constant with time for all averaging radii over the time period of 10 to 40 seconds. The above result indicates that no significant decay of the wake vortex strength occurs in the near wake.

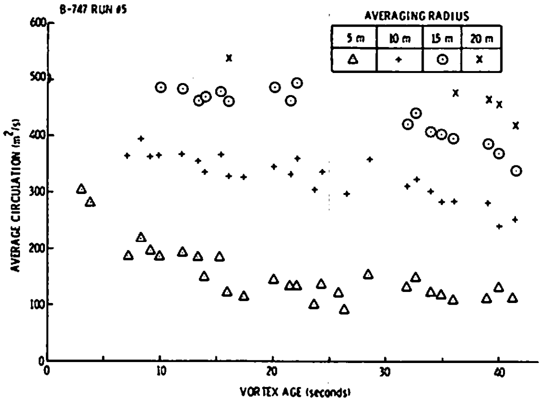

Figure 11. Wake vortex circulation time history for a 30/30 flaps, gear down flyby.

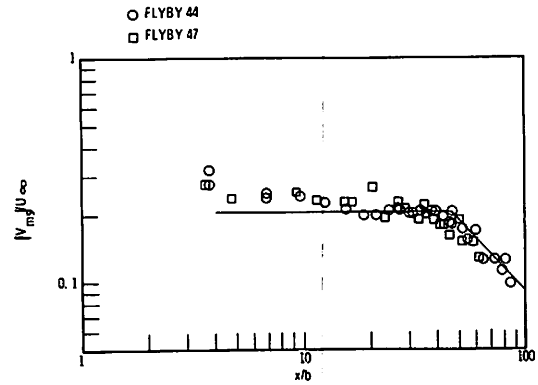

Figure 12. Decay of wake vortex velocity for 0-spoiler configuration.

In order to determine the wake vortex decay characteristics for different aircraft configurations, the time history of the vortex rotational velocity, V_{ms}, has been processed for flybys with 0 and 1, 2, 11, 12 spoilers and the results are shown in Figures 12 and 13. For the 0-spoiler configuration, essentially no decay of vortex rotational velocity is observed in the near wake, followed by a 1/t type of decay 40 or more spans downstream.

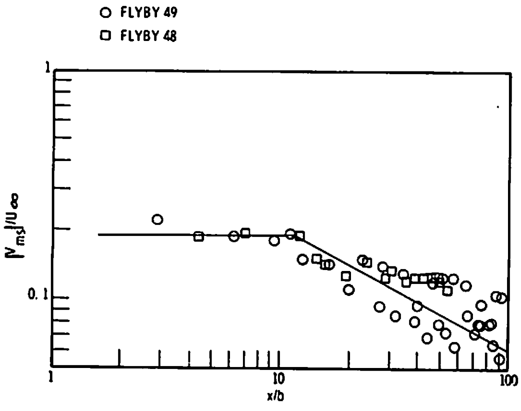

Figure 13. Decay of wake vortex velocity for (1, 2, 11, 12)-spoiler configuration.

For the tip spoiler configuration, the rotational velocity of the vortex is also essentially constant in the near wake followed by a decay beyond 12 semispans with sufficient scatter in the data to make establishment of the decay rate difficult. In comparison with the 0-spoiler case, the 1, 2, 11, 12-spoiler configuration exhibits a slightly lower rotational velocity in the near wake and an earlier onset of decay. However, at distances approaching 80 spans downstream of the aircraft, the 0 and 1, 2, 11, 12 configurations exhibit roughly the same vortex rotational velocities. Thus, deployment of the outboard spoilers enhances the vortex decay in the near wake and does not appear to influence the far wake vortex decay characteristics.

CONCLUSIONS

Laser Doppler velocimeter measurements of the wake vortex characteristics of a B-747 aircraft in various configurations have shown the following trends. For vortex formation:

1. The rollup of the vortex sheet occurred rapidly within a few spans downstream of the aircraft.
2. The peak tangential velocity and circulation of the vortices remained nearly constant in the near wake.

3. The B-747 spoilers affected the vortices, producing vortices with large cores and low peak tangential velocities and the circulation strength remained fixed.

For vortex transport:

1. The wake vortices descended vertically with little horizontal motion under light crosswind conditions.

For vortex decay:

1. A decrease in the peak tangential velocity and circulation and an increase in the core radius were observed in the far wake.
2. Deployment of spoilers and flaps enhanced the vortex peak tangential velocity decay process in the near wake and did not influence the far wake decay characteristics significantly.

ACKNOWLEDGMENTS

The authors are grateful to the NASA-MSFC Optics Branch for making the LDV filter bank and signal processor available for this study and to J.W. Bilbro and H.B. Jeffreys at NASA-MSFC and to W. Keenum, E. Lucas and R. Bynum at Computer Sciences Corporation for processing the high-speed filter bank measurements.

REFERENCES

1. Hallock, J.N., Wood, W.D., and Spitzer, E.A., "Predictive Technique for Wake Vortex Avoidance," AGARD CP-188, May 1975.
2. Tombach, I.H., "Observations of Atmospheric Effects of Vortex Wake Behavior," *J. Aircraft*, Vol. 10, No. 11, November 1973, pp. 641-647.
3. Crow, S.C., "Stability Theory for a Pair of Trailing Vortices," *AIAA J.*, Vol. 8, No. 12, December 1970, pp. 2172-2179.
4. Tombach, I.H., Crow, S.C., and Bate, E.R., Jr., "Investigation of Vortex Stability Near the Ground," AFOSR TR-75-1501, July 1975, AeroVironment Inc., Pasadena, CA.
5. Barber, M.R., Hastings, E.C. Jr., Champine, R.A., and Tymczyszyn, J.J., "Vortex Attenuation Flight Experiments," NASA Wake Vortex Minimization Symposium, Washington, DC, 25-26 February 1976.
6. Hallock, J., Burnham, D.C. Tombach, I.H., Brashears, M.R., and Zalay, A.D., "Ground-Based Measurements of the Wake Vortex Characteristics of a B-747 Aircraft in Various Configurations," AIAA Paper 77-9, AIAA 15th Aerospace Sciences Meeting, Los Angeles, CA, Jan. 1977.
7. Brashears, M.R., Lawrence, T.R., and Zalay, A.D., "Mobile Laser Doppler System Check Out and Calibration," FAA-RD-77-117, 1977, Lockheed, Huntsville, AL.
8. Hoffman, E.R., and Joubert, P.M., "Turbulent Line Vortices," *J. Fluid Mech.*, Vol. 16, Part 3, July 1963, pp. 395-411.

SCANNING LASER-VELOCIMETER SURVEYS AND ANALYSIS OF MULTIPLE VORTEX WAKES OF AN AIRCRAFT

VICTOR R. CORSIGLIA AND KENNETH L. ORLOFF
NASA Ames Research Center
Moffett Field, CA

ABSTRACT: A laser velocimeter capable of rapidly scanning a flow field while simultaneously sensing two components of the velocity was used to measure the vertical and streamwise velocity structure 1.5 spans downstream in the wake of a model typical of a large subsonic transport (Boeing 747). This flow field was modeled by a superposition of axisymmetric vortices with finite cores. The theoretical model was found to agree with the measured velocities everywhere except where two vortices were in close proximity. Vortex strengths derived from the span loading on the wing as predicted by vortex-lattice theory also agree with the present measurements. It was, therefore, concluded that the axisymmetric vortex model used herein is a useful tool for analytically investigating the vortex wakes of aircraft.

NOMENCLATURE

AR	aspect ratio, b^2/s
b	wingspan
$\underline{c}$	wing chord
$\bar{c}$	average chord, s/b
c_l	local lift coefficient, (dL/dy)/qc
C_L	total lift coefficient, L/qs
f	frequency
L	lift
q_∞	$\frac{1}{2}\rho V_\infty^2$
r	radius from center of vortex
S	wing area
U	streamwise velocity component, positive downstream
V	velocity
V_Θ	swirl velocity component
V_∞	free-stream velocity
W	vertical velocity component
x, y, z	coordinate axis: x (positive downstream), y (positive out right wing)
$\bar{x},\bar{y},\bar{z}$,	coordinate axis nondimensionalized by semispan, b/2
α	angle of attack
β	laser tilt angle to obtain directional sensitivity
Γ	circulation
$\bar{\Gamma}$	nondimensional circulation, Γ/bV_∞
λ	wavelength of light, $\lambda_B = 0.488\ \mu m$, $\lambda_G = 0.5145\ \mu m$
Θ	laser beam intersection angle
ρ	air density.

Subscripts

B	blue color channel of laser velocimeter
G	green color channel of laser velocimeter.

INTRODUCTION

Trailing vortex wakes of large aircraft are a hazard to smaller following aircraft. As a result, the separation distances during landing and take-off that must be imposed to maintain safety are now a determining factor in maximizing runway utilization [1]. Future increases in airport capacity are, therefore, limited by required separations between aircraft due to vortices. In recent years, NASA has conducted considerable research into reducing the wake of large aircraft by aerodynamic means [2]. As a result of this research, several techniques have been found to be effective in deintensifying the wake. One of these techniques is to configure the aircraft so that it sheds multiple vortices from the wing in such a way that these vortices interact and merge [3]. A particular configuration that employs this technique is the B747 airplane with the inboard trailing-edge flaps set to the landing position and the outboard trailing-edge flaps retracted [4]. Recent flow visualization studies conducted on various configurations of this aircraft have shown the trajectories of vortices in the wake [5]. The objective of the present study was to measure the velocity distributions in the wake and to determine the size and strength of each of the vortices. A second objective was to investigate the effect of the landing gear on the wake, because it had been found in flight and ground-based tests that, at downstream distances greater than about 30 spans, lowering the landing gear intensified the wake [6, 7].

In an earlier investigation using a rotating-arm hot-wire anemometer [8], the flow field was scanned rapidly along the arc of a circle that passed very near a vortex core. This technique was shown to be effective for the case of simple wakes where only a single vortex pair existed. When this technique was applied to a complex wake involving multiple vortices per side, difficulty was encountered in interpreting the measured results because insufficient data were available to adequately define the various wake vortices. In the present study, an improved technique for the case of complex wakes was used. The flow field was scanned rapidly in the lateral direction at successive vertical locations. Data were accumulated in the vicinity of each vortex to provide more information about the flow as compared to the rotating arm technique. Furthermore, the present measurements were made with a laser velocimeter, which assured that the measuring device did not interfere with the flow field.

The present paper presents the results (obtained by means of a scanning, two-dimensional laser velocimeter) of velocity surveys made in the Ames 7- by 10-Foot Wind Tunnel at 1.5 spans downstream from the generator model. The strengths of the various vortices in the wake were determined by use of a theoretical axisymmetric model for the swirl component of velocity for each vortex. Comparisons are shown between the measurements and this axisymmetric model. An earlier paper [9] describes the apparatus, instrumentation, and the signal processing technique, and shows some sample results from the present tests.

MODEL AND INSTRUMENTATION

The model that was used to generate the vortices was mounted inverted on a single strut at the forward end of the test section (see Figure 2 of reference 9). This mounting provided maximum downstream distance and minimum interference between the strut wake and the wing wake. Angle of attack was varied by adjusting the clevis pivot at the top of the strut. Details of the model, which was identical to that used in earlier studies [4], appear in Figure 1 and Table 1. Two configurations of trailing-edge flap were used in the

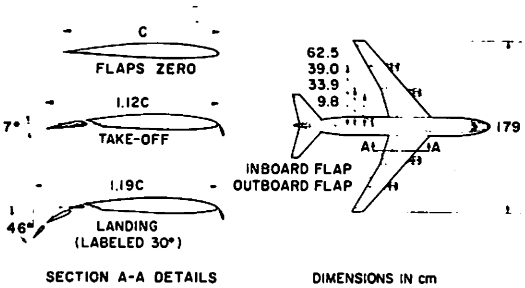

Figure 1. Geometric details of the B747 subsonic transport model.

Table 1. Model Dimensions, Wind-Tunnel and Test Conditions

Generator Model (Boeing 747)	
Wing	
Span, cm (in.)	179 (70.5)
Root incidence	±2°
Tip incidence	−2°
Area, m^2 (ft^2)	0.459 (4.94)
Average chord, cm (in.)	25.6 (10.1)
Aspect ratio	7
Horizontal stabilizer	0°
Wind-tunnel and Test conditions	
U_∞, m/s (ft/sec)	14 (46)
Reynolds number based on average chord	2.5×10^5
Lift coefficient	1.2
Angle of Attack	
Flaps 30°/0°	7°
Flaps 30°/30°	2°

present studies. In one configuration, both the inboard and outboard trailing-edge flaps were set to the landing setting (herein labeled 30°/30°). In the other configuration, the inboard flap deflection was the same, but the outboard flap was set to the zero setting (labeled 30°/0°). The wind-tunnel and test conditions also appear in Table 1.

The laser beams passed through the side window of the wind tunnel to the measuring point, which is indicated by the crossing of the beams (see Figure 2 of reference 9). The velocimeter was capable of scanning this measuring point laterally across the tunnel test section over about 2 m in 3 sec. Both the vertical and streamwise components of velocity were simultaneously measured by arranging an orthogonal array of cross beams in two colors that were available from the laser. Directional sensitivity was obtained by tilting the laser unit approximately 40° so that both laser channels included a free-stream velocity component and, therefore, did not change in velocity direction. The laser velocimeter is further described in references 9 and 10. Details of the signal processing technique used in the present tests are contained in reference 9. Lift coefficient data were obtained by measuring the lift with a strain-gauge balance and the dynamic pressure with a pitot-static tube.

DATA REDUCTION AND ANALYSIS

The measured modulation frequency of the scattered laser light and the laser cross-beam angle were converted to velocity by the following expressions. The velocity normal to the interference fringes is given by

$$V_B = \frac{f_B \lambda_B}{2\sin\theta/2} \text{ and } V_G = \frac{f_G \lambda_G}{2\sin\theta/2}\,, \qquad (1)$$

where subscripts B and G refer to the blue and green color channels, respectively, of the laser velocimeter. The laser cross-beam angle, Θ, which varied across the test section, was calibrated by measuring the beam spacing and the distance to the window of the wind tunnel from the focal point. The vertical and streamwise velocities are given by

$$U = V_B \sin\beta + V_G \cos\beta\,. \qquad (2)$$

$$W = V_B \cos\beta - V_G \sin\beta\,, \qquad (3)$$

where β is the laser tilt angle that was used to provide directional sensitivity. Samples of data records and a processed plot for the vertical and streamwise velocity appear in reference 9. The computed velocities were smoothed by removing obviously bad points which were due to frequency tracker dropout (see reference 9), and by locally least-square fairing the data to a polynominal. Figure 2 contains a typical smoothed data plot.

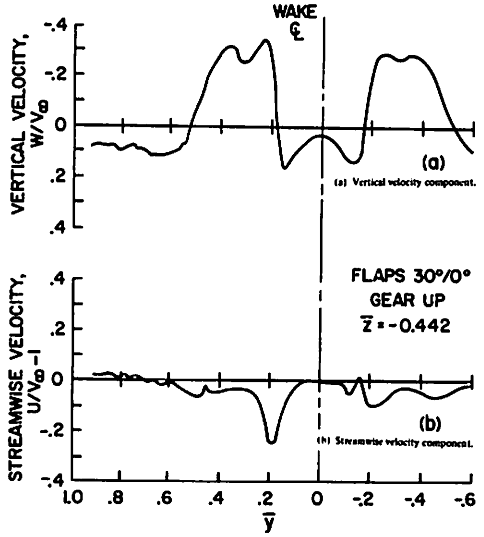

Figure 2. Example of laser velocimeter data after smoothing and replotting. Flaps 30°/0°, gear up, $\bar{z} = -0.442$.

Analysis.

The measured velocity flow field was modeled by superposition of axisymmetric vortices with finite cores. First, it was necessary to locate the centers of vorticity by locating an axial velocity defect coupled with swirl-like vertical velocity. (The location of the vortices for a particular configuration was approximately known from flow visualization (Figure 3 of reference 9) and from earlier flow visualization studies [5].) The first iteration for determining the strength of the vortices was made by using point vortices to match the velocities from the theoretical model with the measured velocities. The circulation distribution in the vicinity of each vortex center was then obtained by first subtracting the vertical component of velocity of all the other vortices in the wake along a horizontal line passing through the vortex center, and then computing the circulation of the unknown vortex from the following expression:

$$\Gamma = 2\pi r V_\theta , \tag{4}$$

where V_θ was set equal to the measured vertical velocity corrected for the induced velocity of all of the other vortices in the flow field.

RESULTS AND DISCUSSION

Effect of Landing Gear.

An investigation was made to measure the effect of the landing gear on the wake behind the 30°/0° configuration. The lateral distribution of the vertical velocity component is shown on Figure 3 for various lateral passes through the wake. These plots were made from smoothed data plots similar to the one shown on Figure 2. Comparison of the velocities between landing gear up and down for all of the vertical locations indicates that no significant effect of the landing gear is apparent. However, an investigation of the streamwise velocity component (not presented here) did indicate a streamwise velocity defect in the wake due to the landing gear. It was, therefore, concluded that the wake vertical velocities at 1.5 spans downstream are only slightly affected by the landing gear and that the reduced alleviation found in earlier investigations at over 30 spans downstream [6] does not manifest itself until further downstream than 1.5 spans.

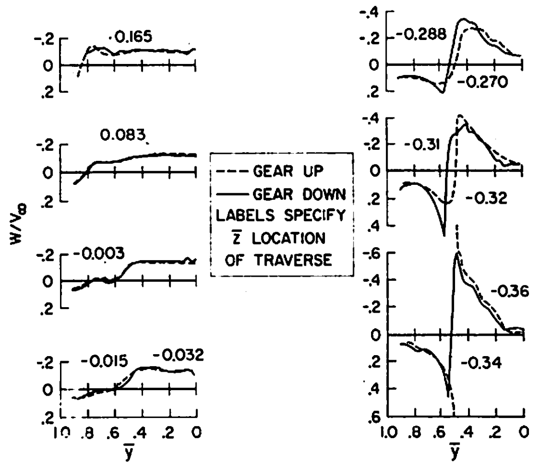

Figure 3. Effect of the landing gear on the variation of vertical velocity. Flaps 30°/0°.

Vortex Locations.

Vortices for the two configurations used in the present study are shed from each flap edge as well as the wing tip (Figure 4). Furthermore, there are vortices shed from the horizontal stabilizer (not shown). Downstream from the generator at distances greater than about 13 spans, the vortices merge into a single pair that is diffuse for the 30°/0° configuration and concentrated for the 30°/30° configuration. At 1.5 spans downstream, the various vortices have not yet completed their merge, so that as many as four and six vortices per side would be expected for the 30°/0° and 30°/30° configurations, respectively.

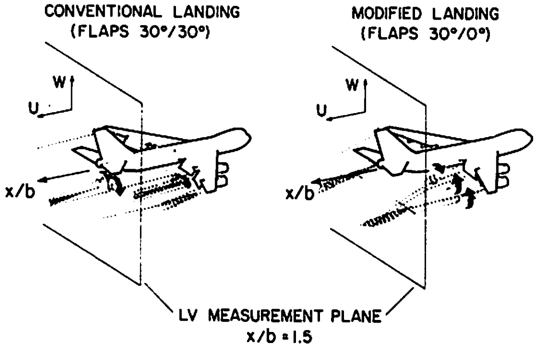

Figure 4. Summary of vortex trajectories from flow visualization studies.

The vortex locations were determined by matching the measured vertical and streamwise velocity components with the axial and rotational properties of vortices near their center; that is, when a lateral scan was made through a vortex center, a swirl-like vertical velocity component coupled with a defect in the streamwise velocity component would occur. As shown in Figure 5, for $\bar{z} = -0.38$, the horizontal scan went directly through the center of the flap outboard vortex. At a slightly greater distance below the wing lower surface ($\bar{z} = -0.44$), the scan went through the center of the vortex shed by the inboard edge of the flap. The presence of the nearby outboard flap vortex, however, also strongly affects the vertical velocity. Similarly, the wing-tip vortex was found above the wing upper surface ($\bar{z} = 0.17$). The streamwise velocity defect associated with each vortex occurs most prominently near the vortex center and helps to locate the various vortices at each vertical location.

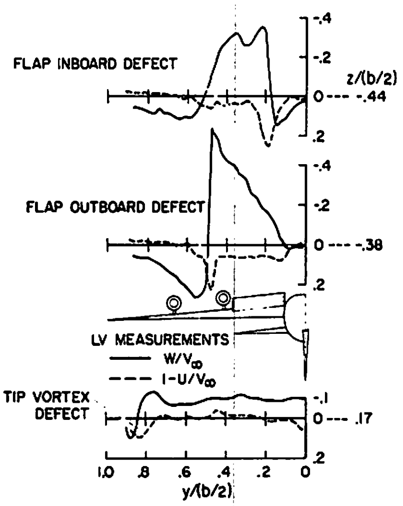

Figure 5. Variation of vertical and streamwise velocity distributions for lateral traverses through each vortex center. Flaps 30°/0°, gear up.

Circulation Distribution, 30°/0°.

The foregoing procedure was used to determine the distribution of vorticity within each vortex shed by the 30°/0° configuration. The vortex locations, strengths, and distributions of circulation are shown on Figures 6 and 7. When all four of the vortices in the wake are included in the theoretical model, good agreement is achieved with the measurements for a wide range of vertical locations. The sensitivity of the agreement between the wake model and the measured data was emphasized by the velocity field of the vortex from the horizontal tail (vortex 4 in Figure 6). The flow was first modeled by using only the three vortices from the wing, because the tail vortex was believed to be too weak to appreciably influence the wake structure. However, it was not until all four vortices were included in the model that the agreement in Figure 8 could be achieved (e.g., see Figure 8 for locations $\bar{z} = -0.408$ and -0.359). In some of the horizontal traverses, it was found that the agreement could be improved by using a slightly different value of $\bar{z}$ in the theoretical model (see Figure 8, $\bar{z} = -0.294$ and -0.246). This is the result of the slight meander of the vortices in the wind tunnel. Although each horizontal scan was made rapidly to avoid the effects of meander, the time between successive vertical locations was large and at nonuniform increments. However, since the meander at the 1.5-span downstream station for these tests was much less than reported for the considerably greater downstream distance used in earlier tests [8], a steady-state model could be deduced from the present test data.

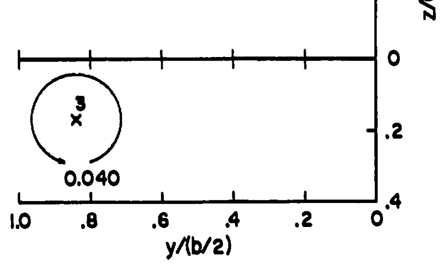

Figure 6. Vortex locations, strengths and regions of varying circulation resulting from analysis of measured velocity. Flaps 30°/0°, gear up.

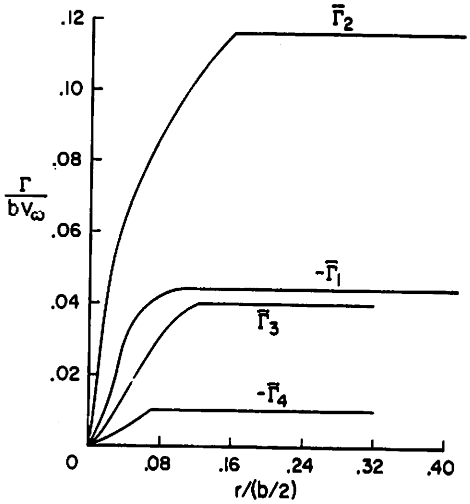

Figure 7. Circulation distributions resulting from analysis of measured velocity. Flaps 30°/0°, gear up.

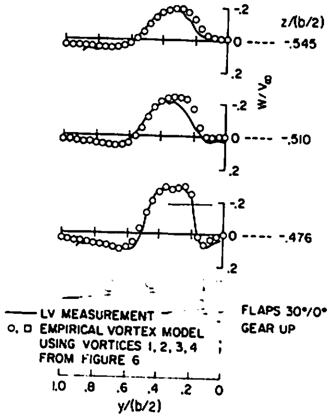

Figure 8. Comparison between measured vertical velocities and the axisymmetric vortex model using the vortices shown on Figures 6 and 7. Flaps 30°/0°, gear up.

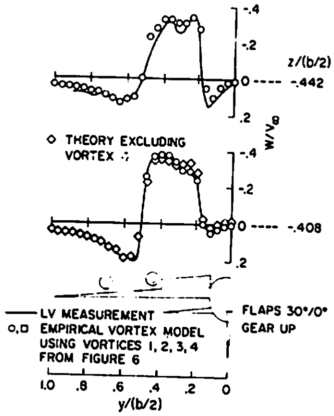

Figure 8. Continued.

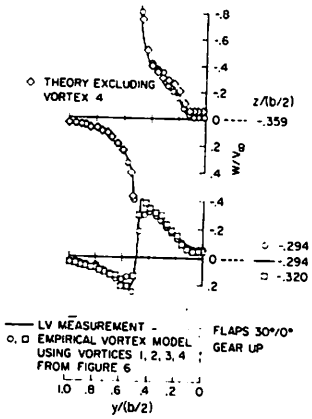

Figure 8. Continued.

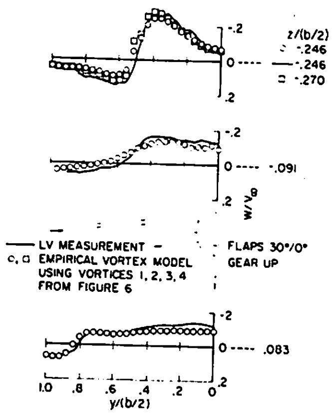

Figure 8. Continued.

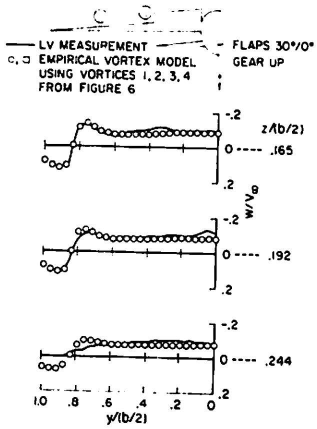

Figure 8. Concluded.

Circulation distributions, 30°/30°.

Figure 9 shows the region of significant measured streamwise velocity defect along with the measured locations of the vortices. The theoretical vortex strengths and distributions are presented in Figures 10 and 11. A much more complex wake than the 30°/0° configuration, containing six vortices per side, was found. The strengths and distributions of circulation were fairly easy to obtain for the 30°/0° configuration. However, for the 30°/30° configuration, the analysis became quite tedious because of the large number of closely-spaced vortices. The analysis could be expedited for this type of configuration by simultaneously evaluating (with a least-square curve-fit procedure) all of the vortex strengths. Once again, good agreement between the theoretical model and the measurements was found everywhere except for a consistent trend to underpredict for $\bar{y}$ greater than 0.8 (Figure 12). Vortices 3 and 5 are overlapping in this region (Figure 10). Modeling the flow as the sum of axisymmetric vortices appears to be inadequate in the overlap regions. Also, the $\bar{\Gamma}$ vs $\bar{r}$ distribution was found to be similar for all of the vortices analyzed except vortex 5 (Figure 11). The unusual shape of this curve may be the result of using an axisymmetric model for vortices undergoing a merger process. Computations of the details of vortex merging [3] indicate that the interactions of closely-spaced vortices can lead to highly noncircular shapes; this finding tends to confirm the foregoing conjecture.

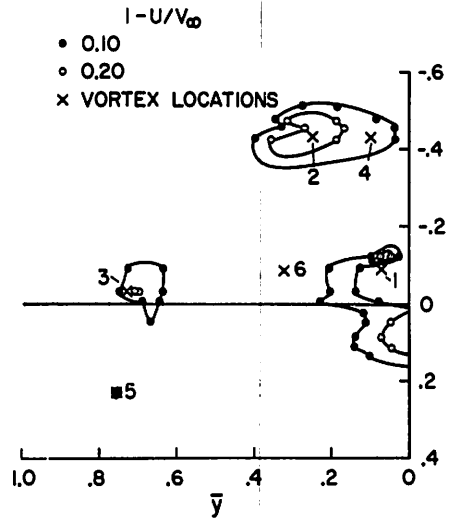

Figure 9. Regions of significant streamwise velocity defect and the locations of the vortices from the analysis of measured velocities. Flaps 30°/30°, gear up.

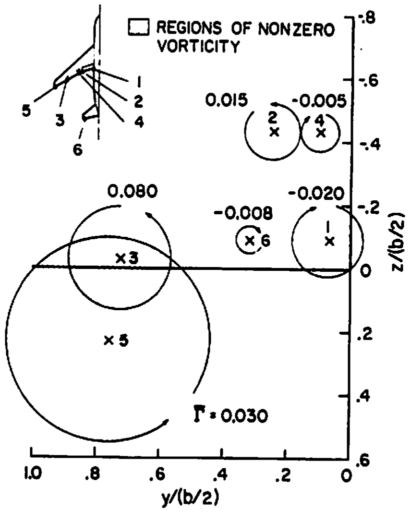

Figure 10. Vortex locations, strengths, and regions of varying circulation resulting from analysis of measured velocities. Flaps 30°/30°, gear up.

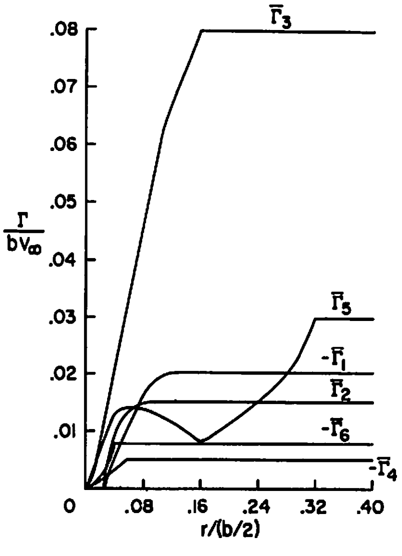

Figure 11. Circulation distributions resulting from analysis of measured velocities. Flaps 30°/30°, gear up.

Comparison with Vortex-Lattice Theory.

The strengths of the wing vortices were estimated from a span loading which was calculated by use of a vortex-lattice theory

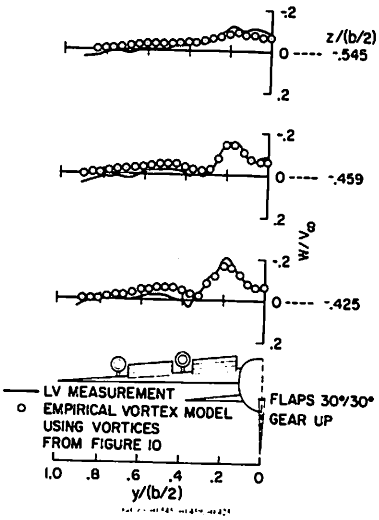

Figure 12. Comparison of maximum vortex circulation from vortex lattice theory and the axisymmetric model for the measured velocities. Gear up.

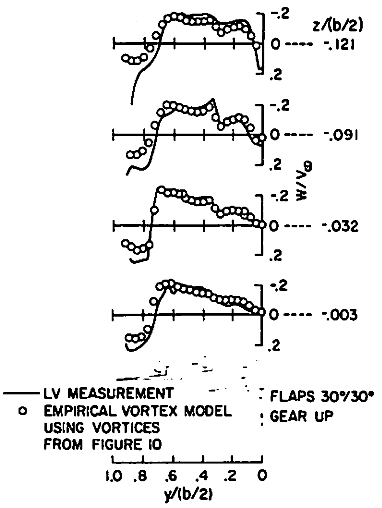

Figure 12. Continued.

developed by Hough [11]. The way in which the span loading for the two configurations is divided to determine the strengths of the vortices from the wing is indicated in Figure 13 (vortex numbers correspond to the numbers used on Figures 6 and 10). The vortex strength is related to the span loading by

$$\bar{\Gamma} = \frac{C_L}{2AR} \frac{c_\ell c}{C_L \bar{c}} . \tag{5}$$

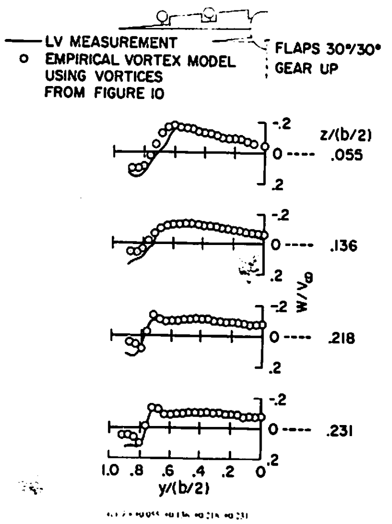

Figure 12. Continued.

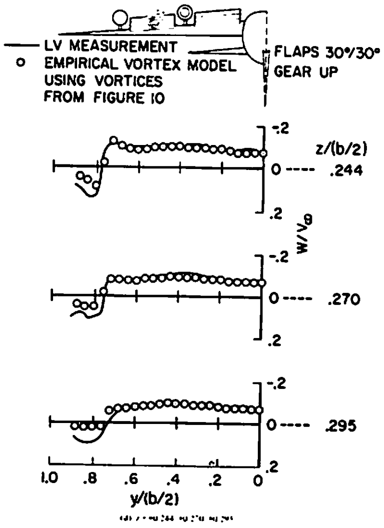

Figure 12. Concluded.

The dividing point between vortices 2 and 3 (Figure 13a) was obtained from the inflection point on the span loading as recommended by Rossow [12]. As can be seen, the comparison between the vortex-lattice theory and the experiment is excellent for vortices 2 and 3. It is believed that the measured strength of vortex 1 is lower than the theory because the vortex-lattice theory ignores the effect of the fuselage on the span loading. Apparently, the lift carry-over across the fuselage in the experiment leads to a weaker flap-inboard vortex than predicted by the theory for the wing alone. An adjusted span loading that takes into account the measured strength of the vortices is shown as a dashed curve in Figure 13.

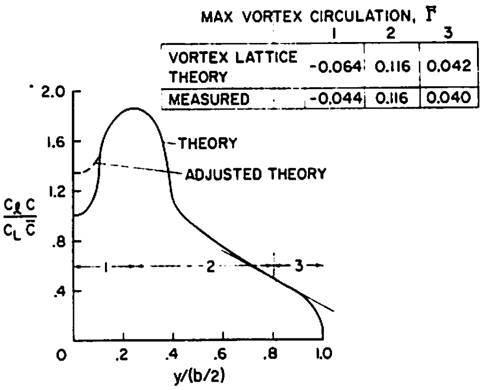
MAX VORTEX CIRCULATION, $\bar{\Gamma}$

	1	2	3
VORTEX LATTICE THEORY	-0.064	0.116	0.042
MEASURED	-0.044	0.116	0.040

Figure 13. Comparison of maximum vortex circulation from vortex lattice theory and the axisymmetric model for the measured velocities. Gear up.

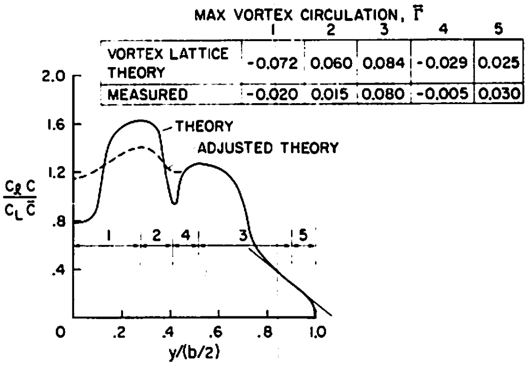
MAX VORTEX CIRCULATION, $\bar{\Gamma}$

	1	2	3	4	5
VORTEX LATTICE THEORY	-0.072	0.060	0.084	-0.029	0.025
MEASURED	-0.020	0.015	0.080	-0.005	0.030

Figure 13. Concluded.

With the 30°/30° configuration (Figure 13b), good agreement was found for the outboard vortices (3 and 5). Exact agreement would be achieved by moving the dividing point from $\bar{y}$ = 0.90 to 0.94; however, as discussed above, there is some uncertainty in the measured strengths of these vortices because of the axisymmetric model. The measurements indicate lower lift on the inboard flap and, as before, better lift carry-over across the fuselage when compared with the vortex-lattice theory for the wing alone.

SUMMARY AND CONCLUSIONS

Presented herein is a technique for experimentally analyzing complex aircraft wakes. First, extensive measurements were made of two components of velocity in a plane downstream of the wake generating model. These vortex wakes were then modeled by a superposition of axisymmetric vortices with finite cores. Good agreement was achieved between the analytical model and the measured velocities everywhere except where the vortices were in close proximity to each other. It is believed that the use of axisymmetric vortices to model the wake is inappropriate when vortices are about to merge. Finally, estimates of vortex strengths made from the span loadings calculated by vortex-lattice theory were also in good agreement with the present measurements in those regions where vortex-lattice theory would be expected to be valid. Therefore, it can be concluded that the superposition of axisymmetric vortices is a useful model for analyzing multiple vortex wakes. Although the analysis procedure was successfully completed for both configurations used in the present study, it was quite tedious for the configuration that contained six vortices per side. The analysis could be expedited by developing a least-square procedure to simultaneously evaluate all of the vortices.

Measurements made to determine the effect of the landing gear on the 30°/0° configuration indicated no significant effect on the vertical-velocity distribution. Additional velocity measurements at greater downstream distance than used in the present tests will be required to analyze the effect of the landing gear.

REFERENCES

1. Gessow, A., "Aircraft Wake Turbulence Minimization by Aerodynamic Means," 6th Conference on Aerospace and Aeronautical Meteorology, El Paso, Texas, Nov. 12-14, 1974.

2. NASA Symposium on Wake Vortex Minimization, NASA SP-409, Feb. 25-26, 1976.

3. Rossow, V.J., "Convective Merging of Vortex Cores in Lift-Generated Wakes," AIAA Paper 76-415, 9th Fluid and Plasma Dynamics Conference, San Diego, CA, July 14-16, 1976.

4. Corsiglia, V.R., Rossow, V.J., and Ciffone, D.L., "Experimental Study of the Effect of Span Loading on Aircraft Wakes," NASA TMX-62,431, May 1975, Ames Research Center, Moffett Field, CA.

5. Ciffone, D.L. and Lonzo, C., Jr., "Flow Visualization of Vortex Interactions in Multiple Vortex Wakes Behind Aircraft," NASA TM X-62, 459, June 1975, Ames Research Center, Moffett Field, CA.

6. Corsiglia, V.R. and Dunham, R.E., "Aircraft Wake-Vortex Minimization by Use of Flaps," in NASA Symposium on Wake Vortex Minimization, NASA SP-409, Feb. 1976, p. 303-336.

7. Barber, M.R., Gatlin, D.H., Hastings, E.C., Jr., and Tymczyszyn, J.J.; "Vortex Attenuator Flight Experiments," in NASA Symposium on Wake Vortex Minimization, NASA SP-409, Feb. 1976, p. 338ff.

8. Corsiglia, V.R., Schwind, R.G., and Chigier, N.A., "Rapid-Scanning Three-Dimensional, Hot-Wire Anemometer Surveys of Wing-Tip Vortices," *J. Aircraft*, Vol. 10, no. 12, Dec. 1973, p. 752-757.

9. Orloff, K.L., Corsiglia, V.R., Biggers, J.C., and Ekstedt, T.W., "Investigating Complex Aerodynamic Flows with a Laser Velocimeter, the Accuracy of Flow Measurements by Laser Doppler Methods," Proceedings of the LDA-Symposium, Copenhagen, 1975. P. O. Box 70, DK-2740 Skovlunde, Denmark, pp. 624-643. (See also NASA TM X-73, 171, Sep. 1976.)

10. Grant, G.R. and Orloff, K.L., "A Two-Color, Dual Beam Backscatter Laser Doppler Velocimeter," NASA TM X-62,254, Mar. 1973, Ames Research Center, Moffett Field, CA.

11. Hough, G., "Remarks on Vortex-Lattice Methods," *J. Aircraft*, Vol. 10, no. 5, May 1973, p. 314-317.

12. Rossow, V.J., "On the Inviscid Rolled-Up Structure of Lift Generated Vortices," *J. Aircraft*, Vol. 10, no. 11, Nov. 1973, p. 647-650.

ROLL UP OF A VORTEX SHEET USING THE "CLOUD-IN-CELL" TECHNIQUE

GREGORY R. BAKER
Applied Mathematics
California Institute of Technology
Pasadena CA 91125

ABSTRACT: The problem of the roll up of a two dimensional vortex sheet generated by a wing in an ideal fluid is phrased in terms of the streamfunction and the vortex sheet strength. A numerical method is used to calculate the time evolution of the vortex sheet by adapting the "Cloud-In-Cell" technique introduced in solving many particle simulations in plasma physics. Two cases are considered for the initial distribution of circulation, one corresponding to an elliptically loaded wing and the other simulating the wing with a flap deployed. Results indicate that small scale behavior plays an important part in the roll up. Typically, the small scale perturbations evolve into ever increasing larger structures by vortex amalgamation. Conclusions are given from a number of tests exploring the validity of the method. Briefly, small scale perturbations are introduced artificially by the grid, but the emerging large scale behavior is relatively insensitive to it. Since clearly defined structures result from the application of this method, it promises to aid considerably in understanding the behavior of vortex wakes.

INTRODUCTION

When a wing of finite span moves at a small angle of attack through the air, it sheds vorticity at its trailing edge which results from the flow of air around the wing tip, driven by the pressure difference between the top and bottom surfaces of the wing. If the speed of the wing is constant and the effect of the viscosity of the air is negligible, vortex lines starting from the trailing edge form a steady surface relative to the wing, which is sharply defined and represents a vortex sheet.

The intractable problem of determining the location of this three dimensional steady vortex sheet is simplified by considering the sheet two-dimensional and unsteady through the relation $z = Ut$ (see Figure 1). This assumption ignores the curvature of the vortex lines and their termination at the trailing edge, and the relation $z = Ut$ assumes there is no variation of the velocity parallel to the z axis. This proves reasonable when sufficiently far downstream of the wing, and Moore and Saffman [1] have provided formal justification. The variation of the vortex sheet strength shed at the trailing edge of the wing depends on the characteristics of the wing and becomes the initial condition for the unsteady two dimensional modelling of the flow. This paper examines two cases of initial vortex sheet strength; one relates to an elliptically loaded wing and the other simulates a wing with a flap deployed.

Before introducing the method, it is instructive to recall previous attempts at solving the model problem. For the elliptically loaded wing, the vortex sheet strength and consequently the velocity is initially infinite at the wing tip. The subsequent motion is the formation of a spiral at the wing tip, and the

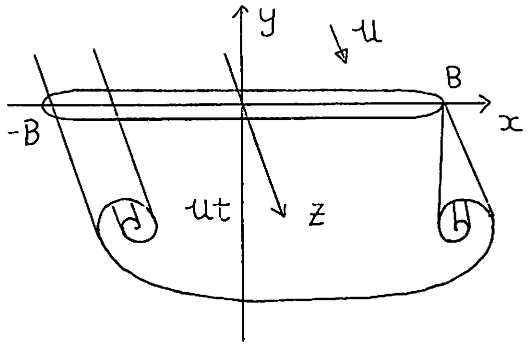

Figure 1. The geometries for the three-dimensional steady flow and two-dimensional unsteady motion.

arclength along the sheet becomes infinite so that the singular nature of the initial flow is removed. Kaden [2] has presented the leading term of an asymptotic expansion describing the spiral and, more recently, more terms have been calculated by Moore [3] and Guiraud and Zeytounian [4]. However, the asymptotic expansion contains unknown parameters which are determined by the flow outside the spiral. In particular, the location of the spiral center is unknown. Thus, a numerical procedure is required to fully determine the motion.

Rosenhead [5] and Westwater [6] were the first to approach this problem numerically. They replaced the vortex sheet by a finite collection of line or point vortices and considered their subsequent motion as marking out the vortex sheet. With the advent of high speed computers, a number of researchers [7-10] have continued this approach but an unsatisfactory feature of the results has consistently emerged. The motion of the point vortices becomes chaotic in the region of the spiral. Different ad hoc modifications have been incorporated in an attempt to regularise the solution. Kuwahara and Takami [11] and Chorin and Bernard [12] introduced different modifications to the velocity field of a point vortex but in a way which is not consistent with the equations of motion. A finite number of point vortices cannot adequately resolve the details of a spiral especially at its center. Moore [13] has addressed this aspect of the numerical calculation by incorporating an amalgamation process at the wing-tip vortex. When the curvature at the nearest point vortex to the wing-tip vortex becomes large enough, the two vortices are combined into one. His spiral appears smooth for greater times than other calculations and more closely resembles the asymptotic nature as found in reference 2.

Unfortunately there has not yet been an adequate accounting of the errors introduced by these modifications. Fink and Soh [14] have pointed out that calculating the velocity at points on the sheet by considering them point vortices is not a good approximation unless the points are evenly spaced in arclength. Consequently, they proposed a method which introduces evenly spaced points at each time level so that the velocity of the vortex sheet will be more accurately determined. When applied to the roll up of the sheet behind an elliptically loaded wing, they obtain results very similar to reference 13. In fact, the redefinition of points in their method results in circulation accumulating at the point near the spiral center and this has a correspondence with the technique of reference 13.

Baker [15] has extended their work by taking some account of the curvature of the sheet when calculating its velocity, resulting in a higher order of accuracy. He applied the refined method to the sheet shed by a ring wing because there is no singularity associated with a wing tip. This provides a definite test of the method. An error analysis shows that, as the number of points increases, the error in calculating the velocity of the vortex sheet (note, not of the point vortices) should decrease. This is not the behavior observed. At a fixed time during the initial roll up, increasing the number of points results in the vortex sheet crossing itself. No consistent solution emerges; the problem appears ill-posed. Clements and Maul [16] also report a failure of the method used in reference 14.

If we are to find reliable numerical procedures, we need to understand the cause of the breakdown commonly obtained. There are several possibilities as follows. The stability of the vortex sheet is generally uncertain. The plane, constant sheet has a known instability, the Kelvin Helmholtz Instability [17], where the modes with the smallest wavelength grow the fastest. However, the effects of curvature and stretching of the sheet may be stabilizing [18]. If the sheet is unstable, the numerical method will reflect this in the growth of round-off errors. In this case, the relevant problem is understanding the nonlinear development of the instability, and this requires a minimum number of points to resolve the important modes. Alternatively, the numerical methods may be unstable independent of the stability of the sheet. The accurate calculation of the vortex sheet motion in the spiral region may require many points because of the close spacing between the turns and their large curvature.

Many of these questions can be explored by increasing the number of points substantially. Adopting a different procedure in calculating the vortex sheet velocity will also increase the breadth of inquiry and give useful information about the basic nature of its motion. This is also desirable for matters of economy. The computer time required to calculate the velocity of N point vortices is $O(N^2)$ and soon becomes expensive for large N. Adapting the "Cloud-in-Cell" technique ensures the calculation of the motion of many vorticity markers at reasonable cost. The purpose of the paper is to describe the method and to discuss the results obtained when applied to the roll up behind an elliptically loaded wing and behind a wing with a flap deployed. The conclusions from several tests to examine the accuracy and reliability of the method are also given.

The technique has already been applied to a number of two dimensional ideal fluid flows [19, 20]. These applications have yielded interesting results, in particular the behaviour of the interaction of finite-sized vortex structures. The primary concern of this paper is the motion of vortex sheets and as far as known by the author, the technique has not been applied and studied in this case.

THE METHOD

Reference 19 was the first to report the use of the "Cloud-in-Cell" technique in studying the motion of a two dimensional, incompressible, inviscid and homogeneous fluid. This paper follows a similar approach and the details are as follows.

If ψ is the streamfunction, ω the vorticity, and u, v the velocity components, the equations of motion are,

$$\nabla^2\psi = -\omega , \tag{1}$$

$$u = \frac{\partial\psi}{\partial y} , \tag{2a}$$

$$v = -\frac{\partial\psi}{\partial x} , \tag{2b}$$

$$\frac{\partial\omega}{\partial t} + u\frac{\partial\omega}{\partial x} + v\frac{\partial\omega}{\partial y} = 0. \tag{3}$$

The vorticity is discretised by introducing N markers,

$$\omega = \sum_{n=1}^{N} \Gamma_n \delta(x - x_n)\delta(y - y_n) , \tag{4}$$

such that

$$\sum_{n=1}^{N} \Gamma_n = \int \omega dA . \tag{5}$$

This reduces Equation (3) to a set of ordinary differential equations,

$$\frac{dx_n}{dt} = u(x_n, y_n) , \tag{6a}$$

$$\frac{dy_n}{dt} = v(x_n, y_n) . \tag{6b}$$

To obtain the streamfunction, a finite-difference approximation is made to Equation (1) on a rectangular grid, $\{x_0 + (i - 1)H_x, y_0 + (j - 1)H_y\}$, $1 \leq j \leq N_y$, where H_x, H_y is the grid spacing assumed uniform in the x, y directions, respectively.

$$\left(\psi_{i+1,j} - 2\psi_{i,j} + \psi_{i-1,j}\right)\Big/H_x^2 + \left(\psi_{i,j+1} - 2\psi_{i,j} + \psi_{i,j-1}\right)\Big/H_y^2 = -\omega_{i,j} , \tag{7}$$

for

$$2 \leq i \leq N_x - 1, \; 2 \leq j \leq N_y - 1.$$

The vorticity is represented at the points (x_n, y_n) and so a redistribution scheme, known as "Cloud in Cell" or area-weighting, is introduced to assign values at the grid points and then Equation (7) can be solved. Figure 2 provides the geometry and notation of the redistribution scheme,

$$\omega(k) = A_k\Gamma_n/H_xH_y , \tag{8}$$

where the A's are the areas shown. The scheme conserves total vorticity and the hydrodynamic impulse.

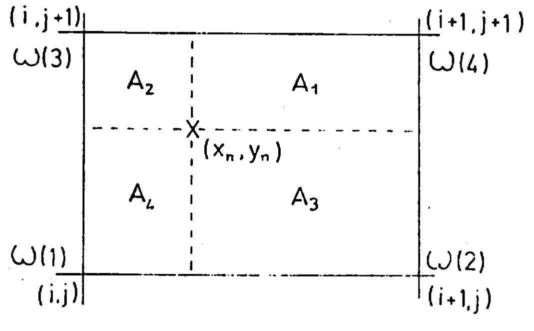

Figure 2. The geometry and notation of the "Cloud in Cell" redistribution scheme.

Equation (7) is easily solved using a Fast Poisson Solver (the optimum FACR(e) method [21]). To determine the velocity of the markers, we calculate the velocity at the nearest four grid points with a central difference formula,

$$u_{i,j} = (\psi_{i,j+1} - \psi_{i,j-1})/2H_y , \tag{9a}$$

$$v_{i,j} = -(\psi_{i+1,j} - \psi_{i-1,j})/2H_x , \tag{9b}$$

and then interpolate bilinearly.

$$u_n = (\sum_{k=1}^{4} u(k)A_k)H_xH_y . \tag{10}$$

The notation of Figure 2 has been followed in Equation (10). The markers are moved forward in time by a finite-difference approximation to Equation (6).

$$x_n(t + \Delta t) = x_n(t) + u_n\Delta t , \tag{11a}$$

$$y_n(t + \Delta t) = y_n(t) + v_n\Delta t , \tag{11b}$$

Where Δt, the time step, must satisfy the Courant-Friedrichs-Levy condition

$$\Delta t < \underset{n}{\mathrm{Min}}\left(\frac{H_x}{u_n}, \frac{H_y}{v_n}\right). \tag{12}$$

In this way, the vorticity distribution at t + Δt has been computed and the procedure repeats to give the motion of the vorticity.

Boundary conditions must be given at the grid edge for a unique solution. The author used a particular Fast Poisson Solver which requires the value of ψ along the boundaries and this may be accomplished in several ways. The author's choice is to calculate local centroids of vorticity over a sufficiently large number of markers and to consider them as point vortices to determine the velocity at the boundaries. Maskew [22] indicates that the resulting error is small provided that the point of velocity determination is at least a distance H away from the nearest vortex point, where H is the maximum distance between adjacent local centroids. The number of local centroids must be judiciously chosen since there is a balance between accuracy and the computer time involved in calculating the velocity at the boundary. As the number of local centroids increases, the accuracy improves but the computer time increases as the square of the number. To off-set some of the computer time, the velocity is calculated at a selected number of grid points at the boundary and the rest of the values are obtained by interpolation using cubic splines [23]. Fixing the number of local centroids, the accuracy can be optimised by choosing the boundary locations a distance H from any vortex marker. This means that the smallest possible grid is placed over the region of interest while keeping the errors at the boundaries reasonably small. The appropriate component of velocity is integrated numerically around the boundary to provide the streamfunction. Since it is singlevalued, it must return to its starting value after a complete circuit around the boundary and this provides a check on the numerical accuracy.

When the flow has a plane of symmetry, a boundary can be chosen along this plane. Special attention must be paid at any intersections of this boundary and the vortex sheet. Large errors can occur arising from the inadequate approximation to the velocity field from the local centroid corresponding to the points nearest the intersection. Following the ideas in reference 22, the local centroid can be ignored and the original markers considered as point vortices to calculate the velocity at a grid point on the boundary whenever the grid point is less than H away from the intersection.

For most of the results presented here, a 129 × 129 grid was used with 2000 vorticity markers, each corresponding to the same constant circulation. There is no reason numerically why the markers should have the same circulation. It merely aids in assessing the vorticity distribution by considering plots of their locations. On an IBM 370/158 computer, it takes 3.8 seconds to update the vorticity distribution; 1.7 seconds of this is spent in solving Poisson's equation, and the rest in calculating its boundary conditions using 40 local centroids and updating the marker's positions.

It is natural to ask which aspect of the procedure limits the accuracy of the numerical solution. Since a vortex sheet is smeared over a region of the order of a cell area, the grid spacing is expected to play an important role. In fact, Langdon [24] presents an analysis of grid effects in calculating the velocity and shows that this is the case. The author has conducted several tests on particular vortex sheets where the velocity field is known analytically at a fixed time. The errors in calculating the velocity depend on the grid spacing. Typically, the calculated sheet velocity resembles the exact velocity, superimposed with a small random component whose wavelength is of the order of the grid spacing. The behavior is most likely a result of the bilinear interpolation used when computing the velocity at the vortex markers. However, it is the growth of the errors in the position of the sheet that is important and analysis in reference 24 does not fully address this aspect of the numerics.

A number of authors [24-27] have explored the errors arising in the "Cloud in Cell" and related methods when applied to the flow of particles in a plasma. They are concerned with the accuracy of the representation of the Columbic force law between charged particles and have shown how the force is modified by the different redistribution techniques. Their particles have a physical reality. Vortex markers, on the other hand, are a result of a numerical discretisation. In other words, whereas the motion of charged particles is the underlying structure to the continuum equations in plasma physics, point vortices are only a numerical representation of continuous vorticity distributions. The main question is how well does the "Cloud-in-Cell" method approximate the motion of continuous vorticity distributions. At present, analysis does not answer this question, and the best approach is to test the method on flows where some information is available.

The author has conducted several tests, the details of which will be reported elsewhere. Before discussing the conclusions of the tests, it is useful to see the results of applying the method to the roll up of vortex sheets generated behind a wing.

FIRST APPLICATION

The vortex sheet lies initially along $-B < x < B$, $y = 0$ and has a strength related to the circulation shed at the trailing edge. For an elliptically loaded wing, the circulation is

$$\Gamma(x) = -2V_0 B\left(1 - (x/B)^2\right)^{\frac{1}{2}}, \qquad (13)$$

where V_0 is the initial downwash velocity. Non-dimensional variables are introduced by scaling distances with B, time with B/V_0, and the circulation with V_0B. Equation (13) reads

$$\Gamma(x) = -2\left(1 - x^2\right)^{\frac{1}{2}}. \qquad (14)$$

The results are shown as a series of vorticity distributions at different time levels in Figure 3. The number of points used is 2000 with each representing the same amount of circulation, but only half are plotted for practical purposes. The grid size is 129 × 129.

The most striking features are the emergence of small scale structure and the smoothing of the spiral core. The large scale structure stays well defined, even though small scale structures developed outside the spiral region are convected into it and absorbed. This behaviour is pleasingly similar to some experimental observations [28], but it is important to understand the generation of the small scale structures.

Figure 3. Vorticity distributions for the rollup behind an elliptically loaded wing at different times.

Several tests conducted by the author indicate that for scales much larger than the grid cell, the flow is accurately computed. The grid introduces scales of the order of the grid spacing, but in an interesting way. Figure 4 shows a vortex sheet intersecting grid lines. The cells in which redistribution takes place are shaded. The smooth vortex sheet is replaced by a jagged array of cells, and it is at the places marked A and B, for instance, that the biggest perturbation to the sheet occurs due to the anisotropic redistribution process. The distance AB is the dominant small scale introduced by the grid while other small scales remain essentially suppressed. By that it is meant that structures are formed along the sheet at places such as A and B, which initially resemble small spirals, and there are relatively smooth sections of the sheet between them. This effect of the grid has been seen before in reference 19 but in a less obvious way and reported merely as an anomalous instability. Increasing the number of vortex markers beyond an average of two per cell, influences the results merely by increased detail of description and does not change the basic behaviour.

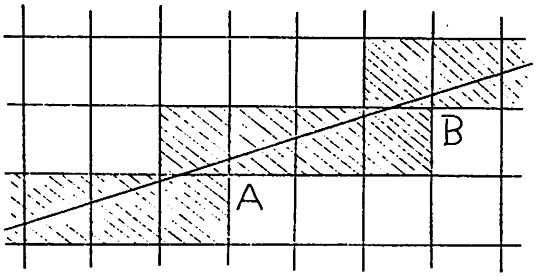

Figure 4. Cells affected in redistribution process.

As indicated in Figure 3, the small scale structures amalgamate, leading to larger sized structures. The question arises to what extent, if any, the emergence of small scale structures, albeit initially created artificially by the grid, and the subsequent amalgamation simulate a physical process. Despite some experimental evidence [29, 30], it is not yet safe to assume the method achieves this in a realistic way.

As a check on the accuracy of the method, two invariants of the motion are monitored during the calculation. One is the spanwise component of the hydrodynamic impulse and its computed value has a relative error of 10^{-4}. The Kirchhoff-Routh path function is the other, but the computed value varies slowly with time. Since it proves too expensive to calculate this function for the complete collection of vorticity markers, only local centroids are used. Tests indicate that the error decreases when more points are included. Although the computed function is approximate, its slow variation suggests reasonable invariance.

The fraction of vorticity rolled up is also calculated using a definition given in reference 13; that is, the fraction of markers with

$n \geqslant N$ where N is determined from $x_N = \max x_n$, and increasing n counts markers along the sheet towards the core center. This fraction is shown in Figure 5 as a function of time. Initially the behaviour follows the similarity solution in reference 2 and agrees well with the results in reference 13. Thus the gross features obtained by point vortices are reproduced. The slight oscillation observed is due to the convection of small structures around and into the rollup region.

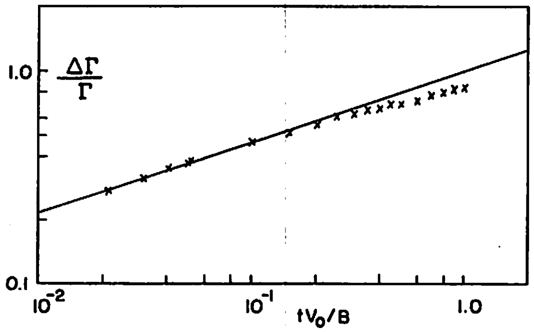

Figure 5. Fraction of circulation in the rollup region as a function of time. Slope of straight line is from Kaden's similarity solution.

Another aspect of the results is presented in the velocity profiles shown in Figure 6. They are spanwise scans through the core center of the vertical velocity component and are a measure of the tangential velocity around the core. The times chosen correspond to two of the four time levels in Figure 3. Turns of the spiral and small scale structure at the core edge are evident by double peaks. The inner region resembles solid-body rotation and this is consistent with radial profiles of the vorticity measured from the core center. A dissipative process related to small scale motion has smoothed the spiral center and, as discussed previously, it is unclear whether this is due to a physical process or merely the numerical method.

The maximum difference in the vertical velocity at a fixed time is a measure of the evolution of the vortex structure. Its time

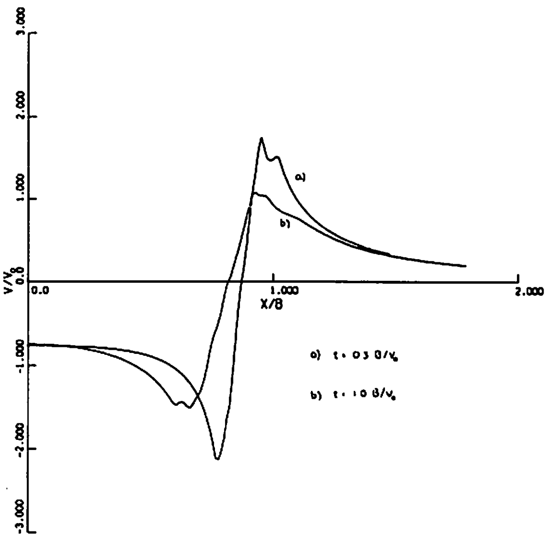

Figure 6. Vertical velocity profiles in the spanwise direction through the core center.

dependence is shown in Figure 7, where double points indicate the presence of double peaks. The behavior is very close to a decay as $t^{-1/4}$, predicted in reference 1 for a vortex structure with a viscous core matched to an outer flow specified by the similarity solution of reference 2. Moreover, the viscous core has solid-body rotation at its center. This interesting parallel in behavior of the results with the work in reference 1 deserves attention. We emphasize that the "Cloud-in-Cell" technique has produced a well defined rolled-up structure unlike the behavior of typical point vortex calculations.

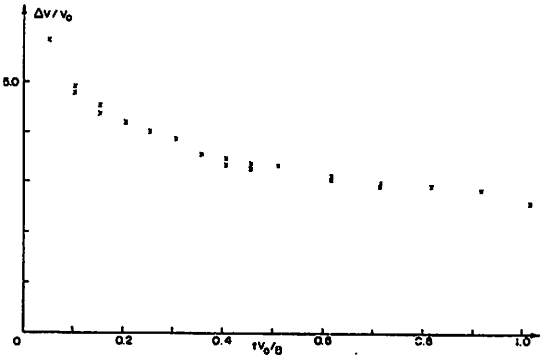

Figure 7. Maximum vertical velocity difference when scanning along spanwise direction through the core center, as a function of time.

SECOND APPLICATION

The second application of the method shows an interesting difference in the roll up of different parts of the vortex sheet. An initial circulation distribution is chosen as shown in Figure 8 by matching three sections so that the circulation and its derivative are continuous. For $0 \leq x \leq A$,

$$\Gamma(x) = \Gamma_0 + \frac{3}{A^2}(\Gamma_1 - \Gamma_0)x^2 - \frac{2}{A^3}(\Gamma_1 - \Gamma_0)x^3 , \quad (15a)$$

where Γ_1 is the maximum circulation. For $A \leq x \leq B$,

$$\Gamma(x) = ax^3 + bx^2 + cx + d , \quad (15b)$$

where $a = -2[\Gamma_1 - (1 - B^2)^{1/2}]/(A - B)^3 - B/[(1 - B^2)^{1/2}(A - B)^2]$, $b = B/[2(1 - B^2)^{1/2}(A - B)] - 3A(A + B)/2$, $c = -3aA^2 - 2bA$, and $d = \Gamma_1 - aA^3 - bA^2 - cA$. For $B \leq x \leq 1$, elliptical loading is assumed, and

$$\Gamma(x) = (1 - x^2)^{\frac{1}{2}} . \quad (15c)$$

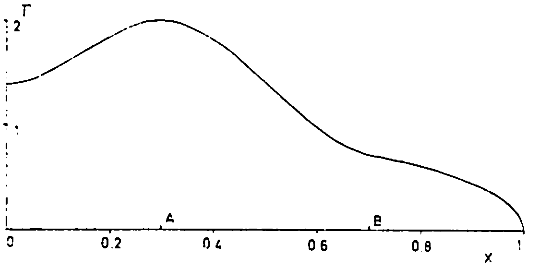

Figure 8. **Profile of circulation along trailing edge for a wing with flap deployed.**

This profile simulates the effect of a flap deployed and the influence of the fuselage near $x = 0$. Roughly speaking, the fuselage influences the region $0 < x < A$, the outboard edge of the flap influences the region $A < x < B$, and the wing tip influences the region $B < x < 1$. The values chosen for the constants are $A = 0.3$, $B = 0.7$, $\Gamma_0 = 1.4$, and $\Gamma_1 = 2.0$, where the units are arbitrary since the interest is to demonstrate the feasibility of the method rather than to obtain precise results. For this configuration three vortex structures are observed to develop, and Donaldson et al. [31] has proposed a criterion which determines which part of the initial vortex sheet is later rolled up into these structures. His criterion corresponds to the regions defined by Equation (15).

Figure 9 gives the vorticity distribution as time progresses and indeed three structures emerge. The grid is 129 × 129 and the total number of points, again with equal circulation, is 1950: 450 for the fuselage region, 964 for the flap region, and 536 for the tip region. Only half the points are plotted and they are marked in different symbols for each region. The results show that the points A and B are the appropriate demarcation of the initial circulation profile as proposed in reference 31.

Unlike the tip vortex, the fuselage and flap vortices emerge by an amalgamation process more reminiscent of the process in a mixing layer than the formation of a spiral. However, the final structures have a form similar to the tip vortex. Since the initial development of the small scales is grid dependent, an important test of the results is to

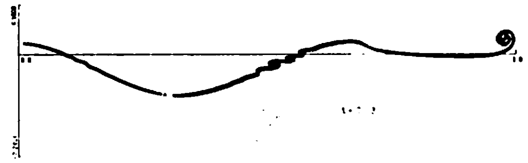

Figure 9. **Vorticity distribution for the roll up behind a wing with a flap deployed at different time levels.**

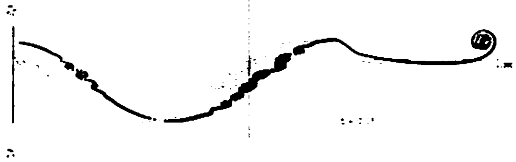

Figure 9. Continued.

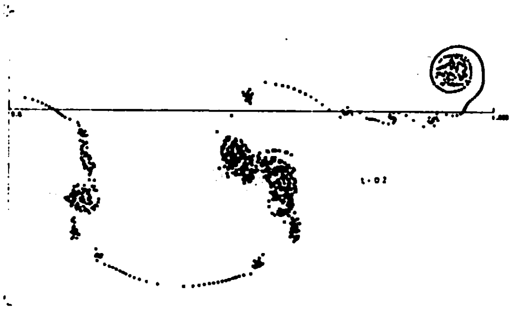

Figure 9. Continued.

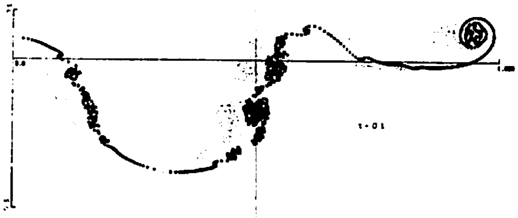

Figure 9. Continued.

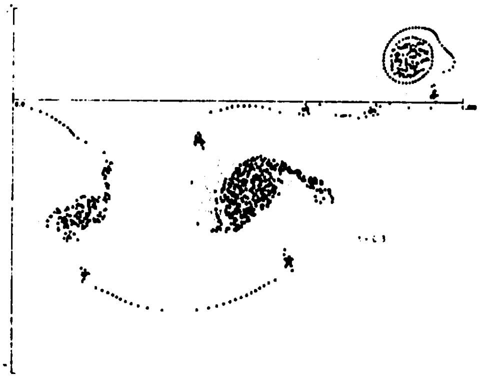

Figure 9. Continued.

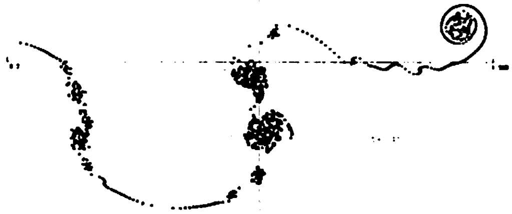

Figure 9. Continued.

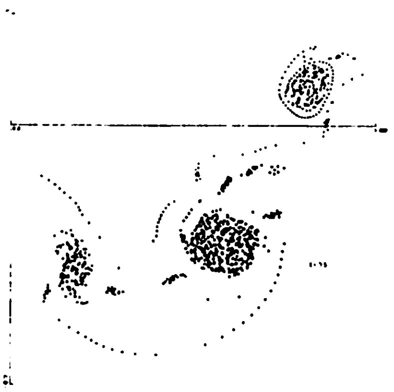

Figure 9. Concluded.

repeat the calculation with a finer grid. Figure 10 shows the result for a 257 × 257 grid at the same times as Figures 9a and 9c. Although the initial small scale structures are different and occur at an earlier time, the emerging large scale structure has remarkable similarity. Even the amalgamation appears reproduced. This illustrates the result found in independent testing: namely, that large-scale motion is accurately computed.

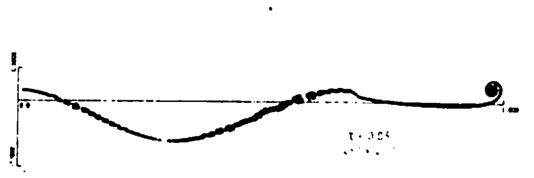

Figure 10. Vorticity distribution for the roll up behind a wing with a flap deployed at different time levels using a refined mesh.

Figure 10. Concluded.

Finally, a comment is in order about the behavior of the angular momentum for both flows considered in this paper. The angular momentum for the region $x > 0$ is not an invariant of the motion. Milinazzo and Saffman [32] have shown that the angular momentum is reliably calculated by the "Cloud-in-Cell" technique. For an elliptically loaded wing, the angular momentum about the centroid increases by 35% at $t = 1.0$ when the roll up is almost completed (fraction of rolled-up vorticity is 85%). This indicates a limitation to the Betz approximation [33]. For the case of a wing with a flap deployed, the angular momentum about the centroids of each region is shown in Figure 11. It is in sharp disagreement with the extension of the Betz approximation in reference 31 and indicates a better understanding for the case of the roll up with more than just a tip vortex may be required. Of course the dissipative process involved in the method will influence the angular momentum and that should be borne in mind when comparing with inviscid estimates.

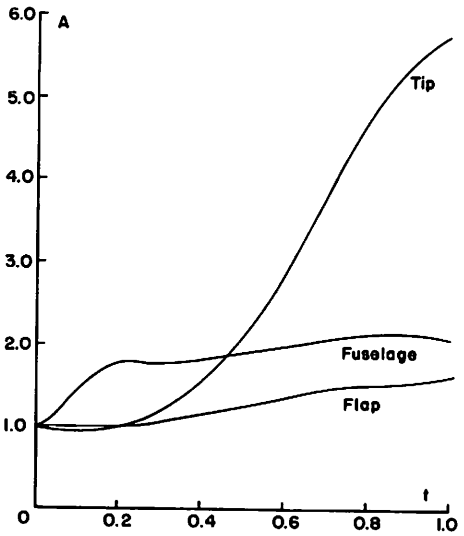

Figure 11. Angular momentum. A, normalised by its initial value for the three vortex structures as a function of time.

CONCLUSION

The "Cloud-in-Cell" technique produces interesting results for the motion of vortex sheets. Although small scale structure is introduced into the sheet by the grid, the resulting large scale motion appears relatively insensitive to its presence. The amalgamation process by which small scale structures evolve into larger structures is an interesting phenomenon requiring further study. Indications are that there is some dissipative process at work in the method and more study is needed to understand this aspect of the results.

ACKNOWLEDGMENTS

I wish to thank Professor Philip G. Saffman for many helpful discussions and Professor Bengt Fornberg for assistance with computer programming. This work was supported by N.S.F. Grant ENG-74-00124.

REFERENCES

1. Moore, D.W. and Saffman, P.G., "Axial Flow in Laminar Trailing Vortices," *Proc. Roy. Soc.*, Vol. A333, 1973, p. 491-508.

2. Kaden, H., "Aufwicklung Einer Unstabilen Unstetigkeitsflache," *Ing. Archiv.*, Vol. 2, 1931, p. 140. (English transl. R.A.E. Library Trans. no. 403.).

3. Moore, D.W., "The Rolling Up of a Semi-infinite Vortex Sheet," *Proc. Roy. Soc.*, Vol. A345, 1975, p. 417-430.

4. Guiraud, J.P. and Zeytounian, R.Kh., "A Double Scale Investigation of the Asymptotic Structure of Rolled Up Vortex Sheets," to appear in *J. Fluid Mechanics* (1977).

5. Rosenhead, L., "Formation of Vortices from a Surface of Discontinuity," *Proc. Roy. Soc.*, Vol. A134, 1931, p. 170-192.

6. Westwater, F.L., "Rolling Up of the Surface of Discontinuity Behind an Aerofoil of Finite Span," Aero. Res. Counc. R & M. no. 1962, Aug. 1935.

7. Birkhoff, G.D. and Fisher, J., "Do Vortex Sheets Roll Up?" Rc. Circ. Mat. Palermo Sec 2, Vol. 8, 1959, p. 77-90.

8. Takami, H., "Numerical Experiment with Discrete Vortex Approximation, with Reference to the Rolling Up of a Vortex Sheet," Dept. Aero. and Astronaut., Stanford Univ., Rep. SUDAER 202, 1964.

9. Moore, D.W., "The Discrete Vortex Approximation of a Vortex Sheet," California Institute of Tech., Pasadena, CA., Rep. AFOSR-1084-69, 1971.

10. Clements, R.R. and Maull, D.J., "The Rolling Up of a Trailing Vortex Sheet," *J. Roy. Aeronaut. Soc.*, Vol. 77, 1973, p. 46-51.

11. Kuwahara, K. and Takami, H., "Numerical Studies of Two-Dimensional Vortex Motion by a System of Point Vortices," *J. Phys. Soc. Japan*, Vol. 34, 1973, p. 247-253.

12. Chorin, A.J. and Bernard, P.S., "Discretization of a Vortex Sheet, with an Example of a Roll Up," Dept. of Engng., Univ. Calif., Berkeley, CA., Rep. FM-72-5, 1972.

13. Moore, D.W., "A Numerical Study of the Roll Up of a Finite Vortex Sheet," *J. Fluid Mech.*, Vol. 63, 1974, p. 225-235.

14. Fink, P.T. and Soh, W.K., "Calculation of Vortex Sheets in Unsteady Flow and Applications in Ship Hydrodynamics," Tenth Symp. Naval Hydrodynamics, Cambridge, MA., 1974.

15. Baker, G.R., "Studies in Vortex Motion," Ph.D. Thesis, 1976, Applied Math. Dept., Calif. Inst. of Tech., Pasadena, CA.

16. Clements, R.R. and Maull, D.J., "The Representation of Sheets of Vorticity by Discrete Vortices," *Prog. Aerospace Sci.*, Vol. 16, 1975, p. 129-146.

17. Batchelor, G.K., *An Introduction to Fluid Dynamics*, Cambridge Univ. Press, England, 1970, p. 511-517.

18. Moore, D.W., Personal Communication.

19. Christiansen, J.P., "Numerical Simulation of Hydrodynamics by the Method of Point Vortices," *J. Comp. Physics.*, Vol. 13, 1973, p. 363-379.

20. Christiansen, J.P. and Zabusky, N.J., "Instability, Coalescence and Fission of Finite-Area Vortex Structures," *J. Fluid Mechanics*, Vol. 61, 1973, p. 219-243.

21. Hockney, R.W., "The Potential Calculation and Some Applications," *Methods of Computational Physics*, Vol. 9, Eds. Alder, B., Fernbach, S. and Rotenberg, M., Academic Press, NY, NY, 1970.

22. Maskew, B., "Subvortex Technique for the Close Approach to a Discretised Vortex Sheet," *J. Aircraft*, Vol. 14, Feb. 1977, p. 188-193.

23. Hamming, R.W., *Numerical Methods for Scientists and Engineers*, 2nd Ed., McGraw-Hill, New York, NY, 1973, p. 349-352.

24. Langdon, A.B., "Effects of the Spatial Grid in

Simulation Plasmas," *J. Comp. Physics*, Vol. 6, 1970, p. 247-267.

25. Birdsall, C.K. and Fuss, D., "Clouds-in-Clouds, Clouds-in-Cells, Physics for Many-Body Plasma Simulation," *J. Comp. Physics*, Vol. 3, 1969, p. 494-511.

26. Eastwood, J.W., "Optimal Particle-Mesh Algorithms," *J. Comp. Physics*, Vol. 18, 1975, p. 1-20.

27. Eastwood, J.W. and Hockney, R.W., "Shaping the Force Law in Two-Dimensional Particle-Mesh Models," *J. Comp. Physics*, Vol. 16, 1974, p. 342-359.

28. Pierce, D., "Photographic Evidence of the Formation and Growth of Vorticity Behind Plates Accelerated from Rest in Still Air," *J. Fluid Mech.*, Vol. 11, p. 460-471.

29. Brown, G.L. and Roshko, A., "On Density Effects and Large Structure in Turbulent Mixing Layers," *J. Fluid Mech.*, Vol. 64, 1974, p. 775-816.

30. Winant, C.D. and Brownand, F.K.; "Vortex Pairing; the Mechanism of Turbulent Mixing Layer Growth at Moderate Reynolds Number," *J. Fluid Mech.*, Vol. 63, 1974, p. 237-255.

31. Donaldson, C.duP., Snedeker, R.S., and Sullivan, R.D., "Calculation of Aircraft Wake Velocity Profiles and Comparison with Experimental Measurements," *J. Aircraft*, Vol. 11, 1974, p. 547-555.

32. Milinazzo, F. and Saffman, P.G., "The Calculation of Large Reynolds Number Two-Dimensional Flow using Discrete Vortices with Random Walk," to appear in *J. Comp. Physics* (1977).

33. Betz, A., "Behavior of Vortex Systems," TM 713, June 1933, NACA.

ON THE OPERATION OF AIRCRAFT IN THE WAKES OF OTHER AIRCRAFT

GUY G. WILLIAMSON, RICHARD S. SNEDEKER, AND COLEMAN duP. DONALDSON
Aeronautical Research Associates of Princeton, Inc.,
Princeton, NJ 08540

ABSTRACT: The study explores the possible benefits of the operation of one aircraft in the wake of another through utilization of the energy contained in the wake vortices.

INTRODUCTION

Aircraft wake studies have generally dealt with the hazard problem and methods of its alleviation. As a result of such studies, considerable progress has been made in recent years in the understanding of wakes, their formation, and dissipation. Less attention has been given, however, to the problem of intentional flight in or near a wake, or to the possibilities of the beneficial utilization of wake energy.

The object of this paper is to describe some preliminary studies of aircraft operation in the wakes of other aircraft. Interest in this problem has arisen in the light of several types of operation in which wake encounter is not only likely but may be intentional. Three such types come to mind: (1) the use of probe aircraft in wake penetration tests for the purpose of determining aerodynamic, structural, and pilot response during an encounter; (2) the problem of possible wake encounter during mid-air refueling; and (3) the possibility of wake riding or convoy formation flight as a means of wake energy utilization and consequent fuel conservation. All of these types of operation involve consideration of the following: (a) intentional flight and maneuvering in close proximity to wake vortices, (b) actual penetration of the vortices, and (c) the imposition of possibly severe structural and control demands on the penetrating aircraft.

Our interest in these types of problems has centered on an investigation of the possibilities of wake riding as a means of wake energy utilization for certain tactical military operations. Specifically, we have determined how a relatively benign wake upwash flowfield can be produced that may be suitable for riding, and we have studied some of the stability and control problems of the riding aircraft.

WAKE RIDING

By "wake riding" we mean the flight of one aircraft in that portion of the wake of another where the upwash flowfield is of sufficient strength, steadiness, and extent to permit flight with a reduced power requirement. Two possible modes of wake riding are illustrated in Figure 1. In the first (a), a single generating aircraft produces a wake which is utilized by one or two riders located in the outboard upwash regions of the vortices. In the second (b), a single aircraft rides in the upwash common to the adjacent vortices of two generating aircraft flying at a constant lateral separation.

The wake riders in the first mode may be considered in two ways. They may either be small, special purpose vehicles which are carried externally for reasons of deployment and mobility, or they may simply be other aircraft of the same type as the generator,

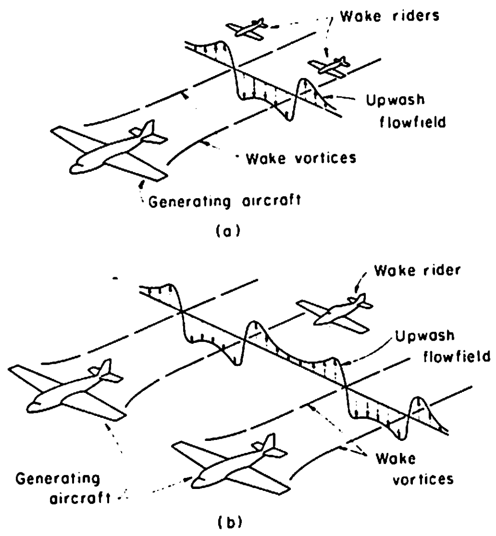

Figure 1. Two modes of wake riding.

flying in formation on a long-range cargo or ferry mission. It is recognized that an important consideration for both arrangements is that of overall power requirement and utilization. That is, with regard to the first arrangement, is it really more efficient in terms of total power required to carry riders in a wake, or is it better to join them to the original aircraft and compensate for their added weight by increasing the aspect ratio of the generating aircraft, thereby reducing its induced drag? The answer to this question obviously involves consideration of the aerodynamic design of both generator and riders, and of what the tactical operating conditions may be for both. For example, if it were necessary for both to fly at the same lift coefficient as well as the same speed, then the wing loadings would also have to match. Under these conditions the mass density of a small rider might be prohibitively high. On the other hand, is it really necessary for both to fly at the same lift coefficient? Clearly, overall power or energy utilization is an important aspect of any type of formation flight, but it is not discussed in detail in this paper. We will assume that wake riding of the type illustrated in Figure 1(a) can be justified in terms of the separate operational capability of the riders.

In the second arrangement of this mode — the long-range cargo mission — it appears that wake riding formation flight does have some advantages in terms of reduced overall power requirement. In their analysis of the formation flight of birds, for example, Lissaman and Shollenberger [1] show that considerable power savings can accrue through reduction in the power needed to overcome induced drag for birds flying in the familiar "vee" formation. They show, for an assumed elliptical spanwise load distribution, that there is an optimum geometry for such a formation in terms of wing-tip spacing and the degree of stagger. The power saving is shown to increase with the number of birds in formation, and it requires that the velocity of the group be lower than that of a single bird if both fly at maximum L/D.

The second mode of wake riding, illustrated in Figure 1(b), appears to be attractive because the upwash flowfield may be inherently more stable with respect to the rider than that of the first mode. Thus it may be useful not only for ferrying operations but as a "safe" test configuration for the sutdy of wake riding and the response to vortex encounter.

Aside from the considerations of overall power requirements, the most important aspects of wake riding which must be assessed are the production of an upwash flowfield that is suitable for riding, the aerodynamic requirements of both the generating aircraft and the rider, and the stability and control problems associated with "station keeping" by the rider. Each of these aspects will now be explored.

THE WAKE FLOWFIELD

For the purposes of wake flowfield calculations, we will use the method first proposed by Betz [2] and later refined by Donaldson [3] and others [4, 5, 6]. This method, which relates the tangential velocities of inviscid wake vortices to the spanwise load distribution on the generating wing, has been shown to give quite accurate results when compared to full-scale [7, 8] and wind-tunnel [9] measurements.

In order to arrive at an upwash flowfield that is desirable for wake riding, we will apply the method to several spanwise load distributions. We also note an important result of the Betz approach, that is that the tangential velocity at the center of a tip vortex is

$$V(0) = \frac{1}{\pi}\left(\frac{\partial\Gamma}{\partial y}\right)_{tip} . \qquad (1)$$

From this result it is clear that an inviscid vortex need not have a highly peaked velocity profile at the center as has often been assumed.

We now consider wings having the four spanwise loads shown in Figure 2. The loads we have chosen are: (a) the elliptic load; (b) a load which falls off linearly at the tip but is constant over 40% of the span (we refer to this as a 60% linear load); (c) an 80% linear loading; and (d) a triangular loading (or a 100% linear load). In Figures 3 through 6 these loads are shown in terms of the nondimensional bound circulation $\Gamma/(W/\rho Ub)$ as a function of $y/(b/2)$, where W is the weight of the aircraft in question. Note that as the load becomes more centered, the centerline bound circulation must increase so the moment of the shed circulation remains constant — all other quantities being held constant. Also shown in Figures 3 through 6 are the distributions of upwash velocity w on a line through the vortex centers. These velocities are plotted in the nondimensional form $w/(W/\rho Ub^2)$ versus $y/(b/2)$ for each vortex separately. It will be noted that as the percentage of linear loading is increased the maximum velocities achieved in the wake decrease, even though Γ_0 increases and even though the induced drags increase significantly. In Table 1 we summarize some of the results of calculations for the four loadings just considered.

Table 1. Characteristics of Elliptically and Linearly Loaded Wings

Loading	$\frac{\Gamma_0}{W/\rho Ub}$	$\frac{V_{max}}{W/\rho Ub}$	$\frac{\Gamma_0}{\Gamma_{0_e}}$	$\frac{C_{D_i}}{C_{D_{ie}}}$
elliptic	1.27	∞	1.0	1.0
60% linear	1.43	1.52	1.12	1.1
80% linear	1.67	1.33	1.31	1.3
100% linear	2.00	1.28	1.57	1.6

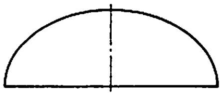
(a) elliptical load

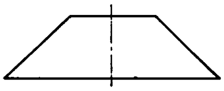
(b) 60% linear load

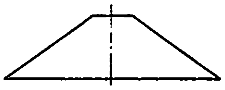
(c) 80% linear load

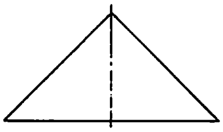
(d) 100% linear load

Figure 2. Four simple spanwise load distributions.

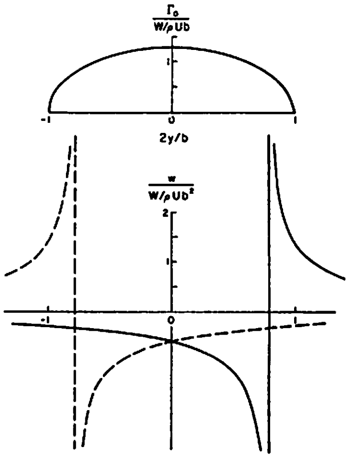

Figure 3. Elliptical load distribution.

Figure 4 figure:

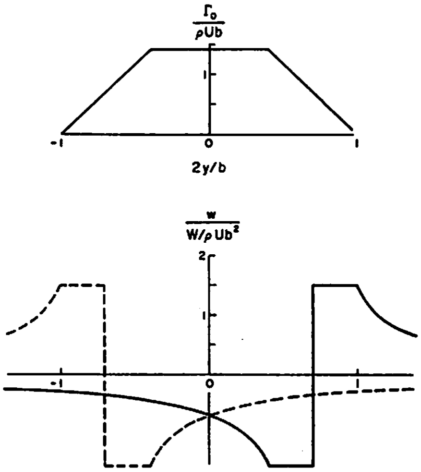

Figure 4. 60% linear load distribution.

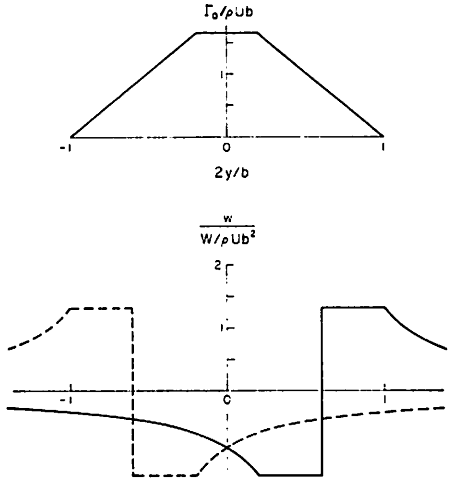

Figure 5. 80% linear load distribution.

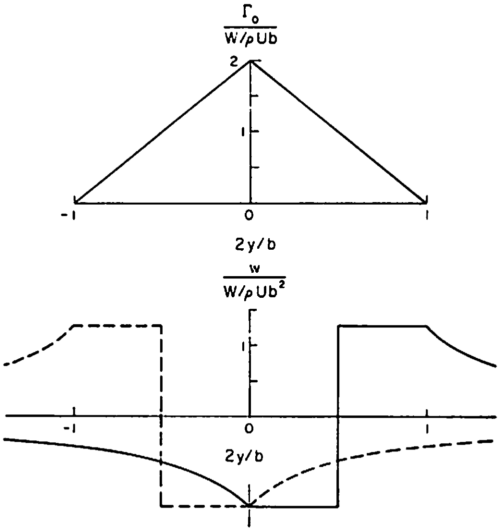

Figure 6. 100% linear load distribution.

What can be learned from Figures 3 through 6 and Table 1? First, we see that by going to linearly loaded wing tips, one can achieve upwash distributions outboard of the vortex center that are reasonably flat and might therefore provide a suitable flowfield for wake riding. Second, we see that the induced drag penalty is not bad (10%) for a wing that has a 60% linear loading. Thus, one might consider the design of a wake rider for a wing with such a load distribution. If it were desired to match the span of such a wake rider to the flat portion of the upwash distribution, the span would be 15% of the span of the generating aircraft.

In the next section of this paper we will consider the requirements for powerless flight in such a wake. First, however, we should assure ourselves that actual aircraft that are reasonably efficient exist with approximately linear loading and that the uniform upwashes discussed do in fact exist behind such aircraft.

In Figure 7 we show the span load distributions for the DC-10 transport aircraft. It is clear from these curves that, except for a possible region of high $\partial\Gamma/\partial y$ near the tip, the span loading for this aircraft in its clean configuration is almost linear for lift coefficients C_L between 0.2 and 0.4. We might, therefore, expect a region of uniform upwash to exist outboard of the vortex center. In Figure 8 we show the confirmation of this expectation. In this figure we have plotted the tangential velocity in the vicinity of the vortex core as measured by the FAA using hot-wire anemometry during tower fly-by tests of the DC-10 aircraft [8]. For this particular test, the airplane was flown at a lift coefficient of 0.28. Also plotted on Figure 8 is a solid curve showing the velocities that might be expected by the simple theory we have discussed here using a load distribution extrapolated from the data shown in Figure 7 for the actual test lift coefficient. It would appear from these data that one can indeed produce, with reasonably efficient aircraft, wakes with characteristics that might be used for wake riding.

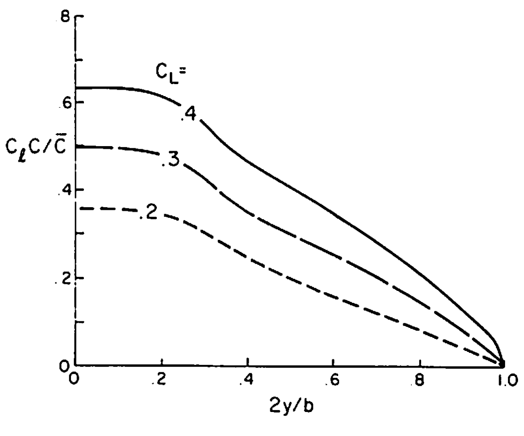

Figure 7. Calculated spanwise load distributions for the DC-10 transport aircraft (reference 8).

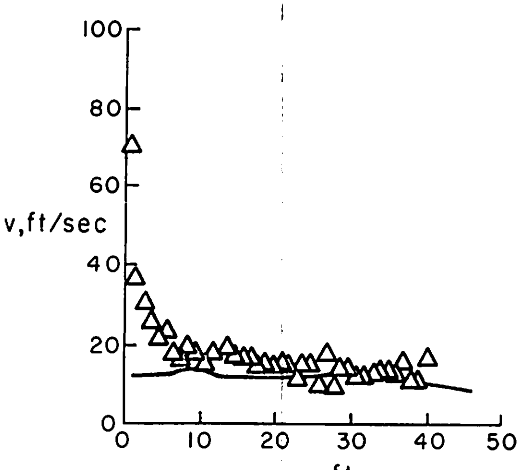

Figure 8. Tangential velocity in the tip vortex of a DC-10 transport aircraft as measured by the FAA (reference 8) in tower fly-by tests ($C_L = 0.28$, vortex age — 26.4 seconds).

REQUIREMENTS FOR WAKE RIDING

In this section we will discuss some of the aerodynamic requirements of wake riding in terms of a single generating aircraft and a pair of small riders or flyers, such as those shown in Figure 1(a). The idealized arrangement for this scheme is shown in Figure 9.

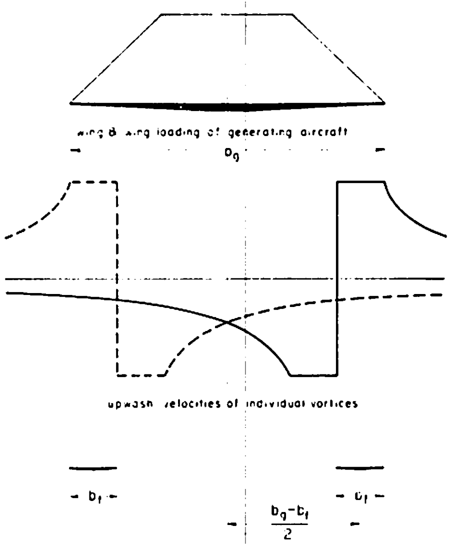

Figure 9. Positions of idealized wake flyers of span b_f located in upwash region of linearly loaded wing of span b_g.

We will first review the well-known formulas for calculating lift-drag ratio, L/D, and the conditions required for optimum L/D.

If an aircraft has a drag polar which is given by

$$C_D = C_{D_o} + \frac{C_L^2}{\pi eA}, \tag{2}$$

where C_{D_o} is the parasite drag coefficient, e is the aircraft efficiency factor, and A is the aspect ratio, then that aircraft will achieve optimum L/D when half the power of the aircraft is used to overcome C_{D_o} and half to overcome the induced drag $C_L^2/\pi eA$. Thus, at optimum L/D, half the power supplied by the engines of the aircraft is used to create the large organized wake vortex motions that were discussed in the previous section. The lift coefficient for optimum L/D is found to be

$$C_{L_{opt}} = \sqrt{C_{D_o} e\pi A}, \tag{3}$$

and the L/D achieved at this optimum C_L is

$$\left(\frac{L}{D}\right)_{opt} = \frac{1}{2}\sqrt{\frac{e\pi A}{C_{D_o}}}. \tag{4}$$

The optimum dynamic pressure q at which to fly is given by

$$q_{opt} = \frac{\frac{W}{S}}{\sqrt{C_{D_o} e\pi A}} \tag{5}$$

where S is the reference wing area on which the coefficients C_L and C_D are based.

One other formula is useful. If one does not fly at optimum dynamic pressure or at the optimum velocity for a given altitude, then the L/D that is achieved is given by

$$\frac{\frac{L}{D}}{\left(\frac{L}{D}\right)_{opt}} = \frac{2}{\left(\frac{U}{U_{opt}}\right)^2 + \left(\frac{U_{opt}}{U}\right)^2}. \tag{6}$$

The behavior of $(L/D)/(L/D)_{opt}$ as a function of U/U_{opt} is given in Figure 10. It is clear from this figure why one seldom flies at the speed required for optimum L/D. For example, if one flies 20% faster than U_{opt}, a penalty of only 6% in L/D is incurred.

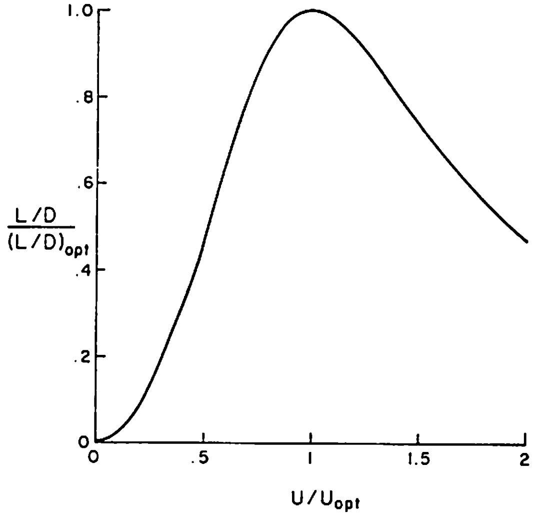

Figure 10. Behavior of L/D when not flying at optimum speed.

To complete our analysis we must derive an expression for the power required for level steady flight at velocity U in an upwash of velocity w compared to that required if no upwash were present. Figure 11 shows the forces and velocities acting on a flyer for such conditions. The thrust in this case is a result of the forward tipping of the lift vector, a situation made possible by the presence of the upwash w. The net longitudinal force is given by

$$F = D \cos\alpha - L \sin\alpha ,$$

for small α, $\cos \alpha \approx 1$ and $\sin \alpha = w/U$, so that

$$F = D - L\frac{w}{U} ,$$

or, in terms of power required $P = UF$,

$$\frac{P}{P_o} = 1 - \frac{L}{D}\frac{w}{U} , \tag{7}$$

where P_o is the power required to overcome drag when no upwash is present.

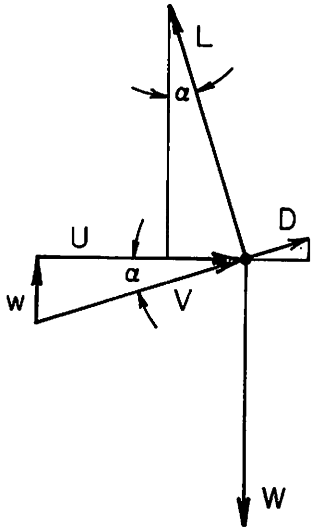

Figure 11. Forces and velocities for a wake flyer in the presence of an upwash w.

Let us now return to Figure 9 and compute the minimum upwash in the vicinity of the wake-flyer wing of span b_f. The center of this wing is located at $y = (b_g - b_f)/2$. We assume the wing is "designed" for the flyer; that is, the linear part of the tip load extends for a distance $2b_f$. Then the upwash velocity due to the near vortex in the vicinity of the flyer is given by

$$w_1 = \frac{1}{\pi}\frac{\partial\Gamma}{\partial y} = \frac{(\Gamma_o)_g}{2\pi b_f} \tag{8}$$

The upwash velocity due to the far vortex is negative. Taking its contribution at the centerline of the flyer ($y = (b_g - b_f)/2$) we have

$$w_2 = \frac{(\Gamma_o)_g}{2\pi(b_g - 2b_f)} , \tag{9}$$

In these equations, the subscript g refers to the wake generating aircraft and the subscript f refers to the wake flyer. The net upwash at the flyer wing is then

$$w = \frac{(\Gamma_o)_g}{2\pi}\left(\frac{1}{b_f} - \frac{1}{b_g - 2b_f}\right). \tag{10}$$

The requirement for powerless flight from Equation (7) is

$$\left(\frac{D}{L}\right)_f = \frac{w}{U} = \frac{(\Gamma_0)_g}{2\pi U}\left(\frac{1}{b_f} - \frac{1}{b_g - 2b_f}\right). \quad (11)$$

Now the bound circulation at the center of the generating aircraft is given by

$$W_g = \rho U(\Gamma_0)_g(b_g - 2b_f) . \quad (12)$$

Using Equation (12) in (11),

$$\left(\frac{D}{L}\right)_f = \frac{W_g}{2\pi\rho U^2}\,\frac{1}{(b_g - 2b_f)}\left(\frac{1}{b_f} - \frac{1}{b_g - 2b_f}\right), \quad (13)$$

The weight of the generating aircraft may be expressed as

$$W_g = C_{L_g}\frac{U^2}{2}\,\frac{b_g^2}{A_g} , \quad (14)$$

so that Equation (13) becomes

$$\left(\frac{D}{L}\right)_f = \frac{C_{L_g}}{4\pi A_g}\,\frac{b_g}{b_f}\,\frac{1 - 3(b_f/b_g)}{1 - 2(b_f/b_g)} . \quad (15)$$

If the generating aircraft is flown at optimum lift coefficient, then

$$\left(\frac{D}{L}\right)_f = \frac{1}{4}\sqrt{\frac{(C_{D_0}e)_g}{\pi A_g}}\,\frac{b_g}{b_f}\,\frac{1 - 3(b_f/b_g)}{1 - 2(b_f/b_g)} . \quad (16)$$

Inverting this expression yields the very least L/D that is required in order for a flyer of span b_f to achieve powerless flight in the wake of a generating aircraft of span b_g having linearly loaded tips and flying at optimum L/D. The expression is

$$\left(\frac{L}{D}\right)_f = 4\sqrt{\frac{\pi A_g}{(C_{D_0}e)_g}}\,\frac{b_f}{b_g}\,\frac{1 - 2(b_f/b_g)}{1 - 3(b_f/b_g)} . \quad (17)$$

Using Equation (4), this may be written

$$\left(\frac{L}{D}\right)_f = \frac{8}{e_g}\left[\left(\frac{L}{D}\right)_{opt}\right]_g\,\frac{b_f}{b_g}\,\frac{1 - 2(b_f/b_g)}{1 - 3(b_f/b_g)} . \quad (18)$$

Let us now consider an example. Suppose one has a generating aircraft with aspect ratio A = 7.6, efficiency factor e = 0.8, and $C_{D_0} = 0.025$. These are numbers typical of an aircraft such as the Navy's P-3. Its optimum L/D will be

$$\left(\frac{L}{D}\right)_g = \frac{1}{2}\sqrt{\frac{.8 \times 3.14 \times 7.6}{0.025}} = 13.8 . \quad (19)$$

Equation (18) then becomes

$$\left(\frac{L}{D}\right)_f = 138\,\frac{b_f}{b_g}\cdot\frac{1 - 2(b_f/b_g)}{1 - 3(b_f/b_g)} . \quad (20)$$

The second column in Table 2 shows the (L/D)'s required for powerless wake riders of various span ratios when the generating aircraft we have assumed is flown at optimum L/D.

Table 2. Wake Rider (L/D)'s Required for a Generating Aircraft Having A = 7.6, e = 0.8, and C_{D_0} = 0.025

b_f/b_g	$(L/D)_f$ for $U = U_{opt}$	$(L/D)_f$ for $U = 0.85U_{opt}$
.15	26.3	19
.1	15.8	11.4
.075	11.4	8.23
.05	7.3	5.27

It will be noted from Equation (13) that if one flies at a speed lower than that required to achieve optimum L/D of the generating aircraft, then the L/D required of the flyer is lowered by the ratio $(U/U_{opt})^2$. Referring to Figure 10, if one were willing to take a 5% range penalty for the generating aircraft, then one could fly at U/U_{opt} of 0.85, or the (L/D)'s given in Table 2 would be reduced by the factor 0.72. The (L/D)'s required for this flight condition for the example we have chosen are shown in the third column of Table 2.

An examination of these results leads one to the conclusion that it may be possible to design long-range patrol aircraft which are capable of taking two smaller (but necessarily denser) vehicles with them wherever they go, with either zero or very small expenditure of power. It is clear from the way in which the analysis has been made that the smaller one makes the wake rider, the smaller will be the L/D required to achieve powerless flight. However, the region in which the wake rider must fly becomes narrower as one decreases b_f/b_g. This increases the problem of density as well as of station-keeping in the wake. The latter consideration will require an additional L/D capability in the wake rider. For powerless flight, it is clear that the way one would have to keep station is to have available more L/D than we have calculated here. Spoilers would then be deployed when on-station in order to achieve the equilibrium L/D. Control would be accomplished by using the excess gliding capability generated by retraction of these spoilers as needed.

It may be worth noting here that the very brief discussion of this type of wake rider would seem to indicate that the design of a wing to be used in an assembly of individual but like wings that are to achieve maximum energy utilization *as an assembly* will be quite different from the design of the wing for solo flight. Our analysis would also seem to suggest that the speed for optimum fuel consumption for such an assembly would be lower than the speed for optimum fuel consumption for any member of the assembly if it were separated from the group. This is in agreement with the conclusion reached by Lissaman and Shollenberger in their analysis of bird formation flight.

A CASE STUDY

A theoretical analysis was made of a possible wake rider flight test based on the concept shown in Figure 1(b), that is, with a single rider or flyer following midway between a pair of generating aircraft and riding the combined upwash of their adjacent vortices. The generating aircraft for this study were two P-3 patrol aircraft and the flyer was a T-2 trainer. The complete results of the study are reported in reference 10. The conditions are illustrated in Figure 12.

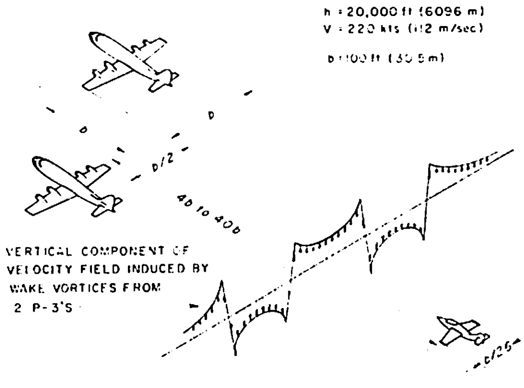

Figure 12. Flight configuration for wake rider study.

The object of the study was to determine what aerodynamic responses would result if the T-2 entered the wake region under several flight conditions and modes of control. Several elements of the study will now be discussed.

Wake Velocity Field.

The wake velocity field was computed by assuming an elliptic load distribution on each P-3 wing and having these distributions roll up into two pairs of discrete vortices as shown in Figure 13. Each vortex is then ideally located at $\pi/8$ b from the centerline of the aircraft. For the P-3 in steady level flight during testing at an altitude of 20,000 ft (6096 m) and at a flight speed of 220 knots (112 m/sec), the strength of each vortex is

$$\Gamma_o = 2{,}700 \ \mathrm{ft}^2/\mathrm{sec} \ (251 \ \mathrm{m}^2/\mathrm{sec}) \ .$$

The flowfield produced by each vortex is characterized by its mean tangential velocity, which is computed by the method of reference 3. The tangential velocity contributions from each of the four vortices are then summed in order to obtain the crossflow velocity at any particular lateral and vertical position. It is assumed, however, that the vortices do not interact with each other and that, therefore, their lateral and vertical positions do not change downstream.

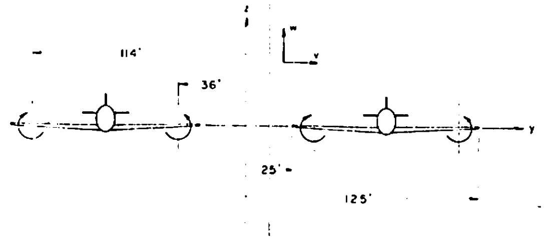

Figure 13. Lateral spacing of P-3 aircraft and their wake vortices.

The crossflow velocity information is then converted to geocentric velocity components v (horizontal) and w (vertical) and stored at 3-foot intervals in y and z over a square area 300 ft (91.4 m) on each side. A program then linearly interpolates among these values and converts to flyer body axes in order to obtain the wake velocity normal to the flyer wing at selected stations.

Forces and Moments on the Wake Flyer.

The forces and moments on the wake flyer are calculated in nondimensional form by summing contributions due to the static aerodynamics, control deflections, and aircraft angular rates. The contributions due to the angular rates are assumed proportional to the rates and not a function of α or β, angle of attack and sideslip angle, respectively. The contributions due to control deflections are proportional to the deflection and a nonlinear function of α and β. Values of each control derivative are stored on a grid of α,β points in a computer file. The four values of the control derivative bracketing the desired α,β are obtained and the desired values found by two-dimensional linear interpolation.

The static aerodynamic coefficients are also nonlinear functions of α and β and are obtained in the same manner as the control derivatives. The values of α and β used in this process include the effect of the wake flow as calculated at the aircraft c.g. In addition to this wake effect on the static aerodynamic coefficients, there is also the spanwise nonuniform flow effect which is evaluated using strip theory.

The really significant effect from spanwise flow variations is the contribution to the rolling moment coefficient C_ℓ. This is shown in Figure 14 as a function of lateral position y for vertical positions z with zero roll. Wind-tunnel test data for the T-2 indicate that full aileron deflection produces a maximum rolling moment coefficient of ±.04. The ailerons will therefore not be able to counterbalance the moment produced by the wake when operating within 15 ft (4.57 m) of the center of a vortex. The aircraft would be automatically rolled out of this region and exit from the wake.

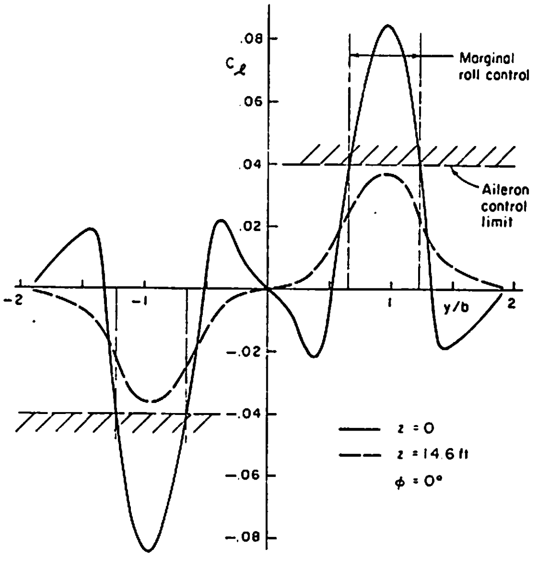

Figure 14. Comparison of computed rolling moment due to wake and from ailerons.

Because of the importance of rolling moment coefficient in the T-2 response, it was decided to conduct wind-tunnel tests to confirm the computed C_l distribution for a wing traversing a multiple vortex flowfield. These tests are discussed later.

Numerical Simulation of Wake-Flyer Dynamics.

A.R.A.P.'s six-degree-of-freedom Aircraft Digital Simulation Program was used to simulate the flight of the T-2 in the wake of the two P-3's. To crudely evaluate the piloting task for wake flying, over forty simulations were run. From these, several have been chosen for discussion here. The first three illustrate the advantage of approaching the wake from above. The others represent worst-case encounters and also give a feel for what the pilot must do in order to ride the wake. These have been portrayed in the form of a computer generated, animated movie for presentation with this paper.

Figure 15 shows the T-2 being flown with altitude stabilization only. The solid curve indicates how a 100-ft (30.5-m) altitude decrease is accomplished with no wake present. The long dashed curve shows what happens with the wake present. Note that the control, while not accurate, is stable. On the other hand, if the approach is made from below, the increasing upwash and high power setting force the aircraft through the center of the wake, and the approach from above must then be used. It, therefore, appears that entry into the wake is more easily accomplished from above.

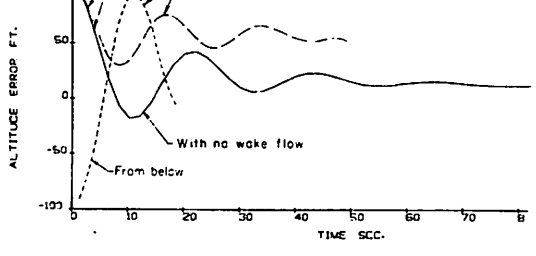

Figure 15. Altitude time history for wake entry from below and from above.

Having chosen this entry technique, the altitude stabilization was removed and entry was studied using a constant thrust reduction such as a pilot might employ. In order for this technique to be successful, the sink rate must be well below the maximum upwash in the wake (say, 5 ft/s (1.52 m/s) sink rate for a 14 ft/s (4.27 m/s) upwash).

For the previous simulations, the aircraft started with no lateral position error in order to concentrate on the longitudinal problems. To examine the combined problem, the aircraft is initially positioned 7 ft (2.13 m) to the right and 50 ft (15.24 m) up. The trajectory of the aircraft with the controls held fixed is shown in Figure 16. The small horizontal wake velocity component v_w causes the aircraft to drift to the right as it descends. The more it drifts to the right, the larger v_w becomes. The aircraft is also rolled by the vortices, causing the vertical component of the lift vector to decrease and the aircraft to descend through the wake.

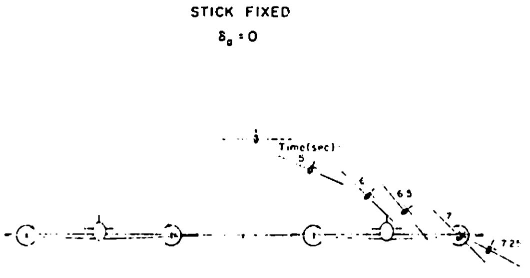

Figure 16. Time sequence of T-2 wake riding with roll angle feedback to ailerons.

In the next simulation (Figure 17), the ailerons are used to help keep the wings level:

$$\delta_a = k_\phi \phi ,$$

$$k_\phi = 1 ,$$

where δ_a = aileron deflection. Again, the aircraft drifts to the right but at a reduced rate since the lift vector is more nearly vertical. The aircraft passes through the wake near the center of the closest vortex and is rolled because the roll torque from the vortex is greater than the maximum aileron roll torque.

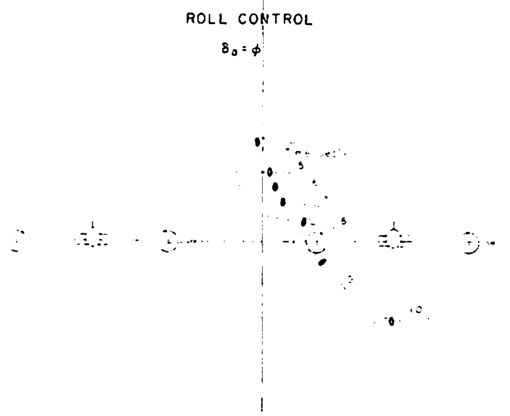

Figure 17. Time sequence of T-2 wake riding with roll angle feedback to ailerons.

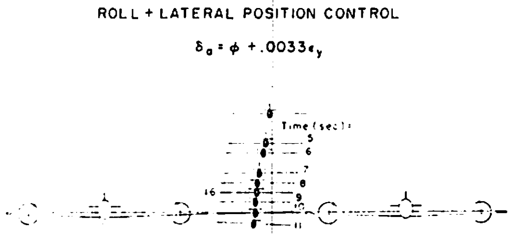

Figure 18. Time sequence of T-2 wake riding with lateral position and roll angle feedback to ailerons.

In the third simulation (Figure 18), the ailerons are used to control lateral error as well as roll angle:

$$\delta_a = k_y y + k_\phi \phi ,$$

$$k_y = .0033 \text{ rad/ft} ,$$

$$k_\phi = 1 .$$

There is, therefore, a slight negative roll due to the initial 7-ft (2.14-m) lateral error. The error is reduced and the vehicle descends slightly into the lower part of the wake but then rises again. At this point, the pilot should further reduce power and attempt to stabilize the aircraft at z = 10 ft (3.05 m). He can then concentrate on holding his lateral position with respect to the vortex field. The small, slow aileron motions required to stabilize the lateral oscillations indicate that a pilot should be able to perform this function if he has good visual cues for locating the vortices. In reality, however, the pilot's task may be complicated by P-3 position-keeping variations, ambient turbulence and crosswind effects on the wake, and turbulence within the wake.

Wind Tunnel Studies of Rolling Moment Coefficient.

In order to support the validity of the theoretical rolling-moment values computed for the T-2, a wind-tunnel test program was carried out in which rolling moment coefficients were measured on a scale T-2 wing immersed in a scale vortex wake. The apparatus and techniques used in this program and the results obtained are described here briefly.

The object of the tests was to measure the rolling moment coefficients on a wing model under conditions which simulated as closely as possible those of a full-scale encounter of a T-2 with the central portion of the wake produced by two P-3's flying side-by-side. The tunnel test section and wake generating system are illustrated schematically in Figure 19, which also shows the flow visualization system available and some examples of vortex flow cross-sections photographed in the course of an earlier study of vortex merging.

The choice of conditions for the tests was dictated by the desire to scale the T-2 wake encounter accurately while minimizing the effects of the tunnel walls and accounting at least crudely for the very large difference in Reynolds number between test and full-

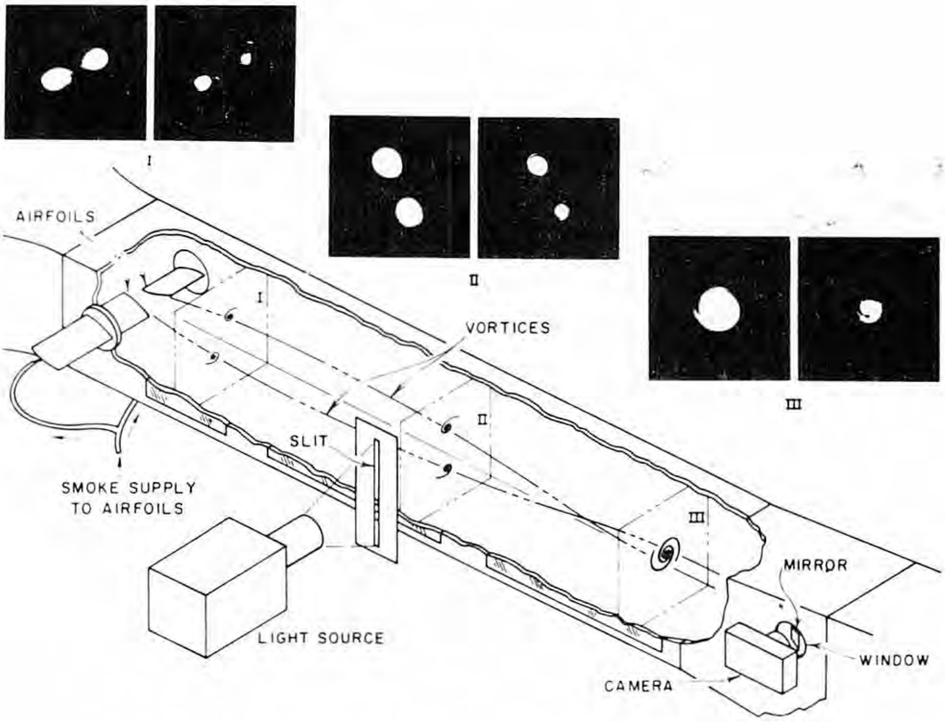

Figure 19. Schematic view of wind tunnel and vortex apparatus.

scale conditions. The conditions chosen were based on a wake vortex spacing of 13.4 cm, or about 44% of the tunnel width. Since the nominal full-scale configuration was to have the vortex spacing equal to twice the T-2 wingspan, the T-2 wing model was made with a wingspan of 6.7 cm.

The measurement of rolling moment on a wing model of this size presented several challenging problems. Not only would the instrument have to be highly sensitive to applied rolling moment, but it would also have to be insensitive to axial and normal forces and other applied moments. At the same time it would have to be small enough so as not to disturb the flow unduly. An estimate of the moments to be encountered revealed that the maximum rolling moment would be of the order of 10 gm-cm.

A torque meter design was finally arrived at which proved satisfactory in all respects [11]. The instrument incorporated a sensitive active element mounted coaxially in a fixed tubular case with the sensitive element suspended on springs of the flexural-pivot type. A very slight angular rotation was allowed in response to the applied torque, and this rotation was sensed by a rotary variable differential transformer (RVDT). The torquemeter and wing model are shown mounted in a traversing mechanism in Figure 20.

To establish the proper wake flowfield for these tests, it was first necessary to determine what vortex circulation strength was needed and what conditions were required to produce it. For the full-scale flight test at 20,000-ft (6096-m) altitude and 220 kts (112 m/s) the lift coefficient for a P-3 is $C_L = .88$ for a gross weight of 100,000 lbs (45,450 kg). The wind-tunnel tests were scaled by adjusting the angle of attack of the vortex-generator airfoils and the tunnel velocity to produce vortices equal in circulation strength Γ to those that would be produced by two hypothetical scale model P-3's flying at $C_L = .88$. To find the proper settings of vortex-generator angle of attack and tunnel speed for the desired match, it was necessary to calibrate the vortex generator system. This was accomplished by deducing the circula-

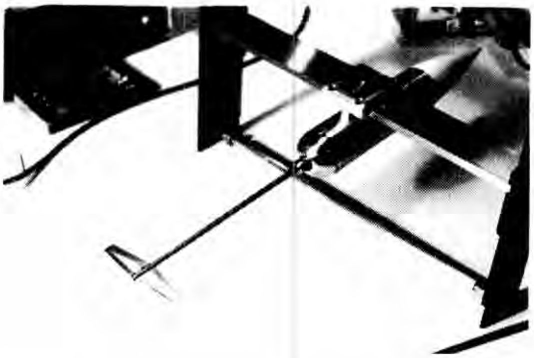

Figure 20. The T-2 wing model and torque meter mounted in the traversing mechanism.

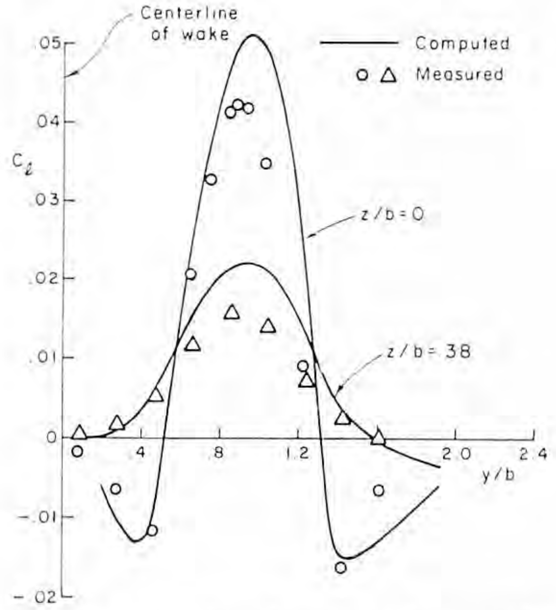

Figure 21. Comparison of computed and measured C_ℓ distributions for model tests of T-2 wing.

tion strength Γ by measuring the mutual rotation induced on each other by a pair of like-sign and equal-strength vortices between two points downstream of the vortex generators. For these measurements, smoke was used to locate the vortices.

Two additional factors which would be expected to affect the rolling moment measurements are the distribution of angular momentum in the vortex, as characterized by its tangential velocity profile, and the Reynolds number. Both of these factors were investigated in a limited way.

Some idea of the tangential velocity profile was gained by holding a rake of sensitive tufts across the flow just upstream of the wing. It was determined that the profile shape relative to the wing was reasonably consistent with the full-scale case. The effect of Reynolds number was explored by referring to data on wing lift-curve slope C_{L_α} measured at low Reynolds number [12]. It was found that C_{L_α} decreases and becomes quite nonlinear at very low Reynolds numbers and that $C_{L_{max}}$ decreases. To minimize this effect on the value of these tests in confirming rolling moment calculations, it was decided to measure $C_{L\alpha}$ and C_{Lmax} for the model wing and to compare the measured rolling moments with those calculated using the measured, low Reynolds number $C_{L\alpha}$ and C_{Lmax}. A comparison on this basis is shown in Figure 21. Since the agreement is reasonable both as to shape and magnitude, it was concluded that the computation method based on strip theory should give reliable results when applied to the full-scale test case. Actual calculations for the full-scale case showed peak values of C_ℓ about twice those measured in the scale model test. Apparently, the difference reflects not only the Reynolds number effect on C_{L_α} and $C_{L_{max}}$, but also the expected tendency for two-dimensional strip theory to overpredict in calculations of this kind. Since the computed peak values of rolling moment were so much higher than the measured ones, however, it was concluded that it would be reasonable to consider them conservative in predicting wake flyer response.

CONCLUDING REMARKS

In this paper we have reviewed some preliminary studies of the possibility of wake riding as a means of wake energy utilization. Obviously, there are many more detailed considerations which must be investigated before the practical value of such flight techniques can be assessed. It is especially important, for example, that the sensing and control requirements for station-keeping be understood. Nevertheless, it does appear that for some tactical purposes there is sufficient promise to warrant further study.

We have described several ways in which aircraft might be arranged in order to take advantage of energy in the wake: small (dense) wake flyers following a single generating aircraft; a formation flight of large cargo aircraft; and a single wake flyer carried behind a pair of generating aircraft. Some of the stability and control problems associated with aircraft attempting to fly in a wake have been discussed and a method of analyzing aircraft response in a wake flowfield has been demonstrated.

REFERENCES

1. Lissaman, P.B.S. and Shollenberger, C.A., "Formation Flight of Birds," *Science*, Vol. 168, 22 May 1970, p. 1003-1005.

2. Betz, A., "Behavior of Vortex Systems," NACA TM-713, June 1933 (transl. from *ZAMM*, Vol. XII, 3, 1932, p. 164-174).

3. Donaldson, C.duP., "A Brief Review of the Aircraft Trailing Vortex Problem," AFOSR TR-71-1910, May 1971 (presented at Nat'l Aerospace Electronics Conf., Dayton, OH, May 1971).

4. Rossow, V., "On the Inviscid Rolled-Up Structure of Lift-Generated Vortices," *J. Aircraft*, Vol. 10, 11, Nov. 1973, p. 647-650.

5. Mason, W.H. and Marchman, J.F., "Farfield Structure of an Aircraft Trailing Vortex," *J. Aircraft*, Vol. 10, 2, Feb. 1973, p. 86-92.

6. Donaldson, C.duP. and Bilanin, A.J., "Vortex Wakes of Conventional Aircraft," AGARDograph No. 204, May 1975.

7. Donaldson, C.duP., Snedeker, R.S., and Sullivan, R.D., "A Method of Calculating Aircraft Wake Velocity Profiles and Comparison with Full-Scale Experimental Measurements," *J. Aircraft*, Vol. 11, 9, Sep. 1974, p. 547-555.

8. Snedeker, R.S. and Bilanin, A.J., "Analysis of the Vortex Wakes of the Boeing 727, Lockheed L-1011, McDonnell Douglas DC-10, and Boeing 747 Aircraft," A.R.A.P. Report No. 245, July 1975.

9. Bilanin, A.J., Donaldson, C.duP., and Snedeker, R.S., "An Analytic and Experimental Investigation of the Wakes Behind Flapped and Unflapped Wings," AFFDL-TR-74-90, May 1974.

10. Donaldson, C.duP., Williamson, G.G., Bilanin, A.J., and Snedeker, R.S., "Study of the Feasibility of Conducting a Wake-Riding Experiment Using a T-2 Aircraft Behind Two P-3 Aircraft," A.R.A.P. Report No. 287, Aug. 1976.

11. Snedeker, R.S., "A Sensitive Torque Meter for Wind Tunnel Applications," *J. Aircraft*, Vol. 14, 3, March 1977, p. 314-315.

12. Jacobs, E.N. and Sherman, A., "Airfoil Section Characteristics as Affected by Variations of the Reynolds Number," NACA Rept. No. 586, 1937.

ALLEVIATION OF LIFT-GENERATED WAKES BY VORTEX INTERACTIONS

VERNON J. ROSSOW
NASA Ames Research Center
Moffett Field CA 94035

ABSTRACT: The requirements for wake alleviation by inviscid convective interaction of vortices are reviewed. It is concluded that these wake structures will disperse and merge to alleviate the wake hazard, but unacceptably large aerodynamic penalties occur when the required loadings are generated by use of trailing-edge flap deflections. It is suggested, therefore, that the vortex pairs of opposite sign be generated above or below the wing with devices such as fins, fences, engine thrust, etc. Guidelines for the effective disposition and strength of these extra or auxiliary vortices are derived and numerical examples are presented for various configurations. Results of some preliminary wind-tunnel experiments confirmed that vortex injection into a wake by fins provides alleviation and warrants further study to optimize the various design parameters.

NOMENCLATURE

AR = aspect ratio
b = wing span
C_L = lift coefficient, lift/$[(1/2)\rho U_\infty^2 S]$
C_ℓ = local lift coefficient
C_l = rolling-moment coefficient, $\dfrac{\text{rolling moment}}{[(1/2)\rho U_\infty^2 S]}$
C_v = vortex interaction parameter (see Equations (4) and (5))
c = wing chord
$\bar{c}$ = mean geometric chord
d_e = effective diameter of vortical region = $7d_v/6$
d_i = spacing between centers of innermost vortices
d_s = spacing between vortex centers
d_v = diameter of outer ring of point vortices in vortical region = $2r_v$, with d_v arbitrarily set at 0.3b
J = second moment of circulation (see Equation (2))
k = vortex core structure parameter
$\ell(y)$ = local spanwise lift
N = number of vortices
r = radius
S = wing area
T = dimensionless time = $4t\Gamma_v/b^2 = 0.36t\Gamma_v/d_v^2$
t = time
U_∞ = free-stream velocity aligned with x axis
u,v,w = velocity components in x, y, and z directions
v_θ = circumferential velocity
v_{sh} = wind-shear parameter (see Equation (1))
x,y,z = coordinates; x, streamwise, and z, vertical
α = angle of attack
Γ = circulation
γ = circulation in point vortices
ρ = air density.

Subscripts

a = auxiliary vortex
f = following model that encounters wake
g = model that generates wake
sh = vortex sheet
v = vortex or vortical region.

INTRODUCTION

Recent research on the wake vortices of large aircraft [1-5] has provided several different methods that reduce the wake hazard by a factor of about 2 at distances 2 miles or more behind the generating aircraft (i.e., $C_{l_f} \approx 0.10$ down to 0.05, where C_{l_f} is the rolling-moment coefficient induced by the wake on a following aircraft). Such a reduction brings the rolling moment induced by the wakes of wide-body subsonic transports to within the roll-control capability of smaller aircraft that might encounter these wakes. However, estimates based on simulator studies and flight encounters [6, 7] indicate that the encountering aircraft may still roll as much as 25°. The studies in references 6 and 7 also indicate that acceptable safe maximum roll angles should be kept below 7° during the landing approach. From these studies of the dynamics of aircraft as they encounter wakes, it is concluded that the rolling-moment hazard in wakes 2 miles behind the generating aircraft must be reduced further by another factor of 3 or 4 if the entire problem is to be solved by aerodynamic alleviation on the generating aircraft only. Then the maximum rolling-moment coefficient induced by a wake on an encountering aircraft should be less than $C_{l_f} = 0.01$ or 0.02.

This paper explores ways in which vortex wakes can be generated so that they leave behind a wake hazard no greater than $C_{l_f} = 0.02$. Previous studies [5] have shown that little or no promise for alleviation can be expected from wings whose span loading is monotonically increasing from the wingtip inboard so that only one vortex is shed per side. However, it has been shown [1-5, 8-11] that span loadings which produce several vortex pairs provide vortex interactions that reduce wake velocities. Therefore, the alleviation techniques considered here require that the span loading be designed (by use of flaps and/or fins) to produce several vortices per side of the wing. Guidelines are sought for the strength, distribution of circulation, and spacing (spanwise and vertically) required of wake vortices so that they interact to merge and/or disperse to substantially reduce the overturning velocities in the wake.

MULTIPLE VORTEX INTERACTIONS

Previous theoretical and experimental studies of wake vortices have identified and demonstrated in flight or in the wind tunnel several schemes for reducing the velocities and overturning moments on encountering aircraft. One of the earlier concepts accelerated the decay or dispersion of vortices by introducing large-scale turbulence [1-6] into or near the center of the vortex. Turbulence, in addition to that produced by the engines, landing gear, boundary layers, etc., was added to the wake by devices such as spoilers on the wing or splines behind the wing. Although several configurations were found to reduce the vortex-induced rolling moment to about the roll-control capability of the encountering aircraft, penalties in drag and aerodynamic buffet raised questions as to whether these devices would become acceptable for alleviation. Furthermore, it was not possible to study the details of the turbulent interactions nor to optimize the configurations theoretically because of the complexity of the flow fields. Even though rather sophisticated numerical simulations of wake turbulence have been made [9, 12], the computer codes are unable to analyze with sufficient accuracy the flow over aircraft equipped with turbulence injection devices. For this reason, it becomes necessary to first measure the wake structure at some station behind the aircraft (as done in reference 13), and then use that data for starting conditions in the computer code. Only then can downstream representations of wakes with turbulence injection be generated theoretically.

Utilization of favorable interactions between vortices in the wake [1-5, 8-11] was also found to reduce the hazard posed by lift-generated wakes. It is well known that wakes with only one vortex pair interact nondestructively with slow diffusion of vorticity across the aircraft centerline. However, vortex wakes with several or many pairs can have extensive random, diffusive velocities. A theoretical example of this kind of wake dynamics was achieved with so-called stepped or sawtooth loadings [8, 10]. Tests with wake-generating models that had three [3, 5] and seven [14, 15] vortex pairs showed that large mixing motions could be induced in the wake so that rolling moments could be substantially reduced for certain flight conditions [2, 5]. Unfortunately, introducing turbulence into the wake by the landing gear (when deployed) or by sideslip of the aircraft reduced substantially the effectiveness of the alleviation in the three-vortex (Boeing 747) case [5]. These results prompted an increased emphasis [10-13] on how vortices interact with one another or with turbulence to increase or decrease their hazard potential.

The following sections consider several kinds of vortex interactions and explore theoretically how they can be used to relieve the hazard potential of lift-generated wakes. The analysis is made using the two-dimensional time-dependent method (used in references 8 and 10) to approximate lift-generated wakes. As a result, the wake-alleviation schemes are assumed to depend mostly on self-induced convective velocities wherein viscosity and turbulence play a secondary role.

Illustrations of Vortex Interactions — Dispersion.

An example taken from reference 10 is presented in Figure 1 to illustrate how the circulation in an originally round vortex can be dispersed in what might be called an ideal way. Each point in the flow field represents a given amount of circulation that convects the other points or vortices about. Dispersion of the originally round vortex core occurs because it is embedded in a flow field that has a velocity gradient in the vertical direction given by [10]

$$v(z) = \frac{z}{r_v} \frac{\Gamma_v}{2\pi r_v} V_{sh} \cdot \qquad (1)$$

(The terms vortex, vortical region, and core are used interchangeably here to denote a region that contains vorticity.) The background flow field therefore has a uniform distribution of vorticity that will disperse the vortex core if it is strong enough [10]. Since the velocity gradient or sheared flow extends indefinitely in the vertical direction, the dispersion also increases indefinitely with time. The velocity field of the vortex then becomes weaker with time as its vorticity is spread more thinly. The background velocity gradient that brings about the dispersion remains unchanged.

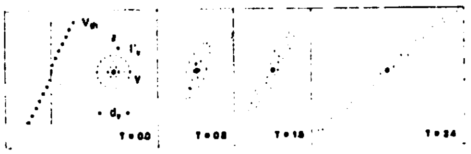

Figure 1. Rankine vortex embedded in a flow field with velocity gradient sufficiently strong to disperse it; $V_{sh} = +0.26$, $k = -1$, $\Gamma_v = 3.6bU_\infty$ (from reference 10).

The situation depicted in Figure 1 approximates the interaction of a vortex with the shear layer on the ground when a crosswind is blowing over an airport. Attempts to achieve comparable dispersion with vortices in the wake [10] (rather than relying on wind shear) brings about a limited amount of dispersion that may be useful in certain circumstances but falls short of that illustrated in Figure 1.

Dispersion of another kind occurs when a large number of positive and negative pairs are produced in the wake by upward and downward flap deflections [8, 14, 15] across the span of the generating wing. The results for the so-called stepped loading [8] suggest that the random motions of the vortices would spread or disperse the wake. Results for a wing with seven flap segments per side [15] showed that the rolling-moment hazard could be substantially reduced by this technique at small lift coefficients ($C_{Lg} \leq 0.4$) and for small following aircraft ($b_f/b_g = 0.14$). These results were encouraging, but a method for making the concept more generally applicable was not apparent at that time.

Vortex Merger.

The process whereby two or more separate vortices combine, merge, or coalesce into a single vortical region is assumed here to be brought about by the inviscid, self-induced velocity fields of the vortices. A sequence wherein two vortices interact to merge quickly and thoroughly is reproduced

[10] in Figure 2. The two initially round vortices distort in shape and combine to form a new circular vortical region that persists. Boundaries that distinguish merging from nonmerging situations [10] were found to be well defined and definite. It was also found that vortices opposite in sign do not merge unless one is at least 5 times as strong as the other. However, merger of two opposite vortices can be induced by having other vortices in the wake.

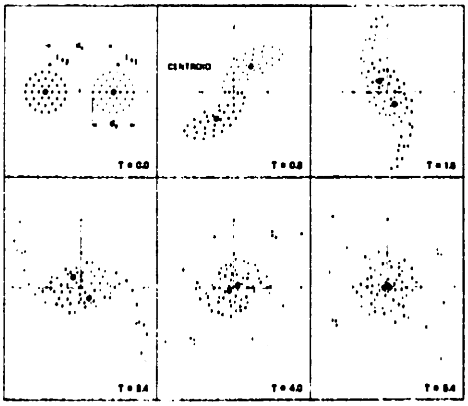

Figure 2. Merging sequence predicted numerically for two Rankine vortices of equal strength; $\Gamma_1 = \Gamma_2 = 3.6bU_\infty$, $d_s = 1.7\,d_v = 1.46\,d_e$, $k = -1$ (from reference 10).

The example [10] shown in Figure 3 brings about merger of the two center vortices at the center plane. The two vortex pairs are opposite in sign and of the same magnitude. The motion toward the centerplane of all four vortices is caused by the slight tilt that develops in the vortex positions. When the two center vortices touch at the centerplane, it is assumed that they would then merge and dissipate by viscosity and turbulent mixing. In this example, the vortex-induced rolling moment is not appreciably changed because the outboard vortices remain unmodified.

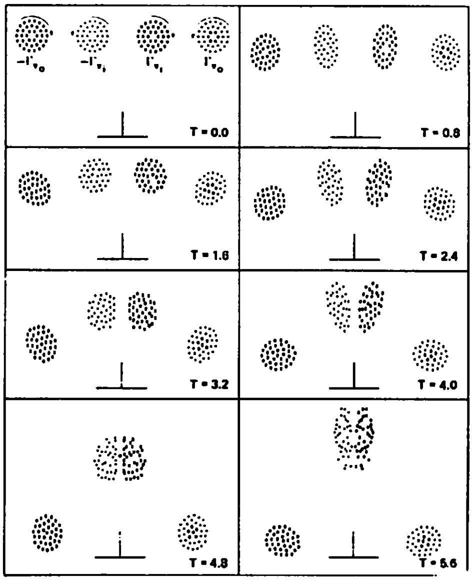

Figure 3. Interaction of two vortex pairs of opposite sign and of the same strength; $\Gamma_0 = -\Gamma_1 = +3.6bU_\infty$, $d_i = d_s = 2.0\,d_v = 1.71\,d_e$, $k = -1$ (from reference 10).

Other wake configurations were also tried with 2, 3, and 4 vortex pairs to find out if the alleviation could be improved. In all cases, the vortex pairs alternated in sign across the span, which was found to be a necessary condition for merger or convergence [11] to the centerplane. Variations in core size and structure, vortex spacing, and strength were found to alter the details of the convergence, but the process occurred for a wide range of parameters. No configurations were found that caused all of the vorticity to converge at the centerplane (or elsewhere in the flow field) or to disperse the wake as thoroughly as depicted in Figure 1. Many were found, however, that brought much of the vorticity to the centerplane, leaving weak remnants of vorticity from the two outboard pairs to move outboard (Figure 4). The net circulation in the outboard group can (by manipulating vortex positions and strengths) be adjusted by a trial and error process to bring about reduced wake velocities when turbulence and viscosity can be relied on to blend the positive and negative circulation in the various groups. These two-dimensional predictions are probably conservative because a detailed study of three-dimensional interactions by Hackett and Evans [11] showed that merger or convergence at the centerplane is more likely to occur when three-dimensional effects are included in the calculations.

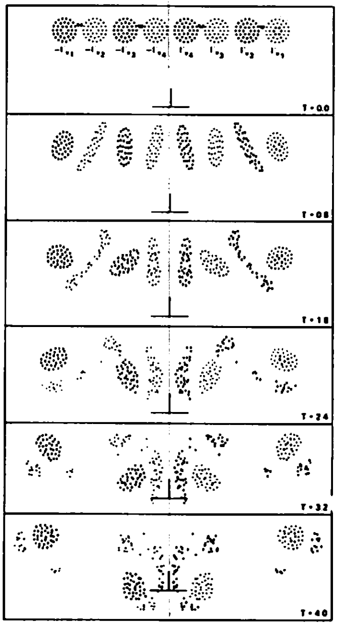

Figure 4. Interaction of four vortex pairs designed to have the same initial downward velocity; $\Gamma_1 = 3.6bU_\infty$, $\Gamma_4 = -0.775\ \Gamma_1$, $\Gamma_3 = +0.853\ \Gamma_1$, $\Gamma_2 = -0.682\ \Gamma_1$, $d_i = d_s = 1.17\ d_v = d_c$, $k=-1$.

AUXILIARY VORTICES FOR WAKE ALLEVIATION

The interactions illustrated in Figures 3 and 4 require that the vortices be of comparable magnitude and that they alternate in strength across the span. An alternative solution is to find sensitive locations in the wake for the negative vortices so that they need not be so strong and that only a few of them are needed to alleviate the wake. Both possibilities are now explored by considering nonplanar vortex wakes rather than the nearly planar ones treated previously. In particular, the effectiveness of vortices located above or below the vortex sheet shed by a wing to disrupt the wake are studied. Although the method for generating these extra or auxiliary vortices is not treated here, they could be produced by the use of fins or fences mounted on the wing, by strakes, by engine-thrust deflected spanwise, or by introducing swirl in the engine exhaust.

Interaction Guidelines from Vortex Invariants.

The invariants for two-dimensional vortex systems are examined here to find directions as to the strength, location, number, etc., for the auxiliary vortices above and below the wing. One property being sought for the final or fully developed vortex wake is to have the vorticity spread over as large a radius as possible. Since the second moment of vorticity for one side of the wake remains constant throughout the wake history in the inviscid approximation, it may provide guidelines for optimum placement and strength for the auxiliary vortices to maximize the area over which the circulation is spread when extra vortices are added above or below the wing. The second moment for the vorticity shed by one side of the wing is given by

$$J = \sum_{i=1}^{N} \gamma_i r_i^2 = \Gamma \bar{r}^2, \tag{2}$$

where r_i is the radius from the centroid of circulation of each point vortex used to represent that half of the lift-generated wake. The symbol Γ represents the circulation for one side of the wake and $\bar{r}$ is the characteristic (or square-root average) of the radius over which the circulation is spread. The objective is to find rules that will maximize $\bar{r}$ with a minimum value of circulation in the auxiliary vortex. This consideration assumes that a large value of $\bar{r}$ indicates that the circulation in the wake is spread out or diffused, which makes it relatively less hazardous than one with a small value of $\bar{r}$. It is necessary then to find those features of the auxiliary vortices that make $\bar{r}$ as large as possible with a minimum addition of circulation. If the lift-generated vortex sheet lies initially on the y axis, the second moment is given by

$$J = \int_0^{b/2} \gamma(y)\left[(y - \bar{y})^2 + \bar{z}^2\right]dy + \gamma_a\left[(y_a - \bar{y})^2 + (z_a - \bar{z})^2\right], \tag{3}$$

where the location of the centroid is given by

$$\bar{y} = \frac{\Gamma_{sh}\bar{y}_{sh} + \gamma_a y_a}{\Gamma_{sh} + \gamma_a}; \quad \bar{z} = \frac{\gamma_a z_a}{\Gamma_{sh} + \gamma_a}$$

These relationships suggest that the auxiliary vortices be placed as far from the sheet centroid as possible. Such a criterion ignores the fact that a vortex far from the sheet will not influence its motion or final structure and would therefore be ineffective in diffusing a wake. The approach will then not be fruitful. If, however, the circulation in the auxiliary vortex is opposite that of the sheet, another maximum in $\bar{r}$ occurs when $\gamma_a = -\Gamma_{sh}$. Then the second moment becomes infinite because the centroid is at infinity, no matter where γ_a is located.

Another approach is to consider the parameter:

$$C_v = \sum_{i=1}^{N-1} \sum_{j=i+1}^{N} \gamma_i \gamma_j r_{ij}^2 , \qquad (4)$$

which is also invariant throughout the history of the vortex wake, and which is independent of the location of the centroid of vorticity because $r_{ij}^2 = (y_i - y_j)^2 + (z_i - z_j)^2$. The double summation characterizes the interaction of all vortices. The parameter C_v is related to the first and second moments by

$$C_v = \left[\sum_{i=1}^{N} \gamma_i\right]\left[\sum_{j=1}^{N} \gamma_j r_j^2\right] - \left[\sum_{i=1}^{N} \gamma_i y_i\right]^2 - \left[\sum_{i=1}^{N} \gamma_i z_i\right]^2 . \qquad (5)$$

Since the distances r_{ij} between vortices determine how strongly they interact, the parameter C_v is a measure of the interaction within the system. A small increase in C_v when an auxiliary vortex is added means, therefore, that the vortices interact strongly and a large value signifies a weak interaction. A minimum contribution to C_v by addition of an auxiliary vortex to the system occurs then at the spanwise station where the vortex interacts most strongly with the vortex sheet. It is found that such optimum position is at the centroid of the sheet vorticity.

Numerical Examples.

Since the guidelines developed in the last section provide only gross directions for the desirable characteristics of the auxiliary vortices, several different situations were analyzed to better define the interaction between the vortex and the sheet. A series of cases was therefore calculated to find how the sign and strength of the extra or auxiliary vortices and the position spanwise and the distance above and/or below would affect the dynamics of several different vortex sheets. It was first found that, as predicted, the spanwise location of an auxiliary vortex that provides the most interaction is near the centroid of the vortex sheet. Because the sheet induces a lateral or spanwise motion on the vortex, the interaction is improved if the vortex is located slightly inboard of the centroid when it is under the sheet and slightly outboard of the centroid when above the sheet. The motion induced by the sheet on the vortex then carries it nearer to and past the centroid, providing a greater interaction on the sheet than when it is initially directly over or under the centroid.

A comparable guideline for the most effective distance for the auxiliary vortex above or below the sheet was not found. Instead, the effectiveness of a vortex did not vary greatly from when it was quite near the sheet to when it was as far away as 30% of the semispan. A difference noted is that a vortex near the sheet has a more localized influence in the early stages of the interaction than a vortex farther away. The $\bar{r}$ guideline derived from the second moment of circulation appears therefore to be valid only when the vortex is very near the sheet. As the distance increases, the dispersion of the sheet does not increase as fast as anticipated by a direct $\bar{r}$ relationship. In the limit wherein the vortex is far from the sheet, the $\bar{r}$ guideline is misleading because no interaction occurs. These numerical examples show that there is not a sharp optimum for vortex height, but that the best distance for the vortex from the sheet depends on the initial spanwise structure of the sheet and on the final wake structure desired.

A similar result was found for the ratio of the strength of the auxiliary vortex to that of the sheet; i.e., stronger vortices have a larger influence on the sheet but they also pose a greater hazard in themselves and impose a larger penalty in drag (and possibly in lift) than weaker vortices. The best strength, location, number, etc., for auxiliary vortices must then be chosen in a trial and error process to provide the desired wake dynamics from a given initial lift-generated wake.

A series of examples is presented in Figure 5 to illustrate the changes in wake dynamics that occur when various auxiliary vortices are added to a wake. For simplicity, the vortex sheet to be modified is assumed to be of constant strength as if it were shed by a wing with triangular span loading. The motion of the vortices was calculated using the numerical technique from references 8 and 10. The process for generating the vortices (whether by fins, fences, strakes, engines, etc.) is set aside for the present, and any effect the vortex-generating process might have on the span loading is ignored. Also, the strengths of all auxiliary vortices were taken to be 20% of the strength of the vortex sheet so that the sheet dynamics would be altered but not dominated by the addition of vortices above and/or below the sheet. The spanwise position chosen for all vortices was near the centroid at a little over halfway out to the wing tip. The interactions in Figure 5 are presented as sequential positions of the vortex elements for the same time increments after the beginning of the event so that comparison can be made of the promptness of or delay in any merger or dispersion. In these examples, the vortex was placed quite near the sheet to ensure a strong interaction and so that the vortices could be produced by short fins on the wing if the configuration were to be tested.

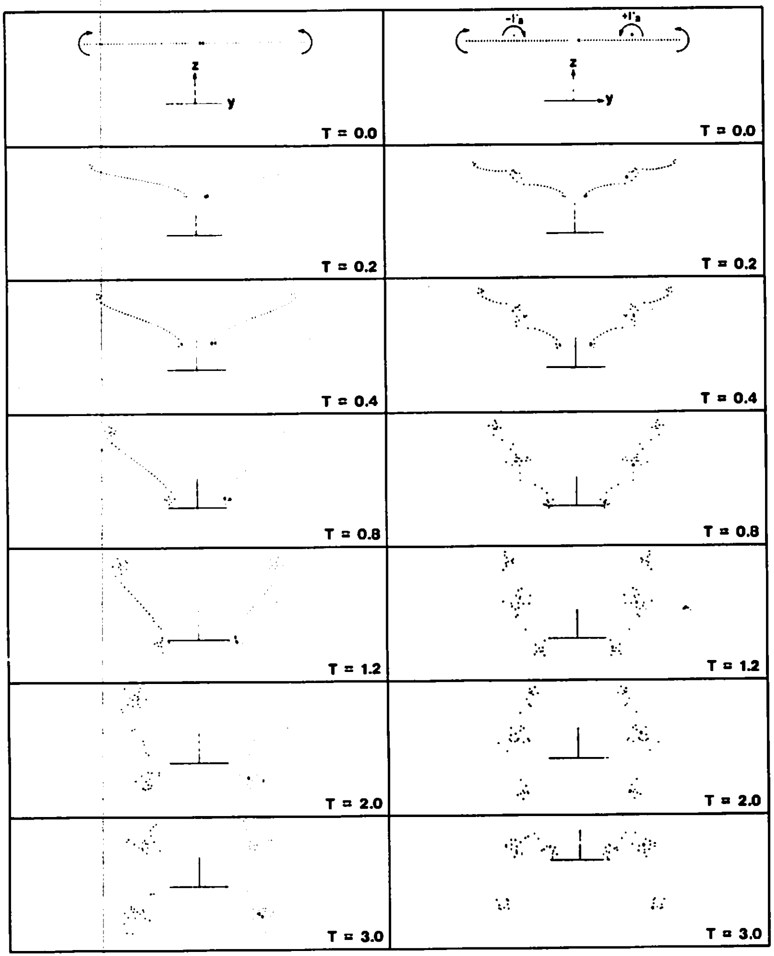

(a) Wake without auxiliary vortices.

(b) Positive vortex over sheet.

Figure 5. Effect of various auxiliary vortices on vortex wake shed by wing with triangular span loading. Vortex strength = ±0.2 × sheet strength = $\pm 0.7 bU_\infty$; vortex distance from sheet = ±0.025 b.

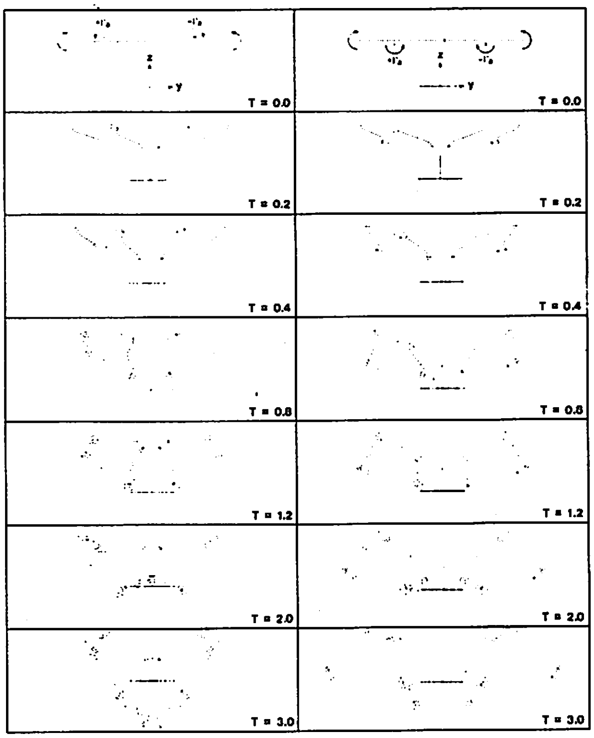

(c) Negative vortex over sheet.

(d) Negative vortex under sheet.

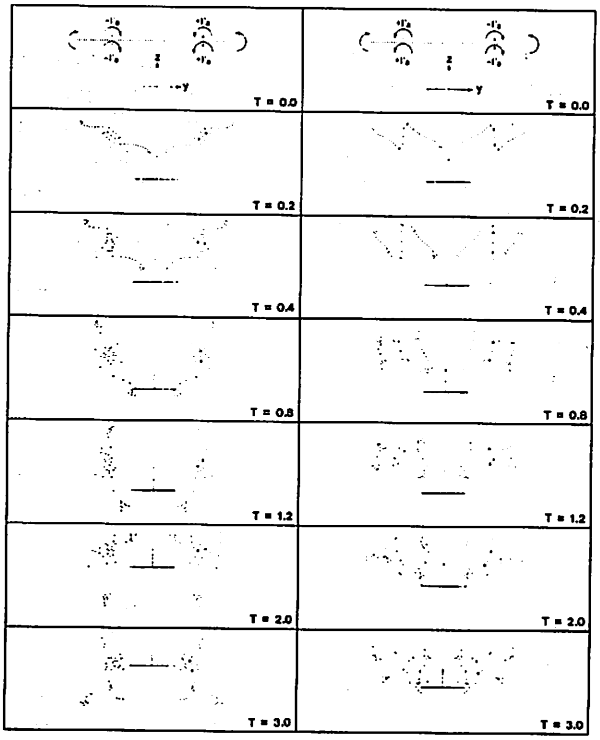

(e) Positive vortex over and under sheet.

(f) Negative vortex over and under sheet.

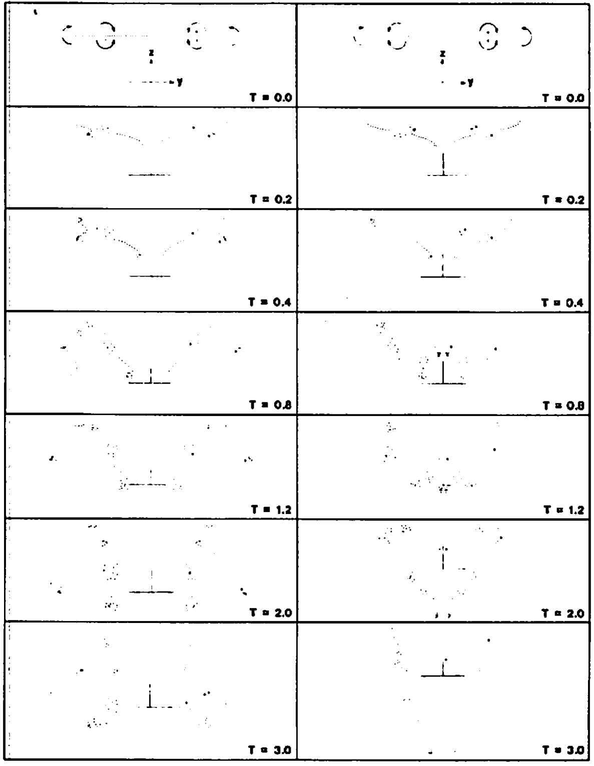

(g) Positive vortex over and negative vortex under sheet.

(h) Negative vortex over and positive vortex under sheet.

The examples in Figure 5 show that some of the details of the wake dynamics depend on whether the vortex is above or below (or both) the vortex sheet, but a great difference does not persist. A greater difference occurs in the subsequent vorticity distributions when the sign of the vortex changes from positive to negative. A negative vortex first tears the sheet and then appears to disperse the sheet more than a positive vortex. A negative auxiliary vortex also has the advantage that it reduces rather than increases the net circulation on each side of the centerline. Negative auxiliary vortices appear to produce wake motions comparable to sawtooth loadings.

The use of a single vortex or of two auxiliary vortices of one sign is interesting from a conceptual point of view but, in practice, vortices can be generated only in pairs. The two situations shown in Figures 5(g) and 5(h) are more realistic in that they approximate a vertical fin crossing a wing with triangular span loading. The net circulation is therefore unchanged from the bare wing shown in Figure 5(a), but the wake motion is quite different. Both the inboard (Figure 5(g)) and the outboard (Figure 5(h)) deflection of the fin leading edge spread the circulation about the same amount. A determination as to which is most effective in practice requires experiments or an analysis that includes viscous and turbulent diffusion.

Wind-Tunnel Tests of Auxiliary Vortices from Wing Fins.

A wind-tunnel test of an aircraft configuration with two wing-fin configurations was used to obtain a preliminary estimate of the effectiveness of auxiliary vortices generated by fins mounted on the wing of a Boeing 747 model. The general test setup in the Ames 40- by 80-Foot Wind Tunnel is the same as that used previously [3]. The planform area of the wing fin in the first configuration was the same as that of two outboard spoilers and it was located at about the same spanwise

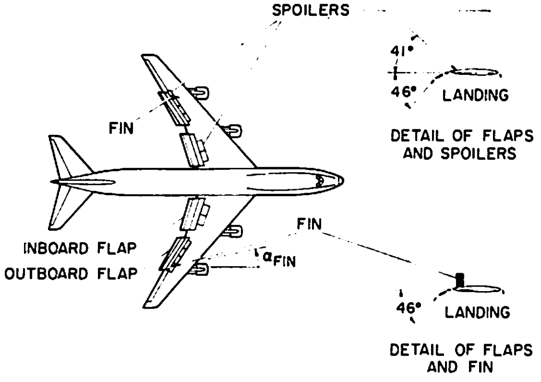

Figure 6. Subsonic transport model used in wind-tunnel tests to simulate a Boeing 747; fin area = area of two spoilers.

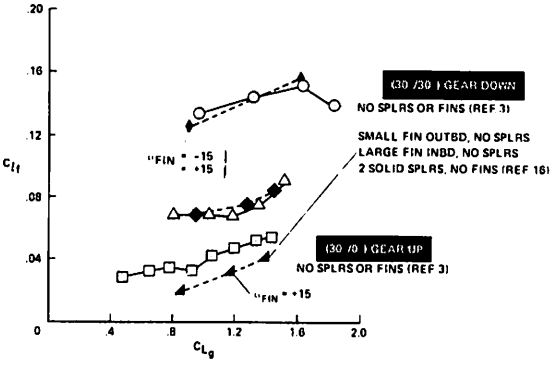

Figure 7. Comparison of maximum rolling moments measured on a wing in the wake of several configurations of a Boeing 747 model: $x_f/b_g = 13.6$, $b_f/b_g = 0.2$.

station (see Figure 6). In the second configuration, the fin was twice as large as in the first configuration, and it was mounted over the inboard engine nacelle. The fins were tested at both positive (i.e., α_{fin} is taken positive when its tip vortex is of the same sign as the wing-tip vortex) and negative deflections up to 15°. The rolling moment measured on a following model whose span is 0.2 of the generator span is compared in Figure 7 with several other configurations of the Boeing 747 tested with the same setup. At the 13.6-span downstream measuring station, the positive fin angles were found to be much more effective in reducing rolling moment than the negative angles. This result seems to contradict the numerical results. From the limited test results obtained so far, it is not certain whether negative fin angles do not provide favorable alleviation on the wing of the B-747 or that the measuring station should be farther downstream, or that another fin location on the wing should have been chosen.

A conclusion drawn from these tests is that the configuration tested with the small outboard fin did yield alleviation equal to the best spoiler configuration [4, 16]. The larger fin, located over the inboard engine nacelle, was even more effective and produced the most alleviation of the configurations tested in the 40- by 80-foot wind tunnel so far. Further tests are required to determine better guidelines for the use of fin-generated vortices for wake alleviation and to optimize the fin configuration for a given wing. A determination whether these devices will reduce the rolling-moment hazard to the level desired can then be made.

CONCLUDING REMARKS

A variety of vortex wakes was studied theoretically to find ways to reduce substantially the hazard posed by the lift-generated wakes of aircraft. Prior research and the first few examples presented here illustrate vortex interactions that lead to reduced wake velocities by either spreading out the vorticity or by combining vortices of opposite sign to neutralize the wake. These interactions require that several vortices be generated in the wake so that they alternate in sign across the span. It is then proposed that the desired dispersion might be achieved if extra vortices are introduced into or near the wake by the use of devices above and/or below the wing such as fins, fences, engines, etc. Some alleviation guidelines for the use of these auxiliary vortices were then obtained by studying the invariants for two-dimensional vortex systems, by calculating a number of numerical examples, and by a preliminary wind-tunnel experiment with a wing-mounted fin on an aircraft model. It was concluded that vortices shed by wing fins are effective in dispersing lift-generated wakes, and that the auxiliary or added vortices should be placed above or below the wing near the centroid of the vortex sheet shed by the lift. The effectiveness of the vortex does not seem to be very sensitive to its distance from the wing, provided it is not greater than about 30% of the semispan away. A determination of the maximum effectiveness of auxiliary vortices for alleviation (i.e., can a level of $C_{l_f} \leq 0.02$ be reached?) and the guidelines for minimizing the penalties associated with the devices that generate the vortex requires further experimental and theoretical research.

REFERENCES

1. Gessow, A., "Aircraft Wake Turbulence Minimization by Aerodynamic Means," 6th Conference on Aerospace and Aeronautical Meteorology, El Paso, TX, Nov. 12-14, 1974.

2. Tymczyszyn, J.J. and Barber, M.R., "A Review of Recent Wake Vortex Flight Tests," 18th Annual Symposium of Society of Experimental Test Pilots, Los Angeles, CA, Sep. 26, 1974, p. 52-68.

3. Corsiglia, V.R., Rossow, V.J., and Ciffone, D.L., "Experimental Study of the Effect of Span Loading on Aircraft Wakes," *J. Aircraft*, Vol. 13, No. 12, Dec. 1976, p. 968-973.

4. Croom, D.R., "Low-Speed Wind-Tunnel Investigation of Various Segments of Flight Spoilers as Trailing-Vortex-Alleviation Devices on a Transport Aircraft Model," TN D-8162, 1976, NASA.

5. Anon., Proceedings, NASA Symposium on Wake Vortex Minimization, Washington, D.C., Feb. 25-26, 1976, SP-409, NASA.

6. Sammonds, R.I. and Stinnett, G.W., Jr., "Hazard Criteria for Wake Vortex Encounters," TM X-62,473, Aug. 1975, NASA.

7. Tinling, B.E., "Estimation of Vortex-Induced Roll Excursions Based on Flight and Simulation Results," Conference on Aircraft Wake Vortices, Cambridge, MA, Mar. 15-17, 1977.

8. Rossow, V.J., "Theoretical Study of Lift-Generated Vortex Wakes Designed to Avoid Roll-Up," *AIAA J.*, Vol. 13, No. 4, Apr. 1975, p. 476-484.

9. Donaldson, C.duP. and Bilanin, A.J., "Vortex Wakes of Conventional Aircraft," AGARDograph 204, May 1975.

10. Rossow, V.J., "Convective Merging of Vortex Cores in Lift-Generated Wakes," *J. Aircraft*, Vol. 14, No. 3, Mar. 1977, p. 283-290.

11. Hackett, J.E. and Evans, P.F., "Numerical Studies of Three-Dimensional Breakdown in Trailing Vortex Wakes," AIAA Paper 76-416, 1976 (see also NASA CR-137,888).

12. Bilanin, A.J., Teske, M.E., Donaldson, C.duP., and Snedeker, R.S., "Viscous Effects in Aircraft Trailing Vortices," NASA Symposium on Wake Vortex Minimization, SP-409, 1976, p. 55-122, NASA.

13. Corsiglia, V.R. and Orloff, K.L., "Scanning Laser-Velocimeter Surveys and Analysis of Multiple Vortex Wakes of an Aircraft," TM X-73,169, Aug. 1976, NASA.

14. Ciffone, D.L. and Orloff, K.L., "Far-Field Wake-Vortex Characteristics of Wings," *J. Aircraft*, Vol. 12, No. 5, May 1975, p. 464-470.

15. Rossow, V.J., Corsiglia, V.R., Schwind, R.G., Frick, J.K.D., and Lemmer, O.J., "Velocity and Rolling-Moment Measurements in the Wake of a Swept-Wing Model in the 40- by 80-Foot Wind Tunnel." TM X-62,414, Apr. 1975, NASA.

16. Corsiglia, V.R. and Rossow, V.J., "Wind-Tunnel Investigation of the Effect of Porous Spoilers on the Wake of a Subsonic Transport Model," TM X-73,091, Jan. 1976, NASA.

MERGING DISTANCE CRITERIA FOR CO-ROTATING TRAILING VORTICES

JAMES D. IVERSEN, STEVEN A. BRANDT, AND PRADEEP RAJ
Iowa State University
Ames IA 50011

ABSTRACT: The merging of co-rotational vortices of equal strength is studied by flow-visualization and hot-wire anemometer wind-tunnel experiments and by preliminary numerical calculation of vortex merging. Wind-tunnel experiments and numerical calculations indicate that the effects of turbulence and viscosity are to decrease merging distance from that predicted by inviscid calculations. Hot-wire anemometer measurements of velocity profiles and rolling-moment measurements on a follower model show reduction of the trailing vortex hazard due to merging.

NOMENCLATURE

b	wingspan
C_{LG}	lift coefficient, generator wing
$C_{\ell F}$	rolling moment coefficient, follower wing
c	wing chord
d	vortex separation distance
d_0	initial vortex separation distance
d_c	vortex core diameter
d_M	vortex core diameter (based on angular momentum defect equal to that in a Rankine vortex)
d_Γ	vortex core diameter (based on circulation defect equal to that in a Rankine vortex)
ℓ	rolling moment
r	vortex radial coordinate
r_v	vortex radius, outer edge of rotational core
s	strain rate
t	time after vortex formation
U_∞	free stream speed
x_m	distance from vortex formation to merger
α	angle of attack
Γ	circulation, $2\pi r$ times tangential speed
Γ_1	circulation at peak tangential speed
Γ_0	large radius circulation
ν	kinematic viscosity
ϵ, ν_T	eddy viscosity.

INTRODUCTION

Among the several attempts at alleviation of the wake vortex hazard, NASA experiments have shown that the hazard to trailing aircraft from existing wide-body jets can be alleviated by alteration of span loading, either by use of spoilers [1] or unconventional flap settings [2]. If an inboard wing flap is deployed, a strong vortex is shed from the outboard edges of the inboard flap as well as from the wing tip. These vortices, of like rotational sense, may merge downstream, leaving a single vortex, more diffuse than that from a clean wing of the same strength, and thus of lesser hazard to trailing aircraft than the clean wing vortex.

To further investigate the vortex merging phenomenon, experimental research is being performed in the Iowa State University low-turbulence open-circuit wind tunnel. Flow-visualization and hot-wire anemometer measurements have been used to determine qualitative and quantitative data for single, interacting, and merged vortices. Two vortices were generated by semi-span wing models. Merging distances and vortex interactions prior to merging have been observed using flow visualization. A two-component hot-wire anemometer was used to measure single and merged vortex tangential speed distributions. Some of these results were presented by Brandt and Iversen [3].

TEST EQUIPMENT AND PROCEDURE

The open-circuit wind tunnel, with a maximum speed of 200 feet per second and a free-stream turbulence level of about 0.1 percent, has a test-section cross section of 30 by 36 inches and an adjustable test-section length ranging from 6 to 28 feet. Figure 1 illustrates schematically the general tunnel layout, showing locations of steam injection through the models or into the inlet, and relative locations of generating and following models. Additional details of the wing models and experimental procedure can be found in references 3 and 4.

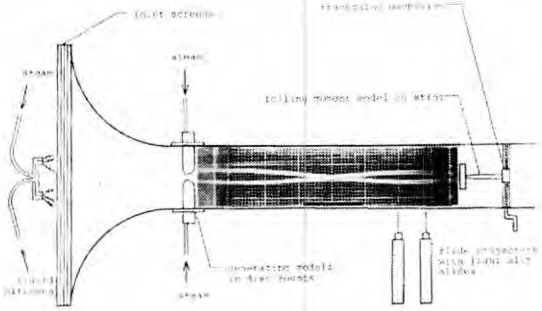

Figure 1. Wind tunnel schematic.

Measurement of merging distances, obtained with flow visualization using steam at maximum tunnel speed, consisted of setting the pair of wing models to given values of span and angle of attack. Figure 2 shows wing models inserted through opposite and adjacent test section walls. These primary models are NACA 0012 airfoils of constant 6-inch chord, except for the outboard 4 inches of the span, where the chord distribution is elliptical. Placing models in adjacent walls allowed equal values of circulation strength as in the opposite wall configuration (same wing span and angle of attack) while allowing a smaller initial vortex separation distance. The wing angles of attack were set to produce vortices of like rotational sense.

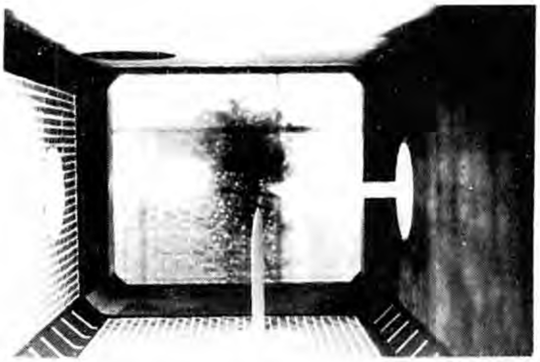

Figure 2a. Ellpitic tip wings mounted in adjacent test section walls.

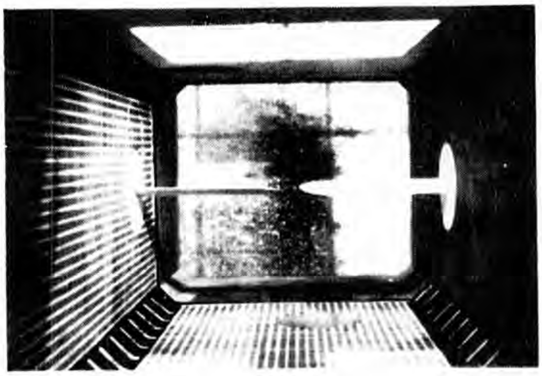

Figure 2b. Wings mounted in opposite walls.

A cross-wire hot-wire probe was inserted into the vortex from the side so as to minimize probe interference. Horizontal traverses through the center of the vortex were made for several vortex configurations. A following model was mounted on a strain-gage internal force balance to measure the rolling moment due to various generator configurations. Flow visualization using steam was used to center the model on the vortex. Fine adjustments of the follower position were then made to obtain maximum rolling moment.

FLOW VISUALIZATION

Steam flow-visualization photographs illustrating the two methods of injection are shown in Figures 3 and 4. In Figure 3, with flow from left to right, five light slits were projected from below the test section to illuminate condensed steam injected through the wings. The light slits are canted with respect to the free stream direction, so that the vortex cross sections can be seen more clearly from the side. The grid lines on the test section wall in the background are one inch apart. Flow visualization with full illumination of the test section with steam also injected through the wings is illustrated in Figure 1. In Figure 4, with three light slits, steam is injected through the inlet, resulting in visibility of a greater portion of the two shed vortex sheets. In both Figures 3 and 4, the separation distance between the two vortices is small, and the rate of rotation with the downstream distance of the line connecting the vortex centers is therefore relatively rapid.

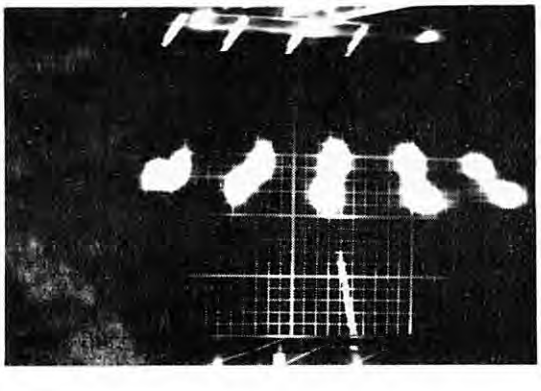

Figure 3. Flow visualization of interacting corotating vortices: flow from left to right; five transverse light slits; speed, 200 ft/sec; steam inserted through wings.

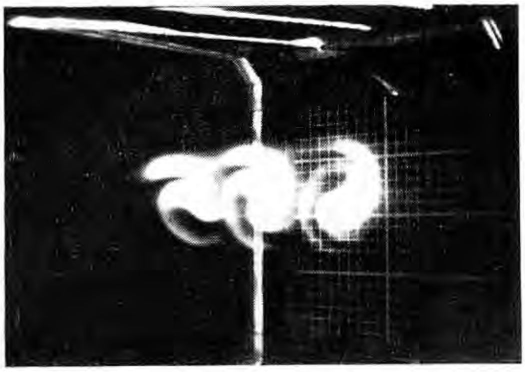

Figure 4. Flow visualization of interacting corotating vortices: flow from left to right; three transverse light slits; speed, 200 ft/sec; steam inserted through inlet.

The merging of two co-rotating vortices is illustrated with full test-section illumination in Figure 5, with steam injected through the wing models. The merging takes place relatively quickly. As discussed in much more detail in references 3 and 4, the separation distance between the two vortex centers decreases gradually with distance downstream until close to the merger point, where the separation distance decreases at a much faster rate and the vortex core shapes also distort rapidly until merger takes place. The unmerged vortices can be seen at the left of the photograph with merger taking place slightly to the left of the center of Figure 5a. In Figure 5b, steam is injected through just one of the wings, and in Figure 5c, it is injected through the other one. The flow patterns are essentially indistinguishable downstream of the merging point, indicating that only one vortex remains.

Figures 6 and 7 illustrate the merged vortex with light-slit illumination. In the second slit in Figure 6 in the newly merged vortex, the vortex cross section appears as the lateral trace of a nested pair of spiral sheets, each sheet originating from one of the two wings. A common feature of vortex flow visualization is the clear area in the center of the core, where visible particles are centrifuged outward by the swirling flow. In the newly merged vortex, the core center appears to be initially filled with visible particles, but farther downstream the centrifuged clear area reappears. A tiny clear area in the center of the merged vortex has begun to appear in the downstream light slit of Figure 7. Measurements of the merging distance for a variety of initial vortex strengths, separation distances, and span-lift distributions were made by passing a single light slit rapidly downstream and noting the merging location as the downstream position where the two clear areas disappeared. The merging distance thus defined could be pinpointed to within an accuracy of 1 to 2 inches. The results of these measurements are presented in a later section.

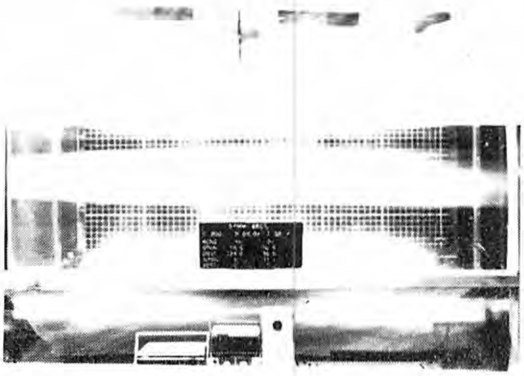

Figure 5a. Flow visualization of merging co-rotating vortices: flow from left to right; full illumination; speed, 200 ft/sec; steam inserted through wings; merging taking place just left of center.

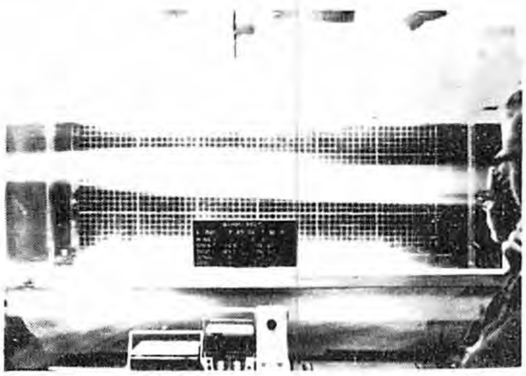

Figure 5b. Steam through one wing only; pattern downstream of merging unchanged.

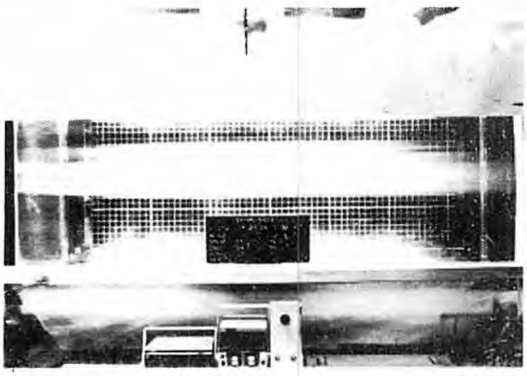

Figure 5c. Steam through other wing only.

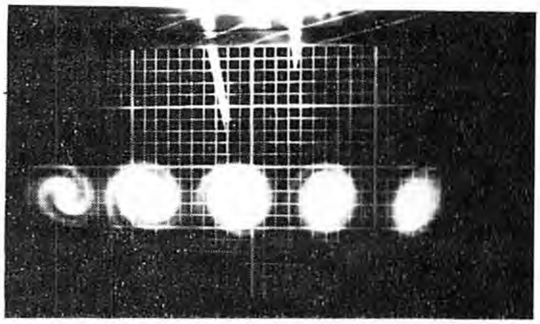

Figure 6. Flow visualization of merged vortex; flow from left to right; note nested spiral pair in second light slit from left.

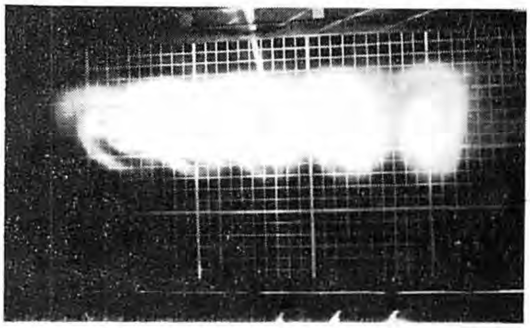

Figure 7. Flow visualization of merged vortex; flow from left to right; note centrifuged clear area in center of vortex at downstream light slit.

HOT-WIRE MEASUREMENTS

One of the major problems in measuring the characteristics of trailing vortices is the effect of measuring probe interference. Figure 8 illustrates one of these experiments with a dummy hot-wire probe and with the vortex illuminated with two light slits. The probe is parallel to the vortex axis and near the center of the core. The second slit illustrates one effect of the presence of the probe which is to enlarge the vortex core size as the vortex flow passes the probe. This is usually an unsteady phenomenon in which the core diameter pulsates at a relatively low frequency. Moving the probe laterally can also cause the vortex to move laterally either toward or away from the probe. Flow-visualization experiments seemed to indicate that a slender probe inserted in a direction normal to the vortex axis caused the least amount of probe interference so subsequent hot-wire experiments are being conducted in that manner. A laser velocimeter is currently being used to measure vortex speeds, and hot-wire measurements will be compared with these results.

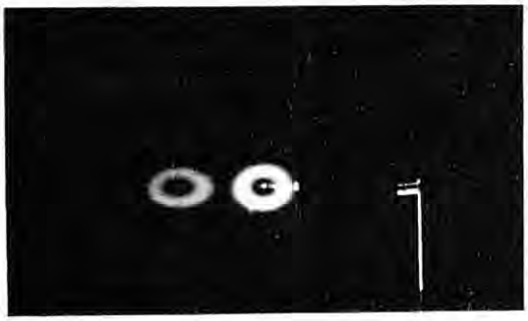

Figure 8. Flow visualization of probe interference; note enlarged core structure as vortex flow passes probe.

Measurements made with a three-wire hot-wire anemometer of the tangential speed (plotted in terms of circulation) in the vortex shed from one of the elliptical-tip wings is illustrated in Figure 9. Also shown is the inviscid Betz circulation profile [5] calculated from the theoretical lifting-line span-load distribution on the wing. Agreement between the inviscid theory and experiment is good except in the viscous core region and for values of large radius where part of the vorticity sheet which is still rolling into the vortex was encountered by the hot-wire probe. It is possible that some of the data scatter at smaller radius is also due to layering of the rolled-up sheet. The data were taken at a distance of 9.6 semi-span-lengths downstream of the wing. The value of circulation Γ_1/Γ_0 at peak tangential speed is 0.456 (or 0.347 from the faired dashed line), and the Reynolds number Γ_0/ν is 110,000.

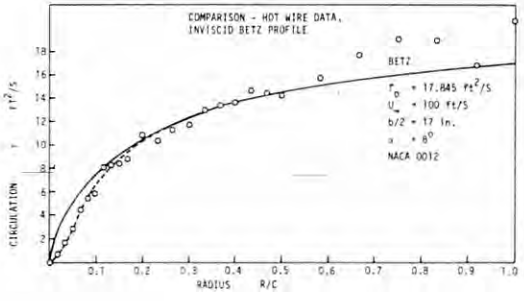

Figure 9. Vortex circulation versus radius — comparison of hot-wire anemometer data with inviscid (Betz) profile (single wing vortex).

Tangential velocity distributions from two-wire hot-wire measurements are presented in Figure 10 for two interacting vortices and for the resulting merged vortex. The upper third of the figure shows the results of a traverse through the two vortices prior to merger. The probe was located 16.8 semi-spans downstream of the wings. In the middle third of the figure, the traverse was taken at the merging point, again at 16.8 semi-spans downstream of the wings (smaller initial separation distance). In this case, only a single merged vortex is evident from the data. Of interest is the fact that the peak tangential speed is about the same for the merged vortex as for the single vortex, although the large radius circulation is twice as great. The lower third of Figure 10 illustrates a traverse taken at 6.5 semi-spans downstream of the merging point (again 16.8 semi-spans downstream of the wings). The peak tangential velocity has decreased slightly from the survey taken at merger. The Reynolds number Γ_0/ν for each single vortex was 250,000 and was twice that for the merged vortex. Since at large radius the circulation in the merged vortex is twice that of a single vortex but the peak tangential velocity is no larger, the relative hazard of a merged vortex would appear to be smaller. This is proven to be the case in the following section.

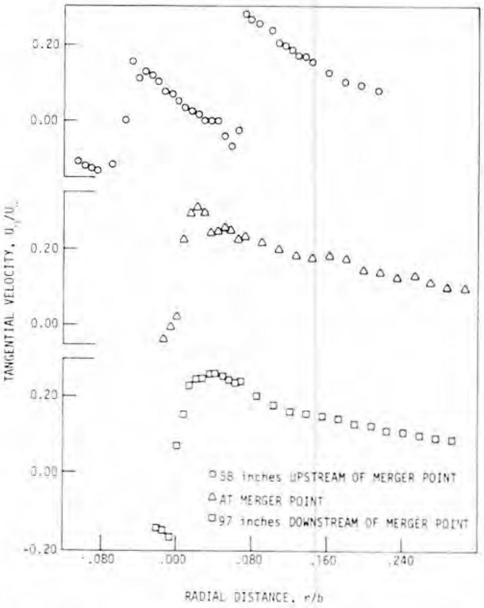

Figure 10. Hot-wire anemometer tangential speed profiles upstream, at, and downstream of merging.

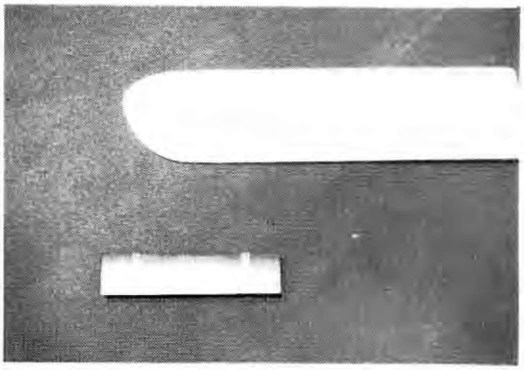

Figure 11a. Elliptic tip generator wing (6-inch chord, NACA 0012 airfoil) and follower wing (2.5-inch chord, 10-inch span, NACA 0015 airfoil).

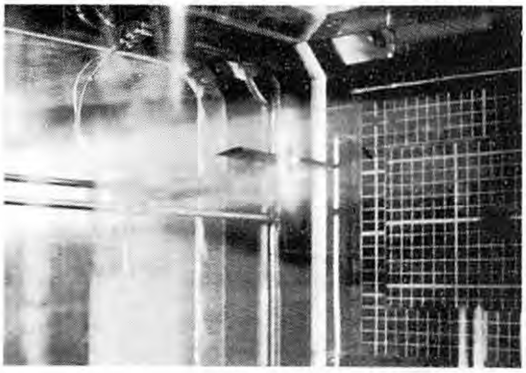

Figure 11b. Follower model mounted on traversing mechanism centered on merged vortex.

ROLLING-MOMENT MEASUREMENTS

The generator and follower models are shown in Figure 11a. The follower model mounted (313 inches downstream from generator) in the wind tunnel is shown in Figure 11b. The follower model is a 10-inch span, 2.5-inch chord NACA 0015 airfoil mounted on an internal strain-gage force balance. The rolling moment was found by first positioning the model in the center of the vortex with flow visualization as shown in Figure 11b, and then measuring the rolling moment maximum by making fine adjustments in the follower model position.

The maximum rolling moment coefficient on the follower model is plotted versus lift coefficient on the generator models in Figure 12. The generator lift coefficient is that for a single wing for the single vortex, but is defined to be twice that for a single wing for the merged vortex. Thus the true relative hazard (dimensionless follower rolling moment versus dimensionless generator lift) is as shown in the figure. The relative hazard for the merged vortex is only about 70 percent that for the single vortex. This reduction in hazard corroborates similar findings for merged vortices shed from transport aircraft [6]. The values of rolling moment obtained are listed in Table 1. Comparing the rolling moment data for one wing at 12-degree angle of attack with the merged data for two wings at 6 degrees (same total circulation, semi-span equal to 15.5 inches) results in a reduction of the rolling moment for the merged case of 31 percent. It can also be noted from the table, particularly for the 6-degree angle of attack, that the rolling moment coefficient appears to be nearly independent of merging distance.

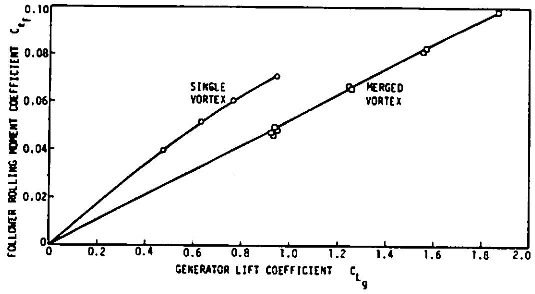

Figure 12. Following rolling moment coefficient versus generator lift coefficient — single and merged vortices.

Table 1. Rolling Moment Data for Single and Merged Vortices.

No. Wings	α	b/2 (in)	x_m (in)	Γ_0 (ft^2/s) (total)	ℓ (in-lb)	C_{ℓ_F}	C_{LG} (each wing)
1	6	15.5	—	26.2	0.223	0.0394	0.471
1	8	15.5	—	35.0	0.293	0.0517	0.628
1	10	14	—	42.7	0.342	0.0604	0.765
1	12	15.5	—	52.5	0.397	0.0702	0.942
2	6	14.25	260	51.4	0.301	0.0473	0.461
2	6	14.5	258	51.7	0.298	0.0468	0.463
2	6	14.75	195	51.9	0.301	0.0473	0.465
2	6	15	92	52.1	0.314	0.0493	0.467
2	6	15.5	0	52.5	0.307	0.0483	0.471
2	8	15	70	68.9	0.361	0.0665	0.623
2	8	15.5	0	70.0	0.419	0.0658	0.628
2	10	15	57	86.8	0.518	0.0813	0.778
2	10	15.5	0	87.5	0.525	0.0825	0.785
2	12	15	48	104.2	0.623	0.0978	0.934

MERGING DISTANCE CRITERIA

If the time measured from formation of two equal-strength infinite co-rotating vortices to the instant of merging into one merged vortex is assumed to be only a function of vortex strength Γ_0, initial separation d_0, and core diameter d_c, then it would be expected that the dimensionless time to merge could be written.

$$\frac{t\Gamma_o}{d_c^2} = f(d_o/d_c) , \qquad (1)$$

or, in the analogous situation for trailing vortices,

$$\frac{x_m\Gamma_o}{U_\infty d_c^2} = f(d_o/d_c) . \qquad (2)$$

To use Equation (2), it is necessary to find an appropriate definition of core diameter d_c (or use another reference length, such as wing span) in order that experimental values of merging distance can be correlated. Rossow's [7] calculation of inviscid merging boundaries led to a search for a normalizing diameter which would not only correlate his merging boundaries for various circulation profiles but also provide the correlation reference diameter for Equation (2). Two such normalizing diameters were found, as discussed in reference 3. The two reference diameters were formulated by equating the defects in circulation and angular momentum for inviscid Betz vortex profiles to the same defects for a Rankine vortex of core diameter d_Γ or d_M respectively, i.e.,

$$d_\Gamma = 3\int_0^{r_v} (1 - \Gamma/\Gamma_o)\,dr\,, \qquad (3)$$

and

$$d_M = 4\left[\int_0^{r_v}\left(1 - \Gamma/\Gamma_o\right) r\,dr\right]^{\frac{1}{2}} \qquad (4)$$

As shown in reference 3, either reference diameter is fairly successful in coalescing Rossow's merging boundary curves to a fairly narrow region (when the ratio of circulation strengths for two vortices is plotted versus the normalized separation distance, d_0/d_Γ or d_0/d_M). The two reference diameters have also proven useful in correlating the wind tunnel merging data as shown in Figures 13 and 14. In Figure 13 the core diameter d_c in Equation (2) is defined as the angular momentum deficit diameter d_M, and in Figure 14 the circulation defect diameter is used. The data in Figures 13 and 14 can be approximately represented by the following straight lines, although there is a considerable amount of scatter for the larger separation distances:

$$\frac{x_m \Gamma_o}{U_\infty d_\Gamma^2} = 55.9(d_o/d_\Gamma) - 37.3\,, \qquad (5)$$

$$\frac{x_m \Gamma_o}{U_\infty d_M^2} = 39.2(d_o/d_M) - 18.3\,\cdot \qquad (6)$$

A correlation with less data scatter is presented in the next section. The numerical values of merging distance are tabulated in reference 4.

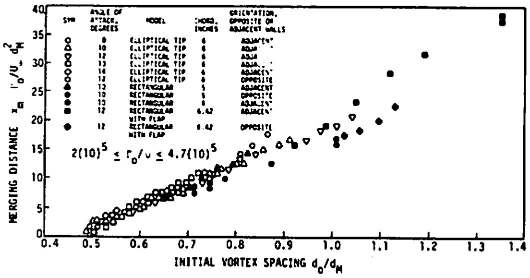

Figure 13. Distance to merge versus initial vortex separation distance (normalized by angular momentum defect diameter).

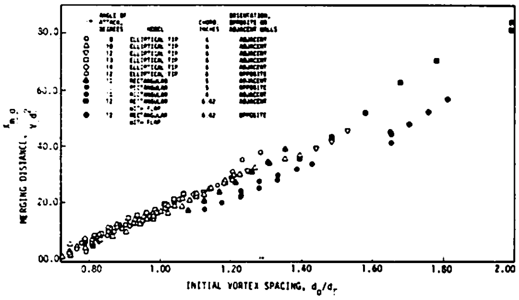

Figure 14. Distance to merge versus initial vortex separation distance (normalized by circulation defect diameter).

EFFECT OF FREE-STREAM TURBULENCE ON MERGING DISTANCE

Two different turbulence grids were fabricated and placed forward of the wind tunnel test section in order to ascertain the effect of ambient turbulence on merging distance. The grid tried first consisted of 0.2-inch wide flat strips arranged in a rectangular grid with a grid spacing of 0.75 inches. The longitudinal turbulence level created at the location of the vortex generating wings, while not determined experimentally, should be on the order of 3 percent. For this grid, there proved to be no discernible effect on merging. A second grid was then tried, this time consisting of 0.63-inch diameter tubes with a 3-inch grid spacing welded in a biplane arrangement. The generator wings were placed 22 inches downstream of the grid where the turbulence level would be approximately 8 to 10 percent. Table 2 lists the merging distances obtained.

Table 2. Merging Distance Measurements with Grid Turbulence.

α^o	b/2 (in)	d_o (in)	d_Γ (in)	d_o/d_Γ	$\Gamma_o/U_\infty b$	X_m (in)	$x_m\Gamma_oU_\infty cb$
10	14	5.5	4.60	1.20	0.0915	101	1.54
10	13.75	5.85	4.55	1.29	0.0927	141	2.18
10	13.5	6.17	4.51	1.37	0.0940	181 to 211	2.84 to 3.31
10	13.25	6.5	4.47	1.45	0.0952	201 to 241	3.19 to 3.83

Merging distance measurements downstream of the large grid were not easy to obtain because of the large amplitude rapid lateral 'meander' due to the high stream turbulence level and large grid spacing. For the larger separation distances the location of the merging distance was very erratic and shifted upstream and downstream with changes in merging distance of 30 to 40 inches taking place quite rapidly. Merging distances were measured at a maximum tunnel speed (with grid) of 125 ft/sec. The normalized merging distances are plotted as a function of the initial vortex spacing in Figure 15. Also plotted in this figure are the low stream turbulence data for comparison. The conclusions from these data are that free-stream turbulence can significantly decrease merging distance, but the integral scale must apparently be on the order of the initial vortex separation distance in order for this to occur. For the high turbulence data presented, the initial separation distance was about twice the turbulence-grid spacing. Also to be noted from Figure 15 is that the normalization $x_m\Gamma_0/U_\infty cb$ seems to coalesce the low turbulence merging data somewhat better than the correlations of Figures 13 and 14. The equation representing a least-squares fit to the data [3] is

$$\frac{x_m\Gamma_o}{U_\infty bc} = 6.69(d_o d_\Gamma) - 4.47 \cdot \qquad (7)$$

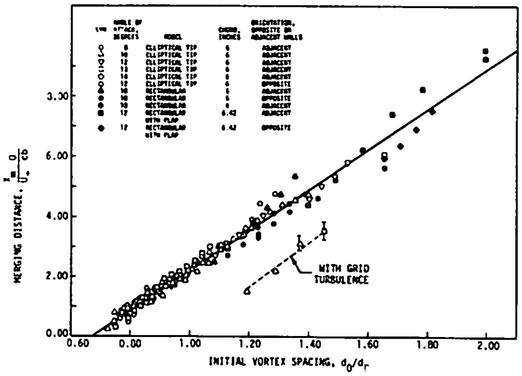

Figure 15. Distance to merge versus initial vortex separation distance — low and high (grid-generated) free stream turbulence.

EXTRAPOLATION FOR UNEQUAL VORTICES

Corsiglia and Orloff [8] have made estimates of multiple vortex circulation strengths and circulation profiles from wind tunnel experiments on a flapped jet-transport model. Ciffone and Orloff [9] presented flow-visualization data for a similar model in a tow-tank from which estimates of merging distance were made for those cases in which wing-tip and flap vortices appeared to merge. Two configurations are of interest. In the first, both inboard and outboard flaps are deployed in a conventional landing configuration. The two vortices, shed on each semi-span from the wing-tip and from the outboard edge of the outboard flap, merge fairly quickly, within one to four span-lengths [8, 9], since the initial separation distance is small. In the second configuration, only the inboard flap is deployed. The tip vortex and that shed from the outboard edge of the inboard flap merge a considerably farther distance downstream (13 span-lengths or greater) since the initial separation distance is 2.4 times larger [8]. Values of circulation defect diameter for each vortex were calculated from the data of reference 8. For each configuration, the values of diameter d_Γ and circulation Γ for the two vortices were averaged, and the merging distance was calculated from Equation (7). The calculated values of merging distance of 1.2 span-lengths for the conventional configuration and 25 span-lengths for the inboard-flap configuration agree qualitatively with the observed values. The extrapolation to this situation is very tentative, however, since the tip and flap vortex strengths differ considerably for both cases and since the correlation curves presented here are strictly only for equal-strength vortices.

PRELIMINARY NUMERICAL CALCULATIONS OF MERGING DISTANCE

It is intended to extend the merging distance criteria presented here to larger downstream distances, nonsimilar circulation profiles, and unequal vortex strengths by means of numerical integration of the two-dimensional Trefftz-plane equations of motion. Preliminary results are shown in Figure 16. The lower curve (curve 4) is Equation (7), representing the experimental data. The remaining merging distance curves shown have been calculated using the basic method of Steger and Kutler [10] but with various viscosity models. The upper curve is the inviscid numerical solution starting with two vortices corresponding to elliptically loaded wings with a semi-span of 15 inches and an angle of attack of 10 degrees and for a variety of initial separation distances. The initial vortex profiles were taken from Iversen [11]. The distance between the vortices is monitored as a function of time by particle tracking. The inviscid solution appears to be approaching a vertical asymptote which would agree with the existence of an inviscid merging boundary as calculated by Rossow [7]. Numerical (artificial) viscosity appears to be pushing the boundary to the right of the $d_0/d_\Gamma = 1.7$ value, however [3, 7].

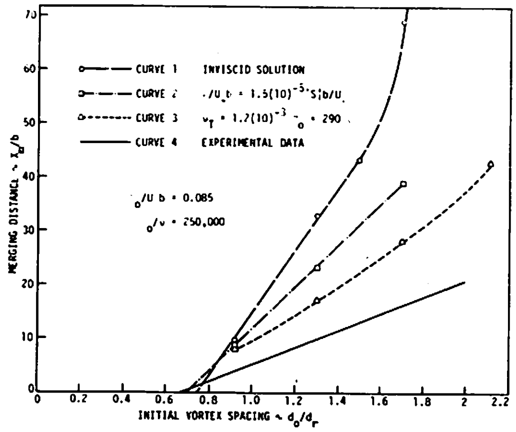

Figure 16. Distance to merge versus initial vortex separation distance — inviscid and viscous two-dimensional numerical calculations.

The two viscous calculations look more like the straight-line fit to the experimental data, except that the values of eddy viscosity chosen are not sufficiently large for the vortices to merge as quickly as in the wind tunnel. Also, the constant eddy-viscosity line is slightly curved rather than straight. Curve 2 represents a simple eddy viscosity mixing-length model (eddy viscosity proportional to magnitude of the strain rate), and curve 3 is the result of a constant eddy-viscosity model. The magnitude of the eddy-viscosity coefficients will be adjusted so as to match the experimental data. These solutions as well as the experimental data show no tendency of approach to a merging boundary for the values of initial separation distance investigated thus far. More sophisticated turbulence models will also be evaluated with the program and eventually full three-dimensional equations may be modeled [10]. The encouraging facets of the numerical predictions thus far are that (1) the eddy viscosity calculations result in straight lines for merging distance versus initial separation distance and (2) all curves intersect the horizontal axis at about the same value of initial separation distance. The merging distances measured in the wind tunnel were all for original vortices still in the so-called 'plateau' region [11-14]. It may be possible that significant changes in the merging phenomenon would occur if merging were to take place in the downstream decay region. Numerical solutions might also be of value in answering that question.

CONCLUSIONS

Flow visualization using condensed steam has been used to obtain a criterion for the distance to merge of two equal-strength, identical profile, co-rotating trailing vortices. The correlation of data represented by the low turbulence curve of Figure 15 is remarkably good considering that it was derived entirely by flow-visualization techniques. Wind tunnel flow-visualization experiments were also used to show that grid-produced turbulence can reduce the merging distance significantly, but the integral-scale of the turbulence must be large enough to be of the same order of magnitude as the initial separation distance.

Comparison of tangential-speed profiles for single and merged vortices shows that, although the merged vortex contains twice the large radius circulation of a single vortex shed from just one wing, the peak tangential speed is no higher for the merged vortex. This change in vortex profile results in reduced hazard to following aircraft. Measurements on a follower model show a 30 to 35 percent reduction in relative rolling moment from the merged vortex. Design of future large aircraft should include the consideration of vortex-hazard reduction devices, but much work remains before such design considerations can be optimized.

Preliminary numerical calculations of vortex merging show good promise of corroborating wind-tunnel results with relatively simple turbulence modeling. It should be possible to perform calculations extending merging distance criteria to include the cases of non-identical profile and unequal-strength vortices.

ACKNOWLEDGMENT

This research is supported by the NASA, Ames Research Center, and the Iowa State University Engineering Research Institute. Appreciation is expressed for help in hot-wire measurements, model design, and other technical problems to L.N. Wilson, V.R. Corsiglia, R.A. Martin, D. Sikavi, and S. Ford.

REFERENCES

1. Croom, D.R., "Wind Tunnel and Flight Evaluation of Spoilers as Trailing-Vortex Hazard Alleviation Devices," AIAA Paper 77-10, AIAA 15th Aerospace Sciences Conference, Los Angeles, CA, Jan. 1977.
2. Corsiglia, V.R. and Dunham, R.C., Jr., "Aircraft Wake-Vortex Minimization by Use of Flaps," NASA Symposium on Wake Vortex Minimization, Washington, DC, SP-409, 303-336, 1976.
3. Brandt, S.A. and Iversen, J.D., "Merging of Aircraft Trailing Vortices," AIAA Paper 77-8, AIAA 15th Aerospace Sciences Conference, Los Angeles, CA, Jan. 1977.
4. Brandt, S.A., "Interaction and Merging of Aircraft Trailing Vortices," Master of Science Thesis, Iowa State University, Ames, IA, 1976.
5. Rossow, V.J., "On the Inviscid Rolled-Up Structure of Lift Generated Vortices," *J. Aircraft*, 10, 647-650, 1973.

6. Corsiglia, V.R., Rossow, V.J., and Ciffone, D.L., "Experimental Study of the Effect of Span Loading on Aircraft Wakes," *J. Aircraft*, 13, 968-973, 1976.

7. Rossow, V.J., "Convective Merging of Vortex Cores in Lift-Generated Wakes," AIAA Paper 76-415, 1976.

8. Corsiglia, V.R. and Orloff, K., "Scanning Laser-Velocimeter Surveys and Analysis of Multiple Vortex Wakes of an Aircraft," NASA TM-X-73,169, 1976, U.S. Department of Transportation Conference on Aircraft Wake Vortices, Mar. 1977.

9. Ciffone, D.L. and Lonzo, C., Jr., "Flow Visualization of Vortex Interactions in Multiple Vortex Wakes Behind Aircraft," NASA TM-X-62,459, 1975.

10. Steger, J.L. and Kutler, P., "Implicit Finite-Difference Procedure for the Computation of Vortex Wakes," AIAA Paper 76-385, 1976.

11. Iversen, J.D., "Inviscid to Turbulent Transition of Trailing Vortices," AIAA Paper 75-883, 1975.

12. Ciffone, D.L. and Orloff, K.L., "Far Field Wake Vortex Characteristics of Wings," *J. Aircraft*, 12, 464-470, 1975.

13. Iversen, J.D., "Correlation of Turbulent Trailing Vortex Decay Data," *J. Aircraft*, 13, 395-411, 1976.

14. Hallock, J., Burnham, D.C., Tombach, I.H., Brashears, M.R., Barber, M.R., and Zalay, A.D., "Ground-based Measurements of the Wake Vortex Characteristics of a B-747 Aircraft in Various Configurations," AIAA Paper 77-9, AIAA 15th Aerospace Sciences Conference, Los Angeles, CA, Jan. 1977.

MEASUREMENTS OF AIRCRAFT WAKE ALLEVIATION AND GROUND PLANE EFFECTS

DONALD L. CIFFONE
NASA Ames Research Center
Moffett Field CA 94035

ABSTRACT: In support of the NASA wake vortex alleviation program, vortex trajectories and velocity profiles were measured in lift-generated wakes. The wakes were generated by towing 0.61-m (2-ft) span models of B-747 and DC-10-30 aircraft under water in a ship model basin. The effects of flaps, spoilers, and ground plane on these wakes were investigated. A laser velocimeter was used to measure vertical (tangential) velocity profiles through primary vortices from 5- to 100-wingspan lengths behind the generating model. A 45° deflection of the two outboard flight spoilers on the B-747 model in the landing configuration resulted in a 40% reduction in wake maximum tangential velocity, in altered velocity profiles, and in erratic vortex trajectories. Similar reductions in maximum tangential velocity were obtained for this model when the outboard flaps were retracted. Presence of a ground plane used to simulate full-scale distances above the ground of 38 m (125 ft) and 21 m (70 ft) modified the vortex trajectories but did not appreciably change vortex interactions and merging. However, at 21 m above the ground plane, the alleviation appeared to be enhanced due to vortex viscous interactions with the ground plane.

NOMENCLATURE

Å = angstrom, units of wavelength (10^{-8} cm)
b = wing span, 0.61 m
C_L = lift coefficient
h = height above ground plane, measured to wing leading edge at wing root
LDG = landing configuration, trailing-edge flaps deflected 46°, leading-edge flaps deployed, landing gear extended, spoilers 0°
LDG (S) = same as LDG but with spoilers deflected upward 45°
LDG/0 = same as LDG but with outboard trailing-edge flaps retracted
LDG/0 (GR) = same as LDG/0 but with landing gear retracted
LV = laser velocimeter
MAC = mean aerodynamic load
U_∞ = towing speed, m/sec
V_x = vortex axial (streamwise) velocity component
V_z = vortex tangential (vertical) velocity component
X = streamwise position, positive downstream of wing tip trailing edge
Y = spanwise position, positive outboard from fuselage centerline in direction of right semispan
Z = vertical position, positive upward from wing tip trailing edge
α = model angle of attack
Δ = unit change.

INTRODUCTION

This experimental study is part of a concerted effort to reduce the hazard potential of lift-generated wake vortices that trail heavy aircraft. Recent research [1] has established that both turbulence produced by flight spoilers and favorable span-load gradients induced by selective flap settings, are effective in alleviating concentrated wake vorticity. Both of these concepts have been shown [1] to be applicable to the B-747 airplane. However, it is not completely understood how landing gear deployment adversely affects wake alleviation obtained by span-load modification [1], what flow mechanisms are responsible for the alleviation achieved with properly placed spoilers [2], or what effect a ground plane has on these wake alleviation concepts.

As part of an experimental investigation to help clarify these uncertainties, quantitative measurements were obtained in the wake downstream of a B-747 aircraft model configured with spoilers and flaps to alleviate concentrated wake vorticity, and in the wake of a model of the DC-10-30 with and without spoilers. The experiment was performed in the University of California's ship model basin at Richmond, California. Vortex trajectory information was obtained from photographic records of dye-marked vortices. Vortex velocity profiles in the wake were measured using a scanning laser velocimeter. Data were obtained to distances of 100 span lengths behind the models; the models were fitted with removable flaps, flight spoilers, and landing gear. The mean chord test Reynolds number was 82,000.

EXPERIMENTAL APPARATUS AND PROCEDURE

Facility and Model Description.

The University of California's ship model basin is 61 m long, 2.44 m wide, and 1.7 m deep. Models are strut-mounted to an electrically driven carriage and towed through the water past a viewing station (Figure 1). At this station, large glass windows in the side of the tank allow the model wake to be observed as it ages and descends. All data were obtained at a model towing speed of 1 m/sec.

Several configurations of a 0.010 scale model of a B-747 aircraft were tested (Figure 2): (1) landing (LDG) with inboard and outboard flaps deflected 46° and leading-edge flaps extended; (2) LDG (S), same as LDG but with two outboard flight spoilers deflected upward at 45°; (3) LDG/0, same as LDG but with outboard flaps retracted; and (4) LDG/0 (GR), same as LDG/0 but with landing gear retracted. The spoilers had a chord of 12% of the MAC and were located forward of the outboard half of the outboard flap with trailing edges along the flap hinge line from 0.59 to 0.69 of the semispan. The 0.011-scale model of the DC-10-30 aircraft was tested (Figure 3) in the landing configuration (LDG) with inboard and outboard flaps deflected 50° and 45°, respectively, and leading-edge flaps extended; and in the LDG (S) configuration. The spoilers had a chord of 8.5% of the MAC and were located forward of the outboard half of the outboard flap with

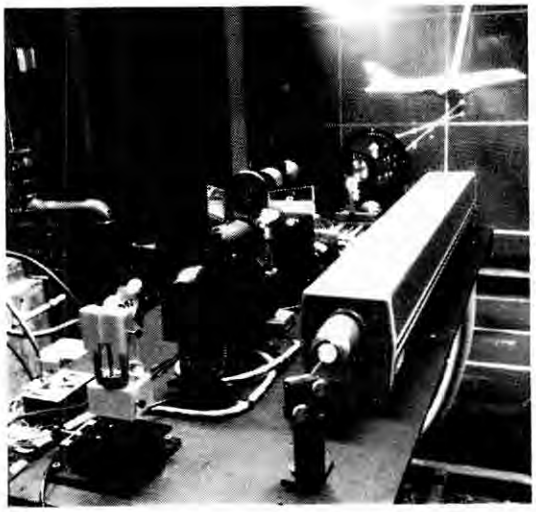

Figure 1. Test installation photograph.

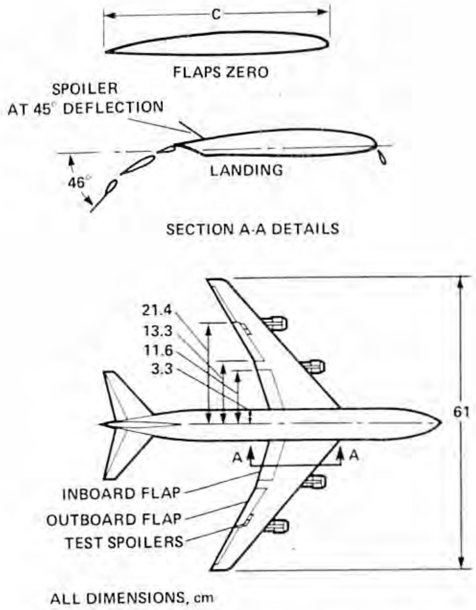

Figure 2. Sketch of 0.010-scale model of B-747.

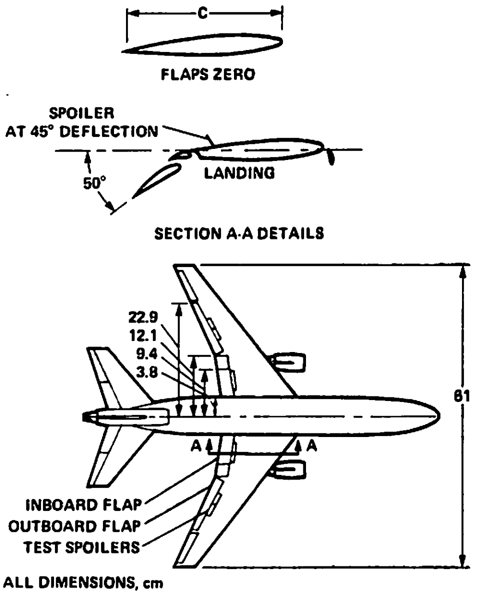

Figure 3. Sketch of 0.011-scale model of DC-10-30.

trailing edges along the flap hinge line from 0.51 to 0.61 of the semispan. With the exception of the B-747 LDG/0 (GR) configuration, all of the models were tested with landing gear extended. The models are equipped with dye-ejection orifices [3] to allow observation of the wake vortices that are generated in the water.

Experimental Procedure.

It has been concluded that the scaling laws for modeling fluid phenomena, pertinent to the study of wake vortices, are essentially the same for tests in water as in air, [4-6], and that the forces acting on hydrofoils operated at depths greater than 2 chord lengths are essentially unaffected by the free surface and are equal to those obtained on a wing operating in an infinite medium [7]. The model centerlines in these tests were located approximately 5 chord lengths below the free surface. Although the test Reynolds number (82,000 based on chord) was considerably less than full scale, general agreement in wake appearance [1] and vortex trajectories [8] was evident when comparisons could be made with flight data; wake data obtained in this test should, therefore, be indicative of flight results. This seeming lack of Reynolds-number sensitivity does not come as a complete surprise because previous wake vortex velocity measurements obtained in the ship model basin [5] on a variety of wing configurations correlated well with both wind-tunnel and flight measurements [9].

Dye was emitted from the models to allow visual and photographic tracking of the wake vortices as they moved through the water. In addition, the viewing section of the tank was seeded with polystyrene copolymer latex spheres to provide sufficient numbers of scattering particles to ensure laser velocimeter (LV) signals with adequate strength and resolution. The combination of a small particle size (diameters of 2 to 15 μ) and a specific gravity of 1.06 for these spheres ensures flow tracing fidelity. Depending on whether trajectory or velocity data were being measured, either the camera equipment or the scanning velocimeter was activated prior to the model's arrival at the viewing station; the timing for a run was initiated as the wing tip trailing edge passed a reference point. For velocity data, the elevation of the velocimeter was kept constant and the aging vortices allowed to descend through the LV's optical axis. After each run, the carriage was returned to the starting end of the tank, and the velocimeter was used to monitor water motion to ensure a calm tank prior to the next run (eddy velocities ≤ 0.004 m/sec). At a towing speed of 1 m/sec, the laser scanning rate was such that the rate of change of the age of the wake with lateral position of the focal point of the laser beams was $\Delta(X/b)/\Delta(Y/b/2) = 2$. Hence, during the scan of the vortex cores, the wake aged approximately 1/3 of a span (~ 0.2 sec).

Data Acquisition and Reference System.

Vortex trajectory data were obtained by illuminating a cross section through the wake (a Trefftz plan view) and photographically recording the positions of the dye-marked vortices as a function of time. An 800-W xenon arc lamp with a specially designed lens and light slit system was used to generate a thin light sheet across the tank. Photographs of vortex position were corrected for both camera viewing and cone angles. Vortex velocity profiles were obtained by spatially scanning the flow field behind the models with the single component laser velocimeter shown installed (Figure 1) at the viewing station of the tank and described in reference 10. A prism splits the green (5145 Å) output beam of the argon-ion laser into two parallel beams that pass through a scanning lens mounted on a motorized slide; the beams are subsequently crossed at a focal point in the water by the collector lens. The crossing angle of the two laser beams and the distance of their focal point from the tank wall are dependent on the scanning lens position. Velocities measured at the focal point represent vortex vertical velocity, V_z, or streamwise velocity, V_x, depending on the orientation of the LV when a core centerline penetration of the vortex is achieved.

Flow field velocities are presented as fractions of towing speed, U_∞, normalized by lift coefficient, C_L. Streamwise position, X, (positive downstream), spanwise position, Y, (positive outboard along the right wing), and vertical position, Z, (positive upward) are nondimensionalized by wingspan, b. The origin of these coordinates is the projected location of the wing tip trailing edge onto the fuselage centerline.

To investigate the effect of the presence of a ground plane on vortex interactions and merging, a 2 m by 2.5 m (7 ft by 8 ft) variable-height table was placed in the tank at the viewing station.

DISCUSSION OF RESULTS

The wakes of four configurations of the B-747 model (LDG, LDG (S), LDG/0, and LDG/0 (GR)) and two configurations of the DC-10-30 model (LDG and LDG (S)) will be discussed. Results from the dominant vortex pair in the wake (as determined from flow visualization studies) are presented as: (1) vortex trajectories in and out of influence of the ground plane, (2) vertical (tangential) velocity profiles, and (3) downstream dependence of maximum vertical velocity. Knowledge of *both* the trajectory and velocity change of a given vortex as different alleviation devices are tried should yield a better understanding of the flow mechanisms associated with a particular alleviation concept.

Vortex Trajectories.

Vortex trajectory data were obtained by marking the vortices and photographing them as they interacted or merged. Figure 4 presents vortex trajectory information for the B-747 model in the LDG configuration at ground plane heights of h/b = 0.63 and 0.35. This and subsequent figures relate the prominent vortex spanwise and vertical location. In addition, the figure includes contour lines of constant downstream position. In the landing configuration, the B-747 sheds five vortices from each side of the wing. Four of these vortices are due to the span-loading gradients caused by the flaps; the fifth is due to the span-load gradient at the wing tip. The dominant vortex is shed from the outboard edge of the outboard flap. At a distance of 5 span lengths behind this configuration, the wing-tip vortex has moved upward and inboard and completely merged with the flap vortex. The result is a persistent vortex. The remaining flap vortices merge with the vortices from the tips of the horizontal stabilizer and form a region of diffused vorticity at and below the aircraft centerline [3].

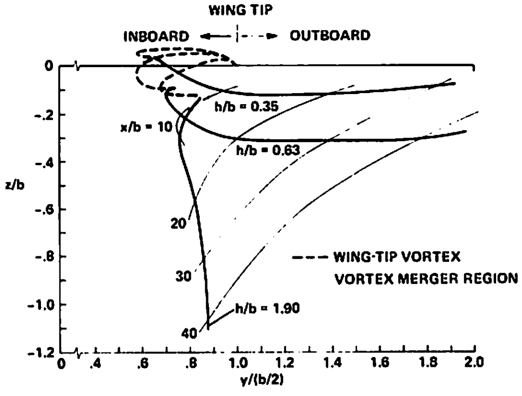

Figure 4. Vortex trajectory data; B-747 LDG configuration: C_L = 1.27, α = 2.9°.

Figure 4 shows a composite trajectory of the wing-tip vortex initially (starting at y/(b/2) = 1.0) and then the dominant flap vortex after merger at 5 span lengths. The merger occurs at the sharp bend in the curve at a z/b ≃ −0.13 for the h/b = 1.9 trajectory. The presence of the ground plane causes the vortex sink rates to be decreased, the tip vortex to move farther inboard, and the merger to take place farther inboard. With the model at an h/b = 0.35 (simulated full-scale height of ~21 m (~70 ft) above the ground) the vortex approached and stayed at a height of ~14 m (~46 ft) above the ground plane to a distance of 20 span lengths behind the aircraft (~0.75 mile). At this downstream position it had moved ~11 m (~35 ft) laterally outboard of the wing tip. In comparison, at an h/b = 0.63 (simulated full-scale height of ~38 m (~126 ft) above the ground) the vortex approached and stayed at a height of ~20 m (~65 ft) above the ground plane to a distance of almost 40 span lengths downstream. At 30 span lengths behind the aircraft (~1 mile) it had moved ~12 m (~40 ft) laterally outboard of the wing tip. These results are in good agreement with the flight measurements and predicted trajectories of reference 11.

The rise of the vortex after the arrest of its sink rate (X/b > 20 for h/b = 0.35 and X/b > 37 for h/b = 0.63) is due to viscous interactions between the descending vortex and the boundary layer directly below it on the ground plane. This effect has been seen both in flight measurements [12] and in the ground-based experiments of Harvey and Perry [13]. As explained in their paper, the vortex induces a cross flow on the ground plane with an attendant suction peak beneath the core (because shear reduces the total head to values below free stream). Consequently, the boundary layer resulting from this cross flow has to negotiate an adverse pressure gradient once it has passed under the vortex. When the vortex is sufficiently near the ground, the pressure gradient is strong enough for separation to occur, and a bubble forms containing vorticity of opposite sense to the main vortex. As the wake ages, the bubble grows rapidly and finally detaches from the floor as a secondary vortex fed by a vortex sheet from the separation point. This secondary core induces an upwash that causes the main vortex to rise. Depending on the model configuration, subsequent trajectory figures all display this viscous interaction to a lesser or greater extent. In all cases, the closer the ground plane to the model, the sooner the vortex rises or "bounces."

Figures 5 and 6 present trajectory data for the B-747 model in the LDG (S) and LDG/0 configurations, respectively. A comparison of Figures 4 and 5 illustrates the effect of two outboard flight spoilers on the vortex trajectory. The model lift coefficient with and without spoilers was kept at a nominal value of 1.3 by adjusting model angle of attack. When spoilers were deployed, the sink rate of the wing tip vortex was increased, and the merging of the wing-tip and flap vortices was delayed to about 15 span lengths. Compared with photographs of the LDG configuration, the wake appeared to be much more disorganized. At an h/b = 0.35, the presence of the ground plane delayed vortex merging until the wake was undergoing a viscous interaction with the boundary layer of the ground plane, and it gave the appearance of an enhanced alleviation. As a consequence of the initially faster sink rate, the vortices moved closer to the ground plane when the spoilers were deployed.

Figure 6 presents the trajectory of the wing-tip vortex as it moved inboard, and

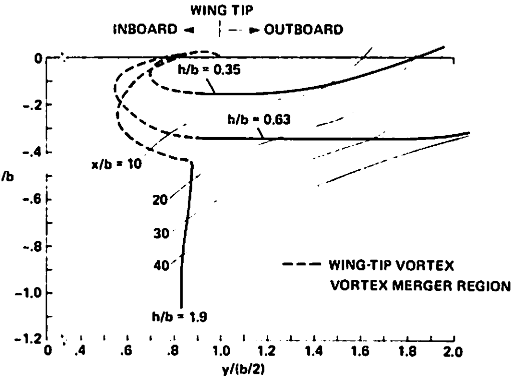

Figure 5. Vortex trajectory data; B-747 LDG (S) (1,2,11,12) configuration: $C_L = 1.35$, $\alpha = 5.8°$

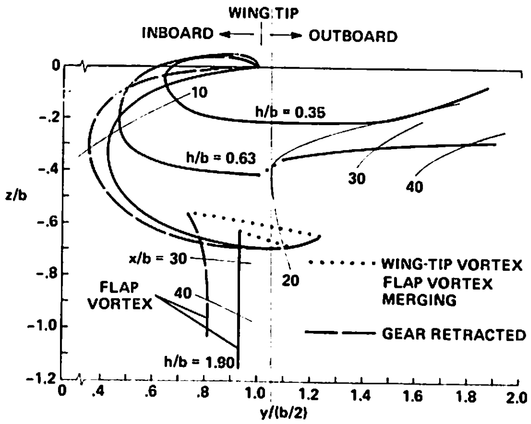

Figure 6. Vortex trajectory data; B-747 LDG/0 and LDG/0(GR) configurations: C_L = 1.16, α = 5.8°.

swung below and merged with the primary wake vortex from the outboard edge of the inboard flap of the B-747 LDG/0 configuration. Three vortices are shed from each side of the wing — one from each side of the inboard flap and the wing tip. First, the vortex from the inboard side of the flap merges with one from the flap's outboard side [14], and the wing-tip vortex then merges with the resulting flap vortex causing a diffuse residual vortex. In this configuration, as the distance between the ground plane and the model decreases, the inboard movement of the wing-tip vortex is reduced — this is a result of the flap vortex moving outboard sooner. The portion of the trajectory where merging takes place is indicated by the dotted lines in Figure 6. At an h/b = 0.35, merging was not complete until after the vortex had begun interacting with the boundary.

At this ground plane height, the flap vortex moves down rapidly, interacts with the ground plane, and then begins to rise. The wing tip vortex moves below and between the flap vortex and the ground plane and interacts with the ground plane before merging is completed. A comparison is shown of the vortex trajectories for this configuration with and without landing gear at an h/b = 1.90. The presence of the landing gear reduced the inboard movement of the wing-tip vortex, and resulted in an earlier merging with the flap vortex and a more outboard location of the final merged vortex. In addition, the velocity profiles of reference 10 showed the wing-tip vortex to be more diffuse and to experience a reduction of 27% in vertical velocity as a result of its inboard movement through the region of the wake being influenced by turbulence shed from the landing gear.

Figures 7 and 8 present the vortex trajectories of the main vortex in the wake of a model of the DC-10-30 in the LDG and LDG (S) configurations with and without ground plane. Lift coefficient was kept at a nominal

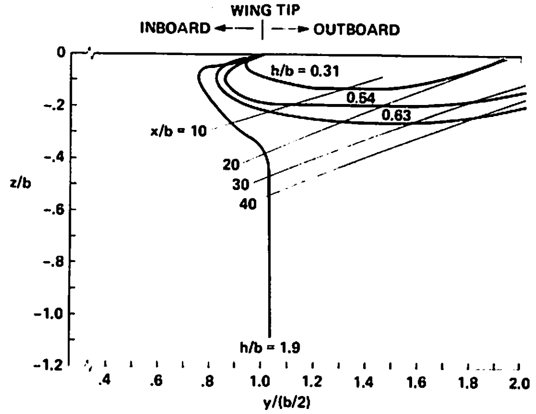

Figure 7. Vortex trajectory data; DC-10-30 LDG configuration: C_L = 1.5, = 7°.

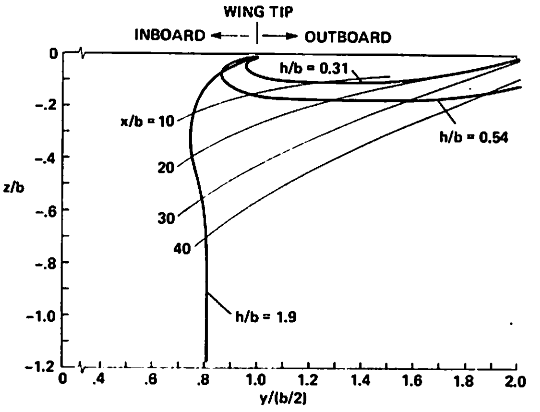

Figure 8. Vortex trajectory data; DC-10-30 LDG (S) (2,3,10,11) configuration: C_L = 1.4, α = 8°.

value of 1.4 by changing model angle of attack. For these configurations, five vortices are shed from each side of the wing with the primary vortex being shed from the wing tip. In interacts with the vortex from the outboard side of the outboard flap, but does not merge with it. When two outboard flight spoilers were deflected upward 45°, there was less interaction between vortices, the wing-tip vortex had less perturbation in its trajectory, and its final location was slightly more inboard.

Vortex Velocity Profiles.

The trailing vortex flow was spatially scanned using the single component argon-ion laser velocimeter (Figure 1) installed at the viewing station of the tank. The velocimeter began scanning the flow field prior to the model's arrival at the viewing station. During each run, the elevation of the velocimeter was kept constant and the aging vortices allowed to descend through the LV's optical axis. Many repeat runs were made for each model configuration. Comparisons of data and verbal comments from an observer about the quality of intersection of the dye-marked vortex and the laser beam focal point were used to determine scans that penetrated the vortex core.

Figure 9 compares the vertical (or tangential) velocity profiles through the vortex from the outboard side of the outboard flap of the B-747 model with and without two outboard spoilers deflected upward 45°. These data are at a downstream distance of 28 wing spans (~ mile). A 40% reduction in velocity occurs when spoilers are deployed. This result is consistent with the differences observed in the flow visualization studies and in wind-tunnel results [2, 15] and flight results [1].

Figure 10 compares the velocity profile in the wake of the B-747 model with the outboard flap retracted, LDG/0, but at a comparable lift coefficient to the LDG configuration. The comparison is made at downstream locations of 53 and 65 span lengths (~2 to 2.5 miles). Once again a 40% reduction in peak velocity results from this favorable span loading. The LDG/0 configuration is compared with the landing gear retracted, LDG/0 (GR), and with it deployed. With the gear extended, the velocities are greater and the alleviation is reduced by about 25% at this downstream location. This trend is also consistent with flight results [1].

A comparison is made in Figure 11 of velocity profiles of the wing-tip vortex of the DC-10-30 model at a downstream position of 16 spans with and without outboard flight spoilers deflected 45°. The small difference in these profiles suggests that the deployment of spoilers enhances the vortex, as the flow visualization studies indicated; the effect, of course, is opposite to that desired.

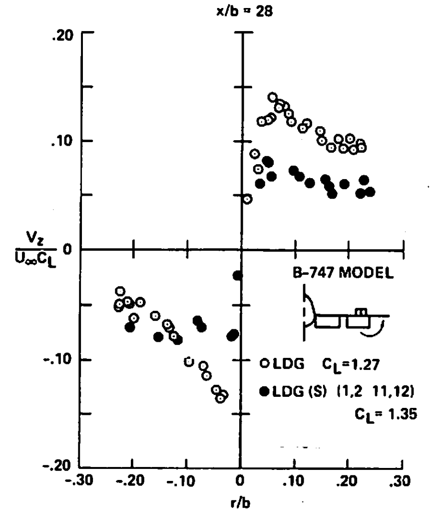

Figure 9. Dominant flap vortex vertical velocity profile, with and without spoilers: X/b= 28, B-747 model.

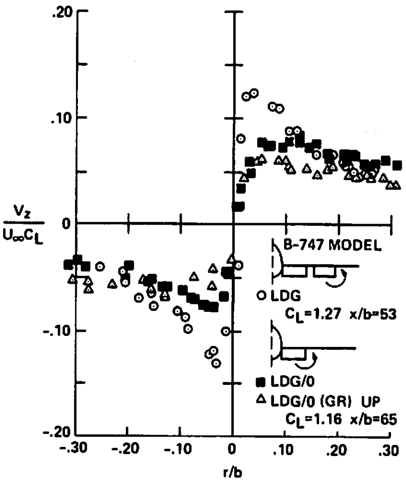

Figure 10. Dominant flap vortex vertical velocity profile, with and without modified span loading: B-747 model.

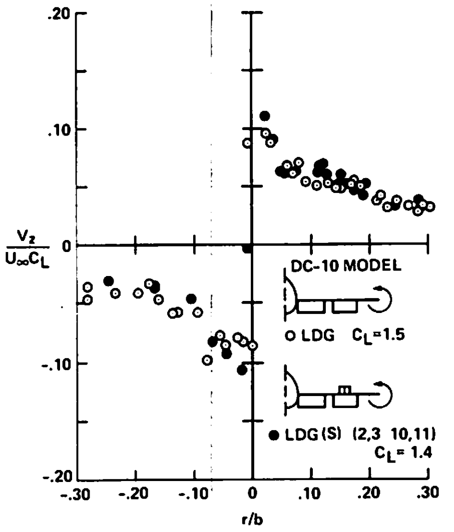

Figure 11. Wing tip vortex vertical velocity profile, with and without spoilers: X/b = 16, DC-10-30 model.

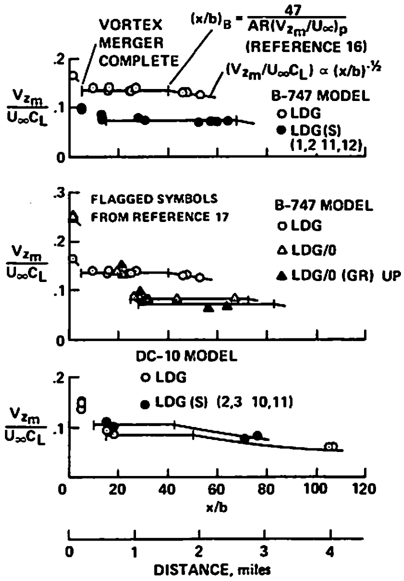

Figure 12. Downstream dependence of vortex maximum vertical velocity.

Vortex Maximum Velocities.

Figure 12 presents the downstream dependence of vortex maximum vertical velocity (normalized by lift coefficient) for each of the configurations tested. Maximum vertical velocity is defined as the average of the inboard and outboard peak vertical velocities from a given velocity profile. Where enough data exist, such as for the B-747 model with and without spoilers and with the flap-modified span loading, the now familiar "plateau" in maximum vertical velocity is identifiable. A 40% reduction in maximum vertical velocity is readily apparent from the data for both of these configurations when compared to the LDG configuration. The first vertical bar or beginning of the lines faired through the data is the approximate downstream distance where vortex interactions or mergers are complete as deduced from the flow visualization studies. The subsequent horizontal line faired through the data is then used to obtain a plateau velocity for use in the empirical correlation of reference 16. The correlation is presented in the figure. The correlation then yields the downstream location where vortex decay begins. This is indicated by the second vertical bar. From this point downstream a line is faired which shows the $(x/b)^{-1/2}$ velocity dependence. The resulting lines through the data are in good agreement with the measurements.

The flagged symbols represent the velocimeter measurements of Corsiglia and Orloff in the 7- by 10-foot wind tunnel at Ames [17]. There is good agreement with the trend of the present data. It can be seen from the data that there is a definite distance required for vortex interaction and merging to be completed, and this distance varies with each configuration. For the B-747 in the LDG configuration the distance is about 5 span lengths. Deployment of spoilers makes the wake more chaotic and the distance is extended to 15 span lengths. In the case of the flap-modified span loading, LDG/0, the distance required for the wing-tip vortex to merge with the flap vortex is 25 span lengths. For the DC-10-30 model, the wake appears less chaotic with the spoilers deployed and the vortex interaction distance is decreased from 15 to 10 span lengths. Since wind-tunnel measurements are limited to distances less than 25 spans, care must be exercised when comparing the wake alleviation potential of one configuration with another in these facilities.

SUMMARY OF RESULTS

Vortex trajectory and velocity measurements made in the wakes of B-747 and DC-10-30 models provide details of vortex interactions in lift-generated wakes. A summary of results of these measurements includes:

1. Near-field reductions of up to 40% in vortex vertical (tangential) velocities are obtainable with flaps or spoilers.
2. Presence of ground plane modifies vortex trajectories but not vortex interactions and merging generated for wake alleviation.
3. At ground plane heights of $h/b = 0.31$ to 0.35, alleviation appeared enhanced due to viscous interactions with the ground plane.
4. For the B-747 model, the chaotic appearance of the wake with two outboard flight spoilers deployed 45° and the resulting delay in main vortex merging by 10 span lengths suggest that the alleviation mechanism of the spoilers is primarily turbulence injection.
5. The distance required for vortex interactions and merging to be completed is configuration dependent and can be as long as 30 span lengths behind the generating aircraft. Therefore, care must be exercised in making comparisons of alleviation concepts based on wind-tunnel measurements at lesser distances behind the generating model.

ACKNOWLEDGMENTS

The author wishes to thank Carolyn Goodwin for supervising the data reduction of the photographic records; Alan Luebs for his assistance in setting up, calibrating and troubleshooting the velocimeter and data reduction instrumentation; and Chris Kralj for assistance with the velocimeter experiment and data reduction.

REFERENCES

1. Anon., NASA Symposium on Wake Vortex Minimization, SP-409, 1976, NASA.
2. Corsiglia, V.R. and Rossow, V.J., "Wind-Tunnel Investigation of the Effect of Porous Spoilers on the Wake of a Subsonic Transport Model," TM X-73,091, Jan. 1976, NASA.
3. Ciffone, D.L., "Vortex Interactions in Multiple Vortex Wakes Behind Aircraft," *J. Aircraft*, May 1977.
4. Kirkman, K.L., Brown, C.E., and Goodman, A., "Evaluation of Effectiveness of Various Devices for Attenuation of Trailing Vortices Based on Model Test in a Large Towing Basin," NASA CR-2202, Dec. 1973, Hydronautics Inc., Laurel, MD.
5. Ciffone, D.L. and Orloff, K.L., "Far-Field Wake-Vortex Characteristics of Wings," *J. Aircraft*, Vol. 12, May 1975, p. 464-470.
6. Ciffone, D.L. and Lonzo, C., "Flow Visualization of Vortex Interactions in Multiple Vortex Wakes Behind Aircraft," TM X-62,459, June 1975, NASA.
7. Wadlin, K.L., Ramsen, J.A., and McGehee, J.R., "Tank Tests at Subcavitation Speeds of an Aspect Ratio 10 Hydrofoil with a Single Strut," RM L9K14a, July 1950, NACA.
8. Brashears, M., Zalay, A., Hallock, J., and Burnham, D., "Laser Doppler Flight Test Measurements of B-747 Wake Vortex Characteristics," Aircraft Wake Vortex Conference, Mar. 15-17, 1977, U.S. Dept. of Trans.
9. Iversen, J.D., "Correlation of Turbulent Trailing Vortex Decay Data," *J. Aircraft*, Vol. 13, May 1976, p. 338-342.
10. Luebs, A.B., Bradfute, J.G., and Ciffone, D.L., "Effects of Spoilers and Gear on B-747 Wake Vortex Velocities," TM X-73,197, Aug. 1976, NASA.
11. Anon., "Preliminary Analysis of Lockheed MVU Measurements Conducted During the Rosamond Wake Decay Task," LMSC-HREC SD D496691, Feb. 1976.
12. Dee, F.S. and Nicholas, O.P., "Flight Measurements of Wing Tip Vortex Motion Near the Ground," British Aeronautical Research Council, London, England, CP 1065, Jan. 1968.
13. Harvey, J.K. and Perry, F.J., "Flowfield Produced by Trailing Vortices in the Vicinity of the Ground," *AIAA J.*, Vol. 9, Aug. 1971, p. 1659-1660.
14. Corsiglia, V.R., Rossow, V.J., and Ciffone, D.L., "Experimental Study of the Effect of Span Loading on Aircraft Wakes," *J. Aircraft*, Vol. 13, Dec. 1976, p. 968-973.
15. Croom, D.R., "Low-Speed Wind-Tunnel Investi-

gation of Various Segments of Flight Spoilers as Trailing-Vortex-Alleviation Devices on a Transport Aircraft Model," TN D-8162, Mar. 1976, NASA.

16. Ciffone, D.L., "Correlation for Estimating Vortex Rotational Velocity Downstream Dependence," *J. Aircraft*, Vol. 11, Nov. 1974, p. 716-717.

17. Corsiglia, V.R. and Orloff, K.L., "Scanning Laser Velocimeter Surveys and Analysis of Multiple Vortex Wakes of an Aircraft," TM X-73,169, Sep. 1976, NASA.

INITIAL DEVELOPMENT OF A WAKE TURBULENCE ASSESSMENT SYSTEM

J.L. LUNDRY
Configurations Concepts Group
Aerodynamics Research Unit
Boeing Commercial Airplane Company
Seattle WA 98124

ABSTRACT: The initial development of a computer software system for wake vortex technology is discussed. The system is intended for use in the preliminary design of new airplanes. Several overall objectives are listed, including the prediction of hazard as a function of geometry and flight conditions of the wake-producing and wake-penetrating airplanes, low cost of use, adaptability to new technology, and an explanation of currently known alleviation concepts. Essential elements of a Wake Turbulence Assessment System are listed, and an upper level system design is presented. Candidate technology for system elements is discussed. Prototype code has been produced for the initial wake rollup and for the wake penetration. Initial results of these two modules are compared with experimental data, and are promising. The comparisons also show the importance of considering the low Reynolds number at which model studies of wake penetration are conducted.

NOMENCLATURE

A	coefficients of Glauert's series
AR	aspect ratio
C_L	lift coefficient
E	strain energy
I	Glauert induction matrix
N	number of terms in series
a	wing lift-curve slope
a_0	airfoil section lift-curve slope
b	wing span
c	wing chord
c_ℓ	rolling moment coefficient
f	lift curve factor (reference 33)
ℓ	local loading = $cc_\ell/4b$
n	summation index
v_n	velocity component normal to wake-penetrating wing
y,z	spanwise and vertical coordinates
ψ	yaw angle
α	angle of attack
δ	lateral control deflection
η	nondimensional spanwise coordinate
$\bar{\eta}$	spanwise centroid of lift
$\bar{\eta}_v(\Theta_2,\Theta_1)$	centroid of vorticity shed between Θ_2 and Θ_1
Θ	transformed lateral coordinate, $\eta = \cos\Theta$
λ	taper ratio
ϕ	roll angle.

INTRODUCTION

The past few years have produced a substantial increase in our knowledge of the vortex wake and its effect on airplanes that encounter it. This knowledge is not yet being used by those responsible for designing new large transport airplanes. This is due primarily to the relative inaccessibility of vortex wake technology, compared with other technologies used in the preliminary design of new airplanes. Although the field of wake vortices is far from being fully mature, it is time to consider the development of a digital software system that will make current and future technology readily accessible to airplane designers.

This paper discusses several objectives for a Wake Turbulence Assessment System (WTAS) to be used by airplane designers. Essential system elements are listed, based on current understanding, and are then incorporated into a digital computer system preliminary design. Candidate technology is identified for most of the elements. Because the technology is still being developed at a rapid rate, the system is designed to permit alteration of, or even substitution for, any technological element. Initial progress toward the development of the WTAS is described, and comparisons are made between analytical predictions and experimental measurements.

A WAKE TURBULENCE ASSESSMENT SYSTEM

Objectives.

Several general objectives can be listed for a WTAS suitable for use in the preliminary design of airplanes. Such a system should provide some measure of the hazard involved when one airplane penetrates the vortex wake of another. It should do so as a function of the geometry of the two airplanes, their flight conditions, and the distance separating them. Highly accurate predictions are always desirable, but even an indication of correct trends would be useful for preliminary design purposes.

The costs of using a WTAS in support of airplane design are important. Iterative studies involving dozens of new airplane configurations are frequently made, and a WTAS should produce supporting results at low cost in terms of both labor and computer resources. A WTAS should therefore be automated to the extent possible.

The technology of the vortex wake is still evolving rapidly, and is likely to do so for some time. A WTAS should therefore be designed to permit easy modification or even replacement of its technical modules.

NASA's wake vortex research program has produced several configuration concepts for reducing hazard [1]. These have been substantiated in wind-tunnel, water-channel, and flight tests. A WTAS should account for the effectiveness of these concepts.

In summary, objectives for a WTAS are:

1) prediction of hazard as a function of geometry and flight conditions of the wake-generating and wake-penetrating airplanes, and their distances of separation;

2) low cost of use in terms of both labor and computing resources;

3) ready adaptability of new technology; and

4) provide explanations of concepts currently known to be effective in alleviating hazard.

Essential Elements.

The elements of a WTAS are defined by the processes and phenomena one considers necessary to model, the results required, and the starting conditions. For some elements of a WTAS, it is desirable to provide the user with more then one calculation method.

Figure 1 indicates the requirements considered here in the initial design of a WTAS. Given geometry and flight conditions of the wake-generating airplane, the spanwise variations of lift and profile drag can be estimated. These define the spanwise distribution of shed vorticity and the wake due to wing profile drag. The latter might be altered locally by the presence of jets from the propulsion system. It might ultimately prove necessary to account also for the shed vorticity and profile drag of the tail surfaces.

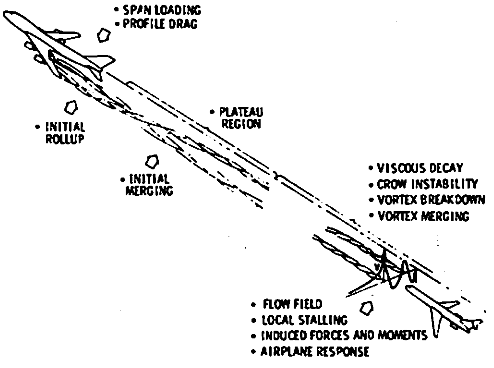

Figure 1. **Essential elements.**

Next, the shed vorticity rolls up into discrete vortices. This process becomes more complicated if the high-lift devices of the wake-generating airplane are extended; multiple vortex pairs are then formed and each has its own tangential and axial velocity profiles.

As soon as the possibility of multiple vortex pairs is introduced, then the possibility of vortex merging must be considered. Merging of adjacent vortices depends on their relative sense of rotation, their relative strengths, their diameters, and the distance separating them.

Once the trailing vortices have formed, their decay must be considered. Three decay mechanisms are shown in Figure 1. Viscous decay produces a gradual reduction in velocities and an increase of vortex core size; the latter makes it necessary to consider vortex merging further downstream. Vortices initially separated by a distance greater than critical grow in diameter with downstream distance, and thus, for those wakes having multiple vortex pairs, the possibility of additional merging remains open. Crow's instability mechanism [2], which depends on atmospheric turbulence or wake dynamics introduced by motions of the airplane or its moveable surfaces, must be considered. Finally, vortex breakdown must be included. The latter two pheonomena lead to a rapid disruption of the ordered vortex structure, and, in effect, greatly accelerate decay rate.

To this point, we have concentrated on the wake-generating airplane and its flowfield. We must now consider the airplane that penetrates the flowfield. The induced flow angles of a vortex wake are sometimes quite high — certainly in excess of the local stall angle on portions of the wake-penetrating wing and tail surfaces. The method of calculating induced forces and moments must account for this, and for unsymmetrically stalled wings, must also account for the increase of separation drag if yaw proves to be important. If the choice of hazard criterion indicates a dynamic analysis, then the inertia and unsteady aerodynamic characteristics of the wake-penetrating airplane become involved.

Computer System Preliminary Design.

The definition of physical processes to be considered in Figure 1 leads directly to a computer software system preliminary design. The blocks in Figure 2 represent computational functions that correspond to the processes indicated in Figure 1, together with an upper level logic that controls the order of the calculations.

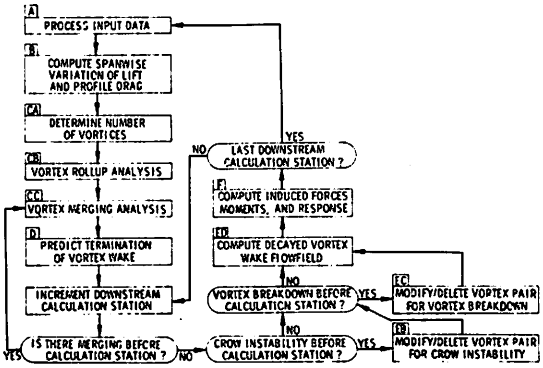

Figure 2. Upper-level logic for the WTAS.

However, Figure 2 does not define the computational reason for the existence of these functions, namely, the data they produce, or the data that each function requires as input; there simply isn't space. This has been done in an overall way in a series of charts in the Appendix. While these appended charts contain no logic, they do define the data produced and required by each function. These charts represent the first steps in a process that, when carried to completion, specifies completely all necessary computational algorithms. Together with Figure 2, they represent a computer software system preliminary design. This type of design can be readily modernized with newly developed technology, since the functions at second and third levels in the design usually become software modules, each of which relates to the overall system primarily by transferring input and output data.

Candidate Technology.

The status of technology selection for the elements of a software system varies during the development of that system. At any given time, technology selection can be divided broadly into four categories:

1) technology already identified for implementation,

2) technology to be identified later in the software system design cycle,

3) technology to be chosen after prototype coding and on the basis of comparisons of numerical results of various methods with experimental data, and

4) multiple technology implementation with choice left to the system user.

For the WTAS, technology selection is currently in all four categories.

The first selection to be considered is a method for predicting span loading. This is not an easy choice. Many methods are available, ranging from lifting-line methods [3, 4] and vortex-lattice theory [5, 6] to advanced panel-aerodynamic methods [7]. Yet, none of these methods are entirely successful for predicting the span-loading of a complex wing-body (-tail?) configuration with high-lift devices extended. The principal difficulty is the modeling of the wake immediately downstream of each lifting element. Reference 8 shows the importance of wake modeling to the calculation of span loading. At this point, vortex-lattice theory appears to be adequate for modeling lift, given the difficulty of wake-shape modeling.

Profile drag is routinely calculated by airplane preliminary design groups. However, they are interested primarily in the overall level, rather than the spanwise variation. It remains to be seen if traditional industrial methods will be adequate, and indeed, the accuracy requirements on profile-drag variation with span have not yet been prescribed. A three-dimensional boundary layer method is available [9] if improved accuracy is required, but its costs are not small.

A number of methods are available for calculating the rollup of the trailing vortex sheet. Only one of these methods [10] provides both axial and tangential velocity profiles, as functions of profile drag and shed vorticity. In fact, reference 10 shows that calculation of the two profiles should not be separated.

Vortex merging should first be considered as soon as rollup is complete. Two vortices either merge or do not merge, depending on their relative sense, their diameters, the distance separating them, and their relative strengths. There are several vortex merging algorithms [11-13] to be compared, and most of these are at least moderately expensive. For preliminary design purposes, it might prove adequate to use a simple separation distance criterion, such as given in reference 11, to determine whether or not merging occurs; if merging is indicated, the Betz conservation laws might then be useful to determine the resulting distribution of vorticity.

There are many sources of methods for estimating viscous decay rates of vortices, and a selection has not been made. Both laminar and turbulent descriptions are available (e.g., references 14 and 15), as well as an empirical description [16]. These methods predict both core growth and decay.

The Crow instability mechanism [2] has been related to atmospheric turbulence by Crow and Bate [17]. This phenomenon is not thought to be responsible for rendering the vortex wake harmless during landing approach, and yet, it cannot be ignored. Figure 27 of reference 18 shows one of several pairs of vortices from a Boeing 747 in nonstandard landing configuration apparently experiencing Crow instability.

Prediction of vortex breakdown is a difficult task. Several studies of breakdown and instability are available [19-28], and more than one method will probably be coded, at least in prototype form. The method of reference 23 is promising for use in a WTAS because it gives conditions downstream of breakdown.

Varying degrees of sophistication can be considered for modeling the effects of the vortex wake on the airplane that penetrates it. These depend on the definition of hazardous conditions. Three possibilities are listed here:

1) Induced rolling moment exceeds half of the available roll control authority.

2) Roll angle exceeds the maximum

permitted by ground clearance or similar restrictions.

3) One or more of roll, pitch, and yaw angles exceed limits which remain to be defined.

Only the static-induced rolling moment need be calculated for the first criterion, and the span-loading methods mentioned earlier are all candidates. The second criterion requires a one-degree-of-freedom dynamic analysis: this permits the effects of roll damping, roll inertia, and pilot roll response to be included. The third requires a six-degree-of-freedom dynamic analysis, and directly predicts the endurance of the encounter.

The prediction of forces and moments induced by the vortex wake should account for the large flow angles that sometimes occur. Local stalling places a limit on the lift that can be produced, in both positive and negative senses.

PROGRESS

The elements of Figure 2 are being studied with the aid of prototype code. The prototype code completed to date has dealt only with the initial rollup of wake vortices, and with wake penetration. Donaldson and Bilanin [10] and Donaldson et al. [29] do not discuss detailed computational algorithms for their implementation of the Betz conservation laws, and initially, there was concern about being able to code fully automatic rollup procedures that would be computationally inexpensive. An additional consideration is that, given geometry, span loading is not usually defined as a continuous function, but rather at only a few points through which a curve must be faired. This leads to some difficulty since both span loading and its derivative are required.

To handle this detail, Glauert's sine series for span loading, in the form

$$\ell = \frac{cc_\ell}{4b} = \sum_{n=1}^{N} A_{2n-1}\sin(2n-1)\theta\ , \qquad (1)$$

where $\cos\Theta = \eta$ has been fitted to the known loading points, while the strain energy,

$$E \sim \int_0^{\pi/2} \left(\frac{d^2\ell}{d\theta^2}\right)^2 d\theta \sim \frac{\pi}{4}\sum_{n=1}^{N}(2n-1)^4 A_{2n-1}^2\ , \qquad (2)$$

in the fitted curve is minimized. This procedure has been in use for sometime as a method for evaluating induced drag [30]. It provides an analytical expression for span loading, which can then be used to evaluate other expressions required in the Betz theory of reference 29; Table 1 summarizes the explicit ones, and others can be evaluated with iterative procedures. This form of implementation produces vortex circulation as a function of radius and in tabular form for each pair of rolled-up trailing vortices. Figure 3 is an example of a curve faired by this method; the span loading is from reference 31.

The wake-penetration element of the WTAS has dealt only with induced lift and rolling moment to this point. Glauert's theory [3] has been used. This simple theory can account for the spanwise variation of chord of the wake-penetrating airplane, but it cannot account for effects of wing sweep, nor for the effects of the boundary layer in

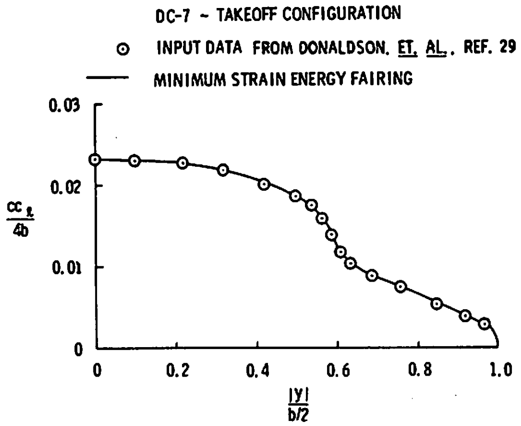

Figure 3. Faired span loading.

Table 1. Explicit Span Loading Relationships

$\frac{d\ell}{d\eta} = -\csc\Theta \sum_{n=1}^{N} (2n-1)\ A_{2n-1} \cos(2n-1)\Theta$
$\frac{d^2\ell}{d\eta^2} = -\csc^2\Theta \sum_{n=1}^{N} (2n-1)\ A_{2n-1} \left\{\cot\Theta \cos(2n-1)\Theta + (2n-1) \sin(2n-1)\Theta\right\}$
$\bar{\eta}_v (\Theta_2,\Theta_1) = \frac{1/2\ A_1 \left\{\Theta_2 - \Theta_1 + 1/2\ (\sin 2\Theta_2 - \sin 2\Theta_1) + f(\Theta_2,\Theta_1)\right\}}{\sum_{n=1}^{N} A_{2n-1} \left\{\sin (2n-1)\Theta_2 - \sin (2n-1)\Theta_1\right\}}$
$f(\Theta_2,\Theta_1) = \sum_{n=2}^{N} (2n-1)\ A_{2n-1} \left\{\frac{\sin 2(n-1)\Theta_2 - \sin 2(n-1)\Theta_1}{4(n-1)} + \frac{\sin 2n\Theta_2 - \sin 2n\Theta_1}{4n}\right\}$

altering the lift-curve slope of the wake-penetrating wing. Corrections for such effects are made in the form of a constant factor based either on a direct measurement of the wake-penetrating wing's lift-curve slope or on a result from a theory more accurate than Glauert's.

Glauert's theory leads to a computationally efficient algorithm for computing lift and rolling moment induced on the penetrating airplane by the vortex wake. The Glauert induction matrix I for the wake-penetrating wing is calculated and inverted. Then, at each Glauert collocation station, the component of velocity v_n normal to the wing and induced by the wake is calculated as shown in Figure 4. The coefficients A are then given, as usual, by

$$\{A\} = [I]^{-1} \{v_n\} \ . \qquad (3)$$

The induced-lift coefficient is

$$C_L = \pi\, \mathit{AR}\, A_1 \ , \qquad (4)$$

and the induced rolling-moment coefficient is

$$C_\ell = \tfrac{1}{2}\, \bar{\eta}\, C_L \ , \qquad (5)$$

where

$$\bar{\eta} = \frac{A_2}{2A_1} \ . \qquad (6)$$

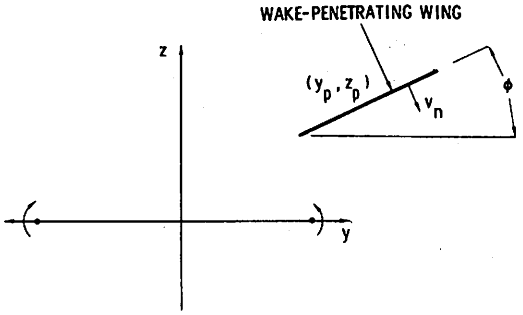

Figure 4. Coordinate system for wake-penetration.

Since only A_1 and A_2 are required to compute induced-lift and rolling-moment coefficients, only the first two rows of I-inverse need to be saved; they can then be multipled by many sets of v_n corresponding to a range of values of y_p, z_p and ϕ in Figure 4.

INITIAL RESULTS

Reference 32 has proved to be particularly valuable for testing the WTAS code. The authors have measured most of the key parameters required to properly test an analytical method. They measured:

1) span loading of a wake-producing wing,

2) tangential velocity profile of the rolled-up vortex,

3) lift-curve slope of the two wake-penetrating wings at their operating Reynolds number, and

4) rolling moments induced on the wake-penetrating wings.

Figure 5 is an experimental span loading for the wake-producing wing of reference 32. The left half of Figure 6 compares the corresponding Betz tangential velocity profiles, calculated by the WTAS prototype code, with experimental data from reference 32. The agreement is quite good, except for the core region.

Also in Figure 6, experimental induced-rolling moments for the two wake-penetrating wings of reference 32 are compared with WTAS results at two lift coefficients of the wake-generating wing. The experimental values of lift-curve slope for the wake-penetrating wings have been used to correct the Glauert theory lift-curve slopes; the correction ratios are 0.846 and 0.789 for the smaller and larger penetrating wings, respectively. The comparison of theoretical and experimental rolling moments is good.

One further test-theory comparison has been made. Iverson of Iowa State provided both a theoretical span loading for a wake-generating wing of 15-inch semispan and measured values of induced rolling-moment coefficient on a following wing; these data are from the vortex merging work at Iowa State. In Figure 7, two theoretical values of induced rolling moment from the WTAS are compared with an experimental one. The upper theoretical value was obtained by using Iverson's theoretical loading directly and Glauert's theory for the penetrating wing, corresponding to an airfoil section lift-curve slope of 2 for both wings. The lower theoretical value corresponds to using a lower value of airfoil section lift-curve slope for both wings, based on section data backed out of the wing lift-curve slopes in reference 32 with a formula from reference 33. The experimental value of induced

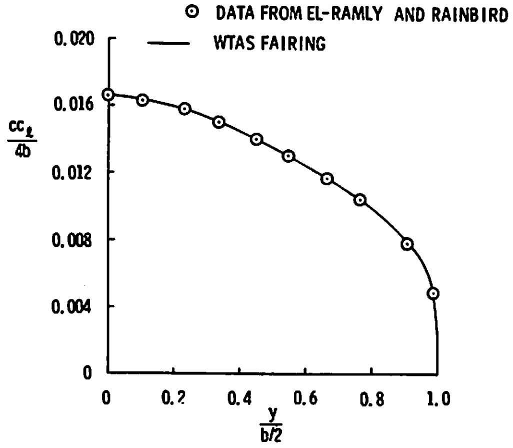

Figure 5. Span loading of wake-generating wing.

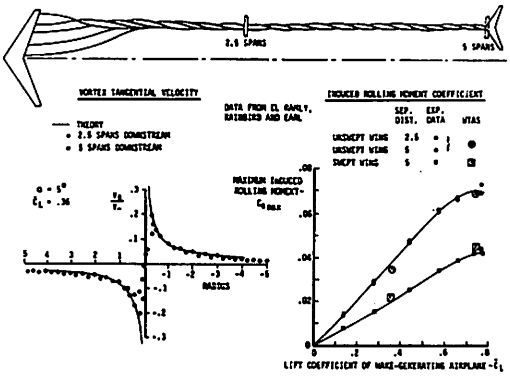

Figure 6. Comparison of WTAS predictions with test data.

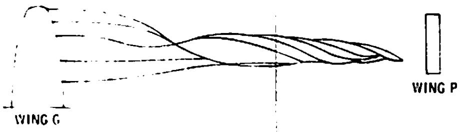

TEST DATUM FROM IVERSON (UNPUBLISHED)

	c_{ℓ_α} per radian	$\left(C_{L_\alpha}\right)_G$ per degree	$\left(C_{L_\alpha}\right)_P$ per degree	INDUCED c_ℓ
THEORY	2π $0.789(2\pi)$	0.0778 0.0664	0.0703 0.0617	0.0806 0.0611
TEST	—	—	—	0.0616

Figure 7. Induced rolling-moment comparison.

rolling-moment coefficient has been interpolated; the range of interpolation is only from 0.0604 to 0.0622, corresponding to wing semispans of 14 and 15½ inches, respectively. The agreement between experimental data and the theoretical result with Reynolds number correction is good. This comparison again demonstrates the importance of considering the effect of low Reynolds number on airfoil section lift-curve slope.

The existing prototype elements of the WTAS have low usage costs. Table 2 lists central-processor execution times for several steps of the case of Figure 7. The existing code requires 32,000 (octal) storage elements.

Table 2. WTAS Execution Time

- CDC 6600 Central Processing Time
- Wake with one vortex pair

WTAS Function	Time (Seconds)
1. Read and print input data	0.05
2. Curve-fit span loading data	0.47
3. Compute and plot fitted span loading	0.42
4. Betz analysis of span loading	1.10
5. Glauert analysis of wake-penetrating wing	0.93
6. Compute flowfield, induced lift, and induced rolling moment at 182 points	5.39
	Total 8.35

CONCLUDING REMARKS

This paper has presented some objectives for a Wake Turbulence Assessment System suitable for use in new airplane design studies. A preliminary design for a digital software system has been developed, and its upper level elements and logic have been shown. Some elements of the system have been implemented in the form of prototype code. The initial results are promising, and demonstrate the importance of accounting for the low Reynolds number of model wings used in vortex wake studies. However, it has yet to be shown that the difficult problems of wake viscous decay and vortex breakdown can be treated with the same degree of success. Ultimately, nonuniform properties of the atmosphere and ground proximity might need to be considered; their effects on the vortex wake flowfield have not yet been considered in the WTAS preliminary design. The definitions of hazardous condition should be reviewed carefully, since they directly influence the wake-penetration elements of a WTAS. Work on these worthwhile goals will continue. It is hoped that this type of effort will one day permit wake vortex hazard and required separation distances to be followed as a function of airplane configuration in much the same way that, say, engine noise, airframe noise, and sonic-boom characteristics are considered now.

REFERENCES

1. Proceedings of "NASA Symposium on Wake Vortex Minimization," Washington, D.C., Feb. 25-26, 1976.
2. Crow, S.C., "Stability Theory for a Pair of Trailing Vortices," *AIAA J.*, Vol. 8, No. 12, Dec. 1970, p. 2172-2179.
3. Glauert, H., *The Elements of Aerofoil and Airscrew Theory*, Cambridge University Press, England, Second Ed., 1948, p. 156-170.
4. Weissinger, J., "The Lift Distribution of Swept-back Wings," NACA TM 1120, 1947.
5. Rubbert, P.E., "Theoretical Characteristics of Arbitrary Wings by a Non-Planar Vortex Lattice Method," The Boeing Company, Commercial Airplane Group, Document No. D6-9244, 1963.
6. Margason, R.J. and Lamar, J.E., "Vortex Lattice

FORTRAN Program for Estimating Subsonic Aerodynamic Characteristics of Complex Planforms," NASA TN D-6142, Feb. 1971.

7. Johnson, F.T. and Rubbert, P.E., "Advanced Panel-Type Influence Coefficient Methods Applied to Subsonic Flows," AIAA Paper No. 75-50, Pasadena, CA, Jan. 1975.

8. Rossow, V.J., "Inviscid Modeling of Aircraft Trailing Vortices," Presented at NASA Symposium on Wake Vortex Minimization, Washington, DC, Feb. 1976.

9. McLean, J.D., "Three-Dimensional Turbulent Boundary Layer Calculations for Swept Wings," AIAA Paper No. 77-3, Los Angeles, CA, Jan. 1977.

10. Bilanin, A.J. and Donaldson, C.duP., "Estimation of Velocities and Roll-Up in Aircraft Vortex Wakes," *J. Aircraft*, Vol. 12, No. 7, July 1975, p. 578-585.

11. Roberts, K.V. and Christiansen, J.P., "Topics in Computational Fluid Mechanics," *Computer Physics Communications* 3, Suppl., 1972, p. 14-32.

12. Lo, R.K.C. and Ting, L., "Studies of the Merging of Vortices," *Physics of Fluids*, Vol. 19, No. 6, June 1976, p. 912-913.

13. Rossow, V.J., "Convective Merging of Vortex Cores in Lift-Generated Wakes," AIAA Paper No. 76-415, 9th Fluid and Plasma Dynamics Conference, July 14-16, 1976, San Diego, CA.

14. Williams, G.M., "Viscous Modeling of Wing-Generated Trailing Vortices," *Aero. Quart.*, May 1974, p. 143-154.

15. Govindarju, S.P. and Saffman, P.G., "Flow in a Turbulent Trailing Vortex," *Phys. Fluids*, Vol. 14, No. 10, Oct. 1971, p. 2074-2080.

16. Iversen, J.D., "Correlation of Turbulent Trailing Vortex Decay Data," *J. Aircraft*, Vol. 13, No. 5, May 1976, p. 338-342.

17. Crow, S.C. and Bate, E.R., Jr., "Lifespan of Trailing Vortices in a Turbulent Atmosphere," *J. Aircraft*, Vol. 13, No. 7, July 1976, p. 476-482.

18. Corsiglia, V.R. and Dunham, R.E., "Aircraft Wake-Vortex Minimization by Use of Flaps," presented at NASA Symposium on Wake Vortex Minimization, Washington, DC, Feb. 1976.

19. Brooke, B.T., "Theory of the Vortex Breakdown Phenomenon," *J. Fluid Mech.*, Vol. 14, 593, 1963.

20. Bossel, H.H., "Vortex Breakdown Flowfield," *Phys. Fluids*, Mar. 1969, p. 498-508.

21. Bossel, H., "Vortex Computation by the Method of Weighted Residuals Using Exponentials," *AIAA J.*, Vol. 9, No. 10, Oct. 1971, p. 2027-2034.

22. Landahl, M.T., "Wave Mechanics of Breakdown," *J. Fluid Mech.*, Vol. 56, pt. 4, 1972, p. 775-802.

23. Mager, A., "Dissipation and Breakdown of a Wing-Tip Vortex," *J. Fluid Mech.*, Vol. 55, Part 4, Mar. 1972, p. 609-628.

24. Uberoi, M.S., Chow, C.Y., and Narian, J.P., "Stability of Coaxial Rotating Jet and Vortex of Different Densities," *Physics of Fluids*, Vol. 15, No. 10, Oct. 1972, p. 1718-1727.

25. Hall, M.G., "Vortex Breakdown," in *Ann. Rev. Fluid Mech.*, Vol. 4, 1973, p. 195-218.

26. Lessen, M., Deshpande, N.V., and Hadji-Ohanes, B., "Stability of a Potential Vortex with a Non-Rotating and Rigid-Body Rotating Top-Hat Jet Core," *J. Fluid Mech.*, Vol. 60, pt. 3, 1973, p. 459-466.

27. Lessen, M., Singh, P.J., and Paillet, F., "The Stability of a Trailing Line Vortex. Part 1. Inviscid Theory," *J. Fluid Mech.*, Vol. 63, pt. 4, 1974, p. 753-763.

28. Lessen, M., and Paillet, F., "The Stability of a Trailing Line Vortex, Part 2. Viscous Theory," *J. Fluid Mech.*, Vol. 65, pt. 4, 1974, p. 769-779.

29. Donaldson, C.duP., Snedeker, R.S., and Sullivan, R.D., "Calculation of Aircraft Wake Velocity Profiles and Comparison With Experimental Measurements," *J. Aircraft*, Vol. 11, No. 9, Sep. 1974, p. 547-555.

30. Lundry, J.L., "The Calculation of Lift and Induced Drag from Sparse Span Loading Data," *J. Aircraft*, Vol. 14, No. 3, March 1977, p. 309-311.

31. Donaldson, C.duP., Snedeker, R.S., and Sullivan, R.D., "Calculation of the Wakes of Three Transport Aircraft in Holding, Takeoff, and Landing Configurations and Comparison with Experimental Measurements," Report No. FAA-RD-73-42, Mar. 1973, Federal Aviation Administration, Washington, DC.

32. El-Ramly, Z., Rainbird, W.J., and Earl, D.G., "Some Wind Tunnel Measurements of the Trailing Vortex Development Behind a Sweptback Wing: Induced Rolling Moments on Intercepting Wings," AIAA Paper No. 75-884, 8th Fluid and Plasma Dynamics Conference, Hartford, CT, June 16-18, 1975.

33. Perkins, C.D., and Hage, R.E., *Airplane Performance Stability and Control*, Wiley, New York, NY, 1949, p. 84-85.

APPENDIX

This appendix contains several figures which specify the type of calculation to be made by the WTAS, the output data produced, and the necessary input data. In the nomenclature of modern software design, these figures represent the upper levels of a functional decomposition for the WTAS.

The process begins with the upper-half of Figure A-1. On the right are the data output by the WTAS. The central block is the function that produces the output data, in this case, the WTAS as a whole. On the left are the necessary input data to the function.

The lower half of Figure A-1 lists six functions which are the components of the WTAS function above and which are labeled alphabetically. For each of these six functions, the decomposition process is repeated in Figures A-2 through A-7. Output data and input data are again defined at this level, and in more detail than before. Each function at this level is again decomposed, and the process should be continued.

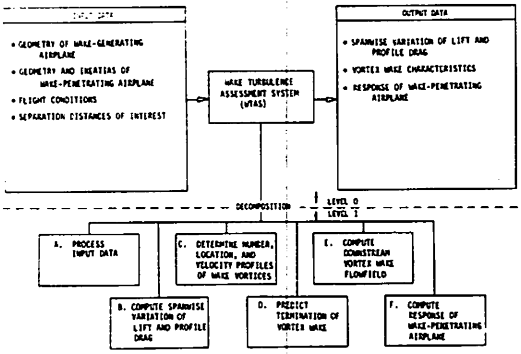

Figure A-1. Functional decomposition of the WTAS.

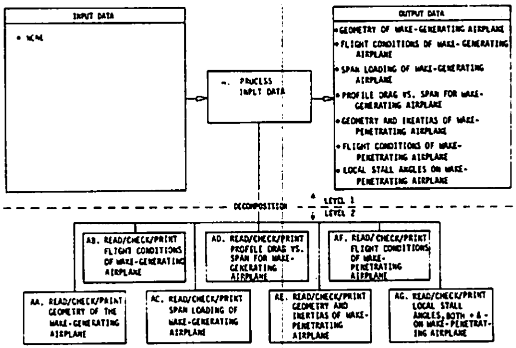

Figure A-2. Functional decomposition of function A.

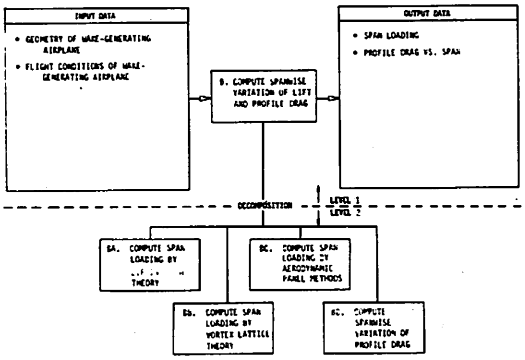

Figure A-3. Functional decomposition of function B.

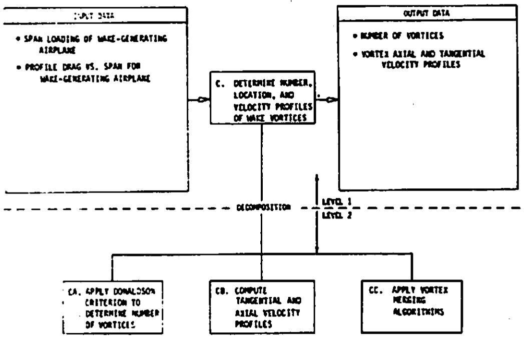

Figure A-4. Functional decomposition of function C.

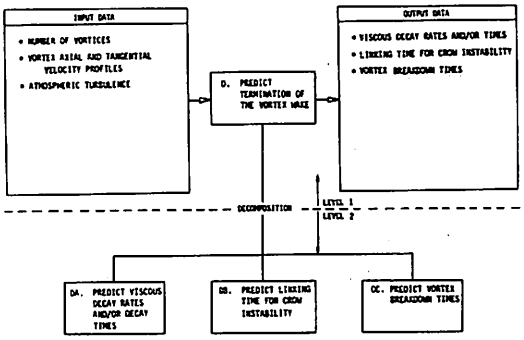

Figure A-5. Functional decomposition of function D.

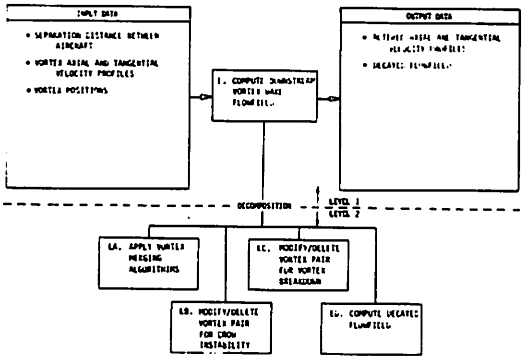

Figure A-6. Functional decomposition of function E.

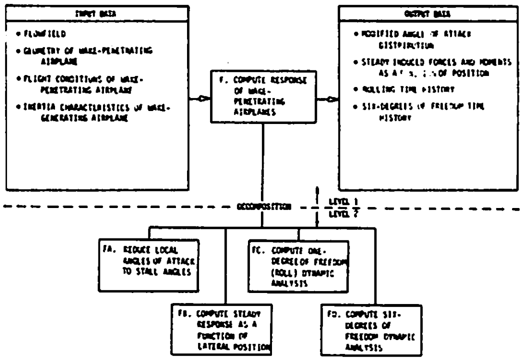

Figure A-7. Functional decomposition of function F.

The final level of decomposition will produce specific computational algorithms. Figure A-8 is an example. For Function DB, the next level of decomposition produces the equations for Crow's instability analysis as a function of atmospheric turbulence.

Figures A-1 through A-7 define the three uppermost levels of a functional decomposition for a WTAS preliminary design. This process ultimately defines all of the *types* of calculations to be made, all of the data produced by these calculations, and all of the data required as input. The *order* of these calculations must be defined by logic diagrams, such as Figure 2.

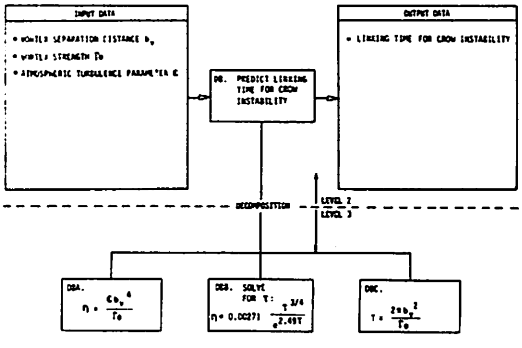

Figure A-8. Functional decomposition of function DB.

EFFECT OF WING-MOUNTED DEVICES ON THE TRAILING VORTEX SYSTEM IN THE NEAR FIELD

Z. EL-RAMLY AND W. J. RAINBIRD
Carleton University
Ottawa ON Canada

ABSTRACT: The paper examines the results of an extensive wind tunnel test program aimed at evaluating the effect of several different devices mounted on a wing on the near field trailing vortex system. The devices used include different wing tip modifications, several spoilers, simulated flap-track fairings, as well as two simulated engines with and without air injection. Only practical tip modifications and spoilers have been incorporated, i.e., only those that appear to be structurally possible with reasonable drag penalties. The devices have been tried first individually and then in combination to see if the reduction in rolling moment is cumulaive. Assessment of the effectiveness of the devices, in reducing vortex hazard, is measured as a reduction in the maximum induced rolling-moment coefficient "$C_{l_{max}}$" on a following wing of fixed span ratio of 0.24, representative of a light aircraft. All devices tested have resulted in decreases of the vortex hazard. However, no single device by itself produced a substantial decrease in maximum induced rolling moment. The maximum reduction in hazard ($C_{l_{max}}/C_{L_{generating}}$) compared to the clean wing case, found in these experiments, is about 25% and occurs when the wing is equipped with a 70° delta-shaped tip, a small spoiler near the tip, 4 simulated flap-track fairings and 2 simulated jet engines. While it is anticipated that similar reduction of vortex hazard will be present at greater downstream distance, the restriction of the present (and all) wind-tunnel experiments to near field conditions is noted.

INTRODUCTION

The problem of aircraft trailing vortices and their effect on flight safety and airport capacity has generated interest and concern in the aviation community in recent years (see, for example, references 1-3 for surveys of the problem). In spite of the large amount of work on the problem there is still a very considerable lack of knowledge about the detailed fluid dynamics of wing-vortex wake formation and decay. In particular there has been a lack of emphasis on viscous fluid considerations such as for the wing three-dimensional turbulent boundary layers and their separation and the subsequent development and roll-up of the resulting shear layers into the vortex wake. Even the allowance for viscous effects on inviscid calculation methods [4] has only been done rather empirically.

However, it appears to be currently impossible to predict the complete viscous and inviscid flow field about a simple lifting wing with its wake let alone a complete trimmed aircraft. Flow details in such highly three-dimensional areas as near wing tips or flap ends, or adjacent to "excrescences" such as pylons, flap tracks or spoilers, defy analysis. The present analytical position [4] appears to rely on inviscid lifting-surface models to predict the wing-load distribution with empirical allowance for viscous effects on $dC_L/d\alpha$ completed with an inviscid Betz-type analysis of the resulting fully developed far wake. Inviscid roll-up calculations and vortex-vortex interaction studies do not appear to have progressed to a point where they can be utilized in an overall predictive scheme.

In order to study the development, stability, dissipation and interaction of wing-generated vortices it is obvious to us that the near field vortical flow on and closely behind the wing must be investigated and understood. Hence our experimental studies concentrated on these near-field problems [5-11].

The use of wind tunnels for such wing-vortex wake work imposes a number of severe limitations. Even for near-field studies (which are just possible!), wing and aircraft models are scaled down thus aggravating

Reynolds number problems; mean chord Reynolds numbers are typically low by a factor of about 10^2 giving severe problems with unrepresentative laminar boundary layers and separations; limitations in $C_{L_{max}}$; difficulties in simulating the correct action of devices like flaps, controls, spoilers, etc.; and, most importantly, an incorrect relative thickness scaling of all boundary layers, free shear layers and resulting concentrated vortical regions. In addition, working-section wall-constraint effects [12] are present and there is the possibility of extraneous axial pressure gradients which can modify vortex structure. Thus the results of wind tunnel studies must of necessity be rather qualitative.

The paper discusses the effect of several different devices mounted on a wing on the near-field trailing vortex system. The devices used include different wing-tip modifications, several spoilers, simulated flap-track fairings as well as two simulated engines with and without air injection. Also tried were simulated smoke generators, similar in external shape to those used by NASA to mark trailing vortices, mounted on the wing undersurface. Only practical tip modifications and spoilers have been incorporated, i.e., only those that appear to be structurally possible with reasonable drag penalties. The devices have been tried first individually and then in combination to see if the reduction in rolling moment is cumulative. Due to the low Reynolds number ($\approx 0.5 \times 10^6$) and the lack of high-lift devices on the model, the present tests are limited to only moderate C_L's representative of cruising flight conditions.

Assessment of the effectiveness of the devices, in reducing vortex hazard, is measured as a reduction in the maximum induced rolling-moment coefficient on a following wing of fixed-span ratio of 0.24 representative of a light aircraft. This coefficient is normalized to the generating wing overall lift coefficient and compared to the clean wing configuration case (in cruise, no high-lift devices, conditions). These rolling-moment measurements were supplemented, in several cases, with detailed pressure plotting of the generating wing (to study the effects on the spanwise load distribution) and with detailed flow field measurements of the vortex system (including deduction of detailed spanwise circulation distribution). All devices tested have resulted in decreases of the vortex hazard. However, no single device by itself produced a substantial decrease in maximum induced rolling moment. The maximum reduction in hazard ($C_{\ell_{max}}/C_{L_{generating}}$) compared to the clean wing case, found in these experiments, is about 25% and when the (half) wing is equipped with a 70° delta-shaped tip, a small spoiler near the tip, 4 simulated flap-track fairings and 2 simulated jet engines. While it is anticipated that similar reductions of vortex hazard will be present at greater downstream distances, the restriction of the present (and all) wind-tunnel experiments to near-field conditions is again noted.

REVIEW OF SOME PREVIOUS WORK

The prospects for attenuating the aircraft vortex wake by aerodynamic means (and thus alleviating the hazard problem) have been reviewed by Lee [22] and many authors at the recent NASA Symposium [4]. While it has been demonstrated that vortex modification is possible using a variety of devices without destroying the wing lift, it is also clear that the precise aerodynamic mechanisms are still elusive and no generalization of results seems possible. The work on some of the more promising devices will be briefly reviewed as a framework for the present work.

Flaps.

The effect of the flaps on the vortex system is a direct consequence of the spanwise load modification. With wing flaps deployed the vortex system consists of multiple cores usually of comparable strength. There is little hope of predicting the generated vortex field and its development. Donaldson and his group (see for example reference 3) presented some simplified inviscid roll-up models and Rossow [13] examined the convective merging of vortex cores using inviscid models.

Several studies by NASA (water tank, wind tunnel and flight — see reference 14) mainly behind a B-747, or model of the same, have shown that big improvements can be obtained with a certain flap configuration (30°/1°). With landing gear retracted the separation requirement for the follower airplane (Learjet and T-37B) was reduced substantially for the 30°/1° configuration compared to the standard 30°/30° landing configuration. Lowering the landing gear, however, increased the separation requirement for all configurations, and especially for the 30°/1° configuration. Sideslip was also found to adversely affect the wake alleviation when the landing gear was up. These conclusions are clearly dependent on the span ratio of the follower/generator; whether it is peculiar to the Boeing 747 still needs further research.

Wing Tips.

At least for cruising flight the wing tip has a dominant effect on vortex structure. Experiments [10, 15, 16] on untapered wings have shown that even for modest C_L's a tip edge separation is present and a concentrated vortex of about 60% of the wing-root circulation has formed at the wing trailing edge.

That wing tip flows are poorly understood is, we feel, self evident; a glance at aircraft through the century will show an incredible variety of wing tip forms — likewise a search of the literature and patents will reveal a wild variety of ideas. Only for the case of slender wings with leading edge separation (which one might say are dominated by the 'tip') has the three-dimensional flow field been thoroughly analyzed — at least in inviscid flow. For more general wings the strongly interactive complex viscous and inviscid flow structure at a wing tip has never been analysed or experimentally explored in detail.

What appears to happen to the flow at wing tips (at least for those formed by a half-body) is as follows: for a small low range of incidence no substantial adverse pressure gradients are generated and the flow passes smoothly around the tip — separation is thus confined to the 'trailing edge'. With increase of incidence steeper adverse gradients are generated (see references 5 and 15) and a tip edge separation line extends gradually forward along the tip from the trailing edge of the tip chord, eventually reaching to near the leading edge (even at a moderate C_L of 0.5 in deVries [15] experiments). Finally, at least on sweptback wings, the separation line runs onward along the leading edge to give tip stall. The behaviour of the flow near a trailing edge flap tip will necessarily be more complex because of the proximity of an adjacent free shear layer from the main wing surface.

In spite of the apparent importance of the details of the tip flow in determining the vortex inner structure, experiments on wing tips [17-20] seem to have been singularly unsuccessful in reducing the vortex hazard. Nevertheless we have designed a series of tips (Figure 1) to spread the spanwise loading more gradually near the tip and to control the tip edge separation.

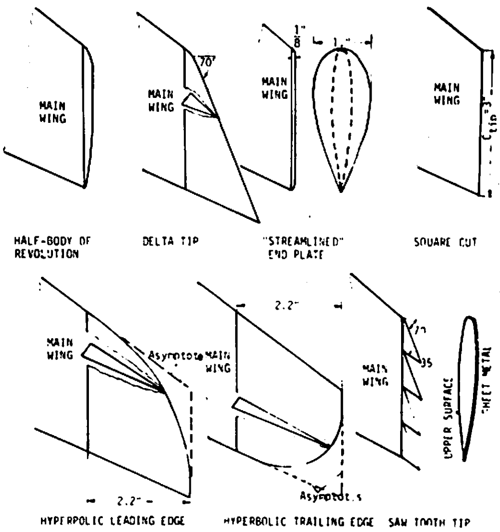

Figure 1. Sketch of tip configurations.

Vortex Generators.

Early water-tank tests by NASA in the Hydronautics Ship Model Basin [21] showed that for a 0.03-scale model of a Boeing 747 aircraft equipped with an array of vortex generators mounted on both the upper and lower surfaces with flaps retracted, the use of the vortex generators diminished the maximum swirl velocity to about one quarter at a full-scale distance of 2.4 n.m. In cruise conditions, the added drag of the vortex generator was about 50 percent with loss of lift of about 5%. In landing, 30°-flaps conditions, the vortex generators were found ineffective, and this, of course, is the practically important case.

Lee [22] suggested the use of special vortex generators on only one surface of the wing. These generators are like those commonly used for boundary layer control but they are larger and project throughout the boundary layer into the main flow and they have a highly swept leading edge. The idea behind Lee's suggestion is to break the vortex wake into a number of 'slender wing wakes' that might wind-up together to give a (favourable) slender-wing-type wake from a conventional attached-flow-type wing.

In principle similar behaviour is expected from large flap tracks as a result of the locally perturbed loading, locally modified and separated boundary layers, and three-dimensional separation. In this investigation we will look at the effect of the large flap tracks — similar to those on the B-747 — on the vortex wake. Following an argument similar to that of Lee's, we used a saw-toothed wing tip (Figure 1) which we were hoping would break the tip vortex into 4 smaller cores.

Spoilers and Other Drag Devices.

Even though several drag devices have been used (see, for example, reference 21) the spoilers seem to be the most promising (see reference 23 for a review of their development), because they could be retracted without any drag penalty when not in use. Croom [23], however, has shown that the effectiveness of the spoilers is critically dependent on their position and on the configuration of the generating aircraft. For example, he found that substantial reduction in the induced rolling moment can be achieved by spoilers near the mid-semispan and well forward on both swept and unswept wings.

The mechanism by which the spoilers work is not really understood. Because we have the capability to measure the detailed loading on the generating wing and the detailed flow field and induced rolling moment on a following aircraft, we tested several spoilers hoping to find one that results in substantial reduced rolling moment and then examine it in details. Since we can only simulate cruise conditions, the spoilers were placed near the tip. Unfortunately, none of the spoilers tested resulted in a large enough reduction to justify detailed investigations.

Power Effects.

The effect of wing-mounted power installation and the hot-jet exhaust on the vortex system have always raised interesting questions. Recent subscale measurements [24] behind a model of the Boeing 747, with flap deflections of the outboard and/or the inboard flap of 30°, show that the jet thrust has an attenuating effect on the vortex. The measured rolling moment, induced on a following model at a separation distance equivalent to 0.88 nautical miles, is reduced by approximately 20 percent of the zero-thrust case. The results also indicate that the attenuation may be maximized by proper engine location relative to the vortex. The results of flight tests [25, 26], using the B-747 aircraft and again with flap deflections of the outboard and/or the inboard flap of 30°, indicate a similar thrust attenuating effect on the vortex system. The inboard and outboard engines of the B-747 airplane are aligned in front of the outboard edges of the inboard and outboard flaps, respectively. With both flaps extended the dominant vortex is the vortex shed from the outboard edge of the outboard flap. With the outboard flap retracted (only the inboard extended), the dominant vortex is that shed from the outboard edge of the inboard flap. In both cases one of the engines is blowing its exhaust directly into the dominant vortex — the jet-mixing region is interfering with the vortex roll-up and formation. Other flight measurements made by the FAA using the CV-880 aircraft with a tower fly-by technique [27] showed that thrust differences (namely all engines at normal power compared to two engines on one side at zero thrust) produced no noticeable changes to the vortex structures (as deduced from recorded data).

The authors have made some systematic investigations of the power installation effects [5, 6] in cruise configuration. The measurements included a comparison of the flow field and induced rolling moment on a trailing wing for a generating wing with and without simulated engines mounted and with and without simulated jet exhaust.

EXPERIMENTAL SET-UP

The apparatus under consideration is the 20-× 30-in. low-speed return-circuit wind tunnel at Carleton University with an extended test section. The axial pressure gradient is essentially zero, and the flow quality is very good. Spatial variation of mean flow angularity is within ±0.15° and the streamwise component of turbulence is approximately 0.1%. Figure 2 shows a schematic of the working-section layout; details of the set-up can be found in references 5 and 9.

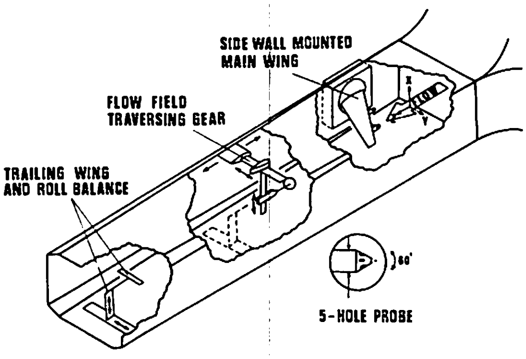

Figure 2. Isometric sketch of working section.

Figure 3 presents sketches of the pressure-plotted generating (half) wing and of the trailing wing, while Table 1 shows the overall dimension of the wings. The vortex generating half wing (herein called the main wing) is sidewall mounted on an incidence gear which also serves as the resistive side of a root-suction system. The intercepting trailing wing is sting-mounted from a floor-mounted x-y traversing strut. The rolling moment on this wing is measured on a simple strain-gauged cantilever-element roll balance. Care has been taken in fixing the transition on the wings because of the relatively low Reynolds number of the test (0.13 to 0.51 × 10^6 based on the mean chord). A surface flow visualization technique using oil dots is used to check the approximate nature of the boundary layer on the wings.

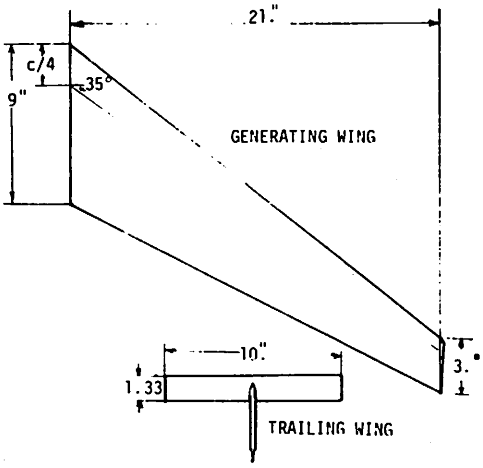

Figure 3. Sketch of generating and trailing wings.

Table 1. Wing Dimensions

	Main (Half) Wing	Trailing Wing
Span	21.0 in. (×2)	10.0 in.
Relative Span	1	0.24
Average Chord	6.00 in.	1.33 in.
Aspect Ratio	7.0	7.5
Taper Ratio	1/3	1
Sweepback (¼c)	35°	0°
Wing Twist	0°	0°
Wing Section	12%, symmetrical	NACA 64_2-015
Tip Form	Half-body	Square cut

Flow field measurements (local total pressures and the three orthogonal velocity components) are made using a precalibrated non-nulling blunted conical 5-hole probe. The probe is also attached to an x-y traversing mechanism. The facility is fully computer controlled, with on-line data reduction and plotting, which made the detailed measurements with such a large number of devices feasible. Details of the computer and control system can be found in reference 8. For this investigation the rolling moment balance and traversing mechanism is also computer controlled. The mechanism can hunt for the position of maximum induced roll and/or produce detailed measurements. After finding the position of the maximum the program generates two scans, a lateral and a vertical, passing through this position.

Wing-Tip Modifications.

Seven different wing tip modifications "tips" are available; a schematic of the tips is shown in Figure 1. The reference tip is the half-body of revolution for which separation is expected throughout the chordwise tip length, at least at moderate incidence. The 70° sharp-edged delta planform was chosen to provide a concentrated standing vortex over the tip which will hopefully have a faster decay rate or possibly even bursting at high incidence. The hyperbolic trailing-edge tip should provide moderation of the spanwise loading near the tip (because of the gradual chord reduction) but retain flow attachment along the wing and tip leading edge. The hyperbolic leading-edge tip (similar to the Kuchemann tip used on aircraft such as the VC-10 and Boeing 707) is used because it combines the advantages, from the hazard point of view, of the delta tip and the hyperbolic trailing edge. This tip is sharp-edged and it was expected that complete separation along the tip leading edge, combined with some moderation of the spanwise loading gradient, would result in a less concentrated standing vortex above the wing. More details of these tips can be found in reference 28. The saw-toothed tip, which is actually like 4 delta wings in tandem, is used with the hope that it will break the tip vortex into 4 smaller cores, one for each leading edge, and that these cores will not merge.

Simulated Jet Engines.

The simulated jet engines (Figure 4) were designed to represent a Boeing 747 with JT9D engines. While the physical scale and position have been approximately represented, the detailed geometry of the pylon and nacelle are not, of course, correct; also, the inlet has been faired in. The jets are supplied with unheated high pressure air (100 psi) through separate ⅜-inch copper tubes embedded in the half-wing. Each supply pipe has four outlets corresponding to alternative spanwise mounting positions for each engine. For the present experiments the inboard engine was attached at a spanwise position $2y/b = 0.40$ and the outboard engine was at 0.67, closely simulating the layout of the B-747.

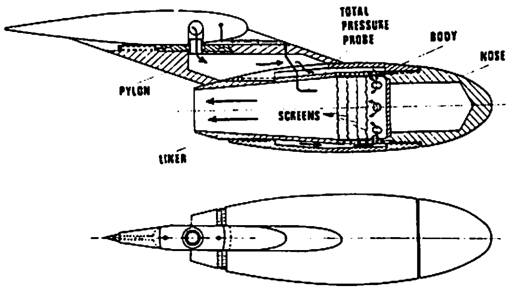

Figure 4. Simulated jet engine.

It is clearly not possible to simulate easily the mixed-flow exhaust of the JT9D engines with the varying exit velocities and densities in the two streams. Instead we have used jets of the correct overall relative scale and have attempted to get the external mixing approximately correct by using a jet-exit velocity to free-stream velocity ratio of 1.5. This ratio is representative of cruising flight conditions and is compatible with the relatively low wing-lift coefficients available with the present small-scale installation. Details of the design, sizing and calibration of the simulated engines can be found in reference 5.

Flap-Track Fairing Simulation.

The simulated flap-track fairings (herein referred to as flap tracks) again represent the Boeing 747; four are used on the (half) wing. Since little pertinent information was available about the structure of these fairings, their size and positioning on the wing are approximate. The spanwise position on the wing was also slightly altered to prevent sealing off the pressure plotting holes (for more details see reference 29). Figure 5 shows a photograph of the flap-track fairings mounted on the wing lower surface; the figure also shows the simulated engines and the 70°-delta tip. Surface flow visualization is also evident.

Figure 5. Surface flow visualization on wing lower surface with flap-track fairings, simulated jet engines and delta tip, $\alpha = 6.25°$.

Spoilers.

The spoilers were mounted near the tip on the wing upper surface. A hinge-like device (Figure 6) can be mounted on the wing and different spoilers could be attached to it. The chordwise position of the hinge as well as the angle with the free stream are adjustable (see Figure 7). Twenty-seven different spoilers were made but only 8 of them were actually used since only small differences in performance were noticed even with drastic variations in size.

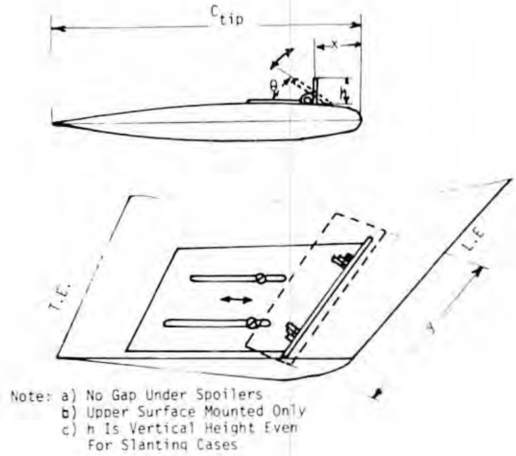

Note: a) No Gap Under Spoilers
b) Upper Surface Mounted Only
c) h Is Vertical Height Even For Slanting Cases

Figure 6. Spoiler mounting device.

Figure 7. Surface flow visualization on wing upper surface with spoiler and delta tip.

Simulated Smoke Generators.

The smoke generators considered are those used by NASA [25, 26] to mark the trailing vortices during their flight tests with the Boeing 747. The authors were concerned about the effects that these smoke generators might have on the vortex structure, especially since they are usually placed near the wing and/or flap tip. The simulated smoke generator used in this experiment is shown in Figure 8. Measurements were made with either one or two generators (on top of one another) mounted on the lower surface near the tip at the trailing edge (Figure 9).

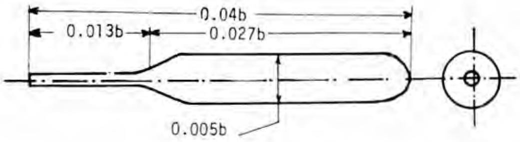

Figure 8. Simulated smoke generator.

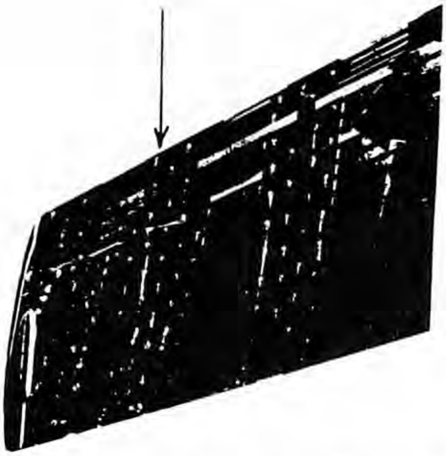

Figure 9. Simulated smoke generator mounted on the wing lower surface and surface flow visualization.

RESULTS AND DISCUSSION

For the clean wing configuration with the half-body-of-revolution tip, the standard case, detailed loading, flow field measurements, and induced rolling moment results are available at several angles of attack and downstream station and have been reported on before. The measurements with different devices have been made over an extended period of time. However, a reference case induced rolling-moment measurement was always made with every new set of measurements, and reproducibility was encouragingly good. A wind-on empty tunnel (generating wing removed) rolling-moment measurement was also always made to remove any non-zero induced roll as a result of machining inaccuracy or flow non-uniformities. Most of the tests with the devices were made with the generating wing at $\alpha = 6.25°$, $\bar{C}_L = 0.46$, at the 2½b station downstream and the trailing wing at nominally zero incidence. These conditions should be assumed unless otherwise mentioned.

Effect of Tip Configurations.

Table 2 summarizes the results of the tip configuration test program. Even though some relatively drastic variations in the tip shape have been attempted the corresponding variation in the induced rolling moment is very small. Surface pressure plotting shows that the effect of the various tips on the spanwise load distribution is limited to less than one tip chord inboard of the original tip. Surface flow visualization as well as wake traverses suggest a diffused core, in some of the configurations tried; however, the reduction in the induced rolling moment, in the near-field study, is very small. The results reported in Table 2 were made with engines mounted (see reference 11 for details); measurements made with the delta tip attached to a clean wing show a relatively higher reduction (~8%).

Table 2. Effect of Different Generator Tip Shape on Maximum Induced Rolling Moment [(a)]

	$\alpha = 5°$		$\alpha = 11°$	
Tip Shape	2½b	5b	2½b	5b
Half Body of Revolution (Standard case)	1	0.95	1	0.89
70° Delta	0.95	0.90	0.97	0.92
Hyperbolic Trailing Edge	0.98	0.92	0.97	0.89
Hyperbolic Leading Edge	0.96	0.91	0.95	0.89
Square Cut	0.99		1	
End Plate	1.01		0.97	

(a) Results presented as $(C_\ell/\bar{C}_L)/(C_\ell/\bar{C}_L)_{\text{standard case}}$ at 2½b station. Standard case, with engine mounted and half body of revolution tip.

The saw-tooth tip produced nearly no change in the rolling moment, see Table 3 and Figure 10(b). There is a slight shift in the position of the maximum induced roll indicating a slight shift of the vortex center. This shift corresponds to the effective outboard extension of the tip. In all probability the smaller cores shed from each leading edge merged forming a single tight core. The higher reduction in maximum induced roll for $\alpha = 11°$ is probably due to the more extensive leading edge separation and stronger tip vortex for this case (see reference 10).

Table 3. Effect of Different Devices Mounted on the Generating Wing on Maximum Induced Rolling Moment [(a)]

Device	$\alpha = 6.25$ $C_{L_{clean}} = 0.46$	$\alpha = 11°$ $C_{L_{clean}} = 0.73$
2 Smoke Generators	1	0.98
Saw Tooth Tip	0.99	0.96
70° Delta Tip	0.93	0.91
Tip Spoiler 0.09C$_t$ × 0.03b (normal, i.e., 90°)	0.91	0.97
Flap-track Fairings	0.97	0.99
2 Simulated Engines	0.92	—

(a) Results presented as

$$\left(\frac{C_{\ell_{max}}}{C_{L_{root_G}}}\right) \Bigg/ \left(\frac{C_{\ell_{max}}}{C_{L_{root_G}}}\right)_{\text{clean wing}}$$

at downstream station 2.5b.

The delta-tip case was considered the most effective for hazard reduction for two reasons. First, surface flow visualization and pressure plotting indicated no deterioration in the flow quality over the wing with this tip, even at $\alpha = 11°$. The flow over the wing with the hyperbolic leading-edge tip, which is as effective, was of unacceptable quality at $\alpha = 11°$ — a large region of spearation existed near the tip. Secondly, flow traverses indicated a tight core for the delta-tip case, leaving even more potential for hazard reduction through core diffusion.

Effect of Simulated Jet Engines and Air Injection.

Results of the program with the simulated engines have been previously reported [5, 6]. The mounting of two simulated engines on the main wing lower surface has resulted in about 8% reduction in the maximum induced rolling moment. Air injection through the simulated engines, with jet to free-stream velocity ratio of 1.5, has resulted in no appreciable change in the induced rolling-moment coefficient as compared to the engine-mounted no injection case. The injection has resulted in small changes in the vortex core position, but the core structure is essentially unchanged.

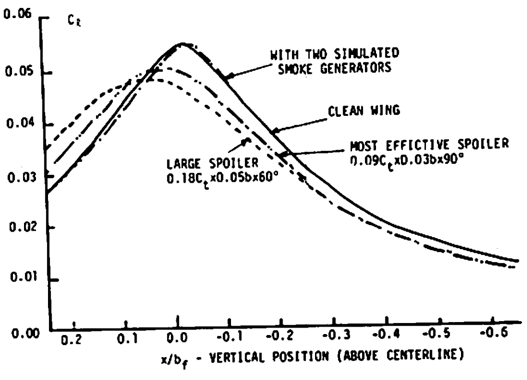

Figure 10a. Effect of spoilers and smoke generator on induced rolling moment coefficient — vertical scan, $\alpha = 6.25°$.

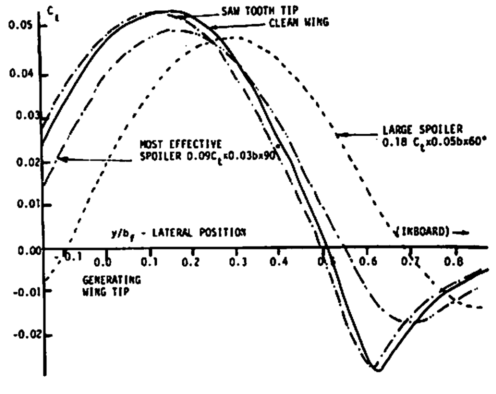

Figure 10b. Effect of spoilers and saw-tooth tip on induced rolling moment coefficient — lateral scan, $\alpha = 6.25°$.

What is important to note is that the reduction in the rolling moment is mainly the result of the interruption of the roll-up. Figure 11 shows a comparison of roll-up (of the viscous wake which contains all the shed vorticity) for the clean case as compared to the engine-mounted case with and without injection. The distortion and consequent interruption of roll-up to the still unrolled shear layer is quite evident.

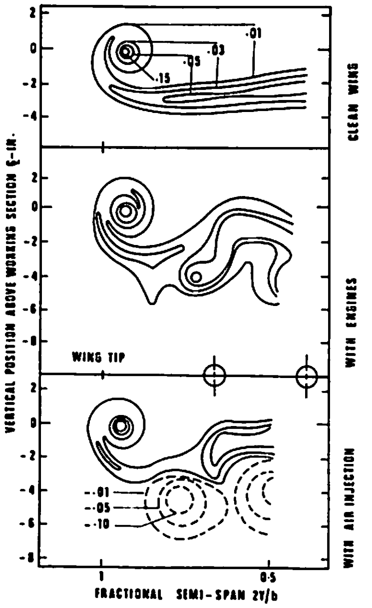

Figure 11. Contours of equal total pressure loss coefficient $(P_\infty — P_0)/\frac{1}{2}\rho V_\infty^2$. Effect of simulated jet engines, ($\alpha = 5°$, 2½b downstream).

Effect of Flap-Track Fairings.

The effects of flap-track fairings were examined at four angles of attack: 5°, 6.25°, 11° and −5° ($\bar{C}_L = 0.36, 0.46, 0.74$ and -0.36, respectively). The negative incidence corresponds to the fairings being effective on the aerodynamic upper surface of the wing (the wing section is symmetrical). It was felt that surface pressure plotting would be inappropriate since fairing effects are local and would not be detected by the coarse (in the spanwise direction) spacing of measuring stations. Instead, the flow field, 0.35b downstream, was mapped and the detailed spanwise distribution of circulation obtained (see reference 10 for details) — Figure 12. It is clear that the overall C_L would be higher with fairings since the loading is fuller. This is due to favourable interference effects of the induced pressure field on the lower surface. Note the local humps in the load distribution near the fairing positions especially for $\alpha = -5°$. Surface flow visualization (Figure 5) and wake traverses also indicate the fairings have only local effects on the wing.

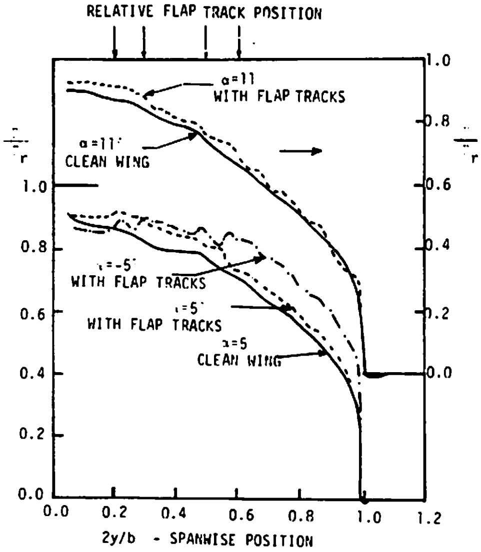

Figure 12. Spanwise circulation distribution; effect of flap-track fairings, 0.35b downstream.

The maximum induced rolling moment with the fairings was found to be more or less equal to or even slightly higher than for the clean wing case for the same incidence. However, if allowance is made for the higher $\bar{C}_L$, $C_{\ell\,max}/\bar{C}_L$ is slightly reduced as a result of mounting the flap-track fairings.

Effect of Spoilers.

The results of measurements with different spoilers are presented in Table 4 and Figure 13(a) and (b). Interestingly enough the maximum reduction in maximum induced rolling moment is very limited, even when very large spoilers were used. Spoilers were tried at several spanwise and chordwise locations and at several angles to the free stream. Figures 13(a) and (b) show that the effect of spoilers is to diffuse the core as is clear from

Table 4. Effect of Different Spoilers Mounted near Generating Wing Tip on Maximum Induced Rolling Moment

Spoiler					
h/c_{tip}	y/b	x/c_{tip}	θ	$C_{l\,max}$	$C_{l\,max}/C_{l\,max_{clean}}$
0.09	0.03	0.25	90°	0.051	0.91
0.18	0.03	0.25	90°	0.051	0.92
0.09	0.05	0.25	90°	0.052	0.93
0.09	0.03	0.25	60°	0.054	0.97
0.09	0.03	0.25	45°	0.054	0.97
0.09	0.02	0.25	90°	0.052	0.94
0.09	0.03	0.70	90°	0.053	0.95
0.18	0.05	0.25	60°	0.049	0.89
Clean Wing				0.056	1

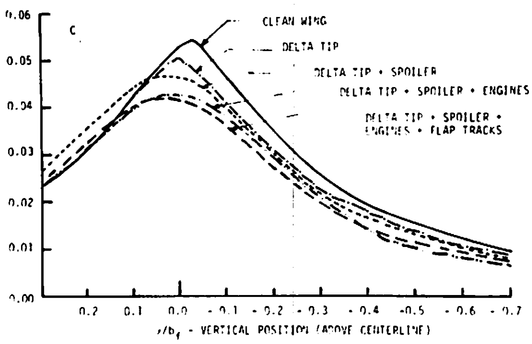

Figure 13a. Effect of combination of devices on induced rolling-moment coefficient; vertical scan, $\alpha = 6.25°$.

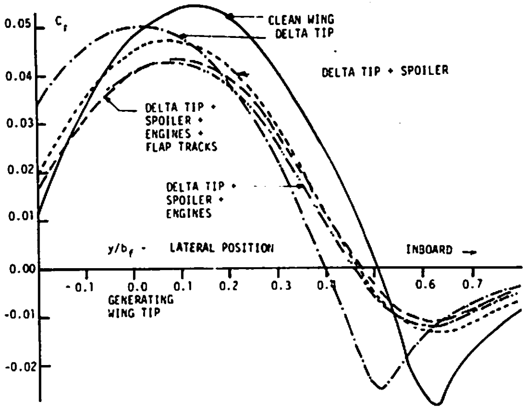

Figure 13b. Effect of combination of devices on induced rolling-moment coefficient; lateral scan, $\alpha = 6.25°$.

the flattening of the maximum and minimum peaks on the graph of the induced rolling moment (large cores with low $V_{\theta max}$). Figure 13(b) also shows that the position of the maximum induced rolling moment (and of course the vortex core) moves inboard, indicating more extensive separation near the tip (see also Figure 7). The closer spacing of the vortices might enhance their decay far downstream, or result in earlier hydrodynamic instability.

It is surprising to notice that increasing the size of the spoiler does not necessarily reduce the induced roll. The spoiler $0.09C_t \times 0.03b \times 90°$ was considered the most effective, since it produces the greatest reduction on induced rolling moment per unit spoiler area or per unit drag increment.

Effect of Simulated Smoke Generators.

It had been expected that the smoke generators would considerably modify the tip-edge separation and therefore the vortex core structure. To our surprise Figure 13(a) and Table 3 show that even with two generators placed on top of the other normal to the wing surface, the effect on the induced rolling moment is almost imperceptible, even at high α. Flow visualization (Figure 9) shows that the smokers disturb the boundary layers, on the lower surface, only near the trailing edge.

Effect of Combination of Devices.

The mechanisms by which the different devices affect the vortex system are different. The question arises whether it is possible to combine some of these devices to achieve a cumulative reduction in hazard.

Table 3 summarizes the effect of the different devices when applied individually. The effect of combination of devices is presented in Table 5 and Figures 13(a) and (b). The delta tip has produced a 7% reduction in hazard. By examining the variation of the induced rolling moment with position it becomes clear that shape of the curve is very similar to that for the clean wing. This is an indication that the reduction in maximum roll is the result of modified spanwise loading near the tip.

Table 5. Effect of Combination of Devices on Maximum Induced Rolling Moment [(a)]

Devices	$(C_{\ell_{max}}/C_{L_{rootG}})/(C_{\ell_{max}}/C_{L_{rootG}})_{\text{clean wing}}$
Clean Wing	1.
With Delta Tip	0.93
Delta Tip + Spoiler	0.87
Delta Tip + Spoiler + Engines	0.79
Delta Tip + Spoiler + Engines + Flap Track Fairings	0.75

(a) $\alpha = 6.25°$, $\bar{C}_L = 0.46$, 2.5b Station

The spoiler used resulted in a reduction of maximum induced roll of 9% when used alone. This reduction is basically due to diffusion of the vortex core (hence very dependent on the span of the following wing). The same spoiler resulted in an incremental reduction of only 7% when added to the wing with the delta tip. The difference is probably due to the fact that the core is now smaller, or contains less vorticity, hence diffusing it results in less hazard reduction.

The engines caused an 8% reduction, as compared to the clean standard case. This reduction is basically due to the interruption of roll-up. When added to the wing equipped with the delta tip and spoiler the relative reduction is even higher (9%). This is because less loading is carried near the tip which means more vorticity in the interrupted unrolled shear layer.

By adding the flap-track fairings an additional 4% reduction is obtained. The effective reduction is probably more because of the higher $\bar{C}_L$ expected. In some cases we have been considering variations of the same order as the uncertainties in the measurements. The only justification we have for this is that usually in these cases the measurements were repeated to ensure, at least, that they indicated the correct trends.

CONCLUSIONS

The results of an extensive wind-tunnel test program seem to suggest that it is not possible to drastically reduce the hazard of trailing vortices using a single device that has reasonable or no drag penalties. However, the results also suggest that if the problem of trailing vortices is considered during the design process, simple modifications or proper location of devices mounted on the wing could prove very helpful.

No device tested gave an effective reduction of maximum induced rolling moment, on a following wing, of more than 10%. However, with combination of devices a reduction of more than 25% was obtained. No effort was made to optimize device positions and it is expected that somewhat greater reduction of hazard is possible.

It should be reiterated that these conclusions are based on wind-tunnel tests (i.e., near field) with one fixed trailing/generating wing-span ratio and only for cruise conditions. Also, it does not make sense to look at the problem as a percentage reduction problem. Once one can get the maximum induced rolling moment down to or below the roll power of the intercepting aircraft the problem may be solved.

REFERENCES

1. Olsen, J., Goldberg, A., and Rogers, M., *Aircraft Wake Turbulence and Its Detection*, Plenum Press, New York, NY, 1971.

2. El-Ramly, Z., "Aircraft Trailing Vortices: A Survey of the Problem," ME/A 72-1, Nov. 1972, Carleton University, Ottawa, ON, Canada.

3. Donaldson, C.duP. and Bilanin, A., "Vortex Wakes of Conventioanl Aircraft," AGARDograph No. 204, May 1975.

4. Rossow, V.J., "Inviscid Modelling of Aircraft Trailing Vortices," NASA Symposium on Wake Vortex Minimization, Feb. 25-26, 1976, Washington, DC, p. 4-54.

5. El-Ramly, Z., "Investigation of the Development of the Trailing Vortex System Behind a Sweptback Wing," ME/A 75-3, Oct. 1975, Carleton University, Ottawa, ON, Canada.

6. El-Ramly, Z. and Rainbird, W.J., "Wind Tunnel Measurements of the Trailing Vortex Development Behind a Sweptback Wing: Effect of Simulated Jet Engines on the Flow Field," *J. Aircraft*, Vol. 14, No. 4, Apr. 1977, p. 343-349.

7. El-Ramly, Z., "Wind Tunnel Flow Field Measurements Behind a Sweptback Wing," Lockheed Georgia Contractor Report, P.O. CK 27059P, Carleton University, Ottawa, ON, Canada, Feb. 1976.

8. El-Ramly, Z. and Rainbird, W.J., "Computer Controlled System for the Investigation of the Flow Behind a Sweptback Wing," Proceedings of the 9th AIAA Aerodynamic Testing Conference, Arlington, TX, June 7-9, 1976, p. 119-128. (to be published in *J. Aircraft*).

9. El-Ramly, Z., Rainbird, W.J. and Earl, D.G., "Wind Tunnel Measurements of Rolling Moment in a Swept-Wing Vortex Wake," *J. Aircraft*, Vol. 13, No. 12, Dec. 1976, p. 962-967.

10. El-Ramly, Z. and Rainbird, W.J., "Flow Survey Behind Wings," AIAA paper #77-175, presented at the AIAA 15th Aerospace Sciences Meeting, Los Angeles, CA, Jan. 24-26, 1977.

11. El-Ramly, Z. and Rainbird, W.J., "Induced Rolling Moment on Trailing Wings," AIAA paper #77-663, to be presented at the AIAA 10th Fluid and Plasma Dynamics Conference, Albuquerque, NM, June 27-29, 1977.

12. Mokry, M. and Rainbird, W.J., "Calculation of Vortex Sheet Roll-up in a Rectangular Wind Tunnel," *J. Aircraft*, Vol. 12, Sep. 1975, p. 750-752.

13. Rossow, V.J., "Convective Merging of Vortex Cores in Lift-Generated Wakes," AIAA paper #76-415, AIAA 9th Fluid and Plasma Dynamics Conference, San Diego, CA, July 14-16, 1976.

14. Corsiglia, V.R. and Dunham, R.E., "Aircraft Wake-Vortex Minimization by Use of Flaps," NASA Symposium on Wake Vortex Minimization, Washington, DC, Feb. 25-26, 1976, p. 303-336.

15. DeVries, O., "Wind Tunnel Investigation of the Development of the Vortex Wake Behind a Sweptback Wing," National Aerospace Laboratory NLR, The Netherlands, TR 72017 C, Mar. 1973.

16. Smith, W.G. and Lozzeroni, F., "Experimental and Theoretical Study of a Rectangular Wing in a Vortical Wake at Low Speed," NASA TN-D-339, Oct. 1960.

17. Dunham, R.E., "Exploratory Concepts Found to be Unsuccessful for Aircraft Wake Vortex Minimization," NASA Symposium on Wake Vortex Minimization, Washington, DC, Feb. 25-26, 1976, p. 123-154.

18. Rorke, J.B. and Moffitt, R.C., "Wind-Tunnel Simulation of Full Scale Vortices," NASA CR-2180, Mar. 1973, Sikorsky Aircraft, Stratford, CT.

19. Thompson, D.H., "A Preliminary Towing Tank Study of the Trailing Vortex Generated by a Rectangular Wing, Including the Effects of Several Tip Modifications," ARL/A 342, Sep. 1973, Aeronautical Research Labs., Melbourne, Australia.

20. Scheiman, J. and Shivers, P., "Exploratory Investigation of the Structure of the Tip Vortex of a Semispan Wing for Several Wing-Tip Modifications," NASA TN D-6101, Feb. 1971.

21. Kirkman, K.L., Brown, C.E., and Goodman, A., "Evaluation of the Effectiveness of Various Devices for Attenuation of Trailing Vortices Based on Model Tests in a Large Towing Tank," NASA CR-2202, Dec. 1973, Hydronautics Inc., Laurel, MD.

22. Lee, G.H., "Trailing Vortex Wakes," *Aeronaut. J.*, Sep. 1975, p. 377-388.

23. Croom, D.R., "Wind Tunnel and Flight Evaluation of Spoilers as Trailing-Vortex Hazard Alleviation Devices," AIAA paper #77-10, AIAA 15th Aerospace Sciences Meeting, Los Angeles, CA, Jan. 24-26, 1977.

24. Patterson, J.C., Jr. and Jordan, F.L., Jr., "Thrust Augmented Vortex Attenuation," NASA Symposium on Wake Vortex Minimization, Washington, DC, Feb. 25-26, 1976.

25. Barber, M.R., Hastings, E.C., Jr., Champine, R.A., and Tymczyszyn, J.J., "Vortex Attenuation Flight Experiments," NASA Symposium on Wake Vortex Minimization, Washington, DC, Feb. 25-26, 1976.

26. Smith, H., "Flight Test Investigation of the Rolling Moments Induced on a T-37B Airplane in the Wake of a B-747 Airplane," NASA TM X-56031, Apr. 1975.

27. Garodz, L.J., "Measurements of Boeing 747, Lockheed C5A and Other Aircraft Vortex Wake Characteristics by Tower Fly-by Technique," in *Aircraft Wake Turbulence and its Detection*, Edited by J. Olsen, A. Goldberg and M. Rogers, Plenum Press, New York, NY, 1971, p. 265-286.

EFFECT OF WHITCOMB WINGLETS AND OTHER WINGTIP MODIFICATIONS ON WAKE VORTICES

HENRY F. FAERY, JR. AND JAMES F. MARCHMAN, III
Virginia Polytechnic Institute and State University
Blacksburg VA 24061

ABSTRACT: Experimental studies of the wake vortices generated behind six different wingtip configurations are presented. It is shown that the Whitcomb winglet configuration produces two distinct wingtip vortices, each of approximately 65% less swirl velocity than that produced by a simple rounded-tip configuration. Strong axial velocity deficits are shown to be characteristic of these vortices with reduced maximum swirl velocities.

INTRODUCTION

The hazard presented to aircraft from wake vortex encounters is well-documented. Naturally, the primary focus of the research into wake alleviation methods is directed toward the far-field case. However, it is also essential that thorough research be conducted in the nearfield so that definitive, quantitative data are available for evaluating and understanding the entire flow field more precisely. It is only through a combination of research into the near-field fluid flow dynamics and the far-field merging and dissipative patterns that a final wake alleviation solution will be found.

Over the past several years a number of researchers at Virginia Polytechnic Institute and State University have conducted investigations into the effects that wingtip modifications have on wake vortex profiles [1, 2, 3]. Due to the facilities available, these experimental studies are limited to the near-field wake. The results, however, not only have direct applicability in terms of helicopter rotor wake problems, but they also provide accurate quantitative vortex data to assist in understanding flow dynamics and in directing further research into areas which show promise of providing significant vortex alterations. It is also felt that these near-field results could be extended into far-field vortex research using the convective and turbulent merging models which have been recently developed [4, 5, 6, 7]. This paper will present the experimental findings from tests conducted on six different wingtip configurations.

PHYSICAL MODELS

The reader is here cautioned that the terminology used to describe some of the wingtip modifications may be misleading. Usually one visualizes the modification as it affects the planform shape. The modifications, discussed herein, however, describe the wingtip as seen by an observer looking along the chord line.

The first configuration tested was a simple "square" tip (Figure 1), a tip normally employed on most helicopter rotor blades and also seen on some fixed-wing aircraft. The base configuration was the "round" tip, a half surface of revolution. From a planform view, the "round" tip also has some aerodynamic streamlining. This tip was chosen to represent a very easily manufactured tip which appears on many fixed-wing aircraft, particularly in the general aviation field. The third configuration was a "pointed" tip, which is simply an aerodynamically streamlined tip that is tapered sharply from the top and bottom surfaces toward the centerline. This shape was chosen to determine the effects that a large shear gradient at the tip would have on the vortex velocity characteristics.

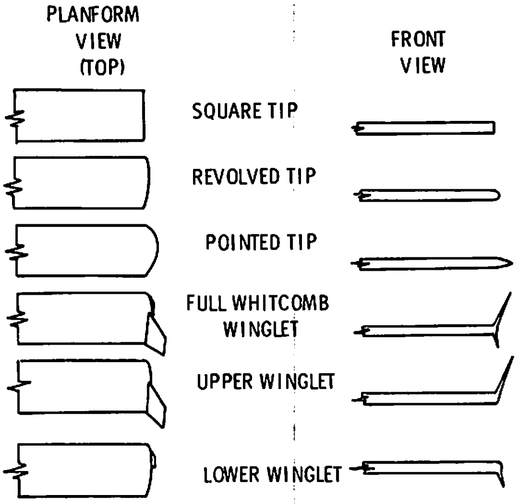

Figure 1. Wing tip test configurations.

The "Whitcomb winglet" was the fourth major configuration tested. Although the major claims for the winglet center around improved aerodynamic efficiency at cruise conditions, it was felt that an obvious side effect should be a less intense trailing vortex since the winglets are said to reduce the induced drag. In fact, Whitcomb gives his winglets an alternate name, vortex diffusers [8]. The winglet configuration tested was constructed from plans obtained from Whitcomb about a year ago and it should be noted that it includes the lower winglet of the original Whitcomb design (Figure 2). NASA has, however, now removed this lower portion of the winglet in their present testing and has also changed the cant angles from those of the original design.

The remaining two configurations were simply the individual components of the winglet: the winglet base with the upper winglet only, and the winglet base with only the lower winglet. It should be noted that the round tip served as the winglet base.

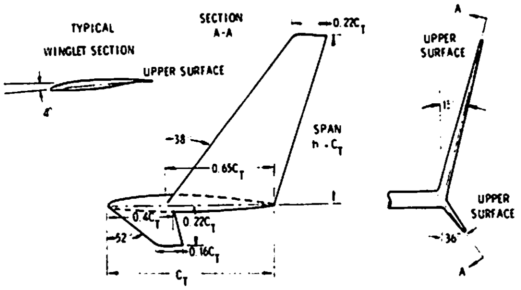

Figure 2. Whitcomb winglet.

All of the wingtip modifications were attached to an untapered NACA 0012 wing of eight-inch chord and four-foot span. The wing was fitted with quarter-chord spanwise pressure taps and chordwise pressure taps immediately adjacent to the tip.

EXPERIMENTAL PROCEDURE

The wing was mounted at a six-degree angle of attack from the test-section ceiling of the Virginia Tech Stability Wind Tunnel, a low-level turbulence wind tunnel having a six-foot square test section (Figure 3). The trailing vortex was probed at five and twenty chordlengths downstream by a ⅛-inch diameter five-hole yawhead probe. The experimental information was obtained in the form of pressure measurements from the yawhead probe and probe-position measurements for displacement from the vortex core. Radial traverses were made from the vortex core to a distance of almost six inches on two sides of each vortex. Data points were established at very close intervals, 0.036 inch, within the vortex core, and spaced at larger intervals outside the core.

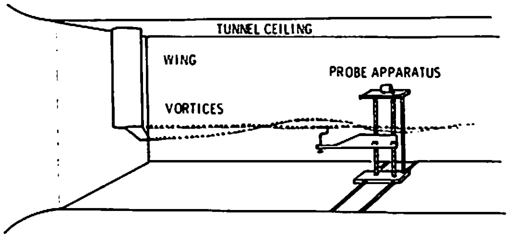

Figure 3. Schematic of test set-up.

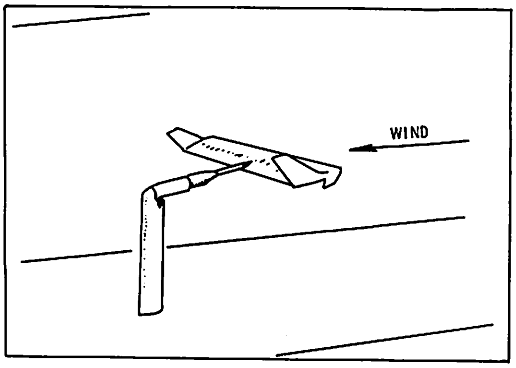

Figure 4. Wing on strain gauge balance system in wind tunnel.

Data reduction was accomplished using a computer program and plotting routine to illustrate the vortex tangential and axial velocity profiles. This data collection and reduction system is the same used in past vortex studies at VPI [1-3]. It was encouraging to note that the previous work done by Mason and Turnage was repeatable with excellent accuracy at each of six stations for five to thirty chordlengths downstream.

Three general assumptions were made: first, the flow was assumed incompressible since the Mach number never exceeded 0.1; second, it was assumed that the vortex path was parallel to the free stream path and unaffected by the tunnel walls, a reasonable assumption since the vortex core was at least 24-core diameters from the nearest wall; third, inviscid theory was used. Spanwise and chordwise pressure measurements were also made for each configuration at the test Reynolds number of 370,000.

As a follow-up to these tests, it was decided to attempt to correlate the wingtip effects on the trailing vortex with the wingtip effects on the wing aerodynamic forces. The identical wingtip modifications were mounted on a smaller aspect ratio, similar wing to compare their lift and drag characteristics. This wing also was placed at a six-degree angle of attack and force readings were obtained through a sting-mounted six-component strain gauge balance (Figure 4). Additionally, the aerodynamic forces were measured on the unattached winglet to assist in determining its contribution to the wing with attached winglet configuration. Spanwise pressure distribution was also obtained for this wing setup.

RESULTS AND DISCUSSION

The experimental vortex data is presented using the familiar plots of the vortex tangential and axial velocities versus vortex radius. Figure 5 compares a typical experimentally-obtained tangential velocity profile with a predicted profile based on the inviscid theory of Betz and also with an empirical prediction proposed by McCormick [1]. As stated previously, it is obvious that the experimental results provided very adequate correlation with theory.

Since this study uses the rounded tip as the "base" tip, then a look at its characteristic profile at the two downstream test locations provides a datum from which to discuss the experimental findings (Figure 6). The vortex is slightly non-symmetrical at the five-chordlength position due to two effects: first, the vortex is still in the roll-up stage;

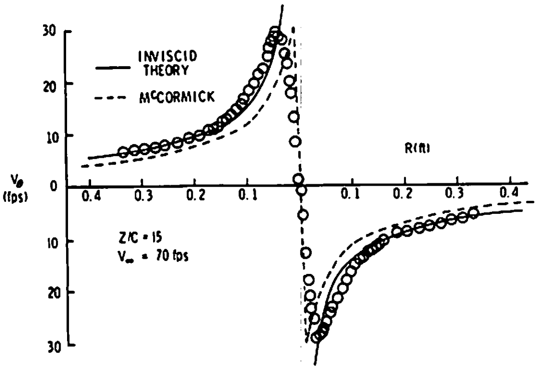

Figure 5. Experimental vs. theoretical tangential velocity profile.

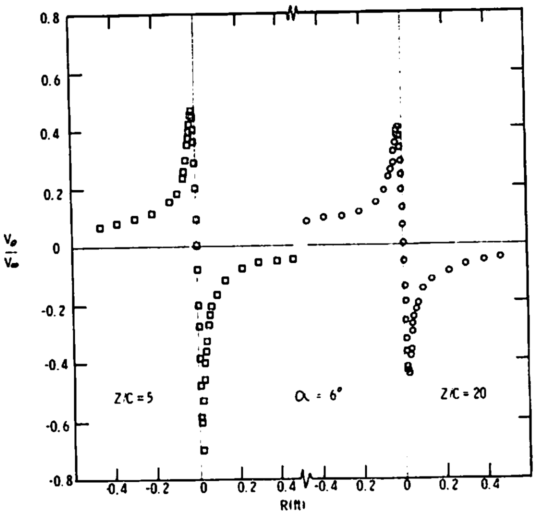

Figure 6. Vortex tangential velocity decay round tip/winglet base.

secondly, the interaction between the inboard side of the vortex and the downwash immediately behind the wing has a tendency to increase the tangential velocities on the inboard side. At twenty chordlengths downstream the vortex has essentially rolled-up, is very symmetrical, and presents almost negligible change in core size. This is typical of most of the tip modifications studied.

A study of the radial circulation distribution for the various wingtips indicates that each vortex has completed the roll-up process by the twenty-chordlength position. In fact, this is in excellent agreement with a theoretical prediction presented by Spreiter and Sacks [9]. Their calculations were based on the theoretical span-load distribution calculated by Glauert using Prandtl lifting-line theory, and depend upon both aspect ratio and the span-load distribution. For the experiment, predicted roll-up occurred between 17 and 20 chordlengths downstream, depending on the wingtip modification.

Further, a comparison of experimental results for the determination of Γ_0, the circulation shed from one side of a wing, with the analytical result presented by Corsiglia, et al., [10], shows excellent agreement for all wingtips studied. Analytical results predict Γ_0 values between 15.8 ft²/sec and 19 ft²/sec, values verified by the experiment. A similar elliptically-loaded wing would have a base circulation of 20–24 ft²/sec for the same conditions.

The remainder of the discussion will primarily focus on the results determined at the twenty-chordlength position. Figure 7 presents a comparison of the round tip with the simple square and pointed tips at this location. Of significant note is the 27% reduction in maximum tangential velocity produced by the pointed tip. It should be further noted that this change is also accomplished by a 5.8% reduction in core size, a fact which contradicts observations of some previous studies [1, 2]. In those studies it was speculated that there was a trade-off between core size and swirl velocity magnitude. If one increased, then the other decreased in order to account for a constant energy within the vortex system. Here, however, a higher energy system is producing a lower velocity vortex with a tighter core. (The circulation shed by the pointed tip is about 9% higher than that shed by the round tip).

The axial velocity profiles are compared in Figure 8 for the same three tip modifications. Although all three profiles exhibit a velocity deficit in the core, the pointed

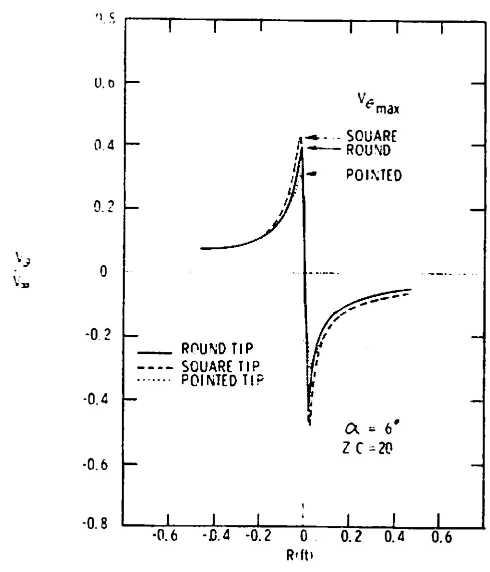

Figure 7. Tangential velocity comparison.

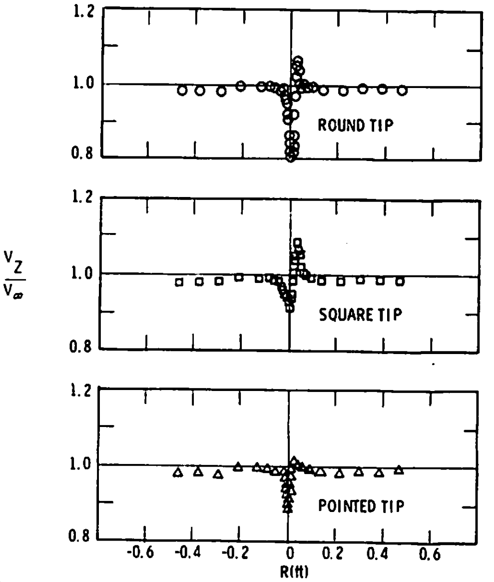

Figure 8. Comparison of axial velocity profiles (z/c = 20).

tip is the only one to show no velocity excess at all. Perhaps this one feature is part of the explanation for the significant reductions in tangential velocity and verifies Bilanin's contention that deficits in axial velocity result in a reduction of the centerline swirl velocity [11]. It is also conjectured that the large shear gradient imposed at the pointed tip is a major causative factor in this vortex behavior.

Figures 9 to 16 depict vortex patterns for the Whitcomb winglet or components of the winglet. In investigating the contributions of the individual components of the winglet on the vortex it was found that three individual vortices of like sign are produced; however, the vortex from the lower, small winglet immediately merges with the main wing vortex. Unlike a previous report [12] which stated that "the addition of the winglets spreads the vorticity . . . to such an extent that a discrete vortex core is not apparent", the present study shows two distinct vortices which persist for the entire downstream distance measured. In fact, a tow-tank observation shows that the two vortices persist downstream for quite some distance, wrapping around each other. This clockwise rotation (as viewed upstream at the left wingtip) is evident in Figures 9 and 10. Also apparent at the twenty-chordlength position is the interference of the two vortices with each other. For comparative purposes, the maximum swirl velocities in each of the two vortices at the twenty-chord length position is about 64% less than that of the round or base tip. Each of the vortices also has a smaller core than the round tip, although once again the circulation shed by this wingtip modification is considerably higher than the rounded tip. In fact, the winglet system shed the most of any tip modification studied. Figures 11 and 12 depict the axial velocity profiles for the winglet, and once again it should be observed that each vortex contains only a strong deficit in axial velocity. It seems that a strong axial deficit is associated with a reduction in tangential velocity.

As previously noted tests were also run using the wing with only one part (upper winglet or lower winglet) of the original Whitcomb design. The contribution of the upper winglet is presented in Figures 13 and 14. Several points can be made concerning the effects of this configuration. First, the maximum swirl velocities have been even further reduced. Secondly, vortex #1 contains an uncharacteristic vortex core spread that has not been seen on the previous tip modifications. Thirdly, once again the axial

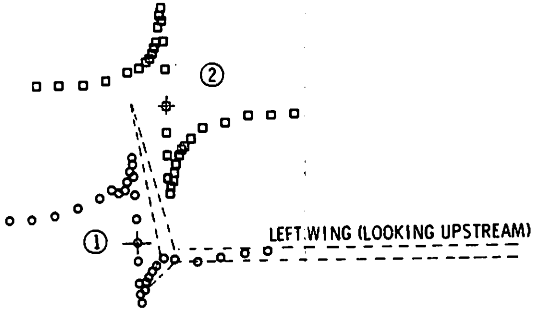

Figure 9. Winglet vortices (z/c = 5).

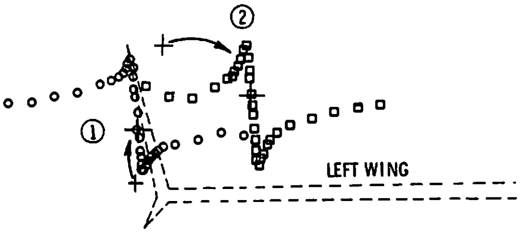

Figure 10. Winglet vortices (z/c = 20).

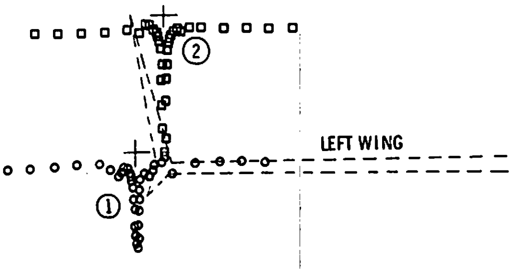

Figure 11. Winglet axial velocity profiles (z/c = 5).

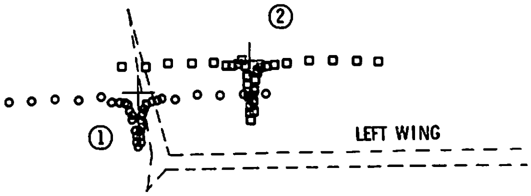

Figure 12. Winglet axial velocity profiles (z/c = 20).

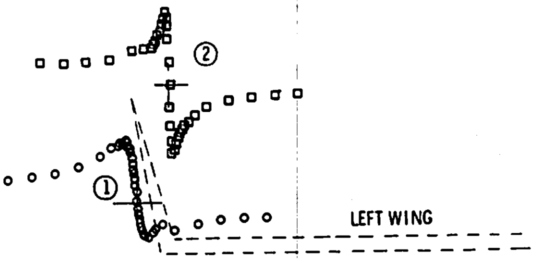

Figure 13. Upper winglet vortices (z/c = 5).

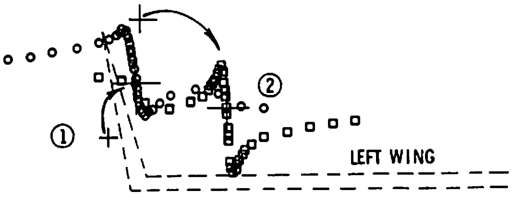

Figure 14. Upper winglet vortices (z/c = 20).

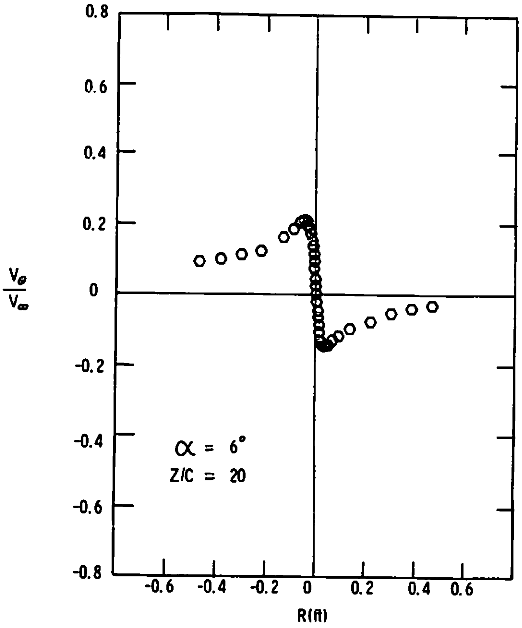

Figure 15. Lower winglet tangential velocity profile.

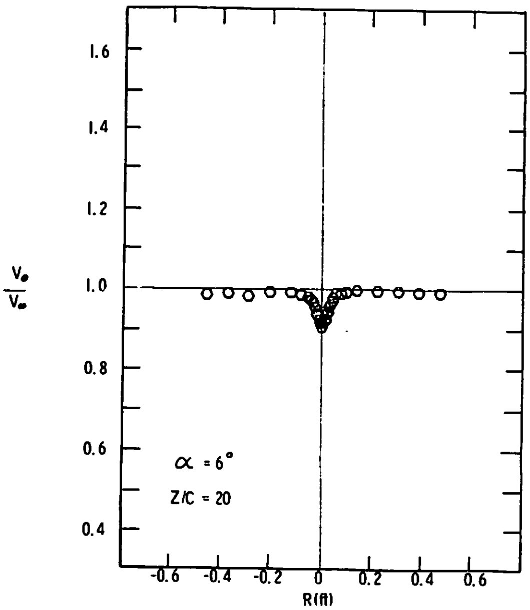

Figure 16. Lower winglet axial velocity profile.

velocity profiles exhibit a strong deficit. These last two observations are also obvious in the vortex profiles of the lower winglet contribution (Figures 15-16). Although the swirl velocity reduction with the lower winglet only is not as great as that with either the upper winglet or with the total winglet, the vortex core expansion is seen to occur. In fact, the lower winglet configuration produces the most dramatic core size increase of all the tip modifications studied.

The variation in vortex core size becomes more apparent in the bar graphs depicting development of maximum swirl velocities and core sizes (Figures 17 and 18). As has been well-documented there is a trade-off between swirl velocity decay and core size increase with downstream distance. However, this experiment does not show that this trade-off occurs so as to keep the product of $V_{\theta_{max}}$ and core radius a constant [13]. It is possible that this relationship does not have validity for this experiment since all data were collected in or immediately aft of the roll-up region. The bar graphs clearly show that: (1) the upper winglet alone is superior to the total winglet, in fact is superior to all modifications studied, in reducing the maximum tangential velocities; (2) the upper winglet vortex cores are substantially more spread than those of the total winglet; (3) the lower winglet alone is nearly as effective as the total winglet in reducing the maximum swirl velocity and has considerably more vortex core spread as it moves downstream. Of course, the lower winglet only produces one distinct vortex, whereas the upper winglet and the total winglet each produce two distinct vortices. This fact alone makes comparison difficult, as in trying to compare the winglet configuration results to those of the round, square, or pointed tips. It would seem, however, advantageous to produce multiple vortices of lesser intensity rather than a single, more intense vortex. Twin vortices provide the possibility of destructive merger; or, if remaining distinct until dissipation, these less intense vortices should present less roll-upset potential to following aircraft.

No discussion of wingtip modifications, particularly the Whitcomb winglet configuration, would be complete without some reference to the aerodynamic performance of these tips. The lift-drag ratio comparison presented in Figure 19 and Table 1 illustrates dramatically the dynamic improvement in aerodynamic efficiency produced by both the

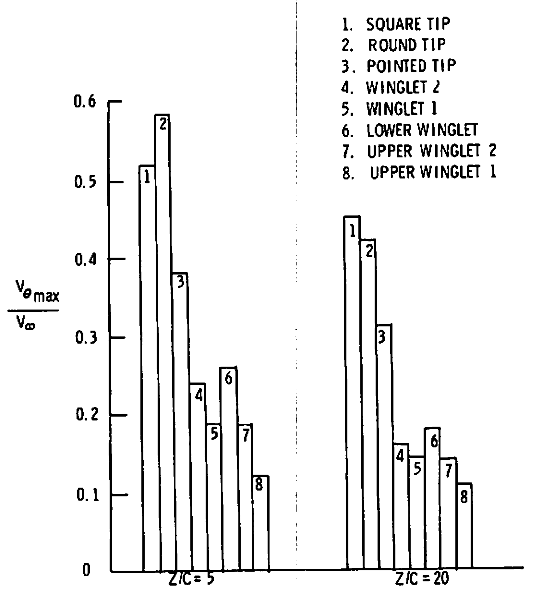

Figure 17. Maximum tangential velocity comparison.

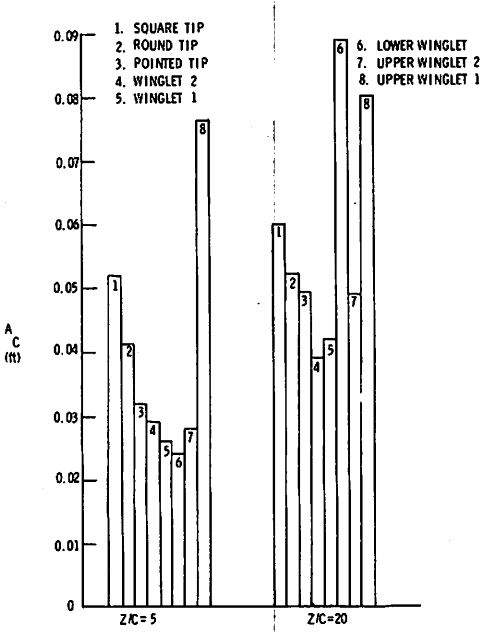

Figure 18. Comparison of core size.

full winglet and the upper winglet alone. At the maximum lift-drag ratio for the winglet there is a 17% increase in L/D over that of the round tip with an accompanying 15% reduction in drag coefficient. Even at this low test Reynolds number the experiments verify most of the trends in aerodynamic improvement presented in Whitcomb's recent paper [8]. At higher lift coefficients than $C_L = 0.55$

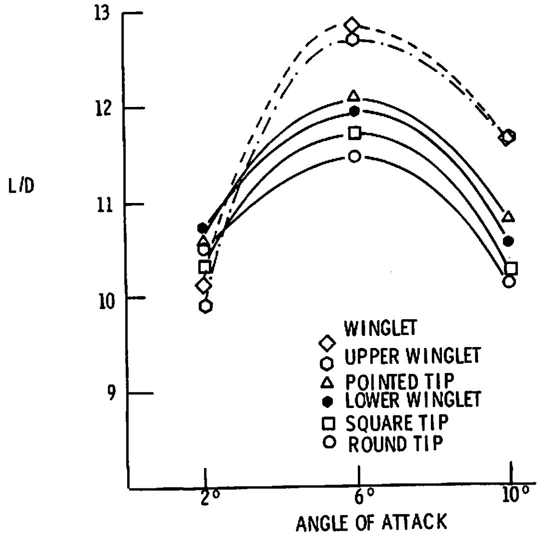

Figure 19. Lift-drag ratio comparison.

even greater reductions in drag coefficient were found although the lift-drag ratio improvement is smaller. The lower winglet provides marginal improvement at all lift coefficients, but its performance is surpassed by that of the pointed tip.

Table 1. Lift and Drag Data

Configuration	α (degrees)	C_L	C_D	L/D
Square Tip	2	.189	.018	10.32
	6	.489	.042	11.69
	10	.718	.070	10.23
Round/Base	2	.193	.018	10.53
	6	.484	.042	11.46
	10	.718	.071	10.13
Pointed Tip	2	.206	.019	10.59
	6	.527	.044	12.08
	10	.785	.073	10.78
Winglet	2	.227	.022	10.08
	6	.578	.045	12.81
	10	.840	.072	11.61
Upper Winglet	2	.214	.022	9.91
	6	.554	.044	12.68
	10	.806	.069	11.63
Lower Winglet	2	.208	.019	10.71
	6	.517	.043	11.94
	10	.748	.071	10.54

The spanwise pressure distribution along the quarter chord for each configuration is presented in Figure 20. The pressure distribution for the total winglet and the upper winglet only are nearly the same and substantially higher on the outboard section of the wing than that produced by the round or square tips. Of interest is the nearly identical distribution for the pointed tip and lower winglet only. A comparison of these pressure distributions with the vortex profiles clearly indicates that a reduction in maximum swirl velocity appears to be linked to a span load increase near the tips.

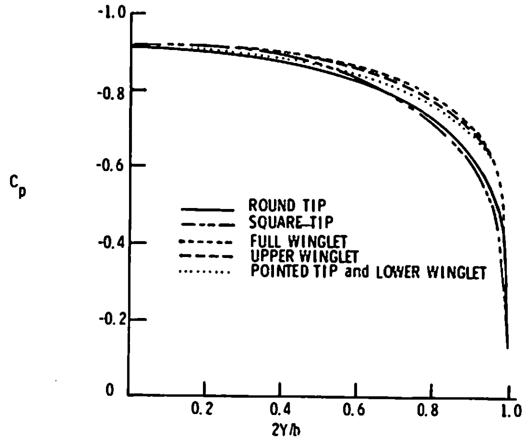

Figure 20. Spanwise pressure distributions.

CONCLUSIONS

A wind-tunnel investigation has been conducted on six different wingtip configurations to determine their vortex characteristics in the near-field and their aerodynamic performance over a limited range of angles of attack. The Whitcomb winglet has been compared with its components and with three simple tip modifications. Several conclusions can be reached:

1) Either the Whitcomb winglet or the upper winglet configuration is superior in all aspects to the tip modifications studied.

a) The winglet's 17% increase in lift-drag ratio, coupled with a 15% reduction in drag coefficient, further substantiate its contribution to aerodynamic performance improvement.

b) The 64% reduction in maximum tangential velocity is a significant achievement. Additionally, it is felt that the twin vortices of lesser intensity have greater potential for wake-alleviation research efforts than a single vortex of larger combined intensity.

2) When comparing the winglet results with those of the upper winglet alone, it would appear that the latter configuration has more promise. Its vortices are less intense and one of them has a tendency for early decay. The lift-drag ratio increase and drag coefficient reduction are very comparable to the total winglet.

3) The lower winglet configuration shows remarkable ability to decrease the vortex tangential velocity and cause early decay. However, its aerodynamic performance improvement is marginal.

4) The pointed tip is very effective in reducing the vortex swirl velocities and also does well in improving aerodynamic efficiency. It is felt that the large shears produced as the flow goes around the pointed wingtip result in vortex velocity reduction and dissipation in much the same manner as the shears caused by the interaction of vortices from the Whitcomb winglet.

5) Further investigation should be made into the use of both the pointed tip and the lower winglet for helicopter blades. They have possible potential in reducing rotor noise and improving blade efficiency.

6) It is felt that fruitful research can be done into optimization of the upper winglet configuration. Analytical merger models should be applied to determine if more rapid vortex dissipation can be produced. The far-field vortex pattern of the upper winglet should be analyzed in facilities capable of this testing. Such testing and analysis could possibly produce an optimum vortex diffuser at minimum loss of current aerodynamic improvement.

REFERENCES

1. Marchman, J.F. and Mason, W.H., "Farfield Structure of an Aircraft Trailing Vortex Including Effects of Mass Injection," NASA Report CR-62078, Apr. 1972.

2. Marchman, J.F. and Uzel, J.N., "The Effect of Wing-Tip Modifications on Aircraft Wake Turbulence," College of Engineering, VPI and SU, VPI-E-72-8, July 1972.

3. Turnage, J.O., "Tip Modification Effects on Helicopter Rotor Vortices," Masters Thesis, College of Engineering, VPI and SU, Aug. 1975.

4. Rossow, V.J., "Convective Merging of Vortex Cores in Lift-Generated Wakes," AIAA Paper No. 76-415, San Diego, CA, July 1976.

5. Rossow, V.J., "Theoretical Study of Lift-Generated Vortex Wakes Designed to Avoid Roll Up," *AIAA J.*, Vol. 13, No. 4, Apr. 1975, p. 476-484.

6. Bilanin, A.J., Teske, M.E., Donaldson, C.duP. and Snedeker, R.S., "Viscous Effects in Aircraft Trailing Vortices," NASA Symposium on Wake Vortex Minimization, Washington, DC, Feb. 1976, p. 55-122.

7. Bilanin, A.J., Teske, M.E., and Williamson, G.G., "Vortex Interactions and Decay in Aircraft Wakes," *AIAA J.*, Vol. 15, No. 2, Feb. 1977, p. 250-260.

8. Whitcomb, R.T., "A Design Approach and Selected Wind-tunnel Results at High Subsonic Speeds for Wing-Tip Mounted Winglets," NASA TN D-8260, July 1976.

9. Spreiter, J.R. and Sacks, A.H., "The Rolling Up of the Trailing Vortex Sheet and Its Effect on the Downwash Behind Wings," *J. Aeronaut. Sci.*, Vol. 18, Jan. 1951, p. 21-32.

10. Corsiglia, V.R., Schwind, R.G., and Chigier, N.A., "Rapid Scanning, Three-Dimensional Hot-Wire Anemometer Surveys of Wing-Tip Vortices," *J. Aircraft*, Vol. 10, No. 12, Dec. 1973, p. 752-757.

11. Bilanin, A.J. and Donaldson, C.duP, "Estimation of Velocities and Roll-Up in Aircraft Vortex Wakes," *J. Aircraft*, Vol. 12, No. 7, July 1975, p. 578-585.

12. Flechner, S.G., Jacobs, P.F., and Whitcomb, R.T., "A High Subsonic Speed Wind-Tunnel Investigation of Winglets on a Representative Second-Generation Jet Transport Wing," NASA TN D-8264, July 1976.

13. McCormick, B.W., Tangler, J.L. and Sherrieb, H.E., "Structure of Trailing Vortices," *J. Aircraft*, Vol. 5, No. 3, May-June 1968, p. 260-267.

DEVELOPMENT OF SPOILERS AS TRAILING-VORTEX HAZARD ALLEVIATION DEVICES

DELWIN R. CROOM
NASA Langley Research Center
Hampton VA 23665

ABSTRACT: This paper presents the results of groundbase and flight investigations that have been performed at NASA for the purpose of development of spoilers as trailing-vortex hazard alleviation devices. Based on the results obtained in these investigations, it was found that the induced rolling moment on a trailing model can be reduced by spoilers located near the mid-semispan of a vortex-generating wing. Substantial reductions in induced rolling moment occur when the spoiler vortex attenuator is located well forward on both unswept and swept wing models. In addition, it was found by groundbased model tests and verified by full-scale flight tests that the existing flight spoilers on the B-747 aircraft are effective as trailing vortex attenuators. Based on the results of wind-tunnel investigations of the DC-10-30 and L-1011 airplane models, the existing flight spoilers on both the DC-10-30 and L-1011 airplanes may also be effective trailing vortex attenuators.

NOMENCLATURE

b	wing span, m
c	wing chord, m
$\bar{c}$	wing mean aerodynamic chord, m
C_L	lift coefficient, Lift/qS_W
$C_{L,trim}$	trimmed lift coefficient
$C_{l,TW}$	trailing wing rolling-moment coefficient, $\frac{\text{Trailing wing rolling moment}}{qS_{TW}b_{TW}}$
C_m	pitching-moment coefficient, $\frac{\text{Pitching moment}}{qS_W\bar{c}_W}$
q	dynamic pressure, Pa
S	wing area, m^2
α	angle of attack, deg.

Subscripts:

W	generating model
TW	trailing wing model
max	maximum.

INTRODUCTION

The strong vortex wakes generated by large transport aircraft are a potential hazard to smaller aircraft. The National Aeronautics and Space Administration (NASA) is involved in a program of model tests, flight tests, and theoretical studies to determine the feasibility of reducing the hazard by aerodynamic means. This hazard is defined schematically in Figure 1. One phase of this program has been devoted to experimental investigations of spoilers as a possible method of trailing vortex attenuation since spoilers can inject turbulence in the wake, and they are also an effective way to alter the span load distribution. This paper will briefly cover the NASA activity in development of spoilers as vortex attentuators.

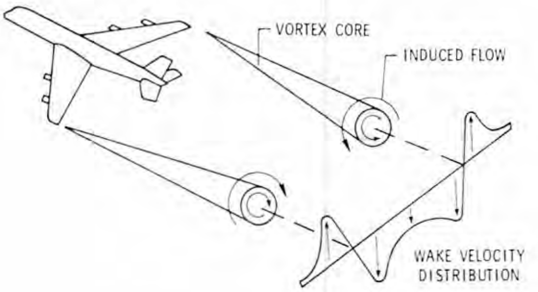

Figure 1. Schematic of aircraft vortex-wake hazard.

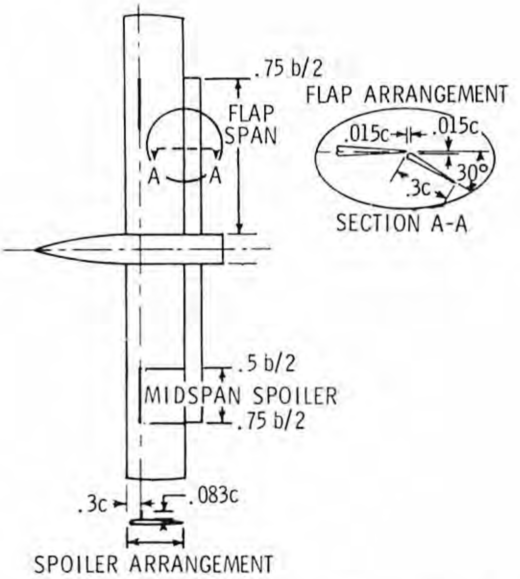

Figure 2. Sketch of aspect-ratio-8 models used in vortex-wake studies.

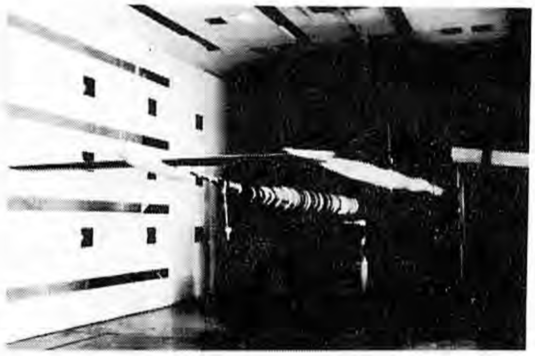

Figure 3. Photograph of aspect-ratio-8 model in the Langley V/STOL tunnel.

SPOILER INVESTIGATIONS

Midspan Spoilers on Untapered Aspect-Ratio-8 Wing Model.

In 1971, experimental work was initiated at the NASA Langley Research Center to investigate spoilers as a possible vortex abatement device. In the first phase of this study, a semispan wing was used in a study to determine the proper location for a spoiler to be installed on the wing to cause the largest apparent alteration to the trailing vortex. To accomplish this, a semispan wing was mounted on the carriage in the Langley tow tank and propelled through a smoke screen at which time observations were made of the behavior of the smoke being entrained in the vortex. After several hundred observations of the smoke patterns with the spoilers positioned at practically every conceivable location on the wing, it was determined that a spoiler of about 8-percent chord projection which was located between the 50- and 75-percent spanwise location near the 30-percent chord line would cause the most alteration to the vortex system, and, in general, the observed vortex motion became essentially nonexistent after a very short time. Based on these observations, a wind-tunnel investigation was made using an unswept aspect-ratio-8 wing model with a spoiler having an 8-percent projection located along the 30-percent chord line between the 50- and 75-percent span station as shown in Figure 2. The three-quarter span flaps used on the model were appended to the wing as is shown in Figure 2. Figure 3 is a photograph of the aspect-ratio-8 model mounted in the Langley V/STOL tunnel.

The spoiler effectiveness was evaluated using the trailing model technique to determine the maximum rolling-moment coefficient (Figure 4) induced by the generating model. It can be seen that the spoiler was effective in reducing the induced rolling-moment coefficient on the following model by about 25 percent throughout the range of downstream distances investigated. The complete results of this investigation are reported in reference 1.

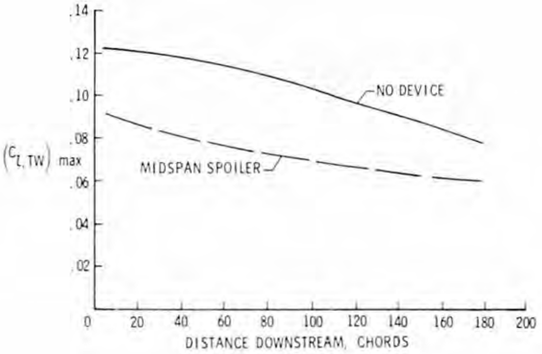

Figure 4. Effect of midspan spoiler on the variation of trailing wing rolling-moment coefficient with downstream distance behind aspect-ratio-8 wing. $C_L = 1.25$; $b_{TW}/b = 0.25$.

Midspan Spoilers on B-747 Airplane Model.

Since the prime concern was the vortex-wake problem behind very large transport aircraft, a decision was made to concentrate groundbased studies on the jumbo-jet class of aircraft. Therefore, a 0.03-scale model of a B-747 airplane (Figure 5) was used for subsequent tests in the Langley V/STOL tunnel. Results of this investigation are reported in reference 2. Figure 6 is a photograph of the B-747 airplane model mounted in the V/STOL tunnel with its landing flaps extended; also shown downstream is the traverse rig for mounting the trailing model.

WING	
SPAN, m	1.79
MEAN AERODYNAMIC CHORD, m	0.25
ROOT CHORD, m	0.497
TIP CHORD, m	0.121
SWEEPBACK AT QUARTER CHORD, deg	37.5
AREA, m^2	0.460
ASPECT RATIO	6.96
FUSELAGE	
LENGTH, m	2.06
HORIZONTAL TAIL	
SPAN, m	0.664
AREA, m^2	0.123
ASPECT RATIO	3.6

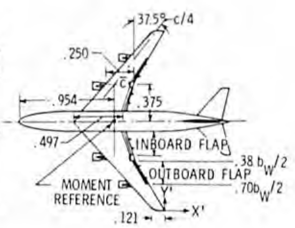

Figure 5. Plainview sketch of 0.03-scale B-747 airplane model.

Figure 6. Photograph of B-747 airplane model and traverse rig in the Langley V/STOL tunnel.

Two sizes of unswept trailing wing models were used during the investigation (Figure 7). One had a span and aspect ratio equivalent to a small business jet aircraft and the other had the span and aspect ratio equivalent to a medium size jet transport aircraft. These trailing models are referenced on the figures as the small and large trailing models.

The first spoiler configuration investigated as vortex attenuators on the B-747

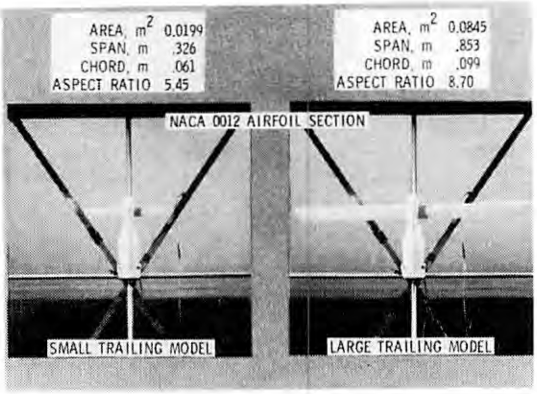

Figure 7. Photographs of unswept trailing wing models on traverse mechanism. (Models used for B-747 airplane model tests.)

airplane model were plain vertical projection spoilers located along the 30-percent chord line between the 50- and 75-percent semispan stations as is shown in Figure 8. Figure 9 is a photograph of the spoilers mounted on the wing of the B-747 airplane model. Figure 10 shows the effect of spoiler projection of the induced rolling-moment coefficient measured on the small trailing wing model when it was located at 6.74 spans downstream of the B-747 airplane model. It can be seen that the maximum reduction in rolling moment was achieved with about an 8-percent spoiler projection. Therefore, subsequent tests were made with the spoiler projected to 8 percent.

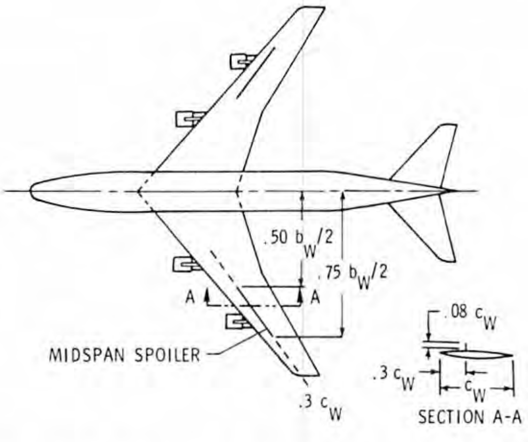

Figure 8. Schematic showing midspan spoiler details on B-747 airplane model.

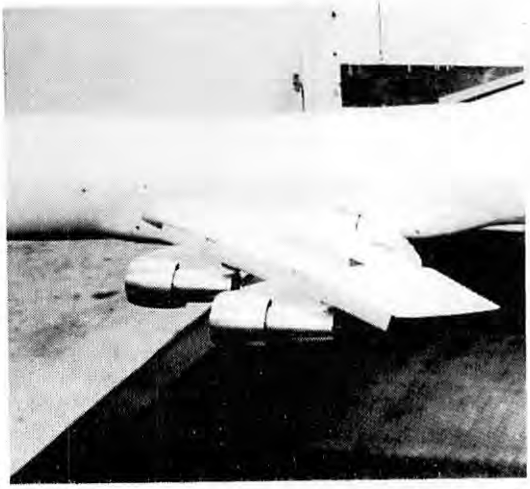

Figure 9. Photograph of midspan spoiler on B-747 airplane model.

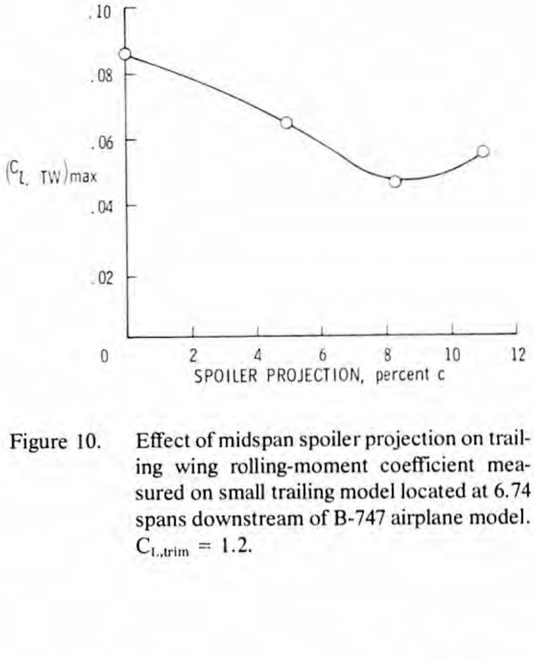

Figure 10. Effect of midspan spoiler projection on trailing wing rolling-moment coefficient measured on small trailing model located at 6.74 spans downstream of B-747 airplane model. $C_{L,trim} = 1.2$.

The effectiveness of the spoilers in reducing the trailing wing rolling-moment coefficient for the two sizes of trailing wing models downstream of the B-747 airplane model is shown in Figure 11. It can be seen that the induced rolling-moment coefficient on the large trailing model downstream of the B-747 airplane model was larger than those induced on the small trailing model. The reduction in induced rolling-moment coefficient on the small trailing model was about 35 to 40 percent over the range of downstream

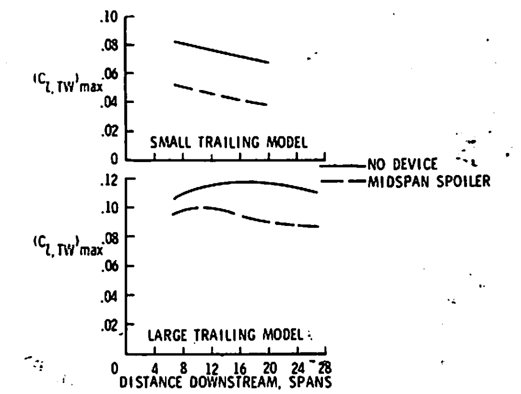

Figure 11. Effect of midspan spoiler on the variation of trailing wing rolling-moment coefficient with distance downstream of B-747 airplane model. $C_{L,trim} = 1.2$; spoiler projection = 0.08 c_W; Langley V/STOL tunnel data.

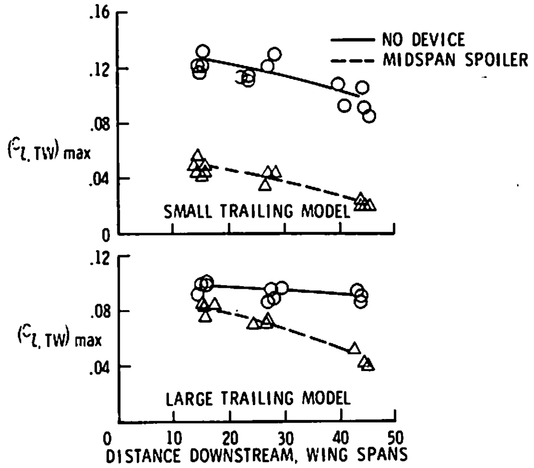

Figure 12. Effect of midspan spoiler on the variation of trailing wing rolling-moment coefficient with distance downstream of B-747 airplane model. $C_L = 1.2$; spoiler projection = 0.08 c_W; water towing tank data.

distances investigated; whereas, the reduction in induced rolling-moment coefficient on the large model was on the order of 15 to 25 percent.

Data obtained in the Hydronautics, Inc. water towing tank on the B-747 airplane model with and without spoilers is shown in Figure 12. This facility allows for data to be taken at a further downstream distance than can be obtained in the V/STOL tunnel. Even though the magnitude of the measured trailing wing rolling-moment coefficients do not agree with those obtained in the V/STOL tunnel, the trends do agree and the effectiveness of the spoilers as vortex attentuators are substantiated over the extended downstream range available in the tow tank.

Flight Spoilers on B-747 Airplane Model.

Even though the spoiler concepts discussed so far did show promise as possible vortex attenuators on the full-scale airplane, their use would require extensive modifications to the airplane. It became apparent that the normal flight spoilers already on the B-747 airplane (Figure 13) should be studied as possible vortex attenuators. Therefore, exploratory wind-tunnel tests were made in the V/STOL tunnel during March 1975 using wooden wedges (Figure 14) that represent the various segments of the flight spoilers noted on Figure 13. These exploratory results, shown in Figure 15, were encouraging; therefore, the model wing was modified so that the flight spoilers would be more representative of those on the full-scale B-747 airplane. Over the section of the wing immediately forward of the outboard flaps, spoilers were constructed that would operate similar to the actual flight spoilers — when retracted the spoilers made the contours of the upper surface of the wing and when they were deflected a large gap was formed forward of the flap. The spoiler segments identified on Figure 13 as 1, 2, 3, and 4 were investigated in the following combinations: 1 and 2; 2 and 3; 3 and 4; and 1 and 4 (Figure 16).

The results obtained for these various combinations of flight spoilers are presented in Figure 17. (Complete test results are available in reference 3.) It can be seen that with either one of these various combinations of flight spoiler segments deflected to 45° that there was a large decrease in the trailing wing rolling-moment coefficient induced on the

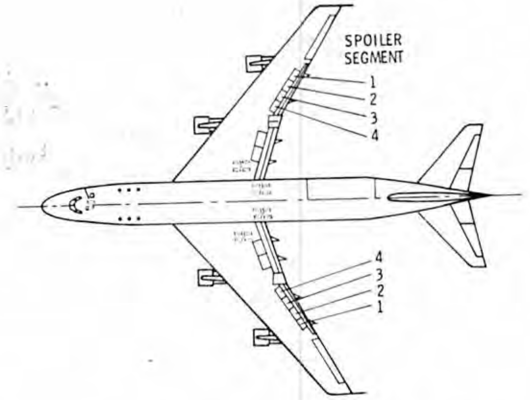

Figure 13. Sketch of flight spoilers on the B-747 airplane.

Figure 14. Photograph of flight spoiler segments 1 and 2 simulated with wedges on B-747 airplane model. Spoiler deflected 45°.

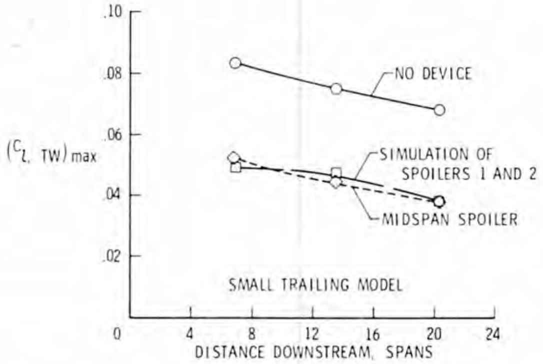

Figure 15. Effect of midspan spoiler and flight spoiler segments 1 and 2 simulated with wedges on the variation of trailing wing rolling-moment coefficient with downstream distance behind the B-747 airplane model. $C_{L,trim} = 1.2$.

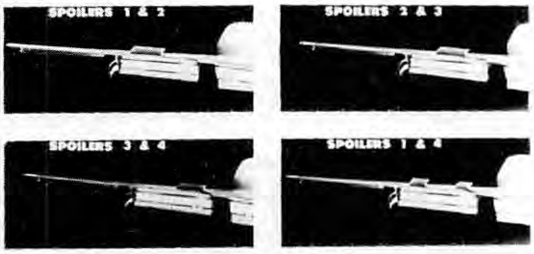

Figure 16. Photographs of various segments of flight spoilers on B-747 airplane model.

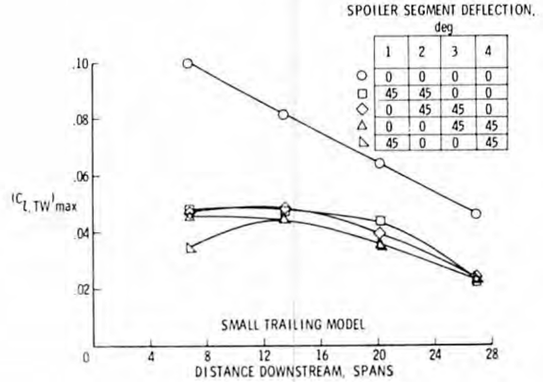

Figure 17. Variation of trailing wing rolling-moment coefficient with downstream distance behind the B-747 airplane model with various segments of the flight spoilers deflected 45°. $C_{L,trim} = 1.2$.

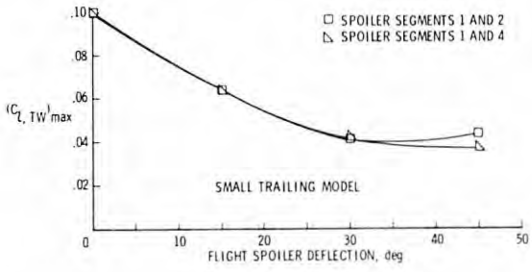

Figure 18. Variation of trailing wing rolling-moment coefficient with flight-spoiler deflection for flight-spoiler segments 1 and 2 and segments 1 and 4. Trailing wing model located 6.7 transport wing spans behind B-747 airplane model; $C_{L,trim} = 1.2$.

small trailing wing model. Two of these configurations (1 and 2 and 1 and 4) were investigated over a spoiler deflection range. The results shown in Figure 18 indicate that essentially all of the effectiveness of the spoilers were obtained at a deflection angle of about 30°.

Data obtained in the V/STOL tunnel using the large trailing wing model (Figure 19) indicate that the induced rolling-moment coefficient is attenuated, however, to a less extent than was noted for the smaller trailing model. Data obtained in the Hydronautics, Inc. water towing tank with the small trailing model (Figure 20) confirmed the foregoing results and also indicated that the large reduction in induced rolling-moment coefficient on the small trailing model was also realized at much further downstream distance than was obtainable in the Langley V/STOL tunnel.

Tests were also made in the Langley vortex research facility of the various flight spoilers as vortex attenuators on a B-747 airplane model, and the results (Figure 21) essentially agree with the results obtained in both the Langley V/STOL tunnel and the Hydronautics, Inc. water tank facility.

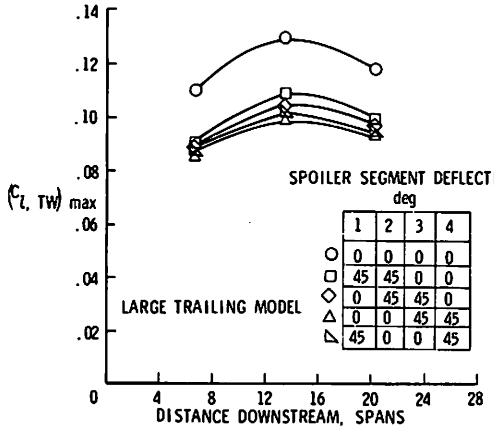

Figure 19. Variation of trailing wing rolling-moment coefficient with downstream distance behind the B-747 airplane model with various segments of the flight spoilers deflected 45°. $C_{L_{trim}} = 1.2$.

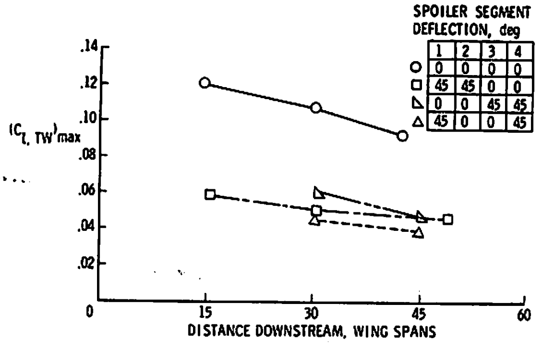

Figure 20. Variation of trailing wing rolling-moment coefficient with downstream distance behind the B-747 airplane model with various segments of the flight spoilers deflected 45°; $C_L = 1.2$, small trailing model. Water towing tank data.

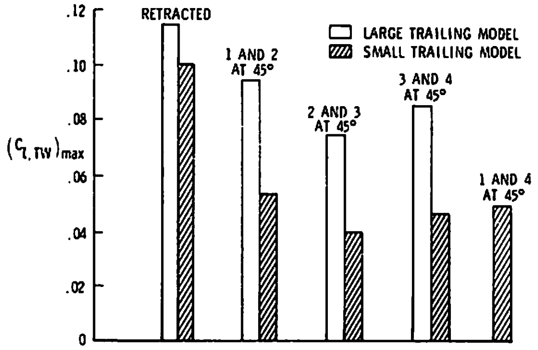

Figure 21. Trailing wing rolling-moment coefficients obtained at 27 spans downstream of the B-747 model with various segments of the flight spoilers deflected 45°; $C_L = 1.45$; Langley vortex research facility data.

Flight Spoilers on B-747 Airplane.

As a result of the findings in the groundbased facilities, a flight program was conducted at the Hugh L. Dryden Flight Research Center which used the existing flight

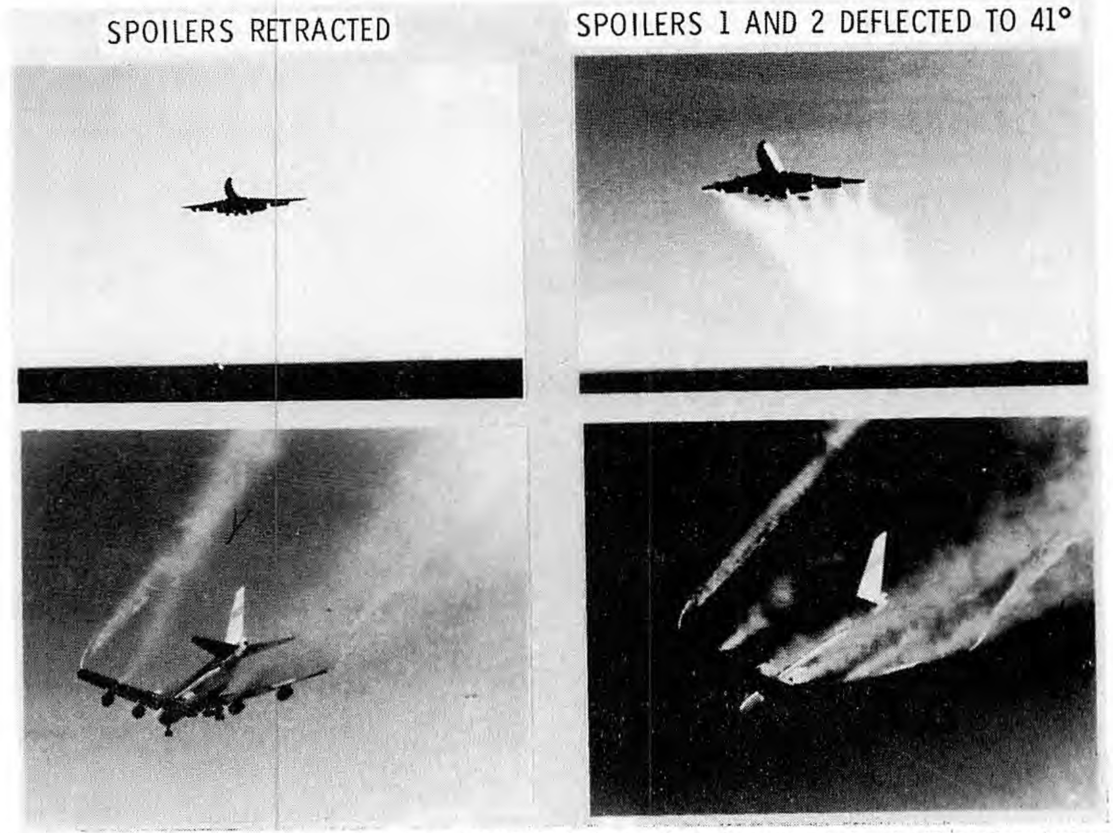

Figure 22. Photographs of trailing vortex-wake of B-747 airplane with spoilers retracted and with spoilers deployed for vortex attenuation. Conventional landing configuration.

spoilers on a NASA-owned B-747 airplane as the vortex attenuating device. (Results of these flight tests are presented in reference 4) The trailing vortex wake was made visible by smoke. Photographs of the B-747 trailing vortex wake with and without spoiler vortex attenuating devices deployed are shown in Figure 22. It can be seen on these photographs that the strong vortex generated at the outboard end of the flaps is altered significantly; in the photographs, it appears just as a turbulent area with no well-defined vortex motion.

A T-37 airplane was used to penetrate the trailing vortex. Penetrations behind the B-747 airplane in its landing configuration on a 3° flight path were limited to about 7 miles. (Pilots qualitative separation requirement was 9 miles (see Figure 23).) With appropriate deflection of the B-747 flight spoilers, penetration as close as about 1½ miles were made. (Pilots qualitative separation requirement was about 3 miles (see Figure 23).) These flight results have verified the trends obtained in the groundbased facilities.

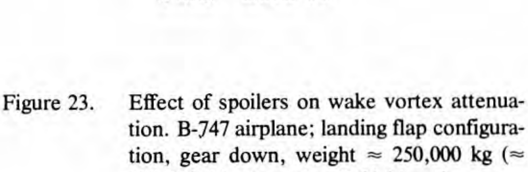

Figure 23. Effect of spoilers on wake vortex attenuation. B-747 airplane; landing flap configuration, gear down, weight ≈ 250,000 kg (≈ 500,000 lb), thrust for 3° flight path.

Flight Spoilers on the DC-10-30 and L-1011 Airplane Models.

The other two American wide-bodied jet transport airplanes (DC-10 and L-1011) have

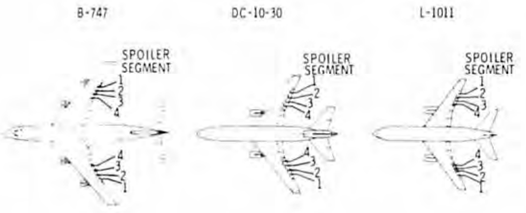

Figure 24. Sketch of flight spoilers on the B-747, DC-10-30, and L-1011 airplanes.

Figure 25. Photograph of the DC-10-30 airplane model and traverse mechanism in the Langley V/STOL tunnel.

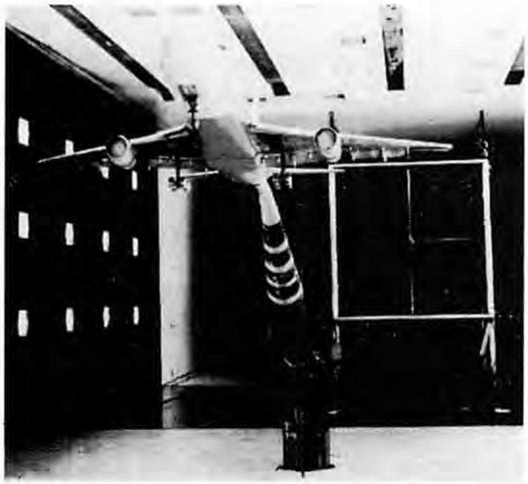

Figure 26. Photograph of the L-1011 airplane and traverse mechanism in the Langley V/STOL tunnel.

flight spoilers that are located forward of the outboard flaps similar to those on the B-747 airplane. Figure 24 shows the flight spoilers on the DC-10-30 and the L-1011 airplanes. Models of both of these airplanes were made available to NASA by the respective aircraft companies at no cost to the Government for tests in the Langley V/STOL tunnel. Figure 25 is a photograph of the test setup of the 0.047-scale DC-10-30 airplane model in the V/STOL tunnel. Figure 26 is a photograph of the test setup of the 0.05-scale L-1011 airplane model in the V/STOL tunnel.

The unswept trailing wing sensor models used during these investigations had a span and aspect ratio equivalent to that of a small business jet aircraft (Learjet). A photograph of the trailing-wing model used to probe the vortex downstream of the DC-10-30 airplane model is shown in Figure 27. A photograph of the trailing-wing model used to probe the vortex downstream of the L-1011 airplane model is shown in Figure 28. These trailing-wing models are referred to on the figures as "small trailing model."

Spoiler segment combinations 1 and 2, 2 and 3, 3 and 4, and 1 and 4 were investigated on both the DC-10-30 and the L-1011 airplane models. The results obtained from tests of these various combinations of flight spoilers on the DC-10-30 airplane model are presented in Figure 29. (Complete test results are available in reference 5.) It can be seen that with either one of these various combinations of flight spoilers deflected to 45° that there was a large decrease in the trailing wing rolling-moment coefficient induced on the small trailing wing model. The largest reduction was noted for the two innermost spoiler segments (3 and 4). These combinations were also investigated over a spoiler deflection range. The results shown in Figure 30 indicate that most of the effectiveness of the spoilers were obtained by the time the spoilers were deflected to 45°.

The results obtained from tests of the various combinations of the flight spoilers on the L-1011 airplane model are presented in Figure 31. (Complete test results are available in reference 6.) It can be seen that with either one of these various combinations of flight spoilers deflected to 45° that there was a large decrease in the trailing wing rolling-

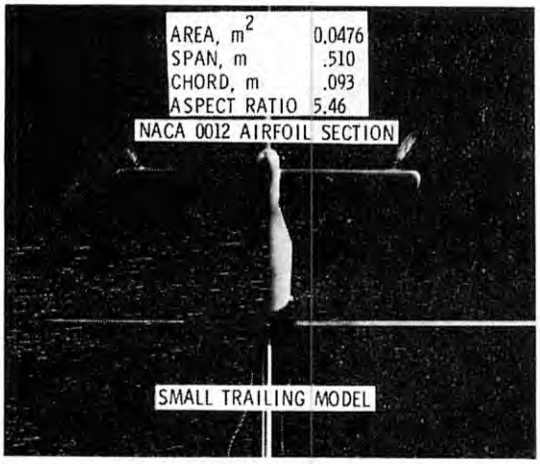

Figure 27. Photograph of unswept trailing wing model on traverse mechanism. (Sensor model used for DC-10-30 airplane model tests.)

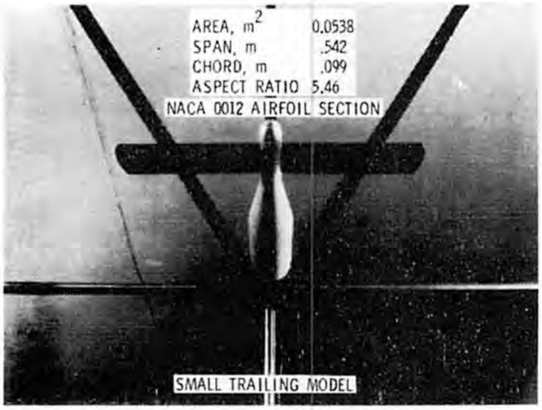

Figure 28. Photograph of unswept trailing wing model on traverse mechanism. (Sensor models used for L-1011 airplane model tests.)

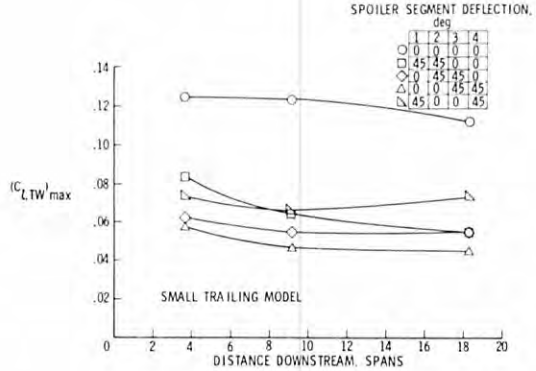
SPOILER SEGMENT DEFLECTION, deg

	1	2	3	4
○	0	0	0	0
□	45	45	0	0
◇	0	45	45	0
△	0	0	45	45
◺	45	0	0	45

Figure 29. Variation of trailing wing rolling-moment coefficient with downstream distance behind the DC-10-30 airplane model with various segments of the flight spoilers deflected 45°. $C_{L,trim}$ = 1.2.

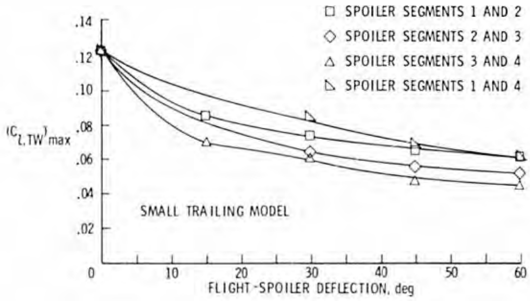

Figure 30. Variation of trailing wing rolling-moment coefficient with flight-spoiler deflection for various flight-spoiler segments on the DC-10-30 airplane model. Small trailing wing model located 9.2 wing spans behind the DC-10-30 airplane model. $C_{L,trim}$ = 1.2.

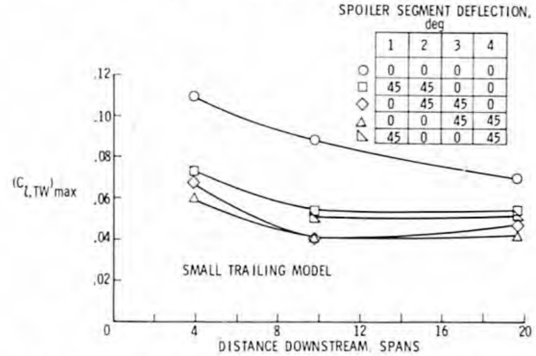
SPOILER SEGMENT DEFLECTION, deg

	1	2	3	4
○	0	0	0	0
□	45	45	0	0
◇	0	45	45	0
△	0	0	45	45
◺	45	0	0	45

Figure 31. Variation of trailing wing rolling-moment coefficient with downstream distance behind the L-1011 airplane model with various segments of the flight spoilers deflected 45°. $C_{L,trim}$ = 1.2.

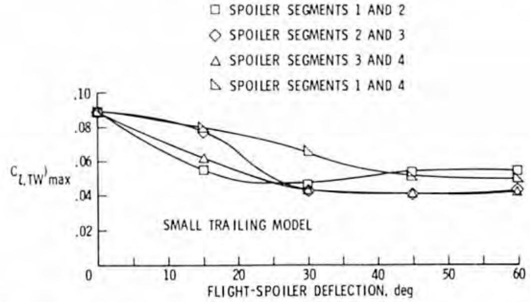

Figure 32. Variation of trailing wing rolling-moment coefficient with flight-spoiler deflection for various flight-spoiler segments on the L-1011 airplane model. Small trailing wing model located 9.8 wing spans behind the L-1011 airplane model. $C_{L,trim}$ = 1.2.

moment coefficient induced on the small trailing wing model. The largest reduction was noted for the two innermost spoiler segments (3 and 4). These combinations were also investigated over a spoiler deflection range. The results shown in Figure 32 indicate that essentially all of the reduction in induced rolling moment on the trailing model was realized at a spoiler deflection of about 45°.

Comparison of Flight Spoiler Effectiveness on Wide-Bodied Transport Airplane Models.

A comparison of the effectiveness of the flight spoilers on all of the wide-bodied transport configurations investigated in reducing the induced rolling moment on the small trailing-wing model is shown in Figure 33. The attenuated $(C_{l,TW})_{max}$ values obtained with flight spoiler segments 3 and 4 on both the DC-10-30 and L-1011 airplane models in the landing flap configuration are comparable with the attenuated values of $(C_{l,TW})_{max}$ obtained in wind-tunnel test of the B-747 airplane model in its landing flap configuration. Flight spoilers were shown to be effective in attenuating the trailing vortex in full-scale flight tests of the B-747 airplane; therefore, it appears that the flight spoilers on both the DC-10-30 and the L-1011 airplanes would also be effective in attenuating the trailing vortex behind both of these airplanes.

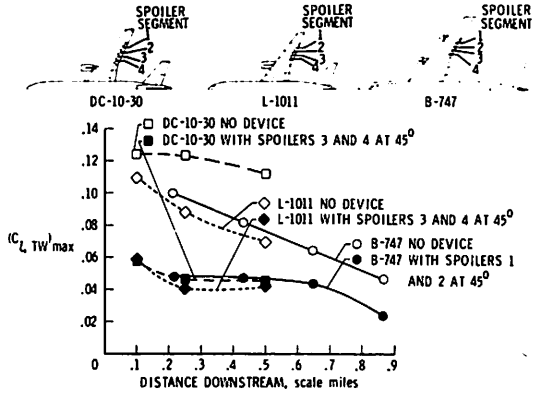

Figure 33. Variation of trailing wing rolling-moment coefficient with downstream distance behind the B-747, DC-10-30, and L-1011 airplane models with and without spoiler trailing vortex alleviators. Landing flap configuration, $C_{L,trim}$ = 1.2; small trailing wing model.

CONCLUDING REMARKS

Based on the results obtained in these investigations, it was found that the induced rolling moment on a trailing model can be reduced by spoilers located near the mid-semispan of a wing. Substantial reductions in induced rolling moment occur when the spoiler vortex attenuator is located well forward on both unswept and swept wing models. In addition, it was found by groundbased tests and verified by full-scale flight tests that the existing flight spoilers on the B-747 airplane are effective as trailing vortex attenuators. Based on the results of wind-tunnel investigations of the DC-10-30 and L-1011 airplane models, the existing flight spoilers on both the DC-10-30 and L-1011 airplanes would also be effective trailing vortex attenuators.

REFERENCES

1. Croom, D.R., "Low-Speed Wind-Tunnel Investigation of Forward-Located Spoilers and Trailing Splines as Trailing Vortex Hazard Alleviation Devices on an Aspect-Ratio-8 Wing Model," NASA TM X-3166, 1975, Langley Research Center, Hampton, VA.

2. Croom, D.R. and Dunham, R.E., Jr., "Low-Speed Wind-Tunnel Investigation of Span Load Alteration, Forward-Located Spoilers, and Splines as Trailing Vortex Hazard Alleviation Devices on a Transport Aircraft Model," NASA TN D-8133, 1975, Langley Research Center, Hampton, VA.

3. Croom, C.R., "Low-Speed Wind-Tunnel Investigation of Various Segments of Flight Spoilers as Trailing-Vortex-Alleviation Devices on a Transport Aircraft Model," NASA TN D-8162, 1976, Langley Research Center, Hampton, VA.

4. Barber, M.R., Hastings, E.E., Jr., Champine, R.A., and Tymczyszyn, J.J., "Vortex Attenuation Flight Experiments," SP-409, NASA Wake Vortex Minimization Conf., Feb. 1976.

5. Croom, D.R., Vogler, R.D., and Thelander, J.A., "Low-Speed Wind-Tunnel Investigation of Flight Spoilers as Trailing-Vortex-Alleviation Devices on an Extended Range Wide-Body Tri-Jet Airplane Model," NASA TN D-8373, 1976, Langley Research Center, Hampton, VA.

6. Croom, D.R., Vogler, R.D., and Williams, G.M., "Low-Speed Wind-Tunnel Investigation of Flight Spoilers as Trailing-Vortex-Alleviation Devices on a Medium-Range Wide-Body Tri-Jet Airplane Model," NASA TN D-8360, 1976, Langley Research Center, Hampton, VA.

EFFECT OF ADDING VORTEX ATTENUATING SYSTEMS ON THE DESIGN, PERFORMANCE, AND OPERATIONS OF A HEAVY COMMERCIAL JET TRANSPORT

JOHN P. MORRIS
Boeing Commercial Airplane Company
Everett WA 98206

ABSTRACT: Various trailing vortex attenuation concepts have been proposed for use on heavy jet transports. A preliminary investigation of the effects of several of these concepts on the design, performance and operations of a model 747-200 airplane has been conducted. Three of these concepts that have been judged to be potentially feasible have been selected for this presentation: retractable splines, modified approach flaps (30° inboard, 0° outboard), and flight spoiler deflection. The effectiveness of these devices in alleviating the wake vortices is not addressed; the discussion is limited to the impact on airplane design requirements and resulting performance characteristics.

NOMENCLATURE

$\bar{c}$	Mean Aerodynamic Chord
CAA	Civil Aviation Authority
C_D	Drag Coefficient
c.g.	Center of Gravity, % MAC
C_L	Lift Coefficient
C_ℓ	Rolling-Moment Coefficient
$C_{m_{0.25\bar{c}}}$	Pitching-Moment Coefficient
DOC	Direct Operating Cost, Cents/Seat-Mile
EPNdB	Unit of Measure of Effective Perceived Noise
EPNL	Effective Perceived Noise Level
FAR	Federal Aviation Regulations
F_N	Net Thrust per Engine
FRL	Fuselage Reference Line
GW	Gross Weight
KEAS	Equivalent Airspeed, Knots
MAC	Mean Aerodynamic Chord
n_z	Load Factor
R.S.	Rear Spar
S_{FRL}	Horizontal Stabilizer Angle Relative to Fuselage Reference Line
T/W	Thrust to Weight Ratio
UWAL	University of Washington Aeronautical Laboratory

V_C	Calibrated Airspeed
V_S	FAR Stall Speed
WRP	Wing Reference Plane
α	Angle of Attack of Wing
β	Sideslip Angle
γ	Flight Path Angle
Δ	Increment Notation
δ	Deflection Angle of Control Surfaces
δ_{AMB}	Ambient Atmospheric Pressure Ratio
Θ	Attitude Angle
$\sqrt{\Theta}$	Square Root of Temperature Ratio.

Subscripts

B	Body
e	Elevator, Used with Control Surface Deflection Angle
F	Wing Flap, Used with Control Surface Deflection Angle
I	Inboard
O	Outboard
R	Rudder, Used with Control Surface Deflection Angle.

INTRODUCTION

During the last 6 or 7 years NASA has investigated ways of attenuating the trailing vortices of heavy commercial jet airplanes. Some of the more promising concepts have been flight tested by the NASA Dryden Flight Research Center to substantiate their effectiveness in reducing the strength or causing early dissipation of wake vortices. The spline concept was tested on a C-54 and the differential flaps and deflection of flight spoilers were tested with a 747 under conservative and controlled conditions. Their overall effect on design, performance and operation of a heavy jet transport were not considered in detail at that time. The Boeing Company under contract with NASA during 1975 and 1976 conducted and documented a detailed evaluation of the above concepts [1,2]. This paper summarizes the results of the evaluation.

Vortex attenuation procedures are assumed to be applicable only on final approach and landing. Operational suitability, performance penalties and design problems of each vortex alleviation concept are identified.

Data used for the evaluation are from wind-tunnel testing and have been provided by NASA or have been previously obtained by The Boeing Company during development of the 747. The 747-200B airplane is used as a baseline in this study. The maximum takeoff and landing gross weight for this model is 775,000 lbs. and 564,000 lbs., respectively.

CONCEPT DESIGN AND ANALYSIS OF SPLINE CONCEPT

Design Concept.

A spline system concept adapted to the 747-200B airplane is illustrated in Figure 1. In this concept, the spline system would be contained in two pods mounted below the wings between the inboard and outboard nacelles. Each pod contains a movable shaft and eight spline blades. The splines are deployed by extending the shaft aft from the pod and unfolding the eight blades from their stowed position around the shaft. The spline system would be deployed only on final approach and landing. During all other phases of flight the system is stowed in the pods.

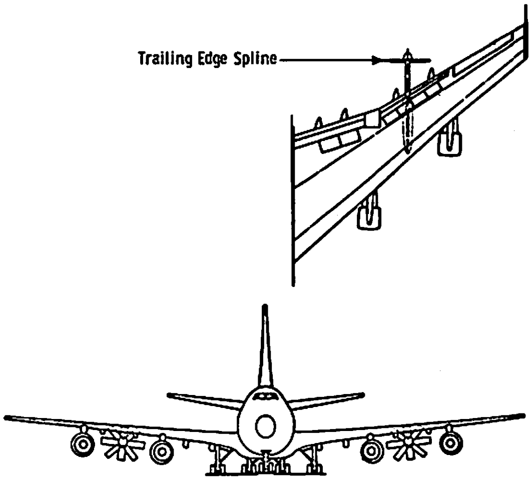

Figure 1. Spline system installation on 747-200B airplane.

Structural Design Considerations.

The eight spline blades fold along the shaft when retracted and unfold when the shaft is fully extended from the pod. The blades extend laterally about 14.5 ft. and vertically only 12 ft. to provide ground clearance. They fold in two groups of four blades each. When folded, the inner group forms a circle 32.0 in. in diameter and the outer group a circle diameter of 40.0 inches. The pods are about 4 ft. in diameter and 21 ft. long. They are hung below the wing at about 55% span on an aerodynamically faired strut which is 6% to 8% thick.

Figure 2 shows that the spline system would interfere with the deflection of the outboard trailing edge flaps when the system is deployed and landing flaps 25 or 30 are selected. The outboard flap modification would include a cutout and a limitation of the maximum deflection to the flaps-25 position when the spline system is deployed.

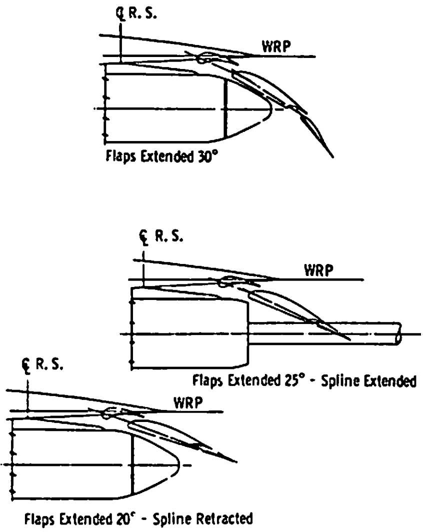

Figure 2. Spline-flap relationship.

Spline Control System.

A control concept has been identified that could extend and retract the splines and establish the required differential-flap configuration (inboard flaps 30, outboard flaps 25). Two independent drive mechanisms would be employed, one for spline shaft extension/retraction and one for spline blade deployment. This type of drive mechanism contains an electric motor as the prime mover. The rotary motion of the electric motor would be converted to linear motion by a transmission gear box, a universal joint and a ballscrew actuator. The estimated time to extend or retract the spline system is 45 seconds.

Following a spline extension command, the outboard trailing-edge flaps would be retracted to the flaps-10 position by a linear actuator making an input to the outboard flap power-pack assembly to provide clearance between the flaps and the folded spline blades when the shaft is in transit (see Figure 2). The spline shaft then extends with the blades retracted. Once the spline shaft reaches the fully extended position, the blades are deployed. When the blades reach their fully deployed position the outboard trailing edge flaps would then extend to the flap-25 position. Spline retraction would be accomplished by the reverse procedure. The spline blades initially fold down to the shaft in an estimated 8 seconds to eliminate their high drag in the event of an aborted landing approach and go around.

Stability and Control.

Stability and control with the spline system installed was evaluated for compliance with Federal Aviation Regulations (FAR) Part 25 requirements and the design objectives for the 747 airplane and appears satisfactory in all areas.

Splines deployed along with the differential flap configuration (30/25) and the effect of the nested aft flap have negligible effect on stability. Although high speed data are not available, previous wind tunnel experience with under wing fairings has indicated that the spline pods (with splines stowed) will not affect high speed stability characteristics.

The requirement to be able to trim throughout the center of gravity range at reasonable low lift coefficients determines the allowable aft center of gravity for a specific flap configuration. It is a design objective that trim be achievable at reasonable low C_L's at the aft c.g. limit with the available airplane nose-down electrical trim. More airplane nose-down trim would be required in the approach and landing configuration not only due to the pitching moment changes

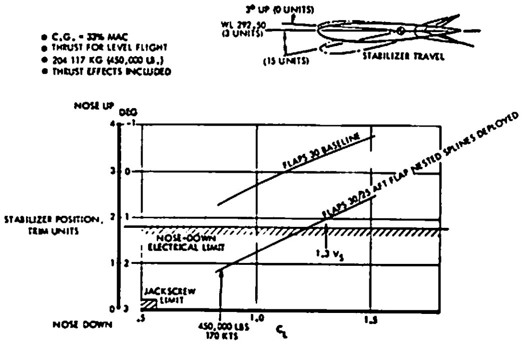

Figure 3. Stabilizer required to trim spline concept.

(nose up) caused by the differential flap configuration, but also due to the additional thrust required when the splines are deployed. The combined effects of differential flap operation and higher power settings require the change in nose-down trim capability shown in Figure 3. An increase in the nose-down electrical trim limit may be required to satisfy a low weight, maximum speed condition.

The effects of the spline system on lateral/directional stability have not been investigated, since these effects are expected to be small and are not expected to affect airplane operation.

Directional control will be unaffected for low sideslip angles. Directional control capability and stability at high sideslip angles would require testing. Adequate directional control exists to control the failure case of only one spline deployed, as shown in Figure 4.

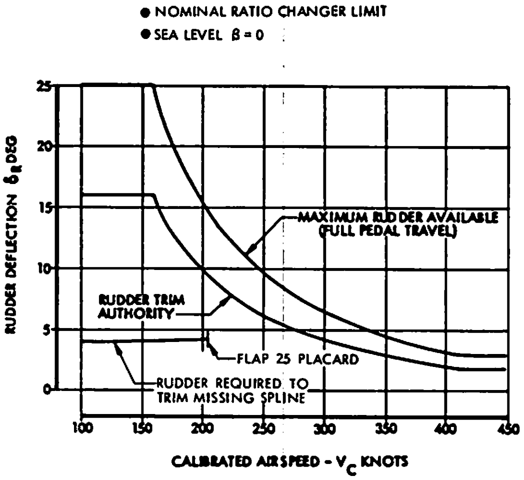

Figure 4. Rudder required to trim missing spline.

AERODYNAMICS AND PERFORMANCE

All phases of flight are effected to some extent by installation of the spline concept on the 747 airplane. During takeoff, climb, cruise and descent the effect is only due to the strut and pod drag with the splines retracted and the cut out in the outboard flap. During approach and landing the required outboard flap modification would introduce performance changes.

The effect of the struts and pods on the 747 drag is given on Figure 5. The incompressible drag coefficient increment is estimated by calculating skin friction and interference drag [3]. The drag variation with increasing Mach number is estimated by the methods described in reference 4. No wind-tunnel testing was conducted for the purpose of measuring the drag of the strut and pod installation.

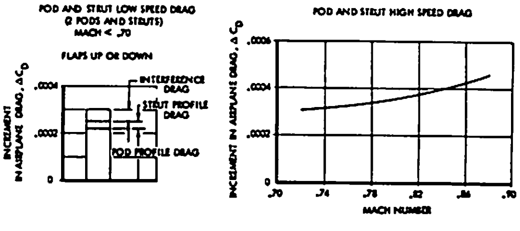

Figure 5. Effect of pods and strut on 747 drag.

During approach and landing the splines can either be extended for vortex alleviation or retracted. In both cases the aft segment of the outboard flap would be nested to the main segment and there would be a 16-inch by 30-inch cutout in the aft flap to clear the spline shaft when the splines are extended. Also, when the splines are extended the outboard flap is restricted to 25°. The changes in the approach and landing performance parameters (C_L and C_D) for the configuration differences from the flaps-30 baseline are summarized in Table 1. The spline drag was derived from NASA wind-tunnel measurements giving very nearly a drag coefficient of 1.0 when applied to the total area required to encircle the spline blades (approximately 280 ft^2). Parameters due to the different outboard flap deflections were obtained from wind-tunnel data accumulated during initial 747 flap development work.

Table 1. Approach and Landing C_L and C_D for Spline System

Configuration	Flap Position	In-Flight		Ground Roll	
		C_L Stall	C_D Approach	C_L	C_D
Baseline	30/30	2.55	0.217	0.525	0.201
Splines Deployed	30/25*	2.35	0.249	0.410	0.242
Splines Retracted	30/30*	2.49	0.217	0.460	0.201

*Aft Flap Segment Nested

Table 2. Baseline 747-200B and Spline System Performance Comparison Summary

Condition	Baseline 747-200B	Spline System 747-200B	Change From Baseline
Takeoff — 351,534 kg. (775,000 lb.) Sea Level, 30° C, Flap 20			
• Field Length, m. (ft.)	3,246 (10,650)	3,274 (10,740)	+28 (+90)
• Climb Limited Weight, kg. (lb.)	358,747 (790,900)	359,246 (792,000)	+499 (+1,100)
Initial Cruise Altitude — 351, 534 kg t.o. wt., m. (ft.)	9,874 (32,100)	9,708 (31,850)	−76 (−250)
Landing — 255,826 kg. (564,000 lb.), Sea Level, 15° C, Flap 30 Baseline, Flaps 30/25 Spline Deployed			
• Approach Speed, Keas	141.5	147.5	+6
• Field Length, m. (ft.)	1,879 (6,165)	1,917 (6,290)	38 (125)
• Landing climb limit, kg. (lb.)	349,040 (769,500)	296,196 (653,000)	52,844 (116,500)
• Landing Climb Gradient, Percent	10.3	7.0	−3.3
• Landing Climb Rate, m/min (ft/min)	451 (1,480)	317 (1,040)	−134 (−440)
• Body Attitude for −3° Glideslope, deg.	2.6	2.1	−.5
Mission — Full Passenger Payload			
• Maximum Range, n.mi.	5,220	5,010	−210
• Payload at 5,220 n.mi., kg. (lb.)	36,977 (81,521)	32,885 (72,500)	−4,092 (−9,021)
• Block Fuel for 5,000 n.mi., kg (lb.)	120,202 (265,000)	124,738 (275,000)	+4,536 (+10,000)
FAR Part 36 Approach Noise, EPNdB	106.2	108.5	+2.3

Based on the above parameters, performance of the model 747-200 with the spline system installed and deployed on landing has been computed. This is compared to baseline performance in Table 2 for all flight modes. The effect of the added drag (and therefore increased engine thrust) on noise during approach is also shown. These changes in aircraft performance are significant during all phases of flight.

MODIFIED APPROACH FLAP CONCEPT

Concept Description.

The modified approach flap concept for vortex alleviation would require a differential flap configuration on the wing trailing edge with the inboard flap deflected to the normal 30° position and the outboard flap at 0° (δF = 30/0). The leading-edge flap system would operate in the normal manner with all leading-edge flaps extended for landing. During takeoff, climb and descent to final approach, the trailing-edge flap system also operates in the normal manner. Approach and landing with vortex alleviation "off" would also result in normal flap operation. Figure 6 shows the location of the various flaps involved and the flap settings used on final approach.

Structural Design Considerations.

Changes to the 747 structure to operate with the modified flap configuration would

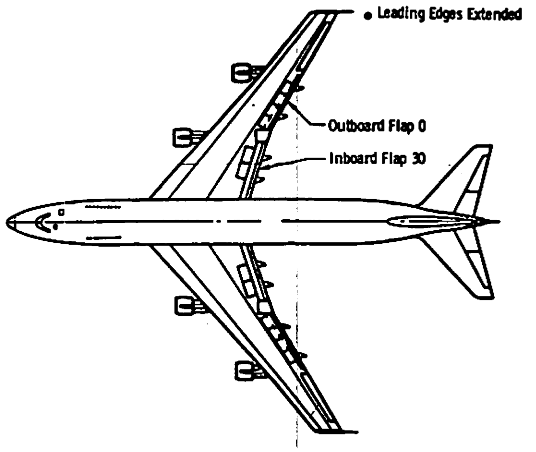

Figure 6. Modified approach flaps.

be necessary to meet trim requirements; also, higher approach speeds would subject the inboard flap system to higher fatigue loads. A change in the range of horizontal stabilizer travel from +3° to −12° to a range of +5° to −10° would be required to meet the landing configuration trim requirements. This modification would take advantage of design modifications developed for the 747SP (also the same as that used for the 747 Space Shuttle Carrier Aircraft project).

The increased approach speeds with the flaps-30/0 configuration are not critical for flap structure ultimate design because design speed is limited by the automatic flap retractor. However, flap fatigue design loads are determined at approach speeds. The increase in approach speed produces higher fatigue loads on the inboard flap requiring more durable structure.

Control System.

The modified approach-flap control system would contain a mechanism to hydraulically retract the outboard trailing-edge flaps independent of the normal command path, which is controlled by two switches on the pilots overhead panel and the flap handle. Also, elevator can be scheduled with speed through additional onboard computers to provide speed stability.

The modified flap control system would be active on final approach and landing when landing flap position 30 and vortex attenuation are selected. The center instrument panel flap position indicators would show the trailing-edge flap configurations at all times. Landing flaps-25 operation is also possible with this system in either the normal mode or the modified flap mode.

A linear actuator (electric-motor-driven ball screw) could be used to retract the outboard trailing-edge flaps by reducing the length of the rod between the wheel-well quadrant and the outboard trailing-edge powerpack assembly input crank. The flaps-30 normal and the modified flap configuration are depicted on Figure 7.

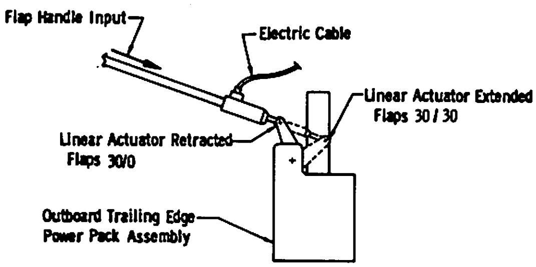

Figure 7. Modified flap mechanism.

With the flaps-30/0 setting stability augmentation by programming elevator with speed is necessary to provide neutral static stability at 33% aft c.g. for the critical case where go-around power is applied at minimum gross weight. This elevator bias is scheduled by speed as shown on Figure 8. The augmentation system would be dual to satisfy requirements for fail-safe protection.

Stability and Control.

Analysis indicates that the proposed use of modified approach flaps for landing is possible but requires several control system changes. The FAA allowable aft c.g. would

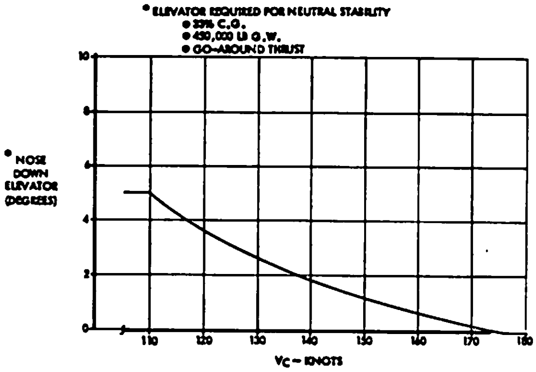

Figure 8. Stability augmentation with modified flaps.

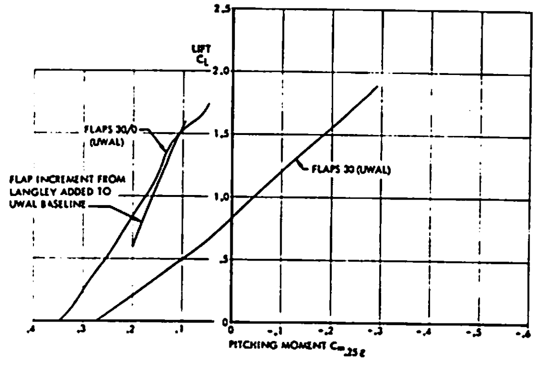

Figure 9. Effect of modified flaps on pitching moment coefficient.

be limited to 31% MAC without stability augmentation. Certification by the British CAA would require stability augmentation or result in a more severe c.g. restriction. The lateral control capability would be reduced 25% at the approach speed.

The effect of modified flaps on pitching moment is presented in Figure 9 using both Boeing data and NASA incremental data. There is reasonably good agreement for the modified increments between the two sources of data. As illustrated, a very large change in pitching moment in the airplane nose-up direction and substantial loss in stability with the modified configuration would occur. Landing trim with modified flaps would be most critical at the aft center-of-gravity position.

Figure 10 shows that trim requirements would be well beyond the current trim capability. The airplane nose-down trim range could be extended two trim units maximum by raising the stabilizer jack-screw assembly in the aft body section and making necessary control system and structural changes.

This change would give trim capability for a c.g. range of 13% to 31% with thrust for level flight. The trim required with go-around thrust would be more severe. To trim 33% c.g. with go-around thrust about 1.5 units more stabilizer is needed. However, further nose-down trim cannot practically be attained with the stabilizer. The easiest change would be to downrig all elevators an additional 3°. This could result in a cruise drag penalty depending on the amount of downrig and the split between inboard and outboard elevators. Another possibility would be to program elevator neutral position with stabilizer deflection, but this would be an extensive change. Relocation of the stabilizer jack-screw assembly upward in the aft body section would reduce available airplane nose-up trim. There is, however,

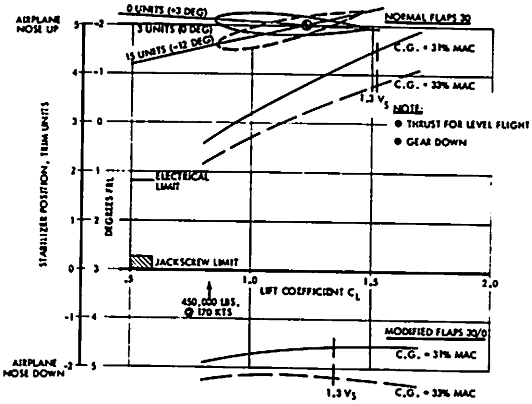

Figure 10. Effect of modified flaps on landing trim.

sufficient trim capability after such a change to trim at the most forward c.g. limit certified for landing to date, 13% MAC, with normal flaps 30 on both inboard and outboard flaps. The electrical trim limit in the airplane nose-down direction is currently set at 1.8 trim units. A revision would therefore be needed to permit full trim capability via the control wheel trim switches when the modified flaps configuration is selected. The existing trim limit at 1.8 units must be retained for flaps-up operation to preserve mistrim dive recovery capability. Dual limit switches would thus be required with trim limit selection dependent on operational mode, landing, or cruise.

Figure 11 shows that the stability would be markedly reduced with modified flaps. The neutral point is approximately 12% MAC more forward when compared to normal flaps 30. Maneuvering stability will be degraded. Both the elevator and stick force gradients versus load factor are reduced, but it is expected that the stick force level at aft c.g. would be adequate. This favorable result is due in part to the pitch damping term, which has a stabilizing effect.

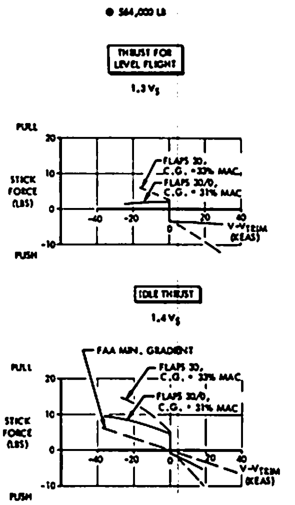

Figure 11. Effect of modified flaps on landing stability.

The airplane must meet the requirements for static stability in the Federal Aviation Regulations. This is demonstrated in flight by varying the speed above and below the trim speed while keeping the airplane in trim (n_z = 1) with the elevator. The stick force gradient versus speed is used as a measure of stability. Figure 11 shows the landing stability with modified flaps, both with idle thrust and also with thrust for level flight. The c.g. would have to be limited to 31% MAC to meet the FAR minimum gradient with idle thrust and to provide acceptable stability with thrust for level flight. Engine thrust is destabilizing for this type of stability test because the engines are mounted below the airplane center of gravity. The effect of thrust on static stability is substantially degrading as shown in Figure 12. Neutral stability with go-around thrust is required to be demonstrated for British CAA certification which would limit aft c.g. to a more forward limit.

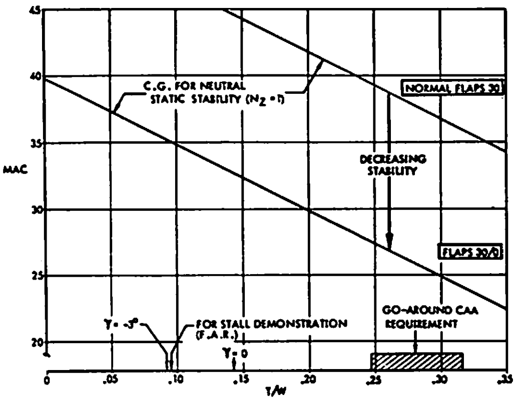

Figure 12. Effect of thrust on static stability with modified flaps.

Stability could be improved with a speed stability augmentation system. Conceptually, elevator or stabilizer deflection could be programmed as a function of speed to increase the stick force gradient similar to a "Mach trim" system. This could be done most conveniently with the elevator. Figure 8 shows the elevator schedule that would give neutral static stability at a c.g. of 33% MAC, light weight, and with go-around thrust.

Lateral control capability with modified approach flaps would be reduced because the outboard spoilers are less effective when outboard flaps are retracted compared to the normal flaps 30. Figure 13 presents rolling moment due to wheel at 1.3 V_S and maximum landing weight. The rolling capability with modified flaps at normal approach speeds would be reduced approximately 25% at this critical design condition. Crosswind landing capability would be reduced about 4 knots assuming that 6% of full lateral control is used for crosswind control (sideslip) and the remaining 40% is reserved for gust control. Lateral control capability with modified flaps would be similar to the capability with hydraulic system No. 2 or No. 3 out and normal flaps 30.

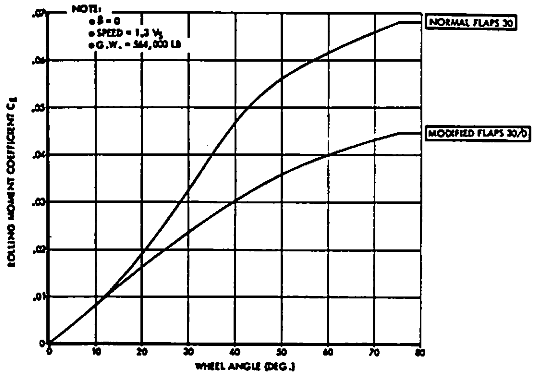

Figure 13. Effect of modified flaps on rolling-moment coefficients.

● FORWARD C.G. LIMIT

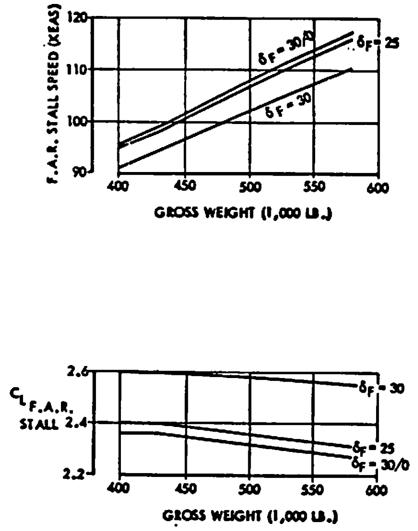

Figure 14. FAR stall speed and stall C_L.

Aerodynamics and Performance.

The flight lift and drag levels for the modified approach flap concept have been predicted by adjusting 747 flight data with wind-tunnel increments. Scale, thrust and trim drag effects have been included. The major differences from the flaps-30 baseline are increased stall speed and an increase in touchdown attitude (see Figures 14 and 15). In either case the values are only slightly greater than the normal flaps-25 configuration, which is used extensively by some airlines.

Takeoff, climb to cruise, cruise and descent to final approach performance would be unaffected since the modified approach flap operation would only be used during the landing segment of the mission. Landing performance is primarily affected by the increase in approach speed due to the reduced FAR stall lift coefficient (Figure 14). The landing performance for flaps 30/0 is compared to the flaps-30 baseline in Table 3. This loss in landing performance is a significant increment and negates the improved technology built into the airplane.

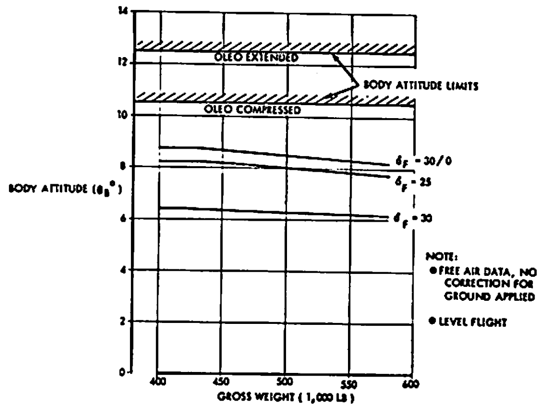

Figure 15. Body attitude at touchdown speed.

Table 3. Baseline 747-200B and Modified Approach Flap Landing Performance Comparison Summary

Condition	Baseline 747-200B Flap 30	Modified Approach Flap 30/0	Change From Baseline
Landing at max. Landing wt. (564,000 lb) Sea Level, std day			
• Approach speed, keas	141.5	150.0	+ 8.5
• Field Length (ft)	6,165	6,800	+635
• Body Attitude for 3° Glide Slope, (deg)	2.5	4.6	+ 2.1
• Landing Climb Gradient (%)	10.3	10.3	0
Landing Climb Limited Weight (lb)	770,000	777,000	+7,000

FLIGHT SPOILER CONCEPT

Concept Description.

The use of spoilers as a vortex attenuating technique on the 747 would involve deflection of two symmetric pairs of the existing outboard spoilers during the landing approach. Outboard spoilers are normally used as lateral control devices and as ground-speed brakes. As vortex attenuation devices, these spoilers would be extended during the landing approach also. During other operations the spoilers operate in the normal manner. Referring to Figure 16 this configuration has spoilers 1, 2, 11 and 12 deflected symmetrically to 45° in conjunction with flaps 30 and gear down. This spoiler combination was chosen because it shows the least loss in stability and is the most practical to mechanize in the existing airplane. It also appears to give the best vortex attenuation in flight tests by NASA.

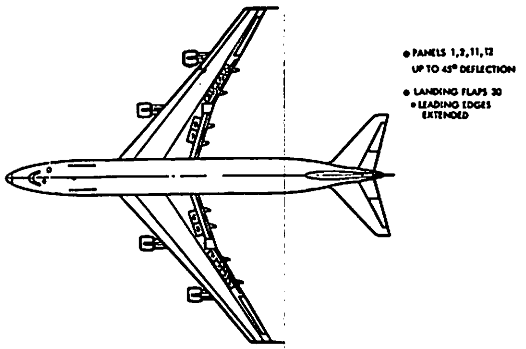

Figure 16. Flight spoilers.

Structural Design Considerations.

The use of flight spoiler combination (1, 2, 11, 12) at flaps 30 would present a unique loading condition on the 747-200 trailing edge structure during final approach and landing, and therefore the outboard trailing-edge wing-flap loads would be affected. The 747 currently is not certified for in-flight deployment of speed brakes with flaps extended during final approach. An estimation of the outboard flap ultimate static pressure loads, reflecting the influence of using flight spoilers for both partial and full deflection with flaps 30, are within the design load envelope for the placard plus roll-maneuver load condition. However, the outboard flap durability and ultimate static strength would experience a degradation because of buffet and head-on gust requirements for the new loading condition. To evaluate the effects of buffet on flap durability and ultimate strength additional testing would be required using flaps 30 with the two outboard spoilers deflected to measure flap static pressures and buffet (frequency) effects.

The effects of spoiler-induced buffet (structural implications and ride quality) may be minimized by modifying the spoiler panel geometry. A porous or perforated spoiler panel is one type. This concept has been tested by NASA on their 747 aircraft. However, since instrumentation to measure flight loads was not used, the reduced buffet levels encountered are only qualitative indications of the success of this concept.

Control System.

A preliminary flight controls evaluation has identified a control system concept that will deploy spoiler panels 1, 2, 11 and 12 to 45° when the airplane is in the landing configuration. The spoiler speed-brake mixer that controls spoilers 1, 2, 11 and 12 is separate from that controlling the other panels. Therefore, it could be modified to accept commands from either the speed brake sequence mechanism or an added linear actuator. Either the linear actuator or the normal speed brake sequence mechanism could then extend the spoiler panels. The linear actuator would be electrically commanded to extend for vortex alleviation.

Full manual control of speed brakes would be retained. Speed brake handle commands would take preference over vortex alleviation signal under all conditions. In failure modes, retract signals would have priority over extend signals. Roll commands would retract the spoilers used for vortex alleviation on the up-going wing. Roll and speed brake control of the spoilers not used for vortex alleviation would remain the same. The vortex alleviation spoilers would be controlled by two switches on the pilot's overhead panel and the flap handle.

Stability and Control.

Analysis indicates that the proposed use of spoilers during landing is feasible not considering spoiler-induced buffet. The stabilizer electrical trim range would have to be expanded in the airplane nose-down direction for landing while the current limit would be maintained for flaps-up operation. The stabilizer trim capability would be marginal and could require some means of increasing nose-down trim capability.

The effect of spoilers on pitching moment is shown on Figure 17. It can be seen that the spoilers cause a large airplane nose-up pitching moment resulting in a substantial trim change. There is also some loss in stability (approximately 3% MAC), which would have only a minor effect on handling characteristics. The effect of spoilers on landing trim is most critical at the aft center-of- gravity position. Figure 18 compares trim requirements with the normal spoilers retracted configuration. Trim on 3° glide slope would be close to the mechanical trim limit at light weight and low C_L. Trimming with increased thrust would require stabilizer beyond the current nose-down mechanical limit. Level flight thrust requires ¼ to ½ unit more, and trim for go-around thrust to demonstrate the go-around condition requires about 1 unit more. The simplest change would be to downrig the elevators. Another possibility would be to raise the stabilizer jack-screw assembly in the aft body section with associated control system changes as in the modified flap concept analysis. The electrical trim limit change required is also similar to the modified flap concept.

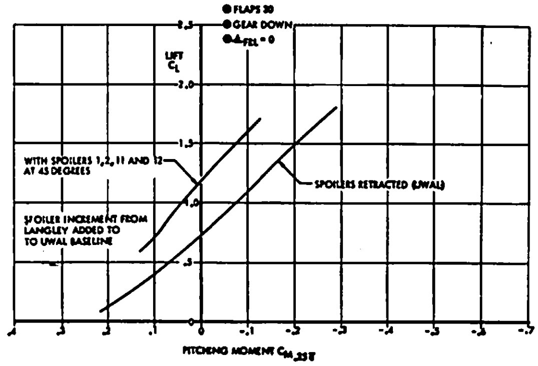

Figure 17. Effect of spoilers on pitching-moment coefficient.

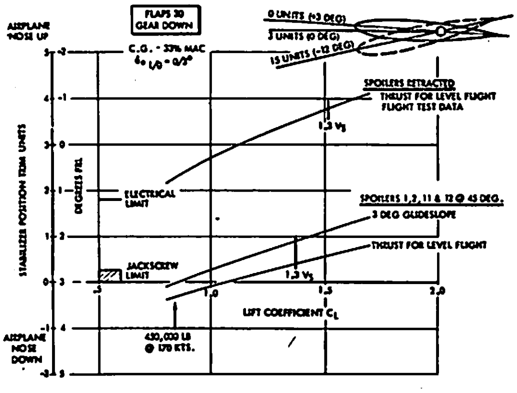

Figure 18. Stabilizer required to trim for landing with spoilers extended.

Aerodynamics and Performance.

The aerodynamic parameters used in the spoiler concept analysis were derived in a manner similar to the method used for the modified flap concept.[1] Lift and drag increments obtained from NASA wind-tunnel data (Figures 19 and 20) were applied to Boeing baseline data. The effect of the spoilers-extended increment on C_L versus α is to lower the baseline flaps-30 wind-tunnel data to a level similar to the baseline flaps-25 level. The full scale FAR C_L stall is derived in the same manner. Figure 21 shows the FAR stall speeds and stall C_L for the spoiler concept and baseline airplane at flaps 30. The full-scale drag is obtained by applying the drag increment from Figure 20 to flight test data.

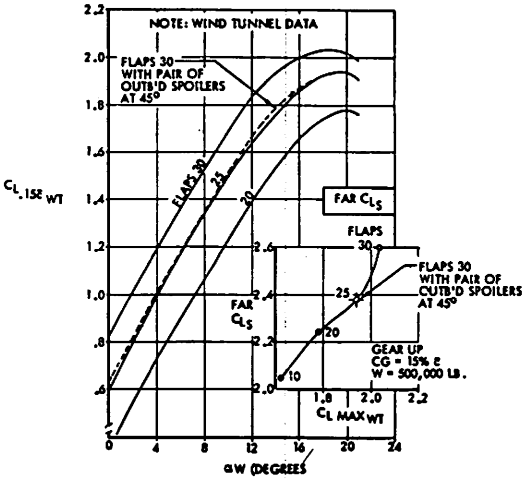

Figure 19. Effect of a pair of outboard spoilers on lift.

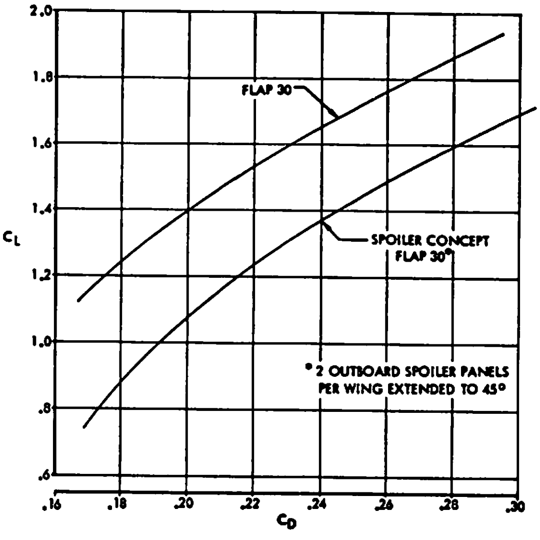

Figure 20. Low-speed data, gear down spoiler

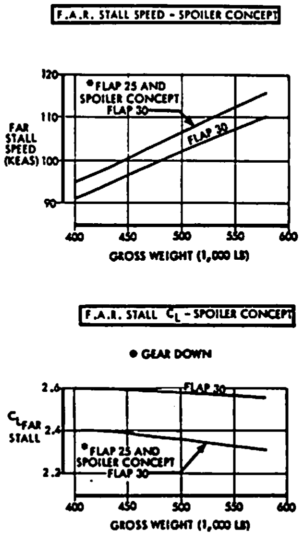

*2 OUTBOARD SPOILER PANELS PER WING EXTENDED TO 45°

Figure 21. FAR stall speed and C_L.

Table 4. Baseline 747-200B and Spoiler Concept Landing Performance Comparison Summary

Condition Sea Level, Std Day	Baseline 747-200B Flap 30	Flight Spoiler Concept Flap 30*	Change From Baseline
Landing at Max. Landing Wt. (564,000 lb)			
• Approach speed, Keas	141.5	148.5	+7
• Field Length (ft)	6,165	6,700	+ 535
• Body Attitude for 3° Glide Slope, (deg)	2.5	4.2	+ 1.7
• Landing Climb Gradient (%)	10.3	6.95	−3.35
Landing Climb Limited Weight (lb)	770,000	655,000	−115,000

*2 Outboard, Spoiler Panels per Wing Extended to 45°

As with the modified flap concept, takeoff, climb to cruise, and descent to final approach performance is unaffected by the spoiler concept. Since the airplane reverts to the normal braking configuration (all spoilers extended) at touchdown, the effects on landing field length are due entirely to the increased approach speed required. Landing performance at maximum landing weight is summarized on Table 4 for the flight spoiler concept as compared to the baseline flaps-30 configuration.

Body attitude on approach increases 1.7° for the spoiler concept as compared to the baseline flaps 30. This is the same as the normal flaps-25 attitude.

NOISE

The use of flaps 30 with the flight spoiler concept would significantly increase 747 approach noise. The primary cause would be the increase in engine noise due to a higher thrust requirement. The basic relationship between EPNL, engine power setting and altitude at reference acoustic conditions were obtained from JT9D-7 flight certification data.

A slight increase in airframe noise was also predicted. However, airframe noise makes a negligible contribution to the increase in total airplane noise for this configuration.

Predicted flyover EPNL are summarized in Table 5. Noise estimates for this configuration indicate that it is 2.1 EPNdB higher than the baseline configuration and 0.3 EPNdB over the FAR Part 36 noise limit of 108.0 EPNdB. This is counter to all recent efforts to reduce aircraft noise.

ECONOMICS

The economic suitability of airplanes can be compared by estimating their direct operating costs under a standard set of conditions. Important parameters in the DOC formula are:

Airframe and engine cost (90% amortized over 15 years)
Airframe and engine maintenance
Fuel cost/fuel burned (trip time and distance)
Insurance costs
Crew salaries
Airport fees.

Airplane cost would be increased by implementing the vortex alleviation concept. However, it is not possible to assess a realiable dollar amount at this preliminary design stage. The sensitivity of increased airframe cost on DOC increase in percent is shown in Figure 22.

A major objective for attenuating the trailing vortex system is to reduce the distance between following airplanes during approach to increase the flow of traffic in air-

Table 5. Approach Noise Estimates—Effect of Flight Spoiler Concept on 747 Approach Noise

Approach Config.	V_{REF}+ 10 (Keas)	$F_N/\delta_{AMB.}$ (lb.)	$N_1/\sqrt{\Theta}$ (rpm)	EPNL (EPNdB)	Traded* EPNL (EPNdB)
Baseline Flap 30	151.5	12,826	2,255	106.2	104.0
Flight Spoiler Concept Flap 30	158.3	17,939	2,580	108.3	105.1

*Takeoff gross weight 351,535 Kg (775,000 lbs)

- 747-200B Airplane
- JT9D-7A Engines
- −200 B Nacelle
- Gross Weight 255,826 Kg (564,000 lbs.)

- FAR Part 36, Appendix C Approach Conditions:
  Airport — Sea Level 25° C
  Relative Humidity 70%
- Speed 1.3 V_s + 10 Knots
- Glide Slope 3° ± 0.5°
- 1.0 n.mi. from threshold

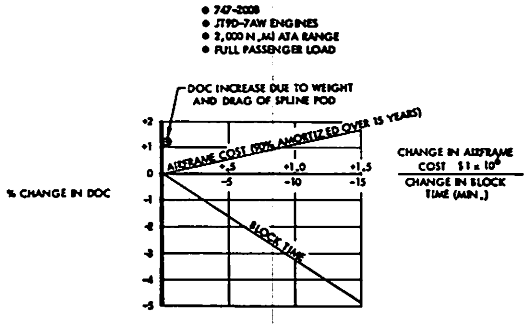

Figure 22. Effect of airframe cost and block time on direct operating cost.

ports and thereby reduce trip delays. The sensitivity of block time reduction on percent decrease in DOC is also shown on Figure 22. An airplane cost increase of $1 × 10^6$, would require an average saving of 3 minutes per trip to break even assuming the costs are depreciated over a 15-year period. However, the saving could not be achieved on all flights since traffic flow problems are limited to relatively few airports. The effect of airplane cost will be proportionately greater for a shorter amortization period, such as a retrofit on a used airplane.

CONCLUSIONS

This preliminary study of vortex attenuation concepts; splines, modified flaps or flight spoilers, indicates that these systems are operationally feasible but require major changes to the airplane. Typically, these systems would require further development including wind tunnel and flight testing and detailed system and structural design. The final configuration would then require certification by the regulatory agencies. In order to be operationally practical, performance losses, system complexities and costs would have to be offset by improvements in terminal area traffic flow and safety through trailing vortex attenuation of significant magnitude.

NASA research has shown that several concepts can have an impact on vortex attenuation but all of these concepts have significant adverse effects. Research should be continued in order to find more attractive methods for vortex alleviation.

REFERENCES

1. Tracy, P.W. and Berger, J.H., "Effects of Installing Vortex attenuating devices on the design, performance and operations of a heavy commercial jet transport," Boeing Document D6-34174, Oct. 1975.

2. Berger, J.H. and Morris, J.P., "Effects of Installing Vortex attenuating devices on the design, performance and operations of a heavy commercial jet transport," Boeing Document D6-34274, July 1976.

3. Hoerner, S.F., "Fluid Dynamic Drag," in *Aerodynamic Drag*, Otterbein Press, OH, 1958. 1958.

4. Berry, J.B., "External Store Aerodynamics for Aircraft Performance Prediction." AGARD lecture series No. 67, Prediction Methods for Aircraft Aerodynamic Characteristics, May 1974, p. 9.1-9.34.

SOME REMARKS ON EN-ROUTE VORTEX ENCOUNTERS

J. W. BRITTON
Royal Aircraft Establishment
Bedford, United Kingdom

ABSTRACT: A number of remarks and observations are given relating to vortex encounters during cruising flight.

INTRODUCTION

Most of the papers for the conference are concerned with vortex wakes as they affect operation in the terminal area and this fact simply reflects the wide appreciation of the potential hazards which can arise from vortex encounters during take off or approach. In the first paper for this conference, however, attention was drawn to the fact that in the UK there is a small but significant proportion (~5%) of all vortex encounters which occur on airways and which involve aircraft in cruising flight. The objectives of this short paper are: (1) to give some details of aircraft response which have been measured during an 'en route wake encounter', (2) to provide some information on the persistence of wakes at altitudes for cruising flight, and (3) to draw attention to a small selection of interesting features of vortex wakes which have been observed at RAE Bedford.

EN ROUTE ENCOUNTERS

At first sight it is reasonable to regard operation of aircraft on the approach and on airways as entirely dissimilar. There is, however, one feature of these types of operation which is, in the context of vortex wakes and wake encounters, common — in both cases the aircraft are regimented into lines. For flight on airways under conditions where there is little lateral movement of the wake, if changes in altitude are required such that a following aircraft has to pass through the flight level of a preceding aircraft or if two aircraft are operated at the same flight level and the prevailing conditions are such that the wake remains at constant altitude rather than descends then there is a chance that wake encounters will occur.

Details of an incident when a medium sized, twin-jet airliner encountered the wake of a large wide-bodied jet in cruising flight are available. The data were recorded via CAADRP (Civil Aircraft Airworthiness Data Recording Programme) which is organized by the CAA with the collaboration of some airlines in the UK, and for which aircraft are fitted with additional sensors and recording facilities. Within this programme, the anonimity of both airline and crew are preserved.

Figure 1, which is presented with the permission of the CAA, shows the flight record for this particular incident which occurred as the smaller aircraft was descending at an altitude of between FL 240 and FL 230. The separation between the two aircraft has been estimated on the basis of ATC information at between 16 and 20 miles. The major features of the response to the encounter are a maximum roll angle of around 70° which was achieved in a period of about 5 seconds and rapid excursions in normal acceleration of up to ±0.6g. As might be expected the record also reveals that the pilot was making large control inputs during the encounter. In many respects this can be regarded as a classic encounter where the encountering aircraft is rolled violently out of the wake and emerges into calmer air with an unusual attitude and with a new heading.

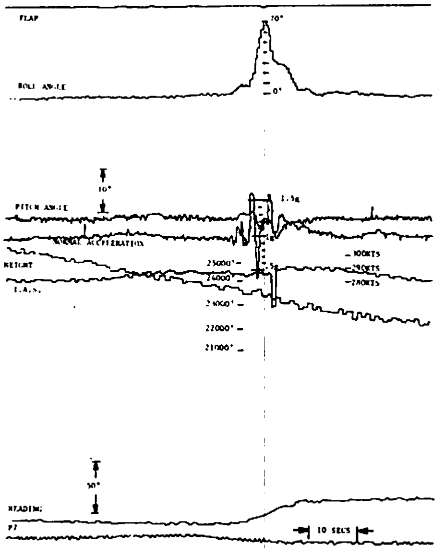

Figure 1. Wake encounter on airway.

PERSISTENCE OF VORTEX WAKES AT CRUISING FLIGHT LEVELS

Knowledge of encounters such as that described above has led to a short programme of research, at RAE Bedford, on the persistence of wakes at high altitudes. In this programme, observations of the behaviour of the vortex wakes of large intercontinental airliners (mainly Boeing 747) were made as the aircraft used the airway which is overhead at RAE Bedford and on those occasions when persistent contrails formed and were entrained in the wake so as to make the vortices visible. Systematic sequences of photographs, which were taken at 5-second intervals using a camera with a telephoto lens, have provided a permanent record of the development of the vortex wakes at a chosen longitudinal station on the airway.

On some occasions the conditions were such that the ice persisted until the dissipation of the wake appeared to be complete and thus the time interval between the passage of the generating aircraft and the disappearance of any visual evidence of organized circulation could be measured. The results of these observations are: 1 wake persisted for 60 sec, 2 for 75 sec, 2 for 110 sec, 1 for 120 sec, 3 for 130 sec, 4 for 140 sec, 1 for 145 sec, 2 for 155 sec, 1 for 160 sec, 1 for 175 sec, and 1 for 185 sec. On about one quarter of the occasions the wake persisted for more than 2½ minutes and on one occasion the persistence exceeded 3 minutes. For aircraft with true airspeeds of typically 8 miles per minute such persistence represent wakes with lengths greater than 20 miles and greater than 24 miles, respectively.

These observations indicate that there is some chance of a wake encounter in cruising flight even with longitudinal separations of 20 miles. As regards the magnitude of the risk, it is felt that direct extrapolation from the limited data base presented here might be unwise. Apart from being a small sample, all the data were collected under one particular atmospheric condition (i.e., when persistent contrails formed) and this may not be typical of "general" meteorological conditions. More particularly, the quoted time intervals relate to the disappearance of visual evidence of circulation — the important issues of vortex strength and associated hazard have not been resolved.

SOME EXAMPLES OF VORTEX BEHAVIOUR

A small selection of photographs of contrails are presented in Figures 2 to 5. The vortex wake of a Boeing 747 is shown in Figures 2 and 3. The photographs were taken 100 sec and 115 sec, respectively, after the passage of the aircraft so that the portions of the wake which are shown are some 14 miles and 16 miles downstream of the generating 747. Four points arise from Figure 2: (1) It can be seen that the Crow instability was already well developed. (2) Another type of instability also arose in which vortex bursts occurred in pairs and appeared to be confined to the outer parts of the vortex since a

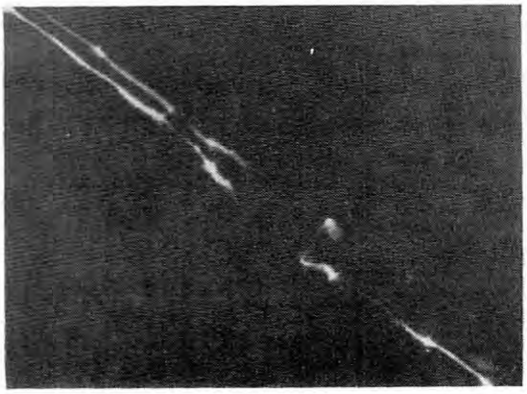

Figure 2. Wake of Boeing 747 (t = 100 sec).

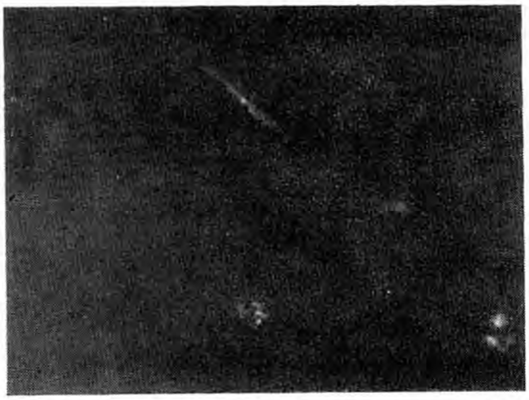

Figure 3. Wake of Boeing 747 (t = 115 sec).

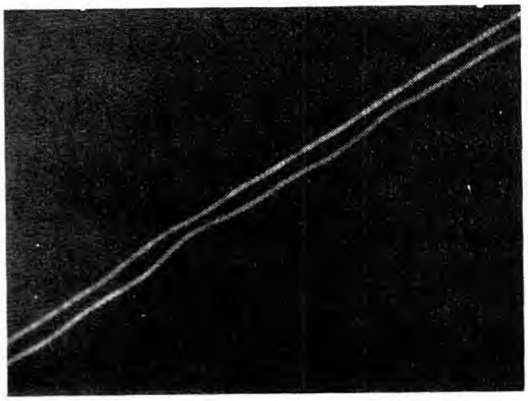

Figure 4. Wake of Boeing 747 (t = 60 sec).

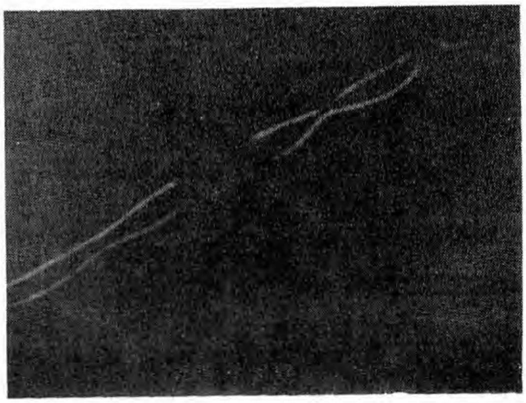

Figure 5. Wake of Boeing 747 (t = 95 sec).

coherent "inner vortex" or residual core appeared to be left behind. This sort of instability seemed to arise about as often as the Crow instability. (3) The ice crystals tended to gather together into a hollow cylindrical mass. Note that the walls of the cylinder do not necessarily occur at the edge of the core of the vortex; the position of the wall depends on the density, shape, and size of the particles themselves. (4) Residual minor cores appeared to persist even during the "breaking and linking process" which is characteristic of the Crow instability.

In Figure 3, the main point of interest is directly related to the fourth point arising from Figure 2. The residual cores which arose from the port and starboard vortices during the breaking and linking process of the Crow instability appeared to have joined and to have formed part of a large vortex ring with a diameter of some 700 to 800 feet.

Figures 4 and 5 show another wake from a Boeing 747; on this occasion the pictures were taken 60 sec and 90 sec after the aircraft passed. The intriguing feature of this wake was that the concentration of ice crystals appeared to have formed a spiral around the usual cylinder. This effect has been seen on a number of occasions, but as yet no explanation is to hand. In Figure 5, in particular, the Crow instability can be seen in various stages on this picture, and the spiral form of the concentration of ice crystals also appears to be able to persist even until this instability is well developed.

CONCLUDING REMARKS

Encounters with vortex wakes can and have occurred during cruising flight on airways. Observations at RAE Bedford indicate that trailing vortices may persist for more than two minutes after the passage of an intercontinental airliner in cruising flight at high altitude.

TECHNIQUES FOR EARLY DEMISE OF VORTICES — A PILOT'S VIEW

JOSEPH J. TYMCZYSZYN
FAA Western Region
Los Angeles CA 90009

AND

MARVIN R. BARBER
NASA Dryden Flight Research Center
Edwards CA 93523

ABSTRACT: The emphasis on full-scale airborne flight testing of wake vortex turbulence has naturally phased into a systematic evaluation of methods for attenuating vortex strength rather than concentrating primarily on the basic consideration of determining separation distances required for safe control of the following aircraft. A brief review of several techniques is provided with emphasis on the most successful configuration explored to date. This configuration change has been the extension of the two most outboard spoiler segments during the landing approach of the B-747. Similar configurations have been successfully tested in wind tunnels by NASA-LRC for the DC-10 and L-1011 and flight tests of the L-1011 are scheduled for the immediate future. An attempt is made to predict the operational, environmental and certification problems which would have to be considered if reduced spacing is dictated by the need to improve airport capacity and general arguments are presented in favor of wake vortex alleviation.

INTRODUCTION

The Wake Vortex hazard is not a new problem. It was described rather accurately in 1909 in a book entitled "Aerodynamics" by an English scientist named Frederick W. Lanchester. Since then, pilots have lived with it under various names such as "prop wash" and "jet wash," and it was considered more of a nuisance than a hazard until the advent of the wide-bodied Heavy jet aircraft and more lately with the need to increase airport capacity as a major national (and international) goal. Like its sister problem of wind shear, the documentation of accident and incident information resulting from wake vortex encounters is much less voluminous than generally reported by most pilots when asked about their experience with the subject. In the last decade, some 200 accidents have occurred to civil, public, and military aircraft as a result of a wake vortex encounter. Most of them have occurred in VFR flight where the pilot is responsible for his own separation. Recent inquires into available records in FAA, NASA (the FAA reporting system) and the Air Force reveal that a surprisingly large number of *incidents* occur particularly to executive jet and small-span military jet aircraft that operate into airports with a wide traffic mix. Again, most of these were operating under VFR conditions. Apparently, the present 6-5-4-3 NM separation standard had served to provide the safety desired under IFR conditions but at a penalty to the potential airport capacity. It suggests that if VFR pilots were more familiar with the 6-5-4-3 NM IFR rule (Table 1), together with a basic understanding of the principles of wake vortices as discussed in Advisory Circular 90-23D for example, they would enjoy a higher level of safety. The IFR separation standards are an excellent guide even under VFR conditions.

Table 1. Present US IFR Landing Separation Requirement

		Trailing Aircraft		
		S	L	H
Lead Aircraft	S	3	3	3
	L	4	3	3
	H	6	5	4
		Nautical miles at threshold		

KEY

S — SMALL (less than 12,500 lbs. GTW)
L — LARGE (12,500 - 300,000 lbs. GTW)
H — HEAVY (more than 300,000 lbs. GTW)

Again, with reference to Table 1, it is obvious that the Large aircraft category, which varies from 12,500 to 300,000 lbs maximum certificated takeoff weight, represents a very wide range of aircraft size and consequently in relative upset tolerance when following another Large or Heavy aircraft. It is equally obvious that this inequity could be solved by establishing more categories of aircraft, but more categories results in too many possible combinations which create additional problems for the human air traffic controller. It is, therefore, apparent that the pilots of aircraft in the lower end of the Large category should be most cognizant and most attentive to this hazard. This classification of aircraft includes the executive jets and small military aircraft which invariably also have a relatively high incidence of exposure to larger and heavier aircraft at busy terminal airports. In addition, in the eyes of the corporate pilot and of the company that owns that "2 or 3 million-dollar beauty," she's as big and as beautiful as her larger sisters, but the executive jet is just a small airplane when you look at it in comparison with the really big vortex generator ahead of her. The same overconfidence may be present in the minds of military pilots flying small high-performance fighters, trainers, and utility aircraft, and it is especially important that they be alert to these problems.

DEMONSTRATED VORTEX ATTENUATION

A complete reporting of the vortex attenuation flight experiments is given in reference 1. A brief review of the results is given here for continuity.

Table 2 summarizes the vortex attenuation flight experiments. The table also lists the aircraft involved in each experiment and gives some idea of the magnitude and timing of the programs.

Table 2. Vortex Attenuation Flight Experiments

Method of attenuation	Means of attenuation	Vortex-generating aircraft	Vortex-probing aircraft	Number of test flights	Time period for test flights
Altered span loading	Altered inboard/ outboard flap deflections	B-747	Learjet-23 (LR-23) Cessna T-37B	≈17	1974
Turbulence ingestion	Splines	C-54G	Piper Cherokee (PA-28)	≈20	1973
Mass and turbulence ingestion	Altered inboard/ outboard engine thrust levels	B-747	LR-23 T-37B	≈2	1974/1975
Altered span loading and turbulence ingestion	Wingtip-mounted spoiler	CV-990	LR-23	≈2	1969
	Altered spoiler deflections	B-747	LR-23 T-37B McDonnell Douglas DC-9	≈15	1975/1976

Span loadings were altered in flight by varying the deflections of the inboard and outboard flaps on a Boeing B-747 aircraft. Figure 1(a) shows the B-747 airplane flying with a conventional or 30/30 landing flap configuration (i.e., inboard flap deflected 30° and outboard flap deflected 30°). Figure 1(b) shows the airplane flying with the 30/1 flap configuration (inboard flap deflected 30°, outboard flap deflected 1°). The following combinations of inboard/outboard flap deflections were tested: 30/30, 30/20, 30/10, 30/5, 30/1, and 5/30. The minimum outboard flap deflection was 1° so that the leading-edge flaps could be kept extended (the leading-edge flap deflections are programmed according to trailing-edge flap deflections). Various span loads were tested because of the attenuation potential forecast by wind-tunnel tests [2]. The results of the flight tests of span loading alterations are reported in references 3 and 4.

(a) 30/30 flap configuration.

(b) 30/1 flap configuration.

Figure 1. B-747 span load test configurations.

Turbulence was created and ingested into the vortices in flight by mounting splines on a McDonnell Douglas C-54G aircraft and by varying the thrust of the engines on the B-747 aircraft. Figure 2 shows the splines on the aircraft in flight, and Figure 3 shows details of the splines. These tests were preceded by wind-tunnel tests which are reported in conjunction with the flight tests in reference 5.

The inboard and outboard engines of the B-747 airplane are alined directly in front of the outboard edges of the inboard and outboard flaps, respectively. Figure 1 illustrates

Figure 2. C-54G aircraft with splines installed.

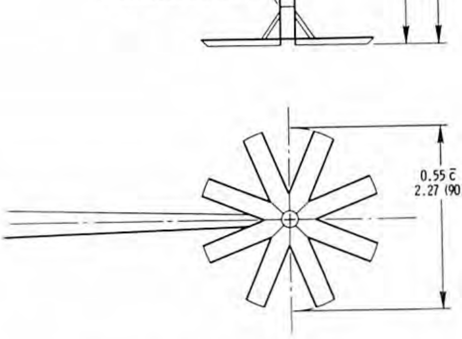

Figure 3. Diagram of spline arrangement. Dimensions in meters (inches).

the engine/flap alinement. This alinement naturally caused curiosity about the effects of changes in engine thrust on the wake vortices of the B-747 airplane in the normal landing configuration and in attenuated configurations; therefore, the effects of engine thrust were evaluated on numerous occasions throughout the B-747 vortex attenuation flight tests.

The combined effects of altered span loading and turbulence ingestion were flight tested in flight by installing a fixed spoiler on the wingtip of a Convair CV-990 aircraft and by deflecting the existing spoilers on the B-747 airplane. Figures 4(a) and (b) show the CV-990 wingtip spoiler from a distance and close up. Wind-tunnel tests of this configuration were conducted and reported in conjunction with flight tests in reference 6.

(a) From a distance.

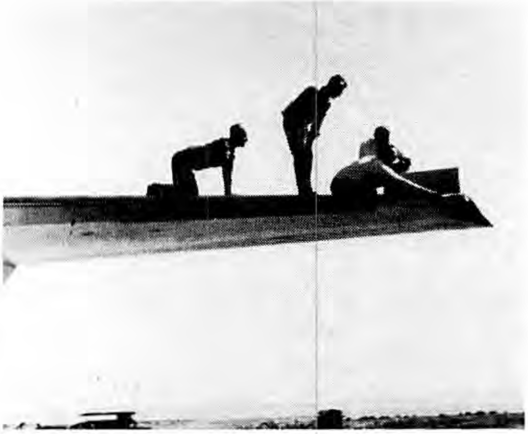

(b) Close up.

Figure 4. CV-990 wingtip spoiler.

Figure 5 is a sketch of the B-747 spoiler/speed brakes, referred to herein as spoilers. The effects of various spoiler segment combinations on vortex attenuation were tested thoroughly in the Langley V/STOL wind tunnel [7]. These results were sufficiently promising to warrant flight test verification. Therefore, the effects of deflecting these spoilers on vortex attenuation have been evaluated in flight tests.

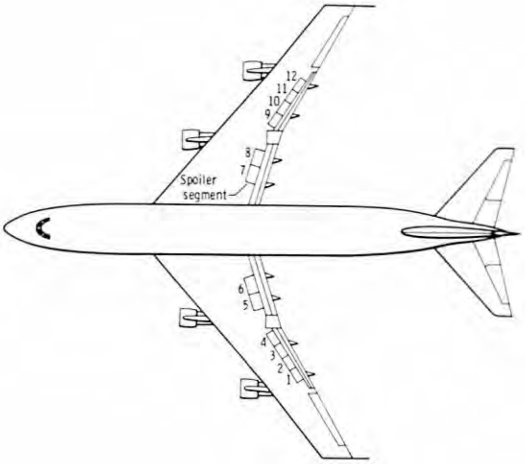

Figure 5. Spoilers on B-747 airplane.

Test Techniques.

The technique of vortex attenuation flight testing has been described in detail in reference 8. However, a review of the techniques from the pilot's standpoint is believed to be appropriate.

The most significant test in a qualitative evaluation of the vortex hazard to a trailing aircraft consists of probing the vortex as it would most likely be encountered in a real landing approach situation. To simulate this situation, the vortices are probed with as small a penetration angle as possible. This type of probe is referred to as a parallel probe (i.e., the probing aircraft's flightpath is approximately parallel to the vortex). The probe aircraft may enter the vortex wake from below, from above, or from either side. The probes result in pitch, roll, and yaw upsets that are representative of those that would be experienced by trailing aircraft in real situations. Qualitative assessments of these upsets enable the probe pilot to select separation distances (or times) behind a generating aircraft that result in acceptable levels of vortex-induced hazard.

The only limitation on a simulation of real vortex encounter situations is test altitude. Statistically it is known that most accidents attributed to trailed wake vortices occur on landing approach at relatively low altitudes. Unfortunately, flight test experience to date has not resulted in sufficient confidence in either predictive techniques or the repeatability of flight test results to permit testing at altitudes less than those required for comfortable recovery from inverted flight. In practice, this means the tests must be conducted no lower than approximately 1500 meters (5000 feet) above ground level; therefore, the probe pilot is evaluating an upset hazard at high altitudes above ground level and attempting to extrapolate his evaluation to low altitudes. This shortcoming has become more and more significant as the attenuated vortex configurations have enabled vortex encounters at closer separation distances, thereby increasing the need to verify the acceptability of the configuration.

In the past, probe pilots have estimated minimum separation distances by determining the separation distance at which the vortex-induced upsets would cause them to decide to execute a missed approach if they were performing an IFR approach. As noted, these determinations were made during parallel probes made approximately 1500 meters (5000 feet) above ground level.

Figure 6 summarizes the data that were obtained from tests reported in references 9 to 12. The correlation of the data throughout the numerous test programs is relatively good and illustrates that the pilots' assessments obtained by using the previously discussed technique agree remarkably well with the minimum separation distances that were established by using the roll-control criterion discussed in reference 8. These data and the techniques for obtaining them were the baseline from which the vortex attenuation flight tests to be discussed herein were initiated. Experience gained in the vortex attenuation flight tests show some shortcomings in these data and indicate areas where present techniques are inadequate.

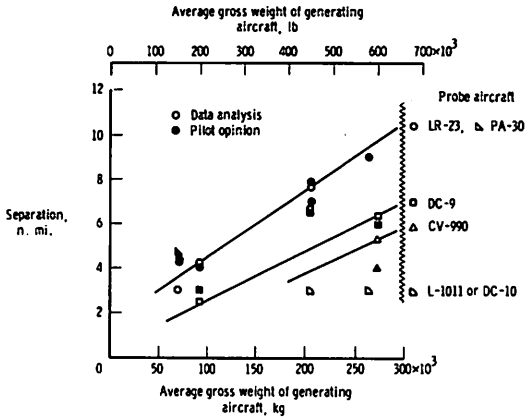

Figure 6. Minimum separation distance based on pilot opinion and roll control criterion. Generating aircraft in landing configuration; $|\dot{p}|_{\text{measured}}/|\dot{p}|_{\delta_{a_{\max}}} = 1$.

Span loadings were altered in flight by varying the deflections of the inboard and outboard flaps on a B-747 aircraft as shown in Figures 1(a) and 1(b). Seventeen flights were flown by the B-747 airplane to complete these tests, and the Cessna T-37B and Learjet-23 (LR-23) aircraft were utilized as the probe aircraft. Both parallel and cross-track probes were performed during this test series. Most of the tests were preceded by the wind-tunnel tests reported in reference 2 and were partially reported in references 3 and 4.

The results of these tests are summarized in Figure 7, which presents the pilot's qualitative assessments of the alleviation provided by retracting the outboard flap on the B-747 airplane. The landing-gear-up data show that a significant amount of attenuation was provided by retracting the outboard flap. These data agree with wind-tunnel data obtained from a model that did not have a landing gear. When the landing gear on the airplane was extended, a significant amount of attenuation was lost.

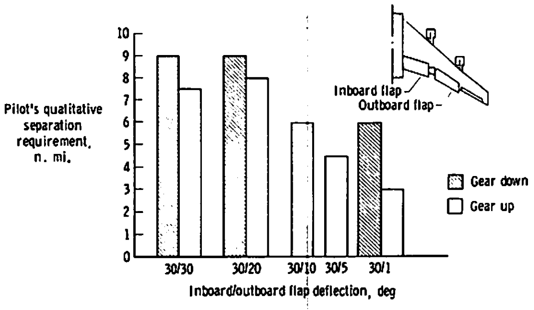

Figure 7. Effect of outboard flap and landing gear on wake vortex alleviation. B-747 airplane; thrust for level flight.

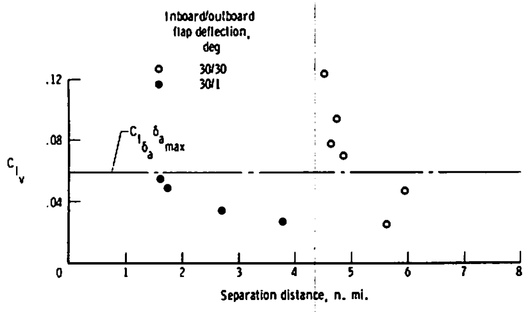

(a) Measured by T-37B airplane. B-747 lift coefficient =1.2.

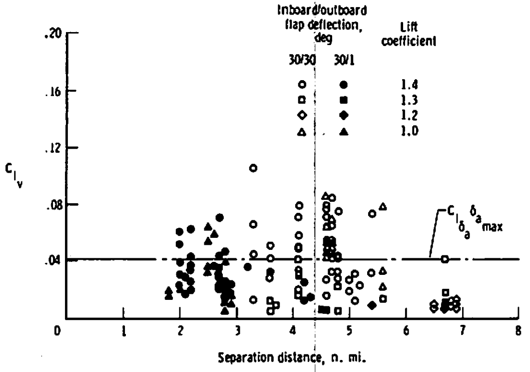

(b) Measured by LR-23 airplane.

Figure 8. Effect of B-747 flap configuration on vortex-induced rolling moments. B-747 gear up; thrust for level flight.

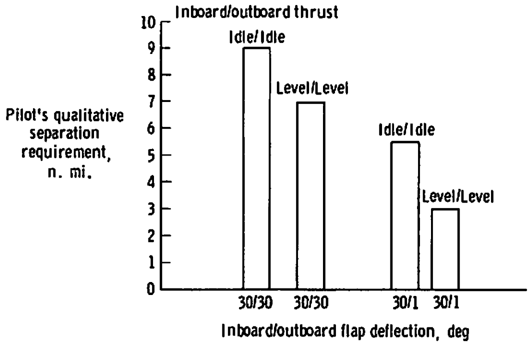

Figure 9. Effect of thrust on wake vortex alleviation. B-747 airplane; gear up.

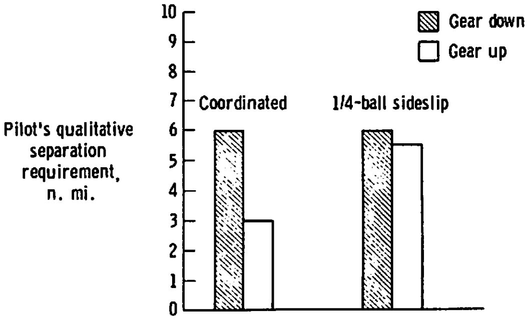

Figure 10. Effect of sideslip on wake vortex alleviation. B-747 airplane; 30/1 flap configuration; thrust for level flight.

Result of Altered Span Loading Tests.

An assessment of the correlation between the pilots' qualitative separation requirements and the requirements that would be dictated by the roll control criterion can be obtained by comparing Figure 7 with Figures 8(a) and 8(b). In general, these data show that the qualitative requirements are in agreement.

During these tests it was also noted that engine thrust and aircraft sideslip had a significant effect on the attenuation provided by the altered span loadings. These effects are illustrated in Figures 9 and 10.

The differences in the B-747 trailed vortex system with and without the outboard flap extended can be evaluated by reviewing the photographs in Figures 11(a) to 11(f) and Figures 12(a) to 12(f). A comparison of Figure 11(a) and Figure 12(a) indicates that with the outboard flap extended the dominant vortex is the vortex shed from the outboard edge of the outboard flap. With the outboard flap retracted, the dominant vortex is that shed from the outboard edge of the inboard flap. In both cases, photographs in Figures 13(a) and 13(b) show that the landing gear diffuses a powerful vortex at the inboard edge of the inboard flap, significantly reducing the attenuation provided by the 30/1 flap config-

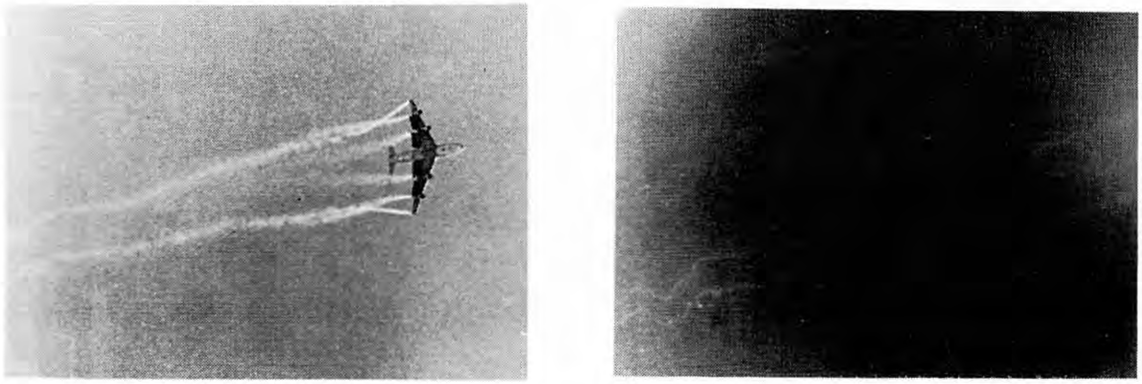

(a) Time = 0 second.

(b) Time = 5 seconds.

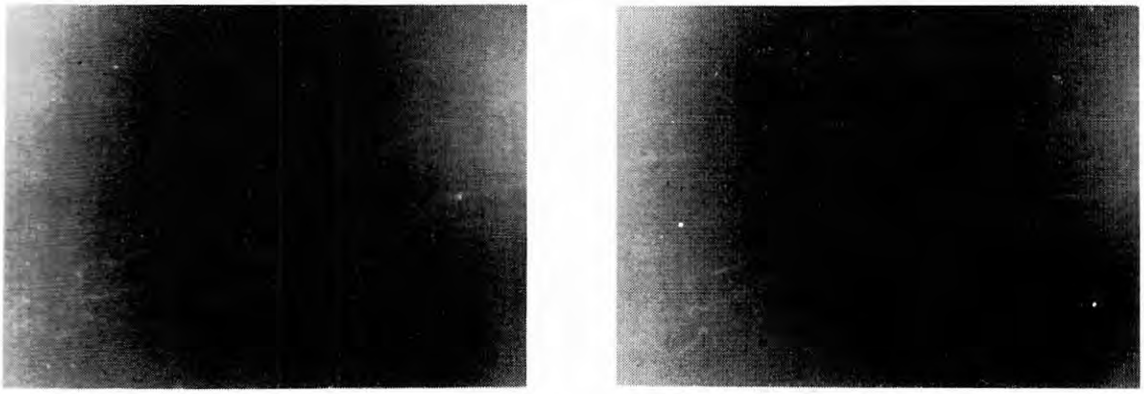

(c) Time = 10 seconds.

(d) Time = 15 seconds.

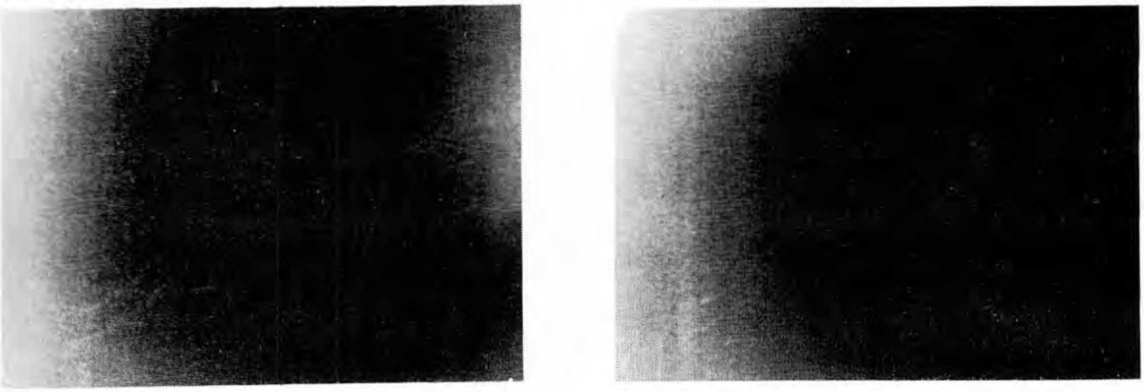

(e) Time = 20 seconds.

(f) Time = 25 seconds.

Figure 11. B-747 wake vortex characteristics. 30/30 flap configuration; gear up; weight = 276,000 kg (607,000 lb); airspeed = 150 knots.

uration. Though not available in the photographic record at this time, visual observations of the inboard vortex showed that it intermingled with the vortex off the outboard edge of the inboard flap when it was not diffused by the landing gear.

Although interesting from a research standpoint, the vortex attenuation afforded by the 30/1 configuration was disregarded for obvious operational reasons when the degrading effects of the landing gear were discovered. It should be noted that this configuration also imposed a center-of-gravity limitation on the B-747 airplane.

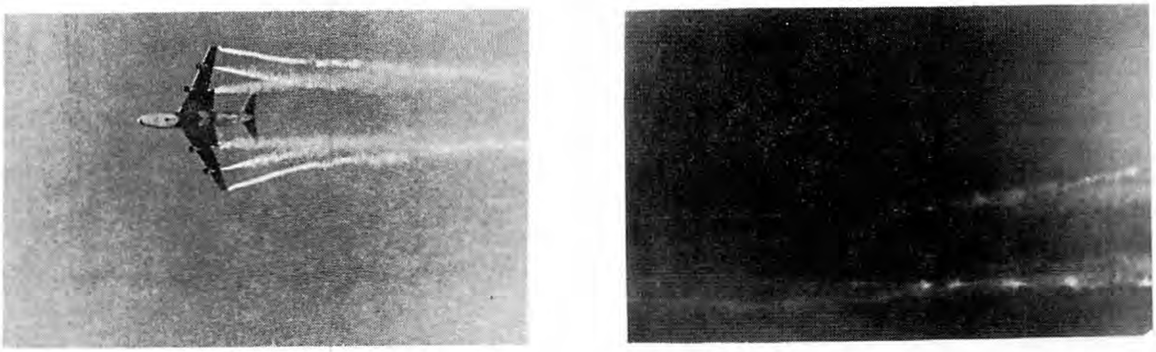

(a) Time = 0 second.

(b) Time = 5 seconds.

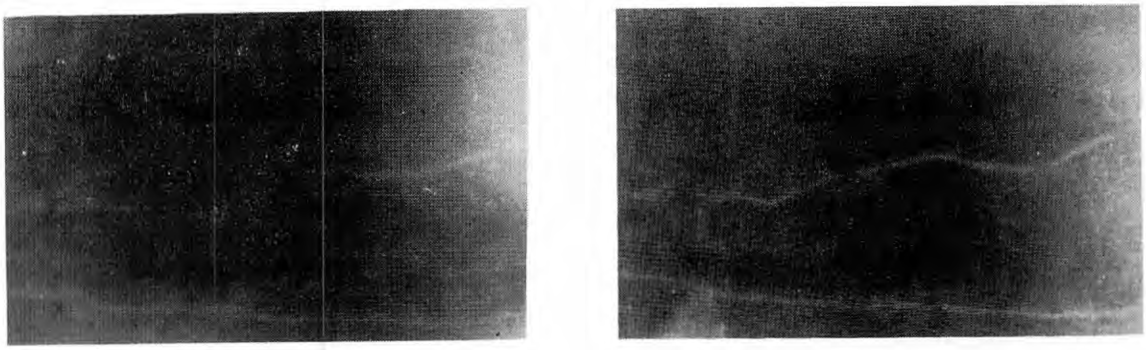

(c) Time = 10 seconds.

(d) Time = 15 seconds.

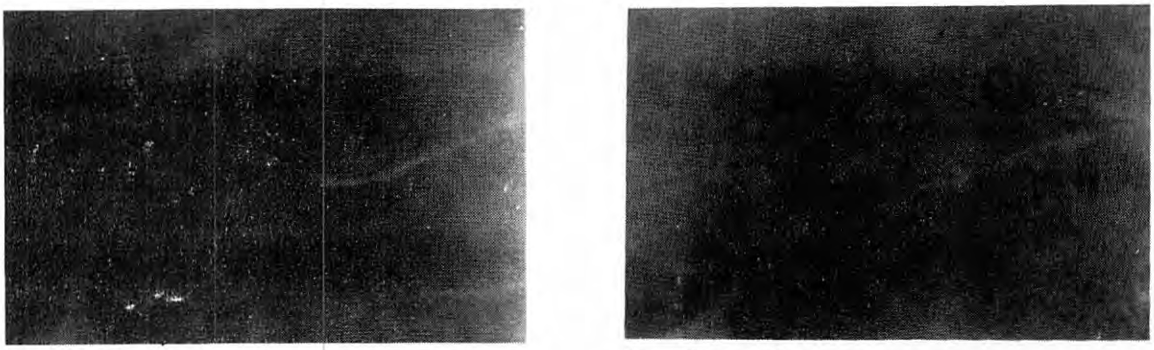

(e) Time = 20 seconds.

(f) Time = 25 seconds.

Figure 12. B-747 wake vortex characteristics. 30/1 flap configuration; gear up; weight = 263,000 kg (578,000 lb); airspeed = 150 knots.

(a) Landing gear extended.

(b) Landing gear retracted.

Figure 13. Effect of landing gear extension on vortex for B-747 30/1 flap configuration.

Undoubtedly, the most violent response of a deliberate exposure of a test airplane to a vortex encounter was that of the T-37B behind the B-747 with a wing-flap configuration opposite to the 30° inboard/1° outboard deflection which was proven to provide attenuation and reduce the vortex hazard. It would be pertinent to look at a time history of this extreme maneuver (Figure 14). The B-747 flap configuration was 30° outboard flap and 5° inboard flaps extended — a thoroughly useless configuration from a practical viewpoint but of extreme interest in the concept of vortex attenuation — since it would prove that if you provided attenuation by decreasing lift at the wing tips you should achieve wake vortex hazard *augmentation* by doing the opposite. It worked! One encounter at 4 miles was so violent and sharp that the probe aircraft dropped back immediately to reenter the vortex at 6.1 miles! The vortex trail was visibly small and tight and the encounter at 6.1 miles resulted in a violent 1½ turn left outside snap roll in which the roll rate exceeded 200 deg/sec and a negative load factor of −2.675g was imposed on the aircraft. The right engine also flamed out in what turned out to be a double inverted snap roll. (All of which convinced us that vortex attenuation in reverse results in vortex augmentation. If anyone ever has a need of increasing separation distances we suggest this type of vortex augmentation.)

Results of Turbulence Ingestion Tests.

The ingestion of turbulence into the vortices in flight was accomplished by mounting splines on the wingtips of a C-54G aircraft (Figures 2 and 3). The Piper Cherokee (PA-28) airplane was used as the probe aircraft for these tests. The vortex attenuation results of these tests are shown in Figure 15, which compares the probe aircraft's roll accelerations in the attenuated and unattenuated vortices. The data show that the PA-28 airplane has insufficient roll control power to overcome the vortices of the basic C-54G airplane at a separation distance of approximately 4 nautical miles and that maximum roll-control roll power is never required to oppose the vortex attenuated by splines. The data generally correlate with the pilots' opinions of the attenuation, which was that roll control become insufficient approximately 2.5 nautical miles behind the unattenuated C-54G airplane but that it was sufficient throughout the entire range of separations

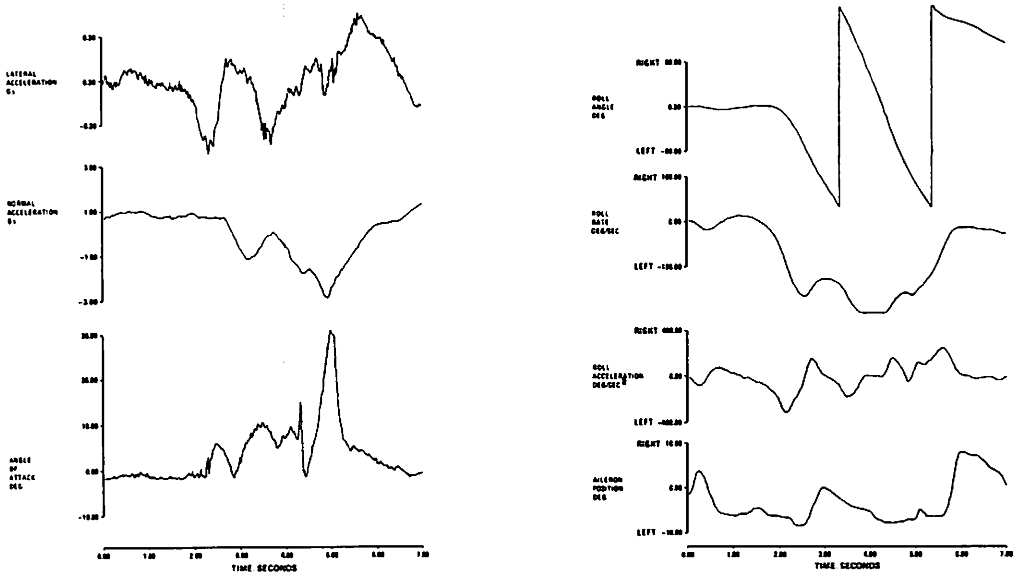

Figure 14. Time history of a T-37B encounter of a B-747 wake (5/30-flap configuration).

tested for the attenuated configuration. The unattenuated data represent the C-54G airplane in the clean configuration and therefore are not directly comparable to the data presented in Figure 6, which are for the normal landing configuration.

The effects of the splines on the performance, handling qualities, and noise of the C-54G airplane were also measured. It was concluded that although the splines significantly reduce the rate of climb of the C-54G airplane, the airplane's four-engine performance was acceptable for this test program. (It should be noted that the splines were not retractable, as they would be for any configuration seriously proposed for operation.) The splines caused no noticeable changes in the handling qualities of the C-54G airplane. Finally, the maximum overall sound pressure level of the C-54G airplane during landing approach with splines on was approximately 4 decibels higher than with splines off.

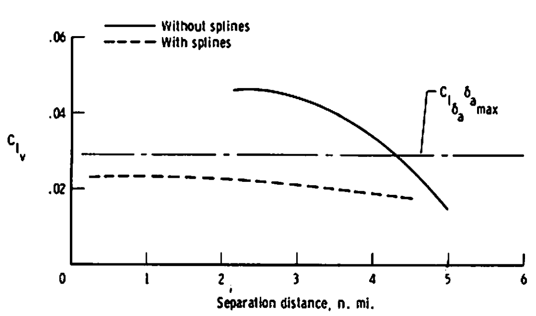

Figure 15. Effect of splines on vortex attenuation. C-54G generator aircraft, gear and flaps up, thrust for level flight; PA-28 probe aircraft.

The vortex attenuation potential of the splines should not be too easily discounted because of what may seem to be rather complex operational problems. An unpublished study concerning the feasibility of producing retractable splines concluded that the concept is practical.

Results of Combinations of Mass and Turbulence Ingestion Tests.

Flight tests were conducted with the B-747 airplane to evaluate the effects of engine thrust on vortex attenuation. In general, most of the B-747 testing has been conducted with thrust for level flight at altitudes of approximately 3000 meters (10,000 feet) because a level flight path makes it easier for the probe pilots to find and encounter the vortices. However, considerable testing has been performed for all the attenuated and unattenuated configurations wherein the thrust was reduced from that required for level flight to that required for a −3° flight-path angle and further to flight idle (approximately −6° flight-path angle, depending on spoiler, flap, and gear configuration). To date, a detailed comparison of the pilots' qualitative assessments of the effects of engine thrust with quantitative data has not been completed. In general, however, it appears that reducing the thrust from that required for level flight to flight idle adds approximately 2 nautical miles to the required separation distance. This generalization is true for both the 30/30 and 30/1 flap configurations (Figure 9).

Tests wherein the inboard and outboard engine thrust levels have been varied alternately have been conducted, but the data are not yet available. Tests to determine the effects of engine thrust on the attenuation provided by deflecting various spoiler segments are yet to be completed.

Results of Combinations of Span Loading Alteration and Turbulence Ingestion Tests.

Wind-tunnel tests made as early as 1969 indicated that the character of the trailing vortex system could be changed significantly by adding a spoiler to the wing in the area of the vortex formation [6]. Flight tests of a spoiler on the wing tip of a CV-990 aircraft (Figure 4) were conducted in 1970 as a result of these wind-tunnel tests. Unfortunately, at that time in-flight vortex marking systems were not available, and therefore the tests were rather inconclusive.

More recently, however, wind-tunnel tests have shown that extending various combinations of the B-747 spoilers is effective in attenuating its vortices [7]. Figure 5 shows that the four outboard spoiler panels on the B-747 airplane are in the vicinity of the outboard flap where the dominant vortex is shed (Figure 11); therefore, it is not surprising that extending these spoilers affects the resulting vortex system. In flight, the spoilers were deflected in the following combinations:

Spoiler Panel											
1	2	3	4	5	6	7	8	9	10	11	12
Spoiler panel deflection, deg											
—	—	37	37	—	—	—	—	37	37	—	—
41	41	—	—	—	—	—	—	—	—	41	41
25	25	—	—	—	—	—	—	—	—	25	25
45	—	—	45	—	—	—	—	45	—	—	45
—	45	45	—	—	—	—	—	—	45	45	—

The deflection angles were chosen as a result of the flight crew's concern about the level of buffet induced by the spoilers and limitations of the control system on the production B-747 airplane. The 37° deflection for spoilers 3, 4, 9, and 10 and the 41° deflection for spoilers 1, 2, 11, and 12 were used because of the crew's concern about the safety of accepting a higher level of buffet. The 25° limit for the deflection of spoilers 1, 2, 11, and 12 was established because it caused the highest buffet level that the flight crew felt passengers would tolerate. The 45° deflections for the spoiler combinations (1, 4, 9, 12) and (2, 3, 10, 11) were limited primarily by the control system. It is interesting to note that the flight crew felt that the buffet level with a spoiler deflection of 45° was excessive for spoiler combination (2, 3, 10, 11) but acceptable for the spoiler combination (1, 4, 9, 12).

Figure 16 summarizes the pilots' qualitative separation requirements from the spoiler flight tests. The data illustrate that with spoilers 1, 2, 11 and 12 deflected 41°, significantly more attenuation is provided than with any other configuration. In fact, it would appear from these data that the 41° deflection of spoilers 1, 2, 11, and 12 could be proposed as an operational configuration that would allow light aircraft to be spaced as close as 3 nautical miles behind heavy aircraft; therefore, a series of tests was developed to investigate the operational feasibility of using this configuration. This investigation was to include actual landings of the B-747 airplane with the spoilers extended and probes of its vortex at landing flare altitudes by the T-37B airplane. Landing the B-747 airplane with the spoilers extended

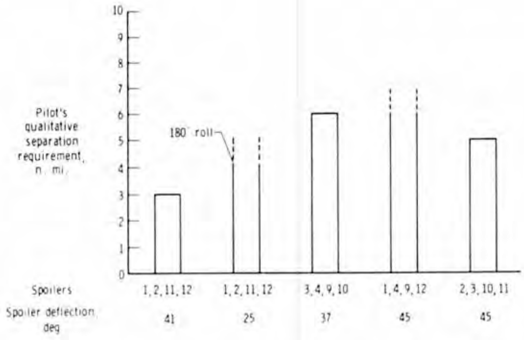

Figure 16. Effect of spoilers on wake vortex attenuation. B-747 airplane; thrust for 3° flightpath; 30/30 flap configuration; gear down; weight ≈ 250,000 kg (≈ 550,000 lb).

was accomplished in a relatively straightforward manner, and the pilots indicated that the spoilers did not significantly detract from the airplane's landing performance.

The proposed low-altitude probes with the T-37B airplane required a reevaluation of the criteria on which probing was based at altitude. The probe pilots used as a criterion the level of upsets which would force them to abandon an approach either on instruments or after breaking out at the bottom of an overcast. Among other factors, a bank angle limit of approximately 30° for the T-37B airplane at altitude was considered as a baseline (with lower limits for aircraft with larger wing spans). The adequacy of this partial criterion was questioned, however, when actual landings were proposed; lower control power, proximity to stalls or spins at low altitude, and the thrust required to overcome the downwash of the generating airplane became additional items of concern.

Intentional probes of the downwash area between the B-747 vortexes were made with the B-747 airplane with spoilers 1, 2, 11, and 12 deflected. The T-37B airplane probed this area to less than 2 nautical miles and found only light to moderate turbulence with an

(a) Front view.

(b) Rear view.

Figure 17. Formation of B-747 wake vortices. Conventional landing configuration.

(a) Front view.

(b) Rear view.

Figure 18. Formation of B-747 wake vortices. Conventional landing configuration with spoiler segments 1, 2, 11, and 12 deflected 41°.

incremental downwash of approximately 150 meters per minute (500 feet per minute). The problem of adequate climb performance at low speeds in the landing configuration had to be considered, even when roll control power was adequate to overcome the vortex-induced roll. An additional unknown was the variation of vortex strength and life as a function of altitude and ground effect. Tests using ground-based sensors were conducted to evaluate the normal and attenuated vortex characteristics, but the results are not yet available.

All T-37B probe pilots agree that the attenuated vortex is much larger in diameter, is less well defined, and has lower tangential velocities than the usual, well-formed vortex tube. A comparison of the photographs in Figures 17(a) and 17(b) with those shown in Figures 18(a) and 18(b) will provide the reader with an illustration of the differences in the formation of the B-747 vortex system with and without spoilers 1, 2, 11, and 12 extended.

FUTURE CONSIDERATIONS

Generating Aircraft.

For the purpose of this discussion, it will be assumed that vortex attenuation is accomplished (in the landing configuration) by extension of specific spoiler segments ahead of the outboard flaps. The most obvious factors to be considered from an operational, environmental and certification viewpoint for a possible retrofit program to the entire fleet of wide-body aircraft would be

a) Landing and Go-Around Characteristics and Performance,

b) Noise,

c) Structural and Passenger Comfort Considerations,

d) Benefits and Cost Effectiveness, and

e) Generating Aircraft Trajectory.

Landing and Go-Around Performance and Characteristics.

At first glance, it would appear necessary to increase the approach speed and determine the increased landing distance required for certification. This need not be the case, however, if the spoilers are mechanized to retract completely at a speed of approximately 1.15 Vso to 1.1 Vso. The spoilers would never be extended at the actual stall or interfere with the stall warning but would be extended during the approach, flare, and landing. The normal landing touchdown speeds in actual service are well above these speeds. This philosophy has already been applied to certification of Direct Lift Control (DLC) where spoiler retraction is initiated by the stall warning system. It could logically be considered as a deliberate increase in drag exactly balanced by an increment of thrust. The spoilers probably would have to be programmed to retract immediately for a missed approach which would be an asset in providing almost instant lift and faster engine response for a windshear or other go-around situations. It would obviously be necessary to recheck the stability, control and trim characteristics as well as the actual landing flare and crosswind landing capacity of the attenuated landing configuration. All of the testing on the NASA B-747 vortex-generating aircraft have been made at normal landing speeds and about a dozen landings have been made with the 1-2, 11-12 spoilers extended through touchdown at normal landing reference speeds. As expected, the pilots reported somewhat less floating after flare but this was not considered unusual or necessarily undesirable for large transport aircraft.

Noise.

Extension of 2 spoiler segments on each wing during final landing approach will obviously increase drag and require some additional thrust with its additional noise increment. Obviously, the noise increment is a liability and will have to be accounted for in terms of increase in safety and airport capacity. Obviously, the optimized spoiler configuration for each of the wide-bodied Heavy aircraft will be influenced by this factor and noise may be the limiting factor in the concept.

Structural and Passenger Comfort Considerations.

One of the parameters in selecting suitable spoiler combinations for vortex attenuation has been consideration of a buffet level acceptable to the passengers in the generating airplane. Some work using perforated spoilers was conducted on the B-747 but resulted in a decrease in effectiveness as vortex attenuators as well as a desired decrease in buffet levels. Wind-tunnel tests have been completed at NASA-Langley Research Center on the Lockheed L-1011 and Douglas DC-10-40 wide-bodied Tri Jets and indicate that the use of spoilers will also work on other wide-body transports although the buffet levels for the several spoiler combinations are not yet known. Flight tests are scheduled for the L-1011 which may also include use of ailerons trimmed symmetrically upward as vortex attenuators and as a factor in development of Active Control Technology. A very brief exposure in the vortex wake trail of a C-5A retrofitted with upward-trimmed ailerons for Lift Distribution Control left some hope that the C-5A with the LDC System installed may already be enjoying some vortex attenuation.

Some quantitative data relating to airplane buffet were obtained on the B-747 and correlated with predicted passenger comfort levels and show an obvious decrease in predicted comfort level although the short period of exposure on final approach is not expected to be a serious problem, but it is one which will require evaluation of any projected increase in flap component fatigue as each configuration is completely defined.

Benefits and Cost Effectiveness.

Increasing airport capacity without compromising safety is a high priority national goal. Obviously, any reduction in the wake vortex hazard at the source would help to achieve this goal as well as to improve economics by reducing delays due to holding. Opposing this factor would be the initial cost of retrofitting the aircraft and the increase in fuel flow during final approach. These and other factors are now being considered in a Cost/Benefit study recently initiated for the FAA by TSC.

Generating Aircraft Trajectory.

Flight tests of the Heavy aircraft have made test pilots appreciate the strength of the vortex trail in the clean, climb or holding configuration to be much more severe than any configuration with flaps extended. Most of the work on vortex attenuation has concentrated on the landing configuration because of the greater exposure and higher accident record. A review of civil, public aircraft, and military accident and incident records reveals unexpected encounters particularly in climb out after flaps have been retracted. One serious attempt to evaluate this hazard during climb out and turning flight recommended a clear corridor 6,000 feet wide, 1,000 feet deep, and a length sufficient to provide for 2.6 minutes × True Airspeed separation [14]. The magnitude of the effort to protect such corridors can be appreciated and the only suggestion which can be offered is for the air traffic controller and pilots to work together to better appreciate this hazard during climb out.

Trailing Aircraft.

The wake vortex hazard is invariably associated with loss of control in roll. In conducting hundreds of deliberate encounters, test pilots have learned to appreciate the imminence of stalling, exceeding safe and sane pitch altitudes as well as actuation of stall-warning stick shakers and pushers coupled with tremendous excursions in yaw. Intentional penetrations of the flow field between the vortices have made them appreciate the rapid settling and loss of airspeed even when no roll and yaw upsets were encountered. Less obvious, however, are the effects of local vortex flow on airspeed and angle of attack and engine control sensors — factors which will have to be analyzed for each aircraft when reduced separations are considered. Another potential problem area in need of analysis and test is the danger of engine flame out and/or compressor stalls when an inlet ingests the vortex of the preceding aircraft. Ironically enough, this may be more of a problem for the Heavy wide-bodied aircraft with their lower potential minimum separation distance. In addition, their engines probably have lower compressor inlet distortion tolerances because of their short inlets and the larger frontal area with consequent higher statistical capability of encountering a vortex. (A parallel, but unrelated problem is the higher statistical probability of bird strikes which is some 7-1/2 times greater than their predecessor engines with less than one half of the thrust [15].) Several instances of deliberate encounters that we have been able to verify to date were:

The right engine of the T-37B vortex probe aircraft flamed out 6.1 nautical miles behind the NASA B-747 with the flaps set in the 30° outboard/5° inboard configuration mentioned previously (the vortex augmented configuration).

C-141 traversing from starboard to port at 1 nautical mile behind another C-141 cruising at 38,000 feet (in order to use the contrail to mark the vortex) suffered compressor stalls on all four engines and flamed out No. 3 engine from the vortex-induced flow perturbation at the compressor inlets.

A third example of an engine "flame out" resulting from vortex ingestion was that of the No. 3 engine of a Convair 990, again at about 38,000 feet while utilizing the contrail as a vortex trailmarker, and at a distance of less than a mile behind an F-104. This flame out was especially insidious because it wasn't even felt by the crew until they saw the engine instruments spooling down!

A review of Air Force accident and incident records reveals many instances of jet and turbo-prop engine compressor stalls and "flame outs" when a vortex was ingested into an engine inlet. Most of these occurred in crossing behind and under other aircraft at relatively close distances, but there are instances documented as far as 1-1/2 miles behind the generator.

Analysis of these engine flame outs reveals similarity in the sense that in most instances the ingested vortices were small in diameter and had peak velocities greatly in excess of those associated with engine inlet distortion tolerance testing. It is conceivable that the threat of possible compressor stalls and engine flame outs may be more limiting in reducing air traffic separation intervals than that associated with upset and control problems. It is only fair to report, however, that there are no flame outs or compressor stalls at distances of 3 to 5 nautical miles for the DC-10-10 and L-1011 probing the vortex wakes of the C-5A and DC-10-40 in level flight at 8,000 to 10,000 feet in the landing configuration. The engine ignition systems were actuated throughout most of these encounters as a precautionary measure. The effects of reduced thrust and higher rate of descent (which result in a smaller tighter vortex) were not appreciated until later and these factors could be significant in reviewing the capability of the airplane from both control and engine flame-out problems in descents if a reduction from the present 4-nautical-mile separation between Heavy aircraft becomes imminent. A similar test or analysis may be necessary in considering the multi-approach capability of future microwave landing systems.

Inadvertent encounters of aircraft during climb out and cruise are obviously less likely to occur than during the landing approach. A review of civil and military accident/incident reports reveals several instances of upsets to aircraft during climb out when they intersect the unseen vortex trail of other aircraft. One such incident, a climb at 23,000 feet at a separation distance of 11 miles, resulted in injury to seven passengers and cabin attendants in a Large tri-jet transport.

The need for decreasing separation intervals between aircraft may dictate the need for training in recognition and wake vortex encounter in much the same manner as the airlines had to introduce recognition and reaction training for windshear problems. One example of the confusion resulting from a wake vortex encounter under VFR conditions was documented by an FAA air carrier operations inspector during a routine inspection. In this case, the first officer of a four-engine turboprop airliner was flying behind a medium size three-engine jet transport on landing approach. The right wing went down at low altitude and the first officer could not raise the wing explaining that he had at first lost one engine and then both engines on the right side. He did not recognize the problems as a wake vortex encounter until the captain applied power to all four engines and ordered a go-around. Training for pilots of non-airline aircraft may also be desirable for both VFR and IFR conditions especially since there is some question as to how to minimize altitude loss when upset in the landing configuration close to the ground. The age-old inference that "one should complete the roll if upset to an inverted position" is seriously in question as a result of the T-37B vortex encounter work and may have to be examined for different aircraft types in different situations. In addition, the very high yaw rates may be unfamiliar and startling at any altitude.

The present desire of pilots to have more information provided to them directly in the cockpit from some sort of aircraft sensors has included wake turbulence. The T-37B probe aircraft is presently equipped with a developmental model of an airborne wake turbulence vortex detector utilizing miniature turbulence sensing pressure transducers in small pitot tubes located at the wing tips. This system when perfected, should be able to point to a vortex to the left or right of the aircraft and would need additional sensors in the vertical plane to provide dimensional information to the pilot. Unfortunately, this project does not enjoy a very high priority at the present time, but the concept appears sound and will have some additional exposure during the forthcoming tests on the L-1011.

CONCLUDING REMARKS

Flight test programs conducted since the advent of the fleet of wide-bodied Heavy aircraft have shown how fortunate it was for the safety of aviation to utilize wing flaps for takeoff, landing, and maneuvering in the terminal area — fortunate, indeed, since wing flaps, unknown to us, have served as vortex attenuators. One needs only a brief exposure to the vicious tight vortex trail of a Heavy aircraft in the clean configuration to appreciate the relatively softer, larger, and more diffused vortices with flaps down. That attenuation was not planned — it was an accident — then why not go one step farther and design for vortex attenuation on purpose.

REFERENCES

1. Barber, M.R. and Tymczyszyn, J.J., "Vortex Attenuation Flight Experiments," in NASA SP-409, 1977.

2. Corsiglia, V.R., Rossow, V.J., and Ciffone, D.L., "Experimental Study of the Effect of Span Loading on Aircraft Wakes," NASA TM X-62431, 1975.

3. Tymczyszyn, J.J., and Barber, M.R., "Recent Wake Turbulence Flight Test Programs," SETP 1974 Report to the Aerospace Profession, Eighteenth Symposium Proceedings, Soc. Exp. Test Pilots, Sep. 1974, p. 52-68.

4. Smith, H.J., "A Flight Test Investigation of the Rolling Moments Induced on a T-37B Airplane in the Wake of a B-747 Airplane," NASA TM X-56031, 1975.

5. Hastings, E.C., Patterson, J.C., Jr., Shanks, R.E., Champine, R.A., Copeland, W.L., and Young, D.C., "Development and Flight Tests of Vortex-Attenuating Splines," NASA TM X-8083, 1975.

6. Corsiglia, V.R., Jacobsen, R.A., and Chigier, N., "An Experimental Investigation of Trailing Vortices Behind a Wing With a Vortex Dissipator," in *Aircraft Wake Turbulence and Its Detection*, J.H. Olsen, A. Goldburg, and M. Rogers, eds., Plenum Press, NY, 1971, p. 229-242.

7. Croom, D.R., "Low-Speed Wind-Tunnel Investigation of Various Segments of Flight Spoilers as Trailing-Vortex-Alleviation Devices on a Transport Aircraft Model," NASA TN D-8162, 1976.

8. Jacobsen, R.A. and Barber, M.R., "Vortex Attenuation Flight Test Techniques," in NASA SP-409, 1977.

9. Andrews, W.H., Robinson, G.H., and Larson, R.R., "Exploratory Flight Investigation of Aircraft Response to the Wing Vortex Wake Generated by Jet Transport Aircraft," NASA TN D-6655, 1972.

10. Robinson, G.H. and Larson, R.R., "A Flight Evaluation of Methods for Predicting Vortex Wake Effects on Trailing Aircraft," NASA TN D-6904, 1972.

11. Andrews, W.H., Robinson, G.H., and Larson, R., "Aircraft Response to the Wing Trailing Vortices Generated by Large Jet Transports," NASA Aircraft Safety and Operating Problems — Vol. 1, NASA SP-270, 1971, p. 115-126.

12. Barber, M.R., Kurkowski, R.L., Garodz, L.J., Robinson, G.H., Smith, H.J., Jacobsen, R.A., Stinnett, G.W., McMurtry, T.C., Tymczyszyn, J.J., Devereaux, R.L., and Boster, A.J., "Flight Test Investigation of the Vortex Wake Characteristics Behind a Boeing 727 During Two-Segment and Normal ILS Approaches," NASA TM X-62398, 1975.

13. Gupta, V.A., "Vortex Related Accidents over the Ten-year Period 1964-1973", FAA-EM-75-6, Apr. 1975.

14. Garodz, L.J. and Miller, N.J., "Investigation of the Vortex Wake Characteristics of Jet Transports during Climbout and Turning Flight," FAA-AEQ-75-1, May 1975.

15. Stout, C.L., "Some Words on Birds," Douglas Aircraft Co. letter to all DC-8, DC-9, and DC-10 operators, CI-270-CLS-L314, 23 Mar. 1976.

AIRCRAFT VORTEX EFFECTS ON GROUND LEVEL POLLUTANT CONCENTRATION AND TRACKING OF VORTEX MOVEMENT IN THE AIRPORT ENVIRONMENT

B. TOD DELANEY
Exxon Research and Engineering
Florham Park NJ 07932

ABSTRACT: The effect on ground level pollutant concentrations of including a mechanism to consider the transport of aircraft-generated pollutants captured in the trailing vortex system is examined by coupling a three-dimensional vortex transport program with a line source dispersion routine. It was found that not only would the ground level concentrations of oxides of nitrogen change but so would the spatial distribution. Echos recorded by a FM-CW radar are shown to be the result of water vapor and pollutants trapped in a descending vortex system.

INTRODUCTION

While visible air pollution from aircraft has decreased over the last 16 years with the introduction of clean combusters, reactive hydrocarbons and oxides of nitrogen have increased. This increase is caused by the increased number of flight operations and the introduction of a new generation of jet engines that produce considerably higher quantities of oxides of nitrogen (NO_x), especially during runway roll and climbout. Since NO_x is a primary constituent of photochemical smog, air pollution from aircraft and airports has come under closer scrutiny.

The increase in the number of flight operations and the size of the aircraft now in common use has also increased the occurrence of another type of air pollutant, the aircraft wake vortex system. The wake vortex system is of major concern in the airport environment because of its possible detrimental effects on encountering aircraft.

These two forms of airport environment air pollution are considered together in this paper; although seemingly unrelated, they each affect one another from the viewpoint of transport and detection, respectively. The two specific areas that are covered are: first, determination of the effect on ground-level pollutant concentration when including aircraft wake vortex transport equations in airport air pollution prediction models and, second, determining if aircraft wake vortices can be tracked by the highly sensitive Frequency-Modulated Continuous-Wave (FM-CW) Radar.

AIRPORT AIR POLLUTION MODELING

An accurate environmental assessment of aircraft operations has three primary components: the measurement of pollutant emissions to categorize the air emissions per engine for each aircraft operational mode, accurate description of the aircraft operational procedures to calculate total emissions released, and dispersion equations to predict ambient air concentrations. This paper reexamines the latter component to determine the effect when aircraft vortex transport equations are included.

The modeling is concerned with the period from climbout to 943 meters. The

Table 1. Airport Air Pollution Diffusion Models

Model Name	Developer	Contracting Agency
AIREC or NREC	Northern Research Engineering Corporation	EPA
GEOMET	Geomet Incorporated	EPA
ERT/MARTIK	Environmental and Research Technology Northern Research Engineering Corporation	FAA
AVAP	Argonne National Laboratory	FAA
AQAM	Argonne National Laboratory	Air Force
GACM	Grumman Aerospace Corporation Model	Unknown
BOEING	Boeing Computer Services	Proposal to FAA
Landrum/Brown	Landrum and Brown	None
LMSC	Lockheed Missile and Space Company	Proposal to FAA

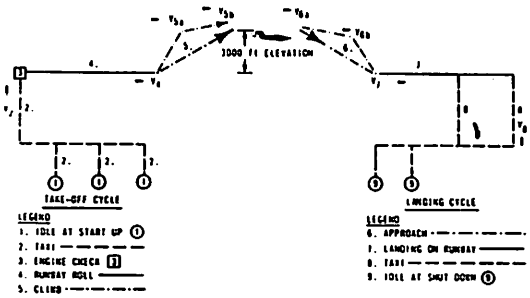

Figure 1. Schematic of aircraft landing take-off cycle (LTO).

Table 2. Aircraft Landing and Takeoff Cycle (LTO)

Operational Modes
a. start-up and idle
b. taxi mode to end of takeoff runway
c. delay at end of runway
d. runway roll
e. climbout to 3000 feet
f. approach from 3000 feet
g. landing on the runway
h. taxi mode to parking area
g. idle at shoutdown
h. a maintenance operation and venting of fuel from the aircraft at one point in the climbout to 300 feet

943-meter cutoff distance is the standard altitude set down by the Environmental Protection Agency (EPA) for consideration of aircraft operations with respect to their contribution to air pollutant concentrations within the mixing layer.

There are presently nine models designed specifically to calculate pollutants generated by aircraft operations in and around airports or military airbases [1]. These nine models are presented in Table 1 along with the contracting agency and developing corporation. All of the modeling efforts subsequent to the NREC model have relied heavily on the basic framework developed in the NREC model. The NREC model was developed to cover all basic operations taking place at an airport with the primary emphasis on development of a typical landing and takeoff cycle (LTO) for passenger aircraft. The LTO cycle developed consisted of ten distinct modes with each being modeled separately. The ten modes comprising the LTO cycle are listed in Table 2 and shown schematically in Figure 1.

Considerable developmental effort has gone into improving the calculation of the quantity of pollutants emitted by individual aircraft during all phases of the LTO cycle, the distribution of the pollutants among the sources defining the LTO cycle, and the dispersion of the pollutants from the source points to the receptors since the NREC model was first published. This developmental effort has resulted in the very detailed airport/military-airbase models represented by AVAP/AQAM of Argonne National Laboratory [2]. This development as applied to the climbout portion of the LTO cycle is as follows: in the NREC model all aircraft (12 classes) followed the same departure path which was approximated as a series of point sources of varying strength in the dispersion algorithm, whereas in AQAM 50 individual aircraft types are represented with each following a different departure path which is treated as an inclined line source using the Argonne developed line-source model (ALSM) [3].

Even with all of the refinements made to the airport air pollution simulation models it has not been possible to obtain conclusive tests of the models predictive capabilities and ambient air data of the three primary pollutants (carbon monoxide, hydrocarbons and oxides of nitrogen). Preliminary tests indicate the models adequately predict carbon monoxide and hydrocarbons but fail with oxides of nitrogen. The usual reasons given for the lack of correlation between observed and predicted values is that material is transported into the sampling area from an unknown source or from sources that have not been modeled adequately, mainly the environs. Another suggestion is that one or more emission sources within the airport or airbase had not been adequately modeled. One emission source that falls into the class of not being adequately modeled is that portion of the LTO cycle that begins when the aircraft leaves the runway and climbs to 943 meters. Neither the NREC nor AVAP/AQAM models adequately modeled this portion of the LTO cycle since both methods assume that the pollutants remain along the aircraft flight path which is not the physical case. This lack of adequate modeling of the physical situation is especially sensitive for NO_x since it is during this portion of the LTO cycle that approximately 40% of the NO_x enter the atmosphere from aircraft operations [4]. Considering the trend toward higher NO_x levels in the new generation of aircraft engines, the accurate modeling of this portion of the LTO cycle becomes more and more important. These reasons point to a need for a refined methodology to determine the effect of the aircraft during climbout as an emission source on the ground-level concentrations predicted at various receptors. The basis of the refined description for the modeling of aircraft emission during the climbout portion of the LTO cycle is that the combustion products are transported from the flight path by the aircraft wake vortex system before dispersion begins.

AIRCRAFT WAKE ENTRAPMENT AND TRANSPORT

Some of the first work performed to determine the dissemination of material from aircraft was done for the U.S. Army's Dugway Proving Ground. The specific series of tests considered are referred to as the Dallas Tower Studies [5]. Some of the important results of this study related to the present subject were the assumption that the aircraft could be treated as a point source for dispersion calculations did not appear to be valid for aircraft releases, that the aircraft wake had some degree of control over the spread of the released material, and that a net downward transport was imparted to the released material.

The action of the aircraft wake and its effect on cloud growth were further studied by Meteorology Research Inc. (MRI). The MRI experimental program consisted of attaching smoke grenades to the wing tips of a Cessna 180 and producing smoke from the aircraft engine by injecting oil into the engine exhaust [6]. This procedure allowed observers to see the wing tip vortices and the entrainment of the engine-exhaust products by the vortex system. The smoke contained in the engine exhaust was captured by the lower portion of the vortex flow field and transported and diffused through most of the oval representing the vortex pair. The oval containing the smoke from the engine and the vortices created by the wings then descended through the atmosphere for 7.6-30.5 meters [6]. The importance of these tests for the present study are that the MRI tests showed that the combustion products from a centrally located engine were drawn into the trailing vortex system, remained there, and were transported with the system as it descended through the atmosphere.

During 1970 the FAA conducted full-scale flight tests to measure the size of vortex cores and duration of the trailing vortex system from some of the commonly used commercial jet aircraft. In this test program aircraft flew upwind of an instrumented tower; the mean wind carried the trailing vortex system to the tower where measurements were made. In an effort to improve the predictability of vortex-tower intercept times, CORVUS-type smoke oil was used in the engines of B-747, B-707 and CV-880 aircraft. The smoke produced become entrained in the rolled-up vortex system and thus marked the position of the trailing vortex system [7].

The test programs cited above show that the trailing vortex system captures the combustion products from aircraft engines either centrally or wing mounted and that the trapped products are transported intact through the atmosphere.

MODEL FORMULATION

A theoretical description of the process of ingestion of the exhaust products has recently been published by Nielson Engineering [8]. Although the emphasis of the study was on supersonic aircraft operations in the stratosphere, many of the analytical methods developed can be used for different flight conditions [8]. Therefore, the Nielson model was used as the basis for describing the capture and radial distribution by density of the aircraft exhaust products in the trailing vortex system.

The prediction of ground-level concentrations of oxides of nitrogen or other pollutants generated by aircraft operations, given a model describing their capture and distribution in the wake vortex system, is dependent on the accurate modeling of the transport of the wake through the atmosphere. Research into devising a model to forecast hazardous situations involving the transport of aircraft wake vortex systems was initiated by the DOT Transportation Systems Center (TSC) in the early 1970's. From this research effort a two-dimensional wake vortex transport model was developed by Brashears et al. [9]. They detailed the development of computer codes for predicting of the aircraft trailing vortex position with time and an analysis of experimental data used to determine the accuracy of the predictive model.

The overall conclusion when the predicted and experimentally obtained tracks were compared was that reliable vortex tracks could be predicted with the accuracy of the prediction being determined by how well the mean wind field was specified. This conclusion was qualified because: (1) the predicted sink rate was less than the observed and (2) the measured upwind vortex transport was greater than predicted.

Some efforts were made in later versions of the model to improve the predictive accuracy especially with regards to the sink rate. The modifications were based on not restricting the model to the use of an elliptically loaded wing. Thus an aircraft with inboard flaps and a non-elliptically loaded wing will generate a wake vortex system that will exhibit a higher sink rate [10].

For the present application of describing the position of the aircraft trailing vortex system (for pollutant dispersion calculations), data on the spatial location with time is required not only on the position of the vortex system with respect to the z axis (altitude) and y axis (cross runway) as provided in the two-dimensional model but also with respect to the x axis (along runway). The extension to the third dimension is required since the mean wind would, except for a purely cross runway wind, translate the vortex position along the x axis with time.

The TSC group took a two-dimensional potential line description of vortex motion and expanded it to the third dimension [11]. The extension was accomplished by using the Biot-Savart principle. The model simulates the position of the inclined vortex system as a sequence of connected straight-line segments.

The three-dimensional TSC model did not have any provision for bouyancy nor for meteorological factors, but the user could input any desired takeoff angle instead of providing only a point location for the aircraft as was the case with the two-dimensional simulation. Therefore, one could simulate the trajectory of the vortex system over the entire range of altitudes instead of only following its progress from a fixed point, and hence account for the unequal effects of the ground plane on the overall vortex system.

The TSC three-dimensional model (VOX3DM) was changed to allow a variation of wind speed and direction with height based on a user input wind profile. The wind profile simulation was adapted from the two-dimensional model.

Comparison of the Two Vortex Transport Models.

Since only the two-dimensional model has been verified by full-scale flight data, comparison tests were undertaken to determine the extent of the variation in predicted vortex position between VOX3DM and the two-dimensional models. The first series of comparison tests was conducted to determine what differences could be expected in the prediction of vortex position with time for a vortex system generated well outside the region of ground effect. In both models the same input parameters were used, including the same wind profile and wind profile interpolation-extrapolation mechanism. Table 3 contains the basic input parameters, the position of the vortex system, time after generation as calculated by both models, and the differences obtained between the two prediction schemes. The most striking result is that the difference in lateral position of the vortex system calculated by the VOX3DM and Lockheed models is less than 30.5 meters even after 120 seconds. It should also be noted that the differences in the positions of the vortices by the two calculation schemes is symmetrical; that is, not all of the calculated differences are associated with either the downwind or upwind vortex but that they vary in the same direction by almost equal amounts. These results show that VOX3DM produces essentially the same vortex trajectory as does the Lockheed model for the vortex system generated out of the ground effect region.

Table 3. Comparison of Predicted Lateral Position from VOX3DM and Lockheed Models

Input Data to Both Models

Aircraft Type: B747
Climbout Angle: 15°
Flight Speed: 243 ft/sec
Wing Span: 195.7 ft
Takeoff weight: 361,000 lbs
Wind Speed: 0 ft/sec

Comparison of Models

Time Sec	Lateral Position (feet)		
	VOX3DM*	Lockheed	Difference
0	±77	±77	0
20	±90	±93	3
40	±149	±167	18
60	±253	±287	34
80	±369	±420	51
100	±489	±558	69
120	±612	±697	85

*Adjusted to same initial position

The next series of tests was conducted to determine what differences existed in the calculated vortex position by using different climbout angle (3°, 5°, 10°, 15°, 20°). The initial position of the vortex for all calculations was 63.4 meters above the ground since this altitude was used extensively in the Lockheed report (this figure represents the altitude of a B-747 at the middle marker location in the landing pattern). Thus, easy comparisons could be made between VOX3DM calculations and reported Lockheed results. As a result of the calculation scheme in VOX3DM, it was not possible to obtain an initial altitude of exactly 208 feet for each of the climbout angles but the initial altitude was never off by more than 8% or 4.9 meters. The results from these comparison runs are presented in Figure 2. Figure 2 shows that computed differences in lateral position with

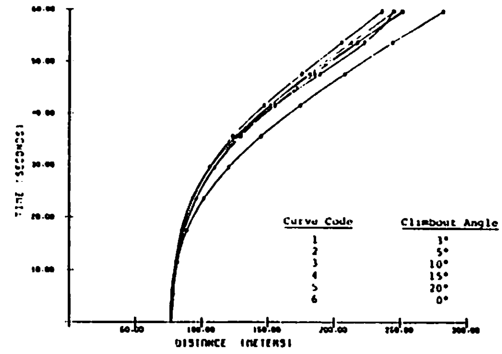

Figure 2. Variation in lateral position of the vortex system with time as a function of aircraft climbout angle.

time after vortex generation is not highly dependent on the climbout angle. For all angles tested the variation among the computed positions was not greater than 5%. The VOX3DM calculated vortex positions were consistently less than the values obtained by the Lockheed model, but always within 15.2 meters. Thus the effect of using different climbout angles in VOX3DM does not lead to any significant change in lateral position of the vortex system with time.

While considerable differences in predicted vortex positions were reported when the Dee and Nicholas two-dimensional study and VOX3DM were compared [12], the results of VOX3DM and Lockheed model comparison showed no significant differences. This result was not expected as the Lockheed model was based on the Dee and Nicholas study. However, for the purposes of this study the similarity in results was a definite bonus as it verified the results of VOX3DM and, with the results verified, allowed its use as the vortex transport model in the proposed method for calculating ground level pollutant levels from aircraft in flight.

COMBINATION OF VORTEX TRANSPORT AND ATMOSPHERIC DISPERSION

For the calculation of ground level pollutant concentrations VOX3DM was used to calculate the wake vortex position and the resulting vortex path was used as input for the Argonne Line Source Model from AQAM, which calculates the dispersion of the engine exhaust. The results of the above routine, the Aircraft Wake Vortex Line Source Model (AWVM), were then compared with the results obtained when the aircraft flight path was input into the Argonne Line Source Model. This second method, the Aircraft Flight Path Line Source Model (AFPM) is currently employed in AQAM. The Argonne Line Source Model from AQAM was used rather than all of AQAM because this study deals only with dispersion of pollutants from jet aircraft.

The differences in the two simulations are in two specific areas: (1) the location of the line source or sources with respect to the aircraft flight path; (2) the manner in which engine emissions are distributed along the designated line source or sources.

Proposed Model.

AWVM models the aircraft emissions as a series of 14 connected (7 for each wing tip vortex) finite line sources which represent the wake vortex trajectory obtained from VOX3DM. AFPM treats the aircraft emissions as a single line source along the flight path of the aircraft.

The line source or sources used to represent the flight path of the aircraft (emission source) in AFPM is dependent only on the climbout angle that applies to a specific aircraft type. This same climbout angle is used in AWVM to provide the initial flight path of the aircraft which is then used to calculate the resultant vortex wake trajectory (and thus the 14 line sources used to describe the position of the pollutants after transport).

The climbout angle for commercial aircraft is dependent on a variety of parameters that are evaluated at flight time. The common range reported is from 5° to 20°. For the present series of comparisons a value of 10° was chosen as being representative.

All simulations using VOX3DM for calculating the position of the vortex system were based on a wake transport that lasted for 60 seconds. The 60-second figure was determined from published data on the lifetimes of measured vortex systems [10]. Also, after about 60 seconds the descent rate is not adequately described by the classical equations used in the computer simulations, although they are used to at least 120 seconds.

For both AFPM and AWVM a starting altitude of one half the aircraft wing span and a final altitude of 943 meters were chosen as the bounds on the flight path. Figure 3 is a representation of the along-the-runway (x axis) versus the across-the-runway (y axis) position of the line sources as is used in AFPM and in the proposed AWVM. The influence of the wind along with the influence of the ground plane vortex interaction is evident in the translation of the line source position from its initial position represented by

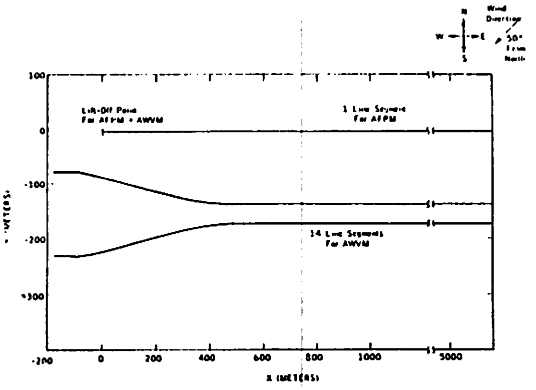

Figure 3. Diagram representing the along-the-runway (x axis) versus the across-the-runway (y axis) positions of the line sources as used in AFPM and proposed AWVM.

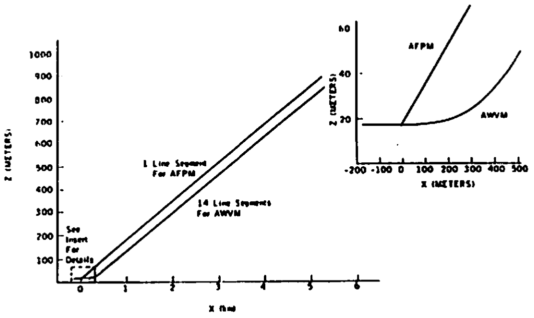

Figure 4. Diagram representing the along-the-runway versus altitude (z-axis) position of the line sources as used in AFPM and proposed AWVM.

the AFPM line source to its final position represented by the pair of line sources used in AWVM. Figure 4 provides a representation of the along-the-runway versus altitude (z axis) position of the line source before and after the 60-second transport period.

The line sources are also further described by an initial vertical and horizontal dimension in which the pollutants are assumed to be fairly uniformly dispersed. For AFPM simulations these values are set at 20 meters for the horizontal and 8 meters for the vertical. The initial vertical and horizontal dimensions for AWVM were set so that the total cross-sectional area of the vortex pair would be slightly larger than the size of 160 square meters currently used in AFPM; thus, they were set at 10 meters each or a total of 200 square meters for the pair. Additional comparisons were undertaken with the initial sizes doubled to 20 by 20 giving a pair cross-sectional area of 800 square meters. The value of 20 meters is based on the size of the field of influence for the vortex from tower fly-by measurements [7].

Emission Source.

The emission rates used for the test purposes were representative of a major airport with a flight takeoff density of about one aircraft every three minutes. The Boeing 707 was chosen as the typical aircraft type for further calculations. The NO_x emission rate for the engine during the climbout portion of the LTO is 6.9 kg of NO_x per 454 kg of fuel consumed at a fuel consumption rate of 4812 kg of fuel per hour resulting in an emission rate of 73.1 kg NO_x per engine per hour.

The aircraft will take approximately 60 seconds to gain the cutoff altitude of 943 meters at a climbout angle of 10° and an average climbout speed of 91 m/sec. Therefore, an average hour would have 20 aircraft climbouts (one every three minutes with each climbout lasting 60 seconds) and an overall average NO_x emission rate of 6.78×10^6 μg/sec per engine. Since the B-707 has 4 engines, the resulting emission rate for the 20 aircraft flights per hour would be 2.712×10^7 μg/sec.

The total emission rate of 2.712×10^7 μg/sec over the entire flight path is used directly by the line source model for the single line source considered in AFPM. Flight conditions presume a takeoff velocity of 83.2 m/sec and a final velocity of 98.9 m/sec at 943 m in computing the emission density at any point along the length of the source. An emission rate must be provided for each individual line segment for the 14 line sources used in AWVM. These emission rates were obtained by apportioning the total emission from the aircraft to each of the line segments on a basis of time.

Receptor Location.

The ground level NO_x concentrations were calculated for a grid of 400 receptors. The distance between grid members was set at 200 meters. Figure 5 depicts the location of the receptor grid in relation to the aircraft flight path that was used for both AFPM (no wingtip vortex consideration) and AWVM (wingtip vortex considered) computer simulations.

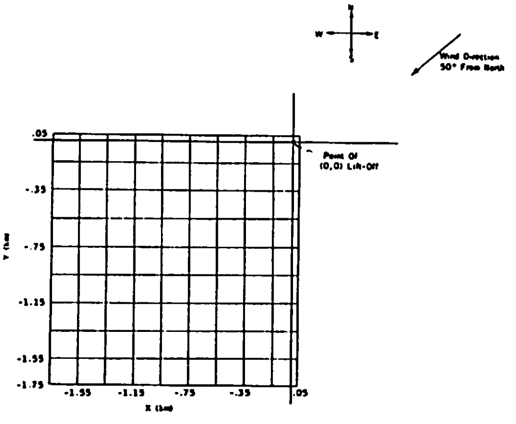

Figure 5. Location of recepter grid in relation to the aircraft flight path for both AFPM and AWVM.

All of the input variables to both AFPM and AWVM are contained in Table 4 for easy reference. The computed ground level concentration at the grid of receptors from the two calculating schemes were entered into a contouring program to provide concentration isopleths. In all of the figures representing the output from the contouring program that follow, the contour lines having the same numerical code designation have the same numerical value. The values corresponding to the code in terms of micrograms per cubic meter are presented in Table 5.

Table 4. Input Variables AFPM and AWVM

Wind Speed	2 m/sec, 4 m/sec, 8 m/sec
Mixing Height	943 m, 100 m
Stability Category	B, C, D, E
Emission Strength	2.717 × 10^7 μgm/sec
Climbout Angle	10°
Initial Horizontal Plume Dimension	2 @ 10 m, 2 @ 20 m, 1 @ 20 m
Initial Vertical Plume Dimension	2 @ 10 m, 2 @ 20 m, 1 @ 8 m
Takeoff Velocity	83.2 m/sec
Velocity at 3000 ft	98.9 m/sec
Number of Line Segments	AFPM 1 line AWVM 14 lines

Table 5. Contour Values

Contour Number	Contour Value in $\mu gm/m^3$
1	1.0
2	10.0
3	20.0
4	30.0
5	40.0
6	50.0
7	75.0
8	100.0

COMPARISON OF PROPOSED-MODEL RESULTS WITH PRESENTLY IN USE MODELS

Examination of Figure 6a-f shows the different ground level concentration patterns that result from changing the Turner Stability from B through D, while maintaining all other parameters constant in the two simulation procedures. The resulting concentration isopleths from the two models are considerably different not only in magnitude but also spatially, especially in the area close to the aircraft departure point. Table 6 presents the maximum values calculated by each of the computational schemes along with the location of the maximum relative to the aircraft liftoff point. A comparison of the data in Table 6 shows that consideration of the wake vortex transport would increase maximum calculated ground level concentrations by a factor of about 3. What is not indicated in Table 6 but is evident from examination of Figures 6a-f is that there are areas where concentration differences of 5, 10, or even 50 times exist. The specific areas where these concentration differences exist differs de-

Table 6. Maximum Predicted NO_x Ground Level Concentrations

Model Used	Stability	Wind Speed (m/sec)	Mixing Height (m)	Concentration ($\mu g/m^3$)	Location x (m)	Location y (m)
AWVM	B	4.	943.	50.2	+50.	−250.
AFPM	B	4.	943.	18.9	−150.	−150.
AWVM	C	4.	943.	50.4	−150.	−350.
AFPM	C	4.	943.	17.0	−250.	−250.
AWVM	D	4.	943.	58.2	−150.	−350.
AFPM	D	4.	943.	14.7	−550.	−450.

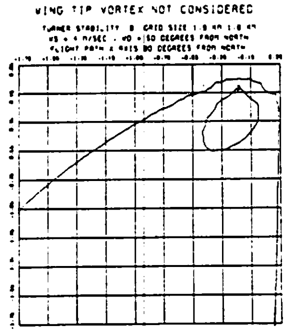

Figure 6a. NO_x concentration isopleths obtained using AFPM—B stability

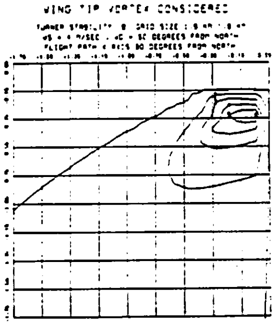

Figure 6b. NO_x concentration isopleths obtained using AWVM—B stability

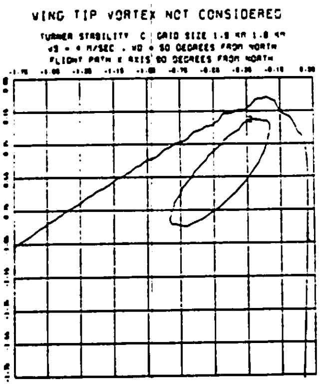

Figure 6c. NO_x concentration isopleths obtained using AFPM—C stability

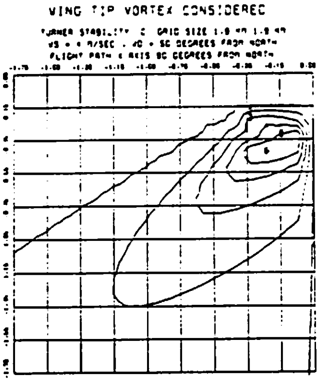

Figure 6d. NO_x concentration isopleths obtained using AWVM—C stability

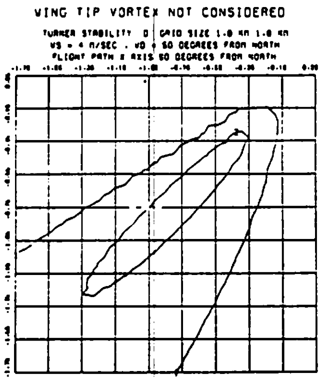

Figure 6e. NO_x concentration isopleths obtained using AFPM—D stability

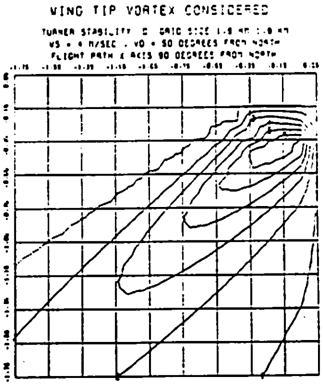

Figure 6f. NO_x concentration isopleths obtained using AWVM—D stability

pending on the meteorological variables chosen, but the extreme cases of factors of 50 or above are confined to about a 200 m^2 area east of the point of maximum concentration. Comparison of Figures 6a-f also shows that considerably larger areas are affected by any specified concentration level when consideration is given to the transport of the wake vortex system.

The D stability case gave the highest ground level concentration of the 3 stability cases chosen for the wake transport model — as shown in Table 6. D stability or a neutral stratification also is the best type of atmospheric condition for the transport of the vortex system.

In addition to considering likely atmospheric conditions as represented by Turner Stabilities B through D with a mixing depth of 943 meters and moderate wind speeds, an additional comparison of the two models was completed using what the Argonne Laboratory has termed as "worst case" conditions; i.e., Turner Stability E, wind speed of 2 m/sec and a mixing depth of only 100 meters. These atmospheric conditions were used in both simulations while maintaining the emission density and wind direction as in previous runs. Examination of the resulting isopleths for consideration of wake vortex transport Figure 7a and no-wake transport Figure 7b and a comparison of the maximum values in Table 7 show that consideration of the wake vortex would give increased concentrations by a factor of about three with a maximum value of 110.0 μg/m^3 being calculated for AWVM compared to a maximum of 37.5 μg/m^3 for AFPM.

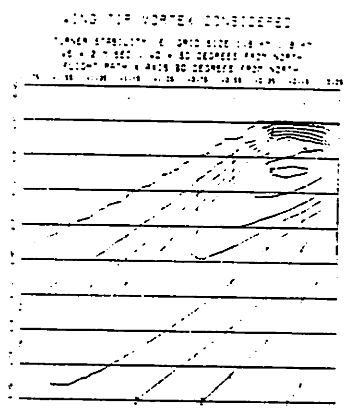

Figure 7a. NO$_x$ concentration isopleths obtained using AWVM—E stability

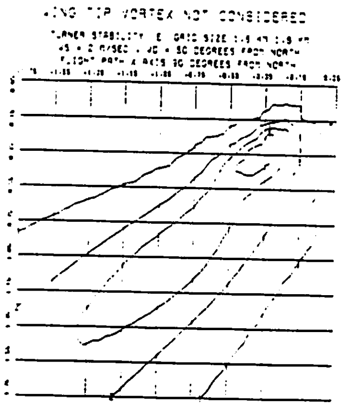

Figure 7b. NO$_x$ concentration isopleths obtained using AFPM—E stability

A comparison of the figures and the associated contour values show that not only does the ground level pollutant concentration pattern change from the use of the two-step procedure, but also the magnitude of the calculated values change by a factor of 3. Therefore, not considering the transport of the vortex system through the atmosphere before starting dispersion calculations leads

Table 7. Worst Case Ground Level NO$_x$ Concentrations

Model	Stability	Wind Speed (m/sec)	Mixing Height (m)	Concentration (μgm/m^3)	Location x (m)	Location y (m)
AWVM	E	2	100.	110.0	−150.	−350.
AFPM	E	2	100.	37.5	−250.	−250.

to substantially different results. The calculated values should not be considered as representative of total airport or airbase values, although representative input from one phase of overall aircraft operation was used in the simulations. The proposed method predicts a change of about 3 times the values calculated by the presently used method and that some results using the input data produced values in excess of the 100 $\mu g/m^3$. The proposed method has a significant effect on calculated total concentrations from the operation of an airport or airbase although the short-term values (1 hour) presented here should not be compared directly with the National Ambient Air Standard for NO_x of 100 $\mu g/m^3$ (annual average). Also, it is noteworthy that approximately one third of the NO_x emitted in the airport environment comes during the climbout portion of the LTO cycle.

CONCLUSIONS

The importance of using the proposed simulation AWVM to predict ground level concentrations over those produced by AFPM, especially at sampling stations close to the runways, is brought out by some of Argonne's work at O'Hare airport. When Argonne compared predicted results using AVAP with observed data, they found that they were generally able to predict NO_x concentrations in relatively good agreement with observations [13]. Although the general prediction tendency was good, the predictions specific to the areas near airport runways were below the observed by a factor of between three and four for most comparison sets. Therefore, the inclusion of AWVM in AVAP/AQAM should bring the predicted result more in line with the observed results based on the comparisons presented previously.

REMOTE VORTEX SENSING

The need to determine the accurate transport of the vortex system is essential in field verifications studies of models such as AQAM/AVAP. Ideally, one would like to observe visually the trajectory of the vortex system throughout its lifetime, but this is only possible at an altitude where contrails form from the water produced from the combustion of fuel. However, these are too far removed from the observer. Also an entirely different set of average meterorological conditions are present in the upper troposphere and lower stratosphere where contrials form from those in the lower troposphere which is of interest here. An alternate method might have been to observe the smoke generated by early jet aircraft, but with the introduction of clean combusters in the late 1960's, the visible smoke trails produced by jet aircraft have virtually become nonexistent. Thus, there is a need for a remote means of sensing the vortex transport through the atmosphere.

In Use Vortex Sensing Instruments.

The need for real time remote vortex tracking was recognized by DOT/TSC and became a primary part of the TSC approach to the development of a Wake Vortex Avoidance System [14]. Five different types of systems are currently being evaluated by TSC as part of the effort at John F. Kennedy International Airport (JFK). The five are broken down as follows: Three systems use acoustic energy for sensing the vortex system (Pulsed, Doppler, and Monostatic Acoustics), one senses the vortex flow field with a series of ground anemometers (Ground Wind System) and the fifth utilizes the backscatter of a laser beam (Scanning Laser Doppler) to detect vortices.

The five systems used in the current tests by TSC offer a wide variety of approaches to vortex detection, but they do not cover all of the possible detection systems that have been suggested [15]. Among the systems not currently being tested but thought to have a possible place in vortex detection is millimetric radar. The FM-CW radar was developed recently by the Naval Electronics Laboratory Center (NELC) by Richter primarily for the purpose of studying the influence of atmospheric refractive structure variations on microwave radio propagation [16]. But the system might be used as a ground-based vortex sensing instrument due to its sensitivity to changes in humidity structure that are likely to result from the injection of water vapor from the aircraft engines to the atmosphere.

To date, studies utilizing the FM-CW radar have indicated that the turbulent distribution of refractive index is due mostly to the presence of water vapor in the atmosphere [16]. For example, the mixing between a rising mass of warm moist air in the surrounding less humid air creates humidity variations at the edge of the mixing region which cause radio refractive index fluctuations. Given sufficiently intense mixing at scales on the order of 1/2 the radar wavelength (5 cm for the FM-CW radar), the regions will produce backscatter echoes detectable by the radar. But the refractive index (N) is dependent also on pressure and temperature gradients and thus it cannot be assumed a priori that only water vapor trapped in the trailing vortex system would be the mechanism which would drive the radar. It is also possible that the pressure and temperature gradients that exist could affect the refractive index to a point of negating any change brought about by the presence of water vapor produced by the combustion of fuel.

Refractivity of the atmosphere N is given by [18]:

$$N = (n-1)\ 10^6 = \frac{77.6\,P}{T} + \frac{3.73 \times 10^5 e}{T^2} , \qquad (1)$$

where n is the index of refraction, T is the absolute temperature °K, P is the atmospheric pressure in millibars, and e is the water vapor pressure in millibars. From the relation it is easy to see that a change in N is directly related to changes in local pressure and water vapor pressure and inversely related to changes in temperature. The trailing vortex system will contain elevated levels of water vapor and there will also likely be a local pressure decrease caused by the tangential velocity distribution and an increase in temperature over ambient values caused by the radial velocity distribution and the entrained exhaust products. Any of the aforementioned facts could provide the required change in radio-refractive index. The magnitude of each of the variables affecting the radio-refractive index will be determined as accurately as possible and these values will then be used to evaluate the effects of the levels within the vortex system as compared with ambient values. The ambient values chosen for each of the variables follow: temperature of 293°K, pressure of 1012 mb, and water vapor pressure of 11.7 mb.

Water Vapor.

The quantity of water vapor produced by a jet aircraft is directly related to the quantity of fuel consumed, the hydrogen content of fuel, and the efficiency of conversion to water vapor during the combustion process. By assuming almost complete combustion of the jet fuel, one obtains an emission rate of 567 kg of H_2O produced per 454 kg of fuel consumed [19]. It is understood that this value will change slightly from aircraft engine (jet) to engine and be affected by meteorological conditions, but it represents a good average value.

The way in which the combustion products are distributed in the vortex system has not been determined as yet by a rigorous test program nor has the total quantity of exhaust products captured and retained in the system been measured. It is known from qualitative studies using intentionally-produced engine exhaust smoke that the combustion products are captured by the vortex system [7]. Also it is very likely that the manner of capture and quantity captured and retained will vary somewhat from aircraft to aircraft. The Nielson model does not provide a specific cross-sectional area over which the water vapor from the engine exhaust (or other exhaust products) would be distributed [8]. An estimate of such distribution has to be made for any calculations of the increase in water vapor concentration in the wake vortex system over the ambient. For this purpose it will be assumed that the size of the annuli containing the water vapor will be represented by the entire core region; this is done with the understanding that there is likely to be some stratification and the probability that higher and lower water vapor concentration will probably exist at various points. The diameter of the vortex cores were presented by Garodz [7] as a fractional range (0.04 to 0.06) of the aircraft wingspan. The midpoint of the range was used as a typical value for calculations here. The results of the calculations show that on a typical B-707 climbout, sufficient water vapor is contained in the trailing vortex system to provide a gradient of humidity (~12 mb over the ambient) and a resulting change in the radio refractive index (of ~40 units).

Temperature.

In the Nielson report a value of 5.16°C above ambient was used as being representative of the temperature in the vortex system of a supersonic aircraft. Using the 5.16°C and taking a ratio of the squared velocities as suggested, one calculates a value of about 0.033°C for a subsonic aircraft of the same aspect ratio.

The only actual flight data found was that obtained by Tombach [20]. By probing the vortices produced by a light twin-engine aircraft (Aero Commander 560 F), Tombach determined that the maximum temperature increase of about 0.5°C was seldom exceeded at any time during the lifetime of the wake.

Therefore, although tests have not been conducted to define the temperature rise in a wake from a typical commercial aircraft, it is reasonable to expect that the temperature rise would not be greater than 1°C based on Tombach's work and the ratio method suggested by Nielson. But for the present study since a value has not been determined from flight tests a value 5 times that suggested (1°C) will be used so as to maximize the effect of temperature change.

Pressure.

Pressure changes are not normally considered to be great enough under most testing conditions to change the radio-refractive index in localized areas. However, with the aircraft trailing vortex system, there are areas of the system (the cores) that experience a pressure below the ambient value [8]. This pressure decrease is brought about by the radial distribution of tangential velocity that surrounds the center of the vortex and by the presence of the axial velocity at the center of the core. Measurements of the pressure defect across the core have not as yet been made. An estimate of the pressure distribution can be obtained by applying the Bernoulli equation to the measured tangential velocities. This type of calculation shows that the velocity-induced pressure differences for most commercial aircraft should not cause a maximum pressure decrease of greater than 2% of the atmospheric value.

Discussion.

The individual values determined for each of the variables in Equation (1): water vapor pressure (e), pressure (P), and temperature (T) in the core region; the ambient values chosen for each (e_a, P_a, T_a); their departure from the assumed ambient values (Δe, ΔP, ΔT) and their fractional changes ($\Delta e/e_a$, $\Delta P/P_a$, $\Delta T/T_a$) are contained in Table 8. The values contained in Table 8 for both the calculated core temperature and pressure changes in relation to the ambient values are the maximum absolute values that could possibly be expected from the type of aircraft that are being considered in this analysis; the

Table 8. Values for Variables in Radio Refractivity Equation

Core Region		
water vapor pressure	(e)	23.65mb
local pressure	(P)	991.76mb
temperature	(T)	298°K
Ambient Values		
water vapor pressure	(e_a)	11.7 mb
local pressure	(P_a)	1012.0 mb
temperature	(T_a)	293°K
Departure From Ambient		
water vapor pressure	(Δe)	11.95 mb
local pressure	(ΔP)	20.24 mb
temperature	(ΔT)	5°K
Fractional Change		
water vapor pressure	($\Delta e/e_a$)	−1.02
local pressure	($\Delta P/P_a$)	− .02
temperature	($\Delta T/T_a$)	− .017
First order relation for ΔN $\Delta N = 268P' + 51e' - 370T' - 102\,e''T'$ where $P' = (\Delta P/P_a)$ $T' = (\Delta T/T_a)$ $e' = (\Delta e/e_a)$ and $P';T' << 1$ $e'' = 0(1)$		

value of water vapor pressure is the minimal expected value. Also presented in Table 8 is a relation describing the change in radio refractive index (N) (through first order in pressure and temperature) in terms of the fractional changes of the variables from Equation (1).

The relationship $\Delta N = 268P' + 51e' - 370T' - 102e''t'$ indicates that ΔN would be most sensitive to fractional changes in temperature $\Delta T/T_a$, followed by changes in pressure $\Delta P/P_a$ and finally water vapor pressure $\Delta e/e_a$. The relation also shows that a decrease in pressure and an increase in temperature ($\Delta P/P_a$, $\Delta T/T_a$) would result in a negative value of ΔN and that a positive fractional change in water vapor ($\Delta e/e_a$) would give a positive ΔN. Using the values for the fractional changes in pressure (−.02) and temperature (+.017) from Table 8 in the relation shows that ΔN would decrease by about 12. To cause no change in ΔN, $\Delta e/e_a$ would have to increase about 0.23 or 23% in the core region. However the minimal change calculated in Table 8 shows a $\Delta e/e_a$ of more than 1.0 or 100%. Therefore, even when worse case conditions for temperature and pressure are used, there is sufficient water vapor in the core region to provide a change in ΔN of approximately 40.

To date the minimum conditions necessary to drive the FM-CW radar have not been determined, but using a value of $\Delta N = 20$ (the value of 20 was determined from published N profiles coinciding with areas of radar signal return) [20] shows that the vortex system of an aircraft would produce a change double that required to drive the radar unit.

Both criteria for using the FM-CW radar as a detection instrument are more than satisfied by the physical properties of the vortex system. The calculated change in the radio-refractive index of 40 is indicative of a sufficient gradient of radio-refractive index between the vortex core area and the surrounding recirculation region, and the required turbulent mixing across the gradient, at a scale size of one-half the probing radar's wavelength should be more than satisfied given the radial velocity distribution within the vortex system.

The assumption that the FW-CW radar has the capability to detect the wake vortex system generated by an aircraft or the decay products from its presence will be tested using the experimental data obtained during the mesoscale program conducted by Noonkester [17], and the prediction of vortex trajectory capability of the three-dimensional VOX3DM described earlier.

Available FM-CW Radar Data.

The FM-CW radar was placed at the east edge of runway 9-27 of Lindbergh Field as part of a mesoscale measurement program being conducted at the Naval Electronics Laboratory, San Diego. The radar unit was in continuous operation at the location from 30 March through 27 April 1973 [17].

A detailed view of the placement of the radar unit with respect to runway 9-27 is shown in Figure 8. The FM-CW radar used during the test series was limited to viewing in the vertical plane so that the echoes received by the radar had to be carried over the radar by the wind. The radar had a total viewing angle of only 4°; Figure 9 provides the vertical cross-section of the resulting radar window.

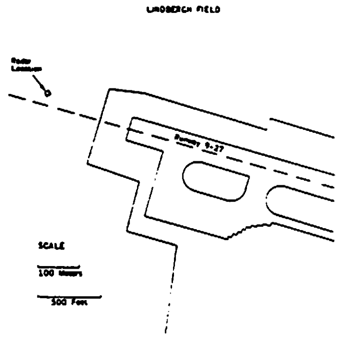

Figure 8. Detailed placement of FM-CW radar on west end of runway 9-22. (Courtesy of R. V. Noonkester, Naval Electronics Laboratory)

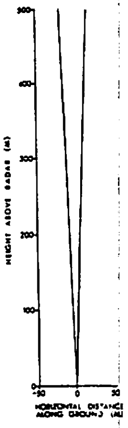

Figure 9. Vertical cross section of the vertical pointing FM-CW radar.

The data obtained from the radar consisted of 35-mm film and magnetic-tape records of the various echo structures that drifted through the radar's viewing volume. The range resolution during the data collection period ranged between 2 and 3 meters. Additional data that were collected either intermittently at the radar site or obtained at other sites, but information which had a bearing on the test program and interpretation of results, were as follows:

1) 35-mm film records of approximately 400 aircraft that passed over the radar. The camera was not operated for all aircraft during all time periods.

2) Accurate time records of when the photographed aircraft passed over the radar and the times of aircraft that were not photographed. These records included the aircraft flight number, type of aircraft and observational notes about the aircraft passage. As with the photographs of the aircraft, data were not recorded for all flights during the sampling period.

3) Continuous records of surface temperature, humidity, wind speed and wind direction for the entire sampling period.

4) Twenty eight pilot ballons (pibals) taken during the data gathering period to provide a wind profile from the surface to approximately 600 meters.

5) Radiosonde data from Montgomery Field, located approximately 11 km from the radar site.

The 35-mm film that recorded the echoes received by the FM-CW radar at Lindbergh Field was examined by personnel at NELC to determine if any unique or unusual echo structures passed through the radar's viewing volume. A unique type of echo structure was found and this echo structure appeared in various forms during the data collection period. The structure was labeled V-echo as a matter of convenience by personnel at NELC. Examples of this unique echo are provided in Figure 10a through Figure 10d. A total of 292 echos are identified as having sufficient detail so that they could be recorded as V-echoes. This same type of echo had been recorded on only a few occasions during hundreds of hours of radar operation at other locations [17]. For each of the 292 V-echoes a slope was calculated by NELC based on the difference between the starting and ending height and the duration of the V-echo. All but 5 of the V-echoes recorded had positive slopes throughout their lifetime. Noonkester et al. [17] proposed a model for analysis of the data with the following assumptions: as an aircraft takes off into the wind, the wind maintains constant direction and speed with height (values are obtained from ground-based measurements); a portion of the aircraft trail is carried through the radar sampling volume by the wind, thus giving an upward sloping echo record on the film. Some of the results that were obtained by applying Noonkester's model to the recorded echoes and ground wind data are that 98% of the V-echoes occurred in the presence of surface winds with westerly components and 63% occurred when the surface wind was between 250° and 300°. Commencement times of the V-echoes and times of aircraft passage indicated a random distribution of delay times between echo detection and aircraft passage.

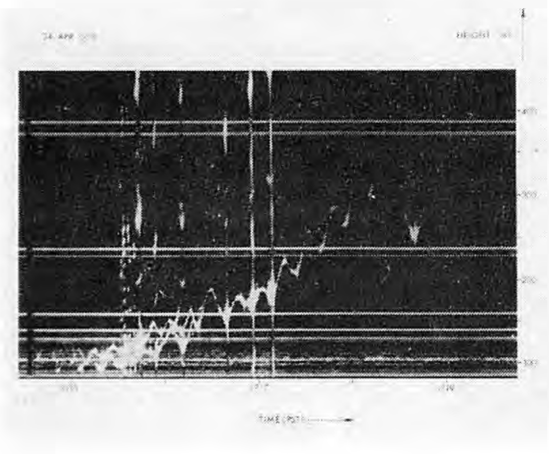

Figure 10a. Trace of a V-echo obtained with the FM-CW radar. (Courtesy of R. V. Noonkester, Naval Electronics Laboratory)

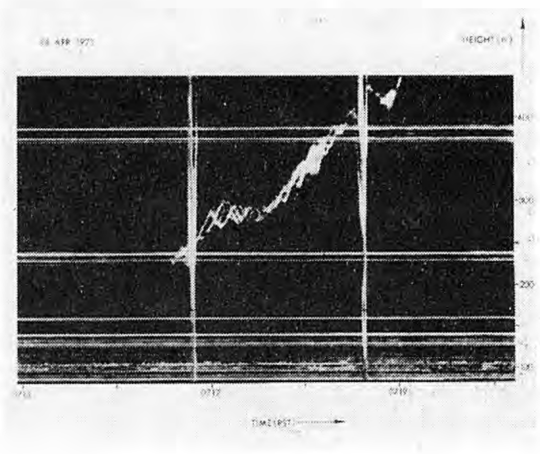

Figure 10b. Trace of a V-echo obtained with the FM-CW radar. (Courtesy of R. V. Noonkester, Naval Electronics Laboratory)

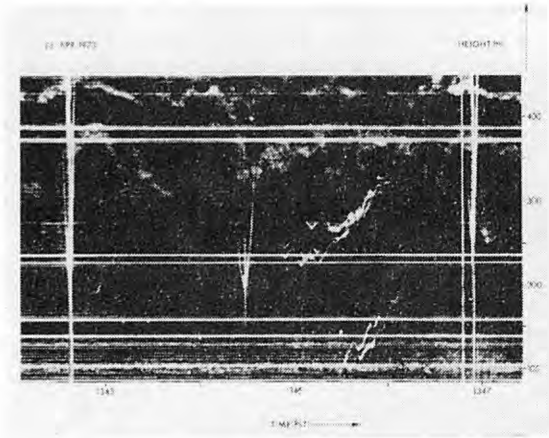

Figure 10c. Trace of a V-echo obtained with the FM-CW radar. (Courtesy of R. V. Noonkester, Naval Electronics Laboratory)

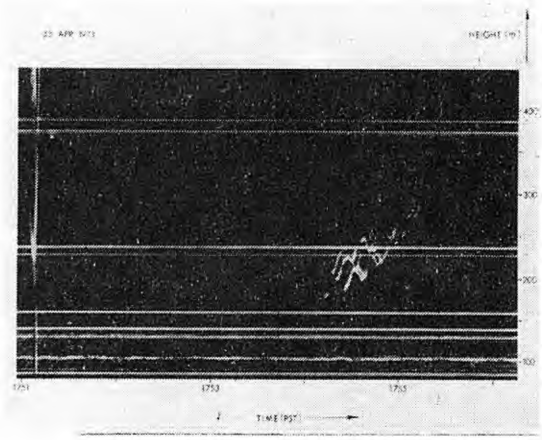

Figure 10d. Trace of a V-echo obtained with the FM-CW radar. (Courtesy of R. V. Noonkester, Naval Electronics Laboratory)

Analysis Procedure.

The data gathered during the 30-day sampling period at Lindbergh Field is analyzed with the basic hypothesis that the echoes are a result of the exhaust products (mainly H_2O) from the engines being entrained into the vortex core, remaining there for sufficient time, and being in sufficient quantity to produce the gradient of refractivity that is required to cause a radar echo.

The angle that the V-echo makes with the ground should be in the same general range as the climbout angle of the departing aircraft if this V-echo is created by the descending vortex system. Most civilian aircraft use a climbout angle of between 5 and 20 degrees, with the majority of flights in the 10- to 15-degree range and most military aircraft (excluding high performance fighter aircraft) use a climbout angle of between 3 and 15 degrees. The angle that each of the

V-echoes made with the horizontal was compared with a flight path climbout angle of 3 to 20 degrees.

Only 279 of the possible 292 V-echo records were used in the analysis, the 13 V-echoes not utilized either had negative slopes, (indicating that they were probably formed along the path of a descending aircraft) or were parallel to the ground. For each of the 279 V-echoes used; the angle between the horizontal and the V-echo trace was determined.

Over 96% (273 of 279) of the V-echoes had angles within the 3- to 20-degree range when the wind speed range was 0.55 m/sec to 10.2 m/sec which represents the range of wind speeds (determined from pilot ballon measurements) that were expected to have occurred during 95% of the time that the V-echoes were observed. Of the 6 V-echoes that were not within the 3- to 20-degree range, 2 were below (maximum of 1.15 degrees below) and 4 were above, with 3 of those above within 7.5% of the range which would require an increase of 4.3 m/sec to bring the farthest of the 3 within the range. The one remaining outside the range would require a wind speed of 23.4 m/sec. By reducing the wind speed range to a level that would contain only 50% of the probable wind speeds shifted only an additional 22 V-echos from the acceptable range which represents less than 10% of the recorded V-echoes.

Since for all wind speed ranges chosen the percentage of V-echoes falling within the 3- to 20-degree range is greater than the corresponding probable wind speed percentage used, the V-echoes could be associated with aircraft during climbout. This conclusion is further supported by the 50% wind speed range's accounting for 88% of the V-echo angles, which also indicates that the upper limit of the acceptable range could be lower than the maximum climbout angle used by aircraft. This finding alone does not prove that the V-echoes are associated with the aircraft climbout. But it does indicate that they could be; if the V-echo angles had not been in the same range as the aircraft flight paths, it would be unlikely that the echoes were associated with aircraft activity.

VOX3DM Program Predictions.

The two controlling factors for the position of the vortex system in space and time were the induced vertical descent rate and the wind field in which the vortex pair was generated. Both of these mechanisms of wake transport were related to the local meteorological conditions that existed during the time period of approximately 6 minutes of generation and transport of the vortex system.

Of the 28 pilot balloon data sets, only 1 set, 1432 hr on the 18th of April, met the criteria of aircraft activity and recorded V-echo or echos occurring within one-half hour of the pilot balloon ascent.

For the particular period chosen two aircraft departed and two distinct V-echos were recorded. The type of departing aircraft, the time that each aircraft passes perpendicular to the radar, the height of each aircraft, the type of aircraft, and the time of commencement and duration of each V-echo are provided in Table 9. The specific inputs for each aircraft type for the computer runs are provided in Table 10.

Table 9. Aircraft Passage and V-Echo Histories

Aircraft	
Type of Aircraft	DC08
Time perpendicular to FM-CW Radar	1409:47
Altitude	849 feet
Type of Aircraft	B737
Time parallel to FM-CW Radar	1411:08
Altitude	731 feet
V-echoes	
Commencement Time	1413:13
Difference Between	206 sec
Aircraft Flight Time + V-echo	1413:13 — 1409:47
Duration of V-echo	74 sec
Commencement Time	1413:45
Difference Between	123 sec
Aircraft Flight Time + V-echo	1413:45 — 1411:42
Duration of V-echo	54 sec

Table 10. Input Data for VOX3DM-V-Echo Comparisons

Aircraft Type	DC08	B737
Climbout Angles	10°, 15°, 20°	10°, 15°, 20°
Flight Speed (FT/sec)	253.5	253.0
Wing Span (FT)	148.4	93
Weight (lbs)	275000	109000
Air Temperature (°C)	25°C	25°C

The basic wind profile input into the VOX3DM program is the 1432 hours time period pilot balloon data. Since the aircraft did not take off during the time that the pilot balloon data was being gathered, a means had to be determined to adjust the 1432 hours data to be representative of the entire one hour segment from which the data were used. In view of the sensitivity of the model to changes in wind direction and wind speed, a conscious effort was made to limit the interval size. The method chosen was based on a determination of the Turner stability class that probably existed (from the surface readings of wind speed, cloud cover, etc.) and the use of the corresponding standard deviation of the horizontal wind component as the measure of the range of variability for the wind direction. For the 1432 hours time period, the Turner stability was determined as D or neutral with an associated standard deviation of 10 degrees, thus the range of wind directions to be used in the simulations would be the 1432 hours readings plus or minus 10 degrees. The variability in the wind speed was designated as plus or minus 1 m/sec which is the maximum accuracy [22] that can be expected from pilot balloon data with the single theodolite method that was used during data gathering.

The VOX3DM program predicted that a wake vortex system would be over the sensing location (when considering the variability of the wind to be 10 degrees) and that the vortex system remained within the sensing region for the entire period that the V-echos were observed. Additional comparisons of the predicted results and the film record show that a V-echo did not occur on the film at any period of time other than when the predicted vortex trajectory was over the sensing region.

From the data base available it was not possible to compare the predicted vortex altitude with the recorded V-echo altitude since data were not available that could be used to determine the time period to be used for vortex descent. But if the assumption was made that the vortex descended for the entire period of time until it was predicted to be over the sensing location, its predicted altitude was within 100 feet of the V-echo record.

Conclusions from FM-CW Data.

The primary conclusion is that the V-echos detected by the FM-CW radar were indeed created by aircraft departing from Lindbergh Field. It is also concluded that the generating mechanism is the water individually or in conjunction with the other exhaust products (particulates and aerosols) from the aircraft propulsion system which is trapped in the descending vortex system, and that it is this vortex system which is the sustaining mechanism, confining the exhaust products to a limited area and thus preventing their dispersal that would otherwise occur. These conclusions are supported by the reanalysis of the FM-CW data presented in this paper when consideration is given to the characteristics of detection of the FM-CW radar, and aircraft wake vortex transport. However, what could be more important in considering the data is that none of the observations, calculations, or comparisons refute any of the assumptions or results on which the conclusion is based.

ACKNOWLEDGMENT

I would like to thank Dr. J.O. Ledbetter, Dr. M.J. Summa, and Dr. N.K. Wagner for their guidance and encouragement during the completion of my dissertation at the University of Texas, from which this paper is derived. I would also like to thank Mr. R.V. Noonkester of the United States Naval Electronics Laboratory who provided all of the data on the FM-CW Radar; Captain D.F. Naugle of the United States Air Force who as project engineer with the Air Force Weapons Laboratory Environics Branch provided access to the Air Force Quality Assessment Model; Dr. M.R. Brashears of Lockheed Missiles and Space Company for use of the two-dimensional model of aircraft vortex transport; and Dr. J.N. Hallock of the Transportation Systems Center for use of the three-dimensional model for predicting vortex transport.

REFERENCES

1. Haber, J.M., "A Survey of Computer Models For Predicting Air Pollution From Airports," J.H. Wiggins Company Tech. Report No. 75-1231-1, May 1975.

2. Rote, D.M. and Wangen, L.E., "A Generalized Air Quality Assessment Model for Air Force Operations," AFWL-TR-74-304, Feb. 1975.

3. Wang, I.T. and Rote, D.M., "A Finite Line Source Dispersion Model for Mobile Source Air Pollution," Paper No. 73-135, 66th Annual APCA Conference, June 1973.

4. Cirillo, R.R., Tschanz, J.F., and Camaioni, J.E., "An Evaluation of Strategies For Airport Pollution Control," Argonne National Laboratory Report ANL/ES-45, Mar. 1975.

5. MacCready, P.B., Jr., Smith, T.B., and Wolf, M.A., "Vertical Diffusion from a Low Altitude Line Source — Dallas Tower Studies," Meteorology Research, Inc., Final Report to U.S. Army Dugway Proving Ground, Dugway, UT, AD298 260 (Vol. I) and AD 298 261 (Vol. II), 1961.

6. Smith, T.B. and MacCready, P.B., Jr., "Aircraft Wakes and Diffusion Enhancement," Meteorology Research Inc., Part B Final Report to Dugway Proving Ground, Dugway, UT, May 1963.

7. Garodz, L.J., "Measurements of Boeing 747, Lockheed C5A and Other Aircraft Vortex Wake Characteristics by Tower Fly-By Technique," in *Aircraft Wake Turbulence and Its Detection*, Edited by J.H. Olson, et al., Plenum Press, 1971, p. 265-285.

8. Nielsen, J.N., Stahara, S.S., and Woolley, J.P., "A Study of Ingestion and Dispersion of Engine Exhaust Products in Trailing Vortex Systems," Nielsen Engineering and Research, Inc., Mt. View, CA, NEAR TR 54, Nov. 1973.

9. Brashears, M.R., Logan, N.A., Robertson, S.J., Shrider, K.R., and Walters, C.D., "Analysis of Predicted Aircraft Wake Vortex Transport and Comparison with Experiment," Rept. FAA-RD-74-74.I, April 1974, Lockheed Missiles & Space Co., Huntsville, AL.

10. Brashears, M.R., Zalay, A.D., Chou, L.C., and Shrider, K.R., "Development of Predictive Wake Vortex Transport Model for Terminal Area Wake Vortex Avoidance," Report LMSC-HREC TR D496597, Sep. 1975.

11. Sheldon, D.B., "Vortex Motion Program," STC-DOT-TSC-297-71-828, June 1971, Service Technology Corp., Cambridge, MA.

12. Dee, F.W. and Nicholas, O.P., "Flight Measurements of Wing-Tip Vortex Motion Near the Ground," RAE Technical Report C. P. — 1065, Jan. 1968, RAE, Bedford, England.

13. Rote, D.M., et al., "Airport Vicinity Air Pollution Study," Report No. FAA-RD-73-113, Dec. 1973.

14. Hallock, J.N., Wood, W.D. and Spitzer, E.A., "The Motion of Wake Vortices in the Terminal Environment," Proceedings of the Sixth Conference on Aerospace and Aeronautical Meteorology, Nov. 1974.

15. Fridman, J.D. and Hallock, J.N., "Airborne Wake Vortex Detection," Proceedings of the Sixth Conference on Aerospace and Aeronautical Meteorology, Nov. 1974.

16. Richter, J.H., "High Resolution Tropospheric Radar Sounding," *Radio Sci.*, 4, 1261-1268, 1969.

17. Noonkester, V.R., Richter, J.H., and Jensen, D.R., "Unique Echoes Observed by FM-CW Radar At A Jet Airport," Naval Electronics Laboratory Center, San Diego, CA, Technical Note TN-2787, Sep. 1974.

18. LaGrone, A.H. and Deam, A.P., "Simultaneous Observations of Disturbed Clear Air Regions with Radar, Pibal, and Instrumental Aircraft," Antennas and Propagation Division, University of Texas at Austin, Report No. P-46, June 1971.

19. Machta, L., "Water Vapor Pollution of the Upper Atmosphere," SAE/DOT Conference on Aircraft and the Environment, Washington, DC, Feb. 8-10, 1971.

20. Tombach, I.H., "Influence of Meteorological Factors on the Vortex Wake of A Light Twin-Engine Aircraft," AFOSR TR-74-1507, March 1974, AeroVironment, Pasadena, CA.

21. Noonkester, V.R., "Convective Activity Observed by FM-CW Radar," Naval Electronics Laboratory Center, San Diego, CA, TR-1919, May 1974.

22. Middleton, W.E.K., and Spichaus, A.F., *Meteorological Instruments*, University of Toronto Press, Toronto ON Canada, 1953.

DEINTENSIFICATION AS A CONSEQUENCE OF VORTEX BREAKDOWN

ALAN J. BILANIN, MILTON E. TESKE AND JOEL E. HIRSH
Aeronautical Research Associates of Princetion, Inc.
50 Washington Road
Princeton NJ 08540

ABSTRACT: The physical mechanisms underlying the phenomenon of vortex breakdown have been the subject of speculation for nearly 20 years. What has become clear from numerous observations of the phenomenon on aircraft trailing vortices is that breakdown can be violently turbulent. This conclusion is drawn from the observation of smoke in the center of the vortex being dispersed with the passage of breakdown along the vortex. The question that has been asked repeatedly by those concerned with the vortex wake hazard is: Does the vortex breakdown phenomenon provide a mechanism of sufficient magnitude to be of aid in lessening the hazard of an aircraft vortex wake? The work reported herein is an attempt to answer this question. Since the vortex breakdown phenomenon is decidedly nonlinear and from observation, violently turbulent, a numerical approach has been undertaken to define the breakdown flowfield. Donaldson's second-order closure turbulent transport model has been coded in circular cylindrical coordinates. The result is an axisymmetric elliptic code in the radial and axial coordinates with time as the marching direction. The code has the capability of computing dispersal of a passive tracer.

NOMENCLATURE

b	turbulent model constant
C	concentration
q	$\sqrt{\overline{u_i u_i}}$, root-mean-square turbulent velocity
$r,\theta,z,$	circular cylindrical coordinates
r_c	viscous core radius
R	Betz tube radius — $\pi s/4$ elliptically loaded wing
s	wing semi-span
s_1,s_2,s_3	turbulent model constants
t	time
U,V,W	velocity components in the r,θ,z directions respectively
v_c	turbulent model constant
Γ	circulation
ζ	axial component of vorticity
η	azimuthal component of vorticity
Λ	turbulent macroscale parameter
ν	kinematic viscosity
ρ	fluid density
ψ	stream function.

INTRODUCTION

The phenomenon of vortex breakdown on aircraft trailing vortices has been thought to be a mechanism which could lessen the hazard of vortex wakes. These thoughts were probably, to a large extent, formed by observing that smoke seeded into the vortex for flow visualization purposes would disappear with the passage of breakdown. One cannot help being impressed by the violence of the phenomenon and it is quite clear that the turbulence levels are very high in the breakdown region. The question which is addressed in this paper is: How much deintensification, in terms of reduction of rolling moment induced on a following aircraft, can be expected with the passage of vortex breakdown? Because the phenomenon is one which involves turbulent transport, our approach will be a simulation of the vortex breakdown flowfield using a second-order closure turbulent transport theory first suggested by Donaldson [1].

First, we would like to briefly review the existing theories of breakdown, as well as comment on past computations of breakdown flowfields. In addition, in this introductory section we will describe our observations of the breakdown phenomenon as it occurs on aircraft trailing vortices. Then we argue for a wave mechanical explanation of vortex breakdown and demonstrate with a simple model that if there is to be any significant reduction in vortex intensity during breakdown, turbulent transport must necessarily be the dominant mechanism by which trailed vorticity is redistributed. Next, A.R.A.P.'s second-order closure model in circular cylindrical coordinates is presented. Here the "super-equilibrium" limit of the model is taken to illustrate the sometimes competing effects of swirl and axial shear on the production of turbulence. Then, two computations of vortex breakdown flowfields are described. Finally, conclusions are offered.

It is quite clear that since the first breakdown flowfield was observed by Peckham and Atkinson [2] in 1960, no universally accepted theory has emerged which can convincingly describe the phenomenon. There are now at least four independent explanations, summarized below:

1. Hydrodynamic instability of a swirling shear flow [3, 4].
2. Stagnation of the axial velocity along the vortex axis [5-7]. (Analogous to boundary layer separation.)
3. Conjugate jump theory [8, 9].
4. A trapped finite amplitude wave [10-12].

There is little doubt that there is a rapid production of turbulence in the breakdown region and, therefore, questions regarding hydrodynamic stability of the flowfield cannot be overlooked. It is also true that in a coordinate system riding with the breakdown phenomenon, the axial velocity is observed to stagnate, and an explanation of breakdown analogous to boundary layer separation is quite appealing. The conjugate jump likens vortex breakdown to a hydraulic jump where the flowfield, upstream of the jump, is supercritical with regard to infinitesimal propagation, while downstream the flowfield is subcritical. What is missing is a unified physical explanation of the phenomenon which can bring together these seemingly differing views. The concept of wave trapping is an attempt to give a unified physical explanation of the phenomenon. Possibility of wave trapping as an explanation of breakdown was implied by Squire [10] in 1960. However, wave trapping has only become a contending explanation of the phenomenon since the recent work of Randall and Leibovich [11], and Bilanin [12]. A qualitative explanation of the wave trapping mechanism will follow in the next section; a more complete description may be found in reference 13.

The phenomenon of vortex breakdown as it is observed and interpreted on aircraft trailing vortices is depicted in Figure 1. Here is shown schematically a vortex whose structure is perturbed by an externally applied pressure gradient and for illustration purposes is shown here to be an atmospheric eddy. This pressure gradient may also result from the proximity of a second vortex or an aerodynamic surface. In fact, the simple aging process of a vortex where axial vorticity is primarily diffused away from the vortex center is sufficient to establish conditions for breakdown to occur. What is *essential* in a breakdown region, is that the vorticity along the centerline of the vortex is *irreversibly* redistributed radially outward by fluid transport. What will be shown in subsequent sections of this paper is that in the breakdown regions turbulence levels are indeed high, such that smoke which is contained in the "laminar" viscous core is rapidly dispersed. Referring to Figure 1c, the region marked out by a dashed box will be the subject of investigation below. Grabowski [14] has numerically (finite difference) investigated this region allowing only laminar transport to occur. His calculations would only converge to a steady state solution for sufficiently low Reynolds numbers ($\Gamma/\nu \leq 200$). One might speculate, taking some liberty, that this convergence problem is a signal that other than laminar transport may in fact be important.

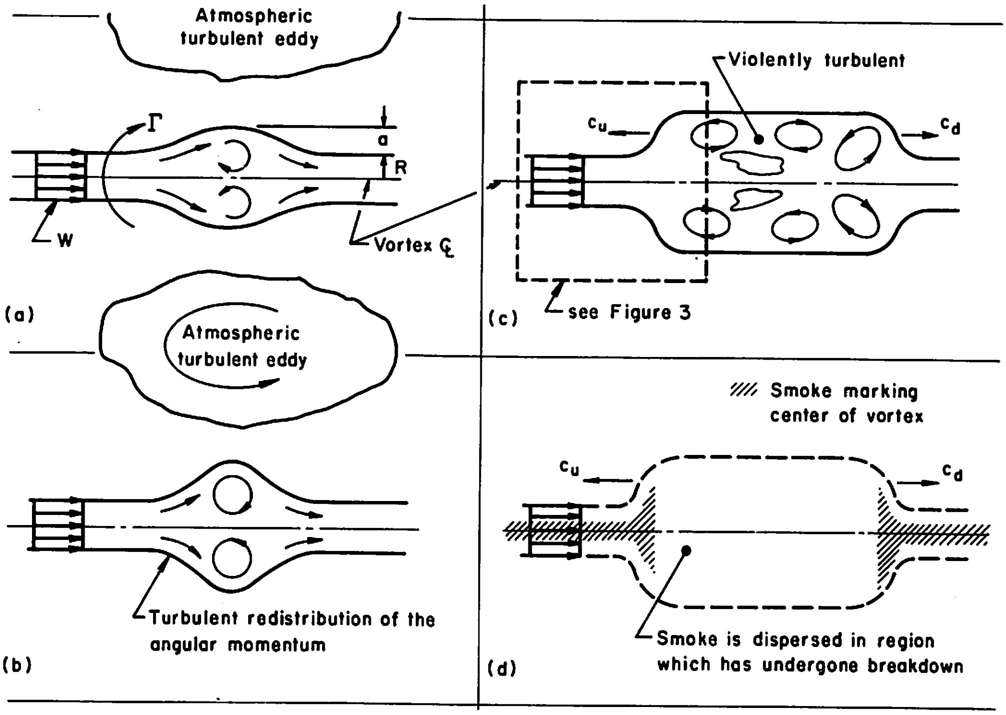

Figure 1. An illustration of the physical mechanisms responsible for vortex breakdown.

PHYSICS OF BREAKDOWN

The simple schematic of breakdown given in Figure 1 illustrates the gross observed features of the phenomenon. The details of the fluid mechanics is obviously somewhat more involved. It is our contention that an understanding of the phenomenon can be obtained from the study of inertial wave motion on vortices. This approach leads to the conclusion that vortex breakdown is a finite amplitude breaking wave. A summary of this approach is described below and further details may be found in reference 13.

The property of vortices to support highly dispersive waves was recognized as early as 1880 by Kelvin. The fact that the waves are dispersive makes it crucial to distinguish between phase velocity and group velocity. The former is the velocity of the wave crests, while the latter is the rate at which energy and information is transmitted. It is the group velocity which is significant in the study of breakdown. It may be shown using linear wave theory that axisymmetric, long wavelength waves have the highest group velocity possible. This is to say that there exists a maximum at which energy can be sent along a vortex. If there is no axial velocity in the vortex, this energy propagation speed is of the order of the maximum swirling velocity V_{max}, and is in either direction along the vortex. With axial velocity present the maximum energy propagation speed is modified by the convective effect of this velocity such that the maximum energy propagation velocity upstream is of the order of $W - V_{max}$ and that downstream is $W + V_{max}$ where W is the characteristic axial velocity, positive downstream. When the axial velocity is larger than the swirl, the vortex is supercritical and upstream propagation of linear waves is not possible. When the axial velocity is less than the swirl, the vortex is subcritical and information can be transmitted in either direction along a vortex.

The critical condition occurs when upstream propagation is just blocked by convection. Here the possibility exists for waves traveling upstream to become blocked or trapped. As more energy from downstream reaches the critical region of the vortex there is an accumulation of wave energy and the wave amplitude grows. A numerical simulation of the trapping process for small but finite amplitude axisymmetric waves has been given in reference 11. It is conjectured that as the amplitude of the trapped wave increases, turbulent processes must become significant. This must necessarily result in the irreversible redistribution of axial vorticity in the vortex.

It should be noted that spiral waves can exist on line vortices, and each of these modes has its own critical condition. In Figure 2 we have attempted to depict the order in which various wave modes will reach their critical states. The vortex is a Rankine vortex with top-hat axial velocity distribution. Far upstream we show axial velocity dominating, and as we move downstream swirl is shown dominating. This effect is a natural result of aging of the vortex or a consequence of an externally applied axial pressure gradient.

The question which we have set out to answer is just how much redistribution of trailed vorticity can result across a breakdown region? The redistribution of axial vorticity arises as a consequence of diffusion, both laminar and turbulent. However, at Reynolds numbers typical of aircraft vortices, laminar diffusion is an extremely slow process. The basic transport mechanism is, therefore, turbulent.

Before undertaking a turbulent computation it is possible to make a simple estimate of the redistribution of axial vorticity which may be attained across a breakdown region. This can be done by balancing the axial flux of angular momentum across a breakdown region. Similar jump conditions across a breakdown region have been investigated in more detail than what is given here [7, 12, 15, 16]. However, this simple example gives a straightforward estimate of the redistribution which might actually be achieved.

The Betz roll-up technique yields the result that the axial flux of angular momentum in the vortex generated by a wing of semi-span s which is elliptically loaded is

$$\int_{\zeta = 0}^{\zeta = \frac{\pi s}{4}} \rho V W 2\pi\zeta^2 d\zeta = \rho W_\infty \Gamma s^2\left(\frac{\pi^2}{16} - \frac{1}{3}\right), \qquad (1)$$

where the upper limit of integration $\pi s/4$ is the Betz tube radius and W_∞ is the flight speed of the aircraft. It has been shown [13] that W does not depart significantly from the

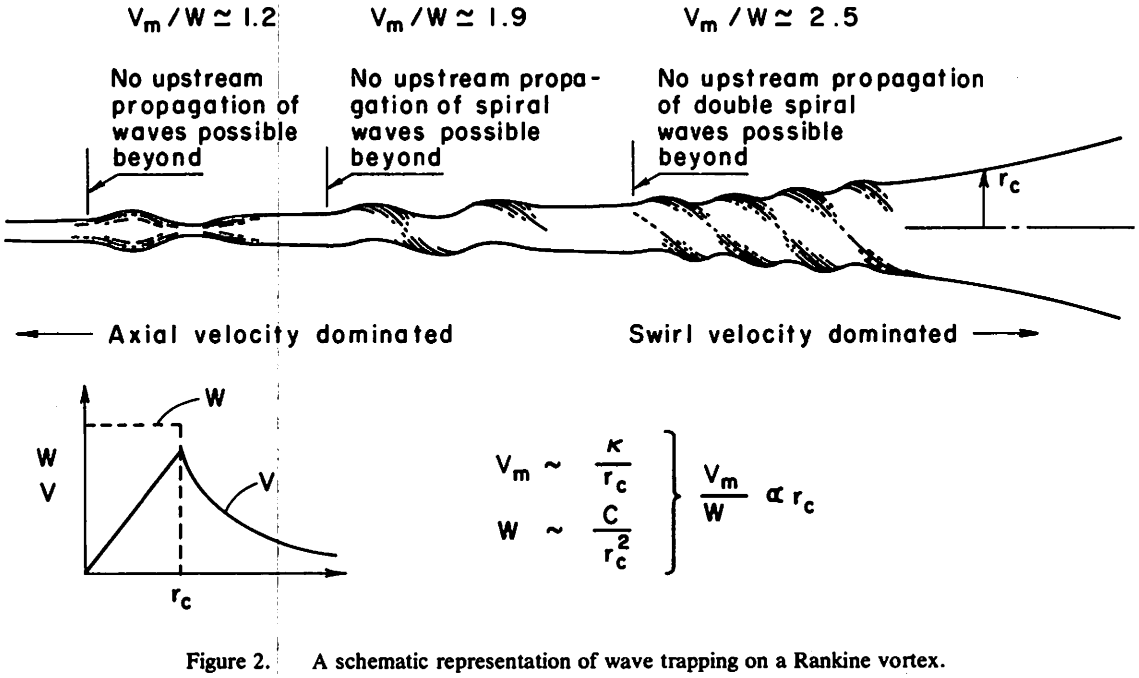

Figure 2. A schematic representation of wave trapping on a Rankine vortex.

free stream value in a vortex, except perhaps along the vortex center. However, the angular momentum contained in this region is very small in comparison with that contained in the entire vortex. We can, therefore, write

$$\int_0^{\zeta = \frac{\pi s}{4}} V 2\pi\zeta^2 d\zeta = \Gamma s^2\left(\frac{\pi^2}{16} - \frac{1}{3}\right) \cdot \quad (2)$$

For estimation purposes, we now take V to be given by a lamb vortex downstream of the breakdown region such that

$$V = \frac{\Gamma}{2\pi r}\left(1 - \exp -\left(\frac{r^2}{r_c^2}\right)\right), \quad (3)$$

where r_c characterizes the viscous core radius. Substituting (3) into (2) and solving for r_c shows that the viscous core radius can be approximately 22% of the semi-span of the wing of the generator. This would indeed represent a sizable reduction in rolling moment induced on a following aircraft. One must next ask: Is there enough turbulence generated in the breakdown region to result in this redistribution? This question is the subject of the remainder of the paper.

TURBULENT TRANSPORT IN VORTEX BREAKDOWN FLOWFIELDS

To estimate the irreversible redistribution of vorticity by breakdown, we have developed an axisymmetric computer code which solves the second-order closure model of turbulent transport which has been under development at A.R.A.P. for the past few years. Recently, Lewellen and Teske [17] reviewed the modeling technique and its flow applications. Bilanin, et al. [18] give the most recent application of the model to vortex interaction flows behind aircraft. We now briefly review the turbulence model used at A.R.A.P., discuss an algebraic limit of the resulting equations relevant to breakdown, and then highlight the numerical scheme used to solve the partial differential equations governing the full vortex breakdown flowfield.

Second-Order Closure Turbulent Modeling.

To obtain a set of equations for the mean velocity components, the fluid velocity is written as the sum of a mean and fluctuating part, and then ensemble-averaged to obtain the mean momentum equations for (U,V,W) in the (r,Θ,z) direction. These equations contain the unknown Reynolds stresses $\overline{u_i u_j}$, whose exact equations may be found by returning to the full momentum equations, subtracting the mean equations, premultiplying by u_i, and averaging [1]. The resulting equations are exact, but contain unknown third-order correlations, other unknown second-order correlations, and their derivatives. Second-order closure models these expressions in terms of the second-order correlations $\overline{u_i u_j}$ and their gradients, mean flow gradients, turbulent velocity scale q, turbulent macroscale Λ, and several model constants. These constants do not change from application to application, yet give a good fit to all flows used to establish their values.

For the axisymmetric flow calculations, we choose to work with an equation for the mean vorticity $\eta = \partial U/\partial z - \partial W/\partial r$ to eliminate a numerical imbalance in the radial momentum equation. This selection requires the solution of a Poisson equation for the stream function ψ. Further, it is advantageous to redefine several dependent variables by normalizing by r; this substitution results in higher accuracy as $r \rightarrow 0$. These variables are denoted by the over-tilde (~). The equations used are listed in the Appendix, with model constants given as $v_c = 0.3$; $b = 0.125$; $s_1 = -0.35$; $s_2 = -0.6$ and $s_3 = 0.375$. Note also that an equation for the macroscale Λ has been included. The derivation of this equation may be found in reference 17.

The model equations are programmed and solved using the procedures discussed below. First, however, it is instructive to examine a limit of the equations to gain some insight into the role of swirl and axial shear on the production of turbulence in axisymmetric vortex flows.

The Super-Equilibrium Limit of Second-Order Closure.

It has often been observed that the center of a vortex appears quite laminar (see Figure 6 of reference 19). Donaldson [20] has demonstrated by use of second-order closure that the central region of a vortex with no axial shear cannot produce turbulence. Therefore, it should not be surprising that observations of smoke in vortices clearly mark the central region of the vortex, while the smoke is dispersed at larger distances from the vortex center. Here, we will include the axial shear in taking a high Reynolds number limit of the rate equations for the velocity correlations. The limit, known as the super-equilibrium limit of the turbulent model, comes from setting the left-hand side of Equations (A.3 – A.8) equal to zero. Therefore, the rate of change of a velocity correlation as it follows the mean motion is assumed small. This is equivalent to saying that the second-order correlations can track their local equilibrium values. In addition, diffusion of correlations is neglected. These assumptions reduce the second-order closure rate equations to an algebraic set of equations which define a simple eddy viscosity model.

If we restrict ourselves to only radial dependence in the swirl velocity $\tilde{V} = V(r)/r$ and axial velocity $W(r)$, the super-equilibrium limit of Equations (A.3 – A.8) yields

$$
\begin{gathered}
4\overline{uv}\tilde{V} - \frac{q}{\Lambda}\left(\overline{uu} - \frac{1}{3}q^2\right) - \frac{2bq^3}{3\Lambda} = 0 \\
2\tilde{V}(\overline{vv} - \overline{uu}) - r\overline{uu}\,\frac{\partial\tilde{V}}{\partial r} - \frac{q}{\Lambda}\,\overline{uv} = 0 \\
2\tilde{V}\tilde{v}\tilde{w} - \frac{\overline{uu}}{r}\,\frac{\partial W}{\partial r} - \frac{q}{\Lambda}\,\tilde{u}\tilde{w} = 0 \\
-4\tilde{V}\overline{uv} - 2r\overline{uv}\,\frac{\partial\tilde{V}}{\partial r} - \frac{q}{\Lambda}\left(\overline{vv} - \frac{1}{3}q^2\right) - \frac{2bq^3}{3\Lambda} = 0 \\
-2\tilde{V}\tilde{u}\tilde{w} - \frac{\overline{uv}}{r}\,\frac{\partial W}{\partial r} - r\tilde{u}\tilde{w}\,\frac{\partial V}{\partial r} - \frac{q}{\Lambda}\,\tilde{v}\tilde{w} = 0 \\
-2r\tilde{u}\tilde{w}\,\frac{\partial W}{\partial r} - \frac{q}{\Lambda}\left(\overline{ww} - \frac{1}{3}q^2\right) - \frac{2bq^3}{3\Lambda} = 0
\end{gathered}
\tag{4}
$$

Assuming the velocity correlations are of the form

$$
\overline{u_i u_j} = \Lambda^2 \left(r\frac{\partial\tilde{V}}{\partial r}\right)^2 U_i U_j \quad , \tag{5}
$$

where U_iU_j as used here is not a velocity but is a dimensionless number (turbulent correlation coefficient). Substituting (5) into (4) yields

$$
\begin{aligned}
&2N(VV - UU) - UU - Q\cdot UV = 0 \\
&2N\cdot VW - A\cdot UU - Q\cdot UW = 0 \\
&-2N\cdot UW - A\cdot UV - UW - Q\cdot VW = 0 \\
&4N\cdot UV + \frac{Q^3}{4} - Q\cdot UU = 0 \\
&-4N\cdot UV + \frac{Q^3}{4} - 2\cdot UV - Q\cdot VV = 0 \\
&-2A\cdot UW + \frac{Q^3}{4} - Q\cdot WW = 0 \ ,
\end{aligned}
\tag{6}
$$

with

$$
Q^2 = UU + VV + WW
$$

and

$$
N = \frac{\tilde{V}}{\left(r\,\frac{\partial\tilde{V}}{\partial r}\right)} \text{, the swirl parameter,}
$$

$$
A = \frac{\frac{\partial W}{\partial r}}{\left(r\frac{\partial\tilde{V}}{\partial r}\right)} \text{, the axial parameter.} \tag{7}
$$

The solution to (6) is an exercise in algebra, yielding a family of solutions in which the turbulent correlation coefficients (UV, UW, etc.) are functions only of the swirl and axial parameters N and A. The solution for Q^2 is shown in Figure 3. The solution for $A < 0$ is a mirror reflection across the $A = 0$ axis and is not shown here. Values of $Q^2 < 0$ denote regions where turbulence is damped. With no swirl, $N = 0$ and $q^2 = 2\Lambda^2 (\partial W/\partial r)^2$, showing that axial shear is always destabilizing. With $A = 0$, the two critical values of the swirl parameter are $N_{crit} = -0.683$ and 0.183, beyond which the production of turbulence is suppressed by the swirl. These critical values of the swirl

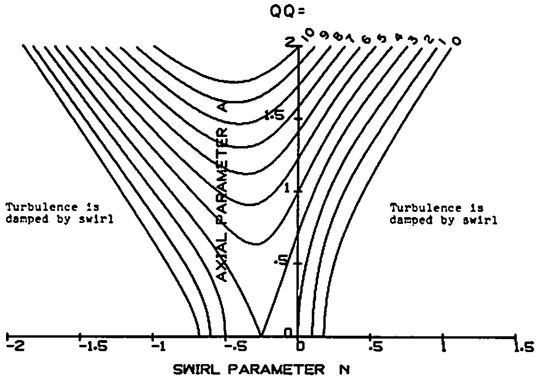

Figure 3. Isopleths of constant QQ showing the dependence on N = V/(r∂V̄/∂r) and A = (∂W/∂r)/(r∂V̄/∂r)

parameter N have been previously given in reference 13.

In the central region of a vortex, known as the viscous core, the swirling velocity is approximately given by V = Ωr, for small r. To illustrate the damping effect of solid body rotation in the center of an aircraft vortex, we can estimate the amount of shear (∂W/∂r) required to overcome the damping of the swirl. In the super-equilibrium limit it can be shown that QQ =2(∂W/∂r/V̄)² − 4, so that when

$$\left(\frac{\Omega}{\frac{\partial W}{\partial r}}\right)^2 > \frac{1}{2} \tag{8}$$

no turbulence can be produced. To get some idea whether this criteria is met in aircraft vortex wakes, consider an approximation to the inviscid swirl velocity distribution for an elliptically loaded wing as given by Betz. It has been shown [20] that

$$v = \frac{\Gamma}{2\pi r}\left[\frac{3r}{s} - \frac{9}{4}\frac{r^2}{s^2}\right]^{\frac{1}{2}} \tag{9}$$

is a good approximation of $0 < r/s \leq 2/3$ where s is the semi-span of the wing. If we then take Ω to be

$$\Omega = \frac{V(r_c)}{r_c}$$

and take as a very conservative estimate of (∂W/∂r)

$$\frac{\partial W}{\partial r} = W_\infty/r_c \ , \tag{10}$$

then $(\Omega/\partial W/\partial r)^2 = 1/2$ when $r_c/s \simeq 8C_L^2/\pi^2A^2$.

In a series of tests, undertaken by NAFEC, the details of the swirl velocities were measured using hot-film probes mounted on a tower. Run 45 contains measurements of the wake of a B-747 in the holding cruise configuration. The aircraft was operated at a $C_L = 0.7$ and the wing load distribution is well approximated by an elliptic load distribution. With aspect ratio A =8, r_c/s is approximately 1/8. Since s ≃ 100 ft, if r_c is of the order of 10 ft and if the axial shears are as large as we have estimated, turbulence can be produced in the vortex. In Figure 4 we show the measured velocity distribution for Run 45. Note that the viscous core is of the order of 1 ft, strongly suggesting that little turbulence is to be found in the central region of this vortex. Since NAFEC measurements for the most part show a small viscous core in the vortex wakes in a variety of aircraft, it is not surprising that smoke is only slowly dispersed from this region.

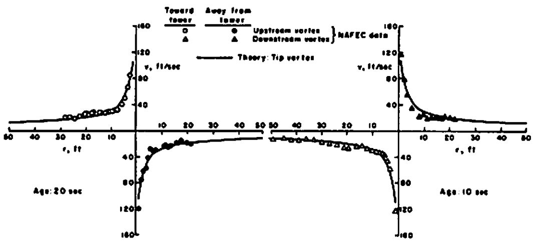

Figure 4. Comparison of measured and computed swirl velocity profiles for a 747 aircraft in holding configuration ($\delta_f = 0°$).

The Numerical Method.

Equations (A.1 – A.10) have been programmed into a two-dimensional, unsteady, radial coordinate code developed for the study of vortex breakdown under support from NASA Ames Research Center and for the study of severe storms (tornados) for the Nuclear Regulatory Commission. The equations are written in Crank-Nicolson form on a centered-space, forward-time finite difference mesh, and solved by an alternating-direction-implicit algorithm. The "correction factors" in the mean equations of motion ($C_{\eta r}$, $C_{\eta z}$, C_{vr}, C_{vz}) are evaluated explicitly at each time step, enabling the two mean equations to be decoupled from the turbulence equations. The numerical simulation begins with a strongly compatible set of initial conditions, and runs at a moderate stepsize until the flow attains steady state. This procedure generally takes several flowtimes to enable information along the inflow boundary to influence every portion of the flow within the computational domain. A detailed explanation of the numerical procedure may be found in Teske [21] for the corresponding two-dimensional Cartesian analogue. Additional boundary conditions are chosen compatible with the inflow conditions. Both initial and boundary conditions will now be discussed in detail, and two calculations of vortex breakdown will be presented.

COMPUTATION OF TURBULENT VORTEX BREAKDOWN FLOWFIELDS

The computation of breakdown flowfields is similar to the computations undertaken by Grabowski [14], except that turbulent transport is included. Figure 5 shows the computational grid as well as the specified boundary conditions. The grid is nonuniform with highest resolution occurring for small r and z. The spacing between points in the r and z directions are increased by the factor 1.1 between successive points. The grid has 40 points in the z direction and 32 in the r direction.

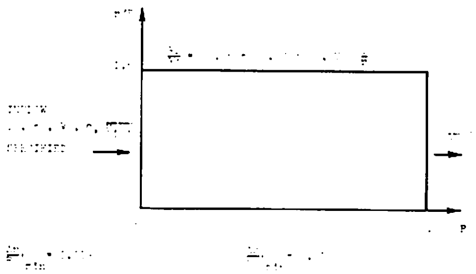

Figure 5. The computational domain used in the simulation of vortex breakdown flowfields.

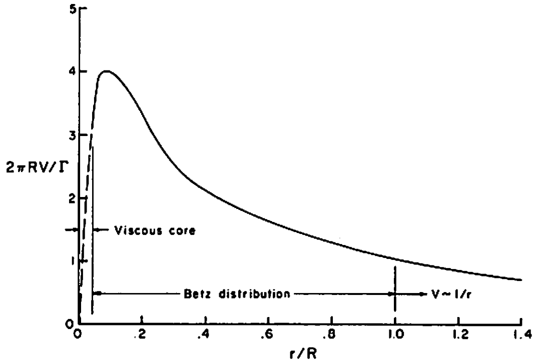

Figure 6. Inflow swirl velocity.

Inflow conditions specified at z = 0 were chosen to approximate the flowfield of an aircraft vortex wake. It was assumed that the aircraft had an elliptic load distribution and the resulting swirl velocity distribution was given by Betz. For an elliptically loaded wing $V \sim r^{-1/2}$; thus, for small r a laminar viscous core correction developed by Moore and Saffman [22] was utilized to eliminate the inviscid singularity. The resulting swirl velocity distribution is shown in Figure 6. The viscous core was scaled to be approximately $r_c/s \simeq 0.08$ for numerical resolution considerations and it could be argued from measurements that r_c should be taken to be smaller.

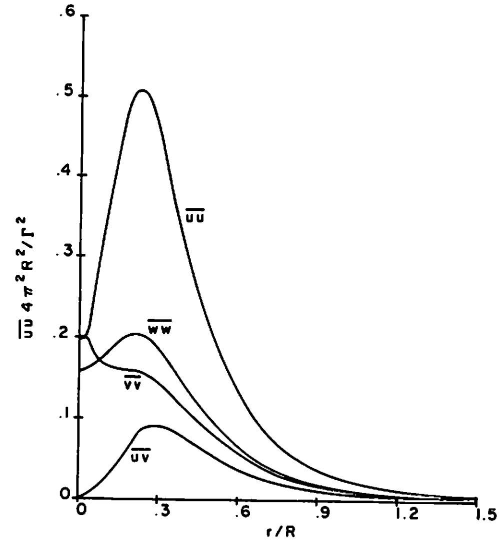

Figure 7. Initial and inflow conditions for the non-zero second-order velocity correlations as computed from the swirl profile shown in Figure 6.

The swirl velocity distribution was then inputed into an axisymmetric vortex code which solves the turbulent decay of a line vortex in the time domain [23]. The code was run with the swirl velocity held fixed and the turbulent velocity correlations permitted to come to equilibrium. The distributions of the non-zero velocity correlations are shown in Figure 7.

These initial conditions on swirl velocity and velocity correlations were then inputed into the axisymmetric code. The inflow axial velocity was taken to be uniform and the integral scale parameter Λ was held constant through the domain and has the value 0.04s. The Reynolds number was 10^4 which past experience has shown to be sufficiently high so as to not affect the turbulent transport. Other boundary conditions are shown in Figure 5. In addition, a passive tracer simulating smoke is specified on the inflow to be

$$c = \exp\,(-117r^2/R^2) \quad . \qquad (11)$$

The equations governing the transport of a passive tracer using second-order closure modeling have not been given here but may be found in reference 17. The only free condition is the inflow axial velocity, and the possibility of specifying non-zero radial outflow at large r, simulating an imposed adverse pressure gradient. By computation, when a breakdown has come to steady state in the computational domain, the inflow axial velocity is the propagation speed of the breakdown region.

Results of two computations are reported here, $W|_{z=0} = 10\Gamma/\pi^2 s$ with $U = 0$ at $r = R$, and $W|_{z=0} = 12.8\Gamma/\pi^2 s$ with $U = 0.1\Gamma/2\pi R$ at $r = R$. In Figure 8 is shown the inflow swirl velocity and the swirl velocity at the outflow boundary. The essential result is that the maximum swirling velocity has been reduced by a factor of approximately 2, but the structure for $r/\pi R > 0.3$ remains essentially unchanged. The streamlines for the two computations are shown in Figures 9 and 10. The comparison of the size of recirculation regions between the two computations is striking. We have found numerically, that the position of the breakdown region in our computation domain is not a stable one. The preference is for the breakdown region to advance upstream and interact with the inflow boundary. This we believe to be the case for the streamline patterns shown in Figure 9. The computation with $W = 12.8\Gamma/\pi^2 s$ was undertaken using an algorithm designed to hold the breakdown region stationary by dynamically adjusting the inflow axial velocity until fluid variables became sufficiently steady. As can be seen from Figure 8, the outflow swirl velocity is not a

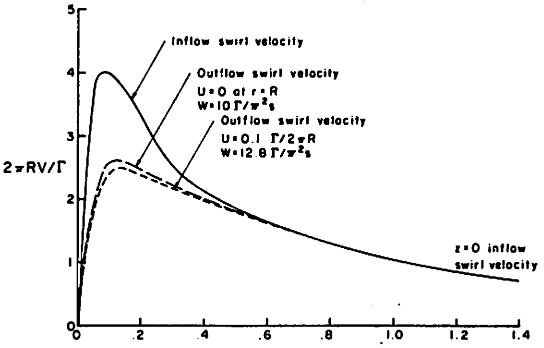

Figure 8. The predicted redistribution of swirling velocity as a consequence of vortex breakdown.

strong function of the size of the recirculation region.

In Figures 11 and 12 are shown the isopleths of turbulent kinetic energy for the breakdown flowfields shown in Figures 9 and 10, respectively. It can be seen that turbulence levels during breakdown can be quite high and are computed to be in excess of 25% of the mean velocity.

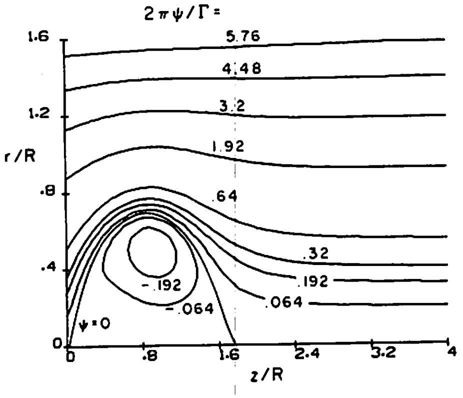

Figure 9. Streamlines for a vortex breakdown flowfield with no imposed axial pressure gradient.

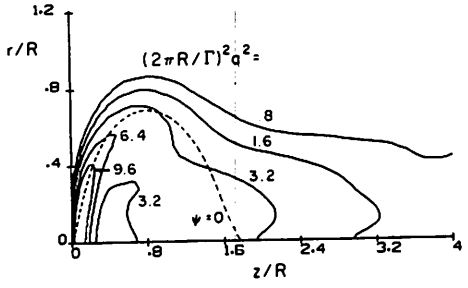

Figure 11. Isopleths of turbulent kinetic energy q^2.

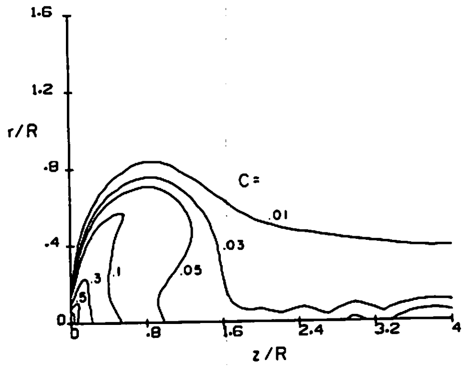

Figure 13. The dispersal of neutrally buoyant smoke. Inflow $C = \exp - 117r^2/R^2$ so that $C_{max} = 1.0$.

Shown in Figures 13 and 14 is the dispersal of smoke by the breakdown flowfields of Figures 9 and 10, respectively, which was placed in the viscous core of the vortex. As expected, higher turbulence levels in the breakdown region effectively disperse the smoke C through the breakdown region. This result is in agreement with observations of breakdown on aircraft vortices.

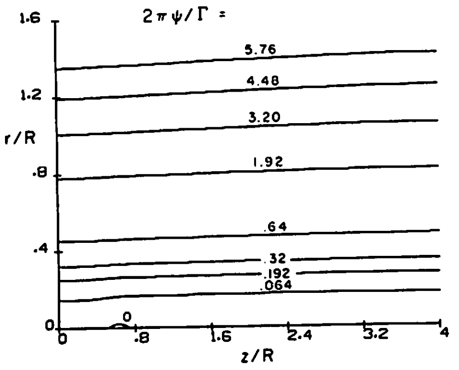

Figure 10. Breakdown flowfield with imposed adverse pressure gradient resulting from $U = 0.1\Gamma/2\pi R$ at $r = R$, $W = 12.8\Gamma/\pi s$.

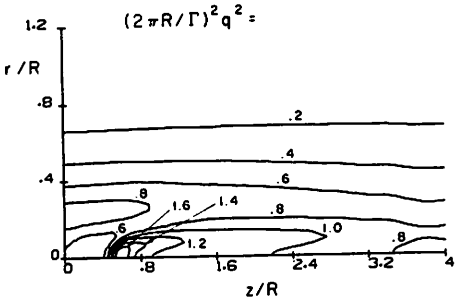

Figure 12. Isopleths of turbulent kinetic energy q^2.

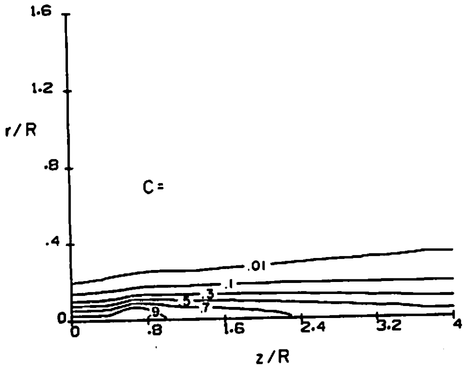

Figure 14. The dispersal of neutrally buoyant smoke. Inflow $C = \exp - 117r^2/R^2$ so that $C_{max} = 1.0$.

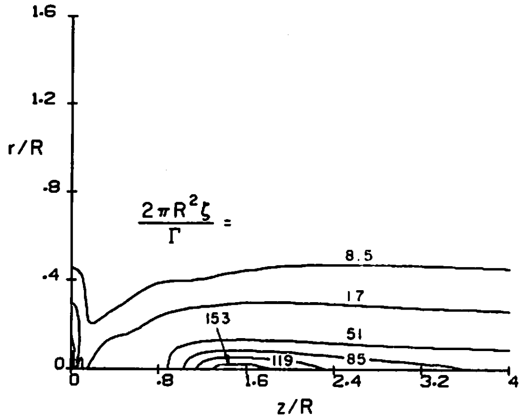

Figure 15. Isopleths of axial vorticity. At $z = r = 0$, $\zeta_{max} = 200\Gamma/2\pi R^2$.

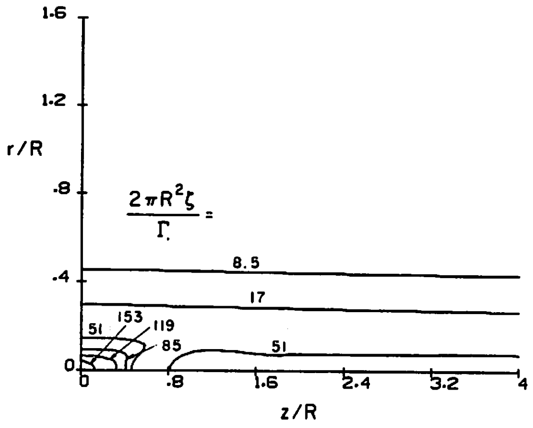

Figure 16. Isopleths of axial vorticity. At $z = r = 0$, $\zeta_{max} = 200\Gamma/2\pi R^2$.

Finally, in Figures 15 and 16 we show isopleths of axial vorticity $\zeta = (1/r)(\partial rV/\partial r)$ for the breakdown flowfields of Figures 9 and 10, respectively, showing that the only substantial redistribution of vorticity occurs very near the vortex axis over radial length scales, which are of the order of the upstream viscous core radius.

To quantify the results as to the level of reduction of rolling moment which may result as a consequence of breakdown, we have computed the function

$$RM = 4\pi\int_0^{s_f} rV\,dr\ , \qquad (12)$$

which is proportional to the rolling moment induced on a follower aircraft, of semispan s_f, during a co-axial vortex encounter. It is assumed that downstream of breakdown the $(W_{\text{inflow}} - W|_{r=0\ \text{outflow}})/W_\infty$ is small. This function is shown in Figure 17, where it is clear that only significant reductions in rolling moment will occur for following aircraft whose semispan is of the order of 2 and 3 times the viscous core radius.

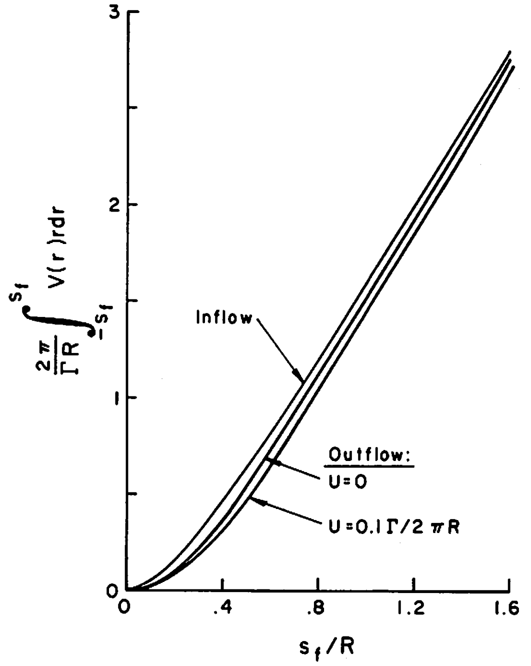

Figure 17. **Rolling momentum upstream and downstream of vortex breakdown as a function of the encountering aircraft's semi-span.**

CONCLUSIONS

Numerical simulation of vortex breakdown flowfields, thought to be typical of that which might occur on aircraft vortices, have shown that sufficient turbulent transport does not exist to bring about extensive redistribution of the trailed vortex. It has been shown by direct computation that an aircraft of a span which is approximately 75% of the span of the generating aircraft will experience a reduction in rolling moment after breakdown of approximately 10%. For trailing aircraft of yet smaller span, the resulting reduction in induced rolling moment is larger, but still appears to not offer the reductions in rolling moment which would permit the operation of a small aircraft in the wake of a larger aircraft.

It has been shown with the use of the super-equilibrium limit of second-order closure theory, that turbulence is in general suppressed in the central region of aircraft vortices. This result is in qualitative agreement with observation of aircraft vortices which have been seeded with smoke to make them visible. It has also been shown that the breakdown phenomenon does disrupt the viscous core in a vortex, and results in high levels of turbulence. This turbulence very effectively disperses the smoke, leaving the impression that the vortex has in some way been destroyed. In reality our calculations show that the large scale structure of the vortex is not significantly altered by the breakdown phenomenon.

ACKNOWLEDGMENT

This research is supported by the National Aeronautics and Space Administration under Contract NAS2-9037.

REFERENCES

1. Donaldson, C.duP., "A Progress Report on an Attempt to Construct an Invariant Model of Turbulent Shear Flows," AGARD CP-93, Sep. 1971.
2. Packham, D.H. and Atkinson, S.A., "Preliminary Results of Low Speed Wind Tunnel Tests on a Gothic Wing of Aspect Ratio 1.0," ARC, London, England, C.P. 508, 1960.
3. Ludwieg, H., "Zur Erklarung der Instabilitat der Uber Angestellten Deltaflugeln Auftretenden Freien Wirbelkerne," *Z. Flugwiss*, Vol. 10, 1962, p. 242-249.
4. Jones, J.P., "The Breakdown of Vortices in Separated Flow," U.S.A.A. Report No. 140, University of Southampton, England, 1960.
5. Hall, M.G., "A Numerical Method for Solving the Equations for a Vortex Core," A.R.C. Rand M. No. 3467, 1967.
6. Gartshore, I.S., "Some Numerical Solutions for the Viscous Core of an Irrotational Vortex," Nat. Res. Lab., Ottawa, ON Canada, Report No. L.R.-378, 1963.
7. Mager, A., "Dissipation and Breakdown of a Wing-Tip Vortex," *J. Fluid Mech.*, Vol. 55, 1972, p. 609-628.
8. Benjamin, T.B., "Theory of the Vortex Breakdown Phenomenon," *J. Fluid Mech.*, Vol. 14, June 1962, p. 38-44.
9. Benjamin, T.B., "Some Developments in the Theory of Vortex Breakdown," *J. Fluid Mech.*, Vol. 28, 1967, p. 65-84.
10. Squire, H.B., "Analysis of the Vortex Breakdown Phenomenon," Part 1, Aero. Dept., Imperial College, London, England, Report 102, 1960.
11. Randall, J.D. and Leibovich, S., "The Critical State — A Trapped Wave Model of Vortex Breakdown," *J. Fluid Mech.*, Vol. 58, 3, 1973, p. 495-515.
12. Bilanin, A.J., "Wave Mechanics of Line Vortices," Ph.D. Thesis, Massachusetts Institute of Technology, June 1973.
13. Donaldson, C.duP. and Bilanin, A.J., "Vortex Wakes of Conventional Aircraft," AGARDograph No. 204, May 1975.
14. Grabowski, W.J. and Berger, S.A., "Solutions of the Navier-Stokes Equations for Vortex Breakdown," *J. Fluid, Mech.*, Vol. 75, 3, 1976, p. 525-544.
15. Landahl, M.T. and Widnall, S.E., "Vortex Control," in *Aircraft Wake Turbulence and Its Detection*, Plenum Press, New York, NY, 1971.
16. Lakschmikantha, H., "Investigation of Two-Phase Vortex Flows with Applications to a Cavity Nuclear Rocket," Ph.D. Thesis, Massachusetts Institute of Technology, Sep. 1973.
17. Lewellen, W.S. and Teske, M.E., "Turbulence Modeling and Its Application to Atmospheric Diffusion," Part 2, EPA Report No. 600/4-75-016b and A.R.A.P. Report No. 254, Part II, Dec. 1975.
18. Bilanin, A.J., Teske, M.E., and Williamson, G.G., "Vortex Interactions and Decay in Aircraft

Wakes," *AIAA J.*, Vol. 15, 2, Feb. 1977, p. 250-260.

19. Garodz, L.J., "Measurements of Boeing 747, Lockheed C5A and Other Aircraft Vortex Wake Characteristics by Tower Fly-By Technique," in *Aircraft Wake Turbulence and Its Detection*, Plenum Press, New York, NY, 1971.

20. Donaldson, C.duP., "A Brief Review of the Aircraft Trailing Vortex Problem," A.R.A.P. Report No. 155 and AFOSR-TR-71-1910, May 1971.

21. Teske, M.E., "Vortex Interactions and Decay in Aircraft Wakes; Volume III — The Vortex Wake Computer Program Programmer Manual," A.R.A.P. Report No. 271, Mar. 1976.

22. Moore, D.W. and Saffman, P.G., "Axial Flow in Laminar Trailing Vortices," *Proc. Royal Society*, Ser. A, Vol. 333, 1973, p. 491-508.

23. Sullivan R.D., "A Program to Compute the Behavior of a Three-Dimensional Turbulent Vortex," ARAP, Princeton, NJ, ARL-TR-74-0009, Dec. 1973.

24. Snedeker, R.S. and Bilanin, A.J., "Analysis of the Vortex Wakes of the Boeing 727, Lockheed L-1011, McDonnell Douglas DC-10, and Boeing 747 Aircraft," ARAP, Princeton, NJ, Report No. 245, July 1975.

APPENDIX

The A.R.A.P. second order closure turbulent model is given below. The equations have been formulated in stream-function vorticity form in circular cylindrical coordinates [(r,Θ,z) → (U,V,W)] for axisymmetric flows.

$$\frac{D\tilde{\eta}}{Dt} = 2\tilde{V}\frac{\partial\tilde{V}}{\partial z} + \frac{1}{r}\frac{\partial}{\partial r}\left\{r\varepsilon_r\frac{\partial\tilde{\eta}}{\partial r}\right\} + \frac{\partial}{\partial z}\left\{\varepsilon_z\frac{\partial\tilde{\eta}}{\partial z}\right\} - \frac{1}{r}\frac{\partial}{\partial r}\left\{C_{\eta r}\right\} - \frac{\partial}{\partial z}\left\{C_{\eta z}\right\}, \tag{A.1}$$

$$\frac{D\tilde{V}}{Dt} + 2\tilde{U}\tilde{V} = \frac{1}{r}\frac{\partial}{\partial r}\left\{r\varepsilon_r\frac{\partial\tilde{V}}{\partial r}\right\} + \frac{2\varepsilon_r}{r}\frac{\partial\tilde{V}}{\partial r} + \frac{\partial}{\partial z}\left\{\varepsilon_z\frac{\partial\tilde{V}}{\partial z}\right\} - \frac{1}{r}\frac{\partial}{\partial r}\left\{r^2C_{vr}\right\} - 2C_{vr} - \frac{\partial}{\partial z}\left\{C_{vz}\right\}, \tag{A.2}$$

$$\frac{D\overline{uv}}{Dt} = 2\tilde{V}\left(\overline{vv}-\overline{uu}\right) - r\overline{uu}\frac{\partial\tilde{V}}{\partial r} - r^2\tilde{u}\tilde{w}\frac{\partial\tilde{V}}{\partial z} - 2\overline{uv}\,\tilde{U} - r\overline{uv}\frac{\partial\tilde{U}}{\partial r} - r^2vw\frac{\partial\tilde{U}}{\partial z} - \frac{q}{\Lambda}\overline{uv} + L(\overline{uv}) - \frac{4v_c\,q_\Lambda}{r^2}\overline{uv}, \tag{A.3}$$

$$\frac{D\tilde{uw}}{Dt} = 2\tilde{V}\,\tilde{vw} - \frac{\overline{uu}}{r}\frac{\partial}{\partial r} - \overline{ww}\frac{\partial\tilde{U}}{\partial z} - \frac{q}{\Lambda}\tilde{uw} + L(\tilde{uw}) + \frac{1}{r}\frac{\partial}{\partial r}\left\{v_cq\Lambda\,uw\right\} + \frac{v_cq\Lambda}{r}\frac{\partial\tilde{uw}}{\partial r}, \tag{A.4}$$

$$\frac{D\tilde{vw}}{Dt} = -2\tilde{U}\,\tilde{vw} - 2\tilde{V}\,\tilde{uw} - \frac{\overline{uv}}{r}\frac{\partial W}{\partial r} - \tilde{vw}\frac{\partial W}{\partial z} - r\tilde{uw}\frac{\partial\tilde{V}}{\partial r} - \overline{ww}\frac{\partial\tilde{V}}{\partial z} - \frac{q}{\Lambda}\tilde{vw} + L(\tilde{vw}) + \frac{1}{r}\frac{\partial}{\partial r}\left\{v_c\,q\Lambda\,\tilde{vw}\right\} + \frac{v_cq\Lambda}{r}\frac{\partial\tilde{vw}}{\partial r}, \tag{A.5}$$

$$\frac{D\overline{uu}}{Dt} = -2r\,\overline{uu}\frac{\partial\tilde{U}}{\partial r} - 2r^2\,\tilde{uw}\frac{\partial\tilde{U}}{\partial z} + 4\overline{uv}\,\tilde{V} - 2\overline{uu}\,\tilde{U} - \frac{q}{\Lambda}\left(\overline{uu} - \frac{1}{3}q^2\right) - \frac{2bq^3}{3\Lambda} + L(\overline{uu}) - \frac{2v_cq\Lambda}{r^2}\left(\overline{uu} - \overline{vv}\right), \tag{A.6}$$

$$\frac{D\overline{vv}}{Dt} = -2\tilde{U}\,\overline{vv} - 4\tilde{V}\,\overline{uv} - 2r\,\overline{uv}\frac{\partial\tilde{V}}{\partial r} - 2r^2\,v\tilde{w}\frac{\partial\tilde{V}}{\partial z} - \frac{q}{\Lambda}\;\overline{vv} - \frac{1}{3}q^2 - \frac{2bq^3}{3\Lambda} + L(\overline{vv}) + \frac{2v_cq\Lambda}{r^2}\left(\overline{uu} - \overline{vv}\right), \tag{A.7}$$

$$\frac{D\overline{ww}}{Dt} = -2r\,u\tilde{w}\frac{\partial W}{\partial r} - 2\overline{ww}\frac{\partial W}{\partial z} - \frac{q}{\Lambda}\;\overline{ww} - \frac{1}{3}q^2 - \frac{2bq^3}{3\Lambda} + L(\overline{ww}), \tag{A.8}$$

$$\frac{D\Lambda}{Dt} = - \frac{s_1\Lambda}{q^2}\left[r\overline{uu}\,\frac{\partial \tilde{U}}{\partial r} + r^2\,\widetilde{uw}\,\frac{\partial \tilde{U}}{\partial z} + \overline{uu}\,\tilde{U} + r\widetilde{uw}\,\frac{\partial W}{\partial r}\right.$$
$$+ \overline{ww}\,\frac{\partial W}{\partial z} - s_2bq + L(\Lambda) - \frac{s_3}{q}\left[\left(\frac{\partial q\Lambda}{\partial r}\right)^2\right.$$
$$\left.\left. + \left(\frac{\partial q\Lambda}{\partial z}\right)^2\right]\right] , \qquad \text{(A.9)}$$

where

$$\frac{D(\ )}{Dt} = \frac{\partial(\ )}{\partial t} + \frac{1}{r}\frac{\partial}{\partial r}\left\{r^2\,\tilde{U}(\ )\right\} + \frac{\partial}{\partial z}\left\{W(\ )\right\} ,$$

$$L(\ ) = \frac{1}{r}\frac{\partial}{\partial r}\left\{rv_c q\Lambda\,\frac{\partial(\ )}{\partial r}\right\} + \frac{\partial}{\partial z}\left\{v_c q\Lambda\frac{\partial(\ )}{\partial z}\right\} ,$$

$$\varepsilon_r = \frac{\overline{uu}\Lambda}{q} , \qquad \text{(A.10)}$$

$$\varepsilon_z = \frac{\overline{ww}\Lambda}{q} ,$$

$$C_{\eta r} = r\varepsilon_r\,\frac{\partial \tilde{\eta}}{\partial r} + \frac{\partial \overline{uu}}{\partial z} - \frac{\partial}{\partial r}\,(r\widetilde{uw}) - \widetilde{uw} ,$$

$$C_{\eta z} = \varepsilon_z\,\frac{\partial \tilde{\eta}}{\partial z} + \frac{\partial \widetilde{uw}}{\partial z} - \frac{1}{r}\,\frac{\partial \overline{ww}}{\partial r} + \frac{1}{r^2}\,(\overline{uu} - \overline{vv}) ,$$

$$C_{vr} = \frac{\varepsilon_r}{r}\,\frac{\partial \tilde{V}}{\partial r} + \frac{\overline{uv}}{r^2} ,$$

$$C_{vz} = \varepsilon_z\,\frac{\partial \tilde{V}}{\partial z} + \widetilde{vw} ,$$

and

$$\frac{\partial^2\psi}{\partial r^2} - \frac{1}{r}\,\frac{\partial\psi}{\partial r} + \frac{\partial^2\psi}{\partial z^2} = - r^2\tilde{\eta} ,$$

with

$$\tilde{U} = - \frac{1}{r^2}\,\frac{\partial\psi}{\partial z} ,$$

$$W = \frac{1}{r}\,\frac{\partial\psi}{\partial r} .$$

AIRCRAFT VORTEX WAKE BEHAVIOR AND DECAY NEAR THE GROUND

IVAR TOMBACH, PETER B.S. LISSAMAN, AND JOHN B. MULLEN
AeroVironment Inc.
Pasadena CA 91107

ABSTRACT: One of the apparent modes of decay of aircraft wake vortices has been variously described as vortex breakdown or vortex bursting, the latter because of the visual appearance of this decay mode when the vortices are marked with smoke. A multi-faceted experimental and analytical research program was carried out to explore the details of vortex breakdown under conditions representative of those which would prevail at low altitudes in the vicinity of airports. Three separate approaches were taken simultaneously. Flight tests with Lockheed L-18 Lodestar and Boeing 747 aircraft flying over an array of ground-based cameras and instrumentation provided data on overall vortex behavior, on the vortex ages at the time of onset of instabilities, and on the changes in the vortex velocity fields which resulted from vortex breakdowns. Analytical work on stability theories identified conditions under which vortices could undergo unstable decay. Experimental tests in a water tank looked at the internal instability of vortices, and also shed light on vortex motion near the ground. Finally, a heuristic modeling approach consolidated the results of these programs into a simple representation of the relationship between the times of vortex breakdowns and the ambient turbulence levels.

INTRODUCTION

This study was concerned with the mechanisms of vortex decay under conditions simulating those present in the vicinity of airports. Although TSC has been studying vortices under operational conditions near airports for several years, much of the fundamental research on wake decay mechanisms has been performed at altitudes well above the ground and with aircraft in a "clean" (flaps up, landing gear up) configuration. Although there were good operational reasons for this emphasis in earlier research, the necessity for measurements in conditions more representative of those of concern mandated that this study emphasize vortices generated by aircraft in landing configuration (landing gear and flaps down).

The specific objective of the study was to achieve some degree of understanding of the phenomena underlying wake decay in the airport terminal environment, with particular emphasis on the vortex core breakdown mode of decay. With regard to that decay mode, the nature of the residual flowfield after the catastrophic breakdown, and the role of axial vortex flows in the breakdown mechanism, were of particular interest. As a goal, some progress in modeling the effect of vortex bursting on vortex strength and lifetime was desired.

A three-pronged study approach evolved, consisting of full-scale flight experiments to provide quantitative information; laboratory experiments to explore details of vortex structure and stability under controlled conditions; and heuristic analysis to meld theoretical concepts and experimental data into a coherent description of the behavior.

DESCRIPTION OF PROGRAM

The in-flight experiments involved generation of smoke-marked vortices by Lockheed Model L-18 Lodestar and Boeing 747 aircraft. A total of 5 days of Lodestar tests and 2 days of 747 tests were flown at a test site established on Rosamond Dry Lake on Edwards AFB, California.

Each test day consisted of a sequence of low level passes by the vortex-generating aircraft over a ground-level anemometer array which recorded the velocities induced by the vortices. The behavior of the smoke-marked vortices was recorded photographically by cameras at various locations on the ground and in a helicopter hovering overhead. To provide data on meteorological conditions, soundings were performed by a tethered balloon on a variable length (7-60 m) tether, by pilot balloon launchings, and by a meteorological aircraft which was instrumented to measure temperature and turbulence. Occasionally, buoyant balloons were released from ground level to enter into and mark the axial flow in the vortex cores. Figure 1 shows a schematic of the instrumentation array which is typical of all test days (except for the array spacing).

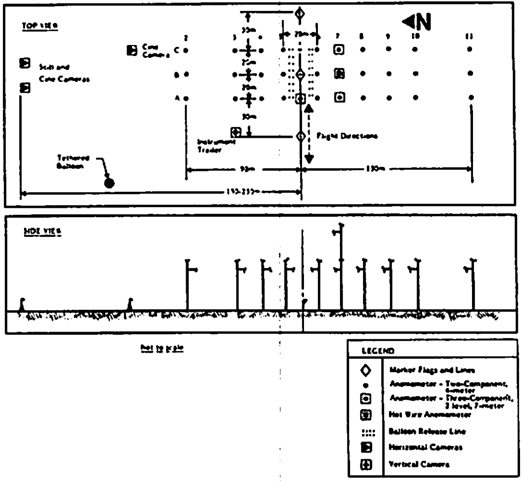

Figure 1. Schematic portrayal of instrumentation array layout for the Lodestar tests.

The laboratory experiments were performed in a water tank using a unique method of generation of a dye-marked vortex pair. The vortices thus generated were short in length relative to the wavelength of the sinuous mutual-induction instability, causing that instability to be suppressed to allow study of vortex motion and internal structure for extended periods. Because of the nature of this experiment, it was not considered as a simulation of a vortex wake, but rather as an analog model of portions of wake behavior which allowed testing of the effects of various input parameters on vortex stability and motion.

The analysis approach was directed toward defining, on the basis of theory and the field and laboratory experiments, those factors which affect the vortex breakdown mode of wake decay. A goal was the development of a model giving the best description of the effects of atmospheric and aircraft parameters on the breakdown, and of the effects of the breakdown itself on the strength and lifetime of the vortices.

Core-Bursting Analysis.

The wake vortex system of an aircraft is subject to two forms of instability: sinuous instability and core-bursting instability. The sinuous mode, known as Crow Instability, is a vortex pair phenomenon, and requires the velocity field of a neighboring vortex to induce instability and subsequent linking of the pair. When near the ground, a single vortex can undergo instability by interaction with its ground-induced image and actually link with the image, so that the vortex has the appearance of a semicircular loop, with both ends terminating on the ground. The motion of the vortex pair in Crow Instability is predominantly an inviscid response and has been considered in detail by Crow [1].

It has been observed [2, 3] that the sinuous instability is excited and driven by the ambient atmospheric turbulence, and the magnitude of this turbulence can be directly related to time-to-link. Crow and Bate [4] have included a turbulent forcing function of this form to develop a universal time-to-link equation, dependent only on the inviscid parameters.

In ground effect, it might be expected that the ground boundary conditions and the different turbulence spectra would have some effect on the sinuous time-to-link. However, Tombach and Crow [5] concluded that although the life span, or time-to-link, is reduced by the presence of the ground, the effect is small (not more than about 10%) when comparable vortices at different heights in the same atmospheric boundary layer are compared with each other.

The other important mode of catastrophic instability, vortex breakdown or core-bursting, is poorly understood to the extent that a precise meaning for the description is not agreed upon, nor is it clear whether there are one or more phenomena under this umbrella description. Most experimental data on this effect have been obtained from visual observation of the behavior of a smoke-marked vortex [2, 3, 6, 7]. The experiments show that the smoke-marked vortex appears to "bunch up" and "break;" that is, the marked core abruptly increases in diameter and then appears to burst, with the burst moving quite rapidly along the vortex axis. Often the smoke which marked the core rapidly dissipates and is no longer visible. Occasionally, a much diminished smaller core remains after the bursting process. The effect of bursting on the velocity fields has not been measured, although inferences from indirect measurements of vortex strength [8] and from the motion of a vortex after its mate had burst [2] suggest significant changes in the structure of the vortical core flow field. On the other hand, in studies of other columnar vortices, Mullen and Maxworthy [9] have observed that highly disruptive core phenomena have had little effect on the outer flow.

It appears likely that core-bursting is a single vortex phenomenon, in the sense that it is not necessarily connected with induced flows associated with the other vortex of the pair. There are, however, frequent occurrences of core-bursting in conjunction with the sinuous instability, in which case the sinuous vortex deformation appears to induce core-bursting.

Much effort has been expended in attempting to analyze the fluid mechanics of core-breakdown. An excellent state-of-the-art review of the theoretical aspects of this problem is given in a monograph by Donaldson and Bilanin [10] which summarizes results to date. Our object here is not to produce yet another analysis, but rather to determine a simple formula or rule by which the time to vortex-breakdown can be approximated from the basic aerodynamic parameters of the generating aircraft and atmospheric properties, in much the same way that the sinuous instability can be predicted.

RESULTS

Vortex Rollup.

The rolling up of the wing vortex sheet into discrete vortices was studied for selected passes of both the Lodestar and the Boeing 747 by examining smoke-marked vortices. Figures 2 and 3 show the rollup sequence for two typical test runs.

Figure 2 shows the smoke filament from the wingtip spiraling around the smoke-marked vortex core while diffusing slowly. The filament retains its identity throughout the sequence, indicating that this is a small vortex itself. Donaldson and Bilanin [10]

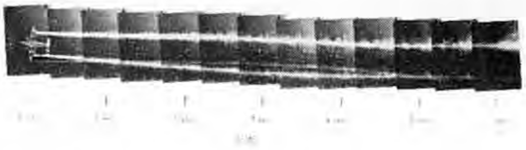

Figure 2. Sequence of photographs showing rollup of Lodestar vortices as seen from below. Although mounted in sequence to show the spatial evolution of the wake, the photos actually all show the same vortex segment at half-second intervals.

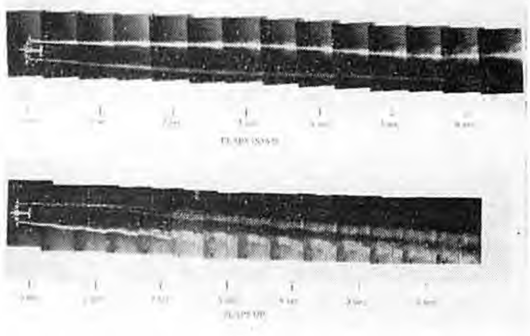

Figure 3. Comparison of smoke visualization of Lodestar vortex rollup with flaps down and flaps up.

have discussed conditions under which two discrete vortices can be formed.

A second smoke source installed inboard of the main smoke generators was also operating in the case shown in Figure 2. Its smoke was wrapped into the main vortex core within one chord length and was thereafter no longer distinguishable from the rest of the vortex in spite of its contrasting color.

The tip vortex should undergo breakdowns and instabilities in much the same way as the main vortex. Although such breakdowns are not seen in Figure 2, some instability in the smoke structure is visible, which appears to be connected with similar phenomena in the main vortices. Perhaps turbulent interaction of the vortex cores is a contributor to the decay of the tip vortex.

Figure 3 shows two more rollup sequences, one with flaps down and the other with flaps up, both without the additional tip smoke. In the clean (flaps up) configuration the vortex should originate at the wingtip; the smoke, however, is being released at the outboard end of the flap. The result is that the smoke never enters into the vortex core, but rather wraps around it, giving a hollow shell-like, diffuse appearance to the vortex. Comparison of the two sequences in Figure 3 can then give rise to misleading results, such as the conclusion that the clean configuration vortex is larger in diameter than the one produced with flaps down. If the smoke generator had been placed at the wingtip for both runs, the opposite conclusion would have been reached. (An example of such a case appears in the Boeing 727 tests reported upon by Barber, et al. [11]). This comparison illuminates one of the weaknesses of flow visualization, and also shows that proper smoke source placement is important for effective long-term visualization of vortex behavior.

Vortex Transport and Decay.

The meteorology which apparently most affects vortex behavior is defined by vertical profiles of temperature and turbulence and by a three-dimensional description of the wind vector field. The temperature profiles at the beginning of a test day (usually dawn) generally indicated a very stable atmosphere. After sunrise, the ground and the air above it gradually warmed until, by mid-morning, the temperature profile was neutrally stable (decreasing adiabatically with height). Further ground heating by the sun caused the atmosphere to become unstable when the warmer-than-adiabatic air near the ground rose vertically and caused a turbulent overturning motion in the atmosphere.

The turbulence levels at the low flight altitudes generally increased as the atmosphere became less stable as the morning progressed. An anomalous situation was sometimes encountered in the very stable early morning period, however, when drainage flow from nearby mountains caused stable layers to slide over one another and the resulting shears generated high levels of turbulence in spite of the very stable density distribution. This situation has been discussed by Tombach, et al. [3].

The desert winds were generally light in the early morning and were mainly caused by drainage. The wind increased as the morning progressed, and was soon dominated by the westerly gradient wind.

Under very stable conditions, the vortices descended in a wavy manner, with descent slowing and often halting in the vicinity of the ground. After halting, the Lodestar vortices rose up again. Sometimes the descent was rapid and the halting and rising occurred quickly enough to give the impression that the vortices had bounced off a layer close to the ground. As wavy or oscillating vortices approached the ground under these stable conditions the amplitude of the waves often appeared to be damped out and the vortex appeared to stiffen and straighten out any kinks that may have developed.

Under neutral to slightly stable conditions, the vortices descended in a lurching, wavy, or sinuous manner to the ground level. They often reached the ground at some point along their length, which immediately initiated a burst breakdown or ground link. The ground-linked vortices, which were only photographed for the Lodestar, resembled dust devils 20 to 30 meters in height. Only the half curved toward the aircraft was visible, indicating that axial flow toward the aircraft was picking up the dust. On a number of occasions the vortices descended at different rates along their length. Portions would rapidly dip, forming deep troughs which often burst near the ground at the point of maximum curvature. At other times the vortices descended rapidly while horizontal, and then in the vicinity of the ground certain portions rose up rapidly, forming humps which again usually burst at the point of maximum curvature.

Under unstable conditions the vortices descended rapidly in a lurching, sinuous manner and often appeared to be detraining fluid, leaving patches of smoke in a wake behind the vortex pair. The vortices contacted or almost contacted the ground on several occasions, which invariably initiated a burst breakdown near the ground.

Regardless of the atmospheric stability, the time of vortex breakdown (as defined by an obvious break in the smoke-marked vortex) was generally earlier in a turbulent atmosphere than in calm conditions.

These observations are a composite of results for both test aircraft and for all flight configurations, although the greater amount of Lodestar data tends to make them particularly representative of the Lodestar observations. The categorization by stability class is unique and has not been observed in prior experimental work, although Tombach, et al. [3], noted the tendency for vortices to descend more rapidly in neutral conditions than in a stable atmosphere.

It should be pointed out for completeness that the vortex behavior description discussed above applies to both vortices if both were visible, or to the one vortex which could be visualized. A few cases were observed where both vortices were visible but behaved differently, as for example would occur if the wake tilted or banked and the vortices then decayed differentially, but such behavior was not analyzed. The wind shear observations of Tombach, et al. [3] discuss such cases. The crosswinds during these tests tended to be small, so such behavior was not a major feature. Because of the difficulties with flow visualization it is possible that some of the rising of vortices which was noted is simply the asymmetric motion of the one visible vortex of a tilting vortex pair.

A limited number of runs was conducted under simulated take-off and landing conditions, so that the aircraft was climbing or descending when passing over the test array. The vortices produced in these situations rapidly approached the ground at an angle to the horizontal and contacted the ground sequentially at points along their entire length. These vortices appeared to break up immediately and then rapidly dissipate. The initiation time of this break up was much shorter than the time to first break up measured when the aircraft maintained constant altitude. No linking was observed in these situations, and normal core bursting was rare.

In contrast to the effects of attitude (and hence thrust), data scatter obscured the effects of landing gear or flap positions on vortex decay times. By inference, then, vortex breakdowns seem to be at most weakly influenced by the aircraft configuration.

Axial Flow.

One interesting aspect of vortex behavior is the axial flow in the core, which is often assigned a contributory role in various vortex decay mechanisms. The Lodestar vortices, when marked by small buoyant balloons invariably showed axial flow toward the aircraft, i.e., a wake-like axial flow. On the other hand, the axial flow in the Boeing 747 vortices was either jet-like (away from the aircraft) or there was no significant axial flow.

Jet-like flow in the cores was found behind the Boeing 747 when in takeoff configuration (10/10 flaps, either spoiler and gear position, aircraft climbing) or in landing configuration (30/30 flaps, gear down, no spoilers, aircraft descending). No significant axial flow was observed when the aircraft was "dirty" (30/30 flaps, gear down, no spoilers) and in level flight.

Local axial flow also occurred whenever a vortex breakdown or vortex pair linking occurred. In such cases the axial flow was away from the instability manifestation, in both directions along the vortex, indicating the presence of higher pressures at the burst or link point. The instability-induced axial flow was stronger than the normal axial flow in the vortex, and thus the local flow was totally dominated by the links or bursts.

Axial flow need not be confined only to the core centerline, and shells of axial motion have been observed in tests of aircraft flying past smoke sources. The flow visualization techniques of these experiments could not illuminate non-centerline core flows, however.

Effects of Core-Bursting.

The smoke marking often showed a small filament of smoke remaining after a burst had occurred, which indicated the continued presence of organized vortical motion. The small balloons released into the cores also showed vortex motion to be present after a visible vortex breakdown. In several 747 cases the balloons were still spinning in the vortex core at a vortex age of around 150 seconds, which is well in excess of the observed core breakdown times. In another case, the balloons in the core were overtaken by a moving breakdown, and then remained firmly trapped in the now-invisible vortex core after the breakdown had passed. Prior work (e.g., Hallock [8]) has also suggested that a vortex breakdown does not necessarily imply a destruction of organized vortex motion, but rather represents a rearrangement of vortex structure. The present work supports this concept, and indicates that the visually observed behavior of the smoke does not always provide a complete picture of the vortex lifetime.

In order to investigate this point further, selected anemometer records on vortex velocities occurring prior to and subsequent to vortex breakdown were examined. The cases studied were ones in which the photography showed a breakdown to have occurred above an anemometer.

A consistent pattern of behavior was observed, which is represented by the three sets of traces in Figure 4. Each trace represents the horizontal wind speed, transverse to the flight path, recorded by an anemometer as a function of time as the vortex traveled horizontally above it in ground effect. For each of the three cases shown, the top trace shows the vortex structure before a burst was seen on the photographs at the array, and the lower trace shows the vortex structure at the next anemometer reached by the vortex.

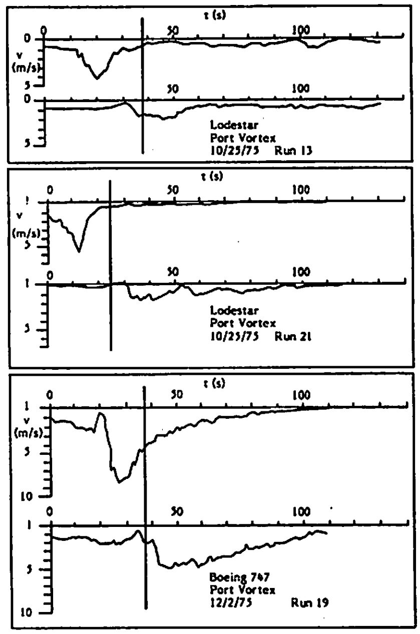

Figure 4. Anemometer records of vortex breakdown. The top graph of each set shows the horizontal speed history at an anemometer before a burst; the lower trace shows the record at the next anemometer after the burst.

In each case, the effect of the vortex burst is to flatten the velocity profile by significantly reducing the peak velocity under the center of the vortex (to about 30% of its prior value), but without major effect on the speeds away from the center of the vortex. A definite vortex flow remains in all of the three cases shown, however, indicating that core bursting did not totally eliminate the vortex, and the persistence of the outer flow speeds suggests that such bursting may not significantly alleviate the vortex hazard to aircraft with wingspans larger than the core size.

A few of the cases studied showed total alleviation of all vortex velocities by a vortex breakdown, with no residual vortex structure remaining. The flow visualization showed no visible difference between the partial and total vortex decay breakdowns, except that the presence of a residual visible core corresponds (obviously) to a case of partial alleviation. Aircraft configuration was not an obvious factor in selecting one form over the other.

Laboratory Results.

The water tank experiments showed that, initially, the vortical scroll rolled up into a finite core vortex (Figure 5a). During the rollup, disturbances developed in the vortex sheet and became amplified (Figure 5b). (This response is somewhat similar to that observed in a free shear layer Kelvin-Helmholtz instability.) The wavelength of this laminar instability increased approximately proportionally to the square root of time until the amplitude was approximately equal to 1/10 of the vortex span, b_v. At this point there was a rapid transition to turbulence, (Figure 5c), with the turbulent transition moving radially both inwards and outwards from the annulus where the instability waves first developed. Within a short time the flow within the vortex cell appeared fully turbulent except for a small region near each vortex center.

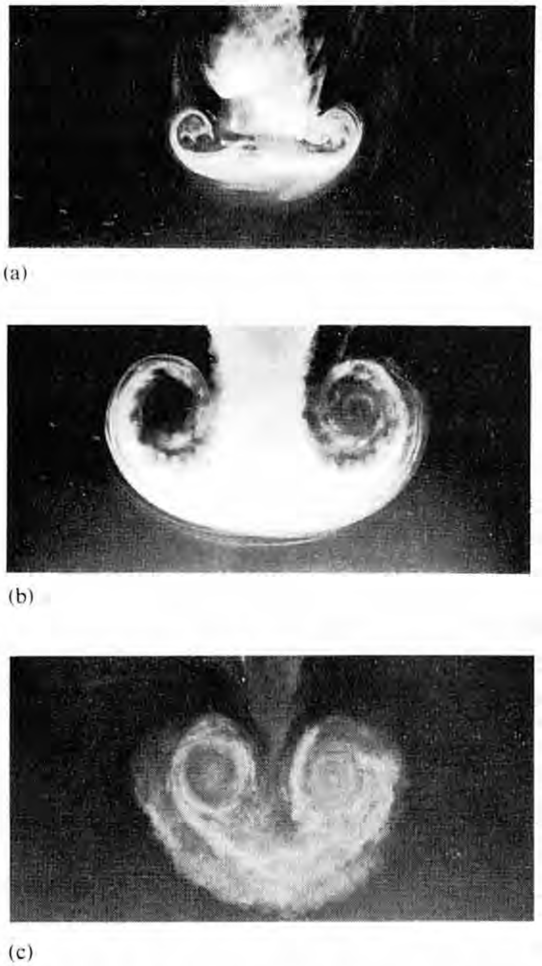

Figure 5. Development of vortex instability in water tank tests. (a) Initial vortex rollup, (b) Later stage of rollup with shear layer instability at inner boundary of smoke, and (c) Transition to turbulence. Vortex pair motion is downward in these photographs.

In further experiments, the initial turbulence in the cell was increased by installing sawtooth vorticity generators at the outlet of the vortex pair generator to simulate the initial turbulence in the aircraft wake vortex which might result from wing flaps, spoilers or engine exhaust. In this case the wavelength of the instability was twice as large as without the sawtooth and the rate of growth of the wavelength also increased. This is qualitatively what one might expect, indicating that initial turbulence will accelerate the turbulent transition in the vortex core.

These experiments indicate that any analytical modeling of core structure should include the effects of internally generated turbulence. However, there was no evidence that this turbulence suddenly caused the size of the core to increase in a manner suggestive of a two-dimensional core burst. Nor did the turbulence affect the translational motion of the vortex pair during the early stages of its descent.

Vortex Pair Descent and Interaction with Ground Plane.

In the water tank experiments the gross character of the motion was only approximately that predicted by inviscid point vortex pair theory. As expected, it was observed that the vortices descended, separated as they approached the ground plane, and then moved apart along the ground plane. However, there were very important distinctions between the real motion and the trajectory computed by a simple analysis such as that in Tombach, et al. [7].

In the water tank experiments, it was noted that the vortex pair never moved as close to the ground as simple theory predicts, and the separated vortices eventually started to move upwards and away from the ground plane. In other words, the vortex appeared to "bounce" when in ground effect. When the vortex pair was generated closer to the ground, this rebound effect was even more pronounced.

The rebound motion observed in the water tank is very similar to that observed in various flight tests, including those of the current program. Tombach, et al. [12] (also Tombach and Crow [5]) measured the lateral transport of vortices in ground effect, and noted that the transport speed slowed significantly after a definite distance of travel along the ground. Figure 6 compares those results, in non-dimensional form, with the water tank data from the present experiment. The agreement is excellent, indicating that vortex rising, not decay, is the main cause for the slowing of transport.

Heuristic Approach to Core-Bursting.

Because of the difficulties of predicting core-bursting by any direct fluid mechanical analysis, a heuristic argument was employed

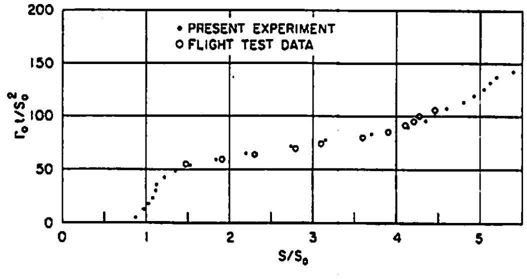

Figure 6. Normalized water tank vortex trajectory compared with flight test data from Tombach, et al. [7].

which appeared to incorporate the main physical terms and correlated with the data. Factors which affected the time-to-breakdown of the vortex core and quantified the relationships between them and vortex lifetimes were identified. Using dimensional and physical arguments the burst time was shown to be of the form

$$T_b = \frac{r_T}{V_T}\left(\frac{V_T^{3}}{\varepsilon r_T}\right) F\left(S^*, R^*\right),$$

where

V_T = Maximum tangential velocity,
r_T = radius of maximum temperature velocity,
ϵ = turbulence,
$S^* = V_T/(V_T + V_W)$,
V_W = maximum centerline speed,
$R^* = r_T/(r_T + r_W)$, and
r_W = effective width of axial flow.

The first term provides the proper dimensions based on the initial tangential flow scales, the second term provides the turbulence scaling and the third term contains the initial axial/tangential flow characteristics. The exponent α appears because the second term is dimensionless. A more general form for the second term would have been an arbitrary function of $V_T^3/\epsilon r_T$.

To evaluate the above equation using available experimental data required a determination of the exponent α and additional simplifying assumptions concerning the function F(S*,R*).

The parameters S* and R* are functions of the induced drag and profile drag of the wing. If the profile drag coefficient of two wings does not vary much, then the function F(S*,R*) should have approximately the same value for both wings if the wings are of comparable aspect ratio and lift coefficient. As a first approximation in this study, the function F(S*,R*) was assumed to be constant for the various aircraft studied. The time-to-burst relation then simplified to the form

$$T_b \sim \frac{r_T^{2}}{\Gamma_o}\left(\frac{\Gamma_o^{3}}{\varepsilon r_T^{4}}\right)^{\alpha}$$

where Γ_0 is the initial circulation of the rolled-up vortex, say a few spans downstream of the wing. As a final assumption, the vortex core size was assumed to be proportional to the wingspan, which is reasonable since the core is made up of the wing boundary layer, and ϵ was assumed to be made up of both ambient turbulence ϵ and mechanical turbulence k. The final form of the time-to-burst relation became

$$T_b = G\,\frac{b^2}{\Gamma_o}\left(\frac{\Gamma_o^{\,3}}{(k+\epsilon)\,b^4}\right)^{\alpha} \qquad (1)$$

with α to be determined experimentally and G a constant of proportionality. A detailed discussion of the derivation of this relation can be found in Tombach, et al. [12].

Functions of the form $T_b = [A/(k+\epsilon)]^{\alpha}$ were fitted to the experimental data. As suggested by the lines in Figure 7, the best fit was obtained for $\alpha = 1/3$, although the sensitivity of the fit to the value of α was fairly weak. Table 1 summarizes the results of the fitting procedure. The correlation of the data with the assumed functional form was fairly good with a mean standard error of estimate of around 10 seconds, which was more governed by the degree of data scatter than by the best curve fit.

The constant k, which can be interpreted as the effective residual aircraft-generated turbulence in the wake, is quite small for the Cessna 170 and Aero Commander 560F, which were flown in the clean configuration with flaps retracted. In terms of $\epsilon^{1/3}$, the value of k for these aircraft corresponds to an ambient $\epsilon^{1/3}$ of 0.2 to 0.4 $cm^{2/3}s^{-1}$ (normally considered as negligible turbulence). For the Lodestar and Boeing 747, which were flown with landing gear and flaps extended, the value of k is significantly higher, and has the same effect as an ambient $\epsilon^{1/3}$ of 1.6 to 1.8, which is typically classed as light turbulence.

The constant A varies significantly over the range of aircraft considered, and generally increases as the aircraft scale increases. Comparing the tested time-to-burst relation with the complete relation in Equation (1), it was hypothesized that

$$A = G^3 b^2 \quad .$$

Note that Γ_0 disappears from Equation (1) for the particular case of $\alpha = 1/3$. Table 2 shows the computation of G for each aircraft. The value of G is very nearly 0.3 for all aircraft except the Lodestar, for which G is 0.46. The different value of G for the Lodestar, which has significant flaps on the inboard third of the wing and thus might have a different form

Table 1. Calculation of the Proportionality Constant G in the Relation $T_b = G[b^2/(k+\epsilon)]^{1/3}$

Aircraft	Configuration	b (cm)	$G = (A/b^2)^{1/3}$
Cessna 170	Clean	1100	0.32
Aero Commander 560F	Clean	1490	0.26
Lockheed L-18 Lodestar	Flaps down	2000	0.46
Boeing 747	Flaps down	5960	0.31

Table 2. Statistical Constants of Fit of Form $T_b = [A/(k+\epsilon)]^{1/3}$ to the Experimental Data

Aircraft	Configuration	No. of points	A (cm^2)	k (cm^2s^{-3})	Correlation Coeff.	Std. Error of Est. (s)
Cessna 170	Clean	43	38,300	0.023	0.76	13.7
Aero Commander 560F	Clean	33	39,100	0.089	0.84	9.5
Lockheed L-18 Lodestar	Flaps down	50	394,000	3.87	0.64	9.6
Boeing 747	Flaps down	21	1,020,000	5.66	0.82	8.5

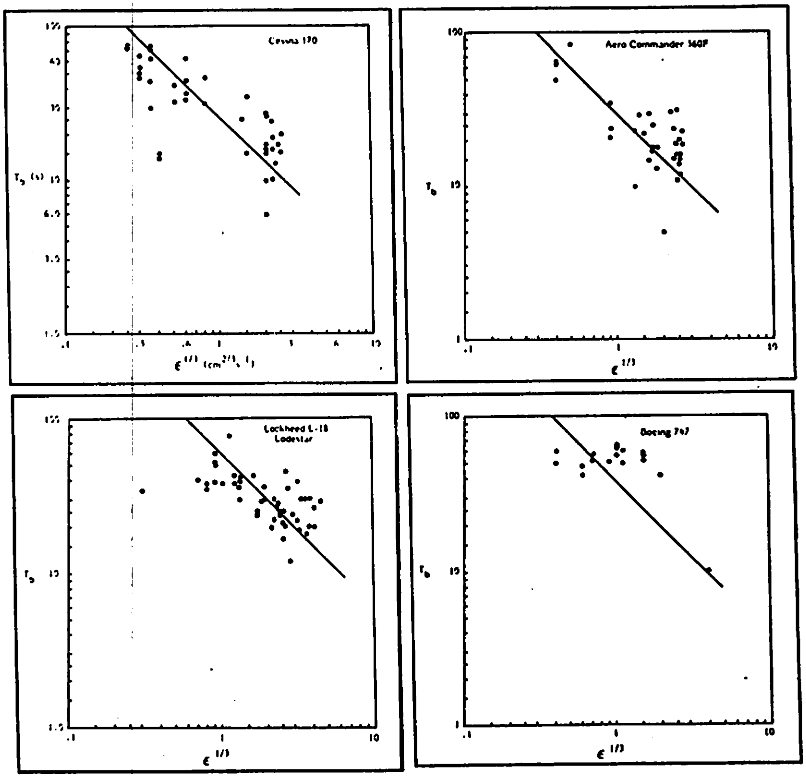

Figure 7. Data on time-to-burst versus turbulence used in the analysis. The lines represent $T_b \sim \epsilon^{-1/3}$.

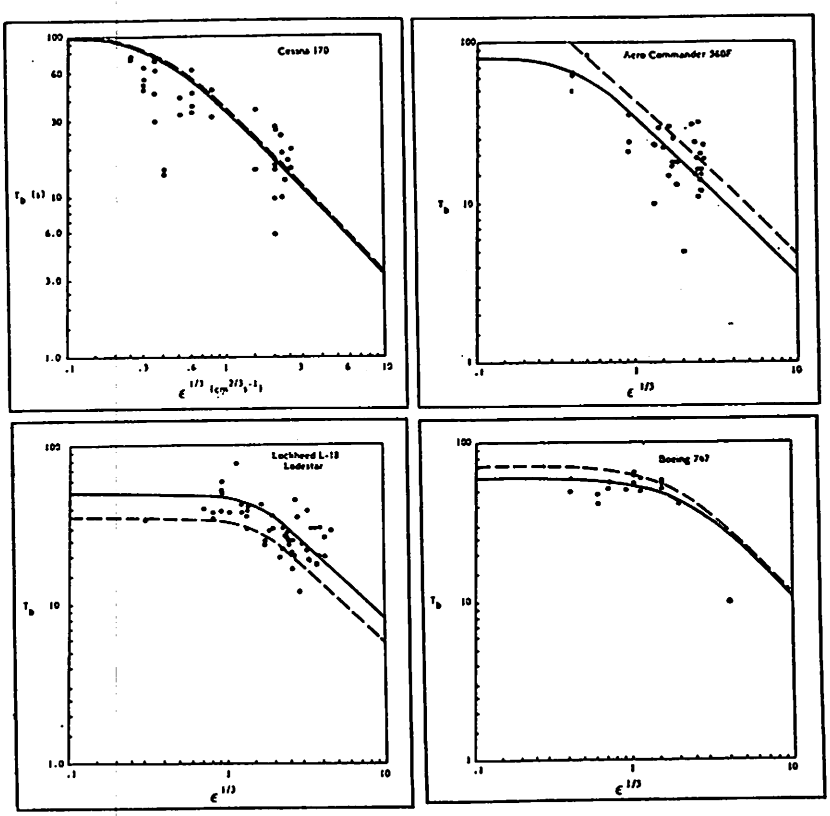

Figure 8. Fitted curves for time-to-burst data for each aircraft from Table 1 (solid lines), and composite function from Equation (2) (broken line). The logarithmic scales emphasize the deviations below the curves.

of the drag-related function F(S*,R*), was not surprising.

Thus a reasonable overall estimate for G is ⅓. For slightly conservative (high estimates of T_b, select $k = 0.05\ \mathrm{cm^2 s^{-3}}$ for the clean configuration and $k = 4\ \mathrm{cm^2 s^{-3}}$ for gear down. Thus the general time-to-burst relation developed here becomes

$$T_b \simeq \frac{1}{3}\left(\frac{b^2}{k + \varepsilon}\right)^{1/3} , \qquad (2)$$

with k selected as noted above.

Figure 8 shows the same data as in Figure 7, with the best fit curves for each aircraft (from Table 1) as well as a composite equation (Equation 2) drawn on each plot. It can be seen that the composite function does not fit the data as well as the individual curves for each aircraft, indicating that not all factors which vary from one aircraft to another are handled by the simplified analysis used here. The deviations are greatest for the two twin-engine propeller aircraft, but not in a constant manner.

Equation (2) can also be written in nondimensional form as

$$\tau_b = \frac{1}{3\eta_b} , \qquad (3)$$

where

$$\tau_b = \frac{T_b\,\Gamma_o}{2\pi b^2} , \qquad (4)$$

and

$$\eta_b = 2\left[\frac{(k+\varepsilon)\,b^4}{\Gamma_o^{\,3}}\right]^{1/3} . \qquad (5)$$

Here, Γ_0 has been reintroduced as a parameter which is required for the non-dimensionalization.

A plot of τ_b versus η_b, with all of the time-to-burst data plotted on it, is shown in Figure 9. Some points for the clean 747 configuration have also been added to this figure, using $k = 0.05\ \mathrm{cm^2 s^{-3}}$ and measured b_v and U to compute Γ_0. Here again there is a definite clustering of points according to aircraft type, showing that the τ_b and η_b nondimensionalization alone does not fully describe all aircraft effects on vortex breakdown. There is a general trend for the clean configuration data (open points) to lie below the general best-fit line and for the flaps-down configuration data (filled points) to lie near or above the line; this is most pronounced at small η_b (low turbulence).

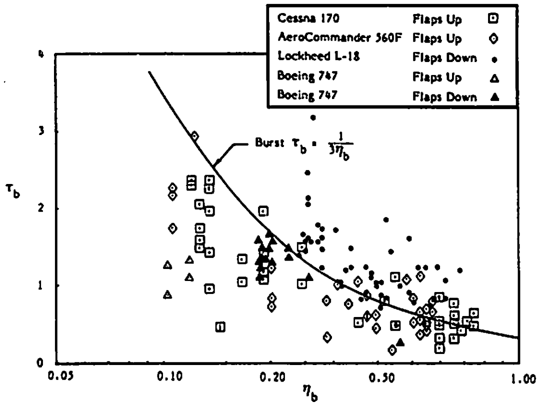

Figure 9. Composite plot of time-to-burst data in dimensionless form, and comparison with model (solid line). The logarithmic scale for η_b emphasizes deviation to the left of the curve at small values of η_b.

An arbitrary choice of a larger value of k, hence a larger value of η, for clean aircraft could improve the fit, but would have to be recognized as an *ad hoc* adjustment in parameters. Nevertheless, the simple curve in Equation (3) is generally good for predicting vortex breakdown times within a factor of 2, except for very small values of η_b, where, however, the experimental data tend to be biased toward shorter T_b as discussed previously.

The significance of the core-bursting time analysis on the prediction of the decay of vortices is more complex than it was for the linking time analysis of Crow and Bate. With linking, it is reasonable to assume that a link rearranges the vortex structure sufficiently to significantly reduce any hazard to a following aircraft. Such is not always the case with core-bursting, however. The experiments performed during this study showed conclusively that a visually apparent vortex core-burst did not necessarily indicate the demise of the vortex structure. Rather, observations of the buoyant balloons showed the continued presence of a vortex after bursting had occurred, and, in several instances, the laser velocimeter, acoustic sensors, and anemometer array also showed continuing vortex structure well after bursting. It is clear, however, that the velocities in the vortex and the overall circulation appear to reduce after core bursting; examples are given by Hallock [8] and Hallock, et al. [13].

CONCLUSIONS

This program set out to study the breakdown phenomenon, in the hope of emulating the success achieved in the prediction of the sinuous instability. The success has been diluted, though, by definite confirmation that vortex breakdown, as it has been defined by everyone who has looked at smoke-marked vortices, is not necessarily a mechanism which destroys a vortex, nor even weakens it significantly. Thus the ultimate destroyer of vortices which avoid linking with each other has still not been captured — it could be a cascade of breakdowns, a new form of mutual interaction, or possibly even decay by turbulent diffusion.

Dramatic differences in descending behavior were noted from hour to hour and day to day. Further analysis showed atmospheric stability to play a role in defining the nature of the descent, with stability suppressing irregular motion and inhibiting descent (and even stopping it).

A mechanism for the slowing down of the lateral motion of a vortex in ground effect was identified in the water tank tests, and was correlated with prior aircraft tests. The cause is a rising of the vortex, which results from rotation of the non-circular vortex core, rather than a dissipative mechanism, as previously believed.

ACKNOWLEDGMENTS

The work described in this paper was supported by the U.S. Department of Transportation, Transportation Systems Center, under contract DOT-TSC-1008. Dr. James Hallock was the Technical Monitor for TSC. The water-tank laboratory tests were performed by Drs. Steven Crow and Steven Barker at Poseidon Research, Los Angeles, California.

REFERENCES

1. Crow, S.C., "Stability theory for a pair of trailing vortices," *AIAA J.*, Vol. 8, No. 12, 1970, p. 2172-2179.
2. Tombach, I.H., "Observations of atmospheric effects on vortex wake behavior," *J. Aircraft*, Vol. 10, No. 11, Nov. 1973, p. 641-647.
3. Tombach, I.H., Bate, E.R., Jr., and MacCready, P.B., Jr., "Investigation of the motion and decay of the vortex wake of a light twin-engine aircraft," AV FR 439, Oct. 1974, AeroVironment Inc., Pasadena, CA.
4. Crow, S.C., and Bate, E.R., Jr. "Lifespan of trailing vortices in a turbulent atmosphere," *J. Aircraft*, Vol. 13, No. 7, July 1976, p. 476-482.
5. Tombach, I. and Crow, S., "Some aspects of aircraft wake behavior near the ground," AMS 7th Conference on Aerospace and Aeronautical Meteorology and Symposium on Remote Sensing from Satellites, Nov. 16-19, Melbourne, FL.
6. Chevalier, H., "Flight test studies of the formation and dissipation of trailing vortices," *J. Aircraft*, Vol. 10, No. 1, Jan. 1973, p. 14-18.
7. Tombach, I.H., Crow, S.C., and Bate, E.R., Jr., "Investigation of vortex wake stability near the ground," AFOSR TR-74-1501, July 1975, AeroVironment Inc., Pasadena, CA.
8. Hallock, J.N., "Monitoring wake vortex strength decay near the ground," *J. Aircraft*, Vol. 13, No. 10, Oct. 1976, p. 830-832.
9. Mullen, J.B. and Maxworthy, T., "A laboratory model of dust devil vortices," *Dynamics of Atmospheres and Oceans*, Vol. 1 (to be published).
10. Donaldson, C.duP. and Bilanin, A.J., "Vortex wakes of conventional aircraft," NATO AGARDograph No. 204, May 1975.

11. Barber, M.R., Kurkowski, R.L., Garodz, L.J., Robinson, G.H., Smith, H.J., Jacobsen, R.A., Stinnett, G.W., Jr., McMurtry, T.C., Tymczyszyn, J.J., Devereaux, R.L., and Bolster, A.J., "Flight test investigation of the vortex wake characteristics behind a Boeing 727 during two-segment and normal ILS approaches," NASA TM X-62,398 and FAA-NA-75-151, Jan. 1975.

12. Tombach, I.H., Lissaman, P.B.S., Mullen, J.B. and Barker, S.J., "Aircraft vortex wake decay near the ground," FAA-RD-77-46, Mar. 1977, AeroVironment, Inc., Pasadena, CA.

13. Hallock, J., Burnham, D.C., Tombach, I.H., Brashears, M.R., Zalay, A.D., and Barber, M.R., "Ground-Based Measurements of the wake vortex characteristics of a B747 aircraft in various configurations," AIAA Paper 77-9, 15th Aerospace Sciences Meeting, Los Angeles, CA, Jan. 1977.

ASSESSMENT OF ATMOSPHERIC EFFECTS ON THE BEHAVIOR OF AIRCRAFT WAKE VORTICES

PAUL B. MACCREADY, JR. AND PETER B.S. LISSAMAN
AeroVironment Inc.
Pasadena CA 91107

ABSTRACT: The transport and decay of an aircraft-generated vortex system depends on the characteristics of the generating aircraft, the proximity to the ground, and on atmospheric factors — the turbulence field, thermal stability, and mean wind shears throughout the region traversed by the vortex system. The number of variables involved, the statistical nature of the phenomena, and the difficulty of performing definitive field tests make the development of a comprehensive theory of vortex transport and decay an elusive goal, but significant strides have been made. This paper seeks to illuminate some of the main points, with more emphasis on dominant factors than on completeness or rigorousness.

INTRODUCTION

The transport and decay of an aircraft-generated vortex system depends on the characteristics of the generating aircraft, the proximity to the ground, and on atmospheric factors — thermal stability, the turbulence field, and wind shears, throughout the region traversed by the vortex system. Field experiments on vortex transport and decay over the years have illuminated some of the complex phenomena involved.

Although the experimental results have emphasized the complexity of the phenomena and the probabilistic nature of vortex evolution, the studies have advanced understanding considerably. This paper seeks to put some of the main factors into perspective.

The initial vortex field — its generation and wrap up — is rather well understood, except for small scale features of the turbulence within the wake and the axial core flow phenomena. Attention here is focused on subsequent events, particularly on those which are dominated by or which override meteorological factors.

DECAY MECHANISMS

The decay mechanism and decay rate for vortices from a given generator aircraft depend primarily on the atmospheric turbulence. Temperature, stability, wind shears, and the ground location all can affect vortex evolution, but the influence of turbulence tends to dominate. The turbulence, either atmospheric or aircraft generated, is in most cases the key to determining the lifetime of the vortex system, which then limits the vertical transport.

Three distinct main decay mechanisms exist:

a) linking (sinusoidal instability of the vortices),

b) bursting (a core-related phenomena), and

c) eddy viscosity (eroding the vortices).

These mechanisms can act independently or in combination. In strong atmospheric turbulence conditions all can be involved, but the vortex system is short lived in such cases and not the subject of study. Some of the main points about decay mechanisms and turbulence, particularly with reference to bursting and its comparison to linking, are given in greater detail in the report by Tombach, Lissaman, Mullen, and Barker [1].

BREAKUP BY LINKING AND BURSTING

Breakup by linking or sinuous instability involves the growth of a rather regular sinusoidal pattern, usually symmetrical for the vortex pair. This is commonly referred to as Crow linking. The time to link T_L has been found to depend, statistically, on atmospheric turbulence within the inertial subrange of eddy sizes, (a size range from a few cm to some hundreds of meters), which can be quantified by ϵ, the turbulence dissipation rate ($\epsilon^{-2/3}$ is proportional to the turbulent energy at any wavelength within the inertial subrange). The scale of the linking varies around nine times the vortex spacing, and so it is turbulence in the size range of one to ten times the span or vortex spacing which has the main effect.

For moderate or strong atmospheric turbulence, the time to link given by Crow and Bate [2] can be put in the form

$$T_L = 0.41\, b_v^{\,2/3} \varepsilon^{-1/3} \quad , \qquad (1)$$

where T_L is the time to link, b_v the vortex spacing, and ϵ the turbulence dissipation rate. For weak turbulence, in which induction between the vortices is at least as important as convection by atmospheric turbulence, a somewhat more complex relation is derived which includes the circulation Γ as a variable as well as b_v and ϵ.

Breakup by core bursting also can be related to the turbulence intensity. The physical mechanism by which turbulence initiates the bursting is unclear. In any case, it appears that smaller wavelengths of turbulence are of significance here than is the case for the sinuous instability — a scale comparable to the vortex core size. A heuristic model [1, 3], which is scaled by an empirical factor, has been found to be in reasonable agreement with results for a wide range of aircraft.

The general time-to-burst relation is

$$T_b \approx \frac{1}{3}\left(\frac{b^2}{k+\varepsilon}\right)^{1/3} \quad , \qquad (2)$$

where T_b is time to burst, b is actual span, and k is an equivalent turbulence created by the airplane (values of $k = 0.05\ \mathrm{cm^2 sec^{-3}}$ and $4.0\ \mathrm{cm^2 sec^{-3}}$ were found to fit experimental data for, respectively, the clean configuration and the landing configuration). The aircraft has an elliptical lift distribution so that $b_v = \pi b/4$, and if Equation (2) is written in terms of b_v, then for $k = 0$ the constant of proportionality in Equation (2) becomes 0.39, virtually identical to the constant in Equation (1). However, the functional and numerical similarity between Equations (1) and (2) is fortuitous, since the basic mechanisms are rather different.

The predicted times are generally within a factor of two of the observed times for both breakup by linking and by bursting. For moderate and strong turbulence the times are virtually the same for either mode. As far as aircraft hazard is concerned, the limiting time for danger to other aircraft is not just the linking or bursting time. The hazard can be expected to disappear within 20-30 seconds following the linking event since the flow quickly becomes rather disorganized. For bursting, the situation is more complex. If the vortex core is marked by smoke the bursting is identified by the disappearance of the smooth core. Upon bursting there quickly occurs a significant change of state of the vortex, to a weaker configuration, but then a residual organized motion of significant intensity often persists. Core bursting is basically a core phenomena, and breaking up or diffusing the core does not directly alter circulation events at larger radii.

DECAY BY EDDY VISCOSITY

Decay by eddy viscosity, rather than the breakup by linking or bursting, can be observed in two distinct regimes. One regime involves very, very calm atmospheric conditions, when linking or bursting may not be operating but when there is still enough turbulence to cause eventual vortex erosion. The turbulence scale of significance is presumably comparable to the vortex spacing or the dimensions of the descending oval containing the two vortices. The other regime involves the turbulence generated by the aircraft itself. Such turbulence can be very strong and can have a large role in the early decay history of the vortex system. The scale of the aircraft induced turbulence is much smaller than the scale of atmospheric turbulence. In clean configuration the aircraft provides turbulence in the boundary layer of the wing which evolves into the vortex cores, and in jet thrust wakes which diffuse into various portions of the organized vortex system. The aircraft in dirty configuration (gear and flaps down), however, will in addition have very strong turbulence added to the wake. The scale of turbulence generated by the dirty aircraft should permit the turbulence to be involved significantly in the eddy viscosity decay of the wake, possibly in core bursting, but not appreciably in linking breakup.

The eddy viscosity-caused decay of vortices behind dirty aircraft is illustrated in Figure 1. Figure 1 presents observational data available two years ago on vortex evolution behind aircraft in landing configuration. The data sources were Hallock's JFK ground-based measurements using doppler acoustic radar, NASA/FAA flight test measurements using probing aircraft (Figure 25, FAA-NA-75-151), as well as NASA's towing tank results. This data base strongly weighs some tests where a Learjet and T-37 were flown behind a 747 and a 727 — important cases for any operation separation matrix.

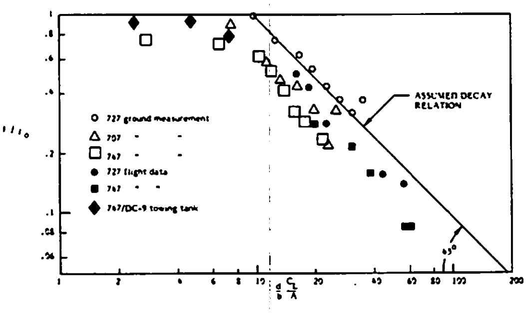

Figure 1. Wake strength decay for landing aircraft as a function of downstream distance.

The definition of vortex "strength" differed for the different tests, but it is felt that the major results will not differ if other definitions were used.

The figure shows that non-dimensionalizing circulation Γ by an effective initial circulation Γ_0, and non-dimensionalizing distance back d by the span of the generator b, its lift coefficient C_L, and its aspect ratio A, the data points coalesce fairly well. Beyond $(d/b)(C_L/A)$ of 10 (corresponding to the region beyond about 100 span lengths), the conservative data fit is

$$\Gamma/\Gamma_0 = 9.6\left(\frac{d}{b}\,\frac{C_L}{A}\right)^{-1.0} .$$

In this region the eddy viscosity acts to diffuse the vorticity within the descending oval, causing wake dissipation to proceed as d^{-1} or $(\text{time})^{-1}$. Earlier, the mixing evidently is not complete enough to cause appreciable sharing of the vorticity from the two vortices in the pair. It is interesting to note that the shape of the curve on Figure 1 showing constant Γ at short distances and thereafter a variation as $(\text{time})^{-1}$ is the same as shown in Figure 5 of Hallock et al. [4] for the core circulation of a B747 in landing configuration measured by a laser-doppler velocimeter. The curve "break" for the velocimeter measurement occurred at $x/b = 33$, a bit closer to the generator aircraft than the "break" shown in Figure 1 wherein much of the data came from observations beyond the core. Other investigators have found slightly different shaped curves or noted decay to be stronger near the ground, but the main feature of constant circulation followed by decay appears consistent with all observations.

Figure 1 shows the circulation is reduced to 20% by $(d/b)(C_L/A) = 50$, about 500 span lengths back. For a jumbo jet at approach speed, this is about 1.8 nautical miles back, at a time of 43 seconds. If ambient turbulence is moderate, exceeding 2 $\text{cm}^{2/3}\text{sec}^{-1}$, it is likely that core bursting will occur before this time with this landing aircraft.

In contrast, aircraft in clean configuration will have only a slow vortex decay from aircraft-generated eddy viscosity, terminated by a breakup by sinusoidal instability or bursting if there is atmospheric turbulence. In extreme cases of clean aircraft, very low turbulence, and a solitary vortex (its mate having become somewhat removed and breaking up independently) the vortex duration can be very long. One case of 6 minutes duration of a contrail has been reported [5], and the senior author of this present report noted another long duration contrail from a jet airliner July 24, 1976, over Iowa. In an ordinary contrail breaking up after about 1½ minutes by an irregular sinusoidal instability there was one section 1 km long where the separation at 1½ minutes became about twice as wide as usual and one vortex broke up independently into loops and shreds. The other portion of the pair remained as a straight rod for 3½ additional minutes, for a five-minute visual lifetime. We have no information on the strength of the circulation for a solitary vortex over these long times; the well-defined core merely gives evidence of a well-organized flow and a lack of significant turbulence. In any case, the hazard to aircraft from such long-lived vortices high aloft seems minimal; there is more than adequate altitude for recovery from an upset. The question arises as to whether or not the phenomenon occurs commonly at low altitudes where a hazard could be created. The lack of contrails at low altitudes makes the probability of occurrence of the phenomenon difficult to ascertain. Fortunately, the amount of time that large aircraft are flown in clean configuration at low altitude (say 1000-2000 feet AGL) is small, and the probability of extremely low turbulence in this region is less than it is high aloft, and so the phenomenon should be uncommon at altitudes low enough to create a hazard due to upset.

OTHER METEOROLOGICAL INFLUENCES

The evolutionary events in the life of a vortex pair in an atmosphere with temperature stability can be considered characterized in the three steps proposed by Lissaman, et al. [6].

1. Inviscid wake — descends at constant speed, constant vortex spacing, no mixing with ambient fluid, acquires buoyancy in a stable atmosphere.
2. Entraining wake — descent rate slows, vortex separation increases, entrainment occurs, wake oval enlares, rate of increase of buoyancy slows down.
3. Decaying wake — descent slows (or stops), buoyancy is dissipated, strong entrainment occurs, vortices decay. (This stage may never be reached because of breakup by an instability.)

In this characterization, atmospheric stability, *per se,* appears to play no significant role, while ambient turbulence very much affects the rate at which wake behavior passes through the three stages.

Although theoretical treatment on the descent of a vortex pair in a stably stratified atmosphere suggests the vortices will draw closer and speed their descent, experiments [7, 8] indicated the descent speed generally stayed the same and then slowed, while the spacing stayed the same and then widened. Strong slowing was symptomatic of the final vortex decay or breakup. Field observations and lab experiments have shown that near the ground there is a tendency for vortices to "bounce" upward above the trajectory which would prevail for line vortices moving under the influence of the normal image vortices.

Close to the ground, with the vortices spreading outward, strong stability appears capable of inhibiting linking interaction with the image vortex, presumably by inhibiting vertical motion of the vortex. In neutral and unstable conditions, the presence of the ground seems to speed decay by any of the breakup/decay mechanisms. The reasons have not been clarified; core-shape distortion and vorticity generated at the ground surface have been implicated.

Wind shear has what appears to be a more significant effect on vortex behavior. The tilting or banking of the plane containing the vortex pair has been observed experimentally at altitude [7] and in ground effect [8], as well as in operational situations [9, 10]. Occasionally, in the light aircraft tests, long segments of the wake were observed to roll past the vertical, resulting in bank angles exceeding 90°. It appears that crosswind shear or crosswind shear gradients are responsible for this observed rolling tendency of wakes.

Theoretical treatments relating the direction of tilt to the direction of shear or to the directions and rate of change of shear are not yet definitive. Nevertheless, the reality of the phenomenon is accepted.

In addition to the tilting, another dramatic (and operationally more significant) aspect of wake behavior occurs simultaneously, at least in the cases in the shear near the ground. When the wake banks, the upper (generally downwind) vortex appears to break up (decay) well ahead of the other vortex, often leaving one vortex drifting alone for some time before it itself decays. Interestingly, the single remaining vortex does not attempt to link with its image below the ground; rather, it invariably experiences vortex breakdown. Thus shear can be a factor in the creation of the long-lived solitary vortices which may constitute a rare but significant operational hazard.

SOME CONCLUSIONS

The reason for developing understanding of aircraft vortex phenomena is to permit design and improvement of an operational system which properly balances safety and efficiency in air traffic movements — and also to aid in the development of devices to augment vortex decay. The present knowledge provides a good framework for the "hazard duration and location" portion of a vortex advisory system. However, examination of any of the experimental data involved in vortex wake research shows that there is always a lot of scatter. Even when the meteorological conditions are being observed carefully, the analyst must be content with scattered data for comparing to theory and the advisory system designer must work with envelopes surrounding points and with wide standard deviations. In an operational advisory system the meteorology will not be known (or forecasted) even as well as it was measured on experimental projects, and so the envelopes will have to be wider.

The conclusion to be drawn from all this is that, for improving an operational advisory system, improving meteorological predictability and improving the predictability of the limiting hazard cases deserve high priority. These are more important than improving understanding of the meteorological influences of the fluid mechanics phenomena of vortex motion and decay. Improving understanding will be helpful for answering one remaining critical and vexing question: how much circulation remains after breakup by core bursting, and for how long does it remain significant?

REFERENCES

1. Tombach, I., Lissaman, P.B.S., Mullen, J.B., and Barker, S.J., "Aircraft vortex wake decay near the ground," FAA-RD-77-46, Mar. 1977, AeroVironment Inc., Pasadena, CA.

2. Crow, S.C., and Bate, E.R., Jr., "Lifespan of trailing vortices in a turbulent atmosphere," *J. Aircraft*, Vol. 13, July 1976, p. 476-482.

3. Tombach, I., Lissaman, P.B.S., and Mullen, J., "Aircraft vortex wake behavior and decay near the ground," Aircraft Wake Vortex Conference, DOT-Transportation Systems Center, Cambridge, Mar. 1977.

4. Hallock, J., Burnham, D.C., Tombach, I.H., Brashears, M.R., Zalay, A.D., and Barber, M.R., "Ground-based measurements of the wake vortex characteristics of a B-747 aircraft in various configurations," AIAA 15th AeroSpace Sciences Meeting, Los Angeles, CA, Jan. 1977.

5. MacCready, P.B., Jr., "An assessment of dominant mechanisms in vortex-wake decay," in *Aircraft Wake Turbulence and Its Detection;* Ed. J.H. Olsen, et al., Plenum Press, NY, 1977, p. 289-304.

6. Lissaman, P.B.S., Crow, S.C., MacCready, P.B., Jr., Tombach, I.H., and Bate, E.R., Jr., "Aircraft vortex wake descent and decay under real atmospheric effects," FAA-RD-73-120, Oct. 1973, AeroVironment Inc., Pasadena, CA.

7. Tombach, I.H., "Observations of atmospheric effects on vortex wake behavior," *J. of Aircraft*, Vol. 10, Nov. 1973, p. 641-647.

8. Tombach, I.H., Bate, E.R., Jr., MacCready, P.B., Jr., "Investigation of the motion and decay of the vortex wake of a light twin-engine aircraft," AV FR-439, Oct. 1974, AeroVironment Inc., Pasadena, CA.

9. Burnham, D.C., Hallock, J., Kodis, R., and Sullivan, T., "Vortex sensing tests at NAFEC,"

DOT-TSC-FAA-72-2, Jan. 1972, DOT Transportation Systems Center, Cambridge, MA.

10. Brashears, M.R., Logan, N.A., and Hallock, J.N., "Effect of wind shear and ground plane on aircraft wake vortices," *J. Aircraft*, Vol. 12, Oct. 1975, p. 830-833.

PREDICTED AND MEASURED WAKE VORTEX MOTION NEAR THE GROUND

M.R. BRASHEARS, A.D. ZALAY, AND W.R. EBERLE
Lockheed Missiles & Space Company, Inc.
Huntsville AL 35807

ABSTRACT: Vortex track and meteorological measurements obtained by the Transportation Systems Center at Kennedy International Airport have been processed and cataloged in a computerized data management system. A total of 1320 flybys have been cataloged. A calculated vortex track using meteorological data measured concurrently with the measured vortex track has been generated and placed in the data management system for each flyby. An analysis of measured vortex parameters and corresponding vortex parameters generated from the analytic model was performed. A comparison of calculated vortex residence time and measured vortex residence time is presented. The reasons for deviations between the calculated residence time and measured residence time are discussed. Design considerations for a wake vortex avoidance system are also discussed.

INTRODUCTION

The Transportation Systems Center (TSC) has been working toward the development of a wake vortex avoidance system which can be implemented at airports to guarantee safe aircraft separations in routine operations [1]. Several tracking systems intended to sense vortices and to determine their positions have been developed. An analytic wake vortex transport model which generates vortex tracks based on aircraft parameters and meteorological conditions has also been developed [2, 3]. A test program was implemented at Kennedy International Airport (JFK) for the purpose of evaluating the candidate sensing and tracking systems, comparing measured vortex tracks with calculated vortex tracks, and refining the analytic model. A large quantity of vortex sensor and meteorological data were recorded during this test program [4, 5]. An aircraft wake vortex data analysis computer program was used to process and present the meteorological data, calculated vortex trajectories, and measured vortex trajectories in such a manner that meaningful comparisons could be made [6]. The data were then incorporated into a data management system (DMS) so that data could be selectively recalled (based on values of meteorological, aircraft, and vortex parameters) and further calculation and/or plotting performed upon the recalled data to permit meaningful analysis of the vortex data to be made. Specifically, it was desired to define the conditions which cause the calculated vortex parameters from the analytic model to deviate from the measured vortex parameters and to identify phenomena which will have a significant impact on the design of an effective operational wake vortex avoidance system.

WAKE VORTEX AND METEOROLOGICAL MEASUREMENTS

As a part of a comprehensive program by TSC to monitor the behavior of wake vortices in the aircraft approach corridor, the meteorological and vortex parameters from aircraft landing on runway 31R at JFK were monitored by an array of ground wind anemometers, two laser-Doppler velocimeter (LDV) systems, and four instrumented meteorological towers. Acoustic vortex sensors were also used, but the results were not placed in the data management system because of unavailability of corresponding meteorological data. A plan view of the test site is given in Figure 1, and a summary of meteorological measurements recorded is presented in Table 1. The table also shows a summary of meteorological parameters which were calculated from the measured parameters and stored in the data management system. Data averages were taken over 128 seconds following aircraft passage.

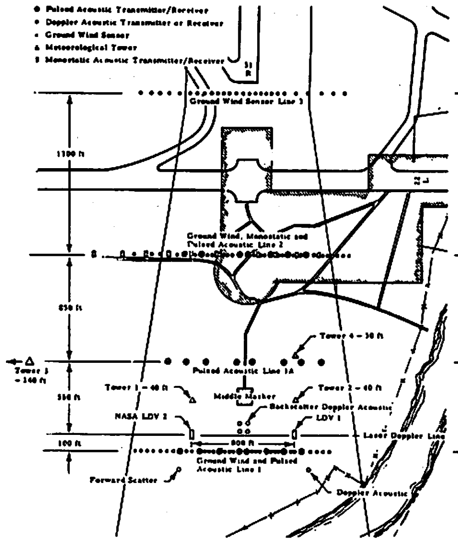

Figure 1. Plan view of JFK vortex test site.

Table 1. Summary of Measured Winds and Calculated Meteorological Parameters

Measured Winds

u = Headwind
v = Crosswind (positive from port side)
w = Vertical Component of Wind (positive upward)

Tower	Altitude (ft) of Wind Measurement
1	20, 40
2	20, 40
3	25, 50, 100, 135
4	20, 30

Calculated Meteorological Parameters

Average of all winds for 128 sec after aircraft passage
Standard deviation of all winds for 128 sec after aircraft passage
Average wind speed for all winds for 128 sec
Average wind direction for all winds for 128 sec
V_{z_0} and p for least-squares fit for wind speed: $V = V_{z_0}(z/z_0)^p$ for tower 3
A and B for least-squares fit for wind direction: $\Theta = A + Bz$ for tower 3

The presence of wake vortices near the ground was detected by each of three rows of single-axis propeller driven anemometers as shown in Figure 1. The propeller anemometers measure crosswind. In the data processing, if the standard deviation of the signal from a single sensor did not exceed 0.14 ft/sec over the 128-second average following aircraft passage, the sensor was declared to be dead. All active sensor data were filtered with a weighted 17-second averaging filter. For the vortex tracking calculation, the anemometer which was determined to be closest to the starboard vortex at a given time was that anemometer for which the filtered value of wind was greater than that for all other active anemometers on the sensor line at the same time. The time of vortex passage over an anemometer which had been determined to be closest to the vortex was the time at which the wind measured by that sensor was a maximum. By plotting the times at which the vortex passed over sensors at the various lateral positions, a plot of vortex lateral position as a function of time was generated. The vortex residence time was generated by smoothing the curve and determining the time at which the vortex crossed the flight corridor boundary. The residence time for the port vortex could be generated in a similar manner by using minimum values of crosswind. (See reference 7 for a definition of residence time and its significance.)

Two characteristics of the ground-wind sensor are important in interpreting data from it. First, reliable data are obtained only when the vortex is close to the ground. This limitation is inherent in the ground wind system. Second, spurious points could be generated after the vortex left the flight corridor; however, these were eliminated in the calculation of residence time.

Measurements of the wake vortex trajectories were also obtained by two laser-Doppler velocimeter (LDV) systems deployed at JFK. The scan pattern used for the test is shown in Figure 2. For the LDV systems, a CO_2 laser was focused at a sequence of points in space as shown in Figure 2. A portion of the beam was backscattered by the atmospheric aerosol. For each position of the focal volume in space, the backscattered laser intensity and the aerosol velocity (line-of-sight velocity relative to the LDV system measured by the Doppler shift in the returned signal) were recorded. In a comparison of data processing algorithms [4], it was determined that the best vortex tracking algorithm is one which identifies the vortex position as the point of maximum returned signal intensity. The vortical motion of the vortex core causes a high concentration of atmospheric aerosol at the vortex core boundary. The high aerosol concentration causes the returned laser intensity to be a maximum at the core boundary. (See reference 8 for a complete description of the LDV and its data.)

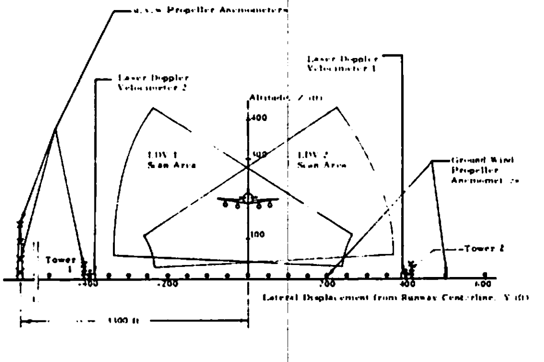

Figure 2. Instrumentation at baseline 1 for JFK wake vortex tests.

The calculated wake vortex trajectories were generated from a theoretical model [3] using the aircraft location, wing span, weight, and airspeed as inputs. The spanwise wing loading was assumed to be elliptic. The input parameters, resulting vortex strength, and number of flybys observed for each aircraft type are shown in Table 2. The aircraft are assumed to be centered on the runway centerlines at an altitude of 200, 172, 135, and 78 ft, respectively, for baselines 1, 2, 3 and 4. Although the complete theoretical vortex transport model contains many transport and decay mechanisms, the calculated trajectories for the data management system considered vortex transport by mutual induction and crosswind only. The trajectories were calculated by a fourth order Runge-Kutta integration of the transport equations

$$\dot{Z} = \frac{-\Gamma}{2\pi(Y_2 - Y_1)} + \frac{\Gamma}{2\pi}\left[\frac{Y_2 - Y_1}{(2Z)^2 + (Y_2 - Y_1)^2}\right]$$

and

$$\dot{Y} = V_\infty \pm \frac{\Gamma}{4\pi Z}\left[\frac{(Y_2 - Y_1)^2}{(2Z)^2 + (Y_2 - Y_1)^2}\right]$$

where Z is the altitude of the vortices, and Y_1 and Y_2 are the lateral positions of the port and starboard vortices, respectively. The + and − signs are applicable to the starboard

Table 2. Aircraft Characteristics for Calculated Vortex Trajectories

Aircraft Type	Wingspan (ft)	Landing Weight (lb)	Airspeed (ft/sec)	Vortex Strength (ft^2/sec)	Number of Flybys Cataloged
B-747	195.7	462,878	237.7	5397	204
B-707	145.0	194,400	231.8	3137	337
B-727	108.0	126,750	212.7	2993	297
B-737	93.0	81,500	183.4	2562	4
DC-10	165.3	335,375	234.7	4689	73
DC-9	89.4	63,544	215.6	1788	152
DC-8	148.4	199,375	230.3	3164	190
L-1011	155.3	298,409	234.7	4441	29
VC-10	146.2	200,000	230.0	3193	9
BAC-111	93.5	64,154	237.7	1553	18

and port vortices, respectively. The calculated residence time was the time for which the upwind vortex reached the flight corridor boundary at Y = ± 150 ft.

DATA MANAGEMENT SYSTEM

Wake vortex and meteorological measurements obtained by TSC at JFK during 1975 have been incorporated into a computerized data management system (DMS). A total of 1320 flybys have been cataloged into the DMS, and the distribution of the number of flybys for various aircraft types is shown in Table 2. The cataloged data files contain vortex trajectories (vortex altitude and lateral position as a function of time) for both LDV systems and the calculated vortex trajectory, vortex trajectories (vortex lateral position as a function of time) for each of the three groundwind anemometer lines, vortex residence times (time for which the vortex remains in the flight corridor) for calculated and measured vortex trajectories, and selected meteorological parameters.

A sample output from the cataloged data files showing the vortex trajectory and plots of vortex altitude and lateral position as functions of time are shown in Figures 3 through 5. The straight lines in Figure 3 connect calculated vortex position with LDV measured vortex position at 20-second intervals. Generally, the LDV measurements give a good indication of the vortex location for the time periods ranging from 10 to 60 seconds where the vortex structure is coherent and drift of the vortex out of the field of view or significant decay of the vortex rotational velocity does not occur. The groundwind anemometers indicate the positions of the vortices from 30 to 128 seconds whenever the vortices have drifted close to the ground and are moving laterally past the ground-wind anemometers. The strength of the vortices, however, is not known.

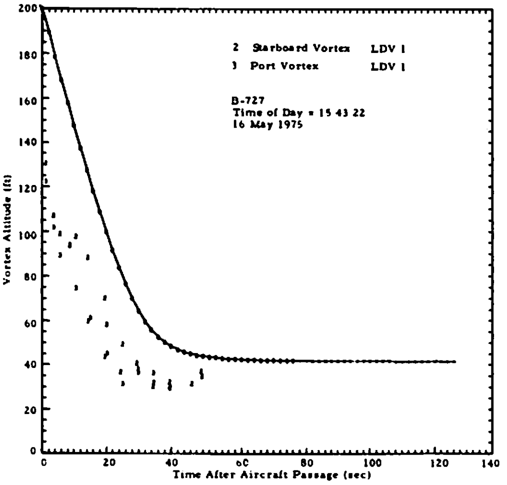

Figure 4. Example of calculated and measured vortex altitude as a function of time.

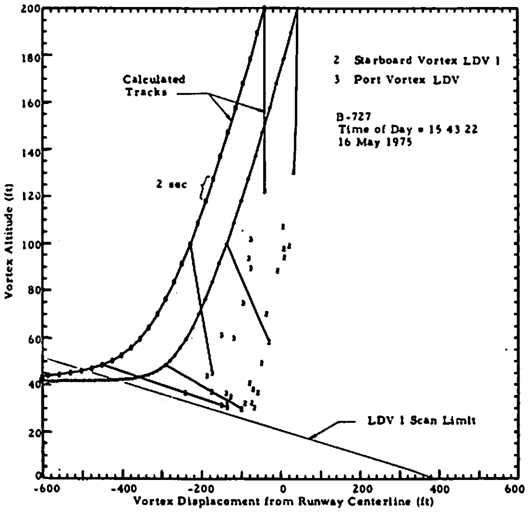

Figure 3. Example of calculated and measured wake vortex trajectories.

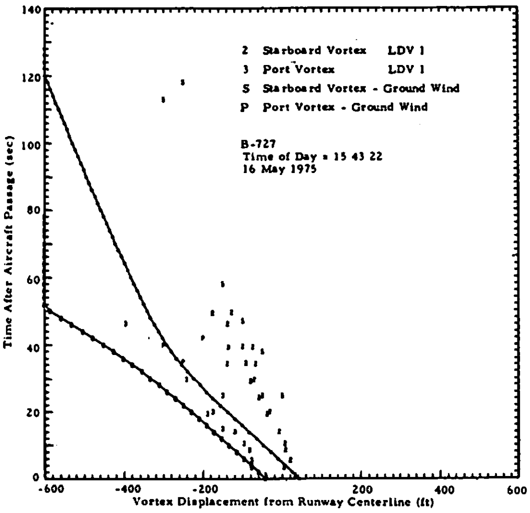

Figure 5. Example of calculated and measured vortex lateral position as a function of time.

Figures 3 and 5 illustrate a problem which is prevalent in all of the data. Although both the calculated and measured vortex trajectories are well defined, they do not agree. The disagreement is due to the fact that the meteorological tower upon which the calculated trajectory is based is located 3300 ft from the runway centerline. For Figures 3 through 5, the average crosswind for tower 1 (40 ft) was −6.32 ft/sec, whereas that for tower 3 (50 ft) was −9.29 ft/sec. Therefore, comparison of calculated and measured vortex trajectories or residence time on a flyby-by-flyby basis has limited meaning.

DATA ANALYSIS

In this section the sources of data scatter are quantified, and the wake vortex avoidance system design implications of the data and data scatter are discussed. In this section, all plots contain data for B-707, B-727, B-737, DC-8 and DC-9 aircraft. Data for wide-body transports were plotted separately. Narrow-body data are presented here because of the number of available flybys. Conclusions for wide-body transports are identical with those presented herein for narrow-body transports.

Meteorological Tower Variations.

A comparison of the wind measured at the 40-ft level of tower 1 (tower closest to the flight path at baseline 1) with that measured at the 50-ft level of tower 3 (tower from which wind data were used for calculated vortex trajectory) is shown in Figure 6. Winds shown are the 128-sec averages following each flyby. The scatter is expected because tower 3 is located 3000 ft from tower 1. Tower 3 was used for the calculated vortex trajectory because it was the only tower with high altitude (~150 ft) wind data.

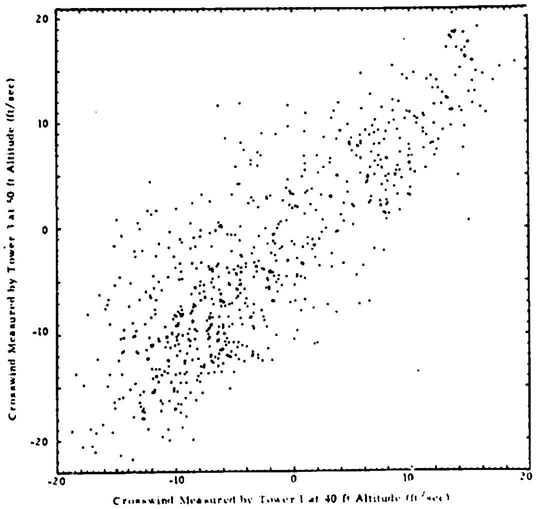

Figure 6. Comparison of crosswind measured by tower 1 and by tower 3.

From an operational viewpoint, the discrepancy between tower 1 and tower 3 does not cause problems for a Wake Vortex Avoidance System. It is expected that the large discrepancy occurs during gusty wind conditions. Vortex life is very short in gusty conditions. In steady wind conditions (when long vortex life may occur) the two towers would be expected to give similar values. Thus, the condition which causes the discrepancy (wind gusts) is the condition which precludes long vortex life.

Figure 6 shows the value of wind measured near the flight corridor. A short tower near the flight corridor may yield better data than a tall tower further from the flight corridor. Wind data measured from the glideslope antenna tower may yield good results.

Because of possible differences in wind between tower 3 (upon which the calculated vortex residence time is based) and tower 1 (near the location where vortex residence time is measured) and for the purposes of this paper, the standard of comparison between calculated and measured residence times is the calculated residence time in a uniform crosswind. For tower 3, the calculated residence time for the complete wind profile is compared with that for a uniform crosswind as measured at the 50-ft altitude of tower 3. The envelope of deviation of the residence time based on a uniform crosswind is thereby established. Measured residence times are then compared with calculated residence times based upon uniform crosswinds measured near the flight corridor. The envelope of deviation is then applied to determine the extent to which non-uniform crosswind effects account for the differences between measured residence times and uniform crosswind residence times.

Effect of Variation of Wind with Altitude.

For the calculated residence time based on a complete wind profile, the wind data measured at 25, 50 and 135 ft were curve-fitted to an analytic form in a least-squares sense. The wind speed was fitted to a power-law curve, and the wind direction was fitted to a linear profile. The form of the crosswind was

$$v = V_{z_0} \, (z/z_0)^P \, \sin(A + Bz)$$

An example of the fitted crosswind profile is shown in Figure 7 with the data measured by the anemometers on the towers. A plot of the individual calculated residence times (based on the curve-fitted wind profile) is shown as a function of crosswind measured at the 50-ft level in Figure 8. The constant crosswind residence time and the residence time for a power-law exponent of 0.2 are shown for reference. While much of the scatter may be attributed to a non-zero power law exponent, some of the scatter results from the condition that the curve fitting implies that the value of wind of the fitted data at 50-ft altitude is not necessarily equal to the measured data at that same altitude. This condition is shown in Figure 7.

A direct comparison of calculated residence time with constant crosswind residence time is shown in Figure 8. There are two conditions worthy of note. The first condition is when the constant crosswind residence time is very large (>120 sec) whereas the calculated residence time is smaller. For the calculated residence time, after the upwind vortex leaves the flight corridor, reentry into the corridor is not considered. For the constant crosswind residence time, reentry is considered. As shown, most of the cases in question are those when reentry occurs. This suggests that the reentry phenomenon may be important.

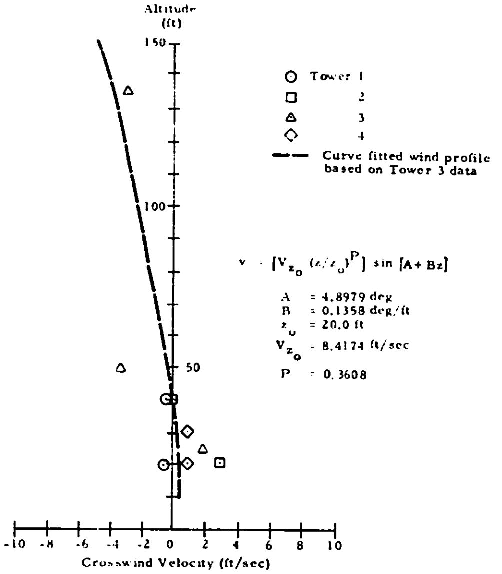

Figure 7. Comparison of measured and curve fitted wind data.

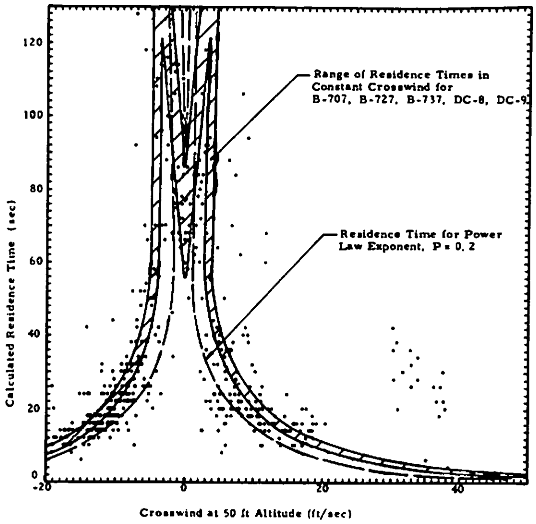

Figure 8. Calculated residence time as a function of crosswind.

The second condition of note is when the calculated residence time is significantly greater than the constant crosswind residence time. In general, wind speed increases as altitude increases. For low crosswinds, residence time increases as wind increases. For equal crosswinds at low altitude, the vortex with the higher wind at high altitude travels further toward the downwind boundary before reversing its direction and exiting from the upwind boundary. Therefore, the residence time for non-constant crosswind is greater than that for constant crosswind.

Unknown Values of Aircraft Parameters.

For measured vortex parameters, significant data scatter can occur from the unknown values of aircraft parameters. The calculated residence time is based on nominal values of aircraft parameters. However, there are unknown variations in aircraft weight (up to ± 25% of nominal values), variations in wing span (due to different models of a given type), variations in spanwise loading factor (due to different flap settings), variations in airspeed, variations in altitude about the glideslope, and variations in lateral position about the runway centerline. For example, the vortex of a B-707-120 at minimum operating weight, spanwise loading coefficient of 0.8, 5 knots above nominal landing speed, and 10 ft above and 20 ft to the side of the ILS at the middle marker has a vortex strength of 1895 ft^2/sec and a residence time of 113 sec for no crosswind. By contrast, a B-707-320C at maximum landing weight, spanwise loading coefficient of 0.75, 5 knots below nominal landing speed, and centered on the ILS has a vortex strength of 4246 ft^2/sec and a residence time of 47 sec for no crosswind. The corresponding values for the nominal values of aircraft parameters shown in Table 2 are a vortex strength of 3135 ft^2/sec and a residence time of 66 sec.

In addition to the direct effect of unknown values of aircraft parameters by virtue of the effect on vortex descent rate, unknown values of aircraft parameters also affect vortex residence time in the determination of the corridor boundary from which the upwind vortex exits. For constant crosswind, the upwind vortex for the B-707-120 described above will exit the upwind boundary for crosswinds less than 3 ft/sec and will exit the downwind boundary for crosswinds greater than 3 ft/sec. By contrast, for the B-707-320C described above, the critical value of crosswind is 6.4 ft/sec. For the nominal condition (Table 2), the critical value of crosswind is 4.5 ft/sec. In a constant crosswind of 5 ft/sec, the B-707-120 would have a residence time of 46 sec whereas the B-707-320C would have an unrealistic residence time of 231 sec. This condition significantly affects a comparison of calculated residence times with measured residence times because the deviations of actual aircraft parameters from values assumed in the analytical models can cause significant variations in vortex behavior.

Measured Vortex Data.

The vortex residence time as a function of crosswind is shown in Figure 9 for LDV measured residence times and in Figure 10 for residence times measured by groundwind anemometers. Constant crosswind residence time curves are superimposed for reference. The LDV measured data agrees well with the constant crosswind residence time.

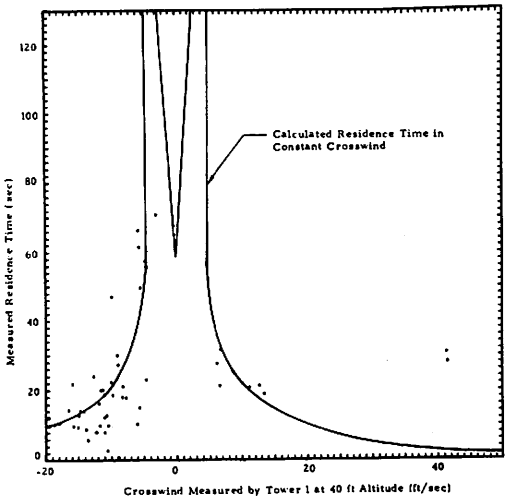

Figure 9. Vortex residence time measured with laser doppler velocimeter.

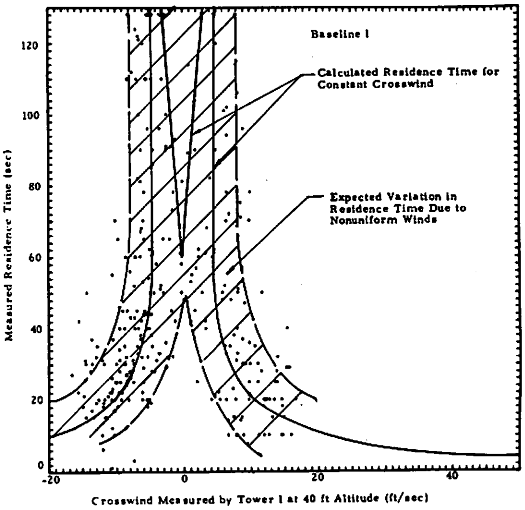

Figure 10. Vortex residence time measured with groundwind anemometers.

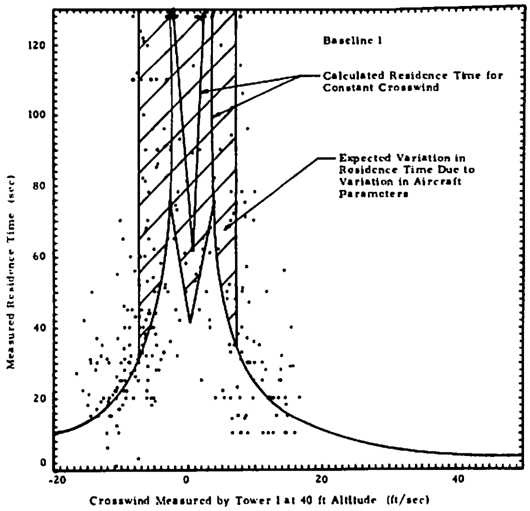

Figure 11. Comparison of residence time measured with groundwind anemometers with expected variation due to variation in aircraft parameters.

For the residence time measured by ground-wind anemometers, the expected variation for non-constant crosswind (i.e., scatter boundaries of Figure 6) is superimposed for reference.

Figure 11 shows the same measured data as Figure 10, but with expected variations due to unknown values of aircraft parameters superimposed. It is obvious that the combination of uncertainties in Figures 10 and 11 account for all scatter in the measured data.

Because there was some disagreement between the wind measured by tower 1 and that measured at tower 2, an attempt was made to reduce some of the scatter in Figures 9 and 10 by better definition of crosswind. It was believed that the crosswind measurements may have been disturbed by the vortices. The measured data were plotted as a function of the upwind tower. The data were also plotted for those points for which towers 1 and 2 agreed within 2 ft/sec. Neither of these attempts yielded any significant reduction in the scatter of the data.

WAKE VORTEX AVOIDANCE SYSTEM DESIGN CONSIDERATIONS

In addition to quantification of the scatter to be expected in the calculation and measurement of wake vortex residence times, analysis of the cataloged data has indicated other trends which have implications related to the design of an effective wake vortex avoidance system.

Multiple Baseline Considerations.

An effective wake vortex avoidance system must assure the absence of vortices at all points in the flight corridor. Therefore, vortex behavior at different baselines (i.e., different initial vortex altitudes) must be considered. From constant crosswind considerations, if the upwind vortex exits from the downwind flight corridor boundary, vortex residence time decreases with increasing initial vortex altitude. However, if the upwind vortex exits from the upwind boundary, vortex residence time increases with increasing initial vortex altitude. Since the latter condition is the condition which gives long residence times, it is the condition of interest.

This phenomenon is shown in Figure 12 for calculated residence times. The residence time at baseline 1 (glideslope altitude = 200 ft) is plotted as a function of residence time at baseline 2 (glideslope altitude = 172 ft). For long residence times, the residence time for baseline 1 is greater than that for baseline 2. The few exceptions are cases for which the power law exponent is negative.

The design implication of this phenomenon is that if a single baseline vortex sensor is used as part of a wake vortex avoidance system, it should be placed at the outermost position (from the runway) at which the vortex is expected to be a problem.

Variations with Time of Day.

Because aircraft spacings must be established up to ten minutes before landing, an effective wake vortex avoidance system must be able to predict vortex behavior. Therefore, variation of vortex parameters with time of day is very important. Figures

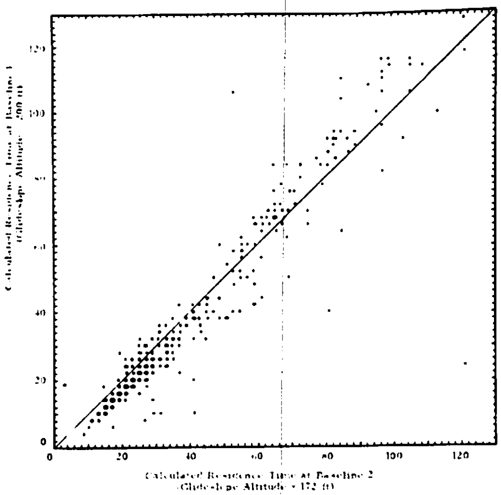

Figure 12. Variation in vortex residence time with distance from runway threshold.

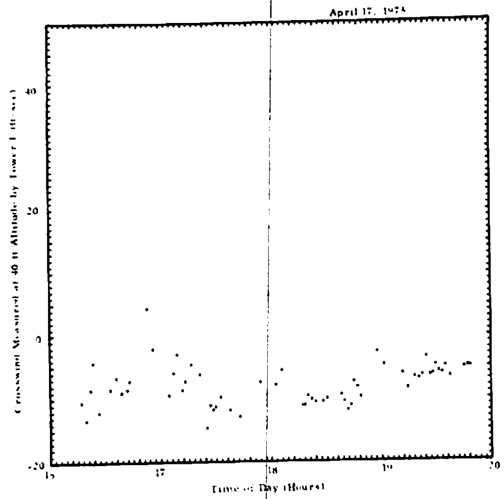

Figure 13. Variation in measured crosswind with time of day.

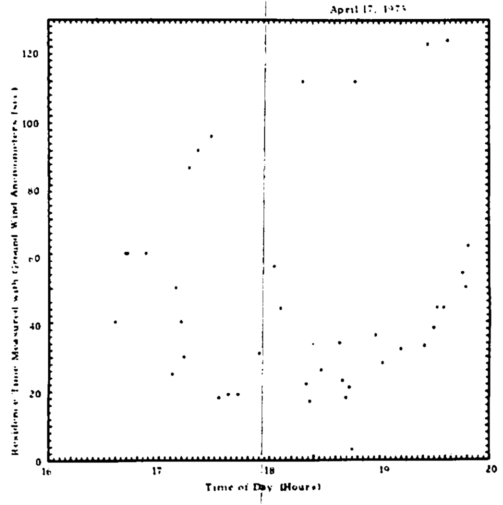

Figure 14. Variation in measured residence time with time of day.

13 and 14 show the variation in crosswind and measured residence time (groundwind anemometer) with time of day for April 17, 1975. It is observed that these parameters may vary significantly over a short period of time. Therefore, separations must be based on residence times which could be expected to occur with reasonable probability.

IMPORTANCE OF VORTEX TRANSPORT AND VORTEX PREDICTIVE MODELS

The data presented herein illustrate the need for both a vortex transport model (model which calculates vortex behavior based on concurrent meteorological data) and a vortex predictive model (model which calculates vortex behavior based on previous meteorological data) for both the development of a Wake Vortex Avoidance System and use in an operational system. In the development context, aircraft spacing must provide protection from anomolous vortex behavior. Therefore, both theoretical and experimental approaches to vortex behavior are appropriate to identify the conditions under which long vortex life may occur.

In addition, there are many meteorological conditions for which vortex considerations do not constrain aircraft separations. An accurate analytic model allows identification of those meteorological conditions. The analytical model provides a theoretical basis for certification of spacings which may be used in conjunction with empirically derived data.

In an operational context, measured vortex parameters for one aircraft are not necessarily indicative of those for the next aircraft. A vortex transport model permits definition of an envelope of possible values of vortex parameters, whereas measurement alone provides specific information for one aircraft passage only. The optimal system is one which calculates envelopes of vortex behavior with a feedback loop provided by measured vortex behavior. Similarly, a predictive model includes an envelope of variation in meteorological parameters which may occur over a specified time interval.

CONCLUSIONS

The set of vortex measurements recorded by TSC at JFK during 1975 have been cataloged and analyzed. On the basis of the data analyzed, several important conclusions have been made. The meteorological tower used for vortex calculations must be located close to the threshold of the active runway. A calculated vortex residence time based on curve-fitted wind profiles can be significantly different from that based on a constant crosswind. The condition in which the upwind vortex exits from the downwind flight corridor and then reenters the flight corridor may be very important. Variations in unknown values of aircraft parameters (actual aircraft weight, wing span, spanwise loading coefficient, airspeed) can have a significant effect on vortex residence time. The scatter in the measured residence time can be easily accounted for by a non-constant crosswind and unknown variations in the value of aircraft parameters. For long vortex residence times, the primary baseline of interest is that farthest from the runway threshold unless there is a negative value of power law exponent. Vortex parameters may vary significantly over a short period of time.

REFERENCES

1. Hallock, J.N., Wood, W.D., and Spitzer, E.A., "Predictive Techniques for Wake Vortex Avoidance," AGARD CP 188, May 1975.
2. Brashears, M.R. and Hallock, J.N., "Aircraft Wake Vortex Transport Model," *J. Aircraft*, Vol. 11, 1974, p. 265-272.
3. Brashears, M.R., Zalay, A.D., Chou, L.C., and Shrider, K.R., "Development of Predictive Wake Vortex Transport Model for Terminal Area Wake Vortex Avoidance," FAA-RD-76-94, May 1976, Lockheed, Huntsville, AL.
4. Bilbo, J.W., Jeffreys, H.B., Weaver, E.A., Huffaker, R.M., Craig, G.D., George, R.W., and Marrero, P.J., "Laser Doppler Velocimeter Wake Vortex Tests," FAA-RD-76-11 (NASA TM X-64988), Mar. 1976, NASA MSFC, Huntsville, AL.
5. Brashears, M.R., Lawrence, T.R., and Zalay, A.D., "Mobile Laser Doppler System Check Out and Calibration," LMSC-HREC TR D497036, Sept. 1976, Lockheed Missiles & Space Company, Huntsville, AL.
6. Brashears, M.R., Shrider, K.R., Love, D.A., Robertson, S.J., and Zalay, A.D., "Wake Vortex and Ground Wind Meteorological Measurements," FAA-RD-76-93, May 1976, Lockheed Missiles & Space Company, Huntsville, AL.
7. Hallock, J., Winston, B, Sullivan, T., and Burnham, D., "TSC Wake Vortex Data Base and Applications," Proceedings of Aircraft Wake Vortices Conference, DOT Transportation Systems Center, Cambridge, MA, Mar. 1977.
8. Bilbro, J., Craig, C., George, R., Jeffreys, H., Marrero, P., Weaver, E., Krause, M., Dunn, T., DiMarzio, C., Harris, C., Sonnenschein, C., and Toomey, D., "Laser Doppler Vortex Measurements at John F. Kennedy Airport," Proceedings of Aircraft Wake Vortices Conference, DOT Transportation Systems Center, Cambridge, MA, Mar. 1977.

STATUS OF THE VORTEX ADVISORY SYSTEM

EDWARD A. SPITZER, JAMES N. HALLOCK, AND WILLIAM D. WOOD
U.S. Department of Transportation
Transportation Systems Center
Cambridge MA 02142

ABSTRACT: A Vortex Advisory System is currently undergoing tests at the Chicago O'Hare International Airport. By measuring the wind magnitude and direction with respect to a runway heading, the VAS indicates via a display when aircraft separations could be safely reduced to three nautical miles for all landing aircraft. The paper presents the rationale for the system, the concept, the system design, how data are being acquired to check the operation of the system, and the test results to date.

INTRODUCTION

A major problem facing our national air transportation system is the restricted capacity and the resulting airline and passenger delay costs at our high density air terminals. The need to increase airport landing and takeoff capacity under all weather conditions without degrading current high levels of air carrier safety is therefore of prime importance to the air transportation system. When the major commercial air terminals operate at or near saturation in the current capacity-demand environment, aircraft delays are commonplace and poor weather only compounds the delay problem. Existing airport and airway system utilizations are projected to increase significantly by 1980 and to quintuple by 1995. Potential capacity relief through construction of more air terminals is not likely in the current or near future economic or environmental climate: expansion of runway quantities at existing terminals is just as unlikely. A solution which must be pursued is to allow increased aircraft operations into and out of the major terminals by decreasing the longitudinal spacings or intervals between successive aircraft operations.

Although the phenomenon of aircraft wake vortices has been known since the beginnings of powered flight, it is only recently that operational problems associated with the phenomenon have been experienced. Aircraft wake vortices now constitute one of the major problems confronting the air traffic control system. Before 1970, landing aircraft maintained 3 nautical-mile separations under Instrument Flight Rule (IFR) conditions. This separation standard was based primarily on radar operating limits and to a lesser extent on runway occupancy limitations. There were no separation standards imposed because of vortex considerations.

With the introduction of the wide-bodied jets and the increasing number of aircraft operations at the major airports, the wake vortex problem has taken on increasing significance. The probability of a vortex encounter is greatest in the terminal area where light and heavy aircraft operate on the same flight path in close proximity and where recovery from an upset may not be possible because of the low aircraft altitude.

Accordingly, the solution implemented by the Federal Aviation Administration (FAA) in March 1970 was to increase the separation standards behind the heavy jets to 4 nautical miles for following heavy aircraft and to 5 nautical miles for a following non-heavy aircraft. In November 1975 the standards were revised to require the addition of an extra nautical-mile separation for following aircraft with a maximum certificated takeoff weight less than 12,500 pounds.

The FAA has a broad objective to increase the airport and airway system capacity fivefold by 1995. The need to increase the capacity of the nation's airports while assuring protection against accidents has led to a program by the FAA to develop an Upgraded Third Generation (UG3) air traffic control system for the 1980's. The success of this system is dependent upon development of techniques for reducing the longitudinal separations required to avoid the hazard from trailing wake vortices, particularly behind heavy aircraft during approach and landing.

The Transportation Systems Center (TSC), under the aegis of the FAA, is developing ground systems which will provide information on the presence or absence of potentially hazardous vortices in the approach corridor such that a following aircraft may completely avoid contact with these vortices. The concept of wake vortex avoidance is based on two considerations which the available wake turbulence data supports:

1. Meteorological conditions exist a large percentage of the time which cause vortices to move quickly off the flight path or decay rapidly in the approach corridor such as to not present a hazard to aircraft following on the same flight path.

2. The duration, intensity and movement of vortices can be reliably predicted if adequate knowledge of existing meteorological conditions and the generating aircraft's characteristics are known.

The feasibility of developing an applicable vortex system which would utilize the above considerations is predicated on the observation that separation criteria are overly conservative most of the time, as they do not consider the meteorological effects on vortex behavior.

RATIONALE FOR VAS

Until recently the lack of knowledge about the life cycle of wake vortices generated by today's large aircraft mandated large separation distances for following aircraft and thus limited approach and landing capacities. Analysis of the extensive data on vortex behavior as a function of meteorological conditions taken during a three-year test program at Denver's Stapleton, New York's John F. Kennedy and London's Heathrow International Airports [1] has indicated that there are wind conditions which predictably remove vortices from the approach corridor.

The objectives of the data collection efforts during the test program were twofold: First, the data could be used to assess how often and under what conditions vortices pose a potential threat to a following aircraft. Second, by identifying correlations between the motion and decay of vortices and various meteorological and aircraft parameters, means for predicting the time history of vortices can be developed. The Stapleton (DEN) test program at runway 26L lasted from August through November of 1973 with vortex tracks from approximately 7000 aircraft landings recorded. The approach zone of runway 31R at John F. Kennedy Airport (JFK) was established as the primary vortex test site from June 1973 until its closing in January 1977. Over 15,000 landings were recorded at JFK. In a joint United States Department of Transportation and British Civil Aviation Authority venture, approximately 13,000 aircraft landings were monitored between May 1974 and June 1975 on runway 28R at Heathrow.

The extensive test and data collection program began with the objective of confirming the adequacy of the current separation standards. The JFK and DEN data demonstrated that the standards were indeed safe vortexwise for commercial airliners; in fact, the data indicated that the separations were almost always too conservative. A subsidiary program at JFK examined the separation standards for light aircraft (less than 12,500 pounds) and led to a recommendation, since adopted, for increasing the separations by one mile behind larger aircraft. The Heathrow effort was initiated to correlate the reported vortex incidents occurring at Heathrow with measured vortex behavior inside the middle marker. Analysis of the data from the three sites contributed significantly to furthering the knowledge about vortex behavior and suggested possible avenues for systems which could specify when the separation standards might be relaxed.

The analysis indicated that a wind rose criterion could be used to determine when the separations could be uniformly reduced to 3 nautical miles for all aircraft types rather than using the 3-, 4-, 5- and 6-mile separations currently required.

A Vortex Advisory System (VAS) was designed to take advantage of the wind rose criterion. The system is based on comparing the measured wind magnitude and direction (with respect to each runway heading) with the wind criterion. The comparison indicates via a simple display when separations could be safely reduced to three nautical miles for all approach and landing aircraft.

A decision was made to test the VAS concept at an airport under actual operating conditions. Since the main objective of the VAS is to allow increases in capacity, the major high density terminals with a significant percentage of jumbo-jet operations and with capacity at or near saturation were considered for the feasibility tests. Chicago O'Hare was selected on the following criteria: adequate available real estate for the VAS equipment and evaluation instrumentation, operations near or beyond saturation during VFR and/or IFR conditions and a significant percentage of jumbo-jet operations in the traffic mix.

The main purpose of the current VAS system at Chicago's O'Hare is to determine the feasibility of reducing longitudinal separations when either the wake vortices have been blown out of the approach corridor, or when the vortices have decayed and no longer present a potential hazard to the following aircraft. VAS testing was implemented by using an instrumentation system to measure the vortex positions and the ambient meteorological conditions and correlating the vortex tracks with the VAS displayed output. The amount of time that the VAS indicates reduced separations could be used will be evaluated to determine how many additional operations could be accommodated if reduced separations to 3 miles for all landing aircraft were in effect. The evaluation will be performed under all combinations of approach and landing runway scenarios as well as under VFR and IFR weather conditions. A combination of simulations by NAFEC [2] and actual operations at O'Hare will be utilized to complete the evaluation. It is anticipated that the system will allow reduced separations up to 60% of the time, and that significant increases in capacity with resultant reduction in delays will be possible, especially during IFR conditions when current capacity is oversaturated.

The current effort at Chicago's O'Hare relative to the VAS involves the evaluation of the system's capability to reliably provide the criteria for reducing longitudinal separations when either the wake vortices have been blown out of the approach corridor or when the vortices have decayed and no longer present a potential hazard to the following landing aircraft. Adequate data must be collected to provide a statistically significant evaluation of the system's ability to determine when the separations may be reduced to 3 miles for all aircraft types and to determine that the criterion algorithm contains adequate safety margins for all meteorological and vortex conditions as applied to all operating runway scenarios. A nine-month evaluation period is planned.

VAS SYSTEM DESIGN

The VAS consists of four major subsystems: a Meteorological Subsystem for the measurement of the meteorological conditions existing in the operating corridors of the airport; a Data Processing Subsystem which processes all meteorological data and, based on the VAS algorithm, determines when spacings between aircraft may be reduced; a Data Display Subsystem for the display of separation requirements and meteorological conditions to the air traffic controllers; and a VAS Performance Monitoring and Data Recording Subsystem which monitors system performance, indicates failures and displays these to maintenance personnel, and records all VAS input and output data.

Meteorological Subsystem.

The meteorological subsystem consists of a network of instrumented meteorological towers placed about the airport perimeter (Figure 1). Ideally, each runway end would be instrumented with a single tower placed approximately halfway between the runway threshold and the Middle Marker and 800-1000 feet to one side in order to prevent vortex impingement on the tower disturbing the meteorological measurements. However, as shown in Figure 1, the proximity of runway thresholds generally allows the placement of a single tower to serve two ap-

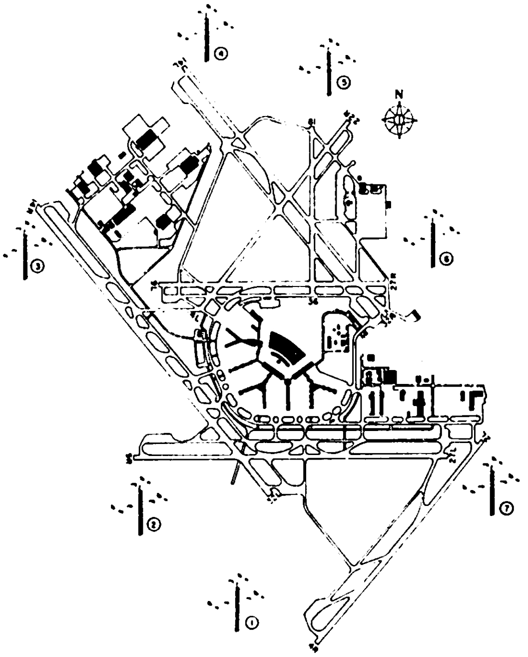

Figure 1. Locations of the VAS meteorological towers at Chicago O'Hare.

proaches, such as tower 1 monitoring wind parameters for the approaches to 4R and 32L at O'Hare.

Each 50-foot tower is instrumented with three sets of wind magnitude and direction sensors, one sensor set located at 50 feet, the remaining two at 47 feet. The redundancy provided by a triple-sensor installation greatly increases system reliability insuring the acquisition of valid data and sensor-failure detection.

The wind sensors presently used are standard cup-and-vane type instruments. The salient characteristics of the wind speed sensor (cup anemometer) are: range of 0-100 knots, accuracy of 0.5 knots or 5%, threshold of 0.75 knots, and a distance constant of 8 feet. The wind direction sensor (vane) has a range of 0-360°, an accuracy of 5°, a 0.75-knot threshold and a distance constant of 30 feet. Both sensors have outputs scaled 0-5 volts.

The instrumentation necessary to transmit the meteorological data from each tower to a central facility (Figure 2) consists of a multiplexer which sequentially samples the sensor output and a line modem which serializes the data and transmits it over a wire pair to receivers located in the central tower. A 16-channel, 12-bit multiplexer is used. The multiplexer operates under the control of the modem which commands the scan rate. The modem operates in a lines-switching mode at a crystal-controlled 5440 Hz bit-rate. Since the modem transmits 34 bits for each 16-bit output from the multiplexer (12 bits of data and a 4-bit channel address), the sampling rate is determined by the number of channels sampled. Thus, if 10 channels are sampled, the per-channel sampling rate is $5440/(34 \times 10) = 16$ samples/second. In addition to the six multiplexer channels used to read the meteorological sensor outputs, four channels are used to monitor the status of the tower electronics by monitoring a precision voltage reference and power supply outputs, enabling the detection of electronic failures which could affect the accuracy of the meteorological measurements.

All tower electronics are housed in an environmental enclosure mounted near the base of each 50-foot tower. Since lightning strikes are a major problem in this type of installation, great care was taken to insure against this type of system damage. All input and output signal lines are protected with transient arrestors. The input 60-Hz power line is regulated and contains a separate transient arrestor.

The O'Hare system does not utilize commercial telephone lines. Instead, standard FAA control lines normally available at various airport NAV-AID sites are used to transmit the data from each meteorological tower to the central tower where the VAS microprocessors are located.

The tower instrumentation channel capacity, scan rate and measurement resolution are obviously in excess of the requirements of this application. The overdesign was deliberate in order to allow system changes without the necessity for major equipment redesign.

Data Processing Subsystem.

The serial data stream from each meteorological tower is received by a modem which converts the input into parallel 16-bit

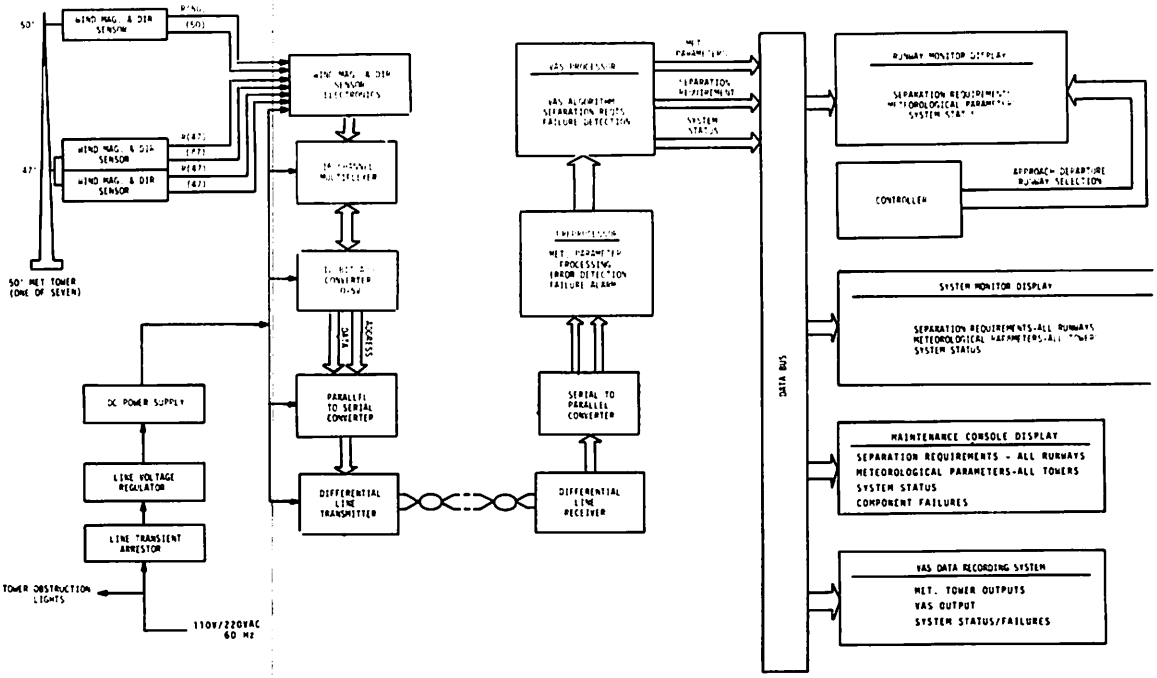

Figure 2. Block diagram of the VAS.

words, representing the output of each channel sampled by the tower instrumentation. The output from each receiving modem is input to individual preprocessors (Intel 8080A microprocessors) packaged on single plug-in boards. The microprocessors sample the meteorological data at a 2 samples/second rate. The sampled wind magnitude (R) and wind direction (Θ) are used to compute a one-minute running average ($\bar{R}$ and $\bar{\Theta}$) by the following scheme: for each sample compute $U=R\sin\Theta$ and $V=R\cos\Theta$; then compute $\bar{U}$ and $\bar{V}$ using a running 128-sample average and compute $\bar{R}=(\bar{U}^2+\bar{V}^2)^{\frac{1}{2}}$ and $\bar{\Theta}=\tan^{-1}(\bar{V}/\bar{U})$.

The preprocessor also calculates wind gusts. A wind gust is defined using a 30-second interval. Within each 30-second interval, the sampled R is averaged using a 4-sample average (2 seconds), thereby eliminating momentary peaks which would not affect aircraft. Any peak measured by the 4-sample average is compared to the current wind average $\bar{R}$; if it is at least 9 knots above $\bar{R}$, it is considered a gust, G. The gust value is the maximum G observed during each 30-second interval. At the end of each 30-second interval, the maximum gust value is compared to that of the previous 30-second interval, and the larger of the two is output to the display.

The preprocessor also performs the important function of failure detection. The sampled R and Θ from each sensor on the tower are compared at the end of each sampling interval and must agree within 3 knots and 10 degrees. Normally, the 50-foot sensor data are selected. If a 50-foot sensor fails, the microprocessor switches to the 47-foot sensor which is not in the wind shadow of the tower. Failure of at least two R's or Θ's to agree for two successive samples causes a tower-failure signal to be generated. The processor also checks the other quantities monitored on the tower as well as the address sum and timing of the incoming data. A deviation beyond preset limits results in a tower-failure signal.

In addition to outputs of $\bar{R}$, $\bar{\Theta}$ and G, the preprocessor outputs system status words to indicate which specific failure is detected. This information is displayed on a system-maintenance console thereby providing maintenance personnel with the means to effect rapid repairs.

A separate microprocessor (VAS processor) receives all inputs from the preprocessors, and using the VAS algorithm shown in Figure 3, determines which aircraft landing separations may be utilized; i.e., the standard 3/4/5/6-nm or a reduced 3-nm separation for all aircraft. As shown in Figure 3, the algorithm consists of an elliptical region with major and minor axes of 12 knots and 5.5 knots, respectively, and a 2-knot guard band around it. The major axis is aligned in the direction of the runway. A wind condition resulting in a wind vector $\bar{R}(\bar{\Theta})$ inside the inner ellipse requires the use of the 3/4/5/6 separation criteria, while a wind vector outside the inner ellipse allows a uniform separation of 3 nm.

The VAS processor utilizes the wind parameters measured near each runway approach region and the elliptical VAS algorithm to calculate separation requirements for each runway approach. This information as well as the calculated $\bar{R}$, $\bar{\Theta}$ and G are output to the displays.

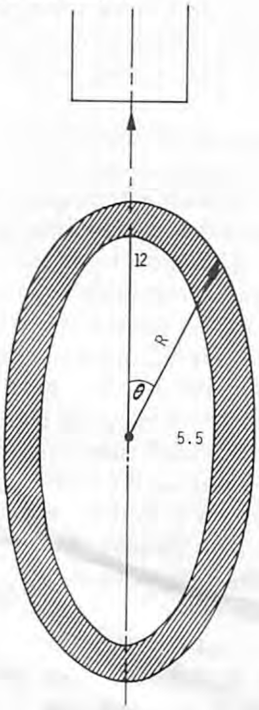

Figure 3. The VAS wind criteria.

Data Display Subsystem.

Two types of displays are used in the VAS, a System Monitor Display (Figure 4) and a Runway Monitor Display (Figure 5).

The System Monitor Display is intended for use by the tower cab and IFR room supervisors. The display indicates in summary form all meteorological tower outputs and the approach/departure corridors for which the wind measurements apply. Its primary function is to provide an overview of the wind conditions across the entire airport enabling the supervisor to select an operating

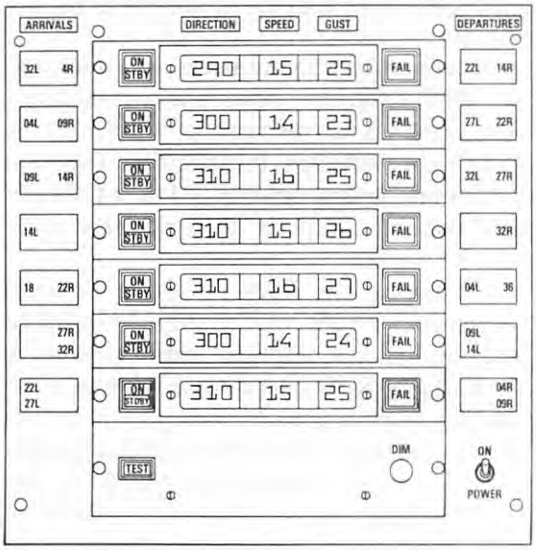

Figure 4. The VAS system monitor display.

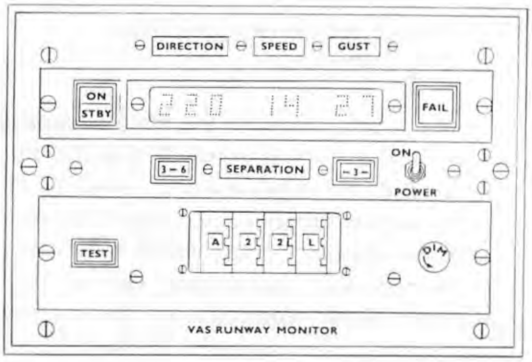

Figure 5. The VAS runway monitor display.

configuration which will maximize traffic flow for the existing meteorological conditions.

The Runway Monitor Display is designed for use by a controller responsible for traffic control on a single runway. As shown in Figure 5, the controller selects a specific runway via a set of thumbwheel switches. The controller must also indicate whether arrival or departure information is desired; e.g., he enters A32L for arrivals to runway 32-Left and D32L for departures from runway 32-Left. The display thereafter accepts data with the corresponding label from the data bus. Thus, if A32L is entered, wind parameters measured by tower #1 are displayed, while a D32L entry causes wind parameters measured by tower #3 to be displayed.

Separation requirements are indicated by "RED-GREEN" lights and are indicated only when an arrival runway is selected. A RED light indicates the need to maintain 3/4/5/6-nm landing spacing, while a GREEN light indicates that an all 3-nm separation may be applied.

Logic in the VAS processor program combined with the use of the 2-knot guard band around the elliptical region separating the GREEN-RED operating conditions combine to insure a gradual transition from one state to the other. When the winds are within the guard-band region, both the RED and GREEN lights are on. This is to provide an early indication of a possible change from GREEN to RED and to provide the controller with perhaps 15 minutes warning that a transition to an increased separation may be required.

Performance Monitoring and Data Recording Subsystem.

In order to facilitate the maintenance of the VAS, the VAS equipment console containing the microprocessors, modem receivers, power supplies, etc., also contains a system maintenance panel which indicates to the maintenance personnel the systems status and repair requirements. The maintenance display has two major display areas:

1. A "scrolling" type of display which sequentially steps through all runways and displays the measured wind and separation requirements for each; and the illumination of the FAIL light alerting personnel to a tower, sensor, or system problem.

2. An LED display indicating in matrix form the specific failure detected by the system. The LED display consists of 7 rows, corresponding to the 7 towers, and columns, corresponding to each sensor or quantity monitored; i.e., when LED (3, 4) is illuminated, it indicates a failure of the wind direction sensor #2 on the tower #3, (6, 8) a loss of transmission from tower #6, and so on.

All data acquired, processed and output by the VAS are recorded by a 9-track digital tape recorder. Each tape contains a complete record of all VAS operations for use in system diagnostics and to meet the FAA's operational requirements for a record of all ATC operations.

DATA ACQUISITION

The performance of the VAS is being evaluated using independent monitors of the vortex motion and decay in the approach corridors of the three most active landing runways at O'Hare. Also being recorded are all incoming VAS data transmitted by the meteorological tower network and the processed VAS data output stream to the displays.

A separate microprocessor in the VAS equipment console is used as a data formatter whose function is to acquire all VAS data necessary for the evaluation of the VAS performance. The data formatter collects the incoming data from all three sensors on each of the seven VAS towers, the sensor selected by the tower preprocessor, the calculated average quantities and gust value, the RED-GREEN calculations for each runway and any indicated sensor/component failures. The collected data are reformatted and transmitted via a modem to a separate data recording and display facility to be described. The validity of the VAS-determined safe landing separations is checked by using Ground Wind Vortex Sensing Systems (GWVSS) deployed for that purpose on the approaches to runways 14R, 27R, 32L.

The detection of vortices by the

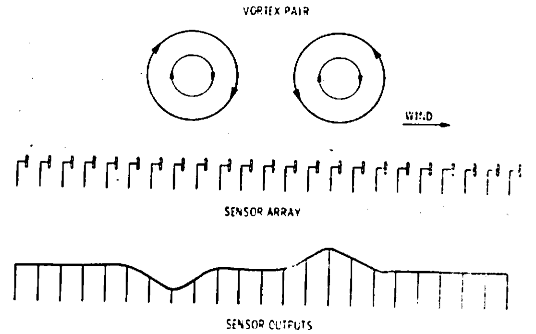

Figure 6. The GWVSS.

GWVSS is based on the fact that the pressure and velocity fields associated with low altitude vortices extend to the ground and can be detected by ground-based sensors. As shown in Figure 6, the GWVSS utilizes an array of propeller anemometers to measure the component of the wind perpendicular to the aircraft flight path. Since most of the vortex flow field is in that direction, the passage of the vortices overhead will cause, as shown in the figure, a large change (increase or decrease) in the crosswind velocity detected by the sensors located directly underneath the vortices.

Currently, Gill-type single-axis propeller anemometers are used in the GWVSS, the anemometers arrayed on a line perpendicular to the extended runway centerline. A fifty-foot spacing between anemometers is used, the sensor lines extending ±350 feet to each side of the extended runway centerline.

Data from each GWVSS are transmitted to a central location using a technique identical to that employed for the transmission of the meteorological tower data. A multiplexer operating under the control of the transmitting modem sequentially samples the output from each sensor of a GWVSS, at a 4-sample/second rate; the formatted data are transmitted over a wire pair to a modem receiver located in the VAS equipment console where the data are input to the data formatter. The data formatter collects all incoming data from the three GWVSS's and the VAS and transmits it via modems to a Mobile Vortex Data Acquisition Facility (MVDAF), where the data are recorded and displayed to the test system's operators.

The MVDAF was designed as an independent vortex data acquisition facility. It contains its own GWVSS lines, meteorological sensors and towers, data acquisition, display and recording equipment. All electronic equipment is housed in a large van which also serves as test headquarters. The van is large enough to carry all the MVDAF equipment to other sites.

At O'Hare the MVDAF van is located near the threshold of runway 32L with its primary function the recording and display of all data pertinent to the evaluation of the VAS. In operation, an observer stationed in the van identifies the type of approaching aircraft; i.e., B747, DC8, B727, etc., and enters this information via a keyboard into the MVDAF computer. An acoustic aircraft detector colocated with the GWVSS generates a run-start signal when the landing aircraft passes overhead. All following data are then logged automatically. Any of the VAS towers or GWVSS lines can be displayed in the MVDAF van by keyboard command.

Data are recorded in two modes:

1. A fast mode when one of the runways instrumented with a GWVSS is used for landing. Under this condition all data are recorded.
2. A slow mode when neither of the instrumented runways is active. Under this condition GWVSS data are obviously not recorded and only every fifth VAS sample is recorded, resulting in a reduction in the amount of tape used, enabling continuous 24-hour data recording.

The digital data tapes are sent daily to TSC for data reduction and analysis.

DATA REDUCTION AND ANALYSIS

At TSC the data are used to check that the microprocessors are operating as intended and that vortices are indeed not posing a threat when the VAS display registers GREEN. Statistics are generated on how often RED and GREEN conditions occur and projections made on how the capacity at O'Hare could have been affected if the VAS were commissioned. Other quantitites such as atmospheric turbulence, temperature, and pressure are also being monitored at each tower. Studies are being conducted to determine if such meteorological variables (or others) could be employed to shrink the dimensions of the ellipse and thereby gain a more effective system.

The GWVSS data are reduced by transforming the anemometer signals into vortex-location histories. These tracks are then examined to find the times for which the port and starboard vortices no longer pose a threat to a following aircraft; i.e., the time when each vortex either dissipated or moved laterally a sufficient distance that a following aircraft would not be subjected to an adverse vortex-induced rolling moment (see reference [1] for details). The times, the VAS-displayed winds and vortex conditions, the aircraft type generating the vortices, etc. are all entered into a data base for further analysis [1].

Vortices from over 13,000 aircraft have been recorded at O'Hare. Included in the 13,000 aircraft are approximately 1000 B-707s, 4900 B-727s, 700 B-737s, 350 B-747s, 700 DC-8s, 2200 DC-9s, 800 DC-10s, and 200 L-1011s. The VAS algorithm has continued to "predict" reliably the times when a RED condition exists.

GREEN conditions have been present more than half the time. Thus, a uniform three-nautical-mile separation could have been used for more than half the time with an attendant decrease in delay. It is of some note that RED conditions most often occur at night and GREEN conditions most often during the day; the VAS thus will permit decreased separations during those times when O'Hare usually experiences delays.

CONCLUSION

The early test results proved very encouraging; the FAA decided to proceed with the full deployment of the VAS at O'Hare. Operational components are now being selected to replace the experimental equipment. The present goal is to have the "hardened" system in place and operating by December 1977.

REFERENCES

1. Hallock, J.N., Winston, B.P., Sullivan, T.E., and Burnham, D.C., "TSC Wake Vortex Data Base and Applications," Proceedings of Aircraft Wake Vortices Conference, DOT Transportation Systems Center, Cambridge, MA, Mar. 1977.

2. Bollman, J.R., "Wake Vortex Advisory System Operational Test and Evaluation," Proceedings of Aircraft Wake Vortices Conference, DOT Transportation Systems Center, Cambridge, MA, Mar. 1977.

WAKE VORTEX ADVISORY SYSTEM OPERATIONAL TEST AND EVALUATION

MAJOR JAMES R. BOLLMAN
U.S. Department of Transportation
Federal Aviation Administration
National Aviation Facilities Experimental Center
Atlantic City NJ 08405

ABSTRACT: The objectives of the operational test and evaluation of the Vortex Advisory System are described.

INTRODUCTION

NAFEC's test and evaluation of the Vortex Advisory System (VAS) covers several different areas of interest to the ultimate user of the system, the FAA. This paper is concerned solely with how the effects of vortices condition the handling of aircraft by a terminal air traffic control facility and the analytical predictions of VAS impact upon airport capacity at Chicago O'Hare International Airport. Other NAFEC personnel are also evaluating system reliability and maintainability to a certain extent. However, that type of evaluation is very straightforward and follows a standard pattern so it will only be mentioned in passing that there is an interest in those aspects of the system. This paper will discuss the system from an air traffic control operational viewpoint.

The project is still in progress and there are no reportable results. However, it was thought that sufficient interest warrants a brief paper on some of the objectives and the technical approach adopted by the NAFEC project team.

CAPACITY

Since air traffic control procedures and separation standards have a major effect upon airport capacity, it is not practicable to uncouple them and examine each in isolation. The history of how procedures, rules, and standards have envolved into what we use today makes an interesting but time-consuming story. Let's simply look at the multiple separation standards which were introduced after the 747 came into use. Prior to the 747, terminal radar separation standards were 3 nmi between all aircraft operating at the same altitude. Now the controller must use 3, 4, 5, or 6 nmi depending upon the weight category and sequence of the landing aircraft. These increased standards obviously reduced capacity for any airport unless it served a single class of either large or small aircraft.

The objective of VAS is to enable some recovery of that lost capacity when conditions are favorable to its use. NAFEC is not involved in validating the system concept or making any input on the questions of safety from an aircraft dynamics standpoint. Our basic assumption is that the system will work as specified; the questions to be answered by the NAFEC project are how much will VAS buy in terms of increased airport capacity and what are the procedural implications which must be fully investigated before implementation of the system?

Before discussing the proposed method of predicting capacity, a simple definition for a complex situation is needed. A good working definition of capacity is: the average number of total aircraft operations (both arrivals and departures) which can be processed on a sustained basis by the air traffic control facility for a given runway configuration, traffic mix, and weather conditions. Many different definitions of capacity can be found in various reports and studies as well as excellent explanations of the factors which cause the numbers to fluctuate from time to time. There are so many independent variables that arriving at a single number which precisely describes the capacity of an airport at some randomly selected time is impossible.

The FAA has funded and conducted many studies on airport capacity and delay; models dating back to at least 1960 can be found. Some fast-time simulation studies of VAS impact upon capacity have been accomplished using recently developed capacity and delay model logic which was validated to yield results within ±15 percent of observed values. The model requires the use of certain implicit assumptions about the distribution of final approach spacing (which may or may not be valid for specific cases). Use of empirical data for those parameters will provide much more accurate results. That greater degree of accuracy is needed to support a cost/benefit analysis for system acquisition decisions.

System benefits can only be quantified by looking at the decrease in airborne delays which result from increased capacity (with unchanged demand levels). Those familiar with the classical queueing theory capacity/demand/delay curves will recall how sensitive average delay is to a very small change in the demand/capacity ratio when demand approaches capacity. The single-channel delay-curve slope rapidly approaches infinity when the utilization factor approaches unity. Although the classical theories do not strictly apply to this problem, the general principles hold fairly well and the delay-curve slope is very steep during busy hours at O'Hare. Capacity, therefore, is only an indirect measure of airport operating efficiency and what is really needed is better information on delays incurred by users of the airport. Capacity estimates of ±15 percent simply are not accurate enough to provide managers with the delay information they require to evaluate the benefits of VAS.

Facility records provide information on how many hourly arrivals and departures were processed for a given configuration and set of weather conditions. If enough hours could be found for the same set of conditions when demand upon the system is sufficiently high; i.e., very large delays experienced by all aircraft, it might be justified to conclude that, for practical purposes, the number of operations conducted is the airport capacity for those conditions. There are not enough such hours for all the configurations which must be considered, however, so smaller time increments must be used to arrive at some average hourly figure. Reduction of recorded radar data will provide that information on current capacity as well as much needed data on final approach spacing.

The ARTS-III data tapes for the time periods of interest will then be reduced to provide some descriptive statistical data on final approach spacing for the different configurations and weather conditions. Aircraft position and altitude information (for properly equipped aircraft) are automatically recorded at 4-second intervals on magnetic tape. This information may be retrieved in its entirety or, with suitable filters, for selected time periods, altitude limits, ranges, etc. The reduction program used for this project provides a computer listing of the following data for each aircraft:

1. Weight category of the landing aircraft and the next aircraft in sequence.
2. Time of landing and time over selected points on final approach.
3. Longitudinal distance between the aircraft pair when the lead aircraft is over each of the selected points.
4. Computed groundspeed of the landing aircraft at the final approach fix.
5. Reported altitude of the landing aircraft at the final approach fix.
6. Aircraft identification and aircraft type.

Analysis of facility records for the calendar year of 1976 were used to segregate hours of operation into three broad weather categories: IFR, VFR (non-visual), and visual approach conditions. The periods when visual approaches may be approved are temporarily set aside and will be investigated only to the extent necessary to confirm the general belief that VAS benefits for those conditions are nil. (In the event recorded data do not support that belief, further analysis will be accomplished.) Final approach spacing during visual approach operations is primarily the pilot's responsibility and capacity becomes more a function of pilot practices than is the case during IFR or VFR (non-visual) operations. Therefore, the project emphasis is placed on those conditions when the air traffic control facility can exercise full control all the way to touchdown.

There are a very large number of possible runway configurations at O'Hare. No attempt will be made to quantify the probable VAS capacity for every configuration; only those which were in actual use for a minimum of approximately 4 hours during periods of heavy demand in either IFR or VFR (non-visual) conditions will be analyzed.

An understanding of the proposed projection technique can best be understood by looking at the simplest of all cases, an independent arrival runway operation (i.e., arrival spacing is accomplished totally independent of any departure aircraft considerations). For this case, the arrival capacity is primarily a function of average spacing between successive arrivals and average groundspeed on final approach. Although there are many other variables which cause those figures, the two which are of most interest (as well as the ones which are most susceptible to analysis) are desired and achieved final approach separation between different aircraft pairs. Desired spacing is a book figure and represents the nominal/standard separation which the controller is permitted to use. Achieved spacing is just that: what is the actual separation between arrivals after everything has been taken into account? The only source of data for this item is the recorded radar data.

Going from the simplest case to the more complex, if all arrivals are in the large category; e.g., 727's, 737's, etc., implementation of VAS would result in no capacity benefits because the allowable radar separation between all aircraft is the same as would be permitted under VAS "green light" operations anyway. Even though the actual average spacing might be 3.75 versus a desired 3 nmi, the difference of 0.75 nmi represents the effect of a plurality of causes which would still be operative and of no consequence (insofar as this project's objective is concerned). However, not all arrivals are in the large category; if so, we wouldn't need VAS! Reduction of the ARTS-III tapes and analysis of that data will provide a means of comparing the "desired" versus "achieved" spacing between all weight category pairs to determine what the distribution is like during periods of time when there is a sustained high demand upon the system. For each runway configuration/operating strategy and weather condition, data such as the following example will be required:

Configuration I — Weather VFR (Non-Visual), Runway 14R
(Independent Arrivals)

Lead A/C	Trail A/C	Desired Spacing (nmi)	Achieved Avg. Spacing (nmi)	Variance (nmi)	Samples
H	H	4	4.95	0.83	100
H	L	5	5.78	0.83	210
H	S	6	6.84	0.83	78
L	H	3	3.90	0.83	160
L	L	3	3.90	0.83	309
L	S	4	4.90	0.83	92
S	H	3	3.90	0.83	40
S	L	3	3.90	0.83	45
S	S	3	3.90	0.83	37

It is unlikely that identical variances in all categories will be found; however, if so, it would certainly make the job easier. Additionally, no a priori assumptions about the normality of those distributions will be made. It is, of course, possible that they will fit the normal bell-shaped curve. However, it is also possible to have extreme skewness in either direction as well as greater or less kurtosis (i.e., sharp or flat peaks) than normal and multi-modality.

Other runway configurations will be accorded the same treatment as the independent arrival case. A full explanation of how other factors (such as exit locations, runway dependencies, percentage of arrivals, weather conditions, and location of crossing runways) affect airport capacity is beyond the scope of this paper. Some appreciation for the way runway dependency affects capacity can be seen by a cursory examination of a fully mixed operation, where arriving and departing aircraft use the same runway. This type of operation results in very low efficiency of runways (in the sense that operations rates are much lower than using separate runways for each type of operation). However, during certain conditions there is no alternative way to operate. Consider the situation when there is a high wind which exceeds tailwind or crosswind limits for all except one runway. Clearly, in that situation, the only possible mode of operation is to conduct both arrival and departure operations on the same runway. When this is done, the average spacing of arrivals on final approach must be much greater than the independent arrival operation because of the necessity of having arrivals spaced sufficiently far apart to enable departures between successive arrivals.

After adequate distribution data are known, it should be fairly easy to project what the achieved spacings would be if the "desired" spacing is 3 miles between all arrivals. Returning to the preceding example, if the data represents 35 hours of operation, the average capacity is 30.6 arrivals per hour; the average in-trail separation is 117.6 seconds with an overall average spacing between all aircraft of 4.67 nmi and an average approach speed of 144 knots.

Assuming that the controllers can maintain the same degree of delivery accuracy when the "desired" spacing is changed to 3 nmi between all aircraft, an example of the projected data would then be:

Configuration 1 — Weather VFR (Non-Visual), Runway 14R
(Independent Arrivals)

Lead A/C	Trail A/C	Desired Spacing (nmi)	Achieved Avg. Spacing (nmi)	Variance (nmi)	Samples
H	H	3	3.95	0.83	100
H	L	3	3.78	0.83	210
H	S	3	3.84	0.83	78
L	H	3	3.90	0.83	160
L	L	3	3.90	0.83	309
L	S	3	3.90	0.83	92
S	H	3	3.90	0.83	40
S	L	3	3.90	0.83	45
S	S	3	3.90	0.83	37

With the same average approach speed and a mean separation between arrivals of 3.88 nmi, the interarrival spacing would be 97 seconds. The average capacity for those parameters is 37.11 arrivals per hour for an increase of about 6.5 aircraft per hour. It is emphasized that the foregoing is merely an example and the actual values for that set of conditions may be quite different from the ones used.

The final step in the capacity analysis will be correlation of VAS history data to runway usage to obtain some measure of system effectiveness. That is, what percentage of time can the "green light" condition be expected for the runways in use? There are also numerous statistical tests which will be applied to help guard against faulty inferences.

In addition to predicting capacity, the team will make recommendations on the value of using VAS information in the runway selection process. Various operational constraints frequently make the highest capacity runway configuration unusable (as in the mixed runway example previously cited). If, however, two or more configurations have equivalent capacity and there are no operational considerations which make one more desirable than another, the use of a configuration which would have a VAS "green light" condition should be selected. Although there may be no operational objections to using VAS in this manner when selection can be made prior to a build-up in demand, changing runways on the basis of VAS lights after demand levels are high may result in unacceptable trade-offs. This will be discussed further in the section on simulation.

Digital Simulation Facility (DSF) Overview.

Research, development, and evaluation of new ATC concepts and subsystems were hampered for many years due to the lack of a suitable laboratory environment. Even when it was possible to use a field facility to check out some promising new procedure, daily operations could be disrupted to an unacceptable degree. In some cases, the possibility of degrading flying safety was great enough that an experiment with real aircraft and real people as test subjects was unthinkable.

This deficiency has been largely overcome by establishing large-scale, computer-assisted laboratories at NAFEC. Concepts may be investigated in sufficient detail to warrant adoption, dismissal, or deferred judgment until some future date. The DSF is one of those laboratories. It is currently being used to develop, evaluate, and gain confidence in the air traffic control procedures required to implement the Vortex Advisory System.

The DSF resembles a modern, automated terminal radar facility. However, the resemblance is restricted to the operations room where controllers use radar displays in the control of traffic. The aircraft targets on the displays are computer-generated and "flown" by a group of pseudo-pilots from their individual consoles in an adjacent room. The system can simulate up to 300 simultaneous targets, 8 radar displays, any desired terminal geography, and route structures sufficiently complex to satisfy the busiest airport requirements.

In addition to valuable insights gained from purely subjective reactions to a given operation, the system provides for the recording and processing of a wide variety of quantified system performance measures. Such items of interest as aircraft conflicts, controller workload, communications requirements, operations rates, route activity, aircraft position history, as well as other information may be recorded from an experiment in real-time or fast-time and then analyzed at length by teams of specialists in various disciplines.

VAS Simulation.

Simulation of the O'Hare terminal environment will be of great value in determining the ATC operational implications of VAS and evaluating the procedural modifications required for system implementation. Additionally, it is hoped the simulation will provide supporting data for the capacity predictions. However, evaluation of the procedures necessary to use VAS in the real world is the principal reason for the simulation and capacity information is of secondary importance.

The procedural questions generally fall into two categories: (1) feasibility of systematic, long-term use of procedures for using dual separation standards in the terminal airspace, and (2) methods for coping with transitions from VAS "green" to "red" modes of operation.

The initial phase of the simulation will be devoted to procedures using a single runway configuration and three different sets of operating conditions. (Note: Conditions B and C both simulate steady state VAS "green" light on.) Condition A: Current separation standards (without VAS) to obtain a data base for comparison with the other two conditions and the ARTS-III data. Condition B: Similar to Condition A with changed separation standards: i.e., use of 3 nmi (minimum) radar separation between all arrivals throughout the terminal airspace. Condition C: Dual separation standards will be employed. Outside the final approach zone current separation standards will be used. After aircraft are established on final approach, 3 nmi may be used. Special emphasis will be placed on evaluation of the methods necessary to safely transition from one separation standard to another in limited airspace during parallel IFR approach operations.

The VAS algorithm will normally provide advance warning that the "green" light may be expected to turn "red" at some time in the future. The duration of the warning period is a function of how rapidly the wind is changing and the specific parameters used in the VAS algorithm. The procedural question arising is: what time period is needed to permit the controller to safely and orderly change from one standard to another? A variety of situations and time periods will be exercised to obtain a reasonable estimate of this critical transition requirement.

The DSF data reduction and analysis programs will provide outputs for comparison between Condition A (current separation standards) and the reduced ARTS-III data. Correlation of the data will verify whether our laboratory environment matches the real world closely enough to justify capacity predictions on the basis of Conditions B and C results. Lack of adequate correlation will not obviate the value of the simulation because, again, the principal reason for the effort is evaluation of procedures. Some capacity results will still be obtained even if adequate correlation between the data bases cannot be found. In addition to procedural questions on the use of dual separation standards, it is uncertain whether the same level of operations can be sustained as in a single separation situation. There is little doubt that those two cases can be rank-ordered regardless of the correlation between data bases.

The final task will be an evaluation of the pros and cons of using VAS information in the runway selection and runway changing decision process. Assuming that two runway configurations have similar capacities, is there any benefit in changing from a "red" configuration to a "green" configuration during a period of heavy traffic or will the loss of operations incurred during the changing process offset that gain produced by a "green" light operation? If one considers only the airside environment, it is possible to imagine that a switch in runways may be desirable. However, complete analysis of that situation cannot be made without a comprehensive look at the groundside constraints and trade-offs as well as possible impact upon center and tower en route operations. It seems, at first look, that any conclusions arrived at in the DSF on this issue would have to be accompanied by the caveat that "the foregoing conclusions are valid assuming that all en route, transition, and ground problems can be satisfactorily resolved."

SUMMARY

The critical issues on the operational test and evaluation of VAS may be simplified as: what are the procedural implications of the system and how will operating efficiency of the airport facilities be affected? The current project will answer the first question by real-time simulation of VAS in the Chicago O'Hare International Airport. The simulation will be of approximately 2 months' duration and will be enhanced by test plan inputs from O'Hare TRACON personnel. Acceptance of the simulation results will be increased by active participation of O'Hare personnel during the simulation. Preliminary discussions on this subject indicate maximum cooperation and support of the project by O'Hare can be expected.

Prediction of the capacity impact will be based on use of empirical data obtained from approximately 15 months of ARTS-III tapes and VAS historical data collected over a 6-month period. Correlation of those two data bases, as well as other sources of information, should give a higher degree of accuracy than attainable through the use of purely analytical or computer models. The sole assumption used in this process is that controllers can maintain the same average delivery accuracy regardless of changes to the "desired" separation standard. That assumption has wide acceptance within the FAA and will be further validated during the simulation activity.

LIST OF PARTICIPANTS

Andersen, James P.
DOT Transportation Systems Center
Kendall Square
Cambridge MA 02142

Avant, Arnold
Mitre Corporation, Metrek Division
1820 Dolley Madison Blvd.
McLean VA 22101

Baker, Gregory R.
California Institute of Technology
Applied Math Department
Pasadena CA 91125

Barber, Marvin R.
Wake Vortex Program Manager
NASA Dryden Flight Research Center
P.O. Box 273
Edwards CA 93523

Barrows, Tim
DOT Transportation Systems Center
Kendall Square
Cambridge MA 02142

Bellantoni, Juan
DOT Transportation Systems Center
Kendall Square
Cambridge MA 02142

Bilanin, Alan J.
Aeronautical Research Associates of Princeton, Inc.
P.O. Box 2229
50 Washington Road
Princeton NJ 08540

Bofah, K.K.
Boeing Company
P.O. Box 3707
Seattle WA 98124

Bollman, James R., Major
FAA-NAFEC
ANA-260
Atlantic City NJ 08405

Brashears, M.R.
Lockheed Missiles & Space Co., Inc.
P.O. Box 1103, West Station
Huntsville AL 35807

Britton, J.W.
Royal Aircraft Establishment
Bedford MK41 6AE
England

Brown, Clinton E.
Hydronautics Inc.
Pindell School Road
Laurel MD 20810

Burnham, David C.
DOT Transportation Systems Center
Kendall Square
Cambridge MA 02142

Cetina, Mike
Kentron-Hawaii Ltd.
Kendall Square
Cambridge MA 02142

Chafe, Ronald E.
Transport Canada
c/o FAA AEM
800 Independence Ave., S.W.
Washington DC 20591

Ciffone, Donald L.
NASA-Ames Research Center
Moffett Field CA 94035

Clapp, David
DOT Transportation Systems Center
Kendall Square
Cambridge MA 02142

Clark, Myron
Federal Aviation Administration
FAA/ARD-402 2100 2nd St., S.W.
Washington DC 20590

Codner, William G.
British Embassy
3100 Massachusetts Avenue
Washington DC 20015

Corsiglia, Victor
NASA-Ames Research Center
Moffet Field CA 94035

Croom, Delwin R.
NASA Langley Research Center
Mail Stop 286
Hampton VA 23665

Daiutolo, Hector
FAA/NAFEC ANA-430
Atlantic City NJ 08405

Delaney, B. Tod
Exxon Research and Engineering
P.O. Box 101
Florham Park NJ 07932

DiMarzio, C.A.
Raytheon Company
Sudbury MA 01776

Dumanian, John
DOT Transportation Systems Center
Kendall Square
Cambridge MA 02142

Dunham, R. Earl, Jr.
NASA-Langley Research Center
Mail Stop 247
Hampton VA 23665

Eberle, William R.
Lockheed Missiles and Space Co.
Box 1103
Huntsville AL 35807

ElRamly, Z.
Carleton University
Department of Mechanical and Aeronautical Engineering
Colonel By Drive
Ottawa ON, Canada K1S 5B6

Faery, Henry F., Jr.
Aerospace & Ocean Engineering Dept.
Virginia Polytechnic Institute
1503 Greendale Drive
Blacksburg VA 24060

Fantasia, John
DOT Transportation Systems Center
Kendall Square
Cambridge MA 02142

Farmer, Herb
DOT Transportation Systems Center
Kendall Square
Cambridge MA 02142

Frankel, Fred
DOT Transportation Systems Center
Kendall Square
Cambridge MA 02142

Fuertas, Lou
DOT Transportation Systems Center
Kendall Square
Cambridge MA 02142

Garodz, Leo J.
DOT, FAA-NAFEC
Atlantic City NJ 08405

Gessow, Alfred
NASA (Code RAA)
Washington DC 20546

Goff, Roger
Raytheon Company
Sudbury MA 01776

Gorstein, Mark
DOT Transportation Systems Center
Kendall Square
Cambridge MA 02142

Greene, Larry
DOT Transportation Systems Center
Kendall Square
Cambridge MA 02142

Grossberg, Mitch
DOT Transportation Systems Center
Kendall Square
Cambridge MA 02142

Hackett, J.E.
Lockheed-Georgia Company
Marietta GA 30063

Haines, Andrew
The Mitre Corporation
Metrek Division
1820 Dolley Madison Blvd.
McLean VA 22101

Hallock, James N.
DOT Transportation Systems Center
Kendall Square
Cambridge MA 02142

Heavener, Arthur A.
Federal Aviation Administration
FAA/NAFEC ANA-321, Bldg. 301
Atlantic City NJ 08450

Iversen, James D.
Aerospace Engr. Dept.
Iowa State University
Town Engr. Bldg.
Ames IA 50011

Jastrzab, Gary
Applications Research Corporation
1300 Industrial Highway
Southampton PA 18966

Johnson, Carl
DOT/FAA Great Lakes Region
2300 E. Devon Avenue
Des Plaines IL 60018

Kalafus, Rudy
DOT Transportation Systems Center
Kendall Square
Cambridge MA 02142

Klass, Philip
Aviation Week & Space Technology
National Press Building
Washington DC 20045

Kolowich, Michael
WGBH-TV
125 Western Avenue
Allston MA 02134

Krawiec, Joseph
DOT Transportation Systems Center
Kendall Square
Cambridge MA 02142

Lev, David
DOT Transportation Systems Center
Kendall Square
Cambridge MA 02142

Lockett, Bascom N.
Federal Aviation Administration
Office of Aviation Safety
800 Independence Ave., S.W.
Washington DC 20591

Lundry, Jerry
Boeing Commercial Airplane Company
M.S. 77-06, P.O. Box 3707
Seattle WA 98124

MacCready, Paul
AeroVironment, Inc.
145 Vista Avenue
Pasadena CA 91107

Maddock, Linda
DOT Transportation Systems Center
Kendall Square
Cambridge MA 02142

Magnant, Eileen
DOT Transportation Systems Center
Kendall Square
Cambridge MA 02142

Marchman, James F., III
Aerospace & Ocean
Engineering Department
Virginia Polytechnic Institute and State University
Blacksburg VA 24061

McCormick, Barnes W.
The Pennsylvania State University
233 Hammond Bldg.
University Park PA 16802

McWilliams, Ian G.
DOT Transportation Systems Center
Kendall Square
Cambridge MA 02142

Meng, James C.S.
Science Applications Inc.
1200 Prospect Street
P.O. Box 2351
La Jolla CA 92037

Meyerhoff, Norm
DOT Transportation Systems Center
Kendall Square
Cambridge MA 02142

Miller, Nelson
FAA-NAFEC (ANA-4B)
Atlantic City NJ 08405

Millikin, Robin L.
Air Traffic Services
Ministry of Transport
Transport Canada ATP
Ottawa ON Canada K1A ON8

Morris, John P.
747 Aerodynamics Staff
Boeing Commercial Airplane Co.
Everett WA 98206

Negron, Caesar D.
Applications Research Corp.
1300 Industrial Highway
Southampton PA 18966

Nielsen, Erling
Directorate of Civil Aviation
G.L. Congevej 60
1850 Copenhagen V, Denmark

Normoyle, Robert H.
Federal Aviation Administration
800 Independence Avenue
Washington DC 20591

Nowark, Dieter
FWG Associates
Tullahoma TN 37388

Ormand, Lowell W.
AFOSR
Building 410
Bolling AFB
Washington DC 20332

Pambookian, Harry
DOT Transportation Systems Center
Kendall Square
Cambridge MA 02142

Patten, Bernie
DOT Transportation Systems Center
Kendall Square
Cambridge MA 02142

de la Pena, Miguel
Federal Aviation Administration
12 N.E. Exec. Park
Burlington MA 01803

Peters, Desmond J.
Aviation Safety Bureau
Ministry of Transport
Transport Canada Building
Place-de-Ville
Ottawa ON Canada K1A ON8

Peterson, Linda
DOT Transportation Systems Center
Kendall Square
Cambridge MA 02142

Pitchford, Lynn D.
Lockheed Missiles and Space Co., Inc.
P.O. Box 1103, West Station
Huntsville AL 35807

Rossow, Vernon J.
NASA-Ames Research Center
Mail Stop N247-1
Moffett Field CA 94035

Rothmel, Bernie
Kentron-Hawaii Ltd.
Kendall Square
Cambridge MA 02142

Rottman, James
Science Applications, Inc.
La Jolla CA 92037

Rudd, Michael J.
Bolt Beranek and Newman Inc.
50 Moulton Street
Cambridge MA 02138

Sabath, Jerrold
DOT Transportation Systems Center
Kendall Square
Cambridge MA 02142

Sharer, K.W.
International Civil Aviation Organization
1000 Sherbrooke Street West, Room 1483
Montreal PQ Canada

Sheldon, Duncan
Kentron-Hawaii Ltd.
Kendall Square
Cambridge MA 02142

Smith, Rene
DOT Transportation Systems Center
Kendall Square
Cambridge MA 02142

Snedeker, Richard S.
Aeronautical Research
Aeronautical Research Associates of Princeton, Inc.
P.O. Box 2229
50 Washington Road
Princeton NJ 08540

Spitzer, Edward
DOT Transportation Systems Center
Kendall Square
Cambridge MA 02142

St. John, O.
Civil Aviation Authority
London Space House
Kingsway WC2
England

Stamison, Rigby
Ministry of Transportation
Ottowa ON Canada

Starkgraf, William
Kentron-Hawaii Ltd.
Kendall Square
Cambridge MA 02142

Sullivan, Thomas E.
DOT Transportation Systems Center
Kendall Square
Cambridge MA 02142

Tartaglione, John J.
1123 Flanner Hall
Notre Dame IN 46556

Thelander, J.A.
Douglas Aircraft Company
3855 Lakewood Blvd.
Long Beach CA 90846

Tinling, Bruce
NASA-Ames Research Center
Moffett Field CA 94035

Tinsley, Guice
Federal Aviation Administration
Washington DC 20590

Todd, Marv
Kentron-Hawaii Ltd.
Kendall Square
Cambridge MA 02142

Tsai, Chon-Yin
NASA-Ames Research Center
Moffett Field CA 94040

Tymczyszyn, Joseph J.
FAA-Western Region AWE-105
P.O. Box 92007
Los Angeles CA 90009

Tymczyszyn, Joe, Jr.
Federal Aviation Administration
Washington DC 20590

VanDuyne, Edward
Federal Aviation Administration
800 Independence Ave., S.W.
Washington DC 20591

VanMeter, David
DOT Transportation Systems Center
Kendall Square
Cambridge MA 02142

Veronda, Carol
DOT Transportation Systems Center
Kendall Square
Cambridge MA 02142

Verstynen, Harry
FAA/HQ AEM-20
800 Independence Ave., S.W.
Washington DC 20591

Vleghert, J.P.K.
National Aerospace Lab N/R
Anth. Fokkerweg 2
Amsterdam 1017
Amsterdam (Netherlands)

Webber, George H.
DOT/OST
400 7th St., S.W.
Washington DC 20590

Wedan, Robert W.
Federal Aviation Administration
2100 Second Street, S.W.
Washington DC 20591

Widnall, Sheila
Massachusetts Institute of Technology
Cambridge MA 02138

Williamson, Guy G.
Aeronautical Research Associates of Princeton, Inc.
P.O. Box 2229
50 Washington Road
Princeton NJ 08540

Winkler, John
Kentron-Hawaii Ltd.
Kendall Square
Cambridge MA 02142

Winston, Berl P.
DOT Transportation Systems Center
Kendall Square
Cambridge MA 02142

Wood, Virginia
Quincy Patriot-Ledger
Temple Street
Quincy MA 02169

Wood, William
DOT Transportation Systems Center
Kendall Square
Cambridge MA 02142

Wright, Hugh
BBN Instruments
50 Moulton St.
Cambridge MA 02138

Yutkins, Joan
Kentron-Hawaii Ltd.
Kendall Square
Cambridge MA 02142

Yutkins, Rich
Kentron-Hawaii Ltd.
Kendall Square
Cambridge MA 02142

Zalay, A.D.
Lockheed Missiles & Space Co.
4800 Bradford Drive
Huntsville AL 35807

400 copies

☆ U. S. GOVERNMENT PRINTING OFFICE: 1978--702-377--337

U. S. DEPARTMENT OF TRANSPORTATION
TRANSPORTATION SYSTEMS CENTER
KENDALL SQUARE, CAMBRIDGE, MA. 02142